Physics of the Solid State, Vol. 42, No. 4, 2000, pp. 589–593. Translated from Fizika Tverdogo Tela, Vol. 42, No. 4, 2000, pp. 577–580.
Original Russian Text Copyright © 2000 by Skobov, Chernov.

METALS AND SUPERCONDUCTORS

Nonlinear Waves in Group III Metals

V. G. Skobov and A. S. Chernov
Ioffe Physicotechnical Institute, Russian Academy of Sciences, Politekhnicheskaya ul. 26, St. Petersburg, 194021 Russia

Received September 17, 1999

Abstract—The effect of nonlinearity on the possibility of Group III metals to support propagating radio waves is investigated theoretically. A nonlinear wave is shown to be able to propagate in a metal when the magnetic field of a wave of a large amplitude traps holes and causes collisionless cyclotron absorption to be suppressed. *© 2000 MAIK "Nauka/Interperiodica".*

INTRODUCTION

Propagation of linear radio waves in Group III metals (aluminum and indium) has been theoretically and experimentally investigated in [1–5]. It was shown that, in addition to helicons, the field of which rotates in the same direction as holes do in a magnetic field, dopplerons can propagate in these metals, which are associated with Doppler-shifted cyclotron resonance (DSCR) for holes. The field of doppleron modes rotates in the opposite direction, and the range of magnetic fields in which these modes exist is situated below that for helicons. In this paper, we consider new effects that occur in these metals when the amplitude of an exciting radio-frequency field is large. A magnetic field of a large amplitude "traps" holes responsible for cyclotron absorption, and the latter becomes significantly lower. Because of this, the collisionless damping of dopplerons decreases and, in magnetic fields much lower than the threshold field for a helicon, the propagation of a new wave becomes possible, which cannot exist in the linear regime. For definiteness, we will consider the propagation of radio waves in aluminum; similar effects should occur in indium.

1. A FERMI SURFACE MODEL AND NONLOCAL CONDUCTIVITY

We consider the propagation of a radio wave in aluminum in the geometry where a static magnetic field **H** and the propagation vector **k** are parallel to a fourfold axis of symmetry (**H** $\parallel$ **k** $\parallel$ [100] $\parallel$ z). The k and H dependences of the nonlocal conductivity and its features are determined by the form of the function $\partial S/\partial p_z$, where S is the area of the cross section of the Fermi surface by a plane p_z = const and p_z is the component of the momentum of a hole along the field **H**. According to calculations performed by Larsen and Greisen [2], the distinctive feature of the Fermi surface of aluminum is that a plot of the derivative $\partial S/\partial p_z$ (in the geometry in question) has two maxima of the same height and a minimum, with the maxima being roughly 10% higher than the minimum. We will use a model Fermi surface for which the function $\partial S/\partial p_z$ has the form

$$\frac{1}{2\pi}\frac{\partial S}{\partial p_z} = -py(p_z)\operatorname{sgn} p_z, \tag{1}$$

$$y(p_z) = (1+2\beta)\sin\frac{\pi p_z}{2p_1}, \quad |p_z| \le p_1, \tag{2}$$

$$y(p_z) = 1+\beta\left(1+\cos\left(\pi\frac{|p_z|-p_1}{p_2}\right)\right), \quad p_1 \le |p_z| \le (p_1+p_2), \tag{3}$$

where β is a dimensionless constant and p, p_1, and p_2 are parameters having dimensions of momentum. In the range $(p_1+p_2) \le |p_z| \le 2(p_1+p_2)$, the function $y(p_z)$ is such that it is symmetric about the point $p_z = p_1 + p_2$; its plot is shown in Fig. 1 for $\beta = 0.05$ and $p_2 = 2p_1 = 0.35\hbar$ Å^{-1}. The symmetry of this function with respect to its minimum point makes calculation of the nonlocal conductivity much easier. The left-hand part of the $y(p_z)$ curve is similar to the corresponding part of the curve calculated by Larsen and Greisen. The dissimilarity between their right-hand portions is of no significance, because holes are predominantly in the region $|p_z| \le (p_1 + p_2)$. The parameter p is taken to be such

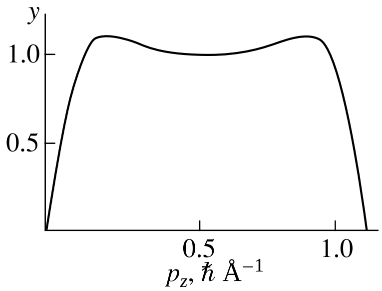

Fig. 1. Graph of the $y(p_z)$ function for $\beta = 0.05$ and $p_2 = 2p_1 = 0.35\hbar$ Å^{-1}.

that the period of doppleron oscillations is equal to that observed in the experiment (in our case, $p = 1\,\hbar$ Å^{-1}).

Although the Fermi surface for aluminum has a fourfold axis of symmetry, we will approximate it by an axially symmetric surface. If there is no axial symmetry, the DSCR will occur at the fundamental and odd higher harmonic frequencies and there will be corresponding multiple doppleron modes [5]. In our model, this is not the case and multiple dopplerons are absent. In actual aluminum, the relative changes in impedance due to multiple dopplerons are much smaller than one percent. At the same time, the nonlinear effect we treat in this paper leads to relative changes in impedance of order unity. For this reason, we will not take into account the existence of multiple dopplerons and restrict our consideration to the case of an axially symmetric Fermi surface, for which calculations are much simpler.

If the vectors **k** and **H** are parallel to the axis of the axially symmetric Fermi surface, the nonlocal conductivity is given by (see, e.g., [6])

$$\sigma_\pm(k, H) = \sigma_{xx} \pm i\sigma_{yx} = \frac{ec}{H}\frac{2}{(2\pi\hbar)^3}\int\frac{S(p_z)dp_z}{\gamma + i[\pm 1 + ku(p_z)/2\pi]}, \tag{4}$$

$$u(p_z) = -\frac{c}{eH}\frac{\partial S}{\partial p_z} = 2\pi\frac{cp}{eH}y(p_z), \tag{5}$$

where

$$\gamma = \frac{\nu}{\omega_c}, \quad \omega_c = \frac{eH}{cm}, \tag{6}$$

e is the absolute value of the electronic charge; c is the velocity of light; m and ω_c are the cyclotron mass and cyclotron frequency of a hole, respectively; ν is the hole collision rate with scatterers; and $u(p_z)$ is the displacement of a particle with the momentum component p_z during a cyclotron period.

In this paper, we will consider the case of a strong magnetic field in which the hole cyclotron frequency ω_c is much larger than the collision rate ν and, hence, $\gamma \ll 1$.

In our model, the function $\partial S/\partial p_z$, and hence the denominator in the integrand in (4), is symmetric with respect to the point $|p_z| = (p_1 + p_2)$. For this reason, it is convenient to represent the function $S(p_z)$ in the numerator in (4) in the form

$$S(p_z) = S_0 + U(p_z), \tag{7}$$

where S_0 is the area of the cross section of the Fermi surface by the plane passing through a point $|p_z| = (p_1 + p_2)$, and $U(p_z)$ is a function antisymmetric with respect to this point. The integral involving U is equal to zero and, hence, the expression for the conductivity becomes

$$\sigma_\pm = \frac{Nec}{H}\frac{1}{2(p_1 + p_2)}\int_0^{p_1+p_2} dp_z \times\left\{\frac{1}{\gamma + i[\pm 1 - qy(p_z)]} + \frac{1}{\gamma + i[\pm 1 + qy(p_z)]}\right\}, \tag{8}$$

where

$$q = \frac{kcp}{eH}, \quad N = \frac{(p_1 + p_2)S_0}{(\pi\hbar)^3}, \tag{9}$$

and N is the concentration of holes. Substituting (2) and (3) into (8) and evaluating the integral with respect to p_z, we arrive at the formula

$$\sigma_\pm = -i\frac{Nec}{H}s_\pm(q), \tag{10}$$

$$\begin{aligned} s_\pm(q) = {} & \pm\frac{1}{3\sqrt{I_\pm^2 - \alpha^2 q^2}} \pm \frac{1}{3\sqrt{(I_\pm - \alpha q)(I_\pm - q)}} \\ & \pm\frac{1}{3\sqrt{(I_\pm + \alpha q)(I_\pm + q)}}, \quad |q| \le \alpha^{-1}, \end{aligned} \tag{11}$$

$$\begin{aligned} s_\pm(q) = {} & \frac{i}{3\sqrt{\alpha^2 q^2 - I_\pm^2}} + \frac{i}{3\sqrt{(\alpha q - I_\pm)(I_\pm - q)}} \\ & \pm\frac{1}{3\sqrt{(I_\pm + \alpha q)(I_\pm + q)}}, \quad \alpha^{-1} < q < 1, \end{aligned} \tag{12}$$

$$\begin{aligned} s_\pm(q) = {} & \frac{i}{3\sqrt{\alpha^2 q^2 - I_\pm^2}} \mp \frac{1}{3\sqrt{(\alpha q - I_\pm)(q - I_\pm)}} \\ & \pm\frac{1}{3\sqrt{(I_\pm + \alpha q)(I_\pm + q)}}, \quad q > 1, \end{aligned} \tag{13}$$

where $\alpha = 1 + 2\beta$ and $I_\pm = \mp 1 + i\gamma$.

In the local regime ($q \longrightarrow 0$), we have $s_\pm \longrightarrow \pm 1$, whereas, in the limit of $q \gg 1$, we have

$$s_\pm(q) \simeq \frac{1}{\alpha(p_1 + p_2)}\left[i\frac{p_1}{|q|} \mp \frac{(1 + \alpha)p_2}{2\sqrt{\alpha}q^2}\right]. \tag{14}$$

2. THE DISPERSION RELATION AND THE PROPERTIES OF MODES IN THE LINEAR REGIME

The properties of radio waves propagating in a metal are determined by the dispersion relation $k^2c^2 = 4\pi i\omega\sigma_\pm$, which is conveniently rewritten in the form

$$\Phi_\pm(q) = \xi, \tag{15}$$

where

$$\Phi_{\pm}(q) = \frac{s_{\pm}(q)}{q^2}, \tag{16}$$

$$\xi = \frac{4\pi\omega N c p^2}{eH^3}. \tag{17}$$

The features of relation (15) can be elucidated by investigating the behavior of the functions $\Phi_{\pm}$. Their imaginary parts are identical, while their real parts are equal in value but opposite in sign. In the limit as $\gamma \longrightarrow 0$, the functions $\Phi'_+ = \mathrm{Re}\Phi_+$ and $\Phi''_+ = \mathrm{Im}\Phi_+$ are plotted in Fig. 2 (in the range $q < 1$, where $\Phi'_+ > 0$). At $q \ll 1$, we have $\Phi_+ \simeq 1/q^2$. This branch of the dispersion curve corresponds to a helicon, the field of which rotates in the same direction as holes. The function Φ'_+ has a minimum at a certain value of q, less than $1/\alpha$, and tends to infinity as $q \longrightarrow 1/\alpha$. Therefore, above the threshold for a helicon, there is a DSCR mode associated with the resonance for those holes the displacement of which during a cyclotron period is maximal. However, this mode is practically impossible to detect, because it occurs at the same polarization of the exciting wave and in the same field range as the helicon, but it has a smaller amplitude.

In the range $\alpha^{-1} < q < 1$, the function Φ_- has a large imaginary part because of the high cyclotron absorption of a wave by holes for which the quantity $\partial S/\partial p_z$ is between $2\pi p$ and $2\pi p\alpha$. Due to this absorption, there are no propagating modes in the range indicated above.

The functions $\Phi'_- = \mathrm{Re}\Phi_-$ and $\Phi''_- = \mathrm{Im}\Phi_-$ are plotted in Fig. 3 in the range $q > 1$, where $\Phi'_- > 0$. In this range, the function Φ'_- monotonically decreases and tends to zero as $q \longrightarrow \infty$. In high magnetic fields, where $\xi \ll 1$, the value of q is close to unity and $\Phi'_- \gg \Phi''_-$. Therefore, in the corresponding range of magnetic fields, there exists a propagating mode due to DSCR for those holes the displacement of which during a cyclotron period is a minimum. The field of this doppleron has a sense of rotation opposite to that of holes (the "plus" polarization), and its damping is due to both collisions and collisionless cyclotron absorption. The corresponding branch of the dispersion relation is

$$k \equiv k' + ik'' \simeq \frac{eH}{cp}\left[1 + \frac{\xi^2}{4(\alpha-1)}\right] + i\left[\frac{\nu m}{p} + \frac{\xi^3}{2(\alpha-1)\sqrt{\alpha^2-1}}\frac{eH}{cp}\right]. \tag{18}$$

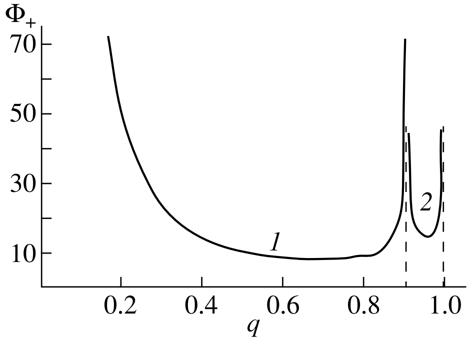

Fig. 2. Graphs (*1*) of the real and (*2*) imaginary parts of the function Φ_+.

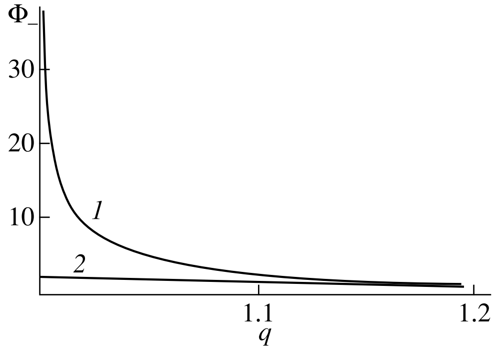

Fig. 3. Graphs of the $\Phi'_-(q)$ (curve *1*) and $\Phi''_-(q)$ (curve *2*) functions in the range of $q > 1$.

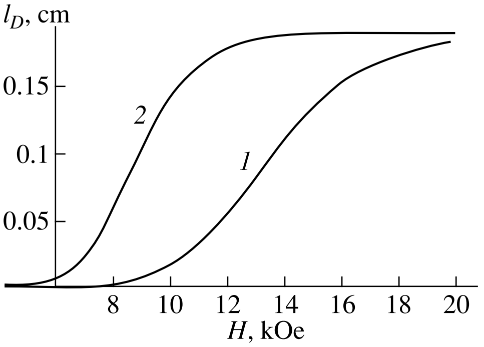

Fig. 4. Doppleron damping length l_D as a function of H in (*1*) the linear and (*2*) nonlinear regimes.

In strong magnetic fields ($\xi \ll 1$), the $k'(H)$ curve asymptotically approaches the straight line $k_0(H) = eH/pc$, which corresponds to the DSCR for holes whose displacement is minimal ($q = 1$). In this field range, the damping of dopplerons is due to collisions; it is practically independent of H, and we have $k'' = m\nu/p$. As H decreases, the $k'(H)$ and $k''(H)$ curves deviate from their asymptotes towards higher values and the contribution to the doppleron damping from collisionless cyclotron absorption becomes dominant. The dependence of the doppleron damping length $l_D = 1/k''$ on the magnetic field H is shown in Fig. 4 (curve *1*). The calculation is performed for the frequency $\omega/2\pi = 100$ kHz,

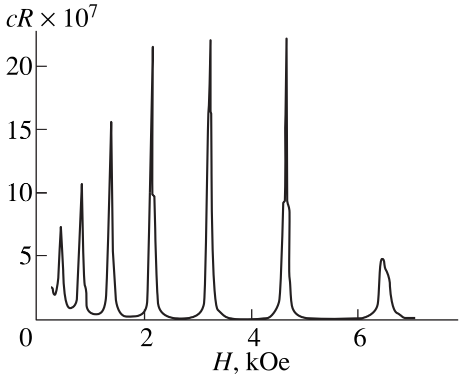

Fig. 5. Surface resistance of a plate of aluminum R_- as a function of H in the nonlinear regime.

concentration $N = 6 \times 10^{22}$ cm^{-3}, hole mass $m = 1.3 \times 10^{-27}$ g, and collision rate $\nu = 4 \times 10^8$ s^{-1}. It is seen that the doppleron damping becomes very great in low magnetic fields.

3. NONLINEAR WAVES AND OSCILLATIONS IN THE IMPEDANCE OF A PLATE

Let us now consider the propagation of waves of a large amplitude. It was shown in [7] that the magnetic field of such a wave "traps" holes with the momentum $p_z = p_{z0}$ satisfying the condition

$$u(p_{z0}) = 2\pi/k. \tag{19}$$

These holes cause cyclotron absorption; their longitudinal velocity is modulated with the frequency

$$\omega_0 \sim \omega_c \sqrt{\frac{H_a}{H}}, \tag{20}$$

where H_a is the amplitude of the magnetic field of the wave in the metal. In the nonlinear regime, when the frequency ω_0 of oscillation of holes trapped by the magnetic field becomes much higher than the collision rate ν, the cyclotron absorption decreases in proportion to the ratio ν/ω_0. Therefore, in the expression for s_- in (13), the first term, which is due to cyclotron absorption, should be multiplied by ν/ω_0. Figure 4 shows the calculated doppleron damping length for the values of parameters indicated above and $H_a = 100$ Oe (curve *2*). It is seen that the trapping of holes in the nonlinear regime results in a considerable increase in the damping length of a doppleron.

The nonlinear effect is even more dramatic in the case of low magnetic fields ($\xi \gg 1$), where there are no propagating modes in the linear regime. If the nonlinearity is strong ($\nu/\omega_0 \ll 1$), the expression for s_- in (14) is replaced by

$$s_-^{(n)} \simeq \frac{1}{\alpha(p_1+p_2)}\left[i\frac{p_1}{|q|}\frac{\nu}{\omega_0} + \frac{(1+\alpha)p_2}{2\sqrt{\alpha}q^2}\right]. \tag{21}$$

When the ratio ν/ω_0 is fairly small, the imaginary part of (21) becomes much smaller than its real part; that is, the metal becomes transparent to radio waves. Substituting (21) into the dispersion relation (15) and solving the latter, we obtain

$$q_1 \simeq (\eta\xi)^{1/4}\left[1 + i\mu\frac{\nu}{\omega_0}(\eta\xi)^{1/4}\right], \quad q_2 \simeq i(\eta\xi)^{1/4}, \tag{22}$$

where

$$\eta = \frac{(1+\alpha)p_2}{2\alpha^{3/2}(p_1+p_2)}, \quad \mu = \frac{p_1}{8\sqrt{\alpha}(1+\alpha)p_2}. \tag{23}$$

The root q_2 describes a damping component of the field, whereas the root q_1 corresponds to a new nonlinear wave for which there is no analog in the linear regime.

Concluding this section, we consider the surface impedance of a plate of aluminum for the excitation being antisymmetric with respect to the electric field. For the case where the reflection of carriers from the surface of the plate is diffuse and the field in the plate consists of two exponential components, the corresponding formula for the impedance was obtained in [6, formula (3.11)]. In the magnetic-field range in question ($\xi \gg 1$), this formula reduces to

$$Z_- \simeq \frac{4\pi\omega}{c^2}\left(\frac{1}{k_1}\frac{1-\exp(ik_1 d)}{1+\exp(ik_1 d)} + \frac{1}{k_2}\right), \tag{24}$$

where

$$k_1 \equiv k_1' + ik_1'' = \frac{eH}{cp_0}q_1(H), \quad k_2 = ik_1', \tag{25}$$

and d is the thickness of the plate. In (24), the first term is due to the excitation of a nonlinear wave in the plate, whereas the second term is due to a damping component.

Figure 5 shows the calculated surface resistance $R_- = \mathrm{Re}Z_-$ of the plate for the values of parameters indicated above, $d = 1$ mm, and $\omega/2\pi = 100$ kHz. The peaks in the resistance occur at the values of H for which the plate thickness is an odd-integer multiple of half the wavelength of the wave, $k_1'(H)d = \pi(2n+1)$, where n is an integer. We note that, in the linear regime, the $R_-(H)$ dependence has no oscillation in the range of magnetic fields in question.

ACKNOWLEDGMENTS

This work was supported by the Russian Foundation for Basic Research (grant no. 98-02-18393).

REFERENCES

1. I. P. Krylov, Zh. Éksp. Teor. Fiz. **54**, 1738 (1968) [Sov. Phys. JETP **27** (1968)].
2. P. K. Larsen and F. G. Greisen, Phys. Status Solidi B **45**, 363 (1971).
3. S. Balibar, B. Perrin, and A. Libchaber, J. Phys. F **2**, 4629 (1972).
4. V. V. Lavrova, V. G. Skobov, L. M. Fisher, *et al.*, Fiz. Tverd. Tela (Leningrad) **15**, 3379 (1973).
5. V. G. Skobov, L. M. Fisher, A. S. Chernov, *et al.*, Zh. Éksp. Teor. Fiz. **67**, 1218 (1974) [Sov. Phys. JETP **40** (1974)].
6. A. S. Chernov and V. G. Skobov, Phys. Rep. **244**, 1 (1994).
7. I. F. Voloshin, G. A. Bugal'ter, V. Ya. Demikhovskiĭ, *et al.*, Zh. Éksp. Teor. Fiz. **73**, 1503 (1977) [Sov. Phys. JETP **46**, 790 (1977)].

Translated by Yu. Epifanov

Physics of the Solid State, Vol. 42, No. 4, 2000, pp. 594–602. Translated from Fizika Tverdogo Tela, Vol. 42, No. 4, 2000, pp. 581–588.
Original Russian Text Copyright © 2000 by Romanov, Shamshur.

METALS AND SUPERCONDUCTORS

Current-Induced Suppression of Superconductivity in a Three-Dimensional Lattice of Weakly Linked Indium Grains in Opal

S. G. Romanov and D. V. Shamshur

Ioffe Physicotechnical Institute, Russian Academy of Sciences, Politekhnicheskaya ul. 26, St. Petersburg, 194021 Russia
e-mail: d.shamshur@shuvpop.ioffe.rssi.ru

Received May 21, 1999

Abstract—The current–voltage characteristics of the metal–dielectric composite have been investigated in the range of the resistive state near the superconducting transition temperature T_c. The composite structure can be represented as a face-centered cubic lattice, which involves a large number of weakly linked indium nanograins and is stabilized in structural cavities of opal. The response to microwave radiation is used to characterize the resistive state of the composite. The comparative investigation into the current–voltage characteristics and the response of the composite to microwave radiation makes it possible to conclude that the weak links are superconducting in the region of critical current (I_c) of the composite as a whole. The transition of weak links to the resistive state occurs at currents immediately preceding the transition of the composite from the resistive state to the ohmic state. The model of resistivity of the indium–opal composite is proposed on the basis of morphological examinations. According to this model, the energy dissipation in the resistive state is brought about by the quasi-discrete (due to the quantization of the magnetic flux in circuits of a three-dimensional lattice comprised of multiply connected grains) redistribution of transport current over the cross-section of composite. *© 2000 MAIK “Nauka/Interperiodica”.*

The construction of regular spatial ensembles involving a great number of identical nanostructures implies the development of materials whose functional characteristics are similar to those of small-sized objects but whose energy parameters reach the values corresponding to the operating range of electronic devices with microscopic sizes [1]. In addition to the extension of operating ranges of currents and voltages, the transport properties of the lattice of interacting nanostructures can exhibit collective effects. An example of the nanostructurized superconductor is provided by a three-dimensional array of Josephson junctions, a the discrete system with a nonlinear dynamics. So far, the physical understanding of similar superconductors, in particular, their interaction with electromagnetic field, remains semiempirical [2]. In this respect, the study of granular superconductors with a known submicrostructure is an urgent problem.

A regular Josephson medium can be treated either as a lattice of weak links or as an array of closed circuits, depending on the nature of the discussed phenomena, for example, the interaction with microwave radiation or the motion of magnetic flux.

The response of a Josephson system to electromagnetic radiation is dual. On the one hand, upon exposure to microwave radiation, the order parameter, critical temperature, and critical current of a superconductor increase at the expense of changes in the distribution of normal electrons with respect to the equilibrium state [3]. On the other hand, the microwave radiation undergoes rectification, which results in an increase in the dc current flowing in a system. The specificity of the microwave radiation response of a Josephson system shifted by the current to the resistive state is determined by the possibility of its resonance at a natural frequency of oscillations of the order parameter in weak links. This resonance was found in natural superlattices of weak links [4] and also in specially constructed Josephson junction arrays [5]. Since the resonance response of a Josephson medium to an applied perturbation requires a coherent change in the phase of the order parameter in single junctions [6], the degree of phase locking of single junctions is an important parameter of their system.

The dynamics of the magnetic flux in a superconducting system governs the critical parameters of the system. The introduction of structural inhomogeneities comparable in size to the penetration depth of a magnetic field leads to an increase in the upper critical field of a system, and the spatial ordering of inhomogeneities, for example, the formation of a two-dimensional lattice of superconducting nanostructures, enhances the possibilities of controlling the properties of an ensemble at a sacrifice in use of the commensurability between the magnetic vortex and nanostructure lattices [7].

Up to now, the creation of three-dimensional ensembles of nanostructures has remained a nontrivial prob-

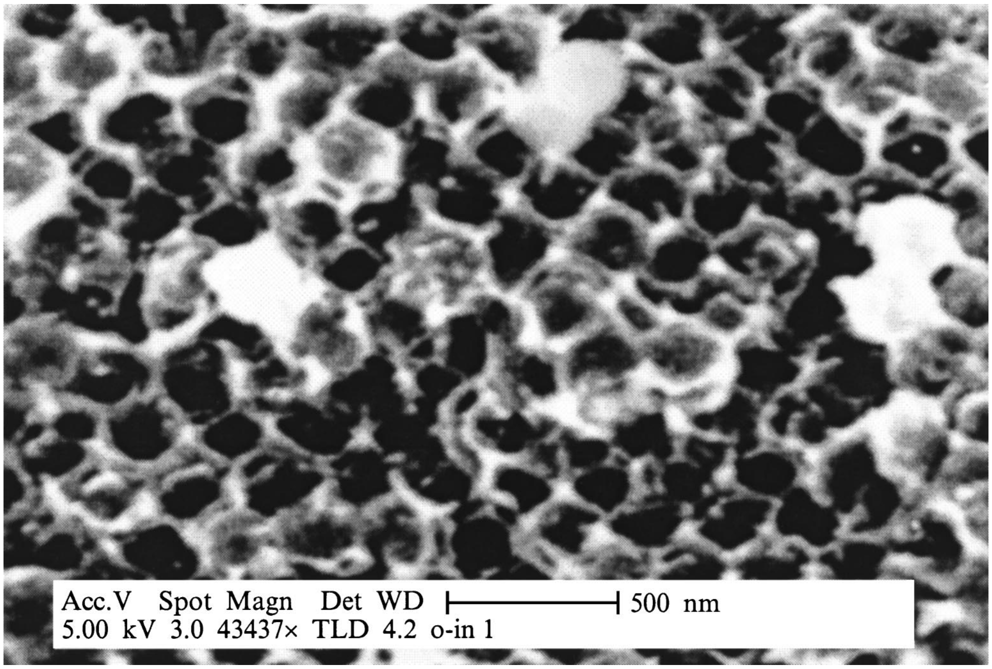

Fig. 1. Electron micrograph of the In–opal composite. Light and dark regions correspond to the metal and dielectric, respectively.

lem for the traditional nanotechnology. However, to a certain degree, this problem has been solved by using a synthetic opal as a matrix for filling with a superconducting metal [8–10]. A superconductor–opal composite can serve as a model object in research into the behavior of three-dimensional Josephson media owing to the known geometry of a system and its controllability. These ordered nanocomposites possess a number of unusual properties, for example, an anomalous hysteresis of current–voltage characteristics (i.e., the situation when the critical current of the reverse branch of the current–voltage characteristic I_{cd} considerably exceeds the critical current of the direct branch I_{cu}) [9] and a discrete penetration of the magnetic field into a lattice [11]. At the same time, the behavior of three-dimensional ensembles is more complex in the interpretation as compared to the two-dimensional systems and has been poorly understood, especially in respect to collective effects.

In the present work, we experimentally studied the resistive state of an ordered lattice involving a large number of weakly linked superconducting indium grains in opal (In–opal) at different currents and under exposure to microwave radiation.

1. MATERIAL AND EXPERIMENTAL TECHNIQUE

Structurally, opal is a regular three-dimensional packing of identical silicate spheres with free cavities between touching spheres. A face-centered cubic packing of spheres involves cavities of two types: octahedral cavities with the characteristic size $d_O = 0.41D$ (O-grains) and tetrahedral cavities with $d_T = 0.23D$ (T-grains), which are connected through bridges with the smallest diameter $d_b = 0.15D$, where D is the sphere diameter [12]. In the present work, we used opal with $D = 260$ nm. In order to increase the $d_{O,T}/d_b$ ratio, we performed 80 cycles of TiO_2 molecular layer deposition [13]. Then, the porous matrix was completely filled with an indium melt under pressure [12, 13]. The electron micrographs (Fig. 1) demonstrate that the metal in opal forms a continuous regular three-dimensional network in the space between dielectric spheres. In the cross-section, the metal network takes the form of a regular lattice of closed circuits containing metal grains, which connect with each other via bridges with a cross-section smaller than that of grains. A fine structure of grains and bridges formed by a filler in opal was discussed in [14].

A sample was prepared in the form of a $5 \times 1 \times 0.5$ mm^3 bar with a local slot in the center to decrease the thickness down to 0.25 mm. Four silver strips were electrochemically deposited onto a larger face of the sample, and electrical leads were soldered to the strips. The current–voltage characteristics were measured using the four-point probe method in a current source mode. The microwave field at a frequency of 1.2 GHz was supplied with a coaxial cable. The induction loop closing a cable and going round the sample served as a coupling element. The traveling-wave mode was created by a directional coupler. The microwave signal with a power of 50 mW at the output of a generator had the pulse modulation with a frequency of 8 kHz. The

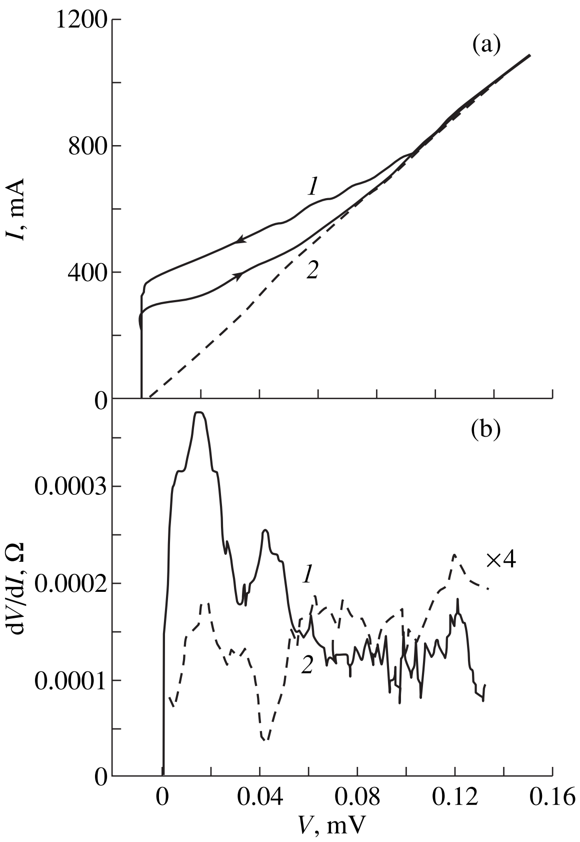

Fig. 2. (a) Current–voltage characteristics and (b) their first derivatives for In–opal composite at T = (*1*) 3.40 and (*2*) 3.45 K (curve *2* in Fig. 2b is shown on an enlarged scale).

sample was excited by the magnetic component of the microwave field in order to increase the efficiency of coupling with the low-resistance sample. The power losses due to the impedance mismatch ranged up to 50 dB. The response to microwave radiation $\Delta V_{res}(V)$ (where V is the dc bias voltage across potential contacts) is the alternating signal with a frequency of microwave modulation. This signal was amplified by a frequency selective voltmeter and then was recorded with a phase-lock detector. No shielding from the earth magnetic field was applied.

2. RESULTS

Figure 2a demonstrates the current–voltage characteristics for In–opal sample at T = 3.45 and 3.4 K, which correspond to the conductivity modes with $I_c = 0$ and $I_c > 0$, respectively. The resistive and ohmic ranges of critical currents can be distinguished in the current–voltage characteristic obtained at T = 3.4 K (Fig. 2a, curve *1*). The current of the reverse branch in the current–voltage characteristic I_{cd} is approximately 30% larger than the critical current of the direct branch I_{cu}; however, the functional dependence $I(V)$ does not change. Note that the current–voltage characteristic of the sample in the resistive state is irreversible at each point; i.e., the current depends on the prehistory of current changes. The first derivative of the current–voltage characteristic (Fig. 2b) indicates that its nonlinearity is predominantly observed in the initial region.

The current–voltage characteristic measured at T = 3.45 K (Fig. 2a, curve *2*) also exhibits a weak nonlinearity. The evaluation of an increase in the T_c temperature due to a change in size of the indium bridges by using the empirical formula $T_c = 3.41 + 5.1/d$ [15] (where the temperature is in degrees Kelvin, and the diameter d is in nanometers) leads to T_c = 3.75 K at d = 15 nm. The applicability of this formula to the determination of the critical temperature for indium in opal was considered in [16]. This estimate allows us to assume the fluctuation superconductivity in the lattice of grains at the given temperature. In this case, the direct and reverse branches of the current–voltage characteristic coincide with each other.

The dependences $\Delta V_{res}(V)$ at the same temperatures are depicted in Figs. 3a and 4a. At T = 3.4 K, the peak of microwave response is observed in a portion of the current–voltage characteristic that does not show pronounced nonlinearity and is located immediately ahead of the ohmic region.

The change in the static current–voltage characteristic $\Delta I_{st}(V)$ upon exposure to external microwave radiation was directly determined by the subtraction of the current–voltage characteristic obtained under microwave irradiation from the initial current–voltage characteristic (Figs. 3b, 4b). At T = 3.4 K, in a certain current range, $\Delta I_{st}(V) < 0$, which corresponds to an increase in the current-carrying capacity of the condensate in response to an external microwave field. The reproducibility of the effect for the current–voltage characteristic in the presence of critical current with a change in the temperature suggests that the microwave radiation stimulates the superconductivity (the critical current or the order parameter, which is insignificant in the context of this experiment). Actually, for the current–voltage characteristic without critical current, the sign of $\Delta I_{st}(V)$ varies in an arbitrary way with a change in the temperature and a change in the bias current (Fig. 4b). The dependences $I_c(T)$ (Fig. 6a) were obtained from the current–voltage characteristics (Fig. 5a, the reverse branches are not shown) and the corresponding responses (Fig. 5b) measured at different temperatures. For uniformity in determination of the peak location, the dependences $\Delta V_{res}(V)$ of the microwave response and the radiation-stimulated static current–voltage characteristics $\Delta I_{st}(V)$ were processed with a Gaussian distribution in order to approximate the peaks. Figure 6a shows the temperature dependence $I_m(T)$ of the current corresponding to a maximum of the microwave response depicted in Fig. 5b, and the dependence $I_{st}(T)$ of the maximum current stimulated by the microwave irradiation is displayed in Fig. 7.

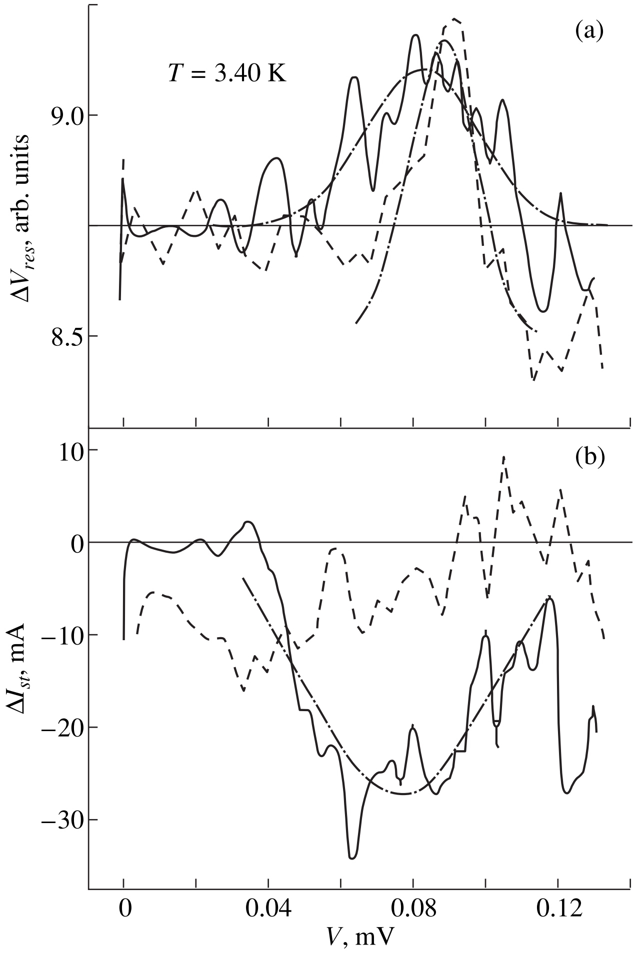

Fig. 3. (a) Microwave responses for the direct (solid line) and reverse (dashed line) branches of the current–voltage characteristic (dot-and-dash lines show the contours of the curves corresponding to a Gaussian distribution). (b) Differences in the current–voltage characteristics obtained without and under microwave radiation for the direct (solid line) and reverse (dashed line) branches (dot-and-dash line shows the Gaussian contour). $T = 3.40$ K.

3. CURRENT–VOLTAGE CHARACTERISTICS

The structure of In–opal can be represented as a face-centered cubic lattice formed by nanostructures of the grain–bridge–grain type. The resistive state of this nanostructure will be taken to mean the state when the flowing current is larger than the critical current of a bridge.

The current–voltage characteristic of the In–opal composite (Fig. 2a) with $I_c > 0$ is adequately described by the relationship $V = (I^2 - I_c^2)^{0.7}$. Such a hyperbolic current–voltage characteristic is typical of a single resistively shunted bridging Josephson junction [17]. On the other hand, similar behavior of the current–voltage characteristic is observed in superconducting films with a regular lattice of pinning centers when the lattices of magnetic vortices and spinning centers are

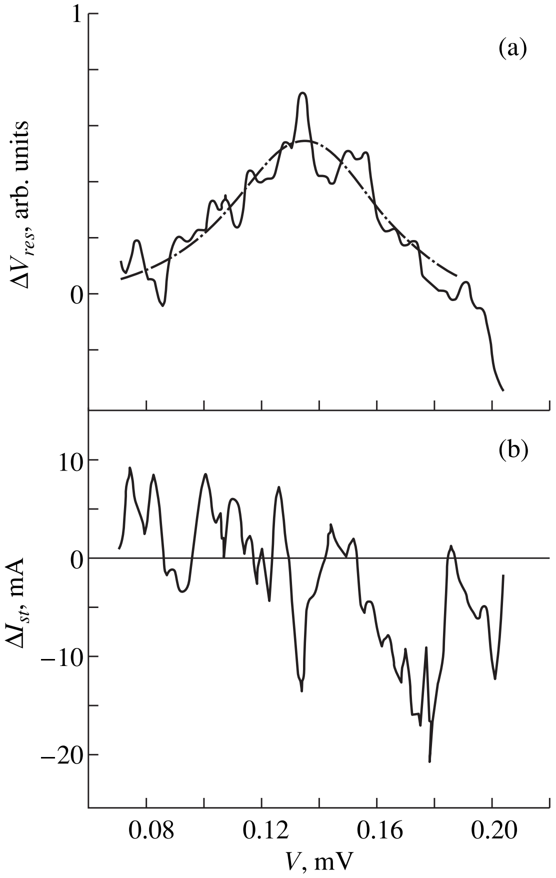

Fig. 4. (a) Microwave response (solid line). The dot-and-dash line shows the Gaussian contour. (b) Difference between the direct branches of the current–voltage characteristics obtained without and under microwave radiation. $T = 3.45$ K.

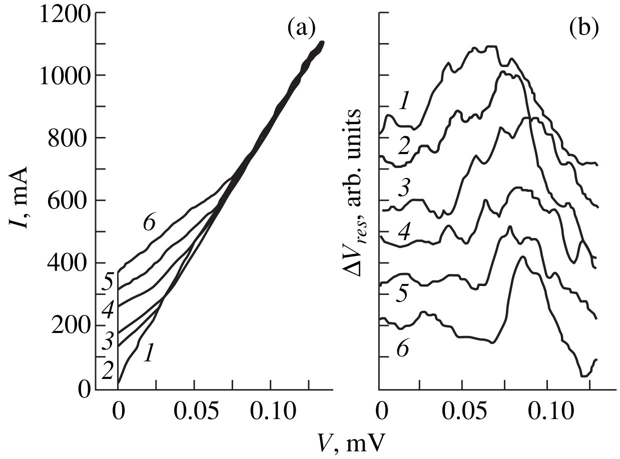

Fig. 5. (a) Current–voltage characteristics and (b) microwave responses at different temperatures T, K: (*1*) 3.45, (*2*) 3.43, (*3*) 3.42, (*4*) 3.4, (*5*) 3.38, and (*6*) 3.36.

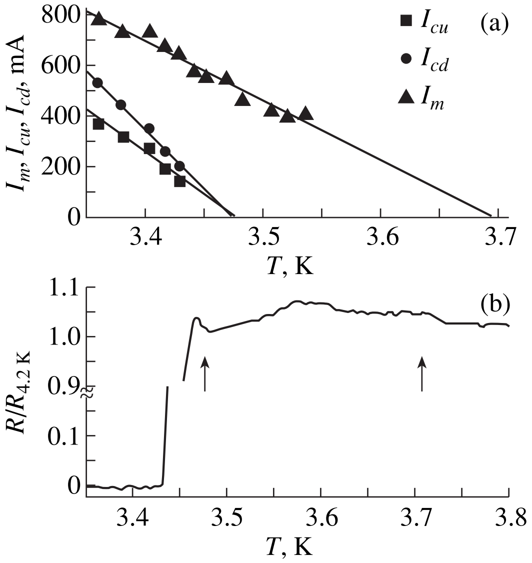

Fig. 6. (a) Dependences of the critical current for the direct I_{cu} and reverse I_{cd} branches of the current–voltage characteristics and the current I_m at a maximum of the microwave response on the temperature. (b) Resistive transition in the In–opal composite. Arrows indicate the transition temperatures obtained by the extrapolation of the data shown in Fig. 6a.

commensurable [18]. For a two-dimensional lattice of Josephson junctions, a hyperbolic current–voltage characteristic corresponds to the junctions with zero McCumber parameter [19], i.e., to bridges with a very low resistance and capacitance. Evidently, the fact that the current–voltage characteristic has hyperbolic behavior is not sufficient to elucidate the mechanism of its formation. However, the shape of the current–voltage characteristic gives grounds to assume that the system of indium grains in opal is regular from the viewpoint of both geometric sizes and the parameters of intergranular links and/or circuits.

Knowing the resistance of the sample and its geometric cross-section, we estimated the resistance of a single bridge in the normal state near the transition temperature as $R_i \approx 0.5\ \Omega$. These bridges are characterized by a high transparency and can be considered within the classical approach to the conductivity [20, 21]. In the general case, the conductivity of single bridging junctions at $I > I_c$ can be described in the framework of the Andreev multiple reflection model [21]. However, this theory cannot be directly applied to the charge transfer in the lattice of multiply connected grains, because the grain sizes are comparable to the coherence length ξ and are substantially less than the relaxation length of quasiparticles.

As the initial approximation, the bridges between the adjacent grains are treated as short ($L < 100$ nm) and narrow neckings of variable cross-section (the minimum diameter $d_b \sim 15$ nm) between superconducting grains. The junction length is considerably less than ξ, which, in bulk indium, is equal to $\xi_0 = 360$ nm. It was demonstrated that, in the case when the ratio between the width of the Josephson bridge necking width and the coherence length is small ($d / 2\xi \ll 1$), the size of the region in which the order parameter is suppressed is comparable to the minimum width of necking and does not depend on the coherence length [22]. It is obvious that this ratio holds for the indium–opal nanostructures. The current–phase relationship for these bridges is purely sinusoidal, as is the case of tunnel junctions. By assuming that the critical current of a lattice is determined by the suppression of superconductivity in bridges, it should be taken into account that the critical current density in a bridge increases with a decrease in its diameter $j_{ci} \sim \xi/d$ [22] and should be larger than the critical current density in a bulk superconductor. However, the estimate of the critical current density j_{ci} in a bridge from $I_c = 280$ mA (the direct branch of the current–voltage characteristic at $T = 3.4$ K) and the number of bridges connected in parallel in the sample cross-section $N \approx 4 \times 10^6$ leads to $j_{ci} \approx 10^8$ A/m^2, which is close in the order of magnitude to the critical current density of bulk indium. On the other hand, since $d_{O,\,T} < \xi$, the grains cannot serve as massive “banks,” and, hence, their critical parameters depend on the state of bridges. This means that the difference in critical currents of grains and bridges cannot be large.

The experimental dependence $I_c(T)$ is close to linear (which is in agreement with the relationship $I_c \sim 1 - T/T_c$ obtained in [22] for short narrow bridges), but exhibits a weak kink at $T \approx 0.9T_c$. This kink is characteristic of the superconductor–opal composites (see, for example, [10, 23]) and can be explained by the correlation between ξ and the unit cell parameter. The critical temperature $T_{c1} = 3.45$ K determined from the intersection of the asymptotics of $I_c(T)$ with the T-axis is the same for the direct and reverse branches of the current–voltage characteristic (Fig. 6a), which suggests that the mechanism of resistivity is identical for both branches of the current–voltage characteristic.

The data discussed above result in a discrepant picture of the resistive state: (i) according to the current–voltage characteristic of the lattice, the resistive state embraces an appreciable current range, whereas the critical currents of grains and bridges should be close to each other; (ii) the current suppression of superconductivity in bridges gives no reasons for an anomalous hysteresis in the current–voltage characteristic; and (iii) the I_c current of the lattice per one bridge is considerably less than the geometry-allowed current. In order to resolve these contradictions, it is necessary to take into consideration the interaction between single nanostructures.

4. MICROWAVE RESPONSE

The response of the indium–opal composite to the microwave radiation can be caused neither by the classical rectification, because the $\Delta V_{res}(V)$ dependence is not proportional to $dV(I) / dI$, nor by the Josephson frequency-selective rectification, since the location of a maximum in the $\Delta V_{res}(V)$ dependence varies with temperature at a constant radiation frequency. Most likely, the observed response is the Josephson wide-band response. The rectification through this mechanism requires that the ensemble involves bridges in the resistive state.

The observed responses $\Delta V_{res}(V)$ are qualitatively similar to each other in the entire studied range of temperatures and currents. The width of the microwave response range is the sole parameter varying in a regular way. For the current–voltage characteristic with $I_c = 0$, the microwave response is observed at any current in the resistivity range (Fig. 4). In the case of the current–voltage characteristic with $I_c > 0$, the width of the peak monotonically decreases with a decrease in the temperature (Fig. 5b), as contrasted to an increase in the voltage range of resistivity in the current–voltage characteristic. Note that the width of the response range for the reverse branch of the current–voltage characteristic is somewhat less than that for the direct branch (Fig. 3a).

Reasoning from these facts, we believe that the maximum of the microwave response corresponds to the current at which a relatively large fraction of bridges is in the resistive state. We also suppose that, in the response range $\Delta V_{res}(V)$, the relationship $I_{cbridge} < I < I_{cgrain}$ is valid, at least, for a part of bridges. A narrowing of the response range with a decrease in the temperature indicates that $I_{cbridge} \longrightarrow I_{cgrain}$ according to the inference drawn from analysis of the bridge structure.

The critical temperature $T_{c2} = 3.7$ K, which is determined from the asymptotic of the $I_m(T)$ dependence, is higher than the temperature $T_{c1} = 3.45$ K obtained from the asymptotics of the $I_c(T)$ dependence (Fig. 6a). This implies that the transition to the superconducting state involves two stages. Let us demonstrate that the difference resides in the state of weak links. A comparison of the T_{c1} and T_{c2} temperatures with the $R(T)$ curve of the resistive transition (Fig. 6b) shows that the former temperature corresponds to the resistive transition temperature, and the latter temperature, to the onset of resistance fluctuations (the $R(T)$ dependence was discussed in [24]). In the temperature range between T_{c1} and T_{c2}, the current–voltage characteristic exhibits a pronounced nonlinearity (Fig. 2b). It is clear that, in the fluctuation pairing mode, the lattice contains superconducting and nonsuperconducting regions whose boundaries are responsible for the microwave response.

In the case of the resistive state of bridges, the oscillating current of quasiparticles in a single bridge necessarily modulates the current flowing through the adjacent bridge; i.e., the oscillations of voltage (order parameter) in the adjacent bridges are phase-locked through the injection of quasiparticles. At the same time, the branching of current flow paths (Fig. 8) can bring about the cross-locking of the lattice as a whole. In the lattice of identical bridges, the effect of phase-locking can be very strong. In the presence of lattice defects, the phase-locking is lost, and the number of bridges phase-unlocked by one defect depends on the path length of quasiparticles. In the case under consideration, the small amplitude of response and the absence of sharp peaks with a change in the voltage across the sample indicate that the oscillations of quasiparticle current are phase-uncorrelated. Therefore, the lattice of weakly linked grains, which is ordered relative to the low-frequency processes, can be considered the so-called Josephson glass with respect to the high-frequency processes.

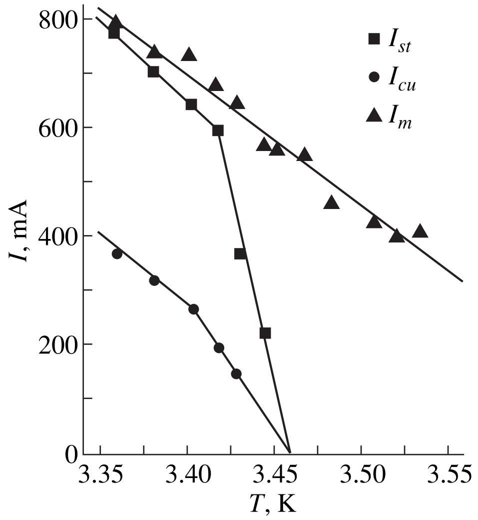

Fig. 7. Dependences of the maximum stimulated current I_{st}, the current I_m at a maximum of the microwave response, and the critical current I_{cu} on the temperature.

As follows from analysis of the microwave response of the indium–opal composite, the critical current of the lattice is determined by a mechanism unrelated to the suppression of superconductivity in bridges, and the bridges undergo a transition to the resistive state when the currents considerably exceed the critical current of the lattice.

5. DISTRIBUTION OF CURRENT OVER THE LATTICE

The close packing of grains in the lattice (the unit cell parameter $f = \sqrt{2}\,D \cong 360$ nm $\sim \xi$) provides a means of describing the vortex dynamics in the indium–opal composite within both the continual and discrete approaches. The continual approach was used by Babaev and Ktitorov [25], who treated the lattice of Abrikosov vortices and the lattice of grains as incommensurable phases; however, the current–voltage characteristics were not considered. We will adhere to the discrete approach under the assumption that vortices in their ordinary sense are absent in the indium–opal com-

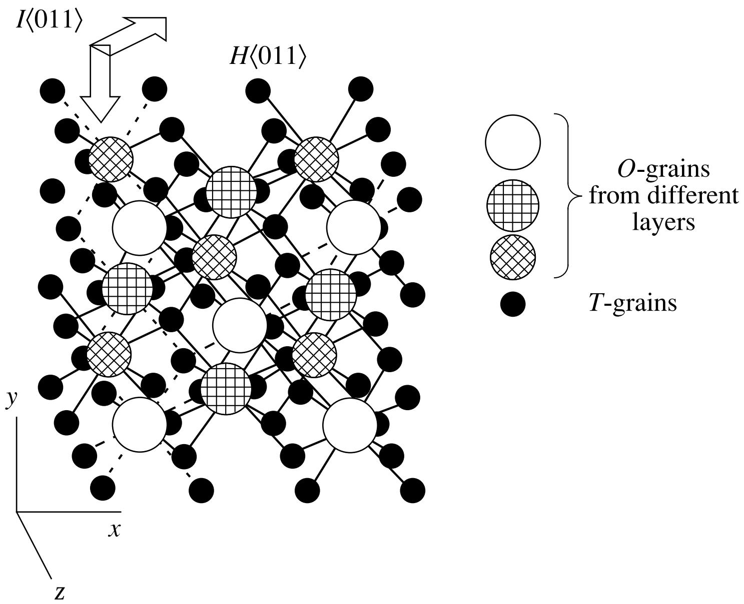

Fig. 8. Schematic representation of the structure of current-carrying paths in the In–opal lattice. The *O*-grains located in the (110) planes outside the figure plane are hatched. Current flowing along the path shown by dashed lines in the [011] direction produces the magnetic field in the [011] direction due to tracing the circuits.

posite, because the size of indium grains corresponds to the London penetration depth of a magnetic field λ_0 = 65 nm and is appreciably less than ξ = 360 nm.

The morphology of the material (Fig. 1) is such that the current flow can be considered as a periodic branching and merging of current-carrying paths at sites of grain lattice. The magnetic field produced by the current affects the interference of the wave functions of carriers by introducing the phase difference in tracing the circuits. Hence, the quantization of the magnetic flux imposes some restrictions on possible paths of the superconducting current and magnitudes of circuit currents. This gives rise to the self-consistent state, which is characterized by a nonuniform distribution of the current throughout the cross-section of the lattice due to the interaction between circuits. This interaction involves circuits whose perimeter allows the wave function of carriers to retain the phase in tracing the circuit, and the weak links involved in the circuits are in the superconducting state. This distribution of current over the lattice will be referred to as the lattice of circuit currents.

Since the circuit currents are self-consistent, the lattice volume is divided into regions, and the transport current flows along their boundaries. The size of a region should be large enough for the circuit to include up to several flux quanta. The accumulation of magnetic flux in a circuit is likely limited by the condition for the retention of superconductivity by weak links, because the resistive link frustrates the interference. By definition, the lattice of circuit currents is commensurable with the grain lattice. As the current increases, these regions undergo a further division to increase the current-carrying capacity of the lattice. At the instant of rearrangement, the lattice of circuit currents becomes unstable; i.e., this lattice can undergo not only division, but also displacement relative to the lattice of grains. A decrease in the circuit size brings about a decrease in the spread of the parameters of weak links involved in the circuit, which becomes more stable to an increase in the magnetic field. The displacement of circuit currents is caused by the Lorentz forces. These forces acting on a circuit current at any nonzero value are induced by the other circuits, because the planes of circuits with different configurations are rotated in the face-centered lattice (Fig. 8). The displacement of magnetic flux produced by the lattice of circuit currents is accompanied by the dissipation of energy and the appearance of voltage across the junctions. The structural defects of opal and the thermal fluctuations also favor the “melting” of the circuit current lattice. Consequently, the critical current determined from the current–voltage characteristic is the critical current corresponding to the onset of the motion of the magnetic flux. However, the motion of magnetic flux is also attended by a further division of the circuit current lattice to the minimum possible size. As is known from the experiments on the penetration of the magnetic field into the indium–opal composite [11], the circuits whose diameters change by a factor of twenty are involved in the process. When the current becomes sufficiently large to destroy the superconductivity of bridges, the lattice as a whole transforms into the normal state.

The change in sign of the current gradient brings about the enlarging of circuits rather than their division. It is evident that, compared to the “wide-mesh” lattice, the “fine-mesh” lattice is capable of carrying a larger amount of current, because the limiting magnetic flux trapped in the latter lattice is larger. The discreteness of the magnetic flux results in the delay of the lattice transformation to the wide-mesh state, which is responsible for the irreversibility of the current–voltage characteristic and anomalous hysteresis.

6. MICROWAVE STIMULATION OF SUPERCONDUCTIVITY

The stimulation of superconductivity by an external microwave field is associated with an additional contribution of the Cooper pairs to the current flow in an ensemble under external irradiation (Fig. 3). It seems likely that the stimulation effect can be interpreted as an increase in the flux trapped in a circuit due to the stimulation of the order parameter, as is the case of the microwave-induced superconductivity in thin superconducting cylinders [26].

The temperature dependence $I_{st}(T)$ of the maximum stimulated current in the temperature range $T < T_c$ is limited from below by the $I_c(T)$ dependence (Fig. 7). This implies that the manifestation of the stimulation effect requires a branched system of current flow paths in the lattice. On the other hand, the $I_{st}(T)$ currents do not exceed the $I_m(T)$ currents; i.e., the microwave stimulation is observed in the range of currents at which the bridges are predominantly in the superconducting state and the system of circuit currents is not disturbed. In this range, the microwave field enhances the stability of weak links with respect to the suppression of superconductivity by current and, hence, provides a way of trapping a larger number of magnetic flux quanta by a circuit. Thus, the fact that the $I_{st}(T)$ currents are intermediate between the $I_c(T)$ and $I_m(T)$ currents indicates the correlation between the microwave stimulation and the stability of circuit current lattice.

No stimulation of superconductivity is found in the reverse branch of the current–voltage characteristic, which can be a consequence of the masking effect of heat release. For the current–voltage characteristic without critical current, the resistivity has a different nature: the circuit currents are absent in the lattice, the stable superconducting state is not observed, and the stimulation effect does not manifest itself.

Therefore, the application of the microwave response allowed us to distinguish between the resistive state of the lattice consisting of multiply connected indium nanostructures in the opal matrix as a whole and the resistive state of nanostructures comprising the lattice. It was demonstrated that, first, the critical current of the lattice is not associated with the suppression of superconductivity in the nanostructures forming the lattice, and, second, the superconductivity in nanostructures can be stimulated by the external microwave field, but this effect does not lead to an increase in the critical current in the lattice as a whole. The proposed model describes the resistive state of the lattice of weakly linked superconducting grains as a result of the self-consistent change in the distribution of the transport current over the lattice. The critical current in the indium–opal composite is determined by the displacement of the lattice of circuit currents with respect to the grain lattice, and the resistive state of the indium–opal composite is predominantly caused by the quasi-continuous rearrangement and displacement of the circuit current lattice. A nonequivalent configuration of circuit currents upon change in the sign of the transport current gradient is responsible for the anomalous hysteresis of the current–voltage characteristic. The external microwave field enhances the stability of circuit currents due to an increase in the critical current of nanostructures, which results in an additional contribution to the current flow in the ensemble.

The shape of the current–voltage characteristic is determined by a collective effect—the interaction of circuit currents in the ordered lattice. The range in which this effect is stable is determined by the current required for the transformation of weak links into the resistive state. At the same time, the achieved degree of crystallinity of the lattice is not sufficient to provide the locking of the lattice with respect to the high-frequency process (microwave response) due to the nonidentity of the parameters of bridges in the resistive state. It seems likely that the phase locking of the dynamic response of junctions requires the fulfillment of considerably more rigorous constraints for the lattice ordering and the coupling of bridges with an external field.

ACKNOWLEDGMENTS

We are grateful to M.P. Volkov for his participation in discussions of the results and C.M. Sotomayor Torres for supplying a scanning electron microscope.

This work was supported by the International Science Foundation (grant no. R53000), the “Superconductivity” Research Program (project no. 96099), and the Russian Foundation for Basic Research (project no. 99-02-18156).

REFERENCES

1. S. G. Romanov and C. M. Sotomayor Torres, in *Handbook of Nanostructural Materials and Nanotechnology,* Ed. by H. S. Halwa (Academic Press, 1999), Vol. 4, pp. 231–323.
2. H.-T. S. Lihn and H. D. Drew, Phys. Rev. B **56**, 5559 (1997).
3. R. Escudero and H. J. T. Smith, Phys. Rev. B **31**, 2725 (1985); T. Kommers and J. Clark, Phys. Rev. Lett. **38**, 1091 (1977); T. M. Klapwijk and J. E. Mooij, Physica B (Amsterdam) **81**, 132 (1976); P. M. Th. M. van Attekum and J. J. Ramekers, Solid State Commun. **43**, 735 (1982); J. E. Mooij and T. M. Klapwijk, Phys. Rev. B **27**, 3054 (1983); D. R. McIntosh and J. Lindesay, Phys. Rev. B **50**, 15852 (1994).
4. R. Kleiner and P. Muller, Phys. Rev. B **49**, 1327 (1994).

5. S. P. Benz and C. J. Burroughs, Appl. Phys. Lett. **58**, 2162 (1991).
6. A. K. Jain, K. K. Likharev, J. E. Lukens, *et al.*, Phys. Rep. **109**, 309 (1984).
7. S. G. Lachenmann, T. Doderer, D. Hoffmann, *et al.*, Phys. Rev. B **50**, 3158 (1994).
8. V. N. Bogomolov, Usp. Fiz. Nauk **124**, 77 (1972).
9. V. N. Bogomolov, V. V. Zhuravlev, A. I. Zadorozhnyĭ, *et al.*, Pis'ma Zh. Éksp. Teor. Fiz. **36**, 298 (1982) [JETP Lett. **36**, 365 (1982)].
10. V. N. Bogomolov, Y. A. Kumzerov, S. G. Romanov, *et al.*, Physica C (Amsterdam) **208**, 371 (1993).
11. S. G. Romanov, Pis'ma Zh. Éksp. Teor. Fiz. **59**, 778 (1994) [JETP Lett. **59**, 809 (1994)].
12. V. G. Balakirev, V. N. Bogomolov, V. V. Zhuravlev, *et al.*, Kristallografiya **38**, 111 (1993) [Crystallogr. Rep. **38**, 348 (1993)].
13. V. V. Tretyakov, S. G. Romanov, A. V. Fokin, *et al.*, Mikrochim. Acta, No. S15, 211 (1998).
14. V. N. Bogomolov, L. M. Sorokin, D. A. Kurdyukov, *et al.*, Fiz. Tverd. Tela (S.-Peterburg) **39**, 2090 (1997) [Phys. Solid State **39**, 1869 (1997)].
15. H. T. Vogel and M. M. Garland, J. Appl. Phys. **38**, 5116 (1967).
16. K. Kh. Babamuratov, V. V. Zhuravlev, Yu. A. Kumzerov, *et al.*, Fiz. Tverd. Tela (Leningrad) **35**, 1577 (1993) [Phys. Solid State **35**, 795 (1993)].
17. K. K. Likharev, Rev. Mod. Phys. **51**, 101 (1979).
18. P. Martinoli, Phys. Rev. B **17**, 1175 (1978).
19. S. G. Lachenmann, T. Doderer, R. P. Huebener, *et al.*, Phys. Rev. B **56**, 5564 (1997).
20. I. O. Kulik and A. N. Omel'yanchuk, Fiz. Nizk. Temp. (Kiev) **3**, 945 (1977) [Sov. J. Low Temp. Phys. **3**, 459 (1977)].
21. T. M. Klapwijk, G. E. Blonder, and M. Tinkham, Physica B + C (Amsterdam) **109–110**, 1657 (1982).
22. J. E. Mooij and P. Dekker, J. Low Temp. Phys. **33**, 551 (1978).
23. S. G. Romanov, in *Critical Currents in Superconductors*, Ed. by H. W. Weber (World Scientific, 1994), p. 473.
24. S. G. Romanov, A. V. Fokin, and K. Kh. Babamuratov, Pis'ma Zh. Éksp. Teor. Fiz. **58**, 883 (1993) [JETP Lett. **58**, 824 (1993)].
25. E. C. Babaev and S. A Ktitorov, Phys. Solid State **39**, 1024 (1997).
26. J. A. Pals and J. Dobben, Phys. Rev. Lett. **44**, 1143 (1980).

Translated by O. Borovik-Romanova

Physics of the Solid State, Vol. 42, No. 4, 2000, pp. 603–608. Translated from Fizika Tverdogo Tela, Vol. 42, No. 4, 2000, pp. 589–594.
Original Russian Text Copyright © 2000 by Vorob'ev, Gaponov, Drozdov, Klyuenkov, Masterov.

METALS AND SUPERCONDUCTORS

Investigation of the Compositional Changes of a Y–Ba–Cu–O HTSC Target under Ion Sputtering

A. K. Vorob'ev, S. V. Gaponov, M. N. Drozdov, E. B. Klyuenkov, and D. V. Masterov
Institute of the Physics of Microstructures, Russian Academy of Sciences, Nizhniĭ Novgorod, 603600 Russia
e-mail: vorobyev@ipm.sci-nnov.ru

Received June 22, 1999; in final form, September 6, 1999

Abstract—An Auger electron spectroscopy study is reported of the elemental depth profile of Y–Ba–Cu–O HTSC targets subjected to ion-plasma sputtering in a magnetron deposition system and ion-beam sputtering in the Auger spectrometer chamber. It has been established that the process consists in all cases of predominant copper sputtering accompanied by the formation of a modified surface layer and of a copper-depleted region. This region is assumed to originate from intense copper diffusion from the bulk to the modified surface layer driven by a concentration gradient. © *2000 MAIK “Nauka/Interperiodica”.*

An analysis of composition-property diagrams [1–4] revealed that Y–Ba–Cu–O (YBCO) superconducting films prepared *in situ* have optimum superconducting properties not at the stoichiometric composition, $YBa_2Cu_3O_{7-\delta}$, but rather when enriched heavily in copper and, less strongly, in yttrium (in the region of the Cu/Ba ≈ 2.2–3.5 and Ba/Y ≈ 1.0–1.5 atomic ratios, respectively). The fact is that at close-to-stoichiometric compositions, there is a high probability of cationic disordering to set in the YBCO unit cell (substitution of barium for yttrium and creation of copper vacancies), processes that distort the lattice and degrade seriously the superconducting properties of a film [2, 5]. As a result, stoichiometric YBCO films with a “smooth” surface (by [3], deviations from the 123 composition should not exceed 1%) exhibit poorer electrical characteristics [6–8]. On the other hand, an excess of copper and yttrium in YBCO films with good electrical parameters precipitates in the form of particles of secondary phases, whose presence is extremely undesirable for most technical applications. Thus, the cationic composition determines practically all properties of YBCO films, namely, the electrical parameters, microstructure, phase composition, and surface morphology. Note that the compositions optimum for various parameters of the YBCO films do not coincide. Preparation of YBCO films with preset properties is obviously possible only if one properly understands the specific features of formation of the cationic composition of films in the course of their growth. This relates primarily to the methods of YBCO film fabrication that employ multicomponent monosources of material (laser-induced evaporation and ion sputtering), because, in this case, unlike the MOCVD and co-evaporation technologies, there is no possibility of controlling the emission of each component. However, monosource-based deposition systems are presently enjoying widespread use, primarily due to their simplicity and reliability; the cylindrical magnetron sputtering system (ICMS) [9] may serve as an example.

One of the reasons that could account for the deviation of the film composition from the starting composition of a multicomponent target in ion sputtering is the variation of the target composition through preferential sputtering and selective diffusion of components from the bulk of the target into the modified surface layer [10]. The present work studies the variation of the YBCO target composition in the course of magnetron sputtering in an ICMS system, as well as a result of ion-beam sputtering in an Auger spectrometer.

1. EXPERIMENTAL

The variation of the elemental composition of YBCO targets was studied with an ÉSO-3 Auger electron spectrometer. The energy of the probing electron beam was 3 keV, and the detection region diameter, 5 μm. The residual pressure in the analytical chamber did not exceed 5×10^{-8} Pa. We analyzed the Auger lines of Y (126 eV), Ba (600 eV), and Cu (920 eV). The KIB-1 ceramic (TU 48-0531-390-88) of the $YBa_2Cu_3O_{7-\delta}$ composition, which was the starting material for the targets, served as a reference. Because the diameter of the Auger detection region was ~5 μm, and the most probable grain size of the KIB-1 ceramic was ~1 μm, it was assumed that local inhomogeneities would not affect the results of measurements. We studied the variations of the YBCO target composition that were produced by ion-beam sputtering directly in the Auger spectrometer and by magnetron sputtering in the ICMS system. The changes in the cation composition of the YBCO targets subjected to ion-beam sputtering were studied by layer-by-layer analysis. We have described the technique of a high-resolution layer-by-layer Auger analysis employed in this work in detail elsewhere [11]. The elemental depth profile was obtained by sputtering

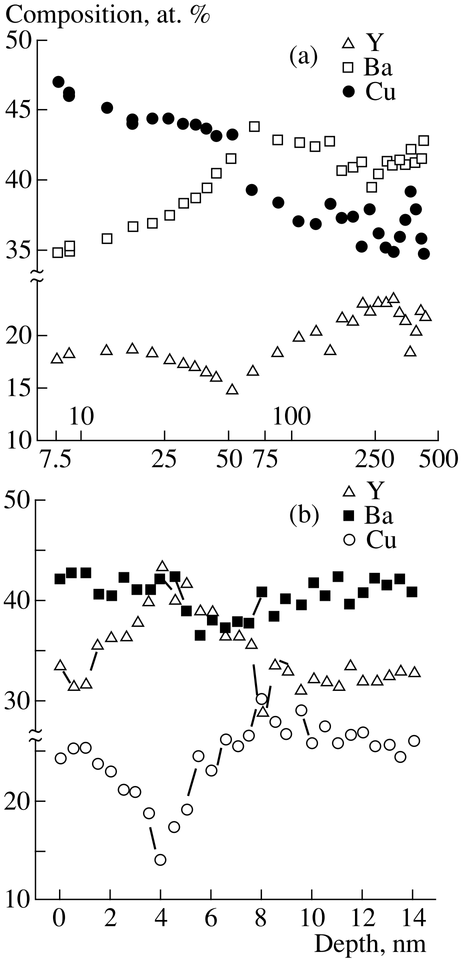

Fig. 1. Elemental depth profile of YBCO targets subjected to ion sputtering: (a) ion-beam sputtering, (b) magnetron sputtering (erosion zone depth 3.5 mm).

the surface of a stoichiometric $YBa_2Cu_3O_{7-\delta}$ target by a 2-keV Ar^+ ion beam incident at an angle of 46°. The ion current density at the target was ~15 $\mu A/cm^2$. The diameter of the sputtered region was ~2 mm. The target sputtering rate in this regime was ~4 nm/min. Operation in this mode produces noticeable compositional changes in the near-surface layer of the target, which are caused by preferential sputtering. The power density released at the target in magnetron sputtering was ~14 W/cm^2, the target voltage was ~150 V, and the working gas pressure was ~40 Pa. The target sputtering rate in this regime was ~150 nm/min. One performed elemental analysis of targets with erosion zones 1.5 and 3.5 mm deep. To make a comprehensive investigation of the composition profile in the modified surface layer of the targets subjected to magnetron sputtering, one carried out layer-by-layer Auger analysis of samples in the region of the erosion zone by sputtering the surface away with a 0.5-keV Ar^+ ion beam incident at an angle of 46°. The measurements made with the reference revealed that the changes in the YBCO target composition introduced by the layer-by-layer analysis in this regime are negligible compared to those produced by magnetron sputtering. The composition profile at larger depths was studied by layer-by-layer Auger analysis of samples with sputtering ions of 2 keV energy. The sputtering rate in the layer-by-layer analysis was calibrated in all cases against a YBCO film of known thickness. To investigate the bulk composition profile of targets subjected to magnetron sputtering, cross cuts of target elements in the region of the erosion zones were made. The spatial distribution of the Cu/Ba concentration ratios were obtained by measuring the peak-to-peak signal intensities of the elements along the surface of the cross cut. A cross cut of the KIB-1 ceramic was employed as a reference.

2. RESULTS OF THE EXPERIMENT

Consider first the variation of the cation composition in a YBCO target, produced by ion-beam sputtering. Figure 1a presents an elemental depth profile of a target derived from a layer-by-layer analysis. One readily sees that this regime of YBCO target sputtering results in a preferential sputtering of copper and yttrium. It is known that preferential sputtering is observed in the case of multicomponent targets where individual components are sputtered in amounts not proportional to the surface concentration of an element and is due primarily to the following factors: (i) a difference in the atomic mass of the target components, which results in different lengths of the collision cascades, and (ii) a difference in surface or chemical binding energy among the target components [12]. Preferential removal of one of the components from the surface gives rise to the formation of the so-called modified surface layer. At temperatures low enough to make diffusion from the bulk negligible, the modified layer retains a fixed thickness, thus making it possible to reach equilibrium conditions at which the sputtered amount of each component is proportional to the bulk concentration of the latter. In this case, the composition of the material lost from the target will be the same as that of the bulk. The situation changes if, at high enough temperatures and/or high diffusion coefficients, the concentration gradient thus produced makes the mass transport of one of the components from the bulk to the modified surface layer prevail over the depletion caused by preferential sputtering. This means that the sputtering is no longer at equilibrium, i.e., the composition of the material being sputtered is no longer the same as in the bulk, and the bulk composition changes continuously. As seen from Fig. 1a, a modified barium-enriched surface layer ~50 nm thick forms in our case. However, equilibrium sputtering conditions are not attained. As the target sputtering continues, the surface layer exhibits a noticeable decrease of the copper concentration (from ~43 down to ~37%) and, accordingly, an increase in the yttrium concentration. This implies the existence of copper mass transport from the bulk to the modified surface layer driven by the concentration gradient. As evident from Fig. 1a, the copper-depleted region extends to ~200 nm in depth.

The data obtained permit one to estimate the relative sputtering coefficients and relative surface binding energies of the YBCO components, as well as the copper diffusion coefficient. In the case of preferential sputtering of a multicomponent material, the following relation holds [12]:

$$Y_A^c/Y_B^c = (c_A/c_B)/(c_A^s/c_B^s), \quad (1)$$

where Y_i^c is the component sputtering coefficient, and c_i and c_i^s are the bulk and surface concentrations of the ith component, respectively. We shall take for c_i^s the concentrations at a depth ~50 nm of the modified surface layer (Fig. 1a), and for c_i, the stoichiometric concentrations of the YBCO components ($c_{\mathrm{Y}} = 17\%$, $c_{\mathrm{Ba}} = 33\%$, and $c_{\mathrm{Cu}} = 50\%$). Equation (1) yields the following relations for the sputtering coefficients of the YBCO components:

$$Y_{\mathrm{Cu}}^c/Y_{\mathrm{Y}}^c = 1.75, \quad Y_{\mathrm{Cu}}^c/Y_{\mathrm{Ba}}^c = 1.68, \quad Y_{\mathrm{Ba}}^c/Y_{\mathrm{Y}}^c = 1.04.$$

Because the sputtering ion energy (2 keV) lies in the range where linear cascades can be initiated, one can use the Andersen–Sigmund model [13], by which

$$Y_A^c/Y_B^c = (M_B/M_A)^{2m}(U_B/U_A)^{1-2m}, \quad (2)$$

where M_i and U_i are the mass and surface binding energy of the atom of the ith component, and m is a parameter depending on the incident ion–target atom interaction potential; typically, $0 \le m \le 0.2$. We set in our calculations $m = 0.2$, i.e., we assume that besides the surface binding energy, the preferential sputtering process is affected also by the mass factor, because the mass of copper atoms is less than that of yttrium atoms approximately by a factor 1.5, and less than that of the barium atoms, by more than a factor of two. Using the sputtering coefficient ratios derived from (1), we obtain from (2) the following surface binding-energy ratios for the YBCO components:

$$U_{\mathrm{Y}}/U_{\mathrm{Cu}} = 2.02, \quad U_{\mathrm{Ba}}/U_{\mathrm{Cu}} = 1.42, \quad U_{\mathrm{Y}}/U_{\mathrm{Ba}} = 1.43.$$

The copper diffusion coefficient D can be estimated using the diffusion models of Pickering (thermal diffusion) [14] and Ho (thermal and radiation-enhanced diffusion) [15]. By these models, the effective thickness of the depleted zone forming as a result of diffusion of one of the multicomponent target components toward the modified surface layer can be written as

$$\delta = D/u, \quad (3)$$

where u is the target erosion rate. In our case, the target sputtering rate in the layer-by-layer analysis regime $u = 4$ nm/min. In accordance with the data of Fig. 1a, $\delta \approx 200$ nm, which yields $D = 1.3 \times 10^{-11}$ cm^2/s.

Consider now the changes in the cation composition produced by magnetron sputtering in a YBCO target. Figure 1b presents an elemental depth profile of a YBCO target with a ~3.5-mm deep erosion zone, obtained by layer-by-layer analysis. As was already mentioned, this analysis does not affect the profile resulting from magnetron sputtering. An analysis of the data obtained permits the following conclusions. The layer from the surface to a depth of ~4 nm is apparently formed by the material deposited on the target surface through back diffusion from the working gas after the discharge turnoff. The reverse flows onto the target must be quite substantial, because straightforward estimation of the lengths of directed motion of the sputtered YBCO component atoms yields about 1 mm for the working gas pressures used (~40 Pa). The next 2 nm in the elemental depth profile correspond to the modified surface layer depleted in copper. Hence, the magnetron sputtering regime employed, as well as the ion-beam sputtering, is characterized by preferential copper removal. As seen from Fig. 1b, the composition of the target bulk differs strongly from the original stoichiometric one ($c_{\mathrm{Y}} = 17\%$, $c_{\mathrm{Ba}} = 33\%$, $c_{\mathrm{Cu}} = 50\%$). This indicates that the equilibrium sputtering conditions were not reached. Just as in the case of ion-beam sputtering, we have here copper diffusion from the bulk of the target to the modified surface layer. The data of Fig. 1b permit one now to calculate the relative sputtering coefficients of the YBCO components using Eq. (1):

$$Y_{\mathrm{Cu}}^c/Y_{\mathrm{Y}}^c = 2.55, \quad Y_{\mathrm{Cu}}^c/Y_{\mathrm{Ba}}^c = 1.90, \quad Y_{\mathrm{Ba}}^c/Y_{\mathrm{Y}}^c = 1.34.$$

The data of Fig. 1b make possible also the determination of the surface binding energies of the YBCO components. Because the sputtering-ion energy in the magnetron process (~150 eV) lies below the energy range where the linear cascade theory [13] is valid, we shall use for the calculations the model of Kelly [16]. This model postulates a change in the composition of the outermost monolayer only, whose atoms are imparted energy in the course of sputtering in the same way as the adsorbed ones are. We believe that this model better reproduces the magnetron sputtering conditions in the given regime, because a substantial part of the sputtered material returns back to the target surface through back diffusion in the working gas and is again resputtered when in the adsorbed state. By the model of Kelly, we have

$$Y_A^c/Y_B^c = [(c_A + c_B\gamma)/(c_B + c_A\gamma)](U_B/U_A), \quad (4)$$

where $\gamma = 4M_A/M_B/(M_A + M_B)^2$. Calculations using (4) yield

$$U_{\mathrm{Y}}/U_{\mathrm{Cu}} = 2.56, \quad U_{\mathrm{Ba}}/U_{\mathrm{Cu}} = 1.96, \quad U_{\mathrm{Y}}/U_{\mathrm{Ba}} = 1.33.$$

The difference of the surface binding energy ratios from the results obtained from (2) reflects the above-mentioned specific features of the state of the target surface under magnetron sputtering in the regime chosen. We see that the surface binding energy of copper

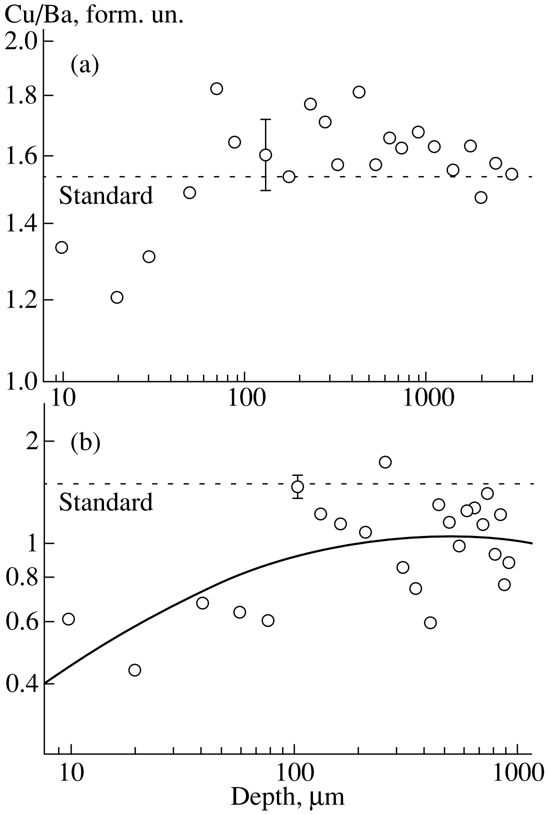

Fig. 2. Composition profile in the bulk of YBCO targets subjected to magnetron sputtering. Erosion zone depth (mm) (a) 1.5, (b) 3.5.

atoms is here still lower than that found for an unperturbed target.

A layer-by-layer Auger analysis of the target with an erosion zone 3.5 mm deep made with 2-keV Ar^+ sputtering ions showed the regions of diffusive depletion in copper to lie deeper than 1.5 μm. Therefore, cross cuts of the target elements in the region of the erosion zone were made in order to probe the bulk composition profiles of the magnetron-sputtered targets. The spatial distribution of the Cu/Ba concentration ratios was studied by measuring the peak-to-peak signal intensities along the surface of the cross cut. Figures 2a and 2b present the Cu/Ba ratios (in formula units) in the bulk of targets with erosion zones 1.5 and 3.5 mm deep, respectively. The dashed line corresponds to the reference value Cu/Ba = 1.5 measured on a cut of the KIB-1 ceramic. The error bars refer to the maximum allowable deviations of the Cu/Ba ratio as specified by TU 48-0531-390-88 Technical Requirements (~7%) for the KIB-1 ceramic. The solid curve in Fig. 2b is a plot of a second-degree smoothening polynomial. The results obtained permit the following conclusions. Magnetron sputtering produces considerable changes in target composition to a substantial depth. The target with an erosion depth of 1.5 mm (Fig. 2a) revealed a depletion in copper to a depth on the order of 100 μm, and the copper content at the surface of the erosion zone is about 90% of that in the reference. In the target with a 3.5-mm deep erosion zone (Fig. 2b), copper depletion is seen to exist throughout the remaining part of the target (~1000 μm), with the copper content at the surface not exceeding 30% of the reference. In the surface region, these results agree well with the figures obtained in target studies by the layer-by-layer Auger analysis. Using the data of Fig. 2a, one can estimate the copper diffusion coefficient D from (3). For $\delta = 100$ μm, we obtain $D \approx 2.5 \times 10^{-9}$ cm^2/s. At the same time, the data of Fig. 2b suggest that if the target is eroded to a depth of 3.5 mm, a steady-state sputtering regime (i.e., with $\delta = \text{const}$) has not been reached at all.

3. DISCUSSION OF RESULTS

The values of D and δ presented here imply that both in magnetron and in ion-beam sputtering of YBCO targets, copper diffuses intensely from the bulk of the target to the modified surface layer. For comparison, consider the results obtained in a study of the concentration profile of a 52 at. % Ni–Cu alloy following its bombardment by 500-eV Ar^+ ions [17]. At a target temperature of 400°C and a fluence of 7.5×10^{17} cm^{-2}, a copper-depleted layer with $\delta \approx 3$ μm forms in the surface region, which corresponds to a copper diffusion coefficient $D \approx 10^{-13}$ cm^2/s. Our values of D are higher by nearly two orders of magnitude in the case of ion-beam sputtering, and by four orders of magnitude for magnetron sputtering. One should apparently take here into account the specific structural features of the YBCO target, which represents fritted ceramic with a density of ~4.5 g/cm^3. The calculated density of the single-crystal $YBa_2Cu_3O_{7-\delta}$ is ~6.3 g/cm^3. This implies that a large fraction of the target volume is occupied by pores and, hence, intense diffusion can take place in the bulk over the grain surfaces.

The conclusion of the existence of mass transport in the bulk of a YBCO target under ion-beam sputtering in an Auger spectrometer was fairly unexpected, because a target subjected to the above-mentioned layer-by-layer analysis is practically not heated. The diffusion in this case has apparently a radiation-induced character. We cannot rule out the possibility that the monotonic nature of the elemental profile at depths of about 50 nm (Fig. 1a) is due to an increase in the diffusion coefficient associated with a buildup of radiation defects. It should be noted that the Ho kinetic model of preferential sputtering used here to estimate the diffusion coefficients assumes, in addition to the conventional thermal, a radiation-enhanced diffusion. Additional experiments are planned in order to confirm the existence of mass transport in the bulk of YBCO targets subjected to ion-beam sputtering in the given regime.

As for the reasons behind the noticeable copper mass transport in YBCO targets under magnetron sputtering, no comprehensive explanation could be proposed for this phenomenon at this stage of the investigation. First of all, one should take into account that a YBCO target subjected to magnetron sputtering in the given regime can be heated to fairly high temperatures. Estimates of the target temperature range from 150 to 500°C. In these conditions, diffusion is more intense. In addition, we believe that magnetron sputtering in this regime could initiate generation of diffusion-stimulating defects, namely, radiation defects themselves and oxygen vacancies. Radiation-enhanced diffusion appears to cause substantial changes in the composition of a multicomponent target under ion-beam sputtering if the target temperature lies within the range $0.2 \leq T \leq 0.6T_m$, where T_m is the melting point [18]. Considering that, for the single-crystal YBCO $T_m \approx 950°C$ [19], and taking into account the above target temperatures, this relation is satisfied in our case. Formation of oxygen vacancies is characteristic of the YBCO material. It is known that various factors, including fairly soft ones, are capable of stimulating oxygen loss and formation of oxygen vacancies in Cu–O chains in the YBCO unit cell [20–23].

Thus, both in magnetron and ion-beam sputtering, the high porosity of YBCO targets is apparently capable of stimulating intense diffusion over the grain surfaces, while the grain bulk diffusion is initiated by the formation of radiation defects and oxygen vacancies. In the conditions of magnetron sputtering, the diffusion rate is higher because of target heating. All this accounts for the anomalously high diffusion coefficients found in our experiments.

The data presented in this study show that the noticeable changes in the composition of a multicomponent target resulting from selective diffusion from the bulk to the modified surface layer are phenomena typical of YBCO film preparation by ion sputtering in general and by the magnetron process in particular. This emphasizes the importance of understanding how the changes occurring in the target composition can affect the properties of thin YBCO films. First of all, one has to stress once more that the superconducting characteristics of YBCO films become optimum in the region of compositions heavily enriched in copper (to an atomic ratio Cu/Ba ≈ 2.2–3.5). Also, the superconducting properties of YBCO films vary insignificantly with the composition changed from the above figure to stoichiometric values and become dramatically degraded only when the copper content drops below the stoichiometric level [2, 5]. One may conjecture that the magnetron process, due to the preferential copper sputtering occurring for a long time (tens of hours [24–26]), produces YBCO films enriched in copper and, hence, with close-to-optimum superconducting properties. We also believe that besides the preferential copper sputtering, the YBCO film composition is determined in a large measure, if not primarily, by selective reevaporation of barium from the condensation surface. We showed [27] that, at substrate temperatures above ~700°C, YBCO films start to become noticeably depleted in barium. By properly optimizing the substrate temperature in accordance with the running target composition, one can prepare YBCO films with an optimum composition and, hence, with optimum superconducting properties. We prepared high-quality thin YBCO films (with a zero resistivity temperature of ~90 K and a critical current density of ~2 MA/cm^2 at 77 K) even in the case where the copper content in the bulk of the target did not exceed 50% of the stoichiometric value (Fig. 1b).

The results presented in this work and in [27–29] permit one to classify the processes accounting for the variation of the cationic composition of YBCO films during their growth in the following way: (i) the use of off-axis deposition systems (in particular, ICMS) rules out variation of the cation composition in the bombardment of the growing film by energetic particles (oxygen ions and secondary electrons) accelerated in the field of the target; (ii) the variation of the film cation composition through selective scattering and diffusion of sputtered YBCO component atoms in the working gas in the typical film preparation conditions does not exceed 15% [28]; (iii) the variation of the film cation composition due to selective desorption of copper and barium adatoms from the surface of a growing film under bombardment by the plasma ions accelerated by the floating substrate potential can reach as high as 30% [29]; (iv) the variation of the film cation composition, caused by preferential sputtering and selective diffusion in the bulk of a monotarget can reach 50%; (v) the variation of the film cation composition induced by selective reevaporation of barium from the surface of the growing film at a growth temperature of about 700°C [27] is apparently the most significant factor, because it makes it possible to prepare films with an optimum composition by properly varying the growth temperature within a narrow interval, even if processes (i)–(iv) are operative.

Thus, the studies described in this paper have demonstrated that an ion beam incident on a Y–Ba–Cu–O HTSC ceramic target gives rise to preferential sputtering of copper with formation of a copper-depleted modified surface layer. In the regimes conventionally employed in ion-beam and magnetron sputtering, copper diffuses from the bulk to the modified surface layer because of a concentration gradient, which may change substantially the target bulk composition. The anomalously large diffusion coefficients may be apparently accounted for by intense diffusion over the grain surfaces because of the high target porosity, and by the onset of grain bulk diffusion stimulated by the formation of radiation defects and oxygen vacancies. The diffusion observed under magnetron sputtering is more intense due to the target heating. The results of this work permit one to classify the processes occurring during the growth of YBCO films and responsible for their cation composition. Our present studies provide a deeper insight into the processes involved in ion-beam sputtering of complex multicomponent and oxygen-containing compounds. The results obtained can be applied to reduce the total time of target sputtering needed to prepare thin YBCO films of a given composition.

ACKNOWLEDGMENTS

This work has been carried out at the Institute of the Physics of Microstructures, Russian Academy of Sciences, within the framework of the "Current Trends in the Physics of Condensed Media" program of the State Committee on Science and Technology "Superconductivity" (grant no. 98064) and "Surface Atomic Structures" and the Russian Foundation for Basic Research (project no. 99-02-18037), whose support is gratefully acknowledged.

REFERENCES

1. E. Waffenshmidt, K. H. Waffenshmidt, F. Arndt, *et al.*, J. Appl. Phys. **75**, 4092 (1994).
2. B. Schulte, M. Maul, P. Haussler, *et al.*, Appl. Phys. Lett. **62**, 633 (1993).
3. N. G. Chew, J. A. Edwards, R. G. Humphreys, *et al.*, IEEE Trans. Appl. Supercond. **5**, 1167 (1995).
4. J. Hudner, O. Thomas, E. Mossang, *et al.*, J. Appl. Phys. **74**, 4631 (1993).
5. T. Yoshitake, W. Hattori, and S. Tahara, J. Appl. Phys. **84**, 2176 (1998).
6. J. Gao, W. H. Wong, and J. Xhie, Appl. Phys. Lett. **67**, 2232 (1995).
7. R. A. Rao, Q. Gan, C. B. Eom, *et al.*, Appl. Phys. Lett. **69**, 3911 (1996).
8. C. S. Huang, T. Y. Tseng, B. C. Chung, *et al.*, J. Appl. Phys. **78**, 7181 (1995).
9. A. K. Vorob'ev, E. B. Klyuenkov, V. V. Talanov, *et al.*, Pis'ma Zh. Tekh. Fiz. **19**, 12 (1993) [Tech. Phys. Lett. **19**, 479 (1993)].
10. *Thin Film Technologies*, Ed. by L. Meissel and R. Glang (New York, 1970; Sov. Radio, Moscow, 1977), Vol. 1.
11. M. N. Drozdov, V. M. Danil'tsev, N. N. Salashchenko, *et al.*, Pis'ma Zh. Tekh. Fiz. **21**, 1 (1995) [Tech. Phys. Lett. **21**, 725 (1995)].
12. *Sputtering by Particle Bombardment*, Ed. by R. Behrische (Springer, Heidelberg, 1983; Mir, Moscow, 1986), Vol. 2.
13. N. Andersen, P. Sigmund, and K. Dan, Vid. Selsk. Math. Fys. Medd. **39** (3), 1 (1974).
14. H. W. Pickering, J. Vac. Sci. Technol. **13**, 618 (1976).
15. P. S. Ho, J. E. Lewis, H. S. Wildman, *et al.*, Surf. Sci. **57**, 393 (1976).
16. R. Kelly, Nucl. Instrum. Methods **132**, 335 (1976).
17. M. Shikita and R. Shimizu, Surf. Sci. **97**, L363 (1980).
18. N. Q. Lam, Surf. Interface Anal. **12**, 65 (1988).
19. M. Maeda, M. Kadoi, and T. Ikeda, Jpn. J. Appl. Phys. **28**, 1417 (1989).
20. V. I. Simonov, V. N. Molchanov, and R. A. Tomazyan, in *Crystals: Growth, Structure, Properties* (Nauka, Moscow, 1993), p. 56.
21. A. Ando, K. Saiki, K. Ueno, *et al.*, Jpn. J. Appl. Phys. **27**, L304 (1988).
22. J. R. Gavaler, J. Talvacchio, and R. W. Weinert, IEEE Trans. Appl. Supercond. **5**, 1173 (1995).
23. Yu. N. Drozdov, S. A. Pavlov, and A. E. Parafin, Pis'ma Zh. Tekh. Fiz. **24**, 55 (1998) [Tech. Phys. Lett. **24**, 24 (1998)].
24. T. I. Selinder, G. Larsson, and U. Helmersson, Appl. Phys. Lett. **52**, 1907 (1988).
25. A. M. Kadin, P. H. Ballentine, J. Argana, *et al.*, IEEE Trans. Appl. Supercond. **25**, 2437 (1989).
26. H. Morita, K. Watanabe, Y. Murakami, *et al.*, Jpn. J. Appl. Phys. **28**, L628 (1989).
27. Yu. N. Drozdov, S. V. Gaponov, S. A. Gusev, *et al.*, IEEE Trans. Appl. Supercond. **7**, 1642 (1997).
28. Yu. N. Drozdov, S. V. Gaponov, S. A. Gusev, *et al.*, IEEE Trans. Appl. Supercond. (in press).
29. A. K. Vorob'ev, S. V. Gaponov, M. N. Drozdov, *et al.*, Pis'ma Zh. Tekh. Fiz. **24** (24), 13 (1998) [Tech. Phys. Lett. **24**, 952 (1998)].

Translated by G. Skrebtsov

Physics of the Solid State, Vol. 42, No. 4, 2000, pp. 609–615. Translated from Fizika Tverdogo Tela, Vol. 42, No. 4, 2000, pp. 595–601.
Original Russian Text Copyright © 2000 by Vykhodets, Kurennykh, Slobodin, Soldatova, Fishman.

METALS AND SUPERCONDUCTORS

Atomic Structure and Diffusion Properties of Superanisotropic Diffusive Systems

V. B. Vykhodets*, T. E. Kurennykh*, B. V. Slobodin, E. E. Soldatova**, and A. Ya. Fishman*****

**Institute of Metal Physics, Ural Division, Russian Academy of Sciences, ul. S. Kovalevskoĭ 18, Yekaterinburg, 620219 Russia*
e-mail: vykhod@imp.uran.ru

***Institute of Solid-State Chemistry, Ural Division, Russian Academy of Sciences,*
Pervomaĭskaya ul. 91, Yekaterinburg, 620219 Russia

****Institute of Metallurgy, Ural Division, Russian Academy of Sciences, Yekaterinburg, 620016 Russia*

Received August 10, 1999

Abstract—The diffusion of oxygen tracer atoms has is, and a diffusion-structural analysis is made of the oxygen subsystem of the $Sr_{2.4}Ca_{1.6}Bi_2O_{8.8}$ oxide representing a copper-free precursor of bismuth high-T_c superconductors. The diffusion in this compound has been shown to be superanisotropic. It has been established that superanisotropic diffusion in the oxygen subsystem of oxide systems, rather than being connected with the high-temperature superconductivity and the existence of CuO_2 planes, is accounted for by the general features of their crystal structure. *© 2000 MAIK “Nauka/Interperiodica”.*

It has been established that the oxygen subsystems of the yttrium- and bismuth-containing HTSC oxides possess unusual diffusion properties, namely, a record-high, at a level of 10^5–10^6, anisotropy in the diffusion coefficients of oxygen tracer atoms and an anomalously high oxygen mobility in the basal planes [1–4]. As a result, Fick's phenomenological equations turn out to be insufficient for a description of diffusion processes in single crystals of these compounds [5]. This accounts for the HTSC oxides having been placed into a specific class of superanisotropic diffusion systems [5]. It appeared of interest to establish the extent to which their anomalous diffusion characteristics are related to the quasiplanar structure of the compounds, their superconducting properties, and the presence in their structure of CuO_2-type planes. This has stimulated our present study of diffusion in the $Sr_{2.4}Ca_{1.6}Bi_2O_x$ oxide.

The choice of the subject was dictated primarily by [6], where this compound was proposed to be considered as a copper-free precursor of bismuth-containing HTSC oxides. The $Sr_{2.4}Ca_{1.6}Bi_2O_x$ bismuthite belongs to perovskite-like $Sr_{3.5-y}Ca_{0.5-y}Bi_2O_7$ solid solutions, with $0 \leq y \leq 1.1$ (monoclinic structure, space group $c2/m$ [7]). A preliminary study of the temperature dependence of the permeability of samples revealed no superconductivity in this compound down to 4.2 K.

The traditional approach to such a problem assumes using single crystals to study diffusion and carrying out complex structural measurements of the compound by means of X-ray, neutron, and electron diffraction techniques, including those on single crystals. This work followed an alternative approach based on the so-called site-plane effect [8]. The phenomenon observed on the HTSC 123 yttrium oxide lies in consecutive filling by ^{18}O atoms of energetically inequivalent lattice sites under isochronous annealing of a sample in gaseous oxygen enriched in the ^{18}O isotope. The isotope exchange kinetics are studied on polycrystalline samples [5, 8]. The possibility of observing the site-plane effect is directly connected with the anomalous diffusion in superanisotropic systems [5, 8]. This permits a comprehensive description of diffusion in the object under study without direct measurements of the diffusion coefficient anisotropy.

Investigation of the site-plane effect can yield information not only on the energy states of oxygen atoms, but on the number of sites of each species as well, i.e., data on the atomic structure of the object. This has initiated an attempt at identification of the atomic structure of $Sr_{2.4}Ca_{1.6}Bi_2O_x$ by diffusion measurements. It can be considered as a method of structural-diffusion analysis. This approach obviously has a methodological potential as well.

1. SAMPLES AND TECHNIQUES

1.1. Samples

The $Sr_{2.4}Ca_{1.6}Bi_2O_x$ bismuthite was prepared by a technique described elsewhere [6] (annealing of a mixture of the starting reagents at 850°C). The X-ray diffraction pattern of the sample was identical with the reference [6], thus indicating it to be single phase.

The powder was pressed into a cylinder 3 mm thick and 10 mm in diameter. The samples were strengthened by annealing for several hours in air at 850°C with subsequent rapid cooling. Next, the pellets were annealed for 4 hours in chemically pure oxygen at 700°C and a pressure of 0.21 atm, followed by rapid cooling. The samples thus obtained were porous. The isotope exchange in such objects was found to proceed with the same kinetics in crystallites on the outer surface of the samples and at a depth of tens of microns, which implies that gaseous oxygen penetrated freely into the intergrain space in the course of annealing.

The concentrations of the metallic components in samples were not monitored and were estimated from the weights of the starting powders. Following the recommendations of [6], the oxygen content in the $Sr_{2.4}Ca_{1.6}Bi_2O_x$ samples was refined. It was found to be $x = 8.8$. The measurements were made by the nuclear microanalysis method (see Section 1.3).

1.2. Isochronous and Isothermal Anneals

Diffusion anneals were carried out in a quartz tube at a pressure of 0.21 atm in an oxygen atmosphere enriched in the ^{18}O isotope to 80%. The isotope composition of the gas phase was constant for the duration of annealing.

Isochronous anneals were carried out in the following way. The samples were kept at the same temperature for 2 h, and the temperature of each subsequent anneal was higher by 20°C than that of the preceding one. In all, 28 isothermal anneals were carried out in the 400–940°C temperature range. After each anneal, the sample was cooled down to room temperature, and the concentration profiles of the oxygen isotopes were measured. The time taken to reach a constant temperature did not exceed 10 min, and the cooling time was approximately 1 min.

The isothermal anneals performed at temperatures from 340 to 450°C and aimed at measuring the diffusion coefficients made up a separate series. These anneals lasted from 20 min to 5 h, and the other conditions were the same as in the isotope exchange kinetics studies.

The temperature was measured to within ±1°C with a chromel–alumel thermocouple. The quartz tube used in the anneals was placed inside a massive metal cylinder. As a result, there was no temperature gradient within the above accuracy at the sample location.

1.3. Concentration Profile Measurements

The concentration profiles of the ^{16}O and ^{18}O isotopes were measured down to a depth of 1 μm by the nondestructive technique of nuclear microanalysis. This technique makes use of the $^{16}O(d, p)^{17}O^*$ and $^{18}O(p, \alpha)^{15}N$ reactions at primary-beam particle energies of 900 and 762 keV, respectively. The diameter of the primary proton and deuteron beams was 1 mm, so that a concentration measurement was actually an average over a large number of grains. The plane surface of the samples was set at right angles to the axis of the primary beam, and the nuclear-reaction products were detected at 160°. The energy spectra of protons and α particles were measured with a silicon surface-barrier detector with a diameter of about 10 mm and an energy resolution of 20 keV. To absorb the back-scattered deuterons and protons, Dacron films 16 and 10 μm thick, respectively, were placed in front of the detector. The deuteron and proton beam currents during a spectrum measurement were determined to within 0.6% with a secondary monitor. The rms errors were less than 10% for the lowest isotope concentrations, and 1% for the high ones. The concentration profiles of the oxygen isotopes were derived from the spectra of the reaction products using data on the stopping powers of the system under study. These data were calculated with the use of tabulated information on the pure components and Bragg's additivity rule [9]. More details on the concentration profile calculation can be found in [10, 11].

After the annealing, we systematically recorded Rutherford backscattering spectra of deuterons at a 900-keV primary beam energy. The quality of these measurements was not high enough to determine, with an acceptable degree of accuracy, the content of all metallic components. These measurements reliably showed, however, that the average bismuth and strontium concentrations in the grain surface layers (down to a depth of ~1 μm) did not change to within an error of 1%.

2. RESULTS AND DISCUSSION

2.1. Isotope Exchange Kinetics in Isochronous Anneals

Figure 1 presents the oxygen isotope concentrations measured in a $Sr_{2.4}Ca_{1.6}Bi_2O_{8.8}$ sample after isochronous anneals. The relative ^{18}O concentration A (at. %) in the oxygen subsystem is reduced to the gaseous phase enrichment factor by the ^{18}O isotope taken as 100%, i.e.,

$$A = (100/\alpha)c_{18}/(c_{16} + c_{18}), \qquad (1)$$

where c_{16} and c_{18} are the ^{16}O and ^{18}O concentrations in the sample, respectively, and $\alpha = 0.8$ is the ^{18}O isotope enrichment factor for the gaseous phase in the experiments. The data relate to the sample surface. Above 550°C, the ^{18}O isotope concentration did not practically depend on depth. Thus, the results displayed in Fig. 1 characterize the whole depth range studied in the sample for $T > 500$°C.

The total oxygen concentration ($c_{16} + c_{18}$) was depth-independent in all experiments. At the same time, the oxygen index of the $Sr_{2.4}Ca_{1.6}Bi_2O_x$ oxide varied with increasing temperature, with $x = 8.8$ at 740°C and $x = 8.0$ for the 760–880°C range. As the temperature was further increased, the value of x decreased continuously. X-ray diffraction measurements detected a structural rearrangement above 880°C, which was accompanied by a change in the sample color. There-

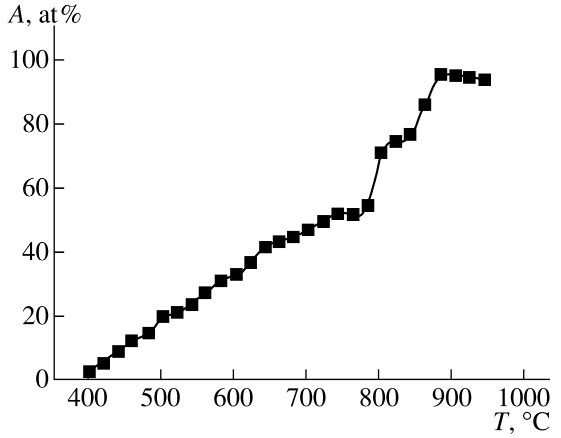

Fig. 1. Relative ^{18}O concentration in $Sr_{2.4}Ca_{1.6}Bi_2O_{8.8}$ *vs* isochronous annealing temperature.

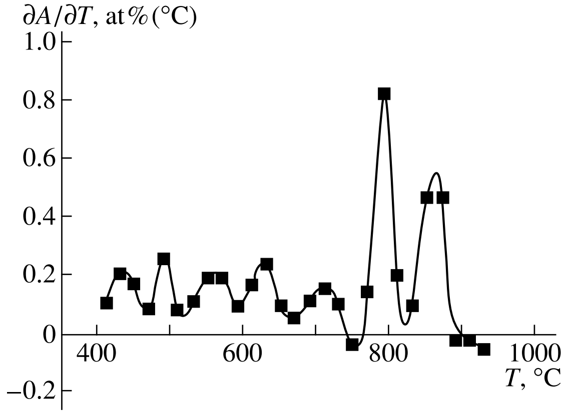

Fig. 2. Isochronous annealing peaks.

fore, our attention was subsequently focused on the results obtained in anneals below 880°C.

The dependence of the $\partial A/\partial T$ function on temperature is presented graphically in Fig. 2. One readily sees seven distinct peaks of isochronous annealing. Thus, we have established a discrete character of the energy spectrum, both for the equilibrium oxygen-atom states and for the heights of the barriers separating the equilibrium sites of various types. The spectrum in Fig. 2 is close in its main characteristics (the peak heights, widths, and spacing) to that obtained earlier for the HTSC 123 yttrium oxide. This may indicate that the oxygen subsystem of the compound under study contains several types of geometrically and energetically inequivalent sites, as is the case, for instance, with HTSC oxides. Alternatively, the observed effect in a solid solution could originate from differences in the metal atom environments of the geometrically equivalent sites occupied by oxygen atoms. In the first case, the density of oxygen distribution over the sites is determined only by the lattice structure of the compound under study, and in the second, by metal atom concentrations and the extent of long- or short-range order in the metal subsystem. These distributions can be expected to be essentially different. Therefore, we are going to analyze in what follows the concentrations A_i of the ^{18}O atoms reached at the moment of completion of each *i*th peak; these data are listed in the table. Also shown for comparison are a scheme of ^{18}O substitutions for the ^{16}O atoms in an HTSC oxide $Bi_2Sr_2CaCu_2O_{8+\delta}$ and the concentrations A_i^{cal} calculated using this scheme for the compound. The table also contains the temperatures $T_m^{(i)}$ corresponding to the maxima of the $\partial A/\partial T$ function for the *i*th peak, and the activation energies E_i for the corresponding isotopic exchange stages.

As seen from the table, the experimental and calculated values of A_i and A_i^{cal} are in almost perfect agreement. Some differences between the first and seventh peaks appear insignificant. As already mentioned, the last peak forms at the destruction of the lattice. Moreover, one cannot exclude the presence in the samples of foreign phases in amounts of a few percent. As for the

Characteristics of isochronous annealing peaks

Peak no., *i*	A_i, at %	A_i^{cal}, at %	Planes and sites in the $Bi_2Sr_2CaCu_2O_{8+\delta}$ lattice entered by ^{18}O atoms in peak *i*	$T_m^{(i)}$, K	E_i, eV
1	13.3 ± 0.5	15.90	Bi–O + δ/2 plane	708	–
2	20.9 ± 0.6	20.45	δ/2	763	2.3
3	31.7 ± 0.6	31.81	Bi–O plane	833	2.5
4	43.3 ± 0.8	43.17	SrO plane	903	2.7
5	50.8 ± 1.0	50.00	″	988	3.0
6	75.0 ± 1.5	75.00	Two CuO_2 planes, half of the sites	1063	3.2
7	94.6 ± 2.0	100.00	″	1133	3.4

first peak, the kinetics of its formation have a complex pattern because of the influence of a surface energy barrier (for more details, see Section 2.2), and the A_1 concentration could be lowered for kinetic reasons.

Consider now the relation between the substitution scheme proposed for the $Bi_2Sr_2CaCu_2O_{8+\delta}$ compound in the table and the isotope exchange kinetics in the subject under study. The fast oxygen diffusion in HTSC oxides is usually related with a modulation of the structure in the double Bi_2O_2 bismuth layers [12]. Taking into account the absence in the compound under study of CuO_2 planes and the presence in it of bismuth in the same compositional ratio with the other metal components as in the HTSC lattices, it appears reasonable to conjecture that, in the $Sr_{2.4}Ca_{1.6}Bi_2O_{8.8}$ compound, the oxygen atoms also have the highest mobility on the Bi–O planes. Judging from its position on the temperature scale, it is peak *1* that should be identified with this mobile oxygen. If this is so, then Fig. 2 and the table (peaks *1*, *3*) suggest that the oxygen atoms can occupy, on the Bi–O planes of the compound under study, energetically inequivalent sites of two types. This result is in accord with the data [13, 14] showing that the bismuth and oxygen atoms in Bi_2O_2 layers of HTSC oxides are distributed statistically between two closely spaced sites. One also cannot rule out that the difference between the values of A_1 and A_1^{cal} in the table is not due to kinetic reasons, but rather to the corresponding statistical distribution of oxygen atoms between two closely spaced sites.

An analysis of isotopic exchange data obtained for the excess oxygen δ also proves the existence of similarities between the bismuth HTSC oxides and the system under study. As seen from the data obtained, the sites occupied by the excess oxygen (peaks *1* and *2*) are replaced in isochronous anneals in the same temperature range as those in the Bi_2O_2 layer (peaks *1* and *3*). These findings obviously imply the geometrical closeness of the two sites in the oxygen sublattice.

We note in this connection that the excess oxygen was shown by neutron-diffraction studies to be located in the Bi_2O_2 layers in bismuth-containing cuprates as well ($Bi_2Sr_2CaCu_2O_{8+\delta}$, $Bi_2SrCa_2Cu_2O_{8+\delta}$ and some others [15]). As already mentioned, $Sr_{2.4}Ca_{1.6}Bi_2O_x$ undergoes at 760°C a discontinuous decrease of the oxygen concentration in a sample down to $x = 8$. Two observations suggest that the sample loses excess oxygen at this temperature. First, starting from 760°C, the chemical formula of the solid solution is $Sr_{2.4}Ca_{1.6}Bi_2O_8$. Second, the measurements revealed a decrease at 760°C of the concentration of the ^{18}O, rather than of the ^{16}O isotope. This becomes manifest in the negative derivative $\partial A/\partial T$ at the completion of peak *5* (Fig. 2).

The interpretation of the isochronous anneal peaks *4–7* appears obvious. Peaks *4* and *5* correspond to the ^{18}O atoms occupying the sites on the SrO-type planes. The presence of two peaks (rather than one) is most likely associated with the oxygen atoms jumping to energetically equivalent final positions from inequivalent starting sites; in other words, oxygen atoms reach the same structural fragments (SrO-type planes) from Bi_2O_2 layers characterized by two different oxygen states. The two-stage substitution on two CuO_2-type planes (peaks *6, 7*) is explained by the existence in the corresponding plane of sites of two types for the oxygens. Studies of the site-plane effect revealed the corresponding feature of the CuO_2 planes in yttrium-based HTSC oxides [8]. It is associated most likely with unequalness of the lattice parameters *a* and *b* in the oxide basal plane.

The above analysis permits a conclusion that the oxygen distribution density over sites in the compound under study is governed by the structure of its lattice rather than by differences in the environment of the geometrically equivalent oxygen positions in a disordered system. The potential barrier distribution established here does not fit into traditional concepts of the barrier shape in systems with compositional disorder. For a given composition, such distributions typically have a maximum and drop rapidly at the edges (see, e.g., [16]). For these reasons, the observed isotope exchange kinetics can be treated as a site-plane effect, in which each isochronous anneal peak corresponds to substitutions by ^{18}O atoms on certain planes or sites on the oxygen sublattice.

The results obtained here do not contradict, even in details, the assumption that the structure of the oxygen sublattice of the compound under study is of the same type as that of the 2212 bismuth-containing HTSC oxide. Both sublattices are made up of four structural formations containing one oxygen atom for each metal atom, and two formations with two oxygen atoms per metal atom, which alternate in the same way. In the HTSC oxide, these are double Bi_2O_2 bismuth layers with sites of two types for oxygen atoms, SrO planes with sites of one type, and CuO_2 planes with inequivalent sites of two types. Both sublattices each have one structural formation, which accounts for fast in-plane diffusion of oxygen atoms. There are sites for the excess oxygen in this formation or near it (in bismuth-containing HTSC oxides, it is the Bi_2O_2 layer). Nevertheless, the above considerations cannot be accepted as firm enough to conclude that the above sublattices are equivalent, because there is no one-to-one correspondence between the isotope exchange kinetics and the crystal lattice structure.

As seen from Fig. 2, the maximum isotopic exchange rate in each annealing stage occurs without any noticeable changes in the filling by ^{18}O atoms of the remaining layers, where the isotopic exchange has practically come to an end or has not yet started. Also, the absence in the sample of a concentration gradient of the ^{18}O and ^{16}O isotopes at temperatures above 500°C suggests that the formation of peaks *2–7* is not connected with conventional diffusion. In all probability, one could assume here jumps over an interatomic distance. This can be used to determine the activation energies E_i of individual annealing stages based only on the temperatures $T_m^{(i)}$ (see the table) at which one observes maxima in the $\partial A/\partial T$ curves. We used for the estimates the equation of first-order solid-phase reactions, which relates the quantities E_i and $T_m^{(i)}$ in the case of constant-rate sample heating [17]:

$$E_i = k_B (T_m^{(i)})^2 \nu_1 \exp\{-E_i/(k_B T_m^{(i)})\}, \quad (2)$$

where k_B is the Boltzmann constant and ν_i is the prefactor, which is actually the oxygen jump frequency for the *i*th peak. The values of E_i listed in the table were obtained for $\nu_i = 10^{12}$ s^{-1}. This value agrees in order of magnitude with the characteristic vibrational frequencies of oxygen atoms in oxides. If oxygen jumps involve structural vacancies, the jump frequencies ν_i may deviate strongly from the above value (by several orders of magnitude). According to (2), a change of ν_i by an order of magnitude brings about a change of E_i in the temperature range considered by 0.15–0.2 eV. Thus, one can maintain that, for some oxygen jump frequencies in the compound under study, the activation energies noticeably exceed 1 eV even in the presence of structural vacancies.

2.2. Diffusion of Oxygen Tracer Atoms

Superanisotropic HTSC oxides are characterized by anomalously fast oxygen-tracer diffusion in the basal planes ($CuO_{1-\delta}$ in the 123 yttrium HTSC oxide and double Bi_2O_2 bismuth layers in the 2212 and 2201 oxides). Studies of diffusion in polycrystals provide a certain idea of the diffusion parameters in the basal plane. If the following condition for the diffusion-coefficient tensor components

$$D_{xx} = D_{yy} \gg D_{zz}, \quad (3)$$

is met, then the diffusion coefficient in a polycrystal, D_{poly}, is related to D_{ij} through $D_{\text{poly}} = (2/3)D_{xx}$, provided that the crystallite distribution is not textured [3].

The mere fact of observation of the site-plane effect is evidence of a strong anisotropy of the diffusion coefficients. Considered from this standpoint, the results obtained in Section 2.1 are in agreement with (3). At the same time, we do not have any information at our disposal on the relative magnitude of the D_{xx} and D_{yy} coefficients for the compound under study.[1] However, even with such an uncertainty, the inequality $D_{\text{poly}} < D_{xx}$ does hold. As a result, by measuring the diffusion coefficient in polycrystals, one can find the lower limit of D_{xx} for the $Sr_{2.4}Ca_{1.6}Bi_2O_{8.8}$ oxide.

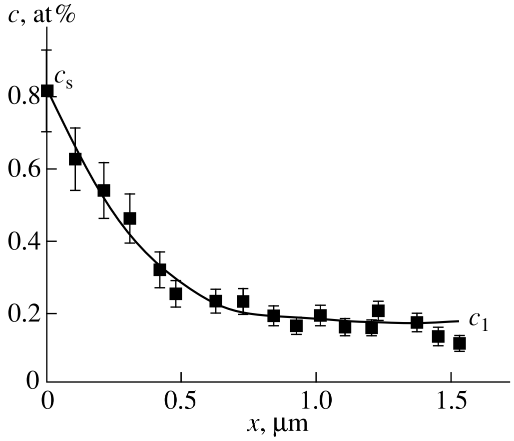

Fig. 3. Concentration profile of the ^{18}O isotope after annealing a polycrystalline $Sr_{2.4}Ca_{1.6}Bi_2O_{8.8}$ sample at 430°C for 0.5 h.

The corresponding values of D_{poly} were derived from the concentration profiles $c(x, t)$ of ^{18}O in the samples which were subjected to diffusion annealing in a ^{18}O-enriched oxygen atmosphere. The diffusion anneals were carried out in conditions that were only favorable for the processes responsible for the first (diffusion) peak in the isochronous annealing plots. We have succeeded in measuring D_{poly} only within a narrow temperature interval from 340 to 450°C.

Figure 3 displays a typical concentration profile. At large depths x, the concentration c_1 is seen to be practically constant. Its values are several times as high as the original concentration of the ^{18}O isotope in the samples, which is determined by the natural oxygen-isotope abundance. The ^{18}O concentrations at the surface, c_s, were found to be lower than the value corresponding to sites of the first type in the Bi–O planes completely filled by ^{18}O. Both c_s and c_1 increased with increasing annealing time t.

The above features in the concentration profiles were observed by us earlier when studying oxygen diffusion in polycrystalline yttrium- and bismuth-based HTSC oxides. An analysis showed that the time dependence of c_s is primarily due to the existence of a surface energy barrier for oxygen atoms. The behavior of c_1 should be assigned most likely to free penetration of oxygen between the grains and subsequent ^{18}O migration in the directions of enhanced diffusion. Therefore, the concentration profiles were fitted by the following

---

[1] Note that, as far as we know, there is no such information on the HTSC oxides either.

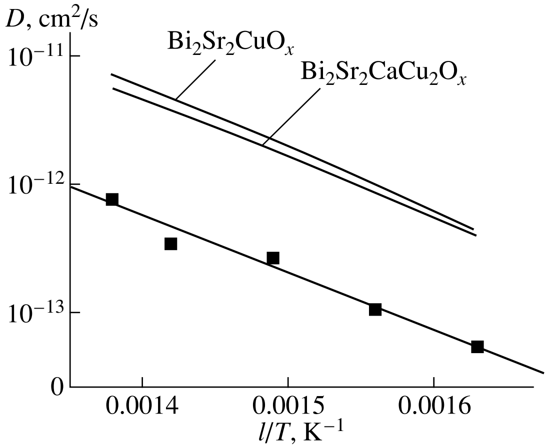

Fig. 4. Temperature dependence of the oxygen tracer diffusion coefficients in polycrystalline $Sr_{2.4}Ca_{1.6}Bi_2O_{8.8}$. The plots for $Bi_2Sr_2CuO_x$ [2] and $Bi_2Sr_2CaCu_2O_x$ [3] are temperature dependences of the diffusion coefficients measured in the basal plane of the single crystals.

asymptotic expression for a semi-infinite sample [5]:

$$[c(x,t)-c_1]/c_0 = \operatorname{erfc}(Z) + \sum_{i=1}^{2}\eta(\eta_i-2\eta)^{-1}$$

$$\times \exp\{\eta_i[x/a+\eta_i t/\tau]\}\operatorname{erfc}\{Z+\eta_i(t/\tau)^{1/2}\}, \qquad (4)$$

$$Z = x/(4D_{\mathrm{poly}}t)^{1/2}, \quad \eta = \tau/\tau_b \ll 1,$$

$$\eta_{1,2} = [1 \pm (1-4\eta)^{1/2}]/2,$$

where c_0 is the equilibrium concentration of ^{18}O atoms at the crystal–gas interface, a is the characteristic jump distance in the direction of the diffusion axis, τ is the time between oxygen atom jumps in the direction of fast diffusion, and τ_b is a time parameter characterizing the potential barrier for oxygen at the crystal–gas interface.

As seen from Fig. 3, the experimental points fit satisfactorily into the $c(x, t)$ curve calculated using (4). The statistical margin of error in diffusion coefficient measurements was 10%.

The temperature dependence of D_{poly} is presented graphically in Fig. 4, with experimental data on D_{xx} obtained on the bismuth-containing $Bi_2Sr_2CuO_x$ and $Bi_2Sr_2CaCu_2O_x$ HTSC oxides [2, 3] shown also for comparison. The values of D_{poly} were found to be very high, which suggests fast diffusion of the oxygen tracer atoms in $Sr_{2.4}Ca_{1.6}Bi_2O_{8.8}$. Considered on diffusion scales, the differences between the data for the HTSC oxides and the copper-free $Sr_{2.4}Ca_{1.6}Bi_2O_{8.8}$ oxide are not large. The corresponding diffusion activation energies for the above oxides are 0.9 eV for $Sr_{2.4}Ca_{1.6}Bi_2O_{8.8}$ and 1.01 and 0.93 eV for the HTSC oxides. The diffusion activation energy found and the earlier isotope-exchange results (see table) show that diffusion in the compound under study and in the HTSC oxides proceeds in similar ways. The activation energy of oxygen tracer diffusion in the basal planes of the latter is close to 1 eV, and, in the perpendicular direction, is in excess of 2 eV [2, 3].

Thus, it has been shown that the oxygen subsystem of the $Sr_{2.4}Ca_{1.6}Bi_2O_{8.8}$ oxide is an analog of the corresponding subsystems of the yttrium- and bismuth-containing HTSC oxides from the standpoint of diffusion. This manifests itself in the fast diffusion in all these compounds and the existence of the site-plane effect in isochronous annealing, which is equivalent to the observation of a strong anisotropy in diffusion. Note that the characteristics of diffusion in the yttrium- and bismuth-containing HTSC oxides and in $Sr_{2.4}Ca_{1.6}Bi_2O_{8.8}$, i.e., all presently known diffusionally superanisotropic objects, are similar. The superanisotropic diffusion in these systems is not connected with the high-temperature superconductivity and the presence of CuO_2 layers in the oxides. The necessary condition for its existence is the quasiplanar pattern of the structure, which includes planes with strongly differing concentrations of structural “defects” responsible for the diffusion characteristics. The role of the planes with high concentrations of these defects is played by the $CuO_{1-\delta}$ planes with structural vacancies (for instance, in the yttrium-containing HTSC oxide), and by the double bismuth layers in modulated structures of bismuth-containing HTSC oxides, as well as probably in the copper-free $Sr_{2.4}Ca_{1.6}Bi_2O_{8.8}$ system.

ACKNOWLEDGMENTS

The authors are indebted to R.G. Zakharov for his interest in this work and stimulating discussions.

Support of the Scientific Council on HTSC within the High-Temperature Superconductivity program (grant no. 96076) and of the Russian Foundation for Fundamental Research (grant no. 96-03-32106) is gratefully acknowledged.

REFERENCES

1. S. J. Rothman, J. L. Routbord, J.-Z. Liu, *et al.*, Defect Diffus. Forum **75**, 57 (1991).
2. M. Runde, J. L. Routbord, J. N. Mundy, *et al.*, Phys. Rev. B **46**, 3142 (1992).
3. M. Runde, J. L. Routbord, S. J. Rothman, *et al.*, Phys. Rev. B **45**, 7375 (1992).
4. S. Tsukui, T. Yamamoto, M. Adachi, *et al.*, Physica C **185–189**, 929 (1991).
5. V. B. Vykhodets, T. E. Kurennykh, K. V. Trifonov, *et al.*, Zh. Éksp. Teor. Fiz. **106**, 648 (1994) [JETP **79**, 355 (1994)].
6. B. V. Slobodin, V. G. Vasil’ev, and E. E. Soldatova, Zh. Neorg. Khim. **42**, 1740 (1997).

7. R. S. Roth, B. P. Burton, and C. J. Rawn, Ceram. Trans. **13**, 23 (1990).
8. V. B. Vykhodets, T. E. Kurennykh, A. A. Fotiev, *et al.*, Pis’ma Zh. Éksp. Teor. Fiz. **58**, 421 (1993) [JETP Lett. **58**, 431 (1993)].
9. *The Stopping and Ranges of Ions in Matter*, Ed. by J. F. Ziegler (Pergamon Press, New York, 1972).
10. V. B. Vykhodets, S. M. Klotsman, T. E. Kurennykh, *et al.*, Fiz. Met. Metalloved. **63**, 974 (1987).
11. V. B. Vykhodets, S. M. Klotsman, and A. D. Levin, Fiz. Met. Metalloved. **64**, 920 (1987).
12. C. J. Zhou, X. M. Xie, and T. G. Chen, Physica C **191**, 185 (1992).
13. M. A. Subramanian, C. C. Torardi, J. Gopalakrishnan, *et al.*, Physica C **153–155**, 608 (1988).
14. M. A. Subramanian, C. C. Torardi, J. C. Calabrese, *et al.*, Science **239**, 1015 (1988).
15. C. N. Rao, Defect Diffus. Forum **75**, 1 (1991).
16. I. M. Lifshits, S. A. Gredeskul, and L. A. Pastur, *Introduction to the Theory of Disordered Systems* (Nauka, Moscow, 1982).
17. M. E. Brown, D. Dollimore, and A. K. Galway, in *Reactions in the Solid State*, Ed. by C. Tipper and C. Bamford (Elsevier, Amsterdam, 1980; Mir, Moscow, 1983).

Translated by G. Skrebtsov

Physics of the Solid State, Vol. 42, No. 4, 2000, pp. 616–620. Translated from Fizika Tverdogo Tela, Vol. 42, No. 4, 2000, pp. 602–605.
Original Russian Text Copyright © 2000 by Bespyatykh, Wasiliewski.

METALS AND SUPERCONDUCTORS

Electric Current Distribution in a Superconducting Film with Ferromagnetic Coatings

Yu. I. Bespyatykh* and W. Wasiliewski**
**Institute of Radio Engineering and Electronics (Fryazino Branch), Russian Academy of Sciences,*
pl. Vvedenskogo 1, Fryazino, Moscow oblast, 141120 Russia
e-mail: svg318@ire216msk.su
***Technical University, Radom, Poland*

Received August 11, 1999

Abstract—This paper reports on a calculation of the spatial electric-current distribution in a superconducting film coated with a ferromagnetic material with one-dimensional surface roughness. It is shown that using coatings with a high magnetic susceptibility permits one to create substantial current nonuniformities in the superconducting-film plane and an anisotropic dependence of the current distribution on its direction relative to that of the nonuniformity. *© 2000 MAIK “Nauka/Interperiodica”.*

The discovery of high-temperature superconductivity and progress in the nanostructure technology have intensified the investigation of systems containing superconducting and magnetic components. It was shown that structures with the ferromagnet spin subsystem exchange-coupled with the conduction electrons of a superconductor can have spatially nonuniform states [1–3] similar to the cryptoferromagnetic state in ferromagnetic superconductors [4, 5]. In layered structures with localized magnet spins interacting electromagnetically with the paired electrons of a superconductor, magnetic domains may be suppressed if the ferromagnetic film has a less than critical thickness [6–11]. The effects associated with the formation of weak bonds through the domain scattering fields in a ferromagnet [9, 12], artificial pinning of Abrikosov vortices by means of magnetic coatings [13, 14], and their depinning by reducing the vortex dissipation fields using magnetic materials with a high static magnetic susceptibility [15, 16] have a considerable application potential.

When analyzing the effect of magnetic inclusions and magnetic coatings on vortex pinning, one usually ignores the action of the transport current on magnetization and the reverse influence of a change in magnetization on the transport current distribution in superconducting films. While in many cases this is justified, in certain situations, for example in the case where the external magnetic field is close to the field of a reorientation phase transition in a magnet, the static susceptibility of the magnet is high, so that the problem of an electric current flowing through a superconductor and of the magnetization distribution in a magnet should be solved in a self-consistent way. This work considers several systems in which the closeness of a superconductor to a ferromagnet results in a substantial redistribution of the transport current in the superconducting film.

1. Calculate the spatial distribution of a superconducting current near a plane surface $y = 0$ of a bulk type-II superconductor ($R \longrightarrow \infty$) adjacent to a uniaxial ferromagnet (Fig. 1). We shall assume the easy-magnetization axis $\mathbf{n}_A$ of the ferromagnet and the current density $\mathbf{j}(\mathbf{r})$ to be parallel to the superconductor surface ($\mathbf{n}_A \| \mathbf{j} \| \mathbf{n}_z$). We neglect the effect of nonuniform exchange and the possible spin pinning at the magnet surface by assuming the characteristic spatial scale of magnetization variation $\Lambda \gg \alpha^{1/2}$ (α is the nonuniform exchange constant).

The magnetic field $\mathbf{H}$ in the system is the sum of the field $\mathbf{H}_0$ associated with the transport current in the absence of the magnet and of the dipole field $\mathbf{H}_D$ created by the magnetization $\mathbf{M}$

$$\mathbf{H} = \mathbf{H}_0 + \mathbf{H}_D. \tag{1}$$

The total field $\mathbf{H}$ and the total current density $\mathbf{j}$ in a

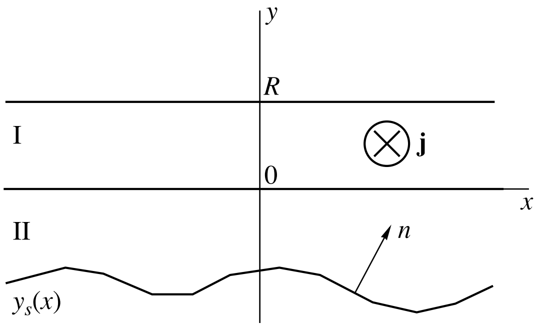

Fig. 1. Geometry of the structure made up of a superconducting film (I) and a ferromagnetic coating with a rough surface (II).

superconductor satisfy the London equation and the magnetostatics equations

$$\mathbf{H} + \lambda^2\nabla\nabla\mathbf{H} = 0, \quad \nabla\mathbf{H} = (4\pi/c)\mathbf{j}, \quad \nabla\mathbf{H} = 0, \qquad (2)$$

where λ is the London magnetic-field penetration depth and c is the velocity of light in vacuum. There is no electric current outside the superconductor, and the distributions of the field **H** and the magnetization **M** are described by the equation of state

$$[\mathbf{M}(\mathbf{H}_0 + \mathbf{H}_D)] = 0 \qquad (3)$$

and the Laplace and Poisson equations for the scalar potentials Ψ_0 and Ψ_D of the magnetic fields $\mathbf{H}_0 = \nabla\Psi_0$, $\mathbf{H}_D = \nabla\Psi_D$

$$\Delta\Psi_0 = 0, \quad \Delta\Psi_D = -4\pi(\nabla\mathbf{M}). \qquad (4)$$

At the interfaces separating the media, the standard electrodynamic continuity conditions for the tangential components of the magnetic field **H** and the normal component of the magnetic induction $\mathbf{B} = \mathbf{H} + 4\pi\mathbf{M}$ are met. The static state of the system in a field $\mathbf{H}_0$ playing the part of an external field corresponds to the minimum of the Gibbs potential G defined as

$$\begin{aligned} G &= \frac{1}{8\pi}\int_V d\mathrm{v}(\mathbf{H} - \mathbf{H}_0)^2 \\ &- \int_{V_f} d\mathrm{v}\left(\mathbf{H}_0\mathbf{M} + \frac{\beta}{2}M_z^2\right) + \frac{\lambda^2}{8\pi}\int_{V_s} d\mathrm{v}(\nabla\mathbf{H})^2, \end{aligned} \qquad (5)$$

where $\beta > 0$ is the uniaxial anisotropy constant of the ferromagnet and V, V_f, V_s are the volumes of the system, ferromagnet, and superconductor, respectively.

Let the lower surface of the ferromagnet be rough, so that its coordinates will be given by the equation $y = y_s(x)$, and its inward normal **n** will be

$$\mathbf{n} = \frac{\mathbf{n}_y - (dy_s/dx)\mathbf{n}_x}{\sqrt{1 + (dy_s/dx)^2}}. \qquad (6)$$

Consider first the case of a small and smooth periodic nonuniformity

$$y_s(x) = -L = a\cos kx, \qquad (7)$$

where $a \ll L$, $ak \ll 1$. We are going to look for the expressions for the field and current density in the form of expansions in powers of the amplitude of the roughness a to first order in a inclusive.

In a zeroth approximation, the superconducting current density $\mathbf{j}_0(\mathbf{r})$ depends on the coordinate y only:

$$\mathbf{j}_0 = -\mathbf{n}_z J_0 \exp(-y/\lambda), \qquad (8)$$

and the magnetic field $\mathbf{H}_0(y)$ is described by the expression

$$\mathbf{H}_0 = \mathbf{n}_x \begin{cases} (4\pi/c)\lambda J_0 \exp(-y/\lambda), & y > 0, \\ (4\pi/c)\lambda J_0, & y < 0. \end{cases} \qquad (9)$$

The magnetization $\mathbf{M}_0$ is parallel to the superconductor surface, and its components $M_{0x,\,z}$ are related to the total current $I_0 = \lambda J_0$ per unit width of the system along the $\mathbf{n}_x$ axis through

$$\begin{gathered} M_{0x} = M_0\sin\vartheta_0, \quad M_{0z} = M_0\cos\vartheta_0, \\ \sin\vartheta_0 = 4\pi I_0/(c\beta M_0), \end{gathered} \qquad (10)$$

where M_0 is the saturation magnetization of the ferromagnet.

The first approximation in the roughness amplitude a for the current density $\mathbf{j}_1$ and magnetic field $\mathbf{H}_1$ in the superconductor can be written as

$$\mathbf{J}_1 = \mathbf{n}_z(kc/4\pi\lambda^2\tau)A_1\cos(kx)\exp(-\tau y), \qquad (11)$$

$$\mathbf{H}_1 = kA_1[\mathbf{n}_x\cos kx - \mathbf{n}_y(k/\tau)\sin(kx)]\exp(-\tau y), \qquad (12)$$

and the dipole-field potential in the ferromagnet Ψ_{D1} is

$$\begin{aligned} \Psi_{D1} &= A_1[\cosh(qy) \\ &- (k^2/q\tau\mu_{yy})\sinh(qy)]\sin(kx), \end{aligned} \qquad (13)$$

where

$$\begin{aligned} A_1 &= 4\pi akM_{0x}[k\cosh(qL) + q\mu_{yy}\sinh(qL) \\ &+ (k^2/q\tau\mu_{yy})(k\sinh(qL) + q\mu_{yy}\cosh(qL))]^{-1}, \\ q^2 &= k^2\mu_{xx}/\mu_{yy}, \quad \tau^2 = k^2 + \lambda^{-2}, \end{aligned} \qquad (14)$$

$\mu_{xx} = 1 + (4\pi/\beta)\cos^2\vartheta_0$ and $\mu_{yy} = 1 + 4\pi/\beta$ are the components of the magnetic permeability tensor μ of the ferromagnet.

The maximum relative change in the transport current density induced by the reverse influence of magnetization, $\varepsilon = j_1(x = 0, y = 0)/J_0$, for a thin ferromagnet, $qL \propto kL \ll 1$, can be presented in the form

$$\varepsilon = \frac{4\pi ak}{\beta\lambda\tau(1 + k\tau + \mu_{xx}kL)}. \qquad (15)$$

In the opposite case of $qL \propto kL \gg 1$, we have

$$\varepsilon \cong \frac{8\pi ka}{\beta}\frac{kq\mu_{yy}}{\lambda(k + q\mu_{yy})(k^2 + q\tau\mu_{yy})}\exp(-qL). \qquad (16)$$

According to (16), for thick magnetic coatings, the effect of their surface roughness on the transport-current distribution is exponentially small. However, for relatively thin coatings (15) with a weak anisotropy, $\beta \ll 4\pi$, $kL\mu_{xx} \le 1$, ε may be appreciable, as a result of which the approximate method of calculation employed by us becomes invalid.

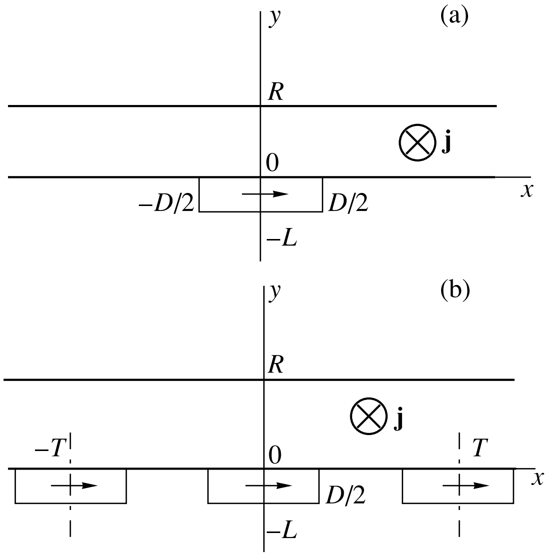

Fig. 2. (a) Superconducting film–ferromagnetic strip system; the arrow shows the projection of the magnetization on the x, y plane; (b) a system made up of a superconducting film and a periodic ferromagnetic-strip array.

For an isolated superconductor of thickness R, the distributions of the transport current and of the internal magnetic field generated by it have the form

$$\begin{aligned}\mathbf{j}_0 &= -\mathbf{n}_z J_0 \cosh[(|y| - R/2)/\lambda]/\cosh[R/(2\lambda)],\\ \mathbf{H}_0 &= \mathbf{n}_x(4\pi\lambda J_0/c)\\ &\times \sinh[(R/2 - |y|)/\lambda]/\cosh[R/(2\lambda)],\end{aligned} \tag{17}$$

and the magnetic-field components in the superconductor, considered in a first approximation in the small parameter a, are equal to

$$\begin{aligned}H_{1x} &= (B_1\cosh\tau y + C_1\sinh\tau y)\cos kx,\\ H_{1y} &= (k/\tau)(B_1\sinh\tau y + C_1\cosh\tau y)\sin kx,\\ B_1 &= kA_1, \quad C_1 = -kA_1(\tau\cosh\tau R\\ &+ |k|\sinh\tau R)/(\tau\sinh\tau R + |k|\cosh\tau R).\end{aligned} \tag{18}$$

The quantity A_1 is described by (14) as before, provided that one makes in it the following replacement:

$$\begin{aligned}&[k^2/(\tau q\mu_{yy})] \longrightarrow [k^2/(\tau q\mu_{yy})],\\ &(\tau\cosh\tau R + |k|\sinh\tau R)/(\tau\sinh\tau R + |k|\cosh\tau R).\end{aligned} \tag{19}$$

As follows from (17)–(19), ε decreases with a decrease in thickness of the superconducting film. In the case of thin magnetic and superconducting layers ($R \ll \lambda$, $qL \ll 1$),

$$\varepsilon \cong \pi aR/(\beta\lambda^2). \tag{20}$$

As λ increases, ε falls off monotonically in absolute magnitude, which justifies our restricting ourselves in what follows to an analysis of the limiting case of $\lambda \longrightarrow 0$.

2. Let us now determine the change in the distribution of surface transport current in a semi-infinite superconductor, induced by a ferromagnetic strip of thickness L and width D (Fig. 2a), and by an array of such strips with a period T (Fig. 2b). We shall use the variational technique to find the current, magnetic field, and magnetization in the system. We shall look for the minimum of the Gibbs potential G (12) of the system, which, in the conditions specified reduces to an integral over the volume of the magnetic material,

$$G = -\int\limits_{V_f} dv\left(\mathbf{MH}_0 + \frac{1}{2}\mathbf{MH}_D + \frac{\beta}{2}M_z^2\right), \tag{21}$$

assuming the magnetization in the strip to be uniform and parallel to the x, z plane. The magnetic field $\mathbf{H}_0$ of the unperturbed transport current in (21) is given by (9), and the potential Ψ_D of the dipole field $\mathbf{H}_D$ satisfies the equation

$$\begin{aligned}\Delta\Psi_D &= -2\pi[\delta(x + D/2) - \delta(x - D/2)]\\ &\times[\theta(y + L) - \theta(y - L)]M_x,\end{aligned} \tag{22}$$

where

$$\theta(y) = \begin{cases}1, & y > 0,\\ 0, & y < 0.\end{cases}$$

We shall subsequently need only the dipole field component

$$\begin{aligned}H_{Dx} &= -M_x\left(\arctan\frac{L + y}{D/2 + x} + \arctan\frac{L - y}{D/2 - x}\right.\\ &\left.+ \arctan\frac{L - y}{D/2 + x} + \arctan\frac{L + y}{D/2 - x}\right).\end{aligned} \tag{23}$$

Taking into account (23), the Gibbs energy of a unit length of the strip g becomes

$$g = 2DL(-H_0M_x + (\beta_{\text{eff}}/2)M_x^2), \tag{24}$$

where $\beta_{\text{eff}} = \beta + \tilde{\beta}$ is the effective-anisotropy constant

$$\begin{aligned}\tilde{\beta} &= (1/\nu)f(\nu),\\ f(\nu) &= [4\nu\,\text{arccot}\,\nu + 2\ln\nu\\ &+ (1 - \nu^2)\ln(1 + 1/\nu^2)],\\ \nu &= D/(2L).\end{aligned} \tag{25}$$

Minimization of (24) yields

$$M_x = H_0/\beta_{\text{eff}}. \tag{26}$$

Substituting (26) into (23) results in the following expression for ε:

$$\varepsilon = (4/\beta_{\text{eff}})\,\text{arccot}\,\nu. \tag{27}$$

For the case of a thin strip, $\nu \gg 1$, we have

$$\tilde{\beta} \cong (3 + 2\ln\nu)/\nu, \quad \varepsilon \cong 4/(\beta\nu + 3 + 2\ln\nu). \tag{28}$$

In cubic ferro- and ferrimagnets, the crystallographic anisotropy is, as a rule, small. To obtain a qualitative estimate of the anisotropy field, take the first cubic-anisotropy constant. For a temperature $t = 300$ K, we have $K_1 = 4.72 \times 10^5$ erg/cm^3 for iron [17], and $K_1 = -5.7 \times 10^4$ erg/cm^3 for nickel [18], where, in order of magnitude, $\beta \propto 0.1$. The values of K_1 for these substances vary little with decreasing temperature, because their Curie temperature is high [19]. For the yttrium–iron garnet, $K_1 \cong 1.5 \times 10^5$ erg/cm^3 at $t = 100$ K, and $K_1 \cong 2.5 \times 10^5$ erg/cm^3 at $t \cong 0$ K [19], which yields $\beta \propto 1$. According to (26), $|\varepsilon| \propto 1$ up to $\nu \propto 10^2$ for iron and nickel, and up to $\nu \propto 10$ for the YIG.

If the system is additionally placed in an external magnetic field $\mathbf{H}_e = H_e\mathbf{n}_z$, $H_e < H_{c1}$ (H_{c1} is the lower critical field of a superconductor), then a term $-2DLH_e(M_0^2 - M_x^2)^{1/2}$ should be added to the energy (24).

For a structure made up of a superconductor and a periodic magnetic strip array (Fig. 2b), the dipole field component H_{Dx} in magnets and in vacuum has the form

$$H_{Dx} = -M_x \sum_{n=-\infty}^{+\infty} \left(\arctan\frac{L+y}{D/2 + x_n} + \arctan\frac{L-y}{D/2 - x_n} \right. \\ \left. + \arctan\frac{L-y}{D/2 + x_n} + \arctan\frac{L+y}{D/2 - x_n} \right), \tag{29}$$

where $x_n = x + nT$ and the energy of the system per unit strip length is given by equation (24), if we set in it

$$\beta_{\text{eff}} = \beta + \tilde{\beta} + \tilde{\tilde{\beta}},$$

$$\tilde{\tilde{\beta}} = (1/\nu)\sum_{n=1}^{\infty}[f(n\delta + \nu) + f(n\delta - \nu) - 2f(n\delta)], \tag{30}$$

$$\delta = T/2L.$$

The appearance in (30) of the $\tilde{\tilde{\beta}}$ term is associated with the dipole interaction of the strip magnetic moments. This interaction reduced somewhat the change of the transport current under the strips, while at the same time increasing its change on the free surface of the superconductor. For $\nu \gg 1$, $\delta \gg 1$, and $\delta - \nu \gg 1$, we obtain

$$\tilde{\tilde{\beta}} \cong \frac{1}{\nu}\left[\frac{1}{3\delta^2}\left(-\frac{\pi^2}{6} - \frac{\delta^2}{2\nu^2} + \frac{\pi^2}{2\sin^2(\pi\nu/\delta)}\right) \right. \\ \left. + 2\ln\frac{\sin(\pi\nu/\delta)}{\pi\nu/\delta}\right]. \tag{31}$$

As seen from (29), the dipole field and the associated effect of the magnetic material on transport current disappear if the gap between the adjacent strips tends to zero.

The assumption of uniform magnetization does not apply to the regions in the bulk spaced from the strip edges by a distance of the order of the strip thickness (see, e.g., [20]). As for estimates of the current and magnetic field near the strip center, they remain correct as long as $\nu \gg 1$, i.e., under the condition that the total volume of these regions is small compared to that of the magnetic material.

If the current flows along the direction of the nonuniformity ($\mathbf{j} \parallel \mathbf{n}_x$), it does not change the state of the magnetic subsystem and remains uniform in the x, z plane, provided that the field $\mathbf{H}_0$ coincides in the direction of the magnetization in the magnetic coating. If, however, the field $\mathbf{H}_0$ is antiparallel to the magnetization, its increase may initiate a first-order phase transition involving magnetization reorientation along the field $\mathbf{H}_0$.

Thus, the distribution of the electric current and magnetic field in structures of the type under study depends substantially on its direction with respect to the symmetry axis of the system. Because a change in the current structure affects the conditions of formation and pinning of fluxons, hybrid systems should exhibit an anisotropy of the critical current as well, provided that the intrinsic vortex pinning in the superconducting film is small enough.

In our analysis of the ground state of the system, we did not touch on the role played by the domain structure in magnets. It is known, however, that the effective static susceptibility of magnetically soft materials in the domain phase is also high (see, e.g., [19]). If the domain dimensions are small compared to the width of the magnetic strips, one can derive an order-of-magnitude estimate of the effect in the presence of a domain structure from the equations presented in the first part of this work by replacing the tensor components of the ferromagnet permeability μ by those of the effective permeability in the inhomogeneous phase.

REFERENCES

1. A. I. Buzdin, L. N. Bulaevskiĭ, M. L. Kulich, *et al.*, Usp. Fiz. Nauk **144**, 597 (1984).
2. A. I. Buzdin and L. N. Bulaevskiĭ, Zh. Éksp. Teor. Fiz. **94**, 256 (1988) [Sov. Phys. JETP **67**, 576 (1988)].
3. M. G. Khusainov, Zh. Éksp. Teor. Fiz. **110**, 524 (1996) [JETP **83**, 533 (1996)].
4. P. W. Anderson and H. Suhl, Phys. Rev. **116**, 898 (1959).
5. *Superconductivity in Ternary Compounds*, Ed. by E. Fisher and M. Maple (Springer, Heidelberg, 1982; Mir, Moscow, 1985), Vol. 2.
6. A. F. Sadreev, Fiz. Tverd. Tela **35**, 2099 (1993) [Phys. Solid State **35**, 1044 (1993)].

7. Yu. I. Bespyatykh, W. Wasiliewski, M. Cajdek, *et al.*, Fiz. Tverd. Tela **36**, 586 (1994) [Phys. Solid State **36**, 323 (1994)].
8. A. Stankiewicz, S. Robinson, G. F. Gering, *et al.*, J. Phys.: Condens. Matter **9**, 1019 (1997).
9. Yu. I. Bespyatykh, W. Wasiliewski, É. H. Lokk, *et al.*, Fiz. Tverd. Tela **40**, 1068 (1998) [Phys. Solid State **40**, 975 (1998)].
10. Yu. I. Bespyatykh and W. Wasiliewski, Radiotekh. Élektron. **44** (9), 1 (1999).
11. Yu. I. Bespyatykh, É. H. Lokk, S. A. Nikitov, *et al.*, J. Magn. Magn. Mater. (in press).
12. É. B. Sonin, Pis'ma Zh. Tekh. Fiz. **14**, 1640 (1988) [Sov. Tech. Phys. Lett. **14**, 714 (1988)].
13. F. M. Sauerzopf, H. P. Wiesinger, W. Kritscha, *et al.*, Phys. Rev. B **43**, 3091 (1991).
14. W. Schindler, B. Roas, G. Saemann-Ischenko, *et al.*, Physica C **169**, 117 (1990).
15. Yu. I. Bespyatykh, W. Wasiliewski, and V. D. Kharitonov, Fiz. Tverd. Tela **39**, 231 (1997) [Phys. Solid State **39**, 203 (1997)].
16. Yu. I. Bespyatykh, W. Wasiliewski, and V. D. Kharitonov, Zh. Tekh. Fiz. **67** (7), 28 (1997) [Tech. Phys. **42**, 741 (1997)].
17. W. L. Becker and F. Döring, *Ferromagnetismus* (Springer, Berlin, 1939), p. 284.
18. W. Heisenberg, Z. Phys. **69**, 287 (1931).
19. S. Chikasumi, *Physics of Ferromagnetism: Magnetic Characteristics and Engineering Application* (Syokabo, Tokyo, 1984; Mir, Moscow, 1987).
20. R. I. Joseph and E. Schlömann, J. Appl. Phys. **35**, 159 (1964).

Translated by G. Skrebtsov

Physics of the Solid State, Vol. 42, No. 4, 2000, pp. 621–625. Translated from Fizika Tverdogo Tela, Vol. 42, No. 4, 2000, pp. 606–610.
Original Russian Text Copyright © 2000 by Nasredinov, N. Seregin, P. Seregin.

METALS AND SUPERCONDUCTORS

Spatial Distribution of Defect Electrons in the $Y_2Ba_4Cu_7O_{15}$ Lattice

F. S. Nasredinov, N. P. Seregin, and P. P. Seregin
St. Petersburg State Technical University, ul. Politekhnicheskaya 29, St. Petersburg, 195251 Russia

Received September 7, 1999

Abstract—The method of emission Mössbauer spectroscopy on the $^{67}Cu(^{67}Zn)$ isotope is used for determining the parameters of nuclear quadrupole interaction at copper sites of the $Y_2Ba_4Cu_7O_{15}$ lattice. The tensor of crystal electric field gradient at all the sites of the lattice is calculated using the model of point charges. A comparison of experimental and calculated parameters leads to the conclusion that holes in the $Y_2Ba_4Cu_7O_{15}$ lattice are localized predominantly at positions of chain oxygen. *© 2000 MAIK “Nauka/Interperiodica”.*

A comparison of experimentally determined and calculated parameters of nuclear quadrupole interaction makes it possible to determine the spatial distribution of defect electrons in the crystal lattice. The most reliable results are obtained when such a comparison is carried out for “crystalline” probes (the electric field gradient (EFG) at the nuclei of such probes is created by ions of the crystal lattice). We proposed and implemented the method of emission Mössbauer spectroscopy (EMS) on $^{67}Cu(^{67}Zn)$ for the experimental determination of the parameters of nuclear quadrupole interaction at copper lattice sites of high-T_c superconductors. In this case, a $^{67}Zn^{2+}$ “crystalline” probe is formed as a result of the decay of the parent isotope ^{67}Cu, and the EFG can be calculated for it by using the point charge model [1, 2].

This research aims to experimentally determine the nuclear quadrupole interaction parameters at copper sites of the $Y_2Ba_4Cu_7O_{15}$ lattice by the EMS method on $^{67}Cu(^{67}Zn)$, to calculate the crystal EFG tensor at these sites, and to obtain information on the spatial distribution of defect electrons in this lattice from a comparison of experimental and calculated parameters. Note that the compound $Y_2Ba_4Cu_7O_{15}$ was investigated earlier by nuclear quadrupole resonance (NQR) and nuclear magnetic resonance (NMR) methods on ^{63}Cu [3] and ^{137}Ba [4] isotopes. This allows one to extend the experimental substantiation of the proposed interpretation of the results of emission Mössbauer spectroscopy on the $^{67}Cu(^{67}Zn)$ isotope.

1. EXPERIMENTAL TECHNIQUE

The experiments were made on ceramic samples having the composition $Y_2Ba_4Cu_7O_{15-x}$. The ^{67}Cu isotope was introduced into the ceramic through diffusion doping in an oxygen atmosphere at 700°C for two hours. A similar procedure with the compounds $YBa_2Cu_3O_7$ and $YBa_2Cu_4O_8$ ensures the intrusion of ^{67}Cu atoms at copper sites in accordance with their natural population density [1,2]. Note that a test annealing of the $Y_2Ba_4Cu_7O_{15}$ sample under similar conditions did not result in a change in T_c ~ 60 K. The Mössbauer spectra on $^{67}Cu(^{67}Zn)$ were recorded at 4.2 K with ^{67}ZnS as an absorber.

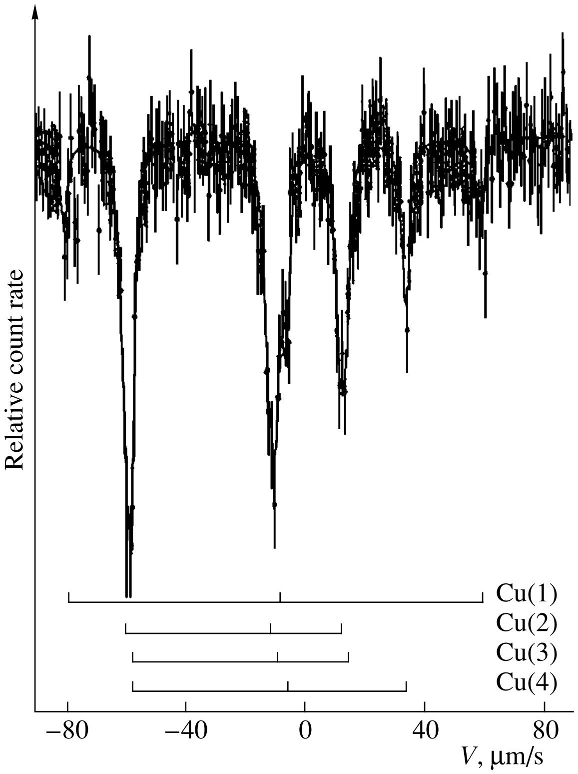

Fig. 1. $^{67}Cu(^{67}Zn)$ emission Mössbauer spectrum of the compound $Y_2Ba_4Cu_7O_{15}$ at 4.2 K. The positions of the components of quadrupole triplets corresponding to the $^{67}Zn^{2+}$ probe at Cu(1), Cu(2), Cu(3), and Cu(4) sites are indicated.

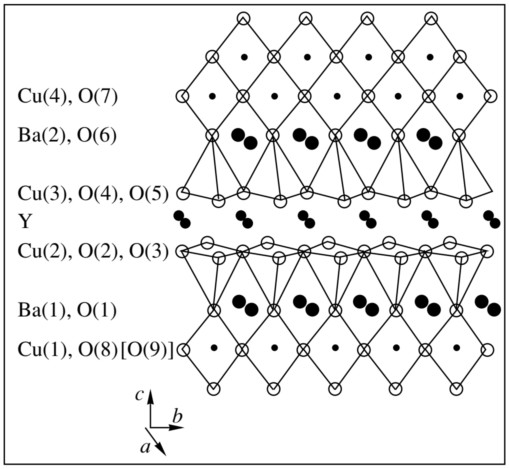

Fig. 2. A fragment of the unit cell of $Y_2Ba_4Cu_7O_{15}$ [5].

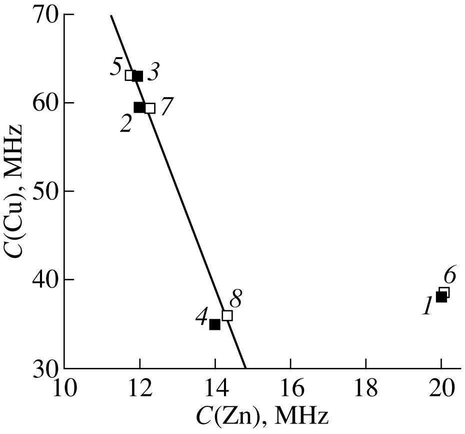

Fig. 3. *C*(Cu) vs. *C*(Zn) diagram for copper metaloxides. Points *1*, *2*, *3*, and *4* correspond to the results for Cu(1), Cu(2), Cu(3), and Cu(4) sites in $Y_2Ba_4Cu_7O_{15}$. The ^{63}Cu NMR data are borrowed from [3]. Points *5* and *6* correspond to Cu(1) and Cu(2) sites in $YBa_2Cu_3O_7$ [1], and points *7* and *8* correspond to Cu(1) and Cu(2) sites in $YBa_2Cu_4O_8$ [2].

2. EXPERIMENTAL RESULTS

The spectra on ^{67}Cu(^{67}Zn) were formed by a set of several lines of different intensity and width (Fig. 1). Since there are four nonequivalent positions of copper in the structure of $Y_2Ba_4Cu_7O_{15}$ (Fig. 2) [5], the experimental spectra were decomposed into four quadrupole triplets. The choice of the decomposition version for the experimental spectra into triplets and the identification of triplets with $^{67}Zn^{2+}$ centers at Cu(1), Cu(2), Cu(3), and Cu(4) sites were determined by the fact that the surroundings of Cu(2) and Cu(3) in $Y_2Ba_4Cu_7O_{15}$ are similar to the surroundings of Cu(2) in $YBa_2Cu_3O_7$ and $YBa_2Cu_4O_8$. It was therefore natural to require that the asymmetry parameter of the EFG tensor for sites Cu(2) and Cu(3) in $Y_2Ba_4Cu_7O_{15}$ be close to zero, as with the Cu(2) lattice sites in $YBa_2Cu_3O_7$ [1] and $YBa_2Cu_4O_8$ [2]. In addition, we took into account the population densities of sites Cu(1), Cu(2), Cu(3), and Cu(4) in $Y_2Ba_4Cu_7O_{15}$. It was found that these requirements are met by the decomposition presented in Fig. 1. The parameters of nuclear quadrupole interaction for the $^{67}Zn^{2+}$ centers at the sites Cu(1), Cu(2), Cu(3), and Cu(4) are shown in Fig. 3.

3. DISCUSSION OF EXPERIMENTAL RESULTS

At the present time, the NMR and NQR experimental data obtained at ^{17}O, ^{63}Cu, and ^{137}Ba isotopes for the compounds $YBa_2Cu_3O_6$, $YBa_2Cu_3O_7$, and $YBa_2Cu_4O_8$ are often interpreted by using the results of calculating the EFG tensor by the quantum-mechanical method of plane waves in the local-density approximation [6–10]. However, this method is invalid for calculating the EFG tensor at Cu(2) lattice sites (the theoretical and experimental values for the above-mentioned compounds differ by more than a factor of two). Moreover, this method is inapplicable for calculating the EFG at the nuclei of impurity atom probes. For this reason, we used the results of EFG analysis for interpreting ^{67}Cu(^{67}Zn) EMS data on the basis of the point charge model.

The measured value of the quadrupole interaction constant *C* is the sum of two terms, i.e.,

$$C = eQU_{zz} = eQ(1-\gamma)V_{zz} + eQ(1-R_0)W_{zz}, \quad (1)$$

where V_{zz}, W_{zz}, and U_{zz} are the principal tensor components of the crystal EFG (created by the ions of the crystal lattice), the valence EFG (created by nonspherical valence electrons of the probe atom), and the total EFG, respectively and where γ and R_0 are the Sternheimer coefficients for the probe atom.

For the $^{67}Zn^{2+}$ probe, the contribution to the total EFG tensor from valence electrons can be neglected, which gives

$$C(\mathrm{Zn}) \approx eQ(1-\gamma)V_{zz}. \quad (2)$$

The crystal EFG tensor was calculated in the point charge model. The components of the crystal EFG tensor were calculated by the formulas

$$V_{pp} = \sum_k e_k^* \sum_i (1/r_{ki}^3)(3p_{ki}^2/r_{ki}^2 - 1) = \sum_k e_k^* G_{ppk},$$
$$V_{pq} = \sum_k e_k^* \sum_i (3p_{ki}q_{ki}/r_{ki}^5)^2 = \sum_k e_k^* G_{pqk}, \quad (3)$$

where *k* is the index of summation over sublattices, *i* is the index of summation over sublattice sites, *q* and *p* are Cartesian coordinates, e_k^* are the atomic charges in the *k*th sublattice, and r_{ki} is the separation between the *ki*th ion and the lattice site under investigation.

The lattice sums G_{ppk} and G_{pqk} were calculated on a computer. We used the structural data obtained in [10] and presented the lattice in the form $Y_2Ba(1)_2Ba(2)_2Cu(1)Cu(2)_2Cu(3)_2Cu(4)_2O(1)_2O(2)_2O(3)_2O(4)_2O(5)_2O(6)_2O(7)_2O(8)_{1-x}O(9)_x$, where $0 \le x \le 1$. The notation of atomic sites corresponds to the results obtained by Hewat *et al*. [5] and is shown in Fig. 2. The index k of summation over sublattices in (3) was ascribed the following values:

$k = 1$	2	3	4	5	6	7	8
atom Y	Ba(1)	Ba(2)	Cu(1)	Cu(2)	Cu(3)	Cu(4)	O(1)
$k = 9$	10	11	12	13	14	15	16
atom O(2)	O(3)	O(4)	O(5)	O(6)	O(7)	O(8)	O(9).

The charges of atoms of the $Y_2Ba_4Cu_7O_{15}$ lattice were determined from the ^{67}Cu(^{67}Zn) EMS data on the basis of a system of eight equations: three equations for the ratio of the quadrupole interaction constants for $^{67}Zn^{2+}$ centers at copper sites, set up for the three pairs of sites Cu(1) and Cu(2), Cu(1) and Cu(3), and Cu(1) and Cu(4),

$$\sum_k e_k^* [G_{zzkl} - P_{lm} G_{zzkm}] = 0, \tag{4}$$

four equations for the asymmetry parameters η of the EFG tensor at the sites Cu(1), Cu(2), Cu(3), and Cu(4),

$$\sum_k e_k^* [G_{xxkl} - G_{yykl} - \eta_{zzkl}] = 0, \tag{5}$$

$$\sum_k e_k^* [G_{xxkm} - G_{yykm} - \eta_m G_{zzkm}] = 0, \tag{6}$$

and the electroneutrality equation

$$\begin{gathered} 2e_1^* + 2e_2^* + 2e_3^* + e_4^* + 2e_5^* + 2e_6^* + 2e_7^* + 2e_8^* \\ + 2e_9^* + 2e_{10}^* + 2e_{11}^* + 2e_{12}^* + 2e_{13}^* + 2e_{14}^* \\ + (1-x)e_{15}^* + xe_{16}^* = 0, \end{gathered} \tag{7}$$

where indices 1 and m label copper sites for which the ^{67}Cu(^{67}Zn) EMS data were obtained and which can assume the values 4 and 5, 4 and 6, and 4 and 7, respectively, for the above-mentioned pairs of sites; η_m and η_1 are the experimental values of the asymmetry parameters of the EFG tensor; and $P_{1m} = eQU_{zzm}/eQU_{zzl}$ is the ratio of the experimental quadrupole interaction constants for $^{67}Zn^{2+}$ at the corresponding sites.

Equations (4)–(7) are all homogeneous, and hence the system comprising them can be used for determining atomic charges only in terms of one of them. It is convenient to choose for this purpose the charge of Y ions, which should be expected to be close to their formal chemical charge (+3e) [1, 2].

Equations (4)–(7) are insufficient for determining the atomic charges of fifteen sublattices. If, however, we take into account the fact that the coefficients of the anion charges are an order of magnitude larger than the coefficients of cation charges, the system (4)–(7) makes it possible to determine anion charges to within small corrections determined by cation charges. We disregarded the solutions for which a negative cation or a positive anion charge was obtained as deprived of any physical meaning.

Proceeding from the symmetry of the local surroundings, we see that the axes z of the crystal EFG tensors for the Cu(2) and Cu(3) sites must coincide with the c axis; and that $V_{zz5} > 0$ and $V_{zz6} > 0$ according to our measurements. For the sites Cu(1) and Cu(4), if only the positions O(8) are populated, we can single out four regions of solutions in which the experimental conditions $\eta_4 \sim 0.95$, $V_{zz4} > 0$ and $\eta_7 \sim 0.70$, $V_{zz7} > 0$ are satisfied: region *AA*, where $|V_{bb4}| < |V_{cc4}|$ and $|V_{bb7}| < |V_{cc7}|$; region *AB*, where $|V_{bb4}| > |V_{cc4}|$ and $|V_{bb7}| > |V_{cc7}|$; region *BA*, where $|V_{bb4}| > |V_{cc4}|$ and $|V_{bb7}| < |V_{cc7}|$; and region *BB*, where $|V_{bb4}| > |V_{cc4}|$ and $|V_{bb7}| > |V_{cc7}|$. However, in all the regions, the axes z of the crystal EFG tensors for the sites Cu(1) and Cu(4) coincide with the crystallographic axis a. If only the position O(9) is populated, the situation does not change radically, but the axes z of the crystal EFG tensors coincide with the crystallographic axis b for the Cu(1) site and with the crystallographic axis a for the Cu(4) site. This remark will be taken into account in the subsequent discussion of the results obtained in the case of population of the position O(8) only.

Charges of oxygen atoms in $Y_2Ba_4Cu_7O_{15}$ lattice

Model	Lattice site							
	O(1)	O(2)	O(3)	O(4)	O(5)	O(6)	O(7)	O(8)
AA	–1.98	–1.98	–1.96	–1.99	–2.00	–1.99	–1.39	–1.44
BB	–1.46	–2.07	–2.04	–1.94	–1.92	–0.55	–2.40	–3.24
AB	–2.37	–2.13	–2.11	–1.90	–1.88	–0.47	–2.33	–1.64
BA	–1.17	–1.93	–1.90	–2.03	–2.03	–2.10	–1.42	–2.85

Note: The charges were obtained from the solution of the system of equations (4)–(6) under the assumption that the charges of Y, Ba, and Cu atoms are equal to +3, +2, and +2 respectively; models *AA*, *BB*, *AB*, and *BA* are described in the text.

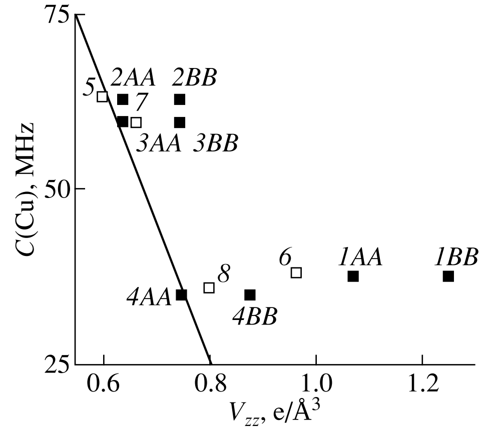

Fig. 4. C(Cu) vs. V_{zz} diagram for copper metaloxides. The notation of points is the same as in Fig. 3. Indices *AA* and *BB* denote the charge distribution models used for calculating V_{zz} for copper sites in the $Y_2Ba_4Cu_7O_{15}$ lattice.

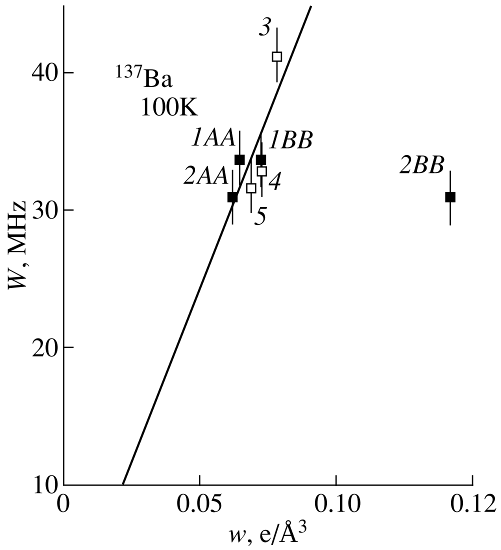

Fig. 5. |w| vs. |W| diagram for barium sites. Notation: *1* and *2* correspond to the Ba(1) and Ba(2) sites, respectively, in $Y_2Ba_4Cu_7O_{15}$; *3*, *4*, and *5* are Ba sites in $YBa_2Cu_3O_6$, $YBa_2Cu_3O_7$, and $YBa_2Cu_4O_8$, respectively. The ^{137}Ba NQR data are borrowed from [4].

In accordance with the presence of the four regions, there must exist four sets of e_k^* (for regions *AA*, *AB*, *BA*, and *BB*) consistent with the experimental values of P_{45}, P_{46}, P_{47}, η_4, η_5, η_6, and η_7. The charges of oxygen atoms obtained under the assumption of standard valences of the Y, Ba, and Cu atoms ($e_1^* = 3$, $e_2^* = e_3^* = 2$, $e_4^* = e_5^* = e_6^* = e_7^* = 2$) are given in the table.

The correlation dependences established between the ^{67}Cu(^{67}Zn) EMS and ^{63}Cu NMR data for copper sites in the copper metaloxide lattices can be used as criteria of the choice among the solutions. It was shown earlier [11] that the quantities C(Cu) (quadrupole interaction constant for a ^{63}Cu probe at copper sites) and C(Zn) (quadrupole interaction constant for a ^{67}Zn probe at copper sites) obey the relation

$$C(\mathrm{Cu}) = 197 - 11.3C(\mathrm{Zn}) \qquad (8)$$

(here, C(Cu) and C(Zn) are given in MHz), and the main reason behind the deviation from the straight line described by (8) is different orientations of the principal axes of the total and the valence EFG tensors. This is observed, for example, for Cu(1) sites in $YBa_2Cu_3O_7$ (Fig. 3) [1].

Moreover, it was proved in [11], that the quantities C(Cu) and V_{zz} satisfy the following relation:

$$C(\mathrm{Cu}) = 179 - 191.4V_{zz}, \qquad (9)$$

and that the main reason behind the deviation from the straight line described by (9) is the inaccurate calculation of the crystal EFG tensor in view of the inferior choice of atomic charges. Consequently, the position of points on the C(Cu) vs. C(Zn) diagrams (Fig. 3) and C(Cu) vs. V_{zz} diagrams (Fig. 4), corresponding to the same position of copper, can be used for selecting possible versions of the charge distribution in the lattice.

Figure 3 shows the lattice sites Cu(1), Cu(2), Cu(3), and Cu(4) in $Y_2Ba_4Cu_7O_{15}$. It can be seen that the points Cu(2), Cu(3), and Cu(4) satisfactorily fit the straight line (8), thus confirming the bivalence of copper at the corresponding lattice sites. The point Cu(1) obviously deviates from the straight line (8), and we can assume, in analogy with the point Cu(1) for $YBa_2Cu_3O_7$, that this is due to different orientations of the principal axes of the total and the valence EFG tensors.

The points Cu(2), Cu(3), and Cu(4), for which V_{zz} are calculated for model *AA*, lie close to the straight line (9) shown in Fig. 4, while the calculations made for model *BB*, as well as for models *AB* and *BA*, lead to considerable deviations in all three points from the straight line (9). This fact can obviously confirm the validity of the model *AA*.

The advantage of an *AA*-type model also follows from an analysis of the ^{137}Ba NQR data for a series of compounds $YBa_2Cu_3O_6$–$YBa_2Cu_3O_7$–$YBa_2Cu_4O_8$–$Y_2Ba_4Cu_7O_{15}$. It should be noted that a $^{137}Ba^{2+}$ probe is crystalline. Lombardi *et al.* [4] used the NQR method to measure the values of $W = (1/2)C(1 + \eta^2/3)^{1/2}$ for this probe in the above series (here, C is the quadrupole interaction constant for the ^{137}Ba probe at the Ba(1) and Ba(2) sites). These experimental values can be compared with the calculated values of $w = (1/2)V_{zz}(1 + \eta_{cr}^2/3)^{1/2}$, where η_{cr} is the asymmetry parameter of the crystal EFG tensor. Figure 5 shows the |W| vs. |w| dependence for barium sites in the above-mentioned compounds. It can be seen that the data obtained for Ba(1) and Ba(2) sites of the $Y_2Ba_4Cu_7O_{15}$ lattice satisfactorily fit to the linear dependence only for values of *w* calculated in the *AA* model.

Thus, the NMR and NQR data obtained on ^{63}Cu and ^{137}Ba isotopes agree with the proposed model of spatial localization of defect electrons.

ACKNOWLEDGMENTS

This work was supported by the Russian Foundation for Basic Research, project no. 97-02-16216.

REFERENCES

1. V. F. Masterov, P. P. Seregin, F. S. Nasredinov, *et al.*, Phys. Status Solidi B **196**, 11 (1996).
2. V. F. Masterov, F. S. Nasredinov, N. P. Seregin, *et al.*, Fiz. Tverd. Tela (St. Petersburg) **41**, 1724 (1999) [Phys. Solid State **41**, 1590 (1999).
3. R. Stern, M. Mali, I. Mangelschots, *et al.*, Phys. Rev. B **50**, 426 (1994).
4. A. Lombardi, M. Mali, J. Roos, *et al.*, Physica C **235–240**, 1651 (1994).
5. A. W. Hewat, P. Fischer, E. Kaldis, *et al.*, Physica C **167**, 579 (1990).
6. K. Schwartz, C. Ambrosch-Draxl, and P. Blaha, Phys. Rev. B **42**, 2051 (1990).
7. J. Yu, A. J. Freeman, R. Podloucky, *et al.*, Phys. Rev. B **43**, 532 (1991).
8. C. Ambrosch-Draxl, P. Blaha, and K. Schwartz, Phys. Rev. B **44**, 5141 (1991).
9. D. J. Singh, K. Schwartz, and P. Blaha, Phys. Rev. B **46**, 5849 (1992).
10. C. O. Rodríguez, G. Fabricius, M. G. Stachiotti, *et al.*, Phys. Rev. B **56**, 14833 (1997).
11. P. P. Seregin, V. F. Masterov, F. S. Nasredinov, *et al.*, Phys. Status Solidi B **201**, 269 (1997).

Translated by N. Wadhwa

Physics of the Solid State, Vol. 42, No. 4, 2000, pp. 626–632. Translated from Fizika Tverdogo Tela, Vol. 42, No. 4, 2000, pp. 611–617.
Original Russian Text Copyright © 2000 by Silin, Studenov.

METALS AND SUPERCONDUCTORS

Cerenkov Losses and the Current–Voltage Characteristic in Sandwich-type Josephson Junctions

V. P. Silin and A. V. Studenov
Lebedev Physical Institute, Russian Academy of Sciences, Leninskiĭ pr. 53, Moscow, 117924 Russia
e-mail: silin@sci.lebedev.ru

Received June 17, 1999; in final form, September 20, 1999

Abstract—An analytic description of stationary chains of Abrikosov–Josephson (AJ) vortices is provided for a Josephson junction (JJ) between two finite-thickness superconductors. The current–voltage characteristic (IVC) determined by the finite conductance and Cerenkov losses is obtained for a JJ with a moving chain of AJ vortices. The law of motion for a solitary vortex is established. *© 2000 MAIK “Nauka/Interperiodica”.*

1. The paper by Mints and Snapiro [1] stimulated interest in the study of the influence of Cerenkov radiation in Josephson junctions (JJ) on current–voltage characteristics (IVC). At the same time, this publication posed a number of questions, including the possibility of analyzing the Cerenkov emission of short Swihart waves by a vortex (or vortex structure) whose small-scale description is constructed using the traditional sine-Gordon equation, which gives a knowingly incorrect description of the internal structure of the vortex and rules out the Cerenkov radiation [1]. Our theory of Cerenkov radiation presented in [2– 4], where we considered the decelerating effect of Cerenkov losses on the motion of an individual vortex in a vortex chain of the JJ between bulk superconductors, is free of this drawback. We also obtained IVCs taking into account the effect of conductance in the contact transition layer, as well as the effect of normal electrons in superconductors (cf. [5]). However, the theory developed in [2–4] pertains to a JJ with a large critical current density, which does not allow us to formally go over to the limit [1] corresponding to a low Josephson critical current density j_c. In the present work, in contrast to [2–4], we consider the Cerenkov radiation in the JJ between two superconductors of finite thickness d_s. Apart from being of interest as such, this structure makes possible a formal transition to a theory differing only slightly from that based on the sine-Gordon equation. Among other things, this allows us to determine the extent of accuracy of the approach used in [1] and associated with the theory of a JJ between bulk superconductors.

Our description of the Cerenkov emission of generalized Swihart waves in JJ structures of the sandwich type described below has made it possible to determine the field of Cerenkov radiation emitted by an infinite moving train of vortices (Section 2). The analysis is based on the equation for the phase difference φ of Cooper pairs located on different sides of the JJ, which was derived by Alfimov and Popkov [6]. In this work, the results of the theory of dislocations [7] are used for the first time to write static solutions for infinite trains of Abrikosov–Josephson (AJ) vortices for a sandwich-type JJ. The steady-state solution corresponding to a nonzero magnetic field is used to determine the field of Cerenkov radiation accompanying the train during its motion. This allowed us to construct the IVC for a sandwich-type JJ with a moving train of vortices in it. Section 3 is devoted to several simple corollaries of the general relation determining the IVC. In Section 4, the law of motion of a solitary vortex exciting Cerenkov radiation in the JJ is considered. The obtained results are discussed in Section 5.

2. In this paper, we use the following equation for the phase difference φ for Cooper pairs on different sides of a JJ between infinitely long planar superconductors of thickness d_s [6, 8]:

$$\sin\varphi + \frac{1}{\omega_j^2}\left(\frac{\partial^2\varphi}{\partial t^2} + \beta\frac{\partial\varphi}{\partial t}\right) - \frac{l}{2d_s}\fint_{-\infty}^{+\infty}\frac{dz'}{\sinh[\pi(z'-z)/2d_s]}\left(\frac{\partial\varphi}{\partial z'} + \frac{\partial^2\varphi}{\partial z'\partial t}\right) = 0. \tag{1}$$

Here we use the following notation:

$$\omega_j^2 = \frac{16\pi|e|j_c d}{\hbar\varepsilon},\quad \beta = \frac{4\pi\sigma}{\varepsilon},$$

$$\tau = \tau_f\frac{n_n}{n_s},\quad l = \frac{\lambda_j^2}{\lambda} = \frac{\hbar c^2}{16\pi|e|j_c\lambda^2},$$

where e is the electron charge; j_c is the critical density of the Josephson current; ω_j and λ_j are the Josephson frequency and length, respectively; β and τ characterize dissipation; σ and ε are the conductivity and dielectric constant, respectively, of the substance of the nonsuperconducting contact layer of thickness $2d$ separating the superconductors; λ is the London penetration depth; n_n

and n_s are the concentrations of normal and superconducting electrons in the superconductor; and τ_f is the effective mean free time for a normal electron in the superconductor. In equation (1), we assume that $d \ll \lambda$.

Let us construct the IVC for a sandwich-type JJ with a moving train of vortices. First of all, we give here steady-state solutions of equation (1), which can be written using the results of the theory of dislocations [7]. The first solution is

$$\varphi_0(z) = \pi + \arctan\left(\frac{\operatorname{sn}(z/B, k)\operatorname{dn}(d_s/B, k')}{\operatorname{cn}(z/B, k)\operatorname{cn}(d_s/B, k')}\right)$$
$$\equiv \pi + 2\arctan\left(\frac{\operatorname{sn}(z/B, k)}{\operatorname{cn}(z/B, k)}\operatorname{dn}\left(\frac{id_s}{B}, k\right)\right), \tag{2}$$

where $0 < (d_s/B) < K'(k)$ and B is defined by the equation

$$\frac{l}{B} = \frac{\operatorname{dn}(d_s/B, k')\operatorname{cn}(d_s/B, k')}{k^2\operatorname{sn}(d_s/B, k')}. \tag{3}$$

Here dn(x, k), sn(x, k), and cn(x, k) denote Jacobian elliptical functions with an argument x, and a modulus k $(0 \le k \le 1)$, $k' \equiv \sqrt{1 - k^2}$, $K'(k) \equiv K(k')$, and $K(k)$ is the total elliptical integral of the first kind (see, for example, [7]). The second solution is

$$\varphi_0(z) = \pi + 2\arctan\left(\frac{k\operatorname{sn}(z/C, k)}{\operatorname{dn}(z/C, k)\operatorname{cn}(d_s/C, k')}\right), \tag{4}$$

where $0 < (d_s/C) < K'(k)$ and C is defined by the equation

$$\frac{l}{C} = \frac{\operatorname{cn}(d_s/C, k')}{\operatorname{sn}(d_s/C, k')\operatorname{dn}(d_s/C, k')}. \tag{5}$$

One can easily verify that expression (2), for example, is a steady-state solution of equation (1) by using the expansion into the Fourier series (see Appendix).

The vortex structure (4) corresponds to zero mean magnetic field. Such a structure in a JJ is usually unstable [9]. For this reason, we consider the vortex structure (2) corresponding to a nonzero mean magnetic field $\bar{H} = (\Phi_0/4\pi\lambda L)$. Here and below, we use the notation $2\pi L \equiv 2BK(k)$ for the period of the structure described by (2). By virtue of this relation, the limit of the infinitely long period of the structure ($L \longrightarrow \infty$) and of the finite thickness d_s of the superconductors corresponds to $k = 1$, because $K(k \longrightarrow 1) \longrightarrow \infty$. In this limit, formula (2) reduces to the relation describing a solitary vortex in a sandwich-type JJ [6]. In the opposite limit, i.e., for infinitely thick superconducting electrodes ($d_s \longrightarrow \infty$) and a finite period L of the structure, formula (2), with the notation $\alpha = 2(K'(k) - d_s/B)$, is transformed into $\varphi_0 = \pi + 2\arctan[\tan(z/2L)/\tanh(\alpha/2)]$, with $\sinh\alpha = (l/L)$. The latter expression is a well-known solution of nonlocal Josephson electrodynamics, which was used, for example, in [3] and [4] in constructing the theory of the IVC for a JJ between bulk superconductors.

In order to find the IVC for a JJ with a vortex train (2), we write the solution of equation (1) in the form

$$\varphi(z, t) = \varphi_0(s) + \varphi_1(s), \quad \varphi_1(s) \ll \varphi_0(s), \tag{6}$$

where $s = z - vt$ and $\varphi_0(s)$ describes the structure (2) moving at a velocity v, which leads to the emergence of perturbation $\varphi_1(s)$. This gives the following equation for $\varphi_1(s)$:

$$\varphi_1\cos\varphi_0 + \frac{v^2}{\omega_j^2}\left(\frac{d^2\varphi_1}{ds^2} - \frac{\beta}{v}\frac{d\varphi_1}{ds}\right)$$
$$-\frac{1}{2d_s}\fint_{-\infty}^{+\infty}\frac{ds'}{\sinh[\pi(s' - s)/2d_s]}\left(\frac{d\varphi_1}{ds'} - \tau v\frac{d^2\varphi_1}{(ds')^2}\right)$$
$$= -\frac{v^2}{\omega_j^2}\left(\frac{d^2\varphi_0}{dx^2} - \frac{\beta}{v}\frac{d\varphi_0}{ds}\right)$$
$$-\frac{\tau l v}{2v_s}\fint_{-\infty}^{+\infty}\frac{ds'}{\sinh[\pi(s' - s)/2d_s]}\frac{d^2\varphi_0}{(ds')^2} \tag{7}$$
$$\equiv \frac{\beta v}{\omega_j^2 L} + \sum_{n=1}^{\infty}\frac{4v}{L}\frac{q^n}{1 + q^{2n}}\left[\frac{nv}{\omega_j^2 L}\cosh\left(\frac{nd_s}{L}\right)\sin\left(\frac{ns}{L}\right)\right.$$
$$\left.+\left\{\frac{\beta}{\omega_j^2}\cosh\left(\frac{nd_s}{L}\right) + \frac{l\tau n}{L}\sinh\left(\frac{nd_s}{L}\right)\right\}\cos\left(\frac{ns}{L}\right)\right],$$

where $q = \exp(-\pi K'(k)/K(k))$. Considering the Cerenkov excitation of short waves and neglecting the difference between $\cos\varphi_0$ and unity (cf. [3]), we immediately obtain a solution of equation (7):

$$\varphi_1 = a_0 + \sum_{n=1}^{\infty}(a_n\cos(ns/L) + b_n\sin(ns/L)). \tag{8}$$

Here $a_0 = (\beta v/\omega_j^2 L)$,

$$a_n = \frac{4q^n\omega_n^2 v\Gamma_n}{(1 + q^{2n})L}\frac{\cosh(nd_s/L)}{[\omega_n^2 - (vn/L)^2] + (\Gamma_n vn/L)^2}, \tag{9}$$

$$b_n = \frac{4q^n\cosh(nd_s/L)}{n(1 + q^{2n})}$$
$$\times\left[-1 + \frac{\omega_n^2(\omega_n^2 - [nv/L]^2)}{[\omega_n^2 - (vn/L)^2]^2 + (\Gamma_n vn/L)^2}\right], \tag{10}$$

$$\begin{aligned}\omega_n^2 &= \omega_j^2[1 + (nl/L)\tanh(nd_s/L)],\\ \Gamma_n &= [\beta + (\omega_j^2\tau nl/L)\tanh(nd_s/L)].\end{aligned} \tag{11}$$

Presuming the smallness of dissipation, we obtain the following condition for the Cerenkov resonance:

$$\frac{n_r^2 v_r^2}{L^2} = \omega_j^2\left[1 + \frac{n_r l}{L}\tanh\left(\frac{n_r d_s}{L}\right)\right], \tag{12}$$

which is satisfied when the velocity of the vortex structure is $v = v_r$, for the term of series (8) with the number $n = n_r$ (it will henceforth be referred to as the resonance term). For small velocities v, the number of the resonance term is large. Moreover, we will assume that

$$n_r \gg (L/d_s), \quad n_r \gg (L/l). \tag{13}$$

Then the Cerenkov resonance condition leads to

$$n_r = (Ll\omega_j^2/v_r^2). \tag{14}$$

The fulfillment of conditions (13) in this case indicates that the following condition is satisfied for the resonance velocity v_r:

$$v \ll \omega_j \min(l, \sqrt{ld_s}). \tag{15}$$

Note that conditions (13) impose the condition $n_r \gg 1$ on the number n_r of the Cerenkov resonance, provided that

$$L \gg \min(l, d_s). \tag{16}$$

If $v = v_r$, the resonance term in (8) with the number $n = n_r$ has the form

$$\varphi_r = \frac{2v_r}{L\Gamma_{n_r}}\exp\left[-n_r\left(\frac{\pi K'}{K} - \frac{d_s}{L}\right)\right]\cos\left(\frac{n_r s}{L}\right). \tag{17}$$

In the vicinity of resonance, when

$$|v - v_r| < (\Delta v_r/2) = (v_r/4n_r) \ll v_r, \tag{18}$$

the resonance term can be written in the form

$$\begin{aligned}\varphi_r &= \frac{2v}{L\Gamma_{n_r}}\exp\left[-n_r\left(\frac{\pi K'}{K} - \frac{d_s}{L}\right)\right]\\ &\times\frac{\cos(n_r s/L) - [2n_r(v - v_r)\Gamma_{n_r}^{-1}L^{-1}]\sin(n_r s/L)}{1 + [2n_r(v - v_r)\Gamma_{n_r}^{-1}L^{-1}]^2}.\end{aligned} \tag{19}$$

The most important difference between this result and the one obtained in the theory of a JJ between bulk superconductors lies in the exponent reflecting the effect of the finite thickness of superconducting electrodes.

The possibility to keep only one resonance term in sum (8) is ensured by the fulfillment of the inequality (see [3])

$$[\omega_n^2 - (vn/L)^2]^2 \gg [\Gamma_n vn/L]^2, \quad n \neq n_r. \tag{20}$$

This inequality can be reduced to the condition

$$v_r \gg L\Gamma_{n_r} = L[\beta + (l^2\tau\omega_j^4/v_r^2)]. \tag{21}$$

Finally, the condition of the smallness of φ_r relative to φ_0 is ensured by the condition

$$\frac{2v}{L\Gamma_{n_r}}\exp\left[-n_r\left(\frac{\pi K'}{k} - \frac{d_s}{L}\right)\right] \ll 1. \tag{22}$$

Taking into account formula (14) for n_r and condition (15) imposed on the velocity, we can easily verify that φ_r satisfies the inequality $|(v^2/\omega_j^2)(d^2\varphi_r/ds^2)| \gg |\varphi_r|$ justifying the substitution $\cos\varphi_0 \longrightarrow 1$ in (7) in the calculation of the resonance term.

Having established the possibility of describing the Cerenkov radiation field with the help of expression (19), we use this result for determining IVC. For this purpose, we write the balance equation for the work done by the current of density j_c flowing through the JJ and the energy loss in the vortex chain due to Cerenkov radiation (cf. [3, 4]):

$$\begin{aligned}\frac{j}{j_c}\int_0^{2\pi L} ds\frac{d\varphi}{ds} &= \int_0^{2\pi L} ds\left\{\frac{\beta v}{\omega_j^2}\left(\frac{d\varphi}{ds}\right)^2\right.\\ &\left.- \frac{l\tau v}{2d_s}\left(\frac{d\varphi}{ds}\right)\fint_{-\infty}^{+\infty}\frac{ds'}{\sinh[\pi(s' - s)/2d_s]}\frac{d^2\varphi}{(ds')^2}\right\}.\end{aligned} \tag{23}$$

After the substitution $\varphi = \varphi_0 + \varphi_r$, we obtain the following velocity dependence of the current density:

$$\begin{aligned}\frac{j}{j_c} &= \frac{\beta v}{\omega_j^2}R(w, k) + \frac{l\tau v}{2B}\frac{dR(w, k)}{dw}\\ &+ \frac{2\omega_j^2 l^2}{vL\Gamma_{n_r}}\frac{\exp[-(2\omega_j^2 ld_s/v_r^2 w)(K' - w)]}{1 + [2\omega_j^2 l(v - v_r/v_r^2\Gamma_{n_r})]^2},\end{aligned} \tag{24}$$

where $\Gamma_{n_r} = \beta + \omega_j^2\tau(l\omega_j/v)^2$, $w \equiv (d_s/B) < K'(k)$, and the following notation have been used:

$$\begin{aligned}R(w, k) &\equiv \frac{1}{2\pi}\int_0^{2\pi L} ds\left(\frac{d\varphi_0}{ds}\right)^2 = \frac{2}{\pi B}\left[\left(\frac{\mathrm{dn}^2(w, k')}{\mathrm{cn}^2(w, k')}\right.\right.\\ &\left.+ \frac{1}{\sinh^2(w, k')}\right)\Pi\left(\frac{k^2\,\mathrm{sn}^2(w, k')}{\mathrm{cn}^2(w, k')}, k\right)\\ &\left.- \frac{1}{\mathrm{sn}^2(w, k')}K(k) + E(k)\right].\end{aligned} \tag{25}$$

Here, $E(k)$ and

$$\Pi(\mu^2, k) \equiv \int_0^1 d\rho(\rho^2\mu^2 + 1)^{-1}[1 - \rho^2(1 - \rho^2 k^2)]^{-1/2}$$

are total elliptic integrals of the second and third kind, respectively. By virtue of relation (3), w can be determined from the equation

$$\frac{l}{d_s}w = \frac{\mathrm{dn}(w, k')\,\mathrm{cn}(w, k')}{k^2\,\mathrm{sn}(w, k')} \equiv \frac{\mathrm{sn}(K' - w, k')}{\mathrm{cn}(K' - w, k')\,\mathrm{dn}(K' - w, k')}. \tag{26}$$

Finally, the modulus k of Jacobian elliptic functions is defined by the equation

$$K(k) = \frac{\pi L}{d_s}w \equiv \frac{\Phi_0}{4d_s\lambda\bar{H}}w. \tag{27}$$

The constant potential difference across a Josephson junction containing the vortex structure (2) moving at a constant velocity is defined as

$$V = -\frac{\hbar}{2|e|}\left\langle\frac{\partial\varphi}{\partial t}\right\rangle = \frac{\hbar v}{2|e|L}, \tag{28}$$

where the angle brackets denote averaging over the period $2\pi L$. Therefore, relations (24)–(27) define the sought IVC. In the limit of bulk superconducting electrodes forming a sandwich, for which $d_s = \infty$, relations (24)–(27) lead to the expression for the IVC from [4].

3. Let us consider some consequences of the general relations (24)–(27) for the IVC of a Josephson junction with a moving chain of vortices. We focus on the case of a large separation L between vortices constituting the chain (much greater than unity). In this case,

$$k' = 4\exp(-\pi Lw/d_s) \ll 1. \tag{29}$$

If equation (26) is written in the form [10]

$$\frac{l}{d_s}w = \frac{\mathrm{dn}(w, k')\,\mathrm{cn}(w, k')}{k^2\,\mathrm{sn}(w, k')} = \frac{\pi}{2k^2K'(k)} \times\left[\cot\left(\frac{\pi w}{2K'(k)}\right) - 4\sum_{n=1}^{\infty}\frac{(q')^n}{1 + (q')^n}\sin\left(\frac{\pi n w}{K'(k)}\right)\right],$$

$$(q') \equiv q(k') = \exp(-\pi K(k)/K'(k)), \tag{30}$$

then, taking into account the fact that $K'(k) \approx \pi/2$ and bearing in mind the estimate of the series

$$\left|4\sum_{n=1}^{\infty}\frac{(q')^n}{1 + (q')^n}\sin\left(\frac{\pi n w}{K'(k)}\right)\right| < 4\sum_{n=1}^{\infty}(q')^n = \frac{4(q')}{1 - (q')} \cong (k')^2/4 = 4\exp(-2\pi Lw/d_s), \tag{31}$$

we can neglect the contribution from this series, provided that

$$4\exp(-2\pi Lw/d_s) \ll (lw/d_s). \tag{32}$$

In this case, equation (26) assumes the following simple form:

$$(l/d_n)w_0 = \cot w_0, \quad w_0 \equiv (d_s/B_1), \tag{33}$$

corresponding to equation (29) in [6] for an individual vortex. Using (33), we can obtain explicit conditions imposed on the separation between vortices. For example, if $l \gg d_s$, we have $B_1 \approx \sqrt{ld_s}$ and $w_0 = d_s/B_1 = \sqrt{d_s/l}$. If, however, $l \le d_s$, we have $B_1 \approx d_s$ and $w_0 \approx 1$. Consequently, inequalities (32) and (29) determining the possibility of application of (33) instead of (26) are reduced to the following inequality:

$$\pi L \gg \max[\sqrt{ld_s}, d_s\ln(4d_s/l)]. \tag{34}$$

Under these conditions, the IVC (24) assumes the form

$$\frac{j}{j_c} = \frac{\beta v}{\omega_j^2 l}\Phi_\beta(w_0) + \frac{\tau v}{2l}\Phi_\tau(w_0) + \frac{2\omega_j^2 l^2}{vL\Gamma_{n_r}}\frac{\exp[-(2\omega_j^2 ld_s/w_0 v_r^2)([\pi/2] - w_0)]}{1 + [(2\omega_j^2 l/\Gamma_{n_r}v_r^2)(v - v_r)]^2}, \tag{35}$$

where

$$\Phi_\beta(w_0) = \frac{2}{\pi}\cot w_0\left(1 + \frac{2w_0}{\sin[2w_0]}\right), \tag{36}$$

$$\Phi_\tau(w_0) = \frac{4}{\pi}\frac{\cot^2 w_0}{\sin[2w_0]}\left(1 - \frac{2w_0}{\tan[2w_0]}\right). \tag{37}$$

Here, in the limiting transition from (24) to (35), we have used the fact that

$$[1 + (k^2/\mu^2)]\Pi(\mu^2, k) - (k^2/\mu^2)K(k) = (1/\mu)\arccos(1/\sqrt{1 + \mu^2})$$

for $k' \ll 1$ [10]. The dependence of the coefficients $\Phi_\beta(w_0)$ and $\Phi_\tau(w_0)$ on the ratio (l/d_s) is plotted in Fig. 1.

In the limit $l \gg d_s$ of thin electrodes, the IVC (35) assumes the form

$$\frac{j}{j_c} = \frac{4}{\pi}\frac{\beta v}{\omega_j v_{s,\,\mathrm{eff}}} + \frac{4}{3\pi}\frac{v}{v_{s,\,\mathrm{eff}}}\tau\omega_j^2 + \frac{2v_{s,\,\mathrm{eff}}}{v}\frac{\omega_j}{\Gamma_{n_r}} \times\frac{l}{L}\sqrt{\frac{l}{d_s}}\frac{\exp[-\pi(v_{s,\,\mathrm{eff}}/v_r)^2\sqrt{l/d_s}]}{1 + [2(v_{s,\,\mathrm{eff}}/v_r)^2(v - v_r)/(\Gamma_{n_r}d_s)]^2}, \tag{38}$$

where we have introduced the notation $v_{s,\,\mathrm{eff}} = \omega_j\sqrt{ld_s}$. The only difference between the term linear in v in the IVC (38) and the term emerging in the energy balance equation for a solitary Josephson vortex in the local theory is the presence of $v_{s,\,\mathrm{eff}}$ instead of the ordinary Swihart velocity $v_s = \omega_j\lambda_j$ (cf. [11]). The last resonance term in the IVC (38), which cannot appear in the local theory, is associated with the excitation of Cerenkov waves by a vortex.

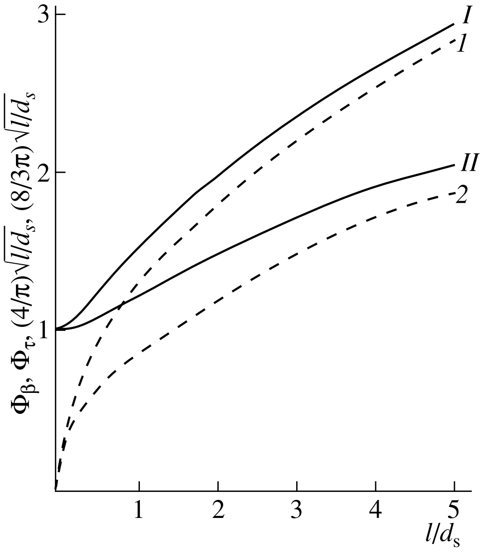

Fig. 1. Dependence of the coefficients $\Phi_\beta(w_0)$ (curve *I*) and $\Phi_\tau(w_0)$ (curve *II*) on the ratio (l/d_s); curves *1* and *2* are described by the functions $(4\pi)\sqrt{l/d_s}$ and $(8/3\pi)\sqrt{l/d_s}$ corresponding to the asymptotic forms of the coefficients Φ_β and Φ_τ, respectively, for $l \gg d_s$.

Let us assess the JJ conductivity σ in which the resonance term in the IVC (38) will manifest itself in the case of relatively low temperatures, where we can neglect the effect of normal electrons ($\tau = 0$). (The effect of normal electrons on IVC is studied in detail in [4].) The resonance term in (38) will be larger than the term linear in v if

$$\left(\frac{4\pi\lambda\sigma}{c}\right)^2\frac{l}{d\varepsilon} \equiv \left(\frac{\beta}{\omega_j}\right)^2 < \frac{\pi}{2}\left(\frac{v_{s,\,\mathrm{eff}}}{v}\right)^2\frac{l}{L}\sqrt{\frac{l}{d_s}}\exp\left[-\pi\left(\frac{v_{s,\,\mathrm{eff}}}{v}\right)^2\sqrt{\frac{l}{d_s}}\right]. \tag{39}$$

If we put $l/d_s = 5$, $L/l = 10$, $v_{s,\,\mathrm{eff}}/v = 3$, $l/d = 10^2$, and $\varepsilon = 10$, we obtain $\sigma_{s^{-1}}\lambda_{\mu m} \le 10^{-1}$, where $\sigma_{s^{-1}}$ is the JJ conductivity in inverse seconds and $\lambda_{\mu m}$ is the London penetration depth in micrometers. This estimate corresponds to relatively low conductivities of JJ. Thus, in the limit of very thin electrodes, which is similar in many respects to the limit of the local Josephson theory, the resonance term in the IVC (38) for low velocities (15) is manifested for relatively low JJ conductivities.

By way of an illustration of the dependence of the IVC shape on the ratio (l/d_s) for somewhat thick superconducting electrodes, Fig. 2 shows the envelope (the curve passing through resonance peaks) of the IVC (35) for $\sigma \sim 10^8$ s^{-1} and $\tau = 0$, which has the form

$$\frac{j}{j_c} = \frac{V}{j_c R_s}\frac{L}{l}\left(\Phi_\beta(w_0) + 2\left(\frac{j_1 R_s}{V}\right)^2 \times \exp\left(-\frac{2V_0^2}{V^2}\frac{[(\pi/2) - w_0]}{\cot w_0}\right)\right), \tag{40}$$

where $R_s = (2d/\sigma)$, $V_0 = (\hbar l\omega_{\mathrm{j}}/2|e|L)$, $j_1 = j_c(l/L)^{3/2}$. It follows from Fig. 2 that the slope of the linear segment of the IVC increases with decreasing d_s and the deviation from linearity occurs at lower voltages.

4. It should be noted that, in the limit $L = \infty$, formula (2) is reduced to one describing a solitary vortex in a JJ:

$$\varphi_0 = \pi + 2\arctan[\sinh(z/B_1)/\cos(d_s/B_1)]. \tag{41}$$

In this case, $(d_s/B_1) \equiv w_0$ is determined by (33). Using (41) as a source of perturbation in equation (7) and proceeding in analogy with [2], we obtain the following field of Cerenkov radiation emitted by a solitary vortex:

$$\varphi_{\mathrm{ch}}(s) = 4\pi\exp\left(\frac{\gamma s}{v}\right)\cos\left(\frac{l\omega_j^2 s}{v^2}\right) \times \exp\left\{-\frac{l\omega_j^2}{v^2}\left(\frac{\pi}{2}B_1 - d_s\right)\right\}\theta(-s), \tag{42}$$

where $\theta(x) = 1$, $x > 0$, $\theta(x) = 0$ for $x < 0$, and $\gamma = \beta + (\tau l^2\omega_j^4/v^2)$. Expression (42) is written under the assumption of weak attenuation of a Cerenkov wave over the length of the vortex, i.e., $v \gg (\beta + \tau l^2\omega_j^2/v^2)\min(l, \sqrt{ld_s})$, and the smallness of expression (42) relative to φ_0 in (41) is ensured by the smallness of velocity (15). Using the field (42) and disregarding the attenuation of the Cerenkov wave ($\gamma \longrightarrow +0$), we can easily find the energy flux behind the vortex and the corresponding frictional force decelerating the vortex (see [1, 2]). For a current of constant density j flowing from an external source through the JJ and accelerating the vortex through the Lorentz force $f_L = \Phi_0 j/c \equiv (\pi\hbar j/|e|)$, we write the balance equation for the force of friction and the Lorentz force and obtain the following dependence of the current density on the vortex velocity:

$$\frac{j}{j_c} = 2\pi\frac{l^2\omega_j^2}{v^2}\exp\left(-\frac{2l\omega_j^2}{v^2}\left[\frac{\pi}{2}B_1 - d_s\right]\right). \tag{43}$$

In the limit of bulk electrodes, $d_s \gg l$, expression (43) coincides with that given in [2]. In the limit of thin film-type superconductors with $d_s \ll l$, formula (43) is transformed into

$$\frac{j}{j_c} = 2\pi\frac{l^2\omega_j^2}{v^2}\exp\left(-\frac{\pi\omega_j^2 l\lambda_{j,\,\mathrm{eff}}}{v^2}\right), \qquad (44)$$

where we have introduced the notation $\lambda_{j,\,\mathrm{eff}} \equiv \sqrt{ld_s}$. It can easily be verified that the limit $d_s \ll l$ is similar to the limit of local Josephson electrodynamics [11]. For example, equation (1) in this limit is transformed into the sine-Gordon equation with dissipation, while expression (41) describing a solitary vortex in a JJ is transformed into the formula for a conventional Josephson vortex:

$$\begin{aligned}\varphi_0(z) &= \pi + 2\arctan\{\sinh(z/\lambda_{j,\,\mathrm{eff}})\}\\ &\equiv 4\arctan\{\exp(z/\lambda_{j,\,\mathrm{eff}})\},\end{aligned} \qquad (45)$$

where the role of the Josephson length is played by $\lambda_{j,\,\mathrm{eff}} \equiv \sqrt{ld_s}$.

Taking into account the above remark, we can state that the dependence (44) of the current density on velocity corresponds to the local limit of (1). Consequently, we could consider the application of the approach developed in [1] for deriving formula (44), in which, during the linearization of equation (1), the approximate expression (45) is substituted instead of the exact expression for φ_0 given by (41). It can be easily verified, however, that the approach used in [1] leads to a considerably larger preexponential factor in formulas (42) and (44). This is due to the inaccuracy of solution (45) just in the range of small distances corresponding to short waves we are interested in, which is manifested directly in the linearization of equation (1), when instead of (7) we have an equation with a right-hand side that does not vanish for $v = 0$. Consequently, formula (44) with the substitution $\sqrt{ld_s} \equiv \lambda_{j,\,\mathrm{eff}} \longrightarrow \lambda_j$ correctly describes the relation between the current and the velocity of a conventional Josephson vortex.

5. Let us summarize the obtained results. The application of solution (41) has made it possible to derive expression (43) relating the velocity of a vortex to the current density through a sandwich-type JJ, inducing the vortex motion.

Among other things, formula (44) that we derived for the local limit proved that the application in [1] of the approximate expression (45) for a vortex source exciting Cerenkov waves during its motion, instead of the exact expression (41) used in this paper, does not lead to the correct preexponential factor in (44).

In order to construct the theory of the IVC for a sandwich-type JJ on the basis of the mathematical theory of dislocations [7], we determined the coordinate dependence of the phase difference for Cooper pairs situated on different sides of the JJ for an infinitely long stationary chain of vortices with a nonzero mean magnetic field (2). Similar expressions were found for a chain of vortices with zero magnetic field (4). Expression (2) was used for deriving a general relation determining the IVC for the JJ under investigation. Cerenkov losses for emission of generalized Swihart waves determine the IVC for small ohmic losses. Since normal electrons are virtually absent in the superconducting electrodes of a sandwich at low temperatures, the effect of Cerenkov radiation on IVC should be sought at just such temperatures.

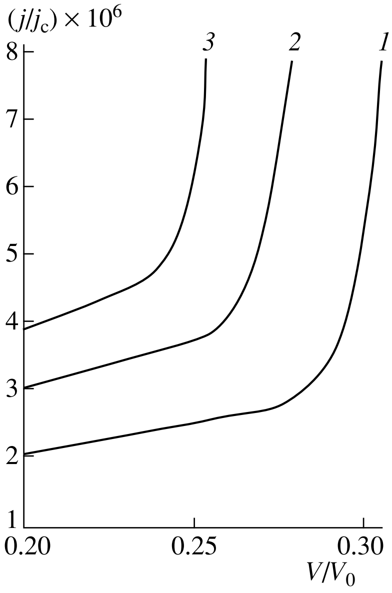

Fig. 2. Current–voltage characteristic for a JJ with a high critical current density for $\tau = 0$, $(l/L) = 10^{-2}$ and $(j_1R_s/V_0) = 10^4$ ($\sigma \sim 10^8\ \mathrm{s}^{-1}$) for different values of the ratio l/d_s: 0.1 (curve *1*), 1 (curve *2*), and 2 (curve *3*).

APPENDIX

Let us verify that expression (2) is a steady-state solution of equation (1). For this purpose, we use the following expansion into Fourier series [10]:

$$\begin{aligned}\frac{d\varphi_0}{dz} &= \frac{2}{B}\frac{\mathrm{dn}(id_s/B, k)\,\mathrm{dn}(z/B, k)}{[1 - k^2\,\mathrm{sn}^2(z/B, k)\,\mathrm{sn}(id_s/B, k)]}\\ &= \frac{1}{B}\left[\mathrm{dn}\left(\frac{z + id_s}{B}, k\right) + \mathrm{dn}\left(\frac{z - id_s}{B}, k\right)\right] \qquad (46)\\ &= \frac{\pi}{BK} + \frac{4\pi}{BK}\sum_{n=1}^{\infty}\frac{q^n}{1 + q^{2n}}\cos\left(\frac{\pi nz}{BK}\right)\cosh\left(\frac{\pi nd_s}{BK}\right),\end{aligned}$$

$$\sin\varphi_0 = -\frac{2\,\mathrm{dn}(id_s/B, k)\,\mathrm{sn}(z/B, k)\,\mathrm{cn}(z/B, k)}{1 - k^2\,\mathrm{sn}(z/B, k)\,\mathrm{sn}(id_s/B, k)}$$

$$= -\frac{\mathrm{dn}(id_s/B, k)}{k^2 \mathrm{sn}(id_s/B, k)\,\mathrm{cn}(id_s/B, k)}\left[\mathrm{dn}\left(\frac{z - id_s}{B}\right) - \mathrm{dn}\left(\frac{z + id_s}{B}\right)\right] = -\frac{\mathrm{dn}(d_s/B, k')\,\mathrm{cn}(d_s/B, k')}{k^2 \mathrm{sn}(d_s/B, k')} \times \frac{4\pi}{K}\sum_{n=1}^{\infty}\frac{q^n}{1 + q^{2n}}\sin\left(\frac{\pi n z}{BK}\right)\cosh\left(\frac{\pi n d_s}{BK}\right). \tag{47}$$

We now use the transformations

$$\frac{1}{2d_s}\int_{-\infty}^{+\infty}\frac{dz'}{\sinh[\pi(z' - z)/2d_s]}\begin{Bmatrix}\cos(nz'/L)\\ \sin(nz'/L)\end{Bmatrix} = \tanh\left(\frac{nd_s}{L}\right)\begin{Bmatrix}-\sin(nz/L)\\ \cos(nz/L)\end{Bmatrix}, \tag{48}$$

where $2\pi L \equiv 2BK(k)$ is the period of the vortex structure (2). Then condition (3) emerges from equation (1) as a condition for its solvability.

This confirms the fact that (2) is a solution of equation (1). Similarly, we can verify the validity of solution (4).

ACKNOWLEDGMENTS

This research was supported by Scientific Council of HTSC (project no. 99002) and the State Program supporting leading scientific schools (grant no. 96-15-96750).

REFERENCES

1. R. G. Mints and I. B. Snapiro, Phys. Rev. B **52**, 9691 (1995).
2. V. P. Silin and A. V. Studenov, Fiz. Tverd. Tela (St. Petersburg) **39**, 444 (1997) [Phys. Solid State **39**, 384 (1997)].
3. V. P. Silin and A. V. Studenov, Zh. Éksp. Teor. Fiz. **113**, 2148 (1998) [JETP **86**, 1177 (1998)].
4. V. P. Silin and A. V. Studenov, Fiz. Tverd. Tela (St. Petersburg) **41**, 582 (1999) [Phys. Solid State **41**, 521 (1999)].
5. Zh. D. Genchev and V. I. Vas'kivskiĭ, Zh. Éksp. Teor. Fiz. **113**, 955 (1998) [JETP **86**, 521 (1998)].
6. G. L. Alfimov and A. F. Popkov, Phys. Rev. B **52**, 4503 (1995).
7. A. Seeger, *Theorie der Gittefehlstellen* (*Handbuch der Physik*), Kristallphysik (Springer, Berlin, 1955), Vol. 17, Part 1.
8. A. S. Malishevskiĭ, V. P. Silin, and S. A. Uryupin, Fiz. Tverd. Tela (St. Petersburg) **41**, 1154 (1999) [Phys. Solid State **41**, 1055 (1999)].
9. G. L. Alfimov and V. P. Silin, Zh. Éksp. Teor. Fiz. **108**, 1668 (1995) [JETP **81**, 915 (1995)].
10. I. S. Gradshteĭn and I. M. Ryzhik, *Tables of Integrals, Sums, Series, and Products* (Nauka, Moscow, 1971).
11. Yu. S. Kivshar and B. A. Malomed, Rev. Mod. Phys. **61** (4), 763 (1989).

Translated by N. Wadhwa

Physics of the Solid State, Vol. 42, No. 4, 2000, pp. 633–637. Translated from Fizika Tverdogo Tela, Vol. 42, No. 4, 2000, pp. 618–622.
Original Russian Text Copyright © 2000 by Vodop'yanov, Kozyrev, Mel'nik.

SEMICONDUCTORS AND DIELECTRICS

Vibrational Spectroscopy of the $Ga_{1-x}Al_xP$ Epitaxial Layers Grown on GaP(111) Substrate by the Liquid-Phase Epitaxial Technique

L. K. Vodop'yanov, S. P. Kozyrev, and N. N. Mel'nik
Lebedev Institute of Physics, Russian Academy of Sciences, Leninskiĭ pr. 53, Moscow, 117924 Russia
e-mail: vodopian@sci.lebedev.ru

Received June 30, 1999

Abstract—The paper reports the results of measurements of the lattice IR reflection and Raman scattering spectra for the $Ga_{1-x}Al_xP$ (x = 0–0.8) films grown on the GaP(111) substrate by the liquid-phase epitaxy technique. The dispersion analysis of the experimental spectra has demonstrated that, for the studied system of the $Ga_{1-x}Al_xP$ alloy, the vibrational spectra of the alloys with different compositions exhibit three modes of the Ga–P vibrations and one mode of the Al–P vibrations. The frequencies of modes only slightly depend on the composition x of the $Ga_{1-x}Al_xP$ alloy, but the composition considerably affects the oscillator strengths of these modes. *© 2000 MAIK "Nauka/Interperiodica".*

Recent renewed interest in semiconducting alloys (solid solutions) is explained by their extensive use in constructing quantum-size electronic structures obtained by the epitaxial growth method. Alloys of III–V semiconducting compounds are very promising materials for these purposes. The vibrational properties of alloys in this system have been studied in detail, for example, in the compounds (GaAl)As [1], Ga(AsP) [2], etc. However, the transformations of the phonon spectra due to variations in the alloy composition have not been adequately investigated for some of these compounds, in particular, (GaAl)P. The lattice IR reflection spectra of the $Ga_{1-x}Al_xP$ bulk crystals were analyzed by Lucovsky *et al*. [3]. Moreover, mention should be made of two works [4, 5] concerned with the investigation of the Raman light scattering in these alloys. Baĭramov *et al*. [4] measured the Raman spectra in the narrow range of compositions at $x < 0.23$. Armelles *et al*. [5] studied the Raman spectra excited at right angles to the surface of thin films grown by the MCVD method on the surface of GaP substrate. Since thin films of the alloy were partially transparent for the exciting lines of a Kr laser, the spectra contained, for the most part, very intense bands of the GaP substrate. This made difficult observation of the fine features associated with the composition transformation of the phonon spectrum.

As far as we know, research works dealing with the lattice IR reflection in the (GaAl)P thin films have never been published. However, this alloy is of particular interest for both investigations into the crystal lattice dynamics and the corresponding model calculations, because the lattice parameters of the terminal binary compounds in this alloy are virtually coincident with each other ($\Delta a/a = 0.003$). This implies that the composition transformation of the phonon spectrum can be observed in the pure form free from the predominant effect of elastic stresses brought about by the difference in lattice parameters.

The present paper has reported the results of the performed measurements of the lattice IR reflection and Raman light scattering spectra for the $Ga_{1-x}Al_xP$ epitaxial films grown on the GaP substrate by the liquid-phase epitaxial technique. The dispersion analysis of the experimental lattice reflection spectra revealed that, for all the studied compositions, their vibrational spectra exhibit modes of the Ga–P and Al–P vibrations, namely, three modes of the Ga–P vibrations and one mode of the Al–P vibrations. The frequencies of modes only slightly depend on the composition x; however, the composition appreciably affects the oscillator strengths of these modes. The results of IR measurements were confirmed by the data obtained from the analysis of the Raman spectra. The Raman scattering technique provides the direct measurements of the characteristics of the TO- and LO-phonons and, thus, makes it possible to determine the type of transformation of the vibrational spectrum. It was found that AlP-like vibrations manifest themselves in one mode, whereas the GaP-like vibrations are characterized by more complex dependences outside the province of classical concepts. These anomalies can be explained in the framework of the quasi-molecular crystal lattice model of the alloy [6, 7].

1. GROWTH OF FILMS AND MEASUREMENTS

The $Ga_{1-x}Al_xP$ epitaxial films with the AlP content varying in the range x = 0–0.8 were grown on the GaP(111) substrate by the liquid-phase epitaxial tech-

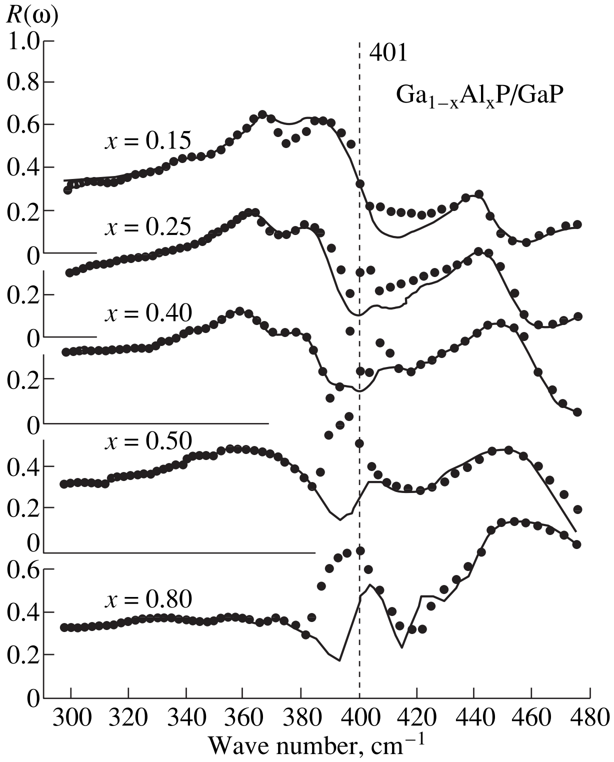

Fig. 1. The lattice reflection spectra of the $Ga_{1-x}Al_xP$ films on the GaP substrate. Points are the experimental spectra and the solid lines correspond to the calculations.

nique from the Ga-enriched melt (GIREDMET). The thickness of the grown layers was 6–10 μm. No additional surface treatment of the films was made to perform the IR and Raman measurements, except the films with composition $x = 0.8$. The films of this composition were coated with a thin organic film to ensure protection against hydrolysis in an air atmosphere.

The chemical composition of the $Ga_{1-x}Al_xP$ films was specified by the composition of the GaP / AlP mixture in the liquid phase. According to Sonomura *et al.* [8], the composition of epitaxial layers in the GaP–AlP system virtually coincides with the composition of the initial mixture in the liquid phase. Moreover, these authors compared the film compositions determined by the electron microprobe analysis and the results of measurements of the cathodoluminescence spectra for the same samples and revealed that the location of the cathodoluminescence peak varies linearly with respect to the frequency as the mole fraction of AlP changes in the $Ga_{1-x}Al_xP$ alloy [8]. For this reason, the electron microprobe analysis was carried out for the samples with compositions $x = 0$ and $x \approx 0.5$, whereas the molar composition of the other films was evaluated from the cathodoluminescence data.

The long-wavelength IR reflection spectra were recorded at room temperature on a laboratory vacuum diffraction IR spectrometer with an OAP-5 opticoacoustic receiver as an infrared detector with a spectral resolution of no worse than 1 cm^{-1}.

The Raman scattering spectra were excited with the 4880 Å line of an argon laser and then were recorded on a double monochromator of an U-1000 spectrometer with a resolution of 1 cm^{-1}. The measurements were performed at room temperature in the backscattering geometry. The preliminary measurements of the Raman spectra with a normal incidence of the exciting beam onto the film surface showed that the TO- and LO-phonon bands of the GaP substrate predominate in the spectrum (it is known that gallium phosphide exhibits a very high Raman scattering efficiency). Hence, in order to tune away from the lines of a substrate, the Raman scattering spectra were excited from the end face of the epitaxial film. For this purpose, we used a microattachment to accomplish the focusing of the laser radiation onto a spot of diameter from 2 to 3 μm. This method of excitation made it possible to obtain the Raman spectra characterizing a thin layer of the GaP alloy.

2. RESULTS AND DISCUSSION

Figure 1 displays the IR reflection spectra in the range of lattice vibrations for the $Ga_{1-x}Al_xP$ films on the GaP(111) substrate with compositions $x = 0.15$, 0.25, 0.40, 0.50, 0.58, and 0.80 at a temperature of 300 K. The experimental and calculated spectra are shown by points and solid lines, respectively.

Earlier [9], we discussed the features of IR reflection spectra in the range of lattice vibrations for the film–substrate structures with a film thickness of 1–2 μm by the example of the $Zn_{1-x}Cd_xSe/GaAs$ structures. The reflection spectra of these films are rather simple in shape. Compared to the reflection spectrum of the substrate in the range of its transparency, the former spectra resemble the absorption curve of the film and are readily amenable to the mathematical treatment with the use of dispersion analysis.

In the case of the film–substrate structures with a film thickness of 6–10 μm, the specific feature of the reflection spectra under consideration (Fig. 1) resides in the fact that the reflection spectrum of a film almost coincides with the reflection spectrum of the bulk material due to strong absorption in the film in the range of lattice vibrations. The skin depth for IR radiation in the range of lattice vibrations turns out to be less than the film thickness. For comparison, Fig. 2 demonstrates the lattice reflection spectra of the $Ga_{1-x}Al_xP$ ($x = 0.25$) film on the GaP substrate (shown by points) and the $Ga_{1-x}Al_xP$ ($x = 0.23$) bulk material [3] (displayed by the heavy solid line). The structures and intensities of the reflection bands almost coincide with each other, respectively. The differences in the spectra are observed only in the range of a relative transparency of the film (i.e., between the bands of “residual beams” corresponding to the GaP- and AlP-like vibrations), where the spectrum of the film on the substrate shows an interference peak near the frequency of the LO-mode of the GaP substrate ($\omega_{LO} \approx 401$ cm^{-1}). An interference effect of this type was observed earlier by Gerbaux and Gadni [10] in the IR reflection spectra of CdTe. In the vicinity of the LO-mode, the substrate is characterized by a strong anomalous dispersion of the refractive index, and, in the case of transparent film, the interference increases at the expense of a multiple reflection in the film.

For interpretation of the lattice reflection spectra measured in this work (Fig. 1), we consider the model structure formed by a thin film on the bulk (semi-infinite) substrate under the assumption that the film is uniform in thickness. In the framework of this model structure for a film of thickness L with the dielectric function $\varepsilon_f(\omega)$ and a substrate with the dielectric function $\varepsilon_s(\omega)$ at a normal incidence of light, the amplitude reflectivity (without regard for multiple reflection in the film) has the form [11]

$$r_{1fs}(\omega) = \frac{r_{1f}(\omega) + r_{fs}(\omega)\exp(i2\beta)}{1 + r_{1f}(\omega)r_{fs}(\omega)\exp(i2\beta)},$$

where

$$r_{1f} = \frac{1-\sqrt{\varepsilon_f(\omega)}}{1+\sqrt{\varepsilon_f(\omega)}},$$

$$r_{fs}(\omega) = \frac{\sqrt{\varepsilon_f(\omega)} - \sqrt{\varepsilon_s(\omega)}}{\sqrt{\varepsilon_f(\omega)} + \sqrt{\varepsilon_s(\omega)}}, \quad \beta = \frac{2\pi L\sqrt{\varepsilon_f(\omega)}}{\lambda}.$$

Here, $\lambda = 10^4/\omega$ is the wavelength. The reflectivity is defined as $R(\omega) = [r_{1fs}(\omega)]^2$. The special features in the interpretation of the reflection spectra of films on the substrate in the range of lattice vibrations were discussed earlier in [9, 12]. Consideration of the multiple reflection in the film at the film–substrate and film–vacuum interfaces leads to a very awkward expression for the reflectivity (see, for example, [13]) and does not provide additional information regarding the lattice vibrations in the film; the sole exception is the demonstration of the complete coincidence between the experimental and calculated spectra even in the range of manifestation of the interference effect.

The dielectric function $\varepsilon_f(\omega)$ of a film was considered in the classical additive form

$$\varepsilon_f(\omega) = \varepsilon_\infty + \sum_j \frac{S_j\omega_{tj}^2}{\omega_{tj}^2 - \omega^2 - i\omega\gamma_j}.$$

In calculations of the reflectivity $R(\omega)$, we varied the following parameters in the formula for $\varepsilon_f(\omega)$: the frequency ω_{tj} of the jth TO-mode, the oscillator strength S_j of the jth TO-mode, and the damping parameter γ_j. The calculated reflection spectra are shown in Fig. 1 by solid lines. Except for the range of manifestation of the interference effect in the vicinity of the frequency $\omega_{LO} \approx 401$ cm^{-1} (LO-modes of the GaP substrate), the experimental and calculated $R(\omega)$ spectra are in good agreement.

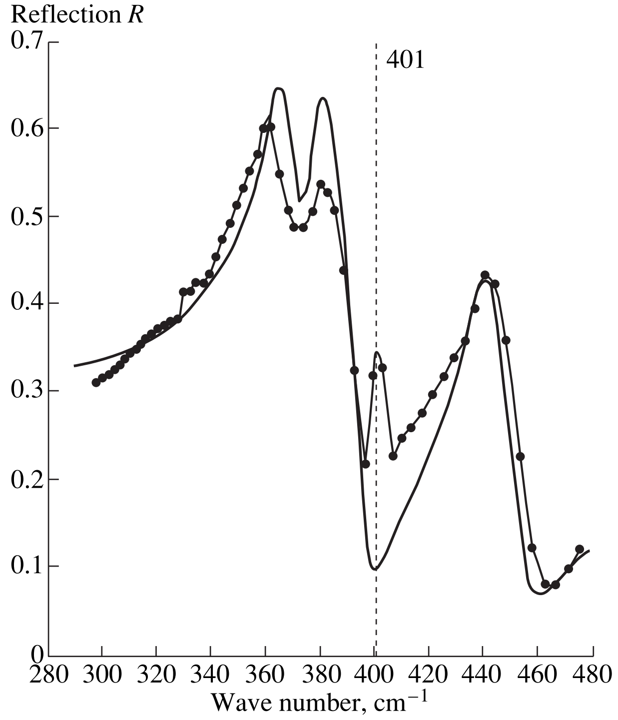

Fig. 2. Comparison of the lattice reflection spectra for the $Ga_{1-x}Al_xP$ film ($x = 0.25$) (shown by points) and the bulk crystal of about the same composition ($x = 0.23$) (displayed by the heavy solid line).

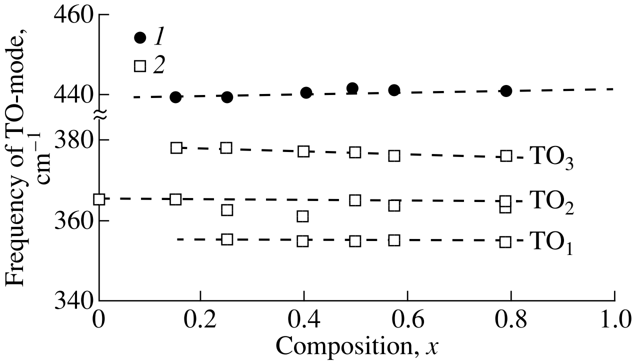

Fig. 3. Dependences of the frequency of TO-mode on the composition of the $Ga_{1-x}Al_xP$ films according to the dispersion analysis of the reflection spectra: (*1*) frequencies of modes of the Al–P vibrations and (*2*) frequencies of modes of the Ga–P vibrations.

The dependences of the frequency of TO-mode on the composition of the $Ga_{1-x}Al_xP$ films are displayed in Fig. 3. The spectra exhibit one mode of the Al–P vibrations ($\omega_t^{AlP} \approx 442$ cm^{-1}) and three modes of the Ga–P vibrations ($\omega_t^{GaP} \approx 365$, 355, and 377 cm^{-1}). The fre-

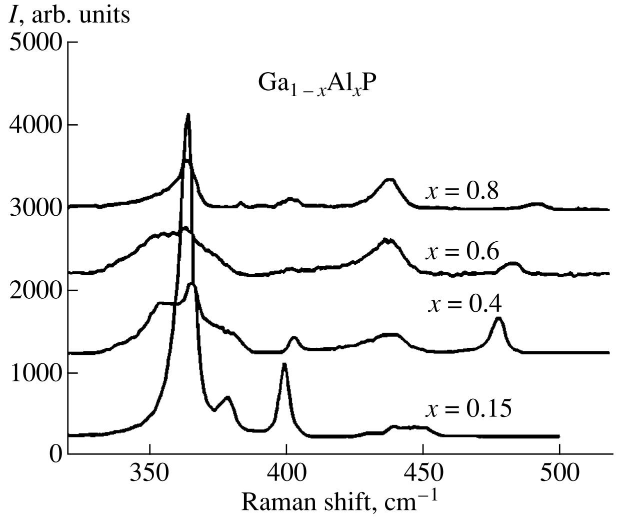

Fig. 4. The first-order Raman spectra for the $Ga_{1-x}Al_xP$ epitaxial films of different compositions upon excitation with the 4880 Å line of an argon laser.

quencies of these modes weakly depend on the composition of the $Ga_{1-x}Al_xP$ film, whereas the transformation of the phonon spectrum with a change in the composition is governed by the oscillator strengths of these modes.

Let us now consider the results obtained by another independent optical method, namely, the Raman scattering technique. Figure 4 depicts typical Raman spectra measured for $Ga_{1-x}Al_xP$ alloys of different compositions $x = 0.15$, 0.4, 0.6, and 0.8 upon excitation with the 4880 Å line of an argon laser. In the high-frequency range, the spectrum contains two bands attributed to AlP-like vibrations. As the GaP content increases, the intensity of a band at ≈ 440 cm^{-1} increases, whereas its frequency location remains virtually unchanged. The second band shifts toward the high-energy range with an increase in x. A more intricate pattern is observed in the low-frequency range of the spectrum, which is characterized by the manifestation of the GaP-like vibrations. There appears a number of bands (not always clearly resolved in frequency) whose intensity changes with a change in x. Figure 5 shows the spectrum of the alloy with $x = 0.25$ in a narrower spectral range. It can be seen that many Raman scattering bands manifest themselves in a veiled form as a shoulder on the slope of a more intense peak or at the background of the noise. The true parameters of these bands were determined with the computer program for contour separation.

In order to interpret the Raman bands observed experimentally, it was necessary to elucidate their nature (longitudinal or transverse). For this purpose, we carried out the polarization measurements. The tensors of effective Raman scattering cross-sections for the polar cubic crystals with a structure of zinc blende were calculated by Loudon [14]. In accord with the selection rules following from consideration of these tensors, upon excitation in the [111] direction, the polarized spectra (parallel polarization of the exciting and scattering light) should manifest only longitudinal phonons. The depolarized spectra (crossed polarizations) can exhibit both longitudinal and transverse phonons. As an example, Fig. 6 displays the polarization spectrum of the alloy with composition $x = 0.5$. It is seen that the intensity of bands at ≈ 405 and ≈ 480 cm^{-1} drastically decreases, which makes possible the assignment of these bands to the LO-phonons.

The dependences of the frequency of TO- and LO-phonons on the alloy composition x (Fig. 7) were obtained from the analysis of the experimental spectra of the $Ga_{1-x}Al_xP$ films. As can be seen, the AlP-like

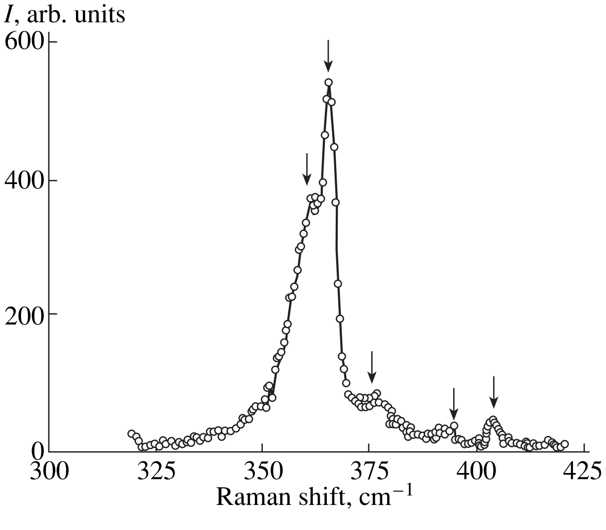

Fig. 5. Raman spectrum for a film of the $Al_{0.25}Ga_{0.75}P$ alloy upon excitation with the 4880 Å line.

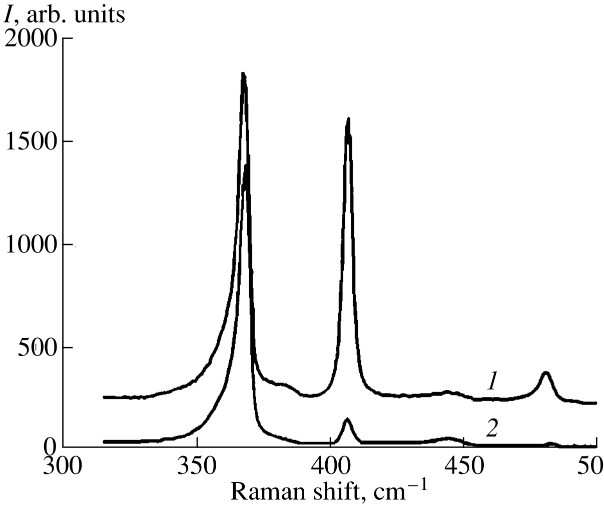

Fig. 6. Polarization spectra for a film of the $Al_{0.5}Ga_{0.5}P$ alloy. Polarization: (*1*) $Z(x, x)\bar{Z}$ and (*2*) $Z(x, y)\bar{Z}$.

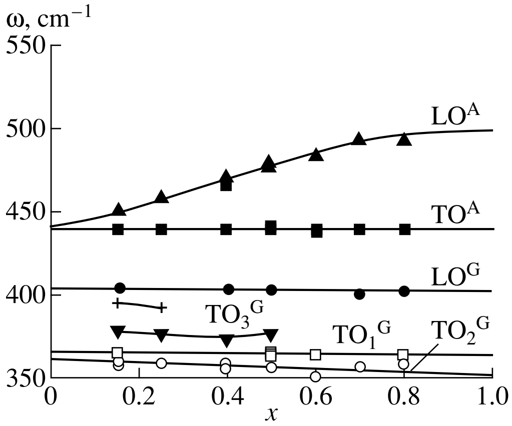

Fig. 7. Dependences of the frequency of TO- and LO-phonons on the aluminum content in films of the $Ga_{1-x}Al_xP$ alloy.

vibrations (two upper curves) follow the classical two-mode scheme of transformations of the phonon spectrum. At a low aluminum concentration, the TO- and LO-branches converge to a common point at the frequency of the local vibration of aluminum replacing phosphorus in the GaP lattice (≈ 440 cm^{-1}), which is in close agreement with the experimental value of this frequency equal to 438 cm^{-1} [15]. Three TO-branches and one LO-branch are observed for the GaP-like vibrations. It is characteristic that, as the gallium concentration decreases, the TO- and LO-branches do not converge to a common point corresponding to the energy-gap mode of gallium in the AlP lattice. A possible reason for such behavior is the absence of AN energy gap between the allowed energy bands of acoustic and optical vibrations in the AlP lattice. Unfortunately, the phonon spectrum of this compound is not clearly understood. The origin of the branch segment at ≈ 393 cm^{-1} in the range of compositions x = 0.15–0.25 remains unknown. It should be noted that the concentration dependences of the TO-branches obtained by the Raman scattering and IR spectroscopic techniques agree closely with each other. Thus, the presence of three branches of transverse optical phonons in the spectra of alloys in the (GaAl)P system was demonstrated by two independent optical methods.

A similar transformation of the phonon spectrum was observed earlier in the thoroughly studied system of the $Hg_{1-x}Cd_xTe$ alloy [6, 7] and explained within the quasi-molecular mode. According to this model, the crystal structure of the alloy is treated as formed from five tetrahedral elementary cells with a common anion at the center of a tetrahedron and various combinations of cations in vertices of the tetrahedron. For each of the Hg–Te and Cd–Te vibrations, four vibrational modes are possible depending on the type of elementary cell. It is assumed that the elementary cells do not interact with each other (by virtue of the domination of the short-range covalent bonding in tetrahedral compounds). Therefore, the frequency of these modes are independent of the alloy composition, and a change in the vibrational spectrum of the crystal with a change in the composition is governed by the concentration ratio of different elementary cells. Note that not all modes can be resolved upon measurements of the vibrational spectrum, because the splitting of modes for different elementary cells depends to a large measure on both the ratio of cationic masses and the ratio between masses of the cation and the anion for each pair. This likely explains the fact that, for the system of the $Ga_{1-x}Al_xP$ alloy, the vibrational spectra measured in this work exhibit one mode of the Al–P vibrations and three modes of Ga–P-like vibrations.

ACKNOWLEDGMENTS

We are grateful to A.A. Shlenskiĭ and L.V. Druzhinina (GIREDMET) for growing the (GaAl)P films.

This work was supported by the Russian Foundation for Basic Research (project no. 97-02-16791) and the State Scientific and Technical Program “Physics of Quantum and Wave Processes” (“Fundamental Spectroscopy,” project no. 0.8.02.73).

REFERENCES

1. M. Bernasconi, L. Colombo, L. Miglio, *et al.*, Phys. Rev. B **43**, 14 447 (1991).
2. M. Teicher, R. Beserman, M. V. Klein, *et al.*, Phys. Rev. B **29**, 4652 (1984).
3. G. Lucovsky, R. D. Burnham, and A. S. Alimonda, Phys. Rev. B **14**, 2503 (1976).
4. B. Kh. Baĭramov, V. N. Bessolov, É. Yane, *et al.*, Pis’ma Zh. Tekh. Fiz. **6**, 1432 (1980) [Sov. Tech. Phys. Lett. **6**, 618 (1980)].
5. G. Armelles, J. M. Calleja, and E. Munoz, Solid State Commun. **65**, 779 (1988).
6. S. P. Kozyrev, V. N. Pyrkov, and L. K. Vodop’yanov, Fiz. Tverd. Tela (Leningrad) **34**, 3695 (1992) [Sov. Phys. Solid State **34**, 1978 (1992)].
7. S. P. Kozyrev, L. K. Vodop’yanov, and R. Triboulet, Phys. Rev. B **58**, 1374 (1998).
8. H. Sonomura, T. Nanmori, and T. Miyauchi, Appl. Phys. Lett. **24**, 77 (1974).
9. L. K. Vodop’yanov, S. P. Kozyrev, and Yu. G. Sadof’ev, Fiz. Tverd. Tela (S.-Peterburg) **41**, 982 (1999) [Phys. Solid State **41**, 893 (1999)].
10. X. Gerbaux and A. Gadni, Int. Conf. Infrared Millimeter Waves **2**, 83 (1981).
11. H. W. Verleur, J. Opt. Soc. Am. **58**, 1356 (1968).
12. S. P. Kozyrev, Fiz. Tverd. Tela (S.-Peterburg) **36**, 3008 (1994) [Phys. Solid State **36**, 1601 (1994)].
13. B. Harbecke, Appl. Phys. B **39**, 165 (1986).
14. R. Loudon, Adv. Phys. **13**, 423 (1964).
15. D. Hon, W. Fost, W. G. Spitzer, *et al.*, Phys. Rev. Lett. **25**, 1184 (1970).

Translated by O. Borovik-Romanova

Physics of the Solid State, Vol. 42, No. 4, 2000, pp. 638–640. Translated from Fizika Tverdogo Tela, Vol. 42, No. 4, 2000, pp. 623–625.
Original Russian Text Copyright © 2000 by Nemov, Musikhin, Osipov, Proshin.

SEMICONDUCTORS AND DIELECTRICS

Energy Spectrum of $(Sn_{0.65}Pb_{0.35})_{0.95}Ge_{0.05}Te$ Solid Solutions

S. A. Nemov, S. F. Musikhin, P. A. Osipov, and V. I. Proshin
St. Petersburg State Technical University, ul. Politekhnicheskaya 29, St. Petersburg, 195251 Russia

Received September 7, 1999

Abstract—The paper reports the study on the resistivity ρ and thermoemf S of the $(Sn_{0.65}Pb_{0.35})_{0.95}Ge_{0.05}Te$ solid solution layers. The dependences of ρ and S on the hole concentrations in the range 3×10^{19}–2×10^{21} cm^{-3} exhibit jumps in the resistivity and thermoemf minima at close hole concentrations $p_1 \approx 9 \times 10^{19}$ cm^{-3}, $p_2 \approx 2.5 \times 10^{20}$ cm^{-3}, and $p_3 \approx 4.5 \times 10^{20}$ cm^{-3}. The observed jumps and minima suggest a complex structure of the valence band and the presence of critical points in the energy spectrum of holes. According to the data for SnTe, the critical points in the energy spectrum at the given hole concentrations are identified as the Σ-extremum, saddle point $L\Sigma$, and Δ-extremum, respectively. *© 2000 MAIK “Nauka/Interperiodica”.*

A specific feature of solid solutions based on tin, germanium, and lead tellurides is the crystallization with a noticeable deviation from the stoichiometry in the direction of excess chalcogen (~ 1 at. % and more). The vacancies formed in the metallic sublattice as a result of this deviation are electrically active. At high concentrations of electrically active defects, the typical concentrations of holes in SnTe and SnTe-based solid solutions can reach $p \sim 10^{20}$–10^{21} cm^{-3} [1]. In this case, the control over the electrophysical properties of the solid solutions with the help of doping becomes inefficient because of very high concentrations of charge carriers and intrinsic defects. The exception is the indium impurity, whose solubility in $Sn_{1-x}Pb_xTe$ is of about 10–20 mol % InTe [2–5]. An interesting feature of $Sn_{1-x}Pb_xTe$ bulk samples doped with indium impurity is the bulk superconductivity through the indium impurity states. In particular, the samples containing 16–20 mol % InTe are characterized by the critical temperature $T_C \approx 4$K. The solid solutions based on SnTe : In with high critical temperatures are promising materials for the production of superconducting bolometers operating at helium temperatures. However, the lack of data on the band structure of the $Sn_{1-x}Pb_xTe$ solid solution over a wide energy range makes difficult the interpretation of experimental data and the determination of the In impurity contribution to the transport phenomena. In this respect, the present work is an attempt to investigate the band spectrum of the $(Sn_{0.65}Pb_{0.35})_{0.95}Ge_{0.05}Te$ solid solution over a wide range of charge carrier concentrations ($p \sim 3 \times 10^{19}$–6×10^{21} cm^{-3}).

1. SAMPLES UNDER STUDY

Possible practical applications of SnTe : In-based solid solutions are connected with preparation of thin layers. In this work, we studied the layers prepared from a batch that was obtained from bulk samples [4] of composition $[(Sn_{0.65}Pb_{0.35})_{0.95}Ge_{0.05}]_{1-x}In_xTe$ with indium content $x = 0.05$–0.20 in the batch. The samples were fabricated by the metal-powder method. The ingots were synthesized under vacuum by melting the initial components of semiconductor purity. After grinding of the ingots (the mean grain size $d \approx 0.1$ mm), the hot pressing was carried out at a temperature of 350°C. Then, the samples were annealed under vacuum at a temperature of 600°C for 120 h. The X-ray microanalysis did not reveal the second phase in the samples.

The layers studied were produced by the pulsed laser deposition method with the use of ceramic samples as targets. The pulsed laser deposition, as a rule, provides a congruent evaporation of many-element targets and makes it possible to obtain films whose composition differs only slightly from the batch composition. However, upon deposition of the $Sn_{1-x}Pb_xTe$: In solid solution, the distribution of indium over the film thickness turns out to be nonuniform. It was established earlier that the uniformity of the indium distribution over the thickness of the $Sn_{1-x}Pb_xTe$ layers can be increased by addition of germanium to the solid solution [6, 7]. This provides an explanation for the choice of the composition of the target material.

A change in the hole concentration in the films and, correspondingly, the shift of the Fermi level in the energy spectrum were accomplished by the variation in deposition conditions (in particular, the substrate temperature, the energy of laser pulse, and the steepness of its leading edge) and indium content in the batch.

The positive signs of the thermoelectric coefficient (S) and Hall coefficient (R) in the thin layers studied indicate the hole-type conduction in the samples. The small values of S and R suggest high concentrations of charge carriers and a strong degeneracy of the hole gas. In this work, the hole concentration in layers was determined from the data on the Hall effect according to the formula $p = (eR)^{-1}$. Since we studied the sufficiently thick films (thickness, 110–190 nm) with a high hole concentration (in the range 3×10^{19}–6×10^{21} cm^{-3}), no effects due to the size quantization manifested themselves in the films, and the electrophysical parameters of the films and bulk samples at the same hole concentrations were close to each other.

2. RESULTS AND DISCUSSION

The temperature dependences of the resistivity (ρ), Hall coefficient (R), and Seebeck coefficient (S) were measured in the temperature range 77–400 K. These dependences are similar to those studied earlier for SnTe [9]. Since distinctive features are not observed in the temperature dependences of the kinetic coefficients, we consider their concentration dependences. Let us take up first the data on the resistivity (see Fig. 1a). It is seen that, as expected, the resistivity of layers, on average, decreases with an increase in the hole concentration. Moreover, the $\rho(p)$ curve shows several abrupt jumps in the resistivity at the hole concentrations $p_1^{\rho} = 9 \times 10^{19}$, $p_2^{\rho} = 3 \times 10^{20}$, and $p_3^{\rho} = 4.5 \times 10^{20}$ cm^{-3}, respectively.

The observed jumps in the resistivity indicate a complex structure of the valence band of the solid solution and also the presence of critical points in the energy spectrum of holes. The resistivity jump is caused by the transition of the Fermi level through a singular point of the energy spectrum. This is accompanied by the appearance of a kink in the energy dependence of the relaxation time, which, in turn, should give rise to a minimum in the thermoemf [as is known, in the case of strong degeneracy, the thermoelectric coefficient $S \sim \left(\left.\frac{d\ln\tau}{d\ln\varepsilon}\right|_{\varepsilon_F} + \frac{3}{2}\right)$]. Therefore, the experimental data on the thermoemf can serve as an additional evidence for the presence of critical points in the energy spectrum.

As is seen from Fig. 1b, the dependence of the thermoelectric coefficient on the hole concentration $S(p)$ also exhibits complex nonmonotonic behavior and shows several clear minima at the critical hole concentrations $p_1^S = 9 \times 10^{19}$, $p_2^S = 2.5 \times 10^{20}$, and $p_3^S = 4.5 \times 10^{20}$ cm^{-3}, respectively. It is worth noting that the aforementioned features are observed both at low temperatures $T \sim 120$ K and at room temperature. A comparison of the data on ρ and S (see Figs. 1a, 1b) reveals a clearly pronounced correlation. The jumps in the electrical resistivity of layers and dips (minima) of the thermoemf in the isotherms of the dependences of ρ and S on the Hall concentrations of holes are observed at close values of the Fermi energy.

The identification of critical points requires information on the valence band structure of the solid solution. Unfortunately, these data for the solid solution studied are not available in the literature. However, with due regard for the structural similarity of the valence bands of A^4B^6 compounds, one can expect that the energy spectra of solid solutions based on SnTe and tin telluride will be similar to each other. The calculations of the band structure for A^4B^6 compounds with a cubic lattice demonstrate that the main extremum of the valence band is located at the L points of the Brillouin zone. Moreover, the valence band is characterized by two groups of singular points of the spectrum, which are situated at the Σ and Δ points on the twofold and fourfold axes, respectively. These axes are characterized by the large effective hole masses (larger than the mass of a free electron). Depending on the sign of heavy masses, these points can be either points of an extremum (the 2nd and 3rd extrema of the valence band), or the saddle points. From the band structure calculations and topological reasons it follows that, if the extrema of valence band are located at the Σ points, one

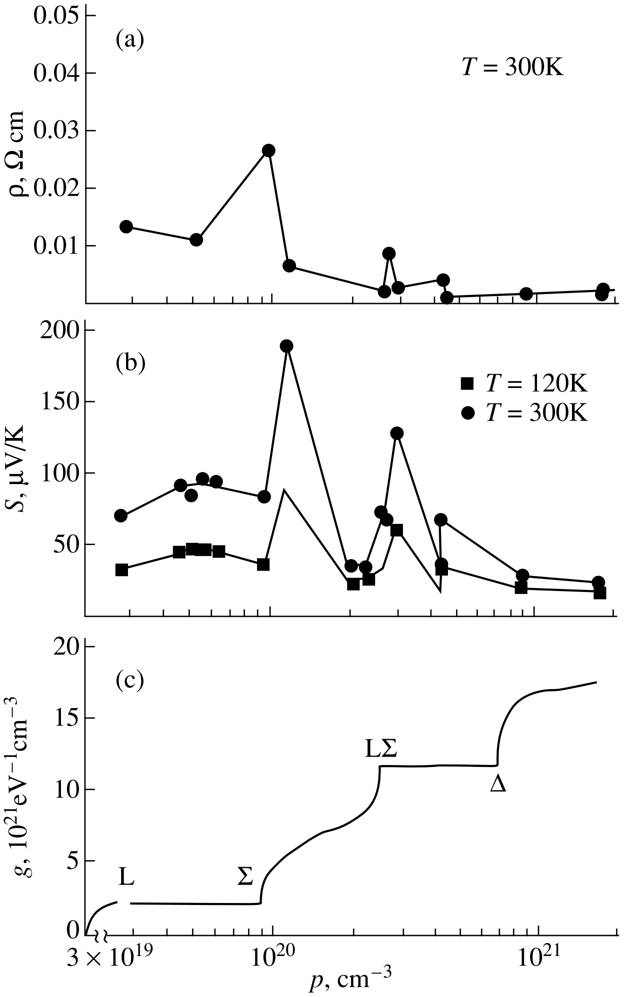

Fig. 1. Isotherms of concentration dependences of (a) the resistivity and (b) the thermoelectric coefficient for the $(Sn_{0.65}Pb_{0.35})_{0.95}Ge_{0.05}Te$: In solid solution. (c) The energy spectrum of SnTe (according to the data taken from [8]).

more group of saddle points arises in the $L\Sigma$ direction. According to [8], the critical points of the spectrum on the twofold Σ and fourfold Δ axes in SnTe are the points of extrema. In this case, as mentioned above, the saddle points appear in the $L\Sigma$ direction (see Fig. 1c).

A comparison of the critical hole concentrations in the $(Sn_{0.65}Pb_{0.35})_{0.95}Ge_{0.05}Te$: In solid solution in SnTe (according to the data obtained in [8]) reveals their closeness (see Fig. 1c). This allows us to identify the critical points of the energy spectrum at the hole concentrations $p_1 = 9 \times 10^{19}$, $p_2 = 3 \times 10^{20}$, and $p_3 = 4.5 \times 10^{20}$ cm^{-3} as the Σ-extremum (~ 9×10^{19} cm^{-3} in SnTe), the saddle point $L\Sigma$ (~ 2.5×10^{20} cm^{-3} in SnTe) and the Δ-extremum (~ 7×10^{20} cm^{-3} in SnTe), respectively. A slight discrepancy between the critical hole concentrations in the solid solution and in SnTe is likely due to the fact that the location of critical points in the spectrum depends on the ratio between components in the solid solution.

REFERENCES

1. N. Kh. Abrikosov and L. E. Shelimova, *Semiconducting Materials Based on* $A^{IV}B^{VI}$ *Compounds* (Nauka, Moscow, 1975).
2. V. I. Kaĭdanov and Yu. I. Ravich, Usp. Fiz. Nauk **145**, 51 (1985) [Sov. Phys. Usp. **28**, 31 (1985)].
3. L. D. Dudkin, N. A. Erasova, V. I. Kaĭdanov, *et al.*, Fiz. Tekh. Poluprovodn. (Leningrad) **6**, 2294 (1972) [Sov. Phys. Semicond. **6**, 1934 (1972)].
4. G. S. Bushmarina, I. A. Drabkin, V. V. Kompaniets, *et al.*, Fiz. Tverd. Tela (Leningrad) **28**, 1094 (1986) [Sov. Phys. Solid State **28**, 612 (1986)].
5. G. S. Bushmarina, I. A. Drabkin, D. V. Mashovets, *et al.*, Physica B (Amsterdam) **169**, 687 (1991).
6. D. I. Popov, S. F. Musikhin, S. A. Nemov, *et al.*, Fiz. Tverd. Tela (S.-Peterburg) **37**, 194 (1995) [Phys. Solid State **37**, 106 (1995)].
7. S. A. Nemov, S. F. Musikhin, R. V. Parfen’ev, *et al.*, Fiz. Tverd. Tela (S.-Peterburg) **37**, 3523 (1995) [Phys. Solid State **37**, 1936 (1995)].
8. G. S. Bushmarina, I. A. Drabkin, M. A. Kvantov, *et al.*, Fiz. Tverd. Tela (Leningrad) **32**, 2869 (1990) [Sov. Phys. Solid State **32**, 1666 (1990)].
9. A. Sagar and R. C. Miller, in *Proceedings of the International Conference on Semiconductor Physics, Exeter, England, 1962* (Exeter, 1962).

Translated by T. Galkina

Physics of the Solid State, Vol. 42, No. 4, 2000, pp. 641–647. Translated from Fizika Tverdogo Tela, Vol. 42, No. 4, 2000, pp. 626–631.
Original Russian Text Copyright © 2000 by Shchennikov.

SEMICONDUCTORS AND DIELECTRICS

Magnetoresistance and Thermopower of Tellurium at High Pressures up to 30 GPa

V. V. Shchennikov

Institute of Metal Physics, Ural Division, Russian Academy of Sciences, ul. S. Kovalevskoĭ 18, Yekaterinburg, 620219 Russia

Received in final form, October 7, 1999

Abstract—Measurements are reported of the transverse magnetoresistance *MR* and of the thermopower *S*, carried out at high pressures *P* on Te single crystals in synthetic-diamond chambers. The *MR* is found to increase with decreasing gas width under a pressure up to 4 GPa as one approaches the semiconductor–metal phase-transition point, to fall off subsequently in the high-pressure metallic phase. The behavior of *S*(*P*) correlates with the pressure dependences of the measured *MR*. A negative *MR* at $T = 77$ K was found within a narrow interval $P = 1.5$–2 GPa, where the valence band of Te is assumed to undergo rearrangement. Above the point of the phase transition to the β-Po structure, *MR* is established to increase with pressure for $P > 12$ GPa. The *MR* data are used to estimate the hole mobility μ for various Te phases. A comparison is made of the mobilities in Te, Se, and high-pressure phases of mercury chalcogenides, which are their structural and electronic analogs, for pressures of up to 30 GPa. © *2000 MAIK “Nauka/Interperiodica”.*

The thermopower (Seebeck coefficient) *S* and the transverse magnetoresistance *MR* characterize the gap width ε_g, concentration, and mobility μ of carriers in semiconductors, and, therefore, investigation of these effects provides information on the character of variation of the electronic structure of both the original and high-pressure phases [1–7]. When deriving μ data from the Hall effect and conductivity, the experimental values can be distorted by the carrier concentration being spatially inhomogeneous. For instance, the room-temperature hole mobility μ in Se obtained from such measurements is less than 1 cm^2/Vs, while *MR* data yield $\mu \approx 50$ cm^2/Vs [5]. Studies of the influence of plastic deformation on the electric properties of Se indicate the existence of potential barriers, which originate from lattice defects and result in spatial concentration inhomogeneities [5]. The conductivity of selenium is determined by the low concentration of holes in depleted zones, while the Hall effect and *S* are accounted for by the high hole concentration in other regions [5]. In contrast to the Hall effect, magnetoresistance permits one to perform direct measurements of μ in selenium, and it does not depend on carrier concentration [5]. The behavior of *MR* permits certain conclusions on the variation of the mobility and other carrier characteristics under a monotonic variation of the parameters of the electron spectrum and in phase transitions in the electron system.

The most convenient chambers for electrical measurements at pressures of up to 50 GPa are those made of synthetic diamond [6, 7]. The technique employed in *MR* and *S* studies at *P* of up to 30 GPa in such chambers [8, 9] was used to investigate the high-pressure phases of Hg, Cd, Zn chalcogenides and such elemental semiconductors as Se and I_2 [9–11]. Some materials (CdTe, CdSe, CdS, ZnSe, ZnS, and I_2 [9]) exhibited a negative *MR*, whereas in the chalcogenides of mercury and Se, one observed *MR* sign reversal in direct and reverse structural phase transformations [9, 10]. The sign reversal of *S* and *MR* reflects changes in the type of the majority carriers and their scattering mechanisms, which occur as a result of an electron structure rearrangement [3, 4, 9, 10].

This paper reports on measurements of *S* and *MR* carried out on Te single crystals at quasihydrostatic pressures of up to 30 GPa. In this pressure region, a semiconductor–metal transition has been revealed [6, 7, 12], and structural changes with increasing lattice symmetry and the coordination number have been found to take place in the following order: trigonal phase I ⟶ monoclinic II (4 GPa) ⟶ orthorhombic III (6.8 GPa) ⟶ rhombohedral IV (10.6 GPa) ⟶ bcc V (27 GPa) [13]. This work aimed to study the changes in the electron structure of Te accompanying the pressure-induced lattice transformation by measuring *MR* and *S*.

1. EXPERIMENTAL

The pressure dependences of *S* and *MR* were studied in two high-pressure chambers, whose anvils made of synthetic diamond had operating diameters of 0.8 and 0.6 mm [8, 9]. For measurements in the pressure region of up to 10 GPa, Toroid-type chambers [14] of a VK6 hard alloy were employed. Catlinite was used as a pressure-transmitting medium. The magnitude of pressure was estimated to within 10% from the calibration graphs relating *P* to the compressive force and constructed for each chamber with the use of the known

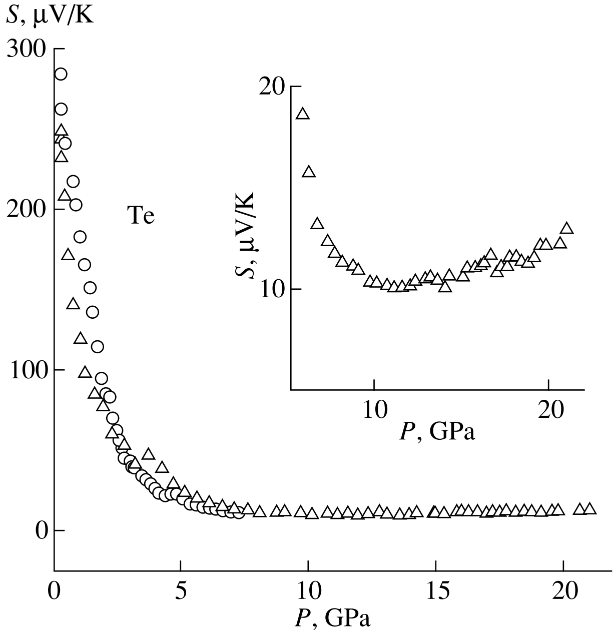

Fig. 1. The thermopower S vs. pressure P dependences obtained at $T = 300$ K on Te samples in chambers of tungsten carbide (circles) and synthetic diamond (triangles). Inset: an enlarged fragment of the plot.

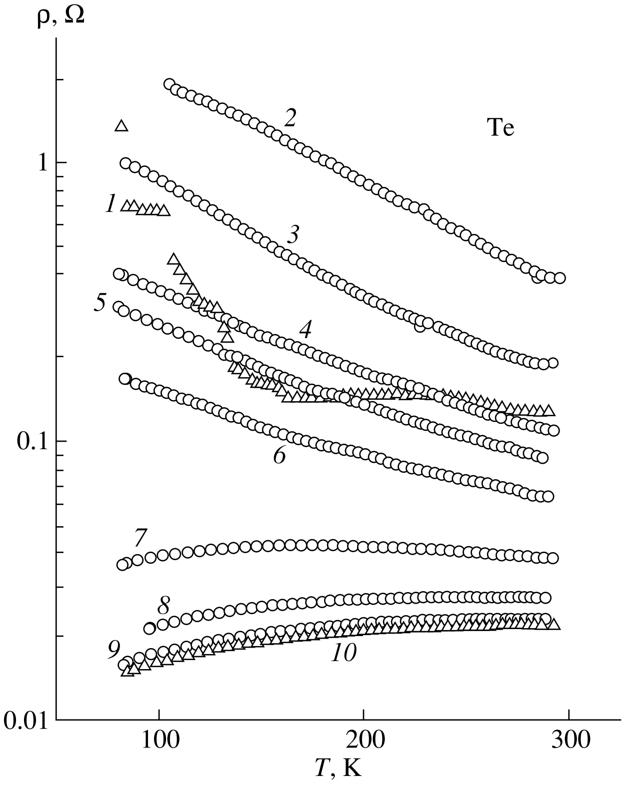

Fig. 2. Temperature dependences of the resistivity of a Te sample obtained in a tungsten-carbide chamber at fixed pressures P (GPa): (*1*) 1.6, (*2*) 2.9, (*3*) 3.4, (*4*) 4.1, (*5*) 5.2, (*6*) 6, (*7*) 6.9, (*8*) 7.7, (*9*) 8.1, and (*10*) 8.5.

phase transitions in such reference substances as Bi, GaP, etc. [4, 6–9].

The samples in the diamond chambers measured typically 0.2 × 0.2 × 0.05 mm, and, in the hard-alloy one, 0.4 × 0.4 × 0.2 mm.

The electrical resistivity ρ, S, and MR were measured by the techniques described in [9, 10]. The electric leads pressed to the samples were made of a 5 μm-thick Pt–Ag ribbon, and the high-conductivity diamond anvils served as current contacts [9, 10]. The temperature dependences of ρ of the samples were obtained in the range from 77 to 300 K at fixed pressures. The pressure and temperature dependences of ρ were measured under the reversal of the current through the sample. The diamond anvils, whose temperature was monitored by thermocouples, served as a heater and a cooler in thermoelectric measurements [4, 9, 10]. The calculated temperature distribution in the diamond chambers [15] permitted an estimate of the error in determination of the temperature drop across the sample. The relative error of ρ and S measurement was 3 and 20%, respectively.

The MR effect was measured by switching the current flow through the sample and the magnetic field B. The MR geometric factor of samples [3] (which was approximately the same for all P) was disregarded. For small MR, the output of the sample potential probes was amplified after compensation. The setup permitted MR measurements starting with 0.01%. Control measurements showed no MR effect with the diamond anvils shorted [9]. The previous MR measurements made in diamond chambers on HgSe, HgSeS, and Se crystals [9–11] agree with the data obtained on large samples of a standard shape at atmospheric [5] and hydrostatic pressures of up to 2 GPa [9, 11]. The total time taken by measurements on each sample of the temperature and field dependences of ρ under pressure was two to three weeks. After each change of pressure, the samples were maintained for 8–12 h to stabilize the resistivity before starting temperature and magnetic measurements [6].

The studies were performed on single crystals of undoped Te. The samples were characterized at atmospheric pressure using the Hall effect and resistivity measurements made in magnetic fields of up to 14 T at temperatures of 4.2–350 K by means of an Oxford Instruments setup. The impurity concentration was estimated as $\sim 2 \times 10^{16}$ cm^{-3}. At all temperatures, the Hall constant was positive.

2. RESULTS

The resistivity and the thermopower of tellurium decreased (Fig. 1), and the temperature dependences of ρ changed their slope (Fig. 2) with increasing pressure. This agrees with the earlier electrical [1, 4, 6, 9, 12, 16] and optical [17] studies. However, at a fixed pressure of 1.5–2 GPa, ρ increased irreversibly as the sample was

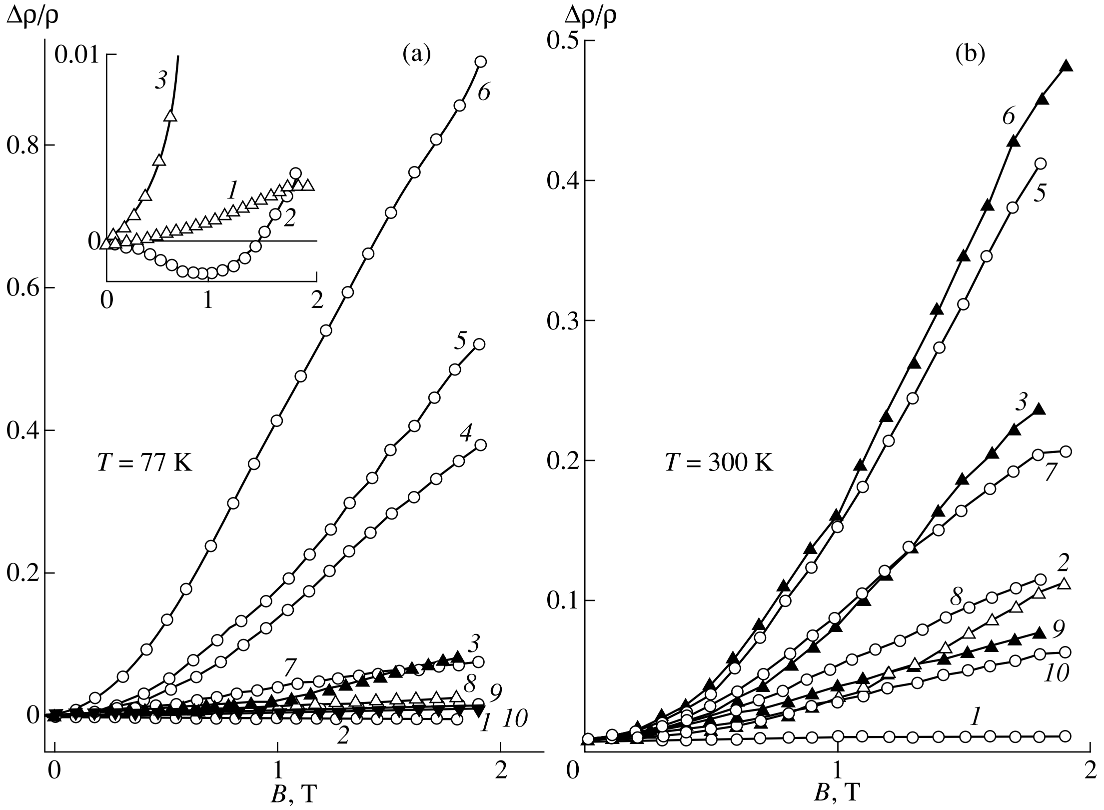

Fig. 3. (a) Magnetoresistance of a Te sample (Fig. 2) obtained at fixed pressures *P* and $T = 77$ K; the curves are labeled in accordance with the values of *P* given in the caption to Fig. 2. Inset shows an enlarged low-pressure fragment of *MR*. (b) Same relations plotted for $T = 300$ K.

cooled (curve *1* in Fig. 2). No such irreversible changes in ρ were observed to occur at higher *P*. The resistivity was also observed to increase after subjecting Te crystals to a hydrostatic pressure of up to 1.2 GPa in [16], where this effect was attributed to an increase of the concentration of defects (dislocations) strongly affecting the electrical properties of Te and Se [5]. At such pressures, Te was reported [18] to transfer from the chain to a Sb-type layered structure (without any change in the volume), but this observation was not confirmed in later studies [19, 20].

The magnetoresistance of Te in fields of up to 2 T was approximated by a parabolic dependence on *B* for all *P* (Figs. 3 and 4). We used the expression for the *MR* of a parabolic-band semiconductor, $\Delta\rho/\rho = a_r(\mu B)^2$, to estimate, assuming the coefficient $a_r = 1$, the hole mobility μ for various Te phases (Fig. 5). The *MR* increased with *P* increasing to 4–6 GPa. The values of *MR* and μ agree with the data of [16] obtained under hydrostatic pressures of up to 1.2 GPa on samples with similar hole concentrations. The pressure dependences of *MR* and μ measured in the hard-alloy (Fig. 3) and diamond chambers (Figs. 4 and 5) coincided. The increase of *MR* and μ and the decrease of *S* with pressure up to 4 GPa should apparently be attributed to the decreasing gap width ε_g [16, 17, 21].

At pressures of 1.5–2 GPa corresponding to the above-mentioned anomaly of ρ, one observed a negative *MR* at $T = 77$ K in different chambers (Figs. 3 and 4). In weak fields, the negative and positive (extrapolated to $B = 0$) *MR* branches could be fitted by approximately the same parabolic dependence on *B*. The high-temperature *MR* for these pressures remained positive and increased with increasing *P* (see Fig. 3).

The *MR* effect decreased rapidly above the pressure where the temperature coefficient of ρ reverses its sign (see Fig. 2). In samples maintained for a long time under a load, the transition to metallic conduction in our experiments occurred at $P > 4$–6 GPa [6, 7, 12]. It should be borne in mind that structural defects emerging even under the hydrostatic pressure *P* strongly affect the electrical properties of Te and Se [16, 21]. In high-pressure metallic phases, the *MR* effect remains positive (Figs. 3 and 4). The structural transformations occurring at high pressures [13] affect the electrical properties of Te [6, 7, 12, 20]. The pressure dependence of *S* reveals anomalies at $P \approx 6$ and 10 GPa (Fig. 1), which can be identified with transitions from the mon-

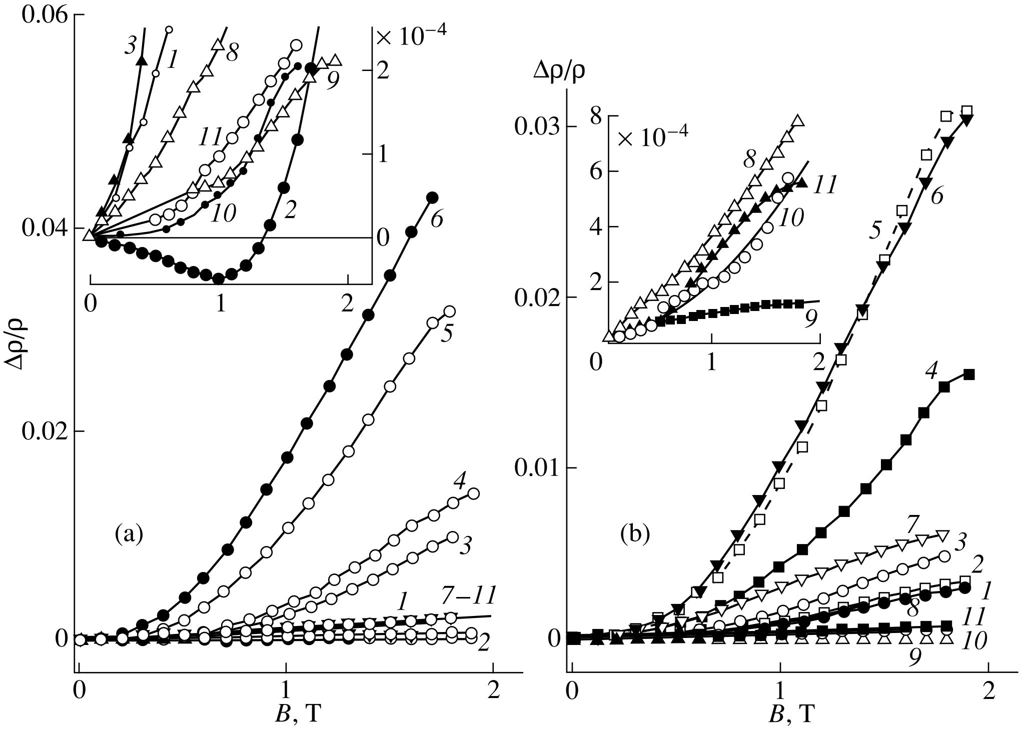

Fig. 4. (a) Magnetoresistance of a Te sample measured at $T = 77$ K in the diamond-anvil chamber at fixed pressures P (GPa): (*1*) 0.3, (*2*) 2.2, (*3*) 3.2, (*4*) 3.2, (*5*) 4.4, (*6*) 6, (*7*) 7.7, (*8*) 10, (*9*) 12, (*10*) 13.7, and (*11*) 14.2. Inset shows an enlarged fragment of the plots. (b) Same dependences measured at $T = 300$ K and P (GPa): (*1*) 0.3, (*2*) 0.6, (*3*) 1.3, (*4*) 2.2, (*5*) 3.2, (*6*) 6, (*7*) 7.7, (*8*) 10, (*9*) 12, (*10*) 13.7, and (*11*) 14.2. Inset shows an enlarged high-pressure fragment of *MR*.

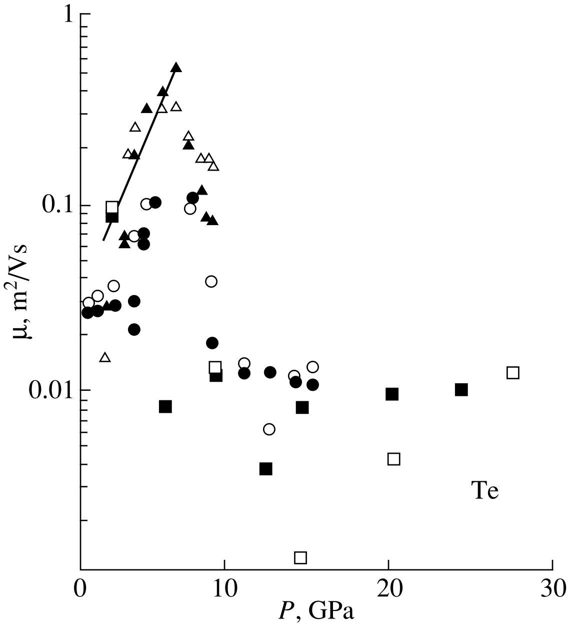

Fig. 5. Hole mobility derived from magnetoresistance for Te samples and presented as a function of pressure for $T = 77$ (open symbols) and 300 K (filled symbols). The data obtained in the hard-alloy chamber are identified with triangles, and those in the diamond chambers, with circles and squares. The straight line is a fit with an exponential (see text).

oclinic to orthorhombic to rhombohedral phase with the β-Po structure [13]. The magnitude of the *MR* effect increases with pressure above 12 GPa (Fig. 4).

3. DISCUSSION OF RESULTS

Calculations of the electron structure of Te and Se under pressure [21, 22], as well as preliminary electrical and optical experiments [1, 4, 7, 12, 16, 17] indicate a strong decrease of the direct energy gap ε_g in the electron spectrum with increasing P. Experimental data for Te (see Figs. 1–5) and Se [10] demonstrate, in accordance with these calculations, a drop in S and an increase of *MR* and μ caused by the pressure-induced decrease of ε_g.

As a result of Te having a complex valence-band structure, several groups of carriers contribute to conduction [16, 17, 21]. To describe the Hall effect and *MR* in strong magnetic fields from 8 to 14 T, two types of holes with different mobilities $\mu = (e\tau/m_p)$ were invoked [16], where e is the electron charge, τ is the momentum relaxation time, and m_p is the hole effective mass [3]. For fields below 2 T, we approximated the positive *MR* with a single-band model, because the contribution of heavy holes is believed [16] to be noticeable for $B > 2$ T. The negative *MR* effect (Figs. 3 and 4), which is tentatively assigned to a pressure-induced change of the valence-band structure [16, 17, 21], is an exception. It will be considered below.

The light-hole mobility in Te at hydrostatic pressures of up to 1.2 GPa was approximated [16, 21] by the $\mu(P) = \mu(0)\exp(\gamma P)$ relation, where the coefficient $\gamma = 0.5$–0.7 GPa^{-1}. This relation is a consequence of the decrease of the gap width ε_g and of the hole effective mass $m_p \sim \varepsilon_g$ according to the same law with $\gamma = 0.5$ GPa^{-1} [16, 17, 21]. The pressure dependences of the hole mobilities for the semiconducting phases of Te (Fig. 5) and Se [10] are fitted satisfactorily by the above exponential function. The coefficient γ for Te up to 4 GPa and for Se within the 6–25 GPa region [10] is, accordingly, 0.5–1 and 0.2–0.3 GPa^{-1}. The strong pressure dependence of μ is accounted for by the fact that ε_g of Te and Se decreases with increasing P much faster than it does for other semiconductors [1], to vanish at 4 and 15–25 GPa, respectively [1, 7, 16, 17, 21]. The trigonal lattices of Te and Se consist of helical chains extended along the c axis, which are forced close to one another by the pressure. This results in a broadening of the electron bands and a considerable decrease of ε_g at the H point of the Brillouin zone [21, 22].

The strong decrease of MR after the transition to the metallic state (Figs. 3 and 4) is accounted for by an electron structure rearrangement [23–25], so that the hole effective mass should obviously increase compared to m_p of the trigonal phase for $\varepsilon_g \longrightarrow 0$. Because the hole gas in metallic phases becomes degenerate, a factor $(kT/E_f)^2 \ll 1$ will appear in the expression for MR [3]. Here E_f is the Fermi energy, and k is the Boltzmann constant.

While the metallic phases of Te have different types of bonding, they still exhibit a certain similarity, which suggests a similarity among their electronic properties [23–25]. The monoclinic phase (II) forms of the trigonal one (I) through rotation of chain segments, which make up weakly bonded, corrugated layers [25]. It is an anisotropic metal, because, along the Γ–X direction in the Brillouin zone, the Fermi level crosses the electron bands, and, along Γ–Y and Γ–Z, it lies in the gap [26]. The orthorhombic lattice (III) forms of the monoclinic one (II) when the angle $\alpha = 92.7°$ decreases down to 90° and the bond lengths in the layers become identical [24]. Phases II and III have corrugated layers, where the conduction along the a axis is metallic, and, along the b, c plane, which is parallel to the zigzag-shaped covalent chains, it is semiconducting [13, 24]. This structure accounts for the noticeable MR effect preserved in these phases (Figs. 3 and 4). The electron structures and properties of phases II and III are identical [13, 25], an assumption confirmed by the measurements of S and MR in this work (Figs. 1 and 5). The rhombohedral lattice of the β-Po (IV) type is a specific case of the orthorhombic one (III), where the compression makes the interatomic distances in a layer equal to the layer separation [25]. Therefore, the transition from lattice III to the more symmetrical structure IV [13, 23] is capable of resulting in the observed increase of MR and of hole mobility μ for $P > 12$ GPa (see Figs. 3 and 4). The three-dimensional semiconducting structures, i.e., IV and the bcc V, are isotropic metals [13, 25].

The crystal structures of group V–VII elements with an unfilled p-shell, including Te, Se, and iodine, are obtained, in the tight-binding approximation, through the Peierls distortion of a simple cubic lattice [26, 27]. The p-electrons play a dominant role in the binding of these crystals [26]. The energy spectrum of the hypothetical cubic phases consists of three overlapping bands p_x, p_y, and p_z, which are partially filled. The linear atomic chains reduce their energy under the Peierls distortion of the lattice, thus creating a gap at the Fermi level. Because the p_z band of Te and Se is filled to two thirds of its capacity, the spectrum undergoes dielectrization through tripling of the unit cell [26, 27]. The deformation stabilizing the structure of the linear Te and Se chains along each coordinate direction at normal pressure P forms helical chains of divalent atoms [26]. In iodine, whose p-band is 5/6-filled, the spectrum dielectrization is produced by a sixfold increase of the cell volume, which corresponds to one short (covalent) bond and five long (Van der Waals) bonds [26]. A molecular crystal forms with the iodine atom having one neighbor only [26]. It was suggested [27] that the spectrum of mercury chalcogenides undergoes dielectrization similar to that for Te and Se, i.e., through a sixfold increase of the unit cell of the cubic praphase. Indeed, the unit cell of the high-pressure HgTe and HgSe semiconducting phases with the cinnabar structure (α-HgS) is actually doubled along the c axis compared to Te and Se [28]. The gap in the spectrum of these phases at the Fermi level emerges apparently from states connected genetically with the p-level of chalcogens [29, 30]. They are structural and electron analogs of Te and Se [4, 28].

Peierls structures have a lower density than unperturbed lattices [26]. When the crystal volume decreases, the atomic core repulsion precludes distortion which becomes energetically disadvantageous starting from a certain pressure [26]. Within this approach, the pressure-induced metallization of Te, Se, halogens (iodine) [1, 6, 7, 21], and mercury chalcogenides [4, 9, 10] is made possible by the removal of the Peierls distortion [26]. However, as follows from calculations made for Te [25] and from structural measurements [13, 19], a simple cubic lattice is unstable for any pressure. The magnitudes of ρ and S of the semiconducting phases of Te, Se, iodine, and mercury chalcogenides decrease with increasing P because of the decreasing ε_g [4, 9, 10]. However, the behavior of MR for $\varepsilon_g \longrightarrow 0$ is essentially different [9, 10]. In the covalent Te and Se, the magnetoresistance and μ of holes increase exponentially with pressure (see Fig. 5 and [10]), whereas the electron mobility in the high-pressure semiconducting phases of mercury chalcogenides is very low ($\mu < 50$ cm^2/Vs [9]) because of the ionic bonding in the chains. The hole mobility μ of holes in the molecular phase of iodine is as low as in amorphous Se, which is accounted for by the smallness of the wave-function overlap integral for neighboring atoms, which determines the electron tunneling rate [31]. These materials with low carrier mobilities exhibit a weak negative *MR* [9, 10], which is probably due to an impurity-band rearrangement in the magnetic field [32].

By contrast, a negative *MR* in Te (Figs. 3, 4) is observed with a high hole mobility. The fact of its appearing at pressures where calculations predict a change in the valence-band shape [16, 17, 21, 33] allows a conjecture that these phenomena are connected. The dispersion relation for the upper valence band of Te near the *H* point of the Brillouin zone has the form $E(k) = -Ak_z^2 - Bk_\perp^2 + (\Delta^2 + C^2k_z^2)^{1/2}$, where k_z and $k_\perp$ are wave-vector components along and perpendicular to the trigonal axis, Δ is the valence-band separation, and the *A*, *B*, and *C* parameters and their variation with *P* were derived from optical and galvanomagnetic measurements up to 1.2 GPa [16, 17, 21]. Along the k_z direction, the valence band has two extrema at $\pm k_{zm}$; the extremum along $k_\perp$ lies at $k_\perp = 0$ and is lower in energy by $\Delta\varepsilon = 2.3$ meV [16, 17, 21]. The existence of a saddle point at $k_z = 0$ (and $k_\perp = 0$) [33, 34] is responsible for a number of effects, including a change in the Fermi surface shape with increasing band occupancy [34] and intraband magnetic breakdown in fields $B > 2$ T (for concentrations 4×10^{16} cm^{-3}) [21, 35]. As *P* increases, $\Delta\varepsilon$ and k_{zm} decrease; i.e., the extrema become closer. Anzin *et al.* [33] were the first to indicate the possibility of a rearrangement of the hole Fermi surface structure at pressures above 1.6 GPa. By the later calculations discussed in [16, 17, 21], extrapolation of the spectrum suggests that the saddle point vanishes in the 1.5–3 GPa interval, where one could expect nontrivial behavior from m_p and μ along the k_z axis, and where our experiments reveal a negative *MR* (see Figs. 3 and 4).

The most probable of all mechanisms capable of creating a negative *MR* at high temperatures are the effects caused by carrier heating by an electric field *E*, where the drift mobility μ_d of “warm” carriers becomes a function of the field, $\mu_d = \mu(1 + \beta E^2)$ [3]. If $\tau \sim (\varepsilon)^r$ is a decreasing function of energy ε (which corresponds to scattering from acoustic phonons, $r = -1/2$), then $\beta < 0$, and μ_d decreases with increasing ε [3]. By deflecting the carriers from the drift direction, the magnetic field reduces the energy gained by the carriers and, hence, increases μ_d. The Hall field generated in the sample changes the direction of the resultant electric field, which also affects m_p, and, hence, μ_d. In weak fields, this results in a quadratic negative *MR*, $\Delta\rho/\rho = -c_r(\mu B)^2$, where $c_r \sim 10^{-2}$ [3]. In the case of two closely lying extrema with different effective masses, the expression for *MR* in weak fields acquires the form $\Delta\rho/\rho = 9\pi/16(\mu_pB)^2[(1 + \eta b^2)/(1 + \eta b) - \pi/4(1 + \eta b^2)^2/(1 + \eta b)^2]$, where *b* and η are the ratios of the hole mobilities and concentrations, respectively, and μ_p is the mobility of light holes [3]. As seen from this expression, a slight decrease in their concentration resulting from a transition between the extrema (for instance, because of cooling of the “warm” carriers) will make the *MR* negative. It can be conjectured that this mechanism is operative in Te close to the vanishing of the saddle point; i.e., in the case where the extrema are the closest to one another and the warming field (in which the carriers gain the energy required for the transition between the extrema) is the lowest [2, 3]. The lower extremum of the valence band can be identified with the region of the spectrum near the saddle point, where this band passes through a local maximum along the $k_\perp$ direction [16, 17, 21, 33].

ACKNOWLEDGMENTS

Support of the Russian Foundation for Basic Research (grant no. 98-03-32656) is gratefully acknowledged.

REFERENCES

1. *Solids under Pressure*, Ed. by W. Paul and D. M. Warschauer (McGraw-Hill, New York, 1963).
2. G. D. Pitt, Contemp. Phys. **18**, 137 (1977).
3. K. Seeger, *Semiconductor Physics* (Springer, Wien, 1973; Mir, Moscow, 1977).
4. I. M. Tsidil’kovskiĭ, V. V. Shchennikov, and N. G. Gluzman, Fiz. Tekh. Poluprovodn. **17**, 958 (1983) [Sov. Phys. Semicond. **17**, 604 (1983)].
5. H. Mell and J. Stuke, Phys. Status Solidi **24**, 183 (1967).
6. F. P. Bundy, Sverkhtverd. Mater., No. 3, 3 (1988).
7. F. P. Bundy and K. J. Dunn, J. Chem. Phys. **71**, 1550 (1979).
8. V. V. Shchennikov and V. A. Smirnov, Patent No. 2 050 180 (1995).
9. V. V. Shchennikov, Fiz. Tverd. Tela (St. Petersburg) **35** (3), 783 (1993) [Phys. Solid State **35**, 401 (1993)]; *ibid.* **37** (4), 1015 (1995) [Phys. Solid State **37**, 551 (1995)]; *ibid.* **38** (9), 2680 (1996) [Phys. Solid State **38**, 1470 (1996)].
10. V. V. Shchennikov and V. I. Osotov, Fiz. Tverd. Tela (St. Petersburg) **37** (2), 448 (1995) [Phys. Solid State **37**, 243 (1995)].
11. V. V. Shchennikov, A. E. Kar’kin, N. P. Gavaleshko, *et al.*, Fiz. Tverd. Tela (St. Petersburg) **39**, 1717 (1997) [Phys. Solid State **39**, 1528 (1997)].
12. F. A. Blum and B. C. Deaton, Phys. Rev. A **137**, A1410 (1963).
13. G. Parthasarathy and W. B. Holzapfel, Phys. Rev. B **37**, 8499 (1988).
14. L. G. Khvostantsen, L. F. Vereshchagin, and N. M. Uliyanitskaya, High Temp.-High Pressures **5**, 261 (1973).

15. V. V. Shchennikov and A. V. Bazhenov, Rev. High Pressure Sci. Technol. **6**, 657 (1997).
16. M. V. Glushkov, E. S. Itskevich, Yu. V. Kosichkin, *et al.*, Fiz. Tverd. Tela (Leningrad) **19**, 3580 (1977) [Sov. Phys. Solid State **19**, 2092 (1977)].
17. M. V. Glushkov, M. I. Eremets, Yu. V. Kosichkin, *et al.*, Fiz. Tverd. Tela (Leningrad) **21**, 499 (1979) [Sov. Phys. Solid State **21**, 295 (1979)].
18. S. S. Kabalkina, L. F. Vereshchagin, and B. K. Shulenin, Zh. Éksp. Teor. Fiz. **45**, 2073 (1963) [Sov. Phys. JETP **18** (1963)].
19. E. Yu. Tonkov, *High-Pressure Phase Diagrams of Elements* (Nauka, Moscow, 1979).
20. V. V. Brazhkin, R. N. Voloshin, and S. V. Popova, J. Phys.: Condens. Matter **4**, 1419 (1992).
21. V. V. Sobolev and A. M. Shirokov, *Electronic Structure of the Chalcogens* (Nauka, Moscow, 1988).
22. Th. Starkloff and J. D. Joannopoulos, J. Chem. Phys. **68**, 579 (1978).
23. A. Nishikawa, K. Nizeki, and K. Shindo, Jpn. J. Appl. Phys. **32**, Suppl. 1, 48 (1993).
24. G. Doerre and J. D. Joannopoulos, Phys. Rev. Lett. **43**, 1040 (1979).
25. F. Kirchhoff, N. Binggeli, and G. Galli, Phys. Rev. B **50**, 9063 (1994).
26. J. P. Gaspard, F. Marinelli, and A. Pellegatti, Europhys. Lett. **3**, 1095 (1987).
27. B. A. Volkov, O. A. Pankratov, and S. V. Pakhomov, Zh. Éksp. Teor. Fiz. **86**, 2293 (1984) [Sov. Phys. JETP **59**, 1336 (1984)].
28. A. N. Mariano and E. P. Warekois, Science **142**, 672 (1963).
29. E. Doni, L. Resca, S. Rodríguez, *et al.*, Phys. Rev. B **20**, 1663 (1979).
30. Z. W. Lu, D. Singh, and H. Krakauer, Phys. Rev. B **39**, 10154 (1989).
31. C. Kittel, *Introduction to Solid State Physics* (Wiley, New York, 1956; Nauka, Moscow, 1978).
32. S. A. Obukhov, Preprint No. 1459 (Ioffe Phys. Techn. Inst., Russ. Acad. Sci., Leningrad) (1991).
33. V. B. Anzin, M. S. Bresler, I. I. Farbstein, *et al.*, Phys. Status Solidi B **48**, 531 (1971).
35. M. S. Bresler, V. G. Veselago, Yu. V. Kosichkin, *et al.*, Zh. Eksp. Teor. Fiz. **57**, 1477 (1969) [Sov. Phys. JETP **30** (1969)].

Translated by G. Skrebtsov

Physics of the Solid State, Vol. 42, No. 4, 2000, pp. 648–652. Translated from Fizika Tverdogo Tela, Vol. 42, No. 4, 2000, pp. 632–636.
Original Russian Text Copyright © 2000 by V. V. Sobolev, Timonov, V. Val. Sobolev.

SEMICONDUCTORS AND DIELECTRICS

Characteristic Electron Energy Loss Spectra for Diamond

V. V. Sobolev, A. P. Timonov, and V. Val. Sobolev

Udmurt State University, Krasnoarmeĭskaya ul. 71, Izhevsk, 426034 Russia

Received March 16, 1999

Abstract—The complete set of optical fundamental functions is determined for diamond in the range from 4 to 32 eV. The features of the bulk and surface characteristic energy loss spectra are elucidated and the functions $n_{\text{eff}}(E)$ and $\varepsilon_{\text{eff}}(E)$ are calculated. The energies of volume and surface plasmons are established. © *2000 MAIK "Nauka/Interperiodica".*

INTRODUCTION

The plasmons hold a unique position among quasiparticles of a solid because of their special features [1]. The spectra of volume and surface plasmons are described by the functions $-\text{Im}\varepsilon^{-1}$ and $-\text{Im}(1 + \varepsilon)^{-1}$, respectively. Experimentally, they are determined by measuring the characteristic electron energy losses (CEELs) W. In the general case, the function W has an intricate form because of the superimposition of various effects, among them the excitation of plasmons, interband transitions, and metastable excitons.

It is a complicated problem to extract the functions $-\text{Im}\varepsilon^{-1}$ and $-\text{Im}(1 + \varepsilon)^{-1}$ from W. For this purpose, various simplifications, approximations, and calibrations are made. The half-width of the principal peak of W typically exceeds 5.5 eV. The intensity of peaks of W critically depends on the orientation of the sample and the energy of the electron beam, their resolution being not finer than 0.5 eV. This severely hampers the determination of the true spectra of plasmons and their energies. For this reason, even for the simplest crystals, such as diamond, the experimental data on the CEEL spectra are highly contradictory as far as the nature and the energies of plasmons of both the types are concerned [2–4]. Of great interest, in this connection, is a calculation procedure in which the experimental data on the reflection spectra and the Kramers–Kronig integral relations are used to determine the plasmon spectra [5].

The objective of this paper is to calculate the spectra of plasmons of both types from experimental data and to correlate the results with the known data on the CEEL spectra for diamond. We also determine the energies of volume and surface plasmons in diamond of the I and IIa types.

1. THE CALCULATION PROCEDURE

The functions for plasmons can be expressed in terms of the ε_1 and ε_2 or of the n and k pair of functions by the formula

$$-\text{Im}\varepsilon^{-1} = \varepsilon_2(\varepsilon_1^2 + \varepsilon_2^2)^{-1} = 2nk(n^2 + k^2)^{-2}, \quad (1a)$$

$$\begin{aligned} -\text{Im}(1 + \varepsilon)^{-1} &= \varepsilon_2[(\varepsilon_1 + 1)^2 + \varepsilon_2^2]^{-1} \\ &= 2nk[(n^2 + k^2)^2 + 2(n^2 - k^2) + 1]^{-1}. \end{aligned} \quad (1b)$$

The complete set of optical fundamental functions, among them ε_1 and ε_2 (or n and k) is commonly calculated from the Kramers–Kronig integral relations and the experimental reflection spectrum in a wide energy range. The calculation procedure we use here for determining the set of optical functions for diamond has been substantiated and employed in many papers [5–8].

2. RESULTS OF CALCULATIONS

The reflection spectra of diamond in the range from zero to 32 eV were measured on three different samples; two of them (1 and 2) were mechanically polished [9, 10], while the third (3) was cleaved [10]. From these spectra, we have calculated the complete set of optical fundamental functions, among them $-\text{Im}\varepsilon^{-1}$, $-\text{Im}(1 + \varepsilon)^{-1}$, $n_{\text{eff}}(E)$, and $\varepsilon_{\text{eff}}(E)$ (see Fig. 1).

The most intense peaks in these reflection spectra are situated at 12.85, 12.55, and 12.77 eV for samples 1, 2, and 3, respectively. On the long-wavelength side, weak peaks are positioned at about 7.25, 7,15, and 7.10 eV for samples 1, 2, and 3, respectively. For samples 2 and 3, these weak peaks have short-wavelength components at about 7.62 and 7.67 eV, respectively. Generously overlapping broad bands are observed in the high energy ranges $E \approx (15–22)$ eV and (22–35) eV,

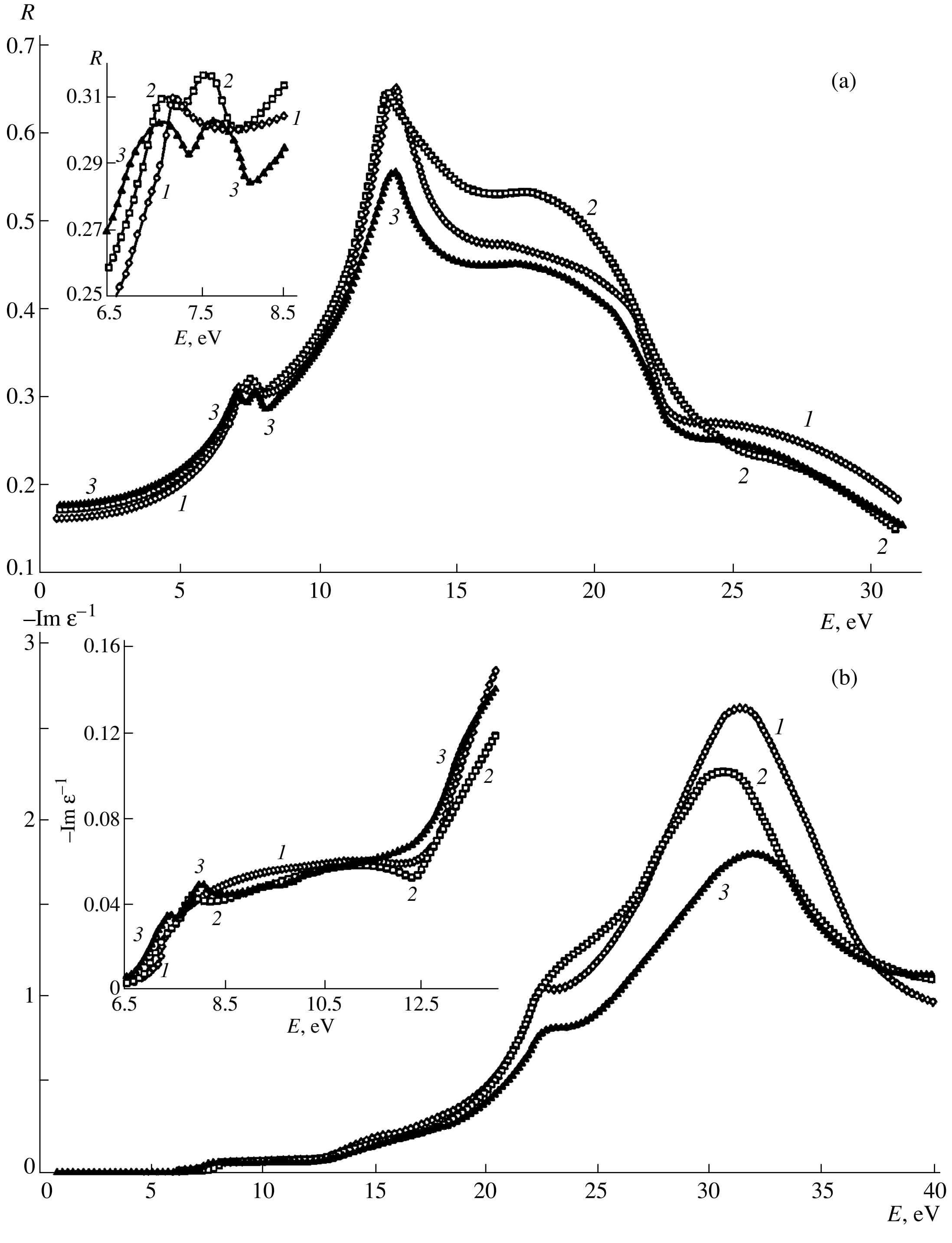

Fig. 1. (a) Experimental reflection spectra $R(E)$; calculated spectra (b) of $-\mathrm{Im}\varepsilon^{-1}$, (c) $-\mathrm{Im}(1+\varepsilon)^{-1}$, (d) n_{eff}, and (e) $\varepsilon_{\mathrm{eff}}$ for three samples of diamond (curves *1*, *2*, and *3*, respectively).

with their maxima estimated very roughly to be at ~18 and 26 eV, respectively.

The spectra of $\varepsilon_2(E)$, which we calculated from the reflection spectra, have a very intense peak at about 11.8 eV, feebly marked peaks at about 7.5 eV (sample 1), 7.3 and 7.75 eV (sample 2), and 7.3 and 7.9 eV (sample 3), and a very weak, broad band at about 23.5 eV. It is interesting to note that the very broad, intense reflection band in the range from 15 to 22 eV does not manifest itself in the spectra of $\varepsilon_2(E)$ for the three samples of diamond.

The calculated spectra of the bulk CEELs, described by $-\mathrm{Im}\varepsilon^{-1}$, have the most intense peaks situated at about 31.5, 30.6, and 32.0 eV for samples 1, 2, and 3, respec-

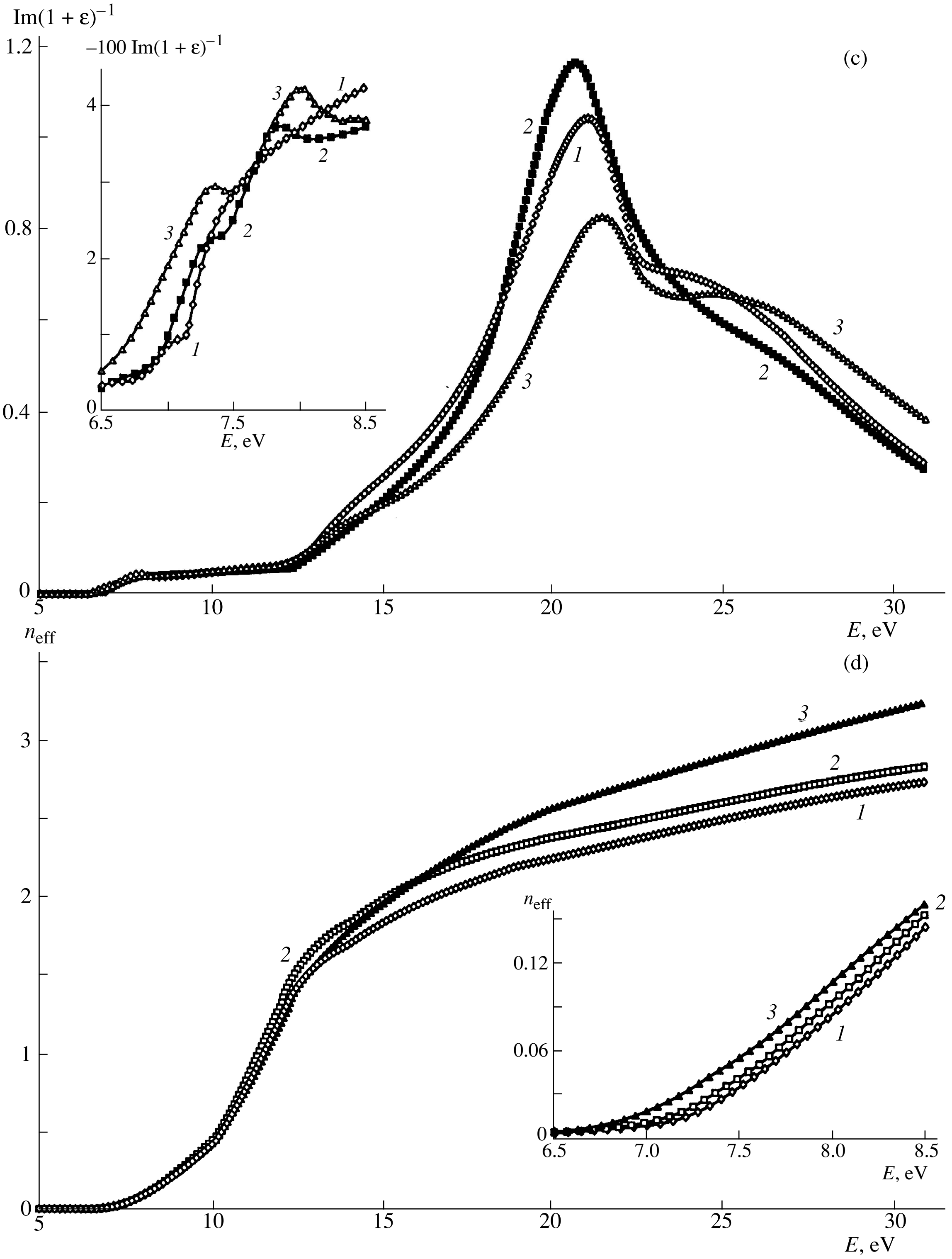

Fig. 1. (Contd.)

tively (see Fig. 1b). Earlier, these peaks were determined to be at about 32 (sample 1) [9], 29 (sample 2), and 29.7 eV (sample 3) [10]. The peak of the CEELs ($-\mathrm{Im}\varepsilon^{-1}$) is situated near the short-wavelength limit of the reflection spectra, which is equal to 35 [9], or 31.5 eV [10]. Using the $R(E)$ spectrum extending to 40 eV allowed us to determine the position of the principal peak of bulk CEELs more correctly than in [9,

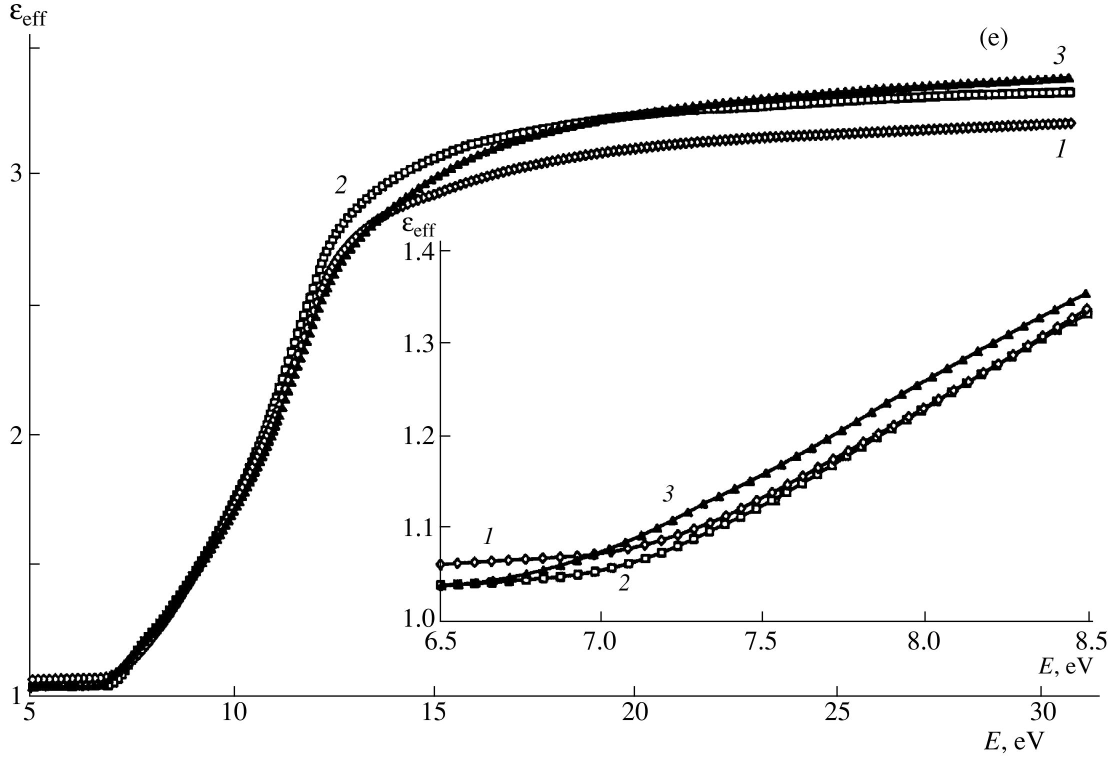

Fig. 1. (Contd.)

10]; the energy of volume plasmons in diamond E_{pv} is found to be 31.2 ± 0.6 eV. This value agrees with the theoretically predicted E_{pv} to be about 31 eV [1].

The experimental CEEL spectra were studied by reflection electron diffraction with energy $E_0 = 1150$ [2], 700, 1500 [3], and 200–1200 eV [4] and a resolution of 1–2 eV. It was found in these three papers, that the energies of volume plasmons lie in the range 31–34 eV.

The surface energy loss spectra, given by $-\mathrm{Im}(1 + \varepsilon)^{-1}$, is first calculated in this paper (Fig. 1c). The principal peak is found to be at about 21.1 (sample 1), 20.8 (sample 2), and 21.6 eV (sample 3). According to our estimates, the energy of surface plasmons for diamond, E_{ps}, is equal to 21.2 ± 0.3 eV. From the experimental data on the CEELs, the quantity E_{ps} was estimated to be 23–25 eV [2–4]. The reasons for the discordance between our calculated values of E_{ps} and E_{pv} and the experimental data [2–4] may be as follows: The positions of the most intense peaks in the spectra of $-\mathrm{Im}\varepsilon^{-1}$ and $-\mathrm{Im}(1 + \varepsilon)^{-1}$ are commonly believed [1, 5, 6] to correspond to the plasmon energies, and our calculations of E_{ps} and E_{pv} are based on this correspondence. The determination of the spectra of these two optical functions from the experimental data on CEELs is an intricate problem, whose solution requires making various simplifications, approximations, and calibrations. In [2–4], the spectra of $-\mathrm{Im}\varepsilon^{-1}$ and $-\mathrm{Im}(1 + \varepsilon)^{-1}$ were not extracted; instead, the energies E_{ps} and E_{pv} were determined directly from the experimentally measured CEELs W. This inevitably introduced some errors into the values of E_{ps} and E_{pv} obtained by this method. Therefore, our data on the energies of volume and surface plasmons for diamond are likely to be more correct.

Let us briefly consider other features of the CEEL spectra. The longest-wavelength doublet in ε_2 at about 7.5 eV is also observed in the spectra of $-\mathrm{Im}\varepsilon^{-1}$ and $-\mathrm{Im}(1 + \varepsilon)^{-1}$, but here it is shifted to a higher energy by ~(0.05–0.1) eV. The transitions occur upon transverse excitation in $\varepsilon_2(E)$ and upon longitudinal excitation in the CEEL spectra. Hence, the difference in the position of the doublet between the spectra indicated above suggests that there is a longitudinal–transverse splitting of transitions in diamond, equal to $\Delta E \approx 0.05$–0.1 eV.

Instead of the most intense, very broad peak at about 11.8 eV in $\varepsilon_2(E)$, a very wide, weak plateau is observed in the range 8–12 eV in both the CEEL spectra. At the same time, the very weak band at about 23.5 eV in $\varepsilon_2(E)$ manifests itself as an intense peak at about 22.4 eV in the spectrum of $-\mathrm{Im}\varepsilon^{-1}$. The specific nature of these spectrum features can be discussed in terms of band models and metastable excitons [11–13]. This will be done in another paper, where the fine structure of the $\varepsilon_2(E)$ spectrum will be considered.

From the reflection spectra for the three samples of diamond, we calculated, for the first time, the number of valence electrons $n_{\mathrm{eff}}(E)$ involved in transitions up to the given energy E, and the spectra of $\varepsilon_{\text{eff}}(E)$ (Figs. 1d, 1e).

Long-wavelength absorption in diamond is due to indirect and direct transitions with $E_{gi} = 5.47$ and $E_{gd} = 7.02$ eV, respectively, at 295 K [6]. The quantity $n_{\text{eff}}(E)$ steeply increases, starting from 7 eV, and becomes equal to about 1.5 at 11.8 eV (the position of the principal peak of ε_2); then it increases slowly to a value of 2.5–3 at 30 eV.

The spectrum of $\varepsilon_{\text{eff}}(E)$ is similar in shape to that of $n_{\text{eff}}(E)$. At $E < 7$ eV, ε_{eff} is equal to unity, then it steeply rises to about 2.8 at ~13 eV, and then it increases to about 3.3 at 30 eV, showing no saturation. According to the definition of $\varepsilon_{\text{eff}}(E)$, the permittivity for very long wavelengths, ε_0, should be roughly equal to ε_{eff} for very high energies.

In [14], the reflection spectrum of diamond was measured in the range 200–610 eV and $n_{\text{eff}}(E)$ was crudely estimated from this spectrum in the range from zero to 900 eV. According to [14], all valence electrons ($n_{\text{eff}} = 4$) will be involved in transitions when the energy E exceeds 200 eV. This correlates well with our result that $n_{\text{eff}}(E)$ and $\varepsilon_{\text{eff}}(E)$ reach their saturation values at energies much higher than the limiting value of the energy (~40 eV) for which our calculations are performed.

CONCLUSION

In this paper, we more correctly determined the bulk and surface characteristic electron energy loss spectra in the range from 7 to 40 eV, as well as the spectra of the effective number of valence electrons involved in transitions. Also, more correct values of the energies of volume and surface plasmons were obtained.

ACKNOWLEDGMENTS

This work was supported by the Center of Fundamental Science (St. Petersburg State University).

REFERENCES

1. D. Pines, *Elementary Excitations in Solids* (W. A. Benjamin, New York, 1963; Mir, Moscow, 1965).
2. N. R. Whetten, Appl. Phys. Lett. **8**, 135 (1966).
3. H. G. Maguire, Phys. Status Solidi B **76**, 715 (1976).
4. H. Armon and J. P. F. Sellschop, Phys. Rev. B **26**, 3289 (1982).
5. V. V. Sobolev and V. V. Nemoshkalenko, *Methods of Calculational Physics in Solid State Theory: The Electronic Structure of Semiconductors* (Naukova Dumka, Kiev, 1988).
6. V. V. Sobolev, *Intrinsic Energy Levels of Group IVA Solids* (Shtiintsa, Kishinev, 1978).
7. V. V. Sobolev and V. Val. Sobolev, Fiz. Tverd. Tela (S.-Peterburg) **36**, 2560 (1994) [Phys. Solid State **36**, 1393 (1994)].
8. V. V. Sobolev, in *Proc. Int. Conf. "Semiconductor Optics"* (Ul'yanovsk. Univ., Ul'yanovsk, 1998), p. 3.
9. H. R. Philipp and E. A. Taft, Phys. Rev. A **136**, 1445 (1964).
10. R. A. Roberts and W. C. Walker, Phys. Rev. **161**, 730 (1967).
11. L. A. Hemstreet, C. Y. Fong, and M. L. Cohen, Phys. Rev. B **2**, 2054 (1970).
12. V. J. Gavrilenko and F. Bechstedt, Phys. Rev. B **55**, 4343 (1997).
13. L. X. Benedict, E. L. Shirley, and R. B. Bohn, Phys. Rev. B **57**, 9385 (1998).
14. J. Nithianandam and J. C. Rife, Phys. Rev. B **47**, 3517 (1993).

Translated by Yu. Epifanov

Physics of the Solid State, Vol. 42, No. 4, 2000, pp. 653–656. Translated from Fizika Tverdogo Tela, Vol. 42, No. 4, 2000, pp. 637–640.
Original Russian Text Copyright © 2000 by Zolotarev, Kim, Neĭfel'd.

SEMICONDUCTORS AND DIELECTRICS

Determination of Relaxation Constants of a Quadrupole Spin System with Many Energy Levels

I. V. Zolotarev*, A. S. Kim*, and P. G. Neĭfel'd**

**Perm State University, ul. Bukireva 15, Perm, 614600 Russia*
e-mail: zolot@psu.ru
***Perm Department of Russian Research Center "Applied Chemistry," Perm, Russia*

Received July 26, 1999

Abstract—The two-frequency nuclear quadrupole resonance method is used to determine the relaxation time for all single-quantum transitions in a quadrupole spin system with many energy levels from the results obtained for a single transition, which is impossible in a one-frequency method. The accuracy is the same as in the measurement of relaxation time in the case of one-frequency pumping of the transition chosen as the "basis." The results of measurements are presented and determination of relaxation constants for $KReO_4$ and $NaReO_4$ as well as $SbCl_3$ and $SbBr_3$ and their complexes at various temperatures with the help of the two-frequency NQR method. *© 2000 MAIK "Nauka/Interperiodica".*

The study of relaxation processes in a quadrupole spin system with many energy levels by a one-frequency NQR method presumes separate pumping of each transition and determination of relaxation constants. This is a difficult technical and analytic problem involving the recording and analysis of all the curves described by multi-exponential functions.

In this paper, we consider the possibility of determining the relaxation constants for all single-quantum transitions in a multilevel spin system under two-frequency pumping.

In the case of separate one-frequency pumping of each transition in a multilevel spin system, the time $T_{2\rho(\mathrm{one})}$ of transverse relaxation in a rotating reference frame (RRF) is determined as in [1]:

$$T^{(i)}_{2\rho(\mathrm{one})} = \frac{2T^{(i)}_2 T^{(i)}_1}{T^{(i)}_2 + T^{(i)}_1}, \tag{1}$$

where $i = a, b, \ldots$ is the number of a transition being pumped, and $T^{(i)}_2$ and $T^{(i)}_1$ are the transverse and longitudinal relaxation times of this transition, respectively.

In the case of two-frequency pumping (see Fig. 1) of two adjacent transitions in a multilevel spin system, the envelope of the echo signal, which is obtained by varying the time interval τ_2, decreases with the time constant $T^{(i)}_{2\rho(\mathrm{two})}$ of transverse relaxation in the RRF.

Let us consider two cases: (1) The pumping pulse is supplied at the lower transition, and the observation of the echo signal amplitude is carried out at the upper transition (Fig. 1a). (2) The pumping pulse is supplied at the upper transition, and the observation of the echo signal amplitude is carried out at the lower transition (Fig. 1b).

The duration t_w of the pumping pulse is associated with transition saturation and detuning required for observing an echo signal in the RRF in the case of two-frequency pumping of a multilevel spin system. In this case, H_1t_w is constant and has a definite value for each transition in a specific multilevel spin system.

The transverse relaxation time in the RRF at the upper transition, in the case of two-frequency pumping

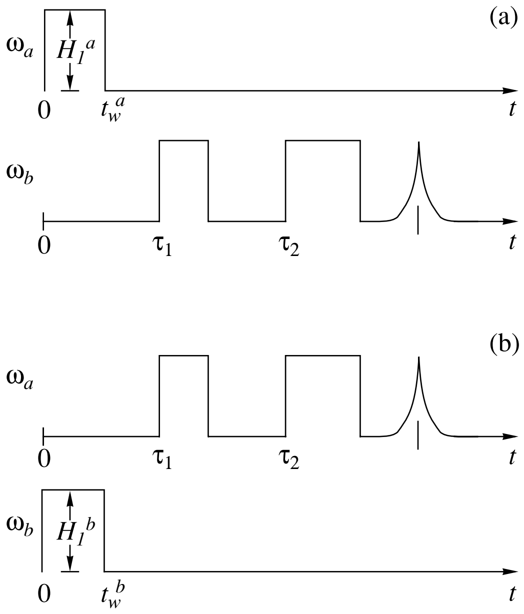

Fig. 1. Pulse program of two-frequency pumping of a multilevel spin system: (a) pumping pulse at the lower transition, observation of the echo signal at the upper transition, and (b) pumping pulse at the upper transition, observation of the echo signal at the lower transition.

Table 1. Results of measurements and calculation of relaxation constants for $^{185,\,187}$Re nuclei in $KReO_4$ by the two-frequency NQR spin-echo method

Isotope	Transition	Frequency, MHz	Temperature, K	$T_{2\rho(\mathrm{two})}$, μs	$T_{2\rho(\mathrm{one})}$, μs	$T_{2(\mathrm{one})}$, μs	$T_{1(\mathrm{one})}$, μs
^{185}Re	1/2–3/2	28.312	296	144	105	66	260
	3/2–5/2	56.600	296	104	143	100	250
^{185}Re	1/2–3/2	29.386	77	1063	378	200	3400
	3/2–5/2	58.746	77	380	1080	630	3800
^{187}Re	1/2–3/2	26.825	296	185	115	70	320
	3/2–5/2	53.626	296	115	184	130	315
^{187}Re	1/2–3/2	27.839	77	715	215	110	4300
	3/2–5/2	55.651	77	215	722	390	4900

Table 2. Results of measurements and calculation of relaxation constants for $^{185,\,187}$Re nuclei in $NaReO_4$ by the two-frequency NQR spin-echo method

Isotope	Transition	Frequency, MHz	Temperature, K	$T_{2\rho(\mathrm{two})}$, μs	$T_{2\rho(\mathrm{one})}$, μs	$T_{2(\mathrm{one})}$, μs	$T_{1(\mathrm{one})}$, μs
^{185}Re	1/2–3/2	44.997	296	99	78	50	180
	3/2–5/2	89.949	296	77	96	68	168
^{185}Re	1/2–3/2	48.628	77	562	175	90	3000
	3/2–5/2	97.207	77	175	568	310	3400
^{187}Re	1/2–3/2	42.600	296	100	72	45	180
	3/2–5/2	85.167	296	73	104	70	200
^{187}Re	1/2–3/2	46.024	77	648	323	170	3300
	3/2–5/2	92.010	77	318	630	360	2500

Table 3. Results of measurements and calculation of relaxation constants for $^{121,\,123}$Sb nuclei in $SbCl_3$ by the two-frequency NQR spin-echo method

Isotope	Transition	Frequency, MHz	Temperature, K	$T_{2\rho(\mathrm{two})}$, μs	$T_{2\rho(\mathrm{one})}$, μs	$T_{2(\mathrm{one})}$, μs	$T_{1(\mathrm{one})}$, μs
^{121}Sb	1/2–3/2	58.162	294	725	441	270	1.2
	3/2–5/2	112.60	294	437	716	520	1.15
^{121}Sb	1/2–3/2	59.730	77	1633	861	440	21.0
	3/2–5/2	114.34	77	856	1614	850	16.0
^{123}Sb	1/2–3/2	37.415	294	576	376	220	1.30
	3/2–5/2	67.776	294	373	569	370	1.23
^{123}Sb	3/2–5/2	67.776	294	806	569	370	1.23
	5/2–7/2	102.78	294	573	815	600	1.27
^{123}Sb	1/2–3/2	39.093	77	2189	1341	700	16.0
	3/2–5/2	68.640	77	1328	2155	1175	13.0
^{123}Sb	3/2–5/2	68.640	77	3315	2155	1175	13.0
	5/2–7/2	104.46	77	2140	3280	1900	12.0

according to the program depicted in Fig. 1a, is given by

$$T_{2\rho(\mathrm{two})}^{(b)} = \frac{2T_2^{(a)}T_1^{(b)}}{T_2^{(a)} + T_1^{(b)}}, \tag{2}$$

while at the lower transition (according to the program in Fig. 1b) this time is

$$T_{2\rho(\mathrm{two})}^{(a)} = \frac{2T_2^{(b)}T_1^{(a)}}{T_2^{(b)} + T_1^{(a)}}. \tag{3}$$

The transverse relaxation times in the RRF under one-frequency and two-pumping of a multilevel spin system satisfy the conditions

$$\begin{aligned} T_{2\rho(\mathrm{one})}^{(a)} &= T_{2\rho(\mathrm{two})}^{(b)}, \\ T_{2\rho(\mathrm{one})}^{(b)} &= T_{2\rho(\mathrm{two})}^{(a)}. \end{aligned} \tag{4}$$

Taking into account expressions (1), (2), and (4), we can write

$$\begin{aligned} T_2^{(a)} &= \frac{T_{2\rho(\mathrm{two})}^{(b)}T_1^{(a)}}{2T_1^{(b)} - T_{2\rho(\mathrm{two})}^{(b)}}, \\ T_1^{(a)} &= \frac{T_{2\rho(\mathrm{two})}^{(b)}T_2^{(a)}}{2T_2^{(a)} - T_{2\rho(\mathrm{two})}^{(b)}}, \end{aligned} \tag{5}$$

while taking into account expressions (1), (3), and (4), we obtain

$$\begin{aligned} T_2^{(b)} &= \frac{T_{2\rho(\mathrm{two})}^{(a)}T_1^{(a)}}{2T_1^{(a)} - T_{2\rho(\mathrm{two})}^{(a)}}, \\ T_1^{(b)} &= \frac{T_{2\rho(\mathrm{two})}^{(a)}T_2^{(b)}}{2T_2^{(b)} - T_{2\rho(\mathrm{two})}^{(a)}}. \end{aligned} \tag{6}$$

The transverse relaxation times $T_{2\rho(\mathrm{one})}^{(a)}$ and $T_{2\rho(\mathrm{one})}^{(b)}$ in the rotating reference frame in the case of one-frequency pumping are determined from the known data on the basis of formula (1), while for two-frequency pumping, the times $T_{2\rho(\mathrm{one})}^{(a)}$ and $T_{2\rho(\mathrm{one})}^{(b)}$ are measured experimentally.

Tables 1–9 contain the results of measurement and calculation of relaxation constants for $KReO_4$ and $NaReO_4$ as well as $SbCl_3$ and $SbBr_3$ and their complexes at various temperatures by using the two-frequency NQR method.

Let us consider the results obtained for one of the samples in greater detail. We assume that no echo signal is observed under one-frequency pumping at the 1/2–3/2 transition in $KReO_4$ (resonance ^{185}Re, ν_1 = 28.312 MHz, $J = 5/2$, $T = 296$ K). We need to determine the transverse relaxation time $T_2^{(1)}$, the longitudinal

Table 4. Results of measurements and calculation of relaxation constants for $^{121,\,123}$Sb nuclei in $SbBr_3$-α at 77 K by the two-frequency NQR spin-echo method

Isotope	Transition	Frequency, MHz	$T_{2\rho(\mathrm{two})}$, μs	$T_{2\rho(\mathrm{one})}$, μs	$T_{2(\mathrm{one})}$, μs	$T_{1(\mathrm{one})}$, μs
^{121}Sb	1/2–3/2	50.263	850	318	160	24.7
	3/2–5/2	99.416	316	849	440	12.0
^{123}Sb	1/2–3/2	31.200	1165	416	220	20.0
	3/2–5/2	60.143	421	1070	600	5.0
^{123}Sb	3/2–5/2	60.143	1438	1070	600	5.0
	5/2–7/2	90.583	1043	1388	840	4.0

Table 5. Results of measurements and calculation of relaxation constants for $^{121,\,123}$Sb nuclei in $SbBr_3$-β at 77 K by the two-frequency NQR spin-echo method

Isotope	Transition	Frequency, MHz	$T_{2\rho(\mathrm{two})}$, μs	$T_{2\rho(\mathrm{one})}$, μs	$T_{2(\mathrm{one})}$, μs	$T_{1(\mathrm{one})}$, μs
^{121}Sb	1/2–3/2	49.302	690	671	340	25.0
	3/2–5/2	94.944	661	680	350	12.0
^{123}Sb	1/2–3/2	31.989	899	649	330	20.0
	3/2–5/2	57.085	646	894	460	16.0
^{123}Sb	3/2–5/2	57.085	1196	894	460	16.0
	5/2–7/2	86.723	880	1096	580	10.0

Table 6. Results of measurements and calculation of relaxation constants for $^{121,\,123}$Sb nuclei in $2SbCl_3 \cdot C_6H_6$ at 77 K by the two-frequency NQR spin-echo method

Isotope	Transition	Frequency, MHz	$T_{2\rho(\mathrm{two})}$, μs	$T_{2\rho(\mathrm{one})}$, μs	$T_{2(\mathrm{one})}$, μs	$T_{1(\mathrm{one})}$, μs
^{121}Sb	1/2–3/2	59.604	710	417	210	26.0
	3/2–5/2	117.60	411	695	360	10.0
^{121}Sb	1/2–3/2	60.008	635	418	210	37.0
	3/2–5/2	116.24	413	633	320	12.0
^{123}Sb	1/2–3/2	37.113	1712	358	180	31.0
	3/2–5/2	71.122	358	1163	880	15.0
^{123}Sb	3/2–5/2	71.122	2393	1163	880	15.0
	5/2–7/2	107.20	1570	2206	1300	7.3
^{123}Sb	1/2–3/2	38.563	1222	299	150	43.0
	3/2–5/2	69.980	299	1215	620	30.0
^{123}Sb	3/2–5/2	69.980	1746	1215	620	30.0
	5/2–7/2	106.11	1139	1595	900	7.0

Table 7. Results of measurements and calculation of relaxation constants for $^{121,\,123}$Sb nuclei in $2SbCl_3 \cdot C_{10}H_8$ at 77 K by the two-frequency NQR spin-echo method

Isotope	Transition	Frequency, MHz	$T_{2\rho(\mathrm{two})}$, μs	$T_{2\rho(\mathrm{one})}$, μs	$T_{2(\mathrm{one})}$, μs	$T_{1(\mathrm{one})}$, μs
^{121}Sb	1/2–3/2	59.460	1558	358	180	30.0
	3/2–5/2	118.94	350	1412	800	6.0
^{123}Sb	1/2–3/2	36.099	3897	691	350	27.0
	3/2–5/2	72.176	689	3834	2100	22.0
^{123}Sb	3/2–5/2	72.176	3174	3834	2100	22.0
	5/2–7/2	108.26	3498	2940	1900	6.5

Table 8. Results of measurements and calculation of relaxation constants for $^{121,\,123}$Sb nuclei in $2SbBr_3 \cdot C_6H_6$ at 77 K by the two-frequency NQR spin-echo method

Isotope	Transition	Frequency, MHz	$T_{2\rho(\mathrm{two})}$, μs	$T_{2\rho(\mathrm{one})}$, μs	$T_{2(\mathrm{one})}$, μs	$T_{1(\mathrm{one})}$, μs
^{121}Sb	1/2–3/2	50.730	594	318	160	30.0
	3/2–5/2	96.441	315	581	300	9.0
^{123}Sb	1/2–3/2	33.562	710	456	230	26.0
	3/2–5/2	57.810	454	705	360	17.0
^{123}Sb	3/2–5/2	57.810	1084	705	360	17.0
	5/2–7/2	86.162	703	1080	560	15.0

Table 9. Results of measurements and calculation of relaxation constants for $^{121,\,123}$Sb nuclei in $2SbBr_3 \cdot C_{10}H_8$ at 77 K by the two-frequency NQR spin-echo method

Isotope	Transition	Frequency, MHz	$T_{2\rho(\mathrm{two})}$, μs	$T_{2\rho(\mathrm{one})}$, μs	$T_{2(\mathrm{one})}$, μs	$T_{1(\mathrm{one})}$, μs
^{121}Sb	1/2–3/2	50.136	877	317	160	17.0
	3/2–5/2	100.45	316	872	450	14.0
^{123}Sb	1/2–3/2	30.650	1548	456	230	24.0
	3/2–5/2	60.945	451	1500	800	12.0
^{123}Sb	3/2–5/2	60.945	1441	1500	800	12.0
	5/2–7/2	91.478	1500	1411	800	6.0

relaxation time $T_1^{(1)}$, and the transverse relaxation time $T_{2\rho(\mathrm{one})}^{(1)}$ of this transition in the RRF from the data obtained for the 3/2–5/2 transition (resonance ^{185}Re, $\nu_2 = 56.600$ MHz).

Using formulas (2), (4), and (5), we obtain $T_2^{(1)} = 65$, $T_1^{(1)} = 251$, and $T_{2\rho(\mathrm{one})}^{(1)} = 105$ μs.

Let us now suppose that no echo signal is observed in the case of one-frequency pumping at the 3/2–5/2 transition (resonance ^{185}Re, $\nu_2 = 56.600$ MHz). In this case, we can determine $T_2^{(2)}$, $T_1^{(2)}$, and $T_{2\rho(\mathrm{one})}^{(2)}$ for this transition from the data obtained for the 1/2–3/2 transition (resonance ^{185}Re, $\nu_1 = 28.312$ MHz).

Using formulas (3), (4), and (6), we obtain $T_2^{(2)} = 100$, $T_1^{(2)} = 250$, and $T_{2\rho(\mathrm{one})}^{(2)} = 143$ μs.

Thus, the formation of quadrupole spin echo in the rotating reference frame under two-frequency pumping of two adjacent transitions makes it possible to determine the relaxation times for all single-quantum transitions in a multilevel spin system. The results obtained for one transition can be used to determine the relaxation parameters of all the remaining single-quantum transitions. The accuracy of the determination depends on the accuracy of measurement of the relaxation time of the transition used as the "basis."

ACKNOWLEDGMENTS

This research was supported by the Russian Foundation for Basic Research (grant "Leading Scientific Schools" no. 96-15-96-636).

REFERENCES

1. Th. Farrar and E. Becker, *Pulse and Fourier Transform NMR: Introduction to Theory and Methods* (Academic, New York, 1971; Mir, Moscow, 1973).

Translated by N. Wadhwa

Physics of the Solid State, Vol. 42, No. 4, 2000, pp. 657–663. Translated from Fizika Tverdogo Tela, Vol. 42, No. 4, 2000, pp. 641–646.
Original Russian Text Copyright © 2000 by Panchenko.

SEMICONDUCTORS AND DIELECTRICS

Photo- and Thermally Induced Optical Absorption and Photoconductivity of Sillenite Crystals

T. V. Panchenko
Dnepropetrovsk State University, pr. Gagarina 72, Dnepropetrovsk, 320635 Ukraine

Received August 19, 1999

Abstract—A study is reported of photo- and thermally induced changes in the optical absorption and photoconductivity spectra of $Bi_{12}SiO_{20}$ crystals in the 0.5–3.5 eV spectral interval, and of the temperature dependence of optical absorption for temperatures from 80 to 600 K. An analysis is made of the electron redistribution processes between the shallow and the deep donor and acceptor levels by invoking the configurational coordinate model. *© 2000 MAIK "Nauka/Interperiodica".*

Photorefractive crystals of the $Bi_{12}MO_{20}$ sillenite family (BMO, M = Si, Ge, Ti) exhibit optically or thermally induced effects associated with changes in optical absorption and photoconductivity.

The BMO response in the 0.5–3.4-eV spectral range can be conveniently characterized by dividing the photon energy range into two regions, $E_1 \approx 2$–3.4 eV (*A*) and $E_2 \approx 0.5$–2 eV (*B*). Illumination in the *A* region induces the photochromic (PC) effect, i.e., the appearance of additional-absorption bands [1–6] and the onset of impurity photoconduction (IPC) [1, 7–9]. Light in the *B* region causes a partial suppression of the PC effect [1, 2], a short-term quenching of the photoconduction, and an increase of the diffraction efficiency when recording holograms in the *A* region [10, 11]. Heating to ~500 K results in the total suppression of the PC effect [1–7] and of (IPC) [1, 11], and for $T < 300$ K, one observes activation and quenching of photoconductivity in the *A* region [11, 12].

The common features in the conditions for photoexcitation and for the optical and thermal suppression of IPC and the PC effect, suggest that these phenomena are inextricably linked. It may be conjectured that they are accounted for by the same electronic transitions and charge transfer processes, for instance, by those of the type deep level–conduction-band–deep level. It does not, however, appear possible to get a clear understanding of the problem from the incomplete available data on the PC effect and IPC obtained in different experimental conditions.

The centers making up a deep level are usually associated with BiO_7 complex ions bound to M-cation vacancies [1] or with an antisite Bi substituting for the M cations in the oxygen tetrahedra [2–4, 13]. Accordingly, there is no consensus on the nature of the PC effect. It is believed that it is induced by the transition of the BiO_7 ions to a metastable state (through many-phonon nonradiative recombination transitions) [1] or by a change in the charge state of the Bi ions [2–4]. Impurity photoconduction is associated with a change in the population of the gap levels [1, 7] and the redistribution of recombination flows between fast and slow recombination centers [11].

One should take into account that the PC effect and impurity photoconduction can involve deep levels with essentially different thermal (E_a^{Th}) and optical (E_a^{Op}) activation energies characteristic of $Bi_{12}SiO_{20}$ (BSO) crystals [14–16]. The difference between the E_a^{Th} and E_a^{Op} is due to the electron–phonon coupling, whose high efficiency in sillenites was demonstrated in studies of Raman scattering [17], photoluminescence [18], and edge optical absorption [19, 20]. Information on these centers can be obtained by investigating the "response" of the optical and photoelectric properties of sillenites to thermal action. While the temperature dependences of the optical absorption of sillenites have recently been attracting interest [5, 6, 17, 21–24], they still remain poorly studied.

In this work, we study the optical and thermal effect on the optical absorption and photoconductivity of BSO crystals and put forward an interpretation for the induced phenomena within a common phenomenological model.

1. EXPERIMENTAL

We studied BSO crystals grown by the Czochralski technique. The total content of the residual impurity did not exceed 10^{-3} wt %. The samples prepared for optical measurements were polished plates $d = 5$ and 0.2 mm thick with (001)-oriented large faces, and the photoconductivity was studied on planar samples with 0.7–1-mm spaced Ag electrodes fired at 780 K into the (001) surface in vacuum.

The spectra of optical absorption $\alpha(E)$ and photoconductivity $\Delta\sigma(E)$ were obtained within the photon energy region $E = 0.5–3.5$ eV. The optical transmission $t(E)$ was measured with a Specord M40 and Specord NIR61 spectrophotometers with 5–10-K steps within the $T = 85–600$ K range. The photoconductivity measurement technique is described elsewhere [11]. The $\Delta\sigma(E)$ dependences were obtained at $T = 90$, 150, 290, and 360 K. The absorption spectra were corrected for reflection in the way this was done in [23].

The PC effects and impurity photoconduction were excited with a 400-W xenon lamp provided with an $E_{\max} = 2.9$-eV interference color filter, and the duration of illumination was 300 s, because this time was long enough for the PC effects to saturate.

Prior to measurements, the samples were heated in the dark in air up to ~800 K. All operations with the samples were carried out in weak red light to reduce uncontrollable photoexcitation to a minimum.

2. RESULTS AND DISCUSSION

2.1. Stationary Spectral Characteristics

The B region is characterized by a fairly good correlation between the positions of the peaks and thresholds in the optical absorption $\alpha(E)$ and stationary photoconductivity $\Delta\sigma(E)$ spectra. Given that the BSO-crystal photoconductivity is n type, we believe that these positions identify the energy of optical activation E_a^{Op} of photoactive optical transitions from donor-type local levels. In the A region, the absorption maximum at the shoulder ($E_a^{Op} = 2.9$ eV) adjoining the fundamental absorption edge and the broad peak of the impurity photosensitivity ($E_a^{Op} = 2.5$ eV) do not coincide, thus implying the existence of nonphotoactive optical transitions (Fig. 1). The values of E_a^{Op}, both new and agreeing with the data found by other authors, are presented in [11].

The $\Delta\sigma(E)$ and $\alpha(E)$ spectra respond to an increase of temperature in somewhat different ways. Within the 85–280-K interval, the photoconductivity and absorption, on the whole, increase, except for the $E \le 1.0$ eV region, where the photoresponse decreases. The components of the $\Delta\sigma(E)$ spectra undergo an intensity redistribution to make the broad impurity photoconductivity peak at $E_a^{Op} \approx 2.5$ eV dominant. The $\alpha(E)$ spectra retain their shape, but the structure $E < 1.5$ eV levels off. Within the $T = 280–300$-K interval, the $\alpha(E)$ spectra exhibit a transformation, namely, the absorption in the $E \le 2.5$-eV region drops dramatically while increasing for $E > 2.5$ eV, with the photoresponse decreasing throughout the spectral range studied (Fig. 1). Further increase of temperature is accompanied by a growth of near-edge absorption and a drop in the photosensitivity.

2.2. Induced Absorption and Photoconductivity

The spectra of the PC effect, $\Delta\alpha^{Ph}(E) = [\alpha^{Ph}(E) - \alpha(E)]/\alpha(E)$, and of the impurity photoconduction, $[\Delta\sigma^{Ph}(E) = [\Delta\sigma^{Ph}(E) - \Delta\sigma(E)]/\Delta\sigma(E)$, normalized against the initial, stationary spectra, exhibit the following features. The maximum values of $\Delta\alpha^{Ph}(E)$ are observed to occur in the region of the broad peak of stationary impurity photosensitivity, where the increase of the induced photoconductivity is smallest (Fig. 2a). At the same time, the IPC is the largest either in the B region (low temperatures) or near the long- and short-wavelength absorption edges ($T > 280$ K). One clearly sees here a level structure E_a^{Op} the values of which are in agreement with those derived from stationary photoconductivity spectra (Fig. 2b). At room temperature, one observes a substantial photoconductivity growth near the absorption edge.

Spectra of thermally induced absorption $\Delta\alpha^{Th}(E) = (\alpha^{Th}(E) - \alpha(E))/\alpha(E)$, normalized against the absorption at $T = 85$ K, are different in the temperature regions $T_1 \le 280$ K and $T_2 > 280$ K. In the T_1 region, they combine the features characteristic of the $\Delta\alpha^{Ph}(E)$ and $\Delta\sigma^{Ph}(E)$ spectra. In the T_2 region, the thermally induced edge-absorption band is similar in position and structure to the IPC band, and the thermal bleaching band coincides in position with the photochromic band in the $\Delta\alpha^{Ph}(E)$ spectrum (Fig. 2c).

Interestingly, the spectra of photo- and thermally induced increments of optical absorption coincide to the smallest of margins (below $T \le 300$ K), and the near-edge IPC spectra correlate with the spectra of near-edge thermally induced absorption for $T > 300$ K (Fig. 2). We also note that $\Delta\alpha^{Ph}(E)$, $\Delta\sigma^{Ph}(E)$, and $\Delta\alpha^{Th}(E)$ spectra have no bands characterizing new optically or photoelectrically active centers, with thermal and optical external action affecting only the relative contribution of the available centers to the resultant spectra.

2.3. Temperature Dependences of Optical Absorption

The $\alpha(T)$ dependences measured in the A and B spectral regions are slightly different. On separating three temperature intervals $\Delta T_1 \approx 80–(280–300)$ K, $\Delta T_2 \approx 300–400$ K, and $\Delta T_3 \approx 400–500$ K, we note that, as the temperature is increased, the slow growth of absorption in the A region alternates with its sharp stepwise falloff, while in the B region the absorption grows in steps (Fig. 3a).

The temperature spectra $d\alpha/dT(T)$ obtained by differentiating the $\alpha(T)$ dependences stress certain features in the thermally induced change of absorption. We note, in particular, that the $\alpha(T)$ dependences obtained for the boundary photon energies ($E \sim 2$ eV) in the ΔT_1 interval are similar to those for the A region of the spectrum, and in the ΔT_2 and ΔT_3 intervals, to those for the

B region. It also appears of interest that the extrema in the $d\alpha/dT(T)$ dependences (Fig. 3b) coincide in position with the maxima of the thermally stimulated currents [1, 25–27]. Impurity absorption is determined by the electron population of the local levels n_t and the cross section of their photoionization ζ, namely, $\alpha(T) \sim \zeta(T)n_t(T)$. Hence, this correlation implies that the thermally induced population variation of $n_t(T)$ determining the ejection of free carriers into the conduction (or valence) band plays a major part in the formation of the $\alpha(T)$ and $d\alpha/dT(T)$ dependences.

3. APPROXIMATION OF THE TEMPERATURE DEPENDENCES OF OPTICAL ABSORPTION

The $\alpha(T)$ and $d\alpha/dT(T)$ dependences for deep levels in the *A* spectral region can be described based on the observation that cooling a BSO crystal to ~80 K is accompanied primarily by the filling of relatively shallow trapping levels by electrons, while the deep levels considered here (donor levels with a thermal activation energy $E_a^{Th} < E_a^{Op}$) are empty (Figs. 1a, 1b). As the crystal is heated, the shallow levels empty, the retrapping of free electrons by the deep levels gives rise to an increase of absorption in the corresponding $\alpha(T)$ band, and the subsequent incremental drop in absorption is caused by the thermally induced emptying of the deep levels.

To approximate the $\alpha(T)$ dependence, we use the solutions to the coupled kinetic equations for the free electron concentration in quasi-steady-state conditions [28]:

$$n_1 = \frac{N_c}{N_{ti}} n_{ti0} \exp\left(-\frac{E_{ai}^{Th}}{kT}\right) \times \left[1 + \int_{T_{01}}^{T} \frac{n_{ti0} N_c S_r v_T}{\beta N_{ti}} \exp\left(-\frac{E_{ai}^{Th}}{kT'}\right) dT'\right]^{-1}, \quad (1)$$

$$n_2 = \tau_t \omega_t n_{t0} \exp\left[-\frac{E_a^{Th}}{kT} - \int_{T_{02}}^{T} \frac{\omega_t \tau_t}{\beta \tau_r} \exp\left(-\frac{E_a^{Th}}{kT'}\right) dT'\right], \quad (2)$$

where N_c is the density of states in the conduction band; N_{ti} is the concentration of *i*th shallow donor centers; n_{ti0} and E_{ai}^{Th} are the initial electron concentration and thermal activation energy, respectively, of the *i*th shallow donor levels; n_{t0} and E_a^{Th} are those of the deep levels in question with concentration N_t and trapping cross section S_t; S_r and τ_r are the recombination cross section and recombination time, respectively, of the centers with concentration M_t; β is the heating rate; v_T is the electron thermal velocity; and τ_t and ω_t are the trapping time and trapping rate coefficient, respectively, of free electrons on deep levels.

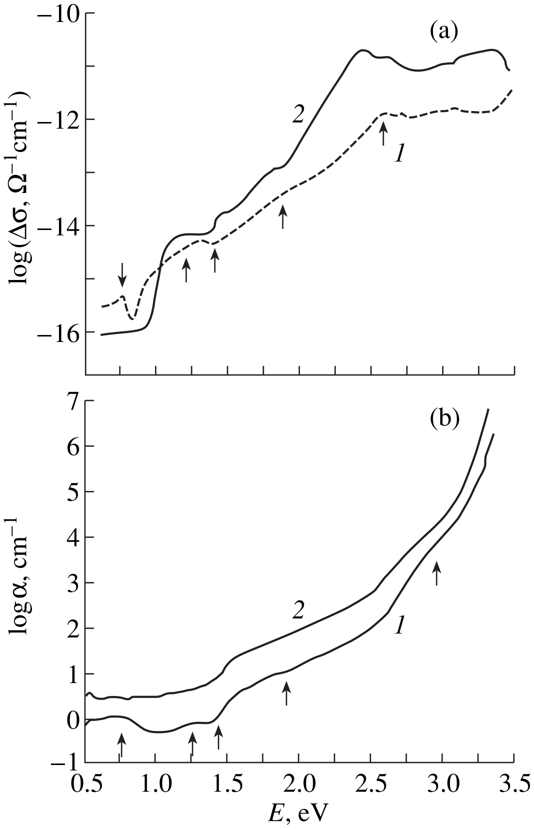

Fig. 1. Stationary spectra of (a) photoconductivity, $\log\Delta\sigma(E)$, and (b) optical absorption, $\ln\alpha(E)$, of $Bi_{12}SiO_{20}$ crystals measured at $T = 85$ K (a, *1*; b, *1*) and 280 K (a, *2*; b, *2*).

The $n_1(T)$ dependence describes the free electron concentration in the course of the emptying of shallow levels with different values of E_a^{Th} under bimolecular-recombination and intense-retrapping conditions. The existence of bimolecular recombination in the ΔT_1 interval is evidenced by studies of the temperature dependences of photoconductivity [11, 12] and of its relaxation time [29]. The $n_2(T)$ dependences characterize electron ejection into the conduction band from deep levels with one value of E_a^{Th}; this ejection occurs within a narrow temperature interval and the recombination time remains practically constant (monomolecular mechanism of recombination).

Further, we assume that, in the course of the emptying of shallow levels, the kinetics of electron concentration variation at deep centers is dominated by the retrapping of free carriers and can be described by the relation

$$\frac{d({}^1n_t)}{dt} \approx \frac{n_1}{\tau_t}, \quad (3)$$

where $\tau_t = 1/(N_t - n_t)S_t v_T \approx 1/(N_t S_t v_T)$, because the filling of the deep levels proceeds slowly and $n_t \ll N_t$. The

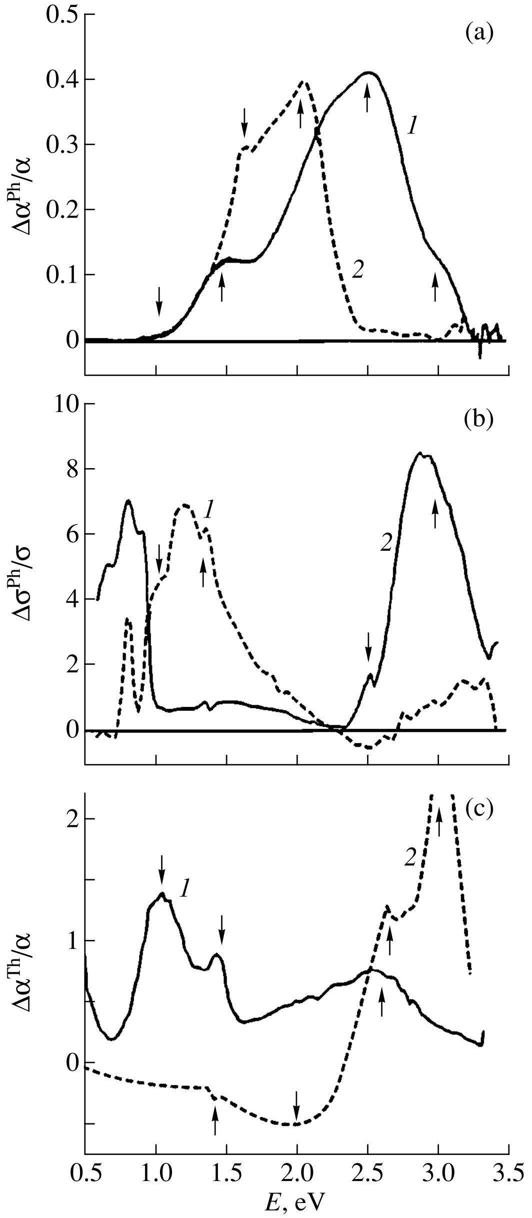

Fig. 2. Normalized spectra of (a) photoinduced photoconductivity, $\Delta\sigma^{Ph}/\Delta\sigma(E)$, (b) photoinduced absorption, $\Delta\alpha^{Ph}/\alpha(E)$, and (c) thermally induced absorption, $\Delta\alpha^{Th}/\alpha(E)$, of $Bi_{12}SiO_{20}$ crystals measured at $T = 85$ K (a, *1*; b, *1*) and 280 K (a, *2*; b, *2*), and after a heating to 200 K (c, *1*) and 350 K (c, *2*).

solution to equation (3) for linear heating, $T = T_{01} + \beta t$, can be written as

$$\frac{{}^1n_t}{n_{t0}} \approx \frac{An^*_{ti}}{n_{t0}}\left(1 + \frac{1}{S_r}\sum_t \frac{N_{ti}S_{ti}E^{Th}_{ai}}{n_{ti0}}\left(\frac{1}{kT_{01}} - \frac{1}{kT}\right)\right), \quad (4)$$

where we set $n^*_{ti} = \sum_t n_{ti0}$; $i = 1, 2, 3, 4$; $E^{Th}_{ai} = 0.2$, 0.36, 0.4, and 0.46 eV (in accordance with [1, 11, 12]); $\frac{1}{S_r}\frac{N_{ti}S_{ti}}{n_{ti}} \approx \text{const} = 0.22$; $A = 0.134$, $T_{01} = 100$ K, and $\frac{n^*_{ti}}{n_{t0}} \approx 10$.

In the stage of thermally induced emptying of deep levels, the concentrations of the electrons trapped by them and of the free electrons are related through [28]

$$\frac{{}^2n_t(T)}{n_{t0}} \approx B(\tau_t\omega_t)^{-1}n_2(T)\exp\left(\frac{E^{Th}_a}{kT}\right). \quad (5)$$

Taking relation (2) for $n_2(T)$, we set $T_{02} = 160$ K and $\omega_t\tau_t/\beta\tau_r = 10^{-2}$ (the latter equality is valid in the case of slow recombination, $\tau_r \gg \tau_t$). The experimentally observed peak in the temperature dependence of the photoconductivity relaxation time in BSO [29] implies a considerable increase of the recombination time near 300 K.

By combining (5) with (4), we come to the temperature dependences of $n_t(T) = {}^1n_t(T) + {}^2n_t(T)$ normalized against the initial deep-level filling n_{t0}, which correlate with the experimental dependences $\alpha(T)$ obtained for the deep levels with an optical activation energy $E^{Op}_a \leq$ 1.7 eV (Fig. 3a). In an early stage of heating, the correlation can be improved by using in (3) the expression

$$n_t \approx \frac{N_c}{S_r}\sum_t S_{ti}\exp\left(-\frac{E_{ai}}{kT}\right), \quad (6)$$

which is valid for bimolecular recombination in the case of weak trapping on shallow levels. Weak trapping is well founded for the high degree of initial shallow-level filling considered here. For deep levels with $E^{Op}_a > 1.7$ eV, the correlation between the approximating and experimental $\alpha(T)$ relations can be improved by taking into account the temperature dependence of the photoionization cross section $\zeta(T) \sim T^{-0.5}$ (Fig. 3a).

The $\alpha(T)$ dependences in the *B* spectral region are dominated by photoionization of the acceptors that compensate the donor levels. The approximating expressions for this case are similar to those derived in [22, 23].

4. CONFIGURATIONAL COORDINATE DIAGRAM

The relation between the photo- and thermally induced effects can be interpreted by taking into account the strong coupling of electronic transitions with phonons by means of the configurational-coordinate diagram (Fig. 4). In Mott's adiabatic approach, these coordinates *Q* denote the radius of a defect producing local lattice distortions, as well as the potential energy *E*(*Q*) of the crystal–defect–electron system. The diagram is based on the Franck–Condon principle and on the concept of the equilibrium state of a system, reached under strong electron–phonon coupling, where

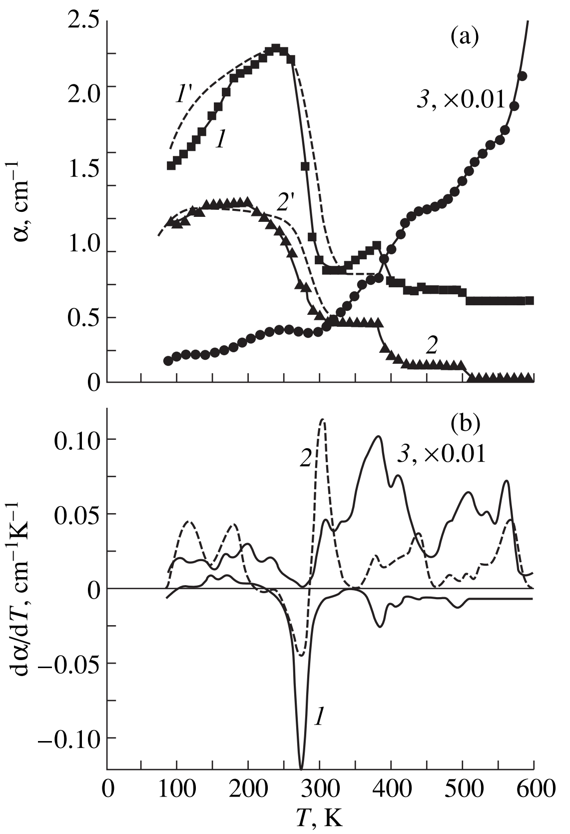

Fig. 3. Experimental (a, *1*, *2*, *3*) and calculated (a, *1*', *2*'; b, *1*, *2*, *3*) temperature dependences (a) of optical absorption $\alpha(T)$ and (b) of its temperature derivative $d\alpha/dT(T)$ in the absorption bands of $Bi_{12}SiO_{20}$ crystals with various values of E_a^{Op} (eV): 1.64 (a, *1*, *1*'; b, *1*), 1.85 (a, *2*, *2*'), 2 (b, *2*), and 3.17 (a, *3*; b, *3*). Curve b, *1* is shifted downwards (along the $d\alpha/dT$ axis) by 0.012 cm^{-1}K^{-1}.

vibrational quanta are imparted to the lattice faster than the energy obtained under photoexcitation can be reemitted [30, 31].

The energy of a system with an electron in the conduction or valence band is represented by parabolas $E_V(Q)$ and $E_c(Q)$. Both bands are centered at $Q = Q_0 = 0$, because in these states the electrons are delocalized and are described by Bloch functions. Next, we introduce two types of centers: relatively shallow, with energies $E_1(Q)$ and $E_2(Q)$, and deeper ones with $E_3(Q)$. The latter can also reside in metastable states $E_8(Q)$ and, besides, they can exist in their own excited localized [$E_4(Q)$ and $E_5(Q)$], [$E_9(Q)$ and $E_{10}(Q)$] and delocalized [$E_6(Q)$] states. The presence of ionized acceptors is taken into account by the $E_7(Q)$ curve.

The diagram is constructed by the following rules: (1) The shift of the minima in the $E_i(Q)$ potential curves (i = 3, 4, 5, and 10) along the E axis, is in direct relation to the electron binding energy with the shallow, deep, and acceptor centers, i.e., its decrease indicates a weakening of the electron–phonon coupling and an increase of the extent of electron delocalization. (2) The optical absorption band width is proportional to the distance along the Q axis between the minima in the $E_i(Q)$ curves between which transitions occur. The energies of the optical and thermal activation of the shallow and deep centers (E_a^{Op} and E_a^{Th}) and the thermal activation energy E_a^S for the trapping cross section (thermal-activation barrier for nonradiative transitions) are defined as this is done in [16]. The electron–phonon coupling constant S (the Huang–Rhys factor) for center-bound electrons is determined by the magnitude of the Stokes shift $\Delta E_{F-C} = 0.5(E_a^{Op} - E_a^{Th}) = S\hbar\omega$, where $\hbar\omega$ is the

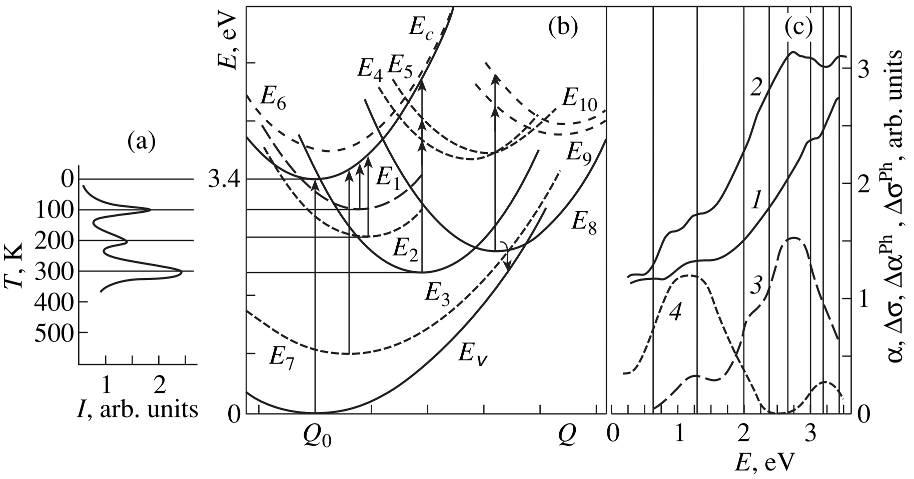

Fig. 4. (a) Model spectrum of a thermally stimulated current, (b) configurational coordinate diagram for $Bi_{12}SiO_{20}$ crystals, and (c) model spectra of (*1*) stationary optical absorption $\alpha(E)$, (*2*) photoconductivity $\Delta\sigma(E)$, (*3*) photoinduced absorption $\Delta\alpha^{Ph}(E)$, and (*4*) photoconductivity $\Delta\sigma^{Ph}(E)$, measured at $T \sim 80$ K. The coordinates of the grid vertical lines correspond to the energies E_a^{Op} of the electronic transitions specified in the configurational diagram.

vibrational energy quantum. We use photoluminescence data [1, 32] to set $\Delta E_{F-C} \approx 0.9$–2.0 eV. Turning now to deep centers associated either with Bi ions substituting for Si in the oxygen tetrahedra or with the BiO_7 molecular ions, we take the LO phonon energies of the BSO phonon spectrum, because they correspond to the vibrations of these structural elements [33]. We come to the estimate $S \approx 6.7$–10.2, which slightly exceeds the value of S obtained for such semiconductors as GaAs, ZnS, and ZnSe [31, 34, 35].

This diagram permits a general description of optical absorption and photoconductivity spectra, as well as of their photo- and thermally induced variations. For instance, at $T = 80$ K, the $\alpha(T)$ dependence displayed in Fig. 1 by curve *1* derives from transitions (shown by arrows in Fig. 4b) from shallow and deep centers and ionized acceptors to the conduction band, intracenter transitions in the centers responsible for the deep levels, and transitions from the density-of-states tails of ionized acceptors (curve *1* in Fig. 4c). Increasing the temperature to $T_{1\max} = 100$ K and $T_{2\max} = 200$ K, which correspond to the maxima of a thermally stimulated current, results in a depletion of the shallow centers with thermal activation energies $E_{a1}^{Th} \sim T_{1\max}$ and $E_{a2}^{Th} \sim T_{2\max}$ (Fig. 4a). This entails an electron transfer to deeper centers and, accordingly, to a thermally induced coloring of BSO crystals (see Fig. 2c, curve *1*). At the higher temperature $T_{3\max}$ corresponding to the peak of the thermally stimulated current, deep levels with a thermal activation energy $E_{a3}^{Th} \sim T_{3\max} = 300$ K start to eject electrons. This corresponds to the thermal bleaching of BSO crystals (curve *2* in Fig. 2c). The same processes govern the $\alpha(T)$ and $d\alpha/dT(T)$ dependences (Fig. 3).

The photoconductivity spectrum $\Delta\sigma(E)$ in the B region correlates with the $\alpha(E)$ spectrum, whereas in the A region, only photoactive transitions from the deep center to the delocalized excited state $E_6(Q)$ contribute to $\Delta\sigma(E)$ (Figs. 4b, 4c). As the temperature increases, the photoconductivity varies in a more complex way than the absorption does, because, in addition to the change in the filling of the shallow and deep centers, the temperature dependence of the recombination time has an effect in this case [11]. Therefore, one could hardly expect the responses of the $\Delta\sigma^{Ph}(E)$ and $\alpha(E)$ spectra to an increase in temperature to correlate. We note only that for $T > T_{3\max}$ the increase in optical transmission of a crystal is accompanied by a drop in its photosensitivity (Figs. 2a, 2c).

Photoexcitation in the B region gives rise not only to an additional filling of both shallow and deep centers [curves $E_1(Q)$ and $E_2(Q)$ in Fig. 4b], but it also transfers the deep centers to a metastable, nonphotoactive state [curve $E_8(Q)$]. This accounts for the difference in position between the main maxima of the normalized spectra $\Delta\sigma^{Ph}(E)$ (impurity photoconductivity) and $\Delta\alpha(E)$ (photochromic effect) (Fig. 4c). At $T = 300$ K, photoexcitation does not transfer the emptied deep centers to the metastable state, and the IPC and PC spectra exhibit only the contributions due to the additional filling of the thermally emptied levels (Fig. 2a).

The photochromic effect in BSO crystals is thermally suppressed by thermal ionization, at $T = T_{3\max}$, of the filled ground-state deep centers and thermalization of electrons (with an activation energy E_a^S) from the metastable state of the deep centers, a process that increases the degree of ionization of the acceptors (the temperature steps in the rise of absorption of the type of ionized acceptor–conduction band correlate with those of the absorption decay in the A spectral region, Fig. 3a).

Thus, the totality of the results obtained can be accounted for by using the configurational diagram proposed in this work and taking into account the considerable difference between the thermal and optical activation energies (the large electron–phonon coupling), the existence of ground and metastable deep-center states, as well as the intracenter optical transitions. The above configurational diagram also allows another important conclusion, namely, that the models of the local gap-level energy structure (similar to those proposed in [1]), which were obtained by a straightforward combination of activation energies found by thermal-activation and optical spectroscopy, are apparently not appropriate for the sillenites.

REFERENCES

1. V. K. Malinovskiĭ, O. A. Gudaev, V. A. Gusev, *et al.*, *Photoinduced Phenomena in Sillenites* (Nauka, Novosibirsk, 1990).
2. T. V. Panchenko and N. A. Truseeva, Ukr. Fiz. Zh. **34**, 1495 (1989).
3. T. V. Panchenko and N. A. Truseeva, Ferroelectrics **129**, 113 (1992).
4. B. Briat, H. J. Reyher, A. Hamri, *et al.*, J. Phys.: Condens. Matter **7**, 6951 (1995).
5. J. Foldvari, L. E. Halliburton, G. J. Edwards, *et al.*, Solid State Commun. **77**, 181 (1991).
6. J. J. Martin, J. Foldvari, and C. A. Hunt, J. Appl. Phys. **70**, 7554 (1991).
7. A. Ya. Volosov, V. Kh. Kostyuk, A. Ya. Kudzin, *et al.*, Fiz. Tverd. Tela (Leningrad) **23**, 2187 (1981) [Sov. Phys. Solid State **23**, 1281 (1981)].
8. I. A. Karpovich, E. E. Kolosov, E. I. Leonov, *et al.*, Izv. Akad. Nauk SSSR, Neorg. Mater. **21**, 965 (1985).
9. T. V. Panchenko, Fiz. Tverd. Tela (S.-Peterburg) **40**, 1027 (1998) [Phys. Solid State **40**, 938 (1998)].
10. A. A. Kamshilin and M. P. Petrov, Fiz. Tverd. Tela (Leningrad) **23**, 3110 (1981) [Sov. Phys. Solid State **23**, 1811 (1981)].
11. T. V. Panchenko and Z. Z. Yanchuk, Fiz. Tverd. Tela (S.-Peterburg) **38**, 2018 (1996) [Phys. Solid State **38**, 1663 (1996)].
12. I. S. Zakharov, Fiz. Tverd. Tela (Leningrad) **27**, 1062 (1985) [Sov. Phys. Solid State **27**, 643 (1985)].

13. R. Oberschmid, Phys. Status Solidi A **89**, 263 (1985).
14. M. G. Ermakov, A. V. Khomich, P. I. Petrov, *et al.*, Mikroélektronika **11**, 424 (1982).
15. V. I. Berezkin, Fiz. Tverd. Tela (Leningrad) **25**, 490 (1983) [Sov. Phys. Solid State **25**, 276 (1983)].
16. T. V. Panchenko, Fiz. Tverd. Tela (S.-Peterburg) **40**, 452 (1998) [Phys. Solid State **40**, 415 (1998)].
17. B. Briat, T. V. Panchenko, H. Bou Rjeily, *et al.*, J. Opt. Soc. Am. **15**, 2147 (1998).
18. V. S. Gorelik and V. N. Moiseenko, KSF FIAN **3–4**, 20 (1991).
19. T. V. Panchenko, S. Yu. Kopylova, and Yu. G. Osetskiĭ, Fiz. Tverd. Tela (S.-Peterburg) **37**, 2578 (1995) [Phys. Solid State **37**, 1415 (1995)].
20. T. Toyoda, H. Nakanichi, S. Endo, *et al.*, J. Phys. C: Solid State Phys. **19**, L259 (1986).
21. M. T. Borowiec, in *Solid State Crystals: Growth and Characterization*, Ed. by J. Zmija, A. Majchrowski, J. Rutkowski, and J. Zellinski [Proc. SPIE **3178**, 173 (1997)].
22. T. V. Panchenko, Fiz. Tverd. Tela (S.-Peterburg) **40**, 1246 (1998) [Phys. Solid State **40**, 1135 (1998)].
23. T. V. Panchenko, Fiz. Tverd. Tela (S.-Peterburg) **41**, 1006 (1999) [Phys. Solid State **41**, 916 (1999)].
24. D. Bloom and S. W. S. McKeever, J. Appl. Phys. **77**, 6511 (1995).
25. T. Takamori and D. Just, J. Appl. Phys. **67**, 848 (1990).
26. D. Bloom and S. W. S. McKeever, J. Appl. Phys. **77**, 6521 (1995).
27. T. V. Panchenko and G. V. Snezhnoĭ, Fiz. Tverd. Tela (Leningrad) **35**, 2945 (1993) [Phys. Solid State **35**, 1598 (1993)].
28. Yu. A. Gorokhovatskiĭ and G. A. Bordovskiĭ, *Thermal Activation Spectroscopy of High-Resistivity Semiconductors and Insulators* (Nauka, Moscow, 1991).
29. V. I. Berezkin, Candidate's Dissertation in Physics and Mathematics, FTI AN SSSR (1983).
30. J. Bourgoin and M. Lannoo, *Point Defects in Semiconductors: Experimental Aspects* (Springer, Berlin, 1983; Mir, Moscow, 1986).
31. B. K. Ridley, *Quantum Processes in Semiconductors* (Clarendon, Oxford, 1982; Mir, Moscow, 1986).
32. T. V. Panchenko and I. V. Solodovnikova, Ukr. Fiz. Zh. **33**, 1014 (1988).
33. S. V. Vagin, R. Jerman, M. Hodoscek, *et al.*, Fiz. Tverd. Tela (Leningrad) **34**, 1384 (1992) [Sov. Phys. Solid State **34**, 736 (1992)].
34. D. Bois and A. Chantre, Rev. Phys. Appl. **15**, 631 (1980).
35. A. A. Kopylov and A. N. Pikhtin, Fiz. Tekh. Poluprovodn. (Leningrad) **8**, 2398 (1974) [Semicond. **8** (1974)].

Translated by G. Skrebtsov

Physics of the Solid State, Vol. 42, No. 4, 2000, pp. 664–669. Translated from Fizika Tverdogo Tela, Vol. 42, No. 4, 2000, pp. 647–651.

SEMICONDUCTORS AND DIELECTRICS

Characteristics of Microwave Photoconductivity of Natural Diamond in the Spectral Range 200–250 nm

A. G. Zakharov*, N. A. Poklonskiĭ*, V. S. Varichenko*, and A. G. Gontar'**

** Belarussian State University, ul. Leningradskaya 14, Minsk, 220050 Belarus*

*** Institute for Superhard Materials, National Academy of Sciences of Ukraine, Avtozavodskaya ul. 2, Kiev, 252153 Ukraine*

e-mail: heii@phys.bsu.unibel.by

Received June 3, 1999; in final form, September 7, 1999

Abstract—Mechanically polished plates of natural diamond of the II*a* and I*a* types were investigated by the microwave photoconductivity (MW PC), conventional (direct-current or, more precisely, low-frequency) photoconductivity (LF PC), and optical-absorption techniques. It is shown that the polycrystalline structure of the samples and high spatial inhomogeneity of the impurity defect distribution provide differences in MW PC and LF PC spectra. It is assumed that nonequilibrium holes in the illuminated diamond are trapped by the crystallite boundaries, while free electrons "oscillate" within the crystallites during their lifetime. The influence of chemical and mechanical treatment on the LF and MW PC is demonstrated. *© 2000 MAIK "Nauka/Interperiodica".*

Conventional (virtually low-frequency) photoconductivity (LF PC) provides one of the most important tools for the investigation of defects in semiconductors and dielectrics [1, 2]. The approach, unfortunately, demonstrates significant disadvantages when it is applied to the research of diamond. First of all, no technique of the ohmic contact formation has been developed for crystals with the *i*- and *n*-type conductivity up to now. Another drawback originates from the sensitivity of the LF PC spectra to the applied voltage [3]. Therefore, the investigation of photoconductivity in diamond calls for contact-free, non-destructive methods, one of which, for instance, implies using microwaves [4].

The present work is aimed at revealing the dependence of MW PC spectra in the wavelength range $\lambda \approx 200$–250 nm on the mechanical treatment of the diamond surface and on impurity defects in the crystal.

1. EXPERIMENTAL TECHNIQUE

The samples tested in our experiments were mechanically polished plates of diamond of the II*a* and I*a* types. The first contained nitrogen in the *A* form with a concentration of $N_A \approx 3 \times 10^{18}$ cm^{-3}, the second contained the same concentration of the *A* form and, additionally, the *B*1 form of nitrogen ($N_{B1} \approx 3 \times 10^{19}$ cm^{-3}). The samples weighed 0.09–0.11 carats and had dimensions 8 × 5 × 0.5 mm. Prior to the measurements, the plates were etched in a mixture of $K_2Cr_2O_7 + H_2SO_4 + H_2O$, then cleaned in boiled distilled water and dried in air. The experiments were conducted at room temperature.

To measure MW PC, the samples were positioned in a potential antinode of the electric field of a wave $E_0\exp(-i\omega t)$ with a frequency of $f = \omega/2\pi = 9.6$ GHz, which corresponded to the central position in a rectangular cavity of the H_{101} type. The amplitude of the electric field in the empty cavity $E_0 \approx 100$ V/cm was estimated from the experimentally found value of the quality $Q \approx 1100$ and the feeding MW power $P = 26$ mW, using the equation $E_0 = \sqrt{2QP/(\omega\varepsilon_0 V)}$ [5]. Here, $V \approx 1$ cm^3 is the portion of the cavity volume that contains the bulk of the electric component of the MW field and $\varepsilon_0 = 8.85$ pF/m is the permittivity of vacuum. The nonequilibrium charge carriers were excited by the light of a xenon arc lamp (1 kW power) transmitted through a MDR-12 monochromator and modulated with a frequency of 300 Hz. The sample plates were exposed to the exciting light alternately from both sides. The intensity of photoexcitation was kept at a level that allowed us to neglect the skin-effect and the reflection of MW radiation from the free carrier plasma in the sample. The reciprocal quality value for the cavity with a sample, when the illumination was out, was taken as zero level of the MW PC signal. The MW PC signals were recorded in the synchronous detection mode. The amplitude of the electric field inside the sample is given by the ratio E_0/ε_r, where $\varepsilon_r = 5.7$ is the dielectric constant of diamond. The microwave radiation power P_a absorbed in the cavity, when the sample volume V_a is exposed to the exciting light, is given by

$$P_a = \frac{1}{2}\left(\frac{E_0}{\varepsilon_r}\right)^2 \int_{V_a} \mathrm{Re}\sigma(\mathbf{r})d^3\mathbf{r} \approx \frac{A}{2}\left(\frac{E_0}{\varepsilon_r}\right)^2 \frac{\mathrm{Re}\sigma}{\alpha(\lambda)}, \qquad (1)$$

where $\mathrm{Re}\sigma(\mathbf{r})$ is the real part of the local photoconductivity, *A* is the illuminated area of the sample, $1/\alpha(\lambda)$ is the depth of free-carrier excitation for the wavelength λ

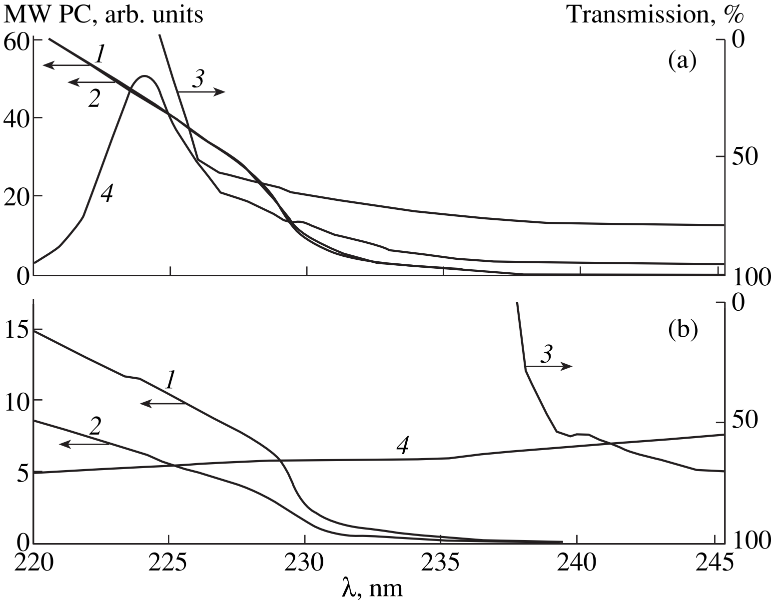

Fig. 1. Typical photoconductivity and transmission spectra measured (a) in the type II*a* diamond ($N_A \approx 3 \times 10^{18}$ cm^{-3}) and (b) in the type I*a* diamond ($N_A \approx 3 \times 10^{18}$ cm^{-3}, $N_{B1} \approx 3 \times 10^{19}$ cm^{-3}). Curves *1* and *2* are MW PC spectra obtained in a diamond plate with both sides illuminated (spectral resolution $\Delta\lambda$ = 2.4 nm); here and below, the MW PC spectra are normalized to the number of exciting quanta; curve *3* is the transmission spectrum ($\Delta\lambda$ = 0.3 nm); and curve *4* is the LF PC spectrum in arbitrary units.

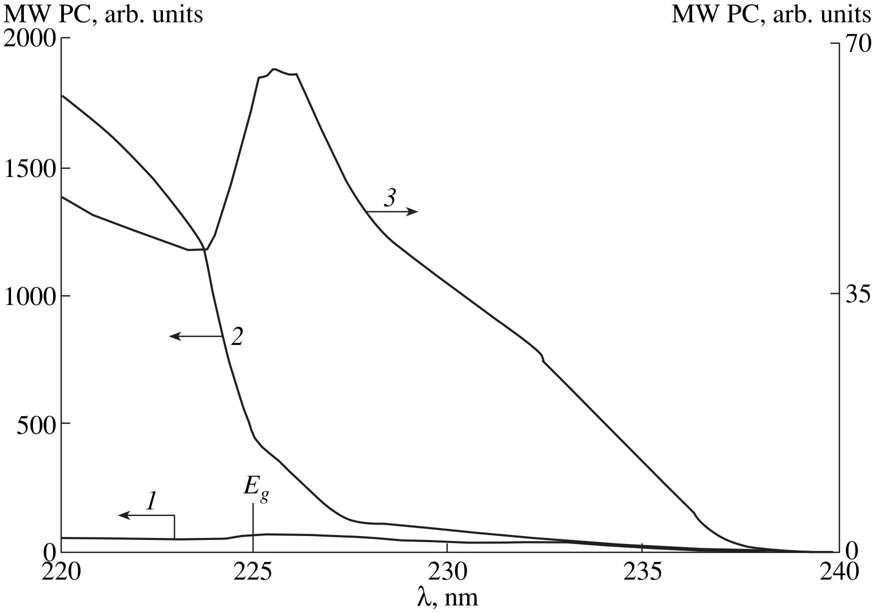

Fig. 2. MW PC spectra of a type II*a* diamond sample prior (*1*) and after (*2*) the chemical etching in $K_2Cr_2O_7 + H_2SO_4 + H_2O$ and subsequent surface polishing with the corundum powder (14 μm grain diameter). The spectral resolution is $\Delta\lambda$ = 1.2 nm for curve *1* and $\Delta\lambda$ = 0.5 nm for curve *2*. Curve *3* represents the scaled up spectrum *1*.

corresponding to the fundamental absorption in diamond, Reσ is the average of the real part of the conductivity induced by exciting light with the absorption constant $\alpha(\lambda)$.

The LF PC was measured using a 25 W deuterium lamp. The external voltage applied to aquadag electrodes on a diamond sample amounted to 50 V ($E_{dc} \approx$ 100 V/cm).

The absorption (transmission) spectra in the samples were measured by a spectrophotometer (SPECORD-M40).

2. EXPERIMENTAL RESULTS AND DISCUSSION

2.1. The typical photoconductivity and absorption spectra are shown in Figs. 1 and 2. As is seen, the MW

PC and the LF PC spectra differ drastically in the spectral range 200–250 nm.

(1) The LF PC spectra of natural diamond of types I*a* and II*a* do not look the same, but are typical of these materials [6, 7], while their MW PC spectral dependences are almost identical.

(2) The LF PC decreases with the exciting light wavelength in the range $\lambda \approx 223$–220 nm, while the MW PC increases in the same range (see Figs. 1a, 1b).

(3) Chemical etching of diamond samples in $K_2Cr_2O_7 + H_2SO_4 + H_2O$, mechanical polishing with corundum powder (14 μm), consequent cleaning in boiling water and drying in air result in an increase of MW PC by more than one order of magnitude (Fig. 2). However, the same treatment of the surface of a diamond sample causes a short circuit during LF PC measurements, either immediately after connection of contacts, or when the exciting light wavelength reaches the range 225–235 nm (in a sweep from longer wavelengths to shorter ones).

2.2. Let us consider the first peculiarity mentioned in Subsection 2.1. It is known that natural diamond is an extremely inhomogeneous material [7, 8]. Moreover, the structure of type II crystals (and of other diamond crystals close to this type) is build of grains. The sizes of these grains (crystallites) L typically belong to the range 1–100 μm, and their orientation mismatch angles may be as large as 1° [8]. Let us discuss the effect of the factors mentioned above on the MW and low-frequency PC.

It was experimentally shown that the exposure of a semiconductor crystal to high-energy particles creates intrinsic radiation defects, which results in a shift of the Fermi level in the band gap to an energy E_F^* independent of impurities and irradiation conditions [9]. According to calculations [9], the Fermi level position in diamond is limited by $E_F^* \approx 0.4E_g$ (with respect to the top of the valence band), where $E_g \approx 5.5$ eV is the gap width in diamond at a temperature of 300 K.

Let us assume that at the boundary between two crystallites the Fermi level position E_F^* is determined by defects of the same type, as in the case of the severe high-energy particle exposure. At the same time, in the bulk of an undoped diamond crystal, the Fermi level is close to the middle of the gap. Therefore, the surface states at the boundaries will be charged positively, while the bulk of a crystallite will be charged negatively. Such a double electrical layer creates an energy barrier for the conduction band electrons [10]. The height of the barrier at the crystallite boundary is $\approx 0.1E_g$, which is much higher than the average thermal energy of electrons $3k_BT/2$. Illumination of the sample in the photoconductivity experiments creates nonequilibrium holes, some of which are trapped at the boundary of a crystallite, and the same number of free electrons is "locked" inside the crystallite and oscillates during their lifetime, which resembles oscillations of an electron within the *F*-center in the lattice of NaCl.

Let us describe the conductivity of a single crystallite in terms of the Drude and Lorentz models and then consider the MW PC in polycrystalline diamond [1, 2, 11, 12]. We assume that the mean free path of an electron is much shorter than the crystallite size L and the lifetime τ_n is much longer than the quasi-momentum relaxation time τ_c.

According to the Drude model, the real part of the conductivity of a crystallite depends on the MW frequency $\omega = 2\pi f$ as [11]

$$\mathrm{Re}\sigma_D = \frac{\sigma_{dc}}{1 + (\omega\tau_c)^2}, \qquad (2)$$

where $\sigma_{dc} = e^2 n\tau_c/m_c$ is the DC conductivity, e is the absolute value of the electron charge, $m_c \approx 0.48m_0$ is the effective mass of an electron in the conduction band of diamond, n is the concentration of nonequilibrium conduction electrons in an "average" crystallite, $\tau_c = \mu_n m_c/e \approx 10^{-12}$ s is the average quasi-momentum relaxation time of conduction electrons in a crystallite, $\mu_n \approx 2000$ cm^2/ (V s) [13] is the electron mobility at a temperature of $T \approx 300$ K (we keep in mind that the MW field $E_{ac} = E_0/(\varepsilon_r\sqrt{2}) \approx 13$ V/cm does not heat electrons).

According to the Lorentz model, the equation of motion of a conduction electron within a crystallite under the action of the MW field is given by

$$\frac{d^2x}{dt^2} + \frac{dx}{\tau_c dt} + \omega_0^2 x = -\frac{eE_0}{m_c\varepsilon_r}\exp(-i\omega t), \qquad (3)$$

where $x(t)$ is the displacement of the electron with respect to the center of the crystallite along the electric component of the MW field, ω_0 is the natural frequency of oscillations of the nonequilibrium electron in the crystallite before its recombination with a hole at the boundary.

The frequency ω_0 can be estimated using an oscillator model in which the quasi-elastic force applied to the electron in the direction to the center of the crystallite is proportional to the displacement of the electron from its equilibrium position and to the elastic constant k; thus, we have $\omega_0 = \sqrt{k/m_c}$. We assume the displacement amplitude to be $L/2$, which means that the electron either reflects from the crystallite boundary or recombines with a hole. Applying the virial theorem [14] to the harmonic oscillator, which states that the average potential energy and the average kinetic energy are equal, we obtain $k(L/2)^2 = 3k_BT$. Hence, $\omega_0 = (2/L)\sqrt{3k_BT/m_c}$.

Solving equation (3) gives the current density $endx/dt$ and the real part of the conductivity for the crystallite, according to the Lorentz model [12],

$$\mathrm{Re}\sigma_L = \sigma_{dc}\frac{(\omega/\tau_c)^2}{(\omega_0^2-\omega^2)^2+(\omega/\tau_c)^2}. \qquad (4)$$

Substituting $\mathrm{Re}\sigma_D$ and $\mathrm{Re}\sigma_L$ into (1), we arrive at the conclusion that, at a frequency of $f = 9.6$ GHz, small crystallites ($L \le 1.5$ μm) do not contribute to the MW PC (see Fig. 3). As is seen, the MW absorption by nonequilibrium electrons in the crystallite (P_a) does not practically depend on the frequency f at $L > 7$ μm. At the same time, the Drude model predicts the independence of the MW absorption on the crystallite size L in the frequency range 0.3–300 GHz (with the proviso that the average crystallite size L is much larger than the mean free path).

It is worth mentioning that the observed peculiarities of the MW PC look similar to the size effect [15], but, in our case, they are of another nature. The size effect arises when the doubled amplitude of conduction electron oscillations $2a = \mu_n E_{ac}/f$ in the electric field alternating with a frequency f exceeds the crystallite size L, so the electron trajectory does not fit the room available, $2a/L \ge 1$. If transitions of the conduction electrons between crystallites are hampered due to interface barriers, the electrons spend a portion of the oscillation period squeezed to the crystalline boundaries and absorb no energy from the MW field. As a result, the power density of MW radiation absorbed in the sample decreases and turns out to be lower than that predicted by the Drude model, $\sigma_{dc}E_0^2/(2\varepsilon_r^2) = \sigma_{dc}E_{ac}^2/\varepsilon_r^2$. The condition $fL \le \mu_n E_{ac}$ gives that, in the case of our MW PC measurements, the size effect can only be observed for the crystallite sizes $L \le 0.03$ μm.

The crystalline boundaries do not manifest themselves if $L > 7$ μm. The MW PC values and spectra, according to the Lorentz model, turn out to be the same as for a monocrystal sample. In LF PC measurements, the presence of crystallites gives rise to the polarization of diamond. The polarization level depends on the position of the electrodes and the relationship between the bulk conductivity and the conductivity in the boundaries between crystallites [16].

Experimental data we obtained for the mechanically polished natural-diamond plates and epitaxial diamond films substantiate the proposed model. We correlated the level of the MW PC in the samples illuminated in the spectral range above the fundamental absorption edge and the spectra of cathodoluminescence (the electron beam diameter ≈1 mm, the acceleration voltage 10 kV, the current 6 μA). We found, that specimens demonstrating free exciton luminescence in the spectral band near 235 nm showed the maximum level of the MW PC. At the same time, a number of samples demonstrating a maximum MW PC signal did not reveal any free-exciton luminescence. This can be explained in terms of the theory of the internal photoeffect [1, 2]. It says that nonequilibrium carriers of the opposite charge are spatially separated at the crystalline boundaries, which excludes the creation of excitons.

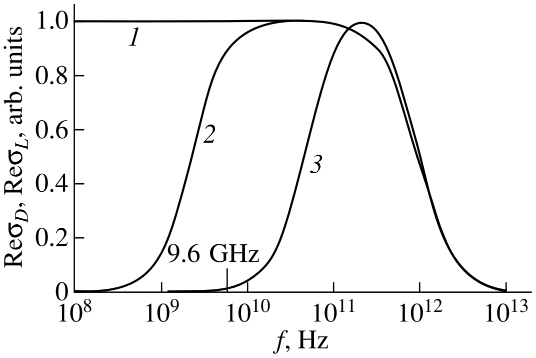

Fig. 3. Absorption of MW power by conduction electrons in a diamond sample (P_a) calculated using equation (1). Curve *1* shows the result of Re σ_D/σ_{dc} calculations according to the Drude model for $\tau \approx 5 \times 10^{-12}$ s; curves *2* and *3* are data for Re σ_L/σ_{dc} obtained by the Lorentz model for polycrystalline diamond ($L \approx 7$ and ≈1.5 μm for curves *2* and *3*, respectively).

Contrary to the data obtained for natural diamond, we found that polycrystalline diamond films reveal no MW PC signal when band-to-band light absorption occurs, even if the free-exciton luminescence is intense compared to that for natural diamond specimens. The theory of the internal photoeffect [1, 2] fails to explain this fact. At the same time, according to estimations derived from (1), (2), and (4), the observations mentioned above may be explained by the fact that the average crystallite size L does not exceed 1.5 μm. Indeed, the natural frequency of oscillations of nonequilibrium electrons inside the crystallite $\omega_0 = (2/L)\sqrt{3k_BT/m_c}$ exceeds $\omega = 2\pi f \approx 60.3$ GHz in the case of $L \le 1.5$ μm and the absorption of MW radiation does not occur.

The results of [17] indirectly confirm the proposed model. In [17], a growth of the conductivity in polycrystalline diamond films ($L \approx 10$ μm, aquadag electrodes) was observed at $T \approx 300$ K with an increase of the electric field frequency according to the law $\mathrm{Re}\sigma \propto f^s$, where $s \approx 0.6$, in the range $f = 10^2$–10^4 Hz. This result agrees with estimations of $\mathrm{Re}\sigma_L$ from (4) (see also the graphs in Fig. 3).

Let us compare data presented in Figs. 1a and 1b, taking into account high spatial inhomogeneity of impurity defects in natural diamond [7, 8]. The cathodoluminescence research using defocused electron beams revealed highly inhomogeneous spatial distribution of $B1$ defects in type I*a* diamond. The $B1$ defects are platelet structures parallel to the (111) plane. They contain nitrogen and show IR absorption in the spectral bands centered at 7.5, 8.5, 9.1, 9.9, and 12.8 μm. The local lifetime of nonequilibrium electrons τ_n and their mobility (quasi-momentum relaxation time τ_c) are also inhomogeneous, they are lower in regions containing

$B1$ defects compared to domains with the perfect crystal structure.

If the excitation depth in diamond $1 / \alpha(\lambda)$ is much more then the average crystallite size L, then the homogeneous illumination of a plate results in different contributions to the MW PC from crystallites without $B1$ defects (index 1) and crystallites with $B1$ defects (index 2), their ratio being equal to [18]

$$\frac{P_{a1}}{P_{a2}} = \frac{\sum_j (KV_1\mu_{n1}\tau_{n1})_j}{\sum_l (KV_2\mu_{n2}\tau_{n2})}, \qquad (5)$$

where μ_{n1}, μ_{n2}, τ_{n1}, τ_{n2} are the mobilities and stationary lifetimes of nonequilibrium electrons in the two kinds of crystallite; V_{1j} and V_{2l} are the volumes of crystallites; and coefficients K_j and K_l take into account the contributions from crystallites j and l, respectively, to the MW PC according to equation (4); their contributions are different depending on the crystallite size along the direction of the electric MW field. At $T \approx 300$ K, we have $K_j = 0$ if $L_j < 1.5$ μm, $K_j = 1$ if $L_j \geq 7$ μm, and $0 < K_j < 1$ if $1.5 < L_j < 7$ μm.

It follows from (5), that crystallites with a more perfect structure (index 1) dominate in the resulting MW PC disregarding their location. If $P_a \gg P_{a2}$, the MW PC values become the same as in crystals free from $B1$ defects, i.e., as in the type II*a* crystals (compare Figs. 1a, 1b).

The processes associated with the charge carrier transport from one electric contact to the other affect the results of LF PC measurements on diamond samples with $B1$ defects. The resulting photocurrent depends on the mobility and carrier concentration everywhere in the region between the electrodes; moreover, it is influenced by the particular location of domains of different photoconductivity and by the presence of boundaries between crystallites. The graphs in Fig. 1b, for instance, illustrate the case of a series arrangement of domains with and without $B1$ defects in the resulting LF PC circuit.

Thus, the first of the differences between the LF and MW PC spectra indicated in Subsection 2.1 can be explained by the inhomogeneity and polycrystalline structure of type II natural diamond (and other materials close to this type) and to the absence of polarization effects in MW PC measurements for crystallite sizes $L > 7$ μm.

2.3. Let us consider the second and the third distinctions between the MW and LF photoconductivity spectra indicated in Subsection 2.1. They are: a growth of the MW PC level (by one order of magnitude) after polishing of diamond with the corundum powder (see Fig. 2), and the impossibility to observe LF PC signals in the same diamond samples after the same surface treatment.

To elucidate the nature of these distinctions, we also applied some other methods of the diamond surface treatment preceding MW PC measurements [19–22]. They were: chemical etching, thermal treatment in air (200–500°C, 1 h), and ion etching. All the treatments did not lead to an increase in the MW PC signal. The etching with Ar^+ ions (1 keV, 1 min), in particular, not only reduced the signal level but also resulted in an irreversible change in the MW PC spectrum. Such a result of the treatment could be caused by the precipitation of components of the etching solutions and etching products on the sample surface [20, 21] (in the case of chemical and thermal treatment), or could be attributed to an increased number of defects (in the case of ion etching). These peculiarities of the MW PC could also origin from the negative affinity of the diamond surface to electron (electron absorbs the energy of the MW PC field being either inside or above the sample).

Thus, we come to the conclusion that the second and third differences of the MW and LF photoconductivity spectra indicated in Subsection 2.1 can be explained by different sensitivity of these two techniques to the condition of the sample surface.

To sum up the results described, we note that the investigation of the same diamond plates by MW PC and LF PC methods results in different photoexcitation spectra in the wavelength range $\lambda = 200$–250 nm. The difference in the MW and LF photoconductivity of type I*a* and type II*a* diamond crystals was explained in terms of a model of the MW PC taking into account peculiarities of the motion of nonequilibrium electrons in polycrystalline samples. It follows from the model developed in this paper, that at $T \approx 300$ K the presence of crystallites of a size L exceeding 7 μm does not influence the results of MW PC measurements ($f \approx 9.6$ GHz), while the crystallites sized below 1.5 μm do not contribute to the MW PC. The chemical and mechanical surface treatment was demonstrated to be crucial for the results of MW and LF photoconductivity spectroscopy in diamond.

REFERENCES

1. A. N. Vasil'ev and V. V. Mikhaĭlov, *Introduction to Spectroscopy of the Solid State* (Mosk. Gos. Univ., Moscow, 1987).
2. P. Y. Yu and M. Cardona, *Fundamentals of Semiconductors* (Springer, Berlin, 1999).
3. P. Gonon, S. Prawer, Y. Boiko, *et al.*, Diamond Relat. Mater. **6**, 860 (1997).
4. V. A. Milyaev and V. A. Sanina, Izv. Vyssh. Uchebn. Zaved., Radiofizika **23**, 407 (1980).
5. Ch. P. Poole, *Electron Spin Resonance. A Comprehensive Treatise on Experimental Techniques* (Wiley, New York, 1967; Mir, Moscow, 1970).
6. P. Denham, E. C. Lightowlers, and P. J. Dean, Phys. Rev. **161**, 762 (1967).

7. V. S. Vavilov, A. A. Gippius, and E. A. Konorova, *Electronic and Optical Processes in Diamond* (Nauka, Moscow, 1985).
8. G. B. Bokiĭ, G. N. Bezrukov, Yu. A. Klyuev, A. M. Naletov, and V. I. Nepsha, *Natural and Synthetic Diamonds*, Ed. By I. I. Shafranskiĭ (Nauka, Moscow, 1986).
9. V. N. Brudniĭ and S. N. Grinyaev, Fiz. Tekh. Poluprovodn. (S.-Peterburg) **32**, 315 (1998).
10. J. M. Palau, A. Ismail, and L. Lassabatere, Solid State Electronics **28**, 499 (1985).
11. P. Grosse, *Free Electrons in Solids* (Springer-Verlag, Berlin, 1979; Mir, Moscow, 1982).
12. P. S. Kireev, *Semiconductor Physics* (Vysshaya Shkola, Moscow, 1975).
13. *Physical Properties of Diamond, A Handbook*, Ed. by N. V. Novikov (Naukova Dumka, Kiev, 1987).
14. B. V. Vasil’ev and V. L. Lyuboshits, Usp. Fiz. Nauk **164**, 367 (1994).
15. É. M. Épshteĭn, Fiz. Tekh. Poluprovodn. (Leningrad) **17**, 2190 (1983).
16. *Polycrystalline Semiconductors: Physical Properties and Applications*, Ed. by G. Harbeke (Springer-Verlag, Berlin, 1985; Mir, Moscow, 1989).
17. G. A. Sokolina, A. A. Botev, L. L. Buĭlov, *et al.*, Fiz. Tekh. Poluprovodn. (Leningrad) **24**, 175 (1990).
18. V. L. Bonch-Bruevich, Usp. Fiz. Nauk **140**, 583 (1983).
19. B. B. Pate, Surf. Sci. **165**, 83 (1986).
20. A. T. Collins and S. Rafique, J. Phys. C: Solid State Phys. **11**, 1375 (1978).
21. A. Lepek, A. Halperin, and J. Levinson, Phys. Rev. B **19**, 2250 (1979).
22. A. Zangwill, *Physics at Surfaces* (Cambridge University Press, Cambridge, 1988; Mir, Moscow, 1990).

Translated by S. M. Klimentov

Physics of the Solid State, Vol. 42, No. 4, 2000, pp. 670–672. Translated from Fizika Tverdogo Tela, Vol. 42, No. 4, 2000, pp. 652–654.
Original Russian Text Copyright © 2000 by Bautin, Gorbunov, Yakovlev, Kruzhalov.

SEMICONDUCTORS AND DIELECTRICS

Metastable Optical Absorption of Exited *F*-Centers in BeO Crystals

K. V. Bautin*, S. V. Gorbunov*, V. Yu. Yakovlev, and A. V. Kruzhalov***
** Ural State Technical University, ul. Mira 19, Yekaterinburg, 620002 Russia*
*** Tomsk Polytechnical University, pr. Lenina 30, Tomsk, 634034 Russia*
e-mail: baut@dpt.ustu.ru

Received June 23, 1999; in final form, September 15, 1999

Abstract—The metastable optical absorption in additively colored BeO crystals is studied. It is found that the optical absorption is induced by transitions between the excited triplet and singlet states of an *F*-center. *© 2000 MAIK “Nauka/Interperiodica”.*

The formation of *F*-centers in BeO crystals under chemical heat treatment in beryllium vapor (additive coloring) was proved in our earlier work [1]. Detailed studies of the optical characteristics of an absorption band at 6.5 eV and luminescence bands at 4.9 and 3.4 eV allowed us to establish their relation to the singlet–singlet and triplet–singlet transitions in an *F*-center [2]. The optical anisotropy of absorption and luminescence of *F*-centers in hexagonal BeO crystals [2] was explained by the splitting of excited states in the crystal field of the C_{3v} symmetry.

In this work, the data on the metastable optical absorption in wide-gap oxides are obtained for the first time. The metastable optical absorption arises upon optical transitions of an electron that relaxes into the lowest-lying excited triplet state of the *F*-center.

The experiments were carried out with BeO single crystals, which were grown from a solution of beryllium oxide in the sodium tungstate melt by V.A. Maslov and were then additively colored in beryllium vapor at $T = 2200$ K according to the procedure described in [1]. Optical measurements in the range 1–5 eV were performed at temperatures of 80–600 K on a setup of pulsed adsorption spectroscopy with a nanosecond temporal resolution (7 ns) [3]. The excitation was achieved using a GIN-600 pulsed electron accelerator with the following parameters of electron beam: $E = 0.2$ MeV, $W = 0.02$–0.25 J/cm^2, and $t_{\text{imp}} = 10^{-8}$ s. Additional studies of the optical absorption in the polarized light were accomplished with the help of a Rochon silica prism.

At 80 K, the kinetics of optical absorption decay in additively colored BeO crystals at about 3.8 eV in the time interval $t > 50$ ms can be described by the superposition of two exponential dependences. The first dominating component has the characteristic decay time $\tau_1 = 740 \pm 40$ ms, which is identical to the decay time of the luminescence at 3.4 eV due to spin-forbidden transitions from the triplet excited state of *F*-centers. The second component of the decay kinetics of the metastable optical absorption has the characteristic time $\tau_2 > 5$ s, which strongly depends on the intensity of the probing light. These trapping centers unstable toward the light are likely associated with shallow traps formed by impurities or defects.

In order to elucidate the nature of the first component of the metastable optical absorption decay, we compared the temperature dependences of the amplitude and relaxation time of the optical density of this component and the temperature dependences of the intensity and decay time of the luminescence at 3.4 eV of *F*-centers (Fig. 1). It is seen that the temperature behavior of the intensity of the first optical absorption component (curve *4* in Fig. 1) agrees well with the temperature behavior of the intensity of the stationary X-ray luminescence at 3.4 eV (curve *3* in Fig. 1) for the additively colored BeO crystals. The symbate quenching of the luminescence at 4.9 eV due to the singlet–singlet transitions in an *F*-center and the luminescence at 3.4 eV upon photon excitation within the *F*-absorption band (curves *1* and *2* in Fig. 1, respectively) reflects the processes of radiationless filling of the triplet state from the higher-lying singlet state. Therefore, a decrease in the amplitude of the first metastable optical absorption component and a decrease in the intensity of X-ray luminescence at 3.4 eV in the range 100–200 K are brought about by the radiationless transitions from the singlet state of the *F*-center. A similar increase in the *F*-luminescence yield and in the optical density amplitude of the first induced-absorption component at $T > 200$ K is caused by an increase in the number of excited *F*-centers due to the energy transfer to the *F*-centers through the thermoactivated migration of the autolocalized electronic excitations in BeO [4].

Moreover, the investigation into the temperature–time characteristics of the relaxation processes of the luminescence at 3.4 eV and optical absorption revealed a number of insignificant differences (curves *5* and *6* in Fig. 1, respectively). A decrease in the decay of the first

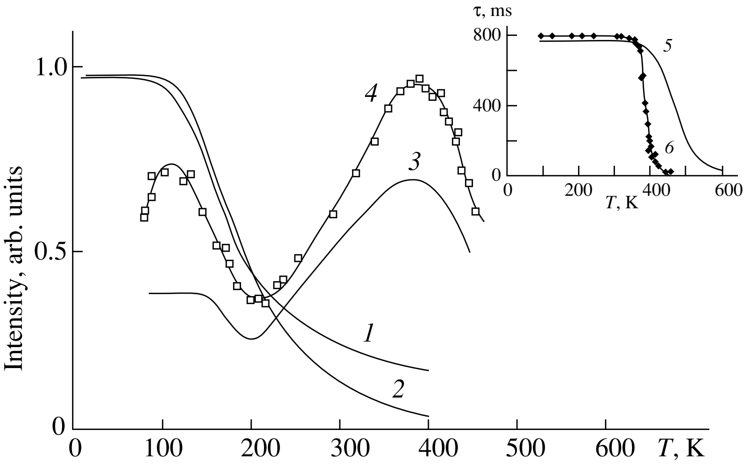

Fig. 1. Temperature dependences of the intensity of (*1*) luminescence at 4.9 eV, (*2*, *3*) luminescence at 3.4 eV, and (*4*) metastable optical absorption of additively colored BeO crystals under excitation with (*1*, 2) the light within the *F*-absorption band, (*3*) X-ray radiation, and (*4*) electron beam. The inset shows the temperature dependences of the decay time of (*5*) luminescence at 3.4 eV and (*6*) metastable optical absorption.

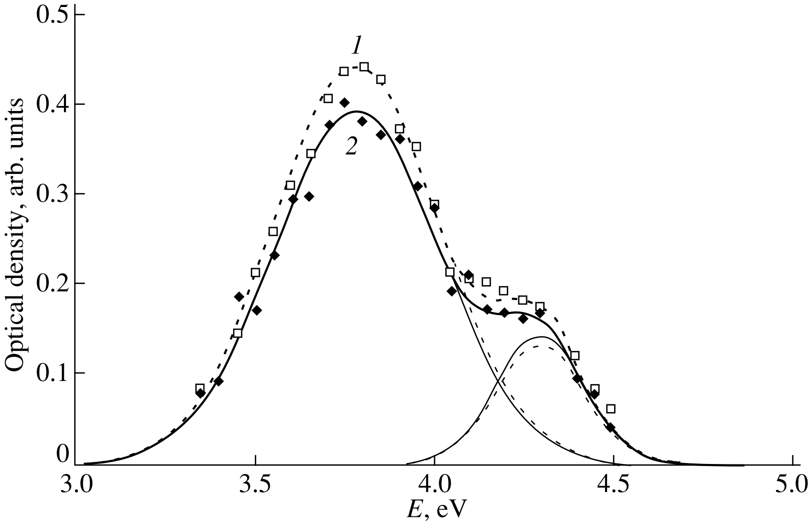

Fig. 2. The spectra of metastable optical absorption of the excited *F*-centers at 80 K for the light polarized at (*1*) **E** ⊥ **C** and (*2*) **E** || **C**. Solid and dashed lines show the resolution into the Gaussian components.

component of the induced optical absorption begins at $T > 350$ K and occurs with the activation energy $E_a = 0.8$ eV. At the same time, a decrease in the decay time of the luminescence at 3.4 eV is observed at $T > 380$ K and proceeds with the activation energy $E_a = 0.53$ eV. These differences can be caused by the probing light, which contributes to an additional decrease in the population of the triplet excited state of the *F*-center upon optical transitions.

Thus, the results obtained indicate the metastable optical absorption of the excited *F*-centers formed upon exposure of additively colored BeO crystals to electron beam. To interpret the optical transitions in the excited *F*-centers, we measured the metastable optical absorption spectra with a temporal resolution in the polarized light at 80 K. As is seen from Fig. 2, the spectrum of the component with a characteristic time of 740 ms consists of two isotropic bands with maxima at 3.8 and 4.3 eV and half-widths of 0.55 and 0.29 eV, respectively. The decay time of this absorption suggests that the optical transitions occur from the triplet excited state of the *F*-center in BeO. We assumed that these transitions are realized to the higher-lying singlet excited states of the *F*-center. In the study of the anisotropy of *F*-absorption band in BeO [2], it was revealed that the singlet excited state of the ^1P-type is split into the $^1A_1$ and ^1E components in the crystal field of the C_{3v} symmetry. The found splitting is equal to 0.3 eV. This value is somewhat less than the separation between the maxima of two bands of the metastable optical absorption (0.5 eV).

The optical transitions $^3P \longrightarrow {}^1P$ between the states with the different multiplicity are forbidden. This forbidding can be partially removed through the spin-orbit interaction resulting in the mixing of singlet and triplet states. However, only the states with a certain symmetry can be mixed. On the basis of the group-theoretic analysis of the spin-orbit interaction, we earlier considered the selection rules for radiative transitions from the triplet excited state—this state is split into the ^3E and $^3A_1$ components in the crystal field of the C_{3v} symmetry—to the ground $^1A_1$ state of the F-center in BeO [2]. A slight anisotropy of the F-luminescence at 3.4 eV was explained in [2] by the $^3E \longrightarrow {}^1A_1$ transitions, because the ^1E state can be mixed with the ^1E and $^1A_1$ states. The observed isotropy of the bands of metastable optical absorption confirms its origin from the $^3E \longrightarrow {}^1A_1$ and $^3E \longrightarrow {}^1E$ transitions between the excited triplet and singlet states of the F-center in BeO.

REFERENCES

1. A. V. Kruzhalov, S. V. Gorbunov, B. V. Shul'gin, *et al.*, Pis'ma Zh. Tekh. Fiz. **10**, 1503 (1984) [Sov. Tech. Phys. Lett. **10**, 635 (1984)].
2. S. V. Gorbunov, A. V. Kruzhalov, and M. J. Springis, Phys. Status Solidi B **141**, 293 (1987).
3. V. Yu. Yakovlev, Fiz. Tverd. Tela (Leningrad) **26**, 3334 (1984) [Sov. Phys. Solid State **26**, 2003 (1984)].
4. V. Yu. Ivanov, V. A. Pustovarov, S. V. Gorbunov, *et al.*, Fiz. Tverd. Tela (S.-Peterburg) **38**, 3333 (1996) [Phys. Solid State **38**, 1818 (1996)].

Translated by T. Galkina

Physics of the Solid State, Vol. 42, No. 4, 2000, pp. 673–682. Translated from Fizika Tverdogo Tela, Vol. 42, No. 4, 2000, pp. 655–664.
Original Russian Text Copyright © 2000 by Moliver.

SEMICONDUCTORS AND DIELECTRICS

An Open-Shell Method for Neutral Vacancy in Silicon and Diamond

S. S. Moliver
Ul'yanovsk State University, Ul'yanovsk, 432700 Russia
e-mail: moliver@sv.uven.ru

Received in final form, September 20, 1999

Abstract—The restricted Hartree–Fock–Roothaan method with closed and open electronic shells projected by electron density matrices and the quasi-molecular large-unit-cell (LUC) model have been applied to calculate the electronic structure of monovacancy and semivacancy in the neutral charge state in the totally symmetric atomic configuration with relaxation and symmetry-lowering distortions. The difference in the energies of states with total spins of 1 and 3/2 for a neutral monovacancy is determined within the ΔSCF approximation. *© 2000 MAIK "Nauka/Interperiodica".*

At present, the quantitative description of a vacancy in silicon and diamond in the framework of the many-electron theory has been obtained by the methods including correlation effects in the self-consistency cycle. As a rule, preference is given to the local-density-functional and pseudopotential calculations [1–3]. The quantum-chemical schemes based on the self-consistent molecular orbital (MO) method were employed within different approximations for the electron correlation, for example, such as, the X_α exchange interaction [4], the perturbation theory for configuration interaction (CI) [5], and generalized valence bond method [6]. For an adequate description of the properties of a vacancy in silicon, diamond, and other covalent semiconductors with the use of the MO method, it is essential to calculate the multiplet structures of open-shell highly symmetric atomic configurations, because the joint inclusion of the electron correlation in the vibronic coupling is of crucial importance for the above systems [7, 8].

A nonreconstructed vacancy has the T_d atomic configuration, whereas a reconstructed vacancy adopts the D_{2d} or C_{3v} configuration. For brevity, these atomic configurations will be referred to as the monovacancy. The saddle point of the vacancy migration is characterized by the D_{3d} symmetry, and this atomic configuration will be designated the split configuration or the semivacancy. The calculation of these atomic configurations with an open electronic shell requires the employment of the MO method that goes beyond the single-determinant Hartree–Fock level: it is necessary to obtain self-consistent spectroscopic combinations of the Slater determinants for the open-shell terms. Only with this constraint, there are grounds to obtain the reliable CI corrections for the electron correlation, because the configuration interaction for non-self-consistent MOs possesses a considerable uncertainty and depends essentially on the parameters [9].

In this work, we used the restricted open-shell Hartree–Fock–Roothaan molecular orbital (ROHF) method, which allows calculations of the multiplet structure composed of self-consistent non-single-determinant terms. Note that self-consistent calculations of determinant combinations in the framework of the ROHF method introduce the correction to the intraconfigurational interaction for the electron correlation. The required spatial symmetry of terms is determined using the group-theoretic analysis of the ROHF coefficients describing the contribution of open-shell MOs to the direct and exchange electron–electron interactions. The restricted method, as applied to these calculations, ensures the spin symmetry of the terms.

The restricted single-determinant closed-shell MO Hartree–Fock (RHF) method cannot be used at all to calculate the totally symmetric atomic configurations of a monovacancy and a semivacancy: the computations at the RHF level make it possible only to estimate one of the terms in the multiplet structure by introducing a small distortion. For vacancies in silicon and diamond, this approach leads to an appreciable error that can be eliminated by the ROHF method.

It should be noted that the quantum-chemical ROHF method is a complementary tool to the density-functional approach. First, unlike the empirical local-exchange-functional method, the electron correlation in the ROHF method is included in *ab initio* calculations as a nonlocal exchange interaction—the intraconfigurational interaction at the self-consistency stage and the interconfigurational interaction in the CI approximation. Second, the multiplet terms in the ROHF method can be determined not only by a unified self-consistency procedure, but, in a number of cases, with the use of more precise separate self-consistent

1063-7834/00/4204-0673$20.00 © 2000 MAIK "Nauka/Interperiodica"

computations (even though not always for all the terms). Third, on the basis of the known experimental properties, the ROHF multiplet structure provides a means of evaluating the ratio of the correlation corrections for certain terms.

The aim of the present work was to comparatively evaluate the correlation energies of different multiplet terms for a neutral vacancy from their (terms) behavior at different distortions in the case when the filling of an open shell changes in character. The results obtained for the correlation energy and other energy parameters associated with the Jahn–Teller effect are in good agreement with a great number of theoretical and experimental data for silicon and diamond and can be characterized as obtained within the one-open-shell approximation. The ROHF method allows the extension to a larger number of open shells [10], but this requires a substantial increase in the computational power.

1. SELF-CONSISTENT OPEN-SHELL CALCULATIONS

The self-consistent restricted open-shell MO method (ROHF) based on a universal technique of projection by electronic-shell density matrices for crystalline systems [10] was realized and described earlier in [11]. Since the computational details are not essential for the understanding of the present work, only the ROHF coefficients required for the calculations are explained below. Similar to the open-shell multiplet, these coefficients are obtained from the group-theoretic analysis.

In the model, N_e electrons are distributed among a closed shell consisting of n_a MOs designated as a' and an open shell composed of n_b MOs denoted by b', so that the Roothaan occupation number for an open shell of a given configuration is equal to

$$f = \frac{N_e - 2n_a}{2n_b} < 1.$$

The ROHF method makes it possible to self-consistently calculate either the energy of the term or the Slater diagonal sum of terms [12, 13]. This energy involves two terms formed according to the Slater rule from the matrix elements of the one-electron part h and two-electron part g of the Hamiltonian.

The first term in the total energy does not depend on the distribution of electrons over the open shell, is identically written for all terms and diagonal sums of the given configuration, and is equal to the closed-shell energy plus one-electron open-shell energy and the energy of interaction between all the closed-shell MOs and all the open-shell MOs (the last two energies are proportional to the occupation number f).

The second term in the total energy is the interaction energy in the open shell and depends on a specific distribution of electrons over the open-shell MOs in determinants involved in the spectroscopic sum (term), that is,

$$g^{(b)} = \sum_{b'}^{n_b}\sum_{b''}^{n_b}[2A_J\langle b'b''|g|b'b''\rangle - A_K\langle b'b''|g|b'b''\rangle] + \sum_{b'}^{n_b}A_I\langle b'b'|g|b'b'\rangle. \qquad (1)$$

The essence of the ROHF method is that the self-consistent calculation can be carried out only when the interaction energy (1) takes the form similar to that of the part describing the closed shell, which is possible if the coefficient A_I is equal to zero. Therefore, after the symmetry selection of determinants into the term, it is necessary to find its interaction energy (1) according to the Slater rules and to calculate the A_I, A_J, and A_K ROHF coefficients. If $A_I = 0$ for the given term, its energy can be calculated by a self-consistency procedure. Otherwise, this term should be included in the Slater diagonal sum (several sums are possible) with $A_I = 0$. The energy of each term entering into the diagonal sum can be derived by using MOs of the diagonal sum and the ROHF coefficients of the given term.

According to the variational principle in the presence of an open shell, two electron density matrices constructed on the LCAO coefficients of closed and open electronic shells should be computed in each self-consistency cycle. The Fock matrix in each self-consistency cycle is calculated by the density-matrix projection with allowance made for the ROHF coefficients determined for the calculated term or diagonal sum [11]. The eigenvalue problem for the Fock matrix is solved in each self-consistency cycle, and the total energy of the term or Slater diagonal sum can be found upon reaching the specified convergence level.

It should be remarked that the radical difference from the closed-shell case is not energy modification (1) with the ROHF coefficients, but the Fock matrix projection providing an orthogonal set of MOs for all shells [10]. The projection procedure takes a larger part of the computer time and considerably increases the computation time as compared to the closed-shell case. However, the open-shell computational schemes without projection lead to a nonorthogonal set of MOs, which complicates the calculations of observables and requires the elaboration of a special approach to the determination of the multiplet structure.

2. MULTIPLET STRUCTURES AND VACANCY DISTORTIONS

An open shell of a vacancy consists of either orbital triplet, or orbital doublet, or one orbital depending on the atomic configuration. The group-theoretic analysis of the Slater determinant combinations is required only in the first two cases. The results of the analysis performed are presented in the table. The designations of the terms are obtained by adding the left superscript of

Multiplet structure and ROHF coefficients for the neutral vacancy in open-shell states with orbital degeneracy

V^0 configuration $t^2\left(f=\frac{1}{3}\right)$			A_J	A_K	A_I
$t_2^2\,(T_d)$	s^2p^2				
${}^1A_1$ (■, ■■)	${}^1S$	$\frac{1}{\sqrt{3}}(t't' + t''t'' + t'''t''')\alpha\beta$	0	–3	0
${}^1E$ (■)	${}^1D$	$\frac{1}{\sqrt{6}}(2t't' - t''t'' - t'''t''')\alpha\beta;\ \frac{1}{\sqrt{2}}(t''t'' - t'''t''')\alpha\beta;$	0	$\frac{3}{2}$	$\frac{9}{2}$
${}^1T_2$ (□)	${}^1D$	$\frac{1}{\sqrt{2}}t't''(\alpha\beta - \beta\alpha)$; + CR	$\frac{3}{4}$	$-\frac{3}{2}$	–3
${}^3T_1$ (□, □□)	${}^3P$	$\frac{1}{\sqrt{2}}t't''(\alpha\beta + \beta\alpha)$; $t't''\alpha\alpha$; $t't''\beta\beta$; + CR	$\frac{3}{4}$	$\frac{3}{2}$	0
E_1'' (□■)		$\frac{1}{6}({}^1A_1 + 2\cdot{}^1E + 3\cdot{}^1T_2)$	$\frac{3}{8}$	$-\frac{3}{4}$	0
E_2'' (■□)		$\frac{1}{9}({}^1A_1 + 2\cdot{}^1E + 3\cdot{}^1T_2 + 3\cdot{}^3T_1)$	$\frac{1}{2}$	0	0

V^0 configuration $e^2\left(f=\frac{1}{2}\right)$						
$e_g^2, e_u^2\,(D_{3d})$	$e^2\,(C_{3v})$	$e^2\,(D_{2d})$				
${}^3A_{2g}$ (□□)	${}^3A_2$ (□□)	${}^3A_2$ (□□)	$\frac{1}{\sqrt{2}}e'e''(\alpha\beta + \beta\alpha)$; $e'e''\alpha\alpha$; $e'e''\beta\beta$;	1	2	0
		${}^1B_1$ (□)	$\frac{1}{\sqrt{2}}e'e''(\alpha\beta - \beta\alpha)$	1	–2	–4
${}^1A_{1g}$ (■■)	${}^1A_1$ (■■)	${}^1A_1$ (■, ■■)	$\frac{1}{\sqrt{2}}(e'e' + e''e'')\alpha\beta$	0	–2	0
		${}^1B_2$ (■)	$\frac{1}{\sqrt{2}}(e'e' - e''e'')\alpha\beta$	0	2	4
${}^1E_g$ (■□)	${}^1E$ (■□)		$\frac{1}{\sqrt{4}}[(e'e' - e''e'')\alpha\beta \pm e'e''(\alpha\beta - \beta\alpha)]$	$\frac{1}{2}$	0	0
		E_1'' (■□)	$\frac{1}{3}({}^1B_1 + {}^1A_1 + {}^1B_2)$	$\frac{1}{3}$	$-\frac{2}{3}$	0
		E_2''	$\frac{1}{4}({}^1B_1 + {}^1A_1 + {}^1B_2 + 1\cdot{}^3A_2)$	$\frac{1}{2}$	0	0
		E_3''	$\frac{1}{6}({}^1B_1 + {}^1A_1 + {}^1B_2 + 3\cdot{}^3A_2)$	$\frac{2}{3}$	$\frac{2}{3}$	0

Note: t', t'', t''' and e' and e'' in the Slater determinants are the radial parts of MOs (components of triplet and doublet representations) in the configurations; α and β are the basis spin functions. CR indicates that the triplet terms contain the determinant combinations obtained from the given combination by the cyclic rearrangement of the orbital functions. The terms of the s^2p^2 dominant valence atomic configuration are presented.

the spin multiplicity to the symbol [7] involved in the irreducible representation of the spatial part of MOs. Here, the determinants are written in the short form as products of their constituent MOs. Note that the closed-shell orbitals (the same set for all the terms of a specific configuration) are omitted, and the orbital and spin MO components are separated. In addition to the terms, the table also lists the Slater diagonal sums of the terms, which have the ROHF coefficients $A_I = 0$ and, hence, can be obtained by the self-consistent method. The reliability of the results can be improved with several Slater sums by extracting individual terms with the use of their ROHF coefficients.

Distortions—atomic displacements leading to the lowering of the symmetry of an atomic configuration—are classified by the T_d group representations for a monovacancy and the D_{3d} group representations for a semivacancy. An arbitrary displacement of the nearest neighbor separated from the monovacancy by the $\left[\frac{1}{4}\frac{1}{4}\frac{1}{4}\right]$ distance is expanded in normal modes in the form [8]

$$\begin{aligned}&(A_1)[111] + (E, 1)[\bar{1}\bar{1}2] + (E, 2)[1\bar{1}0]\\&+ (T_2, 1)[101] + (T_2, 2)[0\bar{1}\bar{1}] + (T_2, 3)[\bar{1}\bar{1}0],\end{aligned} \tag{2}$$

where the dimensionless nonnormalized modes are enclosed in parentheses. The first mode—the relaxation—is the normal mode corresponding to identical displacements of the nearest atoms along the $\langle 111\rangle$ directions, which does not lead to the symmetry lowering. The relaxation (A_1) for a monovacancy was simulated by the displacement of its four nearest neighbors toward an empty lattice site, and the relaxation (A_{1g}) for a semivacancy was modeled by the displacement of the six nearest neighbors toward two empty lattice sites.

In accord with the vibronic-coupling theory of orbital electronic MO triplet with modes identified by two-dimensional and three-dimensional irreducible representations [8], the minima of the adiabatic electronic energy are matched by two possible distortions (with the appropriate removal of MO degeneracy):

(i) the tetragonal distortion with the $\langle 001\rangle$ axis

$$\begin{gathered}q = (E, 1) \neq 0,\\(E, 2) = (T_2, 1) = (T_2, 2) = (T_2, 3) = 0,\\T_d \longrightarrow D_{2d}, \quad t_2 \longrightarrow e + b_2,\end{gathered} \tag{3}$$

(ii) the trigonal distortion with the $\langle 111\rangle$ axis

$$\begin{gathered}2q = (T_2, 1) = -(T_2, 2) = -(T_2, 3) \neq 0,\\(E, 1) = (E, 2) = 0,\\T_d \longrightarrow C_{3v}, \quad t_2 \longrightarrow e + a_1.\end{gathered} \tag{4}$$

It is these displacements determined by the relaxation and the sole dimensionless parameter q that were used in the present work. The q parameter measured from the distortion axis is the argument in Fig. 1.

In addition to the open-shell states given in the table, there are the closed-shell configurations in the states with a lowered symmetry. For example, tetragonal distortion (3) splits the MO triplet, and the neutral vacancy, except the e^2 configuration (see table), can also adopt the closed-shell configuration b_2^2 with a single ${}^1A_1$ term. This term can be self-consistently determined by the closed-shell RHF method [14, 15]; however, the subsequent use of the CI calculation [5] can appear to be inefficient, because the closed-shell configuration is not treated as a ground configuration within the Hartree–Fock approximation. As follows from the performed calculation (see Fig. 1 and the discussion given below), the ${}^1B_1$ term of the open-shell configuration e^2 has a lower energy, and just this term should be primarily taken into consideration in the CI calculations.

The states with one open shell are given in the table. For states with two open shells, e.g., for the ${}^5A_2(T_d)$ excited state experimentally observed for the neutral vacancy in diamond, the ROHF method, even if applicable, requires calculations that are too large (Fock's matrices should be projected by three, rather than two, density matrices). However, it is possible to use the non-self-consistent approximation known in quantum chemistry as the ΔSCF method [10] when the state sought is constructed as a superposition of the determinants formed by one-electron excitations of the self-consistent ground state. The Hamiltonian is not diagonal for the determinants involved in the superposition, and the mean energy of the state sought is determined by the minimization, which is equivalent to the solution of the eigenvalue problem. Omitting the formulas used in the formulation of the Hamiltonian matrix, we note that the matrix elements are written similarly to the elements defined by relationship (1), but with contributions from both open shells (each contribution is characterized by its own occupation number f and ROHF coefficients) and also with the contribution from the interaction between open shells. For numerical calculations according to the described scheme, the ΔSCF matrix was formalized by two occupation numbers, six ROHF coefficients for both open shells, and two ROHF coefficients for the open-shell crossing energy terms, which were introduced into the program on the basis of group-theoretic analysis.

3. INDO PARAMETRIZATION AND QUASI-MOLECULAR LUC MODEL

The ROHF method, as applied to crystalline systems, has been realized on the basis of the quantum-chemical semiempirical (INDO) program for closed

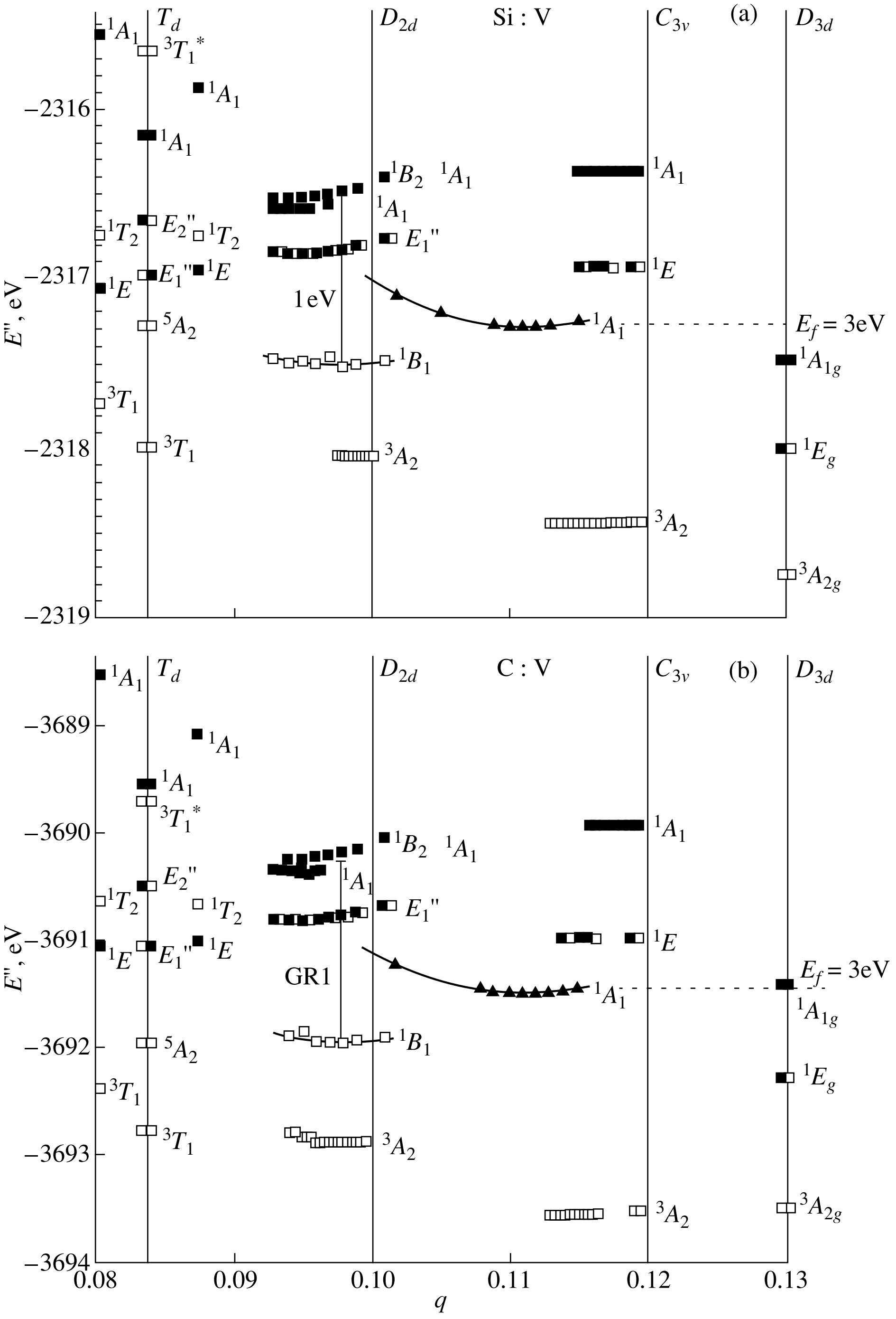

Fig. 1 Multiplet structure of the neutral vacancy in (a) silicon and (b) diamond. The dimensionless parameter q is measured from the D_{2d} tetragonal (3) and C_{3v} trigonal (*4*) distortion axes. All the levels near the T_d axis correspond to the atomic configuration of the monovacancy without distortion, and the level marked by asterisk matches the atomic configuration without relaxation. The D_{3d} axis corresponds to the semivacancy.

shells and the quasi-molecular large-unit-cell (LUC) model [11, 14, 16]. The choice of the parametrization procedure was dictated by the computational capability and experience gained in calculations of the systems consisting of Si and C atoms. The ROHF method, as such, in no way involves the parametrization procedure, and the programs implementing this procedure can be employed in any method, including *ab initio* calculations.

The parametrization procedure and computational features, such as the inclusion of the interaction between valence electrons and cores and also the cutoff of direct and exchange integrals upon summation over the extended Bravais lattice in the quasi-molecular LUC model, were chosen identical to those used by Shluger and co-workers in the CLUSTER program [17]. The lattice sums of the direct Coulomb integrals and the Hartree sums were calculated with a large cutoff radius, so that its further increase led to small variations. Although the calculation of the Hartree sums outside the cutoff radius can be refined by introducing the Madelung correction for the periodic atomic potential [13], this would be an unjustified increase in the accuracy for the nonpolar crystals under consideration, especially, in view of the semiempirical parametrization level and the restrictions imposed on the model size and on the number of displaced atoms near the defect. In accord with the recommendations following from analysis of the exchange interaction for this crystal model [19], the cutoff radius for the exchange lattice sum was chosen to be equal to approximately one-half the quasi-molecular LUC translational vector. The adiabatic dependence of the energy on the atomic displacement was calculated with the constant number of terms in the direct and reciprocal lattice sums.

The Slater valence AOs of the Si and C atoms were optimized using the parameters (lattice constant, binding energy, bulk modulus, and valence band structure) for silicon, diamond, cubic silicon carbide, and graphite crystals. The optimization technique and the physical meaning of parameters were described earlier in [16]. Since that time, the parameters were somewhat refined and included in a large number of calculations of defects and surfaces with broken bonds in the systems consisting of silicon and carbon atoms.

The wavevectors of MOs in the quasi-molecular LUC model form a set of k points [20], which coincide with the centers of the narrowed Brillouin zones filling the crystalline Brillouin zone. All the calculations were carried out with the symmetrically extended body-centered quasi-molecular LUC, which contains 32 atoms, has the k set $\{\Gamma + 12\Sigma + 3X\}$, and well reproduces the valence band structure in crystals with diamond and sphalerite structures [16]. As a whole, the semiempirical INDO parametrization employed for silicon and carbon atoms is completely determined by the properties of the above crystals (including the valence band levels); i.e., in actual fact, the calculation of defects was not semiempirical in character.

The point defects form a periodic structure and interact with each other via the four nearest neighbors in the 32-atom quasi-molecular LUC model. However, the interaction is weak for small charges on atoms. In the case when the defect is charged, the quasi-molecular LUC charge is translated over the entire crystals, which brings about the physically meaningless increase in the energy. In order to avoid this situation, upon simulation of the charged state of a defect, the charge of electrons added or removed from the neutral defect model was taken with opposite sign and uniformly distributed among all cores of the model. For the large quasi-molecular LUC, this small change in the core charges is physically equivalent to the shift of the chemical potential (the Fermi level of semiconductor).

4. RESULTS OF CALCULATIONS

Figure 1 displays the multiplet structure determined for the neutral vacancy, depending on the relaxation and distortions. The self-consistent energies (found as a result of the separate ROHF calculation in each case) of terms and diagonal sums (see table) are shown by double squares in the T_d axis for the totally symmetric monovacancy and in the D_{3d} axis for the semivacancy. Single squares near the axes indicate the energies of terms extracted from the diagonal sums. The same designations (single and double squares) are used for the monovacancies with tetragonal (3) and trigonal (4) distortions. The triangles correspond to the energies of the closed-shell configuration b_2^2, which were calculated at the RHF level. All the data were obtained at the relaxations providing the minimum energy of a given term. The exception is the $^3T_1$ term marked by asterisk whose energy, for comparison, was calculated without relaxation.

The terms shown in Fig. 1 by open and full symbols are classified in two types, which are characterized by the different structure and, as a consequence, by the different nature of the correlation correction to the ROHF approximation: (i) the covalent terms (full symbols), for which the open-shell MOs are either doubly occupied or empty, and (ii) the exchange terms (open symbols), for which the open-shell MOs are either singly occupied or empty.

The formation energy E_f for the vacancy was determined from the level indicated by the horizontal dashed line. Since this energy is calculated by subtraction of the defect-free quasi-molecular LUC energy within the RHF approximation, the level should also be specified by the energy of the closed-shell configuration to obtain the correlation corrections of the same order. The results involve the systematic error due to a spurious interaction between vacancies in the periodic quasi-molecular LUC model.

For diamond, the formation energy for the vacancy $E_f[V^0]$ is equal to 5.0 eV, whereas the *ab initio* calculation leads to an energy of 7.2 eV [21], which is in close agreement with the empirical description of the electronic properties on the basis of a large number of experimental data [22].

For silicon, the energy $E_f[V^0] = 3.0$ eV agrees well with the experimental data (3.6 ± 0.2 eV [23]).

The systematic error decreases with an increase in the quasi-molecular LUC size owing to the weakening of the vacancy–vacancy interaction.

In order to emphasize the importance of the self-consistency achieved prior to the CI calculations, let us compare the self-consistent multiplet structure shown in Fig. 1 with that obtained within the empirical model of defect molecule. The parameters of the empirical model are the matrix elements of the electron–electron interaction for open-shell MOs of the vacancy. In particular, the exchange integral $K = \langle b'b''|g|b''b'\rangle$ for the monovacancy in diamond was determined as $K = 0.58$ eV in [24] and $K = U/4 = 0.65$ eV in [22]. These values determine the relative energies of terms in the model of defect molecule. The separate self-consistent calculations of the terms give different values of the exchange integral, and the spread in the values is comparable to the correlation corrections. Upon self-consistent calculations, the other integrals used in the empirical approximations also become dependent on the terms.

The effective exchange integral without correlation correction can be determined within the ROHF approach from the splitting of the t_2^2 multiplet terms for the monovacancy. The value close to this integral was obtained using the MOs of diagonal sums. The K value calculated in the present work is equal to 0.7 eV for diamond and 0.4 eV for silicon. In the framework of the density-functional method, the quantity referred to as the singlet–triplet splitting is determined in a similar way from the terms of the total Slater diagonal sum. This quantity accounts for the electron correlation (but contains the error due to the impossibility of separate self-consistent calculations of the terms) and is found to be equal to 0.6 eV for diamond [21] and 0.33 [1] and 0.2 eV [21] for silicon.

5. RELAXATION AND RECONSTRUCTION

The main findings characterizing the lattice distortion near the vacancy are as follows.

(1) The relative equilibrium values of relaxation and distortion for vacancies in diamond and silicon are approximately identical; i.e., the atomic displacements near the vacancies in these crystals are geometrically similar, which renders the dimensionless distortion parameter q [see relationships (3) and (4)] especially convenient.

(2) For both the neutral V^0 state and the singly charged $V^{\pm}$ states, the equilibrium relaxation is directed inward and amounts to 21–25% (of the bond length) for the monovacancies (the spread is observed for all the terms) and about 16% for the semivacancies. Undoubtedly, the magnitudes of atomic displacements in different crystals differ because of different lattice constants and are equal to 0.53–0.58 and 0.32–0.37 Å for the monovacancies in silicon and diamond, respectively.

(3) The distortions are small compared to the relaxation. In the dimensionless form (2), the ratio between the distortion and relaxation enclosed in parentheses is about 20% for tetragonal distortion (3) and about 10% for trigonal distortion (4). The corresponding magnitudes of atomic displacements in the $\langle 112\rangle$ directions for the tetragonal distortion are equal to 0.15 Å for silicon and 0.11 Å for diamond. The tetragonal, rather than trigonal, distortion is energetically more favorable, which is observed in the experiment.

For lack of the experimental data, the theoretical works disagree on the direction of relaxation near the vacancy, irrespective of the computational method and the defect-crystal model. The outward relaxation is interpreted as a tendency for the first threefold-coordinated neighbors of the vacancy to form the sp^2 hybridized flat configurations with the second neighbors. It is these atomic displacements that were obtained, for example, by the density-functional method [2] (0.2 Å for diamond), the MO method at the *ab initio* RHF level [5] (the sum of relaxation and distortion is equal to 0.12 Å for silicon), and within the valence bond approach [6] (0.08 Å for silicon), even though the sizes of model clusters used in these calculations differed considerably: hundreds of atoms in the first case, tens of atoms in the second case, and the first and second coordination spheres in the third case. By analogy with the case of divacancy [25], the outward relaxation can be referred to as resonant in distinction to the pairing inward relaxation. The latter relaxation is more preferable with respect to the restoration of chemical bonds between the first neighbors of the vacancy instead of broken bonds. These inward displacements of atoms were obtained, for example, by applying different methods to the same 64-atom quasi-molecular LUC model: the density-functional method [3] (0.4 Å for silicon—a somewhat lesser value as compared to the atomic displacement obtained in the present work), which, in addition, made it possible to reproduce the experimental energy of formation of the monovacancy [23], and the semiempirical MO method [26] (0.77–0.93 Å for diamond—a larger value as compared to that found in the present work).

The relaxation direction (inward) found in the present work in the vicinity of the vacancy corresponds to the pairing relaxation mode and agrees in magnitude with the calculations performed by different methods for a similar periodic model. It is quite possible that the domination of the pairing relaxation over the resonant relaxation is associated with the limited basis set of AOs, which are centered on the atoms and poorly reproduce the delocalized unoccupied (virtual) one-electron states of the conduction band. The discrepancy in the relaxation directions near the vacancy can be caused by the fact that the model of perfect crystal, in which the vacancy is introduced, either does not account for the initial relaxation or does not reproduce the experimental elastic moduli. In this work, the models of all the crystals were optimized with particular care in order to eliminate this error [16]. A similar preliminary optimization was also performed in other works dealing with the pairing relaxation of the monovacancy [3]. The importance of considering the relaxation in the modeling of the structure and processes involving the vacancy follows from the difference between two energies of the $^3T_1$ term shown in Fig. 1. These energies were obtained for the relaxed and unrelaxed atomic configurations of the monovacancy (the latter value is marked by asterisk in Fig. 1). Their difference is the stabilization energy upon relaxation and covers the entire energy range of the multiplet structure.

The ROHF method allows the self-consistent calculation of individual terms and makes it possible to evaluate the error of calculations in which the self-consistency is achieved only for the diagonal sum [1, 2, 4]. Single squares to the right and to the left of the T_d axis indicate the term energies extracted from two diagonal sums E_1'' and E_2'', which can be obtained for the totally symmetric monovacancy. By comparing the energy of the $^3T_1$ term separately determined in a self-consistent way (double squares in the axis) and the energy obtained from the diagonal sum (squares to the left of the axis), the error of the procedure of computing the energies of terms from the diagonal sum is estimated at 0.25 eV for silicon and at 0.6 eV for diamond. Both diagonal sums lead to close values for the $^1T_2$ and ^1E terms.

6. ELECTRON CORRELATION AND JAHN–TELLER EFFECT

For the central vacancy in silicon and diamond, the triplet states ($^3T_1$ for the totally symmetric monovacancy, $^3A_2$ for the monovacancy subjected to distortions, and $^3A_{2g}$ for the semivacancy) calculated within the ROHF approximation lie below the singlet states, as in the other MO calculations [4]. From the results of calculations it follows that, if the ground state was actually triplet, this state in silicon would be stabilized by the Jahn–Teller trigonal distortion $^3T_1(T_d) \longrightarrow {}^3A_2(C_{3v})$ (Fig. 1a), and, in diamond, the state of the semivacancy, rather than the monovacancy, would be ground $^3T_1(T_d) \longrightarrow {}^3A_{2g}(D_{3d})$ (Fig. 1b).

It is well known from the experiment that the ground state of the neutral vacancy is singlet in both crystals. In this respect, the potentialities of the MO method in the description of the vacancy came under criticism. It was argued [6] that the CI corrections to the Hartree–Fock MOs are so large that it is necessary to employ the valence bond method. This assertion was based on the calculation of an insufficiently realistic small cluster model for the totally symmetric monovacancy. Moreover, the authors did not take into account that the distortion leads to the appearance of such terms in the MO scheme that can be characterized by smaller correlation corrections than the corrections applied to the totally symmetric states (of course, the revelation of this fact requires the use of the open-shell method).

This situation is actually realized in the case of the monovacancy (see Fig. 1). The stabilization of the degenerate ^1E term for the totally symmetric monovacancy due to the Jahn–Teller effect upon tetragonal distortion is described by the closed-shell configuration b_2^2 with a single $^1A_1$ term. It is the adiabatic parabola formed by triangles, which, in the ROHF approximation, approaches the level of the $b_2^2(^1E)$ term with a decrease in the distortion. However, in the ROHF approximation, the whole of the adiabatic parabola of the $^1B_1$ term for the open-shell configuration e^2 (open squares) is shifted downward with respect to its $b_2^2(^1A_1)$ counterpart in the Jahn–Teller splitting and does not reach the $t_2^2(^1E)$ level with a decrease in the distortion.

The discontinuous behavior of the energies of terms—the components in the splitting of the ^1E doublet—is not a computational error, but is the many-electron effect due to the application of the ROHF method. Indeed, within the independent electron approximation, the separation between the e doublet MOs and the t_2 triplet is two times less than the separation between the b_2 singlet and the t_2 triplet, and both separations are continuous with respect to the distortion. Therefore, the b_2^2 configuration should be energetically more favorable [8] when the distortion direction corresponds to the b_2 low-lying level (to the right of the D_{2d} axis in Fig. 1). The discontinuity in the separation of the terms within the ROHF approximation demonstrates that the correlation energies for the $t_2^2(^1E)$ and $b_2^2(^1A_1)$ covalent terms are identical to each other and exceed the correlation energy of the $e^2(^1B_1)$ exchange term. The true totally symmetric ground state ^1E involves other configurations in addition to the t_2^2 ground configuration. These configurations consist of two and more open shells and, unlike the ground configuration, are not purely covalent in character. If the CI calculations were performed with these configurations, this would provide such a correlation correction that the Jahn–Teller splitting would be continuous with respect to the distortion. Thus, the energy discontinuity between the covalent totally symmetric term and its exchange Jahn–Teller component in the ROHF approximation is the correlation energy E_{corr} in the one-open-shell approximation.

The quantum-chemical rule stating that the MO methods, without applying CI corrections, systematically underestimate the energies of triplet states as compared to the energies of the singlet states can be generalized in the following way: Within the ROHF approximation, the correlation energies of the exchange-type (both triplet and singlet) terms, like, for example, the $E^2(^1B_1)$ term for the neutral monovacancy, are less than those of the covalent-type terms. Therefore, the ROHF approximation permits one not only to independently determine single terms of the multiplet structure in a self-consistent way, but also to evaluate the correlation corrections from the behavior of the terms with a lowering of the symmetry. In the one-open-shell approximation, the correlation energy of the ^1E ground state in the totally symmetric neutral monovacancy is determined by the difference between the ROHF energies of the covalent and exchange components of the Jahn–Teller splitting ($E_{\mathrm{corr}} \approx 0.5$ eV for silicon and 0.7 eV for diamond). This energy for diamond is in satisfactory agreement with the empirical CI correction equal to 0.63 eV for the ^1E term [22].

In the ROHF approximation, the energy of the zero-phonon dipole-allowed optical electron transition, ΔE, which was determined from the terms of the totally symmetric monovacancy as $^1E \longrightarrow {}^1T_2$ [8, 22], is underestimated because of the difference between the correlation corrections of the covalent and exchange terms, as discussed above. In the one-open-shell approximation, the ΔE value is determined by the terms of the e^2 configuration with the tetragonal distortion as the energy difference $^1B_1 - {}^1B_2$. This difference is shown by the vertical line in Fig. 1 and has the following values.

For diamond, $\Delta E \approx 1.8$ eV. A good agreement with the experimental data is illustrated in Fig. 1b by the vertical segment (along which the ΔE energy is determined) whose length is taken to be equal to the energy (1.673 eV) of the corresponding GR1 band in the optical spectrum [8].

For silicon, $\Delta E \approx 1.0$ eV. Within the accuracy of the ROHF approximation, this value coincides with the experimental band gap and agrees with the result obtained by the valence bond method, i.e., $\Delta E = 1.32 \pm 0.54$ eV [6], which gave grounds to conclude that the optical spectrum of the vacancy in silicon is not observed because of the overlap with interband transitions.

7. EXCITED STATE WITH SPIN 3/2

The non-self-consistent ΔSCF approximation was used for the states with two open shells. In order to employ this method in calculating the energy of the $^5A_2(T_d)$ excited state experimentally observed by the electron paramagnetic resonance (EPR) technique [27] for the neutral vacancy in diamond, let us choose the $^3T_1$ term with appropriate single excitations (see table). The single excitations of required spatial and spin symmetry can be obtained by the transfer of one electron from the a_1 MOs of the closed shell to the MOs of the open-shell triplet

$$(t_2't_2''\alpha\alpha) \longrightarrow \sum_{a_1}(a_1\alpha)(t_2't_2''t_3'''\alpha\alpha\alpha)C_{a_1}. \qquad (5)$$

As in the table, we represent the Slater determinants in the short form by indicating only the MOs involved in their construction and omitting all the closed-shell MOs. Specifically, in the left-hand side of relationship (5), we omit all the doubly occupied MOs ($a_1a_1\alpha\beta$), which participate in the formation of the second open shell in the right-hand side (there are the five thus occupied MOs in the 32-atom quasi-molecular LUC vacancy model). The components of irreducible representations are numbered by primes, and the α and β spin parts of MOs are separated from spatial parts.

The minimum eigenvalue of the Hamiltonian matrix with determinants of the right-hand side of relationship (5) is the energy of the $^5A_2$ state, and the corresponding eigenvector of the C_{a_1} coefficients describes the configuration mixture within the ΔSCF approximation. With this method, we determined the difference in the energies of the states with spins $S = 1$ and 3/2 for the neutral monovacancy.

For diamond, the difference in the energies of the $^5A_2$ and $^3T_1$ states is equal to 0.8 eV, which agrees with the empirical estimate (about 1 eV [27]) made from the shift of the g factor in the EPR spectrum and with the theoretical value (0.87 eV [6]) obtained by the valence bond method. The discrepancy between the aforementioned data and the empirical estimate (1.6 eV [22]) is possibly caused by the fact that the latter estimate was made without invoking the experimental data on the states with nonzero spin and all the terms were calculated with the same values of two-electron integrals (non-self-consistent CI).

The difference in the energies of the $^5A_2$ and $^3T_1$ states for silicon is equal to 0.7 eV, which, unlike diamond, agrees not so well with a similar value (0.42 eV [6]) found by the valence bond method. This disagreement is likely explained by the difference between diamond and silicon in the location of the a_1 resonance states of the vacancy in the valence band and its localization, which cannot be taken into consideration in the framework of the small cluster model used in [6]. The location of the vacancy resonance a_1 can be evaluated from the energies of MOs whose excitations predominantly contribute to configuration sum (5), i.e., from the maximum ΔSCF coefficients. The squares of these coefficients (indicating the contribution of the configurations to the $^5A_2$ term in the order of the "deepening" of the a_1 MO orbital energies into the valence band) and the estimates for the energies of the resonance state of the vacancy (measured from the top of the valence band) were determined from the two most important configurations and have the following values:

$$C_{a_1}^2 = \begin{cases} 53, 38, 6, 3, 1\% \\ 29, 58, 8, 4, 0\% \end{cases},$$

$$a_1 = \begin{cases} E_V - (3.9\text{–}4.8)\ \text{eV} & \text{for diamond} \\ E_V - (2.3\text{–}3.0)\ \text{eV} & \text{for silicon} \end{cases},$$

which can indicate the larger contribution of crystalline states to the vacancy resonance in silicon as compared to diamond.

Therefore, the ROHF method made it possible to calculate the multiplet structures of highly symmetric atomic configurations of the neutral vacancy in silicon and diamond, which is the necessary condition for analyzing the electron correlation and the vibronic coupling with the use of configuration interaction. The ROHF correlation corrections for the intraconfigurational interaction differ in the order of magnitude, depending on the type of filling of the open-shell MOs. When the splitting of the highly symmetric term due to the Jahn–Teller effect is accompanied by the appearance of the configuration with a different occupation type, the discontinuity arises in the ROHF multiplet structure: the adiabatic energy of the split-off term does not approach the energy of the totally symmetric term with a decrease in the lattice distortion. The energy discontinuity is the correlation energy in the one-open-shell approximation used in the present work, even though the method can be extended to a larger number of open shells.

The difference in the energies of states with spins $S = 1$ and 3/2 for the neutral monovacancy is determined within the ΔSCF approximation. These triplet and quintet states being the low-lying excitations play an important part in the general pattern of physical properties of the vacancy (the quintet state in diamond is observed in the EPR spectrum).

ACKNOWLEDGMENTS

I am grateful to Prof. S.V. Bulyarskiĭ for his support of this work.

This work was supported by the Russian Foundation for Basic Research, project no. 98-02-03327.

REFERENCES

1. M. Lannoo, G. A. Baraff, and M. Schlüter, Phys. Rev. B: Condens. Matter **24** (2), 943 (1981); Phys. Rev. B **24**, 955 (1981).
2. S. J. Breuer and P. R. Briddon, Phys. Rev. B **51**, 6984 (1995).
3. H. Seong and L. J. Lewis, Phys. Rev. B **53**, 9791 (1996).
4. G. D. Watkins and R. P. Messmer, Phys. Rev. Lett. **32**, 1244 (1974).
5. M. A. Roberson and S. K. Estreicher, Phys. Rev. B **49**, 17040 (1994).
6. G. T. Surratt and W. A. Goddard, III, Solid State Commun. **22**, 413 (1977); Phys. Rev. B **18** (6), 2831 (1978).
7. M. Lannoo and J. Bourgoin, *Point Defects in Semiconductors: I* (Springer-Verlag, Heidelberg, 1981; Mir, Moscow, 1984).
8. J. Bourgoin and M. Lannoo, *Point Defects in Semiconductors: Experimental Aspects* (Springer-Verlag, Heidelberg, 1983; Mir, Moscow, 1985).
9. F. P. Larkins, J. Phys. Chem. Solids **32**, 965 (1971).
10. R. McWeeny, *Methods of Molecular Quantum Mechanics* (Academic, London, 1989), Vol. 15.
11. S. S. Moliver, Fiz. Tverd. Tela (S.-Peterburg) **41**, 404 (1999) [Phys. Solid State **41**, 362 (1999)].
12. J. C. Slater, Phys. Rev. **34**, 1293 (1929).
13. D. Hartree, *The Calculation of Atomic Structures* (New York, 1957; Inostrannaya Literatura, Moscow, 1960).
14. S. S. Moliver, Fiz. Tverd. Tela (Leningrad) **33**, 929 (1991) [Sov. Phys. Solid State **33**, 527 (1991)].
15. S. S. Moliver, J. Phys.: Condens. Matter **4**, 9971 (1992).
16. S. S. Moliver, Fiz. Tverd. Tela (S.-Peterburg) **38**, 2029 (1996) [Phys. Solid State **38**, 1119 (1996)].
17. A. Shluger, Theor. Chim. Acta (Berlin) **66**, 355 (1985); A. Shluger and E. Stefanovich, Phys. Rev. B **42** (15), 9664 (1990); E. Stefanovich, E. Shidlovskaya, A. Shluger, *et al.*, Phys. Status Solidi B **160**, 529 (1990).
18. P. Saalfrank, J. Phys.: Condens. Matter **3**, 2621 (1991).
19. R. A. Evarestov, V. A. Lovchikov, and I. I. Tupitsin, Phys. Status Solidi B **117**, 417 (1983).
20. R. A. Évarestov, *Quantum-Chemical Methods in the Solid-State Theory* (Leningr. Gos. Univ., Leningrad, 1982).
21. J. Bernholc, A. Antonelli, T. M. Del Sole, *et al.*, Phys. Rev. Lett. **61**, 2689 (1988).
22. A. Mainwood and A. M. Stoneham, J. Phys.: Condens. Matter **9**, 2453 (1997).
23. S. Dannefaer and P. Mascher, Phys. Rev. Lett. **56**, 2195 (1986).
24. J. E. Lowther, J. Lumin. **60–61**, 53 (1994).
25. M. Saito and A. Oshiyama, Phys. Rev. Lett. **73**, 866 (1994).
26. A. Mainwood, J. Phys. C: Solid State Phys. **11**, 2703 (1978).
27. J. A. van Wyk, O. D. Tucker, M. E. Newton, *et al.*, Phys. Rev. B **52**, 12657 (1995).

Translated by O. Borovik-Romanova

Physics of the Solid State, Vol. 42, No. 4, 2000, pp. 683–688. Translated from Fizika Tverdogo Tela, Vol. 42, No. 4, 2000, pp. 665–670.
Original Russian Text Copyright © 2000 by Dubovskiĭ.

SEMICONDUCTORS AND DIELECTRICS

New Type of Breathers near Fermi Resonance of Optical Oscillations in Crystals

O. A. Dubovskiĭ

State Scientific Center Institute of Physics and Power Engineering, pl. Bondarenko 1,
Obninsk, Kaluga oblast, 249020 Russia

Received September 28, 1999

Abstract—It has been shown that in crystals, near the Fermi resonance of optical excitons, in addition to the solitons discovered before, such as multi-exciton bound complexes of cusp-, crater-, and dark-type possessing a single carrier frequency, amplitude, and envelope, there are nonlinear soliton excitations of a crucially new, breather-type. Such periodic soliton oscillations exhibit slowly pulsing amplitudes of high-frequency oscillations, with the carrier frequency being a multiple of the frequency of pulsations. In accordance with the multiplicity, the depth of pulsations defines a series of the carrier frequencies, which are condensed near the basic frequency of optical oscillations. The spatial dependence of the two envelopes of new solitons of the cusp type is determined. With the increase in multiplicity, the sharpness of the space envelope of a soliton decreases, while the localization radius increases. Some other features of the solitons of new type are listed. *© 2000 MAIK “Nauka/Interperiodica”.*

INTRODUCTION

At present, the experimental and theoretical studies of nonlinear optical excitations of high-energy and amplitude—solitons—are performed. Such excitations consist of bound multi-exciton complexes, which are formed due to the Fermi resonance (FR) of oscillations, which gives rise to exciton–exciton interaction of the third order. When the energy $\hbar\omega_C$ of excitons of one type (C) is close to the total energy $2\hbar\omega_B$ of two excitons of another type (B), and the $BB \longleftrightarrow C$ interaction takes place, the FR causes a series of features in the vibration spectra of ionic, molecular, and other crystals of different structures and dimensions [1]. A typical value of the vibration energy in the FR is equal to 300 meV for NH_4Cl ionic crystals, 350 meV for $LiNbO_3$, etc. Recently, nonlinear optical oscillations have been investigated in superlattices of different types with a predetermined order of monomer layers (e.g., of organic molecules in PTCDA and NTCDA superlattices with exciton energies of ≈2 meV [2]), and concurrently, new technologies for multilayer lattice formation are elaborated. Such multilayer lattices hold much promise for nonlinear devices that are meant for use in optic computers in the future [2–4]. In [5–7], attention was called to the important role of the spatial FR of optical vibrations in adjacent crystal planes, when the exciton energy $\hbar\omega_C$ in one of the planes is close to the total energy $2\hbar\omega_B$ of two excitons in the neighboring plane of the interface. In [7], it was shown that, in some systems such as superlattices, due to the FR leading to the nonlinear third-order exciton–exciton interaction, specific mixed $BB + C$ exciton excitations—Fermi resonance interface modes (FRIMs)—may propagate along the interface. Quantum and classical FRIMs are responsible for the effect of bistability [8]. In [9–11], it was shown that it is possible to generate nonlinear soliton excitations of high energy that are bound complexes of FRIM excitations. In [12–14], it was shown that the solitons examined in [9–11] are the only elements of the whole class of soliton excitations that possess symmetric [12] or antisymmetric [13] envelopes of different types (cusp, crater, dark). In [14], it was shown that the solitons studied in [12, 13] may exist not only in one- or two-dimensional crystal lattices, for example, on the superlattice interfaces, but also in three-dimensional crystals. Various nonlinear optical effects associated with the generation of the solitons found in [9–14] were discussed in later works [15, 16]. It should be noted that the FR may significantly affect the spectra of optical and acoustic multiphonon vibrations in light-weight metals, such as beryllium, which are widely used in technology [17]. The investigation of the soliton energy transfer (~0.5 eV) in biological albumen structures is also of importance [1].

We note that all FRIM solitons investigated earlier have the same fundamental feature, namely, they are excitations of the single-frequency type, in which the intercoupled carrier frequency and the amplitude of oscillations at this frequency, together with the FR anharmonism constant, are the only basis parameters even in the isolated pair of B and C monomers. These parameters determine the space dependence of the individual envelopes of various solitons in a crystal.

In this work, it has been shown that, near the FR in crystals, soliton periodic oscillations of a crucially new type may be generated with the amplitude–frequency characteristics being essentially different from those of the previously described type. These oscillations refer to breather-type solitons with amplitudes (corresponding to the carrier frequency) pulsing periodically in a certain interval of values and with high carrier frequencies that are multiples of the low frequency of the amplitude modulation. The breathers are solitons with a more complex space–time dependence ("breath") than in [9, 10] (in continual approximation); they are intensively investigated in very different fields of physics. It is of some interest to study the question of existence of these breather-type solitons in the FRIM–type oscillations. In the appropriate temporal Fourier-representation, the periodic nonlinear oscillations of such a type have an infinite set of frequencies. However, in what follows, we will use, rather than the Fourier transformation, the exact solutions of the corresponding nonlinear equations. It is a feature of these nonlinear oscillations that, at a fixed modulation depth, which determines the frequency of the pulsations, there is a series of carrier frequencies condensing near the basic monomer frequency $\omega_C \cong 2\omega_B$. The interaction of monomers (nonlinear oscillators) causes the formation of new-type solitons in a crystal, which, unlike the solitons discovered earlier, are characterized by the same feature, namely, the presence of low-frequency pulsations of the amplitude of oscillations with the carrier (high) frequency, the latter being a multiple of the frequency of pulsations. In a crystal, this results in a space distribution of the pulsation amplitude and of the pulsation depth in the soliton tails with the corresponding space dependence of already two envelopes for an individual soliton. In this case, a number of features arise that are associated with the character of oscillations in the breather soliton. Among them is the fact that in the soliton tails the envelope steepness decreases as the corresponding multiplicity increases; that is, the radius of the localization of excitations in the soliton increases.

In what follows, we investigate the oscillations of this new type, which, according to the shape of their envelope, should be classified as cusp-type solitons with the finite negative derivative of the soliton envelope in its center. The investigation of the problem of crater- and dark-type soliton existence [12–14] is now faced with serious difficulties due to dramatic complications in the analytical description of such a type of oscillations. There is no question that, as a development of the present work, the solution of this problem would be of a certain interest. In the future, as the first step in this direction, it seems to be necessary to study the nonlinear effects (studied earlier [9–16] for the old-type FRIM solitons) associated with the new type of solitons discovered in our work.

FORMULATION OF THE PROBLEM AND BASIC EQUATIONS

In the case of the optical FR in a crystal system of monomers, for example, of molecules in organic superlattices, in the site representation of secondary quantization, the Hamiltonian H of the crystal system takes the form

$$H = H_B + H_C + H_{int},$$

$$\begin{aligned} H_B &= \sum_n \hbar\omega_B b_n^+ b_n + \sum_{n\neq m} V_{nm}^{(B)} b_n^+ b_m, \\ H_C &= \sum_n \hbar\omega_C c_n^+ c_n + \sum_{n\neq m} V_{nm}^{(C)} c_n^+ c_m, \end{aligned} \tag{1}$$

$$H_{int} = \Gamma\sum_n [(b_n^+)^2 c_n + c_n^+ (b_n)^2].$$

In (1), b_n^+, c_n^+ and b_n, c_n are the creation and annihilation boson operators of B- and C-type excitonic excitations at the nth site, e.g., for a pair of B and C molecules on both sides of the interface; $V_{nm}^{(B,C)}$ are the matrix elements of the intermolecular interaction operator describing the translation of excitons. In the term of the Hamiltonian responsible for the FR of oscillations, the constant Γ determines the energy of the anharmonic $C \longleftrightarrow BB$ interaction of the third order, and this energy may be as large as ≈1000 cm^{-1}. The detailed discussion of Hamiltonian of this type is given in [7].

The Heisenberg equations for the operators b_n and c_n

$$i\hbar\frac{db_n}{dt} = -[H, b_n], \quad i\hbar\frac{dc_n}{dt} = -[H, c_n] \tag{2}$$

in the case of the nearest-neighbor interaction, $V_{nm}^{(B,C)} = V_{B,C}\delta_{n,m+1}$, take the form

$$\begin{aligned} i\hbar\frac{db_n}{dt} &= \hbar\omega_B b_n + V_B\sum_1 b_{n+1} + 2\Gamma b_n^+ c_n, \\ i\hbar\frac{dc_n}{dt} &= \hbar\omega_C c_n + V_C\sum_1 c_{n+1} + \Gamma b_n^2. \end{aligned} \tag{3}$$

Usually, to describe intense nonlinear oscillations in the case of large occupation numbers at high laser pumping, a quasi-classical approach is used, in which all operators in (3) are replaced by their average values $\langle b_n\rangle = B_n$, $\langle c_n\rangle = C_n$, where B_n and C_n are the corresponding displacements. In this case, equations (3) for averaged values become [9, 10]

$$i\hbar\frac{dB_n}{dt} = \hbar\omega_B B_n + V_B\sum_1 B_{n+1} + 2\Gamma B_n^* C_n,$$
$$i\hbar\frac{dC_n}{dt} = \hbar\omega_C C_n + V_C\sum_1 C_n + \Gamma B_n^2. \qquad (4)$$

TWO-FREQUENCY SOLUTIONS

In [9–16], standing-soliton solutions, i.e., non-shifting solitons, were sought in a one-frequency (simplest, as it has become clear now) form

$$B_n(t) = B_n\exp\left(-i\frac{\Omega}{2}t\right), \quad C_n(t) = C_n\exp(-i\Omega t). \qquad (5)$$

The substitution of $B_n(t)$ and $C_n(t)$ having the time dependence (5) into (4) and a subsequent analysis of the nonlinear equations for the B_n and C_n amplitudes gave the corresponding form for the envelope that had a one-to-one relationship to the carrier frequency Ω. The basic form of this relation is seen just from the dependence of the amplitudes B_0 and C_0 on Ω for an isolated pair

$$B_0 = \hbar(2\Gamma)^{-1}((\Omega - 2\omega_B)(\Omega - \omega_C))^{1/2},$$
$$C_0 = \hbar(4\Gamma)^{-1}(\Omega - 2\omega_B), \qquad (6)$$

which can be easily obtained from (4).

It is clear that the solutions of the system (4) depend on the parameter $\Gamma/\hbar$ as on a scale factor, and, that is why it is natural to introduce the variables $b_n = (\Gamma/\hbar)B_n$, $c_n = (\Gamma/\hbar)C_n$, which have the dimensions of frequency.

As will be shown later, the nonlinear equations (4) have another, also periodic, but much more complex solution describing an isolated B, C pair. For brevity, we will show here only the structural solving scheme and the final result, without the full analytical procedure. We present equations (4) for an isolated pair in terms of quantities b_0^2, c_0 in the form

$$i\hbar\frac{db_0^2}{dt} = 2\hbar\omega_B b_0^2 + 4|b_0|^2 c_0,$$
$$i\hbar\frac{dc_0}{dt} = \hbar\omega_C c_0 + b_0^2 \qquad (7)$$

and seek a solution to the first of the equations in the form

$$b_0^2(t) = \rho(t)\exp(-i\varphi(t)) \qquad (8)$$

separating the time-dependent modulus and phase of the quantity b_0^2. Substituting (8) in the first equation in (7), we obtain the dependence of c_0 on ρ and φ

$$c_0(t) = \frac{1}{4}\exp(-i\varphi(t))\left(i\frac{1}{\rho}\frac{d\rho}{dt} + \frac{d\varphi}{dt} - 2\hbar\omega_B\right). \qquad (9)$$

To simplify the fairly cumbersome calculations, we will assume the FR to be absolute, i.e., $\omega_C = 2\omega_B$ exactly, though, as it is seen from the solution, it is not crucial. The substitution of (9) into the second equation in (8) and separation of the real and imaginary parts lead to two coupled second-order nonlinear differential equations for ρ and φ, which, through the proper procedures, are reduced to the first-order differential equations for ρ and φ

$$\frac{d\rho}{dt} = \pm\sqrt{8(\rho_1 - \rho)(\rho - \rho_2)(\rho + (\rho_1^{-1} + \rho_2^{-1})^{-1})}, \qquad (10a)$$

$$\frac{d\varphi}{dt} = \omega_C - \frac{2\rho_1\rho_2}{\rho}\sqrt{\frac{2}{\rho_1 + \rho_2}}. \qquad (10b)$$

In (10a), two signs (upper and lower) result from the associated square equation solution, the quantities ρ_1, ρ_2 are the integration constants, which specify the limits of $\rho(t)$ pulsations: $\rho_2 \le \rho \le \rho_1$. The solution of (10a), in the form $t = t(\rho)$, is

$$t(\rho) = \frac{1}{\sqrt{2q}}F(\psi(\rho), k), \quad 0 \le t \le \frac{T}{2}, \qquad (11a)$$

$$t(\rho) = T - \frac{1}{\sqrt{2q}}F(\psi(\rho), k), \quad \frac{T}{2} \le t \le T, \qquad (11b)$$

where $F(\psi, k)$ is the elliptic integral of the first kind of the modulus k. The constant q, modulus k, and the pulsation period T are defined by the ρ_1 and ρ_2 values:

$$q = \rho_1 + (\rho_1^{-1} + \rho_2^{-1})^{-1},$$
$$k = \sqrt{\frac{\rho_1 - \rho_2}{q}}, \quad T = \sqrt{\frac{2}{q}}K(k), \qquad (12)$$

where $K(k)$ is the full elliptic integral of the first kind. In (11), the function $\psi(\rho)$ is of the following form:

$$\psi(\rho) = \arcsin\left(\frac{1}{k}\sqrt{\frac{\rho_1 - \rho_2}{\rho + (\rho_1^{-1} + \rho_2^{-1})^{-1}}}\right). \qquad (13)$$

The time reference is chosen so that at $t = 0$, the quantity $\rho = \rho_2$ is minimal and $\psi = 0$, while at $t = T/2$, the quantity $\rho = \rho_1$ is maximal; at the end of the period ($t = T$), the values of ρ repeat those at $t = 0$. We note that in the first half-period, $t(\rho)$ in (11a) is taken with the plus sign, while in the second one, with the minus sign. In its turn, using (10a) and taking the periodic nature of ρ into account, the phase $\varphi(t)$ is determined from equation (10b) after integrating with respect to ρ as follows:

$$\varphi(\rho) = \omega_C t - \frac{[(2\rho_1+\rho_2)\Pi(n,\psi(\rho),k)-(\rho_1+\rho_2)F(\psi(\rho),k)]}{\sqrt{\rho_1(\rho_1+2\rho_2)}}, \quad 0 \le t \le T/2, \tag{14a}$$

$$\varphi(\rho) = \omega_C t - \left[J - \frac{2[(2\rho_1+\rho_2)\Pi(n,\psi(\rho),k)-(\rho_1+\rho_2)F(\psi(\rho),k)]}{\sqrt{\rho_1(\rho_1+2\rho_2)}}\right], \quad T/2 \le t \le T. \tag{14b}$$

In (14), the first relation defines the phase growth with ρ increase, while the second one, with ρ decrease. The function $\Pi(n, \psi, k)$ is a known tabulated special function as well, namely, the elliptic integral of the third kind of the parameter n. This parameter and the quantity J take the following values:

$$\begin{gathered} n = \frac{\rho_1-\rho_2}{\rho_1+2\rho_2}, \\ J = \frac{4[(2\rho_1+\rho_2)\Pi(n,\pi/2,k)-(\rho_1+\rho_2)K(k)]}{\sqrt{\rho_1(\rho_1+2\rho_2)}}. \end{gathered} \tag{15}$$

The periodic continuation of (14) over the further periods shows that the phase has a component linear in t, which is coupled not only with ω_C, but also with J, there with the opposite sign, and, thus, the linear phase growth takes place during each period T. Therefore, the carrier frequency Ω, which determines the full phase growth after each period of pulsations of the frequency $\omega = 2\pi/T$, is equal to

$$\Omega = \omega_C - \frac{J}{T}, \tag{16}$$

where J and T are specified by (15) and (12), respectively. The complex functional dependencies $t(\rho)$, or, inversely, $\rho(t)$ and $\varphi(t)$, given by (11) and (14), may be significantly simplified in the limit of similar ρ_1 and ρ_2 values. At the condition $\rho_1 - \rho_2 \ll (\rho_1 + \rho_2)/2$, when $F(\psi) \approx \Pi(\psi)$, the feature parameters take the values $n = 0$, $k = 0$, $J = 2\pi/\sqrt{3}$, $T = \pi\sqrt{2/(3(\rho_1+\rho_2))}$, and the time dependence of the modulus and phase take the following, more simple, form:

$$\begin{gathered} \rho(t) = \frac{\rho_1+\rho_2}{2} - \frac{\rho_1-\rho_2}{2}\cos(\omega t), \\ \varphi(t) = \Omega t - \frac{\rho_1-\rho_2}{(\rho_1+\rho_2)\sqrt{3}}\sin(\omega t). \end{gathered} \tag{17}$$

They give us an idea about the character of the nonlinear oscillations under consideration. We note that it is the phase oscillating character that is the distinctive feature of the nonlinear oscillations, in contrast with usual harmonic beats.

The purely periodic oscillating process takes place only when the low-frequency pulsation period T is a multiple of the period $2\pi/\Omega$ of the oscillations of the carrier frequency Ω

$$m\frac{2\pi}{\Omega} = T, \quad m = 1, 2, 3, \dots. \tag{18}$$

The substitution of (18) into (16), after simple manipulations, reveals Ω and ω dependencies upon the multiplicity m, namely,

$$\begin{gathered} \Omega_m = \omega_C\left(1 - \frac{1}{1+m(2\pi/J)}\right), \\ \omega_m = \omega_C\frac{1}{m+(J/2\pi)}, \end{gathered} \tag{19}$$

where $\Omega = \Omega_m$ are the carrier frequencies, and the quantities ω_m arbitrarily specify the frequencies ω of pulsations (14). It is clear that Ω_m represents the series of terms $\Omega_1 < \Omega_2 < \dots < \omega_C$, which concentrate near ω_C similarly to the series of atomic levels of hydrogen. The fact $\Omega_m < \omega_C$ associates with the choice of the integration constants. A preliminary analysis had shown that at other values of these constants, at the same time, there is a similar high-frequency series $\Omega_j > \omega_C$, but the time dependence of the module $\rho(t)$ differs from (11). There is no question that henceforth, a comprehensive study of this fact is necessary. Detail analysis of the presented relations shows that the multiplicity m, the quantity $x \equiv \rho_2/\rho_1$ as a depth of pulsations, and, naturally, ω_C are the basic parameters of the nonlinear oscillations under consideration. With fixed m and x, by use of (11), (15), and (19), the quantities k, n, J, ρ_1, ρ_2, T, Ω_m, ω_m can be determined, and then, through the inverse function $t = t(\rho)$, the functions $\rho(t)$, $\varphi(t)$, and $c(t)$. Immediately from (14), with use of the known elliptic Jacobi functions sn and cn, the direct representation of the function $\rho = \rho(t)$ is also possible, but its analytical form is not presented here for brevity. It is the outlined algorithm that was used in our numeric calculations for determination of $t(\rho)$, $\varphi(\rho)$, $c(\rho)$ with the consequent direct graphic presentation of $\rho = \rho(t)$ and other time dependencies.

DETAILS OF CALCULATIONS AND NUMERICAL RESULTS

The above-described oscillations are naturally collectivized. For their investigation, we will use the procedure that was used before in investigations of the cusp-, crater-, and dark-type solitons [12–14]. As the first step, let us consider a one-dimensional crystal chain of *BC*-molecule pairs, and, in the same way as in [12], let us study only symmetric standing soliton solutions. The generalization of the solving procedure for the case of an antisymmetric solution, and for two- and three-dimensional crystals, seems to meet no major difficulties [13, 14]. As in [12–14], to reduce the number of parameters in use, we will suppose that $V_C = V_B = \hbar v$ and that the ratio $\alpha \equiv |v|/\omega_C$ is small, as it takes place for Frenkel excitons in molecular crystals, where $\hbar\omega_C \approx 2 \times 10^4$ cm^{-1}, and $|\hbar v| \approx 10^2$ cm^{-1}. At small $\alpha \approx 10^{-2}$, the above-mentioned procedure of a one-frequency solution search for equation (4), for the case of symmetric states of the chain of $2N - 1$ BC-molecule pairs, led to a set of N coupled nonlinear equations. In the process, at small α and large N, for cusp, crater, and dark solitons, it makes no difference whether the chain being closed or unclosed due to a steep decline of the space envelope in the soliton tails. At $N = 2, 3, 4$, the corresponding equations were solved analytically, and the solutions thus obtained showed the possibility of cusp, crater, and dark solitons existing. Then, these solitons were used as input data for the computer calculation of soliton envelopes for large N. In doing so, due to small α, which caused a dramatic reduction in the size of the envelopes in the tails of cusp solitons, the results of exact calculations might be analytically approximated using the model of pair of nonlinear BC oscillators successively interacting with each other (with the energy V) without feedback. Such oscillators were assumed to be of large oscillation amplitudes b_0, c_0 at the site $n = 0$ and of small amplitudes b_n, $c_n \approx \alpha b_{n-1}$, αc_{n-1}, at the nth sites in the tails. Because the amplitudes are small in the tails, nonlinearity is of no significance there, and the oscillations may be considered as harmonics in these nodes.

Because the time dependence of nonlinear oscillations considered in this work is very complex and even at $N = 2$ causes significant difficulties in the analytical and computer only solving of the problem, at first, the above procedure was used for the closed chain with the nonlinear oscillator located at the center, at the site $n = 0$, and forced oscillators driving without feedback in the sequence $n \longrightarrow 0 \longrightarrow 1 \longrightarrow 2 \ldots$. The last assumption referred to the negligibility of the small terms of order α_2 in comparison with terms of order α. In so doing, the sequence of decreasing amplitudes b_n, c_n associated with the space envelope of the breather soliton of the new type was determined. To calculate the solution of (4) more precisely, the foregoing procedure was employed as the first step. Further, the calculated space–time solutions were used in solving (4) by means of a recurrent correction procedure, which was employed up to the acceptable reproduction of the results.

The results of calculations, obtained by a PC Pentium using MATHCAD, are shown in Figs. 1 and 2. The values of parameters used are: $m = 8$, $x = 0.7$, $\alpha = 0.01$. In Fig. 1, the functions $\mathrm{Re}(c_0(t))$ (curve *1*), $\mathrm{Im}(c_1(t))$ (curve *2*), and $B_0(t) = \mathrm{sgn}(f(t))\sqrt{|f(t)|}$, where

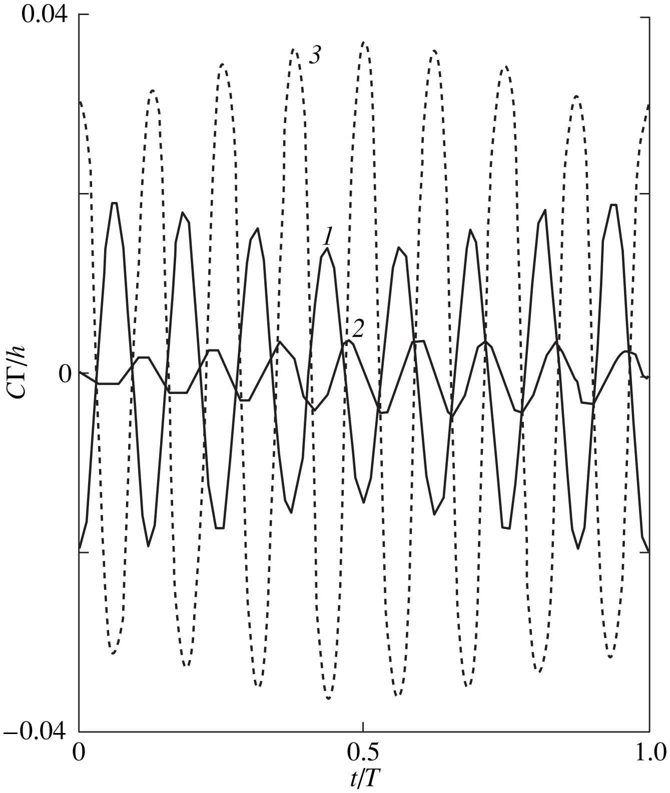

Fig. 1. Nonlinear high-frequency oscillations and low-frequency pulsations of the amplitudes of the new-type breathers near the Fermi resonance of optical excitations.

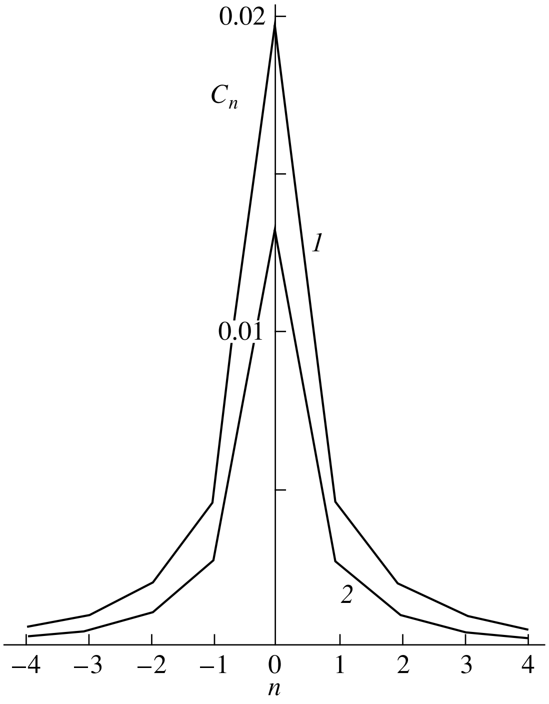

Fig. 2. Binary space envelopes of the new-type breathers.

$f(t) \equiv \rho(t)\cos(\varphi(t))$ (curve *3*), are presented in the time interval $0 \le t \le T$. They display the oscillations of the carrier high frequency Ω accompanied by the low-frequency pulsations of the amplitudes. These functions give you an example of *B*- and *C*-oscillations in the central site and in those nearest to the center. For $f(t)$, the root dependence was chosen in order to separate curves *2* and *3*, the last represents the modulus time dependence of *B*-type oscillations with the time-dependent phase $\varphi(t)/2$, naturally. It should be emphasized that, in this case, we do not observe the usual harmonic two-frequency beats, but nonlinear oscillations with the pulsing phase, which produces an infinite series of frequencies in the Fourier-transform. The time dependencies of the real and imaginary parts of $c_n(t)$, $b_n(t)$, which are not shown here, have mainly the same form as in Fig. 1. Their amplitudes decrease with n growth, as is seen from comparing curves *1* and *2*. Some discontinuities in the slope of the curves are caused by the technical possibilities of the plotter. The curves of Fig. 1 were plotted using 100 points that were chosen from 200 points calculated by MATHCAD. The last ones depicted the absolutely smooth curves. The results of calculations and respective curves for $n = 2, 3, ..., 8$ ($n = 8$ is the limiting value from the standpoint of computer resources) provided support for the assumption of the existence of the discussed type of soliton solution and allowed us to clear up the space form of the corresponding envelopes, but these results are not presented here for brevity. In Fig. 2, the space forms of two envelopes are shown, namely, $\max|c_n|$ (curve *1*) and $\min|c_n|$ (curve *2*), which are drawn through minimal and maximal values of the modulus of $c_n(t)$. It is seen that the amplitude decrease associated with n growth is not of the first order in α, but is slower, which is connected with the value of the multiplicity parameter m. As numerical calculations and analytical estimations indicated, the larger m is associated with slower decay of an envelope and with larger localization radius of soliton excitations. The investigations of all details of soliton oscillations of the type considered here, which are related to this, as well as other effects, is of further interest.

ACKNOWLEDGMENTS

The author wishes to thank V.M. Agranovich for his useful comments and advice.

This work was performed under the support of the Russian State Scientific and Technical Program “Actual Problems of Condensed Matter Physics,” RFBR, and INTAS.

REFERENCES

1. V. M. Agranovich and Ĭ. Ĭ. Lalov, Usp. Fiz. Nauk **146**, 267 (1985).
2. F. F. So, S. R. Forrest, Y. Q. Shi, *et al.*, Appl. Phys. Lett. **56**, 674 (1990).
3. F. F. So and S. R. Forrest, Phys. Rev. Lett. **66**, 2649 (1991).
4. V. M. Agranovich, Mol. Cryst. Liq. Cryst. **230**, 13 (1993).
5. V. M. Agranovich, R. D. Atanasov, and G. F. Bassani, Chem. Phys. Lett. **199**, 621 (1992).
6. V. M. Agranovich, Phys. Scr. T **49**, 699 (1993).
7. V. M. Agranovich and O. A. Dubovskiĭ, Chem. Phys. Lett. **210**, 458 (1993).
8. V. M. Agranovich and J. B. Page, Phys. Lett. A **183**, 651 (1993).
9. V. M. Agranovich and A. M. Kamchatnov, Pis’ma Zh. Éksp. Teor. Fiz. **59**, 397 (1994).
10. V. M. Agranovich, O. A. Dubovskiĭ, and A. M. Kamchatnov, J. Phys. Chem. **98**, 13 (1994).
11. V. M. Agranovich, S. A. Darmanyan, O. A. Dubovskiĭ, *et al.*, Phys. Rev. B **53**, 15451 (1996).
12. O. A. Dubovskiĭ and A. V. Orlov, Fiz. Tverd. Tela (St. Petersburg) **38**, 1221 (1996).
13. O. A. Dubovskiĭ and A. V. Orlov, Fiz. Tverd. Tela (St. Petersburg) **38**, 1931 (1996).
14. O. A. Dubovskiĭ and A. V. Orlov, Fiz. Tverd. Tela (St. Petersburg) **41**, 712 (1999).
15. S. Darmanyan, A. Kobyakov, and F. Lederer, Phys. Rev. E **57**, 2344 (1998).
16. V. M. Agranovich, S. A. Darmanyan, O. A. Dubovskiĭ, *et al.*, Phys. Rev. B **57**, 2461 (1998).
17. O. A. Dubovskiĭ and A. V. Orlov, Fiz. Tverd. Tela (St. Petersburg) **39**, 542 (1997).

Translated by N. Ostrovskaya

Physics of the Solid State, Vol. 42, No. 4, 2000, pp. 689–693. Translated from Fizika Tverdogo Tela, Vol. 42, No. 4, 2000, pp. 671–675.
Original Russian Text Copyright © 2000 by Panchenko, Karpova, Duda.

SEMICONDUCTORS AND DIELECTRICS

Dielectric Relaxation in $Bi_{12}SiO_{20}$: Cr Crystals

T. V. Panchenko, L. M. Karpova, and V. M. Duda
Dnepropetrovsk State University, pr. Gagarina 72, Dnepropetrovsk 10, 320625 Ukraine

Received July 8, 1999; in final form, October 7, 1999

Abstract—A study is reported of the temperature and frequency dependences of the permittivity and losses in Cr-doped $Bi_{12}SiO_{20}$ crystals at sonic frequencies and in the range 300–800 K. A number of dielectric anomalies and a close-to-linear Cole–Cole diagram have been observed. The results are discussed by invoking the concepts of electron hopping and screening of the induced polarization through the relaxation of local lattice distortions. *© 2000 MAIK “Nauka/Interperiodica”.*

A large number of studies of $Bi_{12}MO_{20}$ crystals (BMO, where M = Si, Ge, or Ti) have paid only scant attention to their interesting dielectric properties. Some authors reported the high room-temperature permittivity $\varepsilon = 30–160$ [1–4] and a strong dependence of ε on the growth factors governing the content of intrinsic defects in these crystals [2–4]. An increase in ε observed in a number of bismuth oxide crystalline compounds is associated with an increase in the Bi_2O_3 content [4]. The BMO crystals were shown to be promising for microwave technologies [5].

The temperature and frequency dependences of $\varepsilon(\nu, T)$ and loss tangent $\tan\delta(\nu, T)$ at the frequency $\nu = 10^2–10^4$ Hz and in the microwave range reveal anomalies near 4.2 K, which are characteristic of “virtual” ferroelectrics [4–6]. The anomalies are assigned to relaxation processes involving a low relaxator potential barrier $E_a \simeq 0.05$ eV [5]. This value of E_a agrees with the estimated activation energy $E_a = 0.044$ eV for “dipole” impurities, which are responsible for the relaxation maximum in $\varepsilon(T)$ and $\tan\delta(T)$ in the range $T = 20–40$ K at sonic frequencies [6]. The relaxation “strength” of these impurities and the intensity of yellow coloring of the $Bi_{12}GeO_{20}$ (BGO) crystals were found to be correlated [6]. In the same temperature range, the ultrasound damping was observed in BGO and $Bi_{12}SiO_{20}$ (BSO) crystals, which increased with introduction of Cr [7] and decreased under Ga and Al doping [8].

The features in $\varepsilon(\nu, T)$ and $\tan\delta(\nu, T)$, which are characteristic of the relaxation polarization, have been observed also near room temperature (BSO crystals, sonic frequencies [9]). Consideration was given to the mutually correlating anomalies in the internal friction $Q^{-1}(T)$ and $\varepsilon(T)$ at temperatures $T = 500–700$ K ($\nu = 10^3$ Hz), which depend on the actual impurity species (Al or Cr) and annealing of BSO crystals under vacuum [10]. They are believed to originate from impurity–vacancy-type dipoles with a trigonal lattice-site symmetry.

Studies of static thermally stimulated polarization and depolarization of BSO crystals revealed participation of the quasi-dipoles in the formation or destruction of the thermoelectret state. In this case, the contribution of the quasi-dipole mechanism of polarization increases upon doping BSO crystals by Al, Ga, Cr, and Mn ions [11, 12]. The thermoelectret state of BSO : Al and BSO : Ga crystals also exhibits a substantial enhancement of the anomalies in $\varepsilon(\nu, T)$ and $\tan\delta(\nu, T)$ at temperatures $T = 400–800$ K [13].

Thus, defects in BMO crystals manifest themselves over a wide range of temperatures $T = 4–800$ K in the relaxation processes, which can be identified with quasi-dipole polarization. Further investigation of the nature of these processes and the possibilities of their control through doping appear to be of interest. Of particular importance are the iron-group transition metals forming multiply charged impurity ions, which produce deep strong-localization centers capable of efficiently interacting with the strongly polarizable BMO lattice.

This work presents the results of our investigation of dielectric relaxation processes in BSO : Cr crystals transferred to the thermoelectret state.

1. EXPERIMENTAL

The optically homogeneous BSO : Cr crystals were grown by the Czochralski method. The Cr content was varied from 0.0004 to 0.02 wt %, and the total content of residual impurities did not exceed 10^{-3} wt %. The samples were polished bars $(0.5–1.5) \times 3 \times 7$ mm in size. Pt electrodes were deposited by cathode sputtering under vacuum on the 3×7 sides cut in the (001) plane. To bring the electronic subsystem to the initial equilibrium state, the samples were heated in air before measurements up to 800 K with subsequent slow (~2 days) cooling to room temperature.

The dependences $\varepsilon(\nu, T)$ and $\tan\delta(\nu, T)$ were studied in the frequency range $\nu = 10^2–10^5$ Hz at temperatures $T = 300–800$ K by means of an E8-2 bridge,

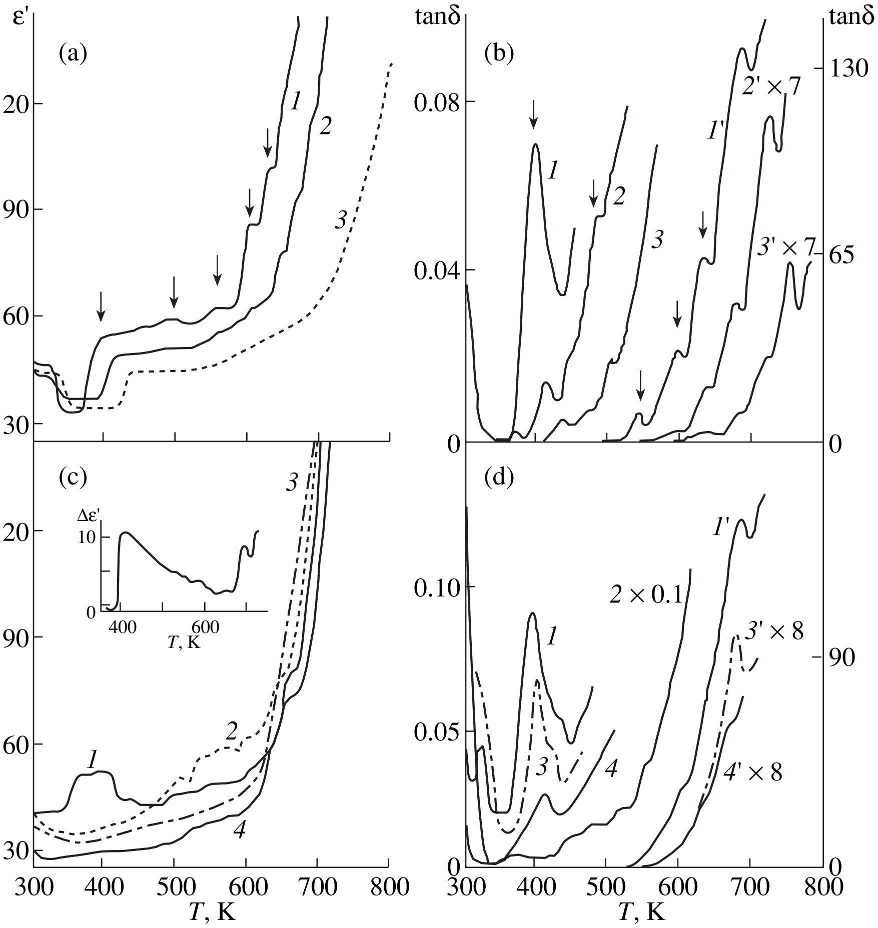

Fig. 1. Temperature dependences of (a, c) the permittivity ε'(T) and (b, d) loss tangent tanδ(T) of BSO : Cr crystals (0.03 wt % Cr, d = 0.9 mm): (a, b) for the same conditions of prepolarization U_p = 100 V, T_p = 300 K, and different measuring-field frequencies ν = (a, *1*; b, *1*, *1'*) 5×10^2, (a, *2*; b, *2*, *2'*) 10^3, and (a, *3*; b, *3*, *3'*) 3×10^3 Hz; and (c, d) for fixed frequency ν = 5×10^2 Hz and different prepolarization conditions: (c, *1*; d, *1*, *1'*) U_p = 300 V, T_p = 370 K; (c, *2*; d, *2*) U_p = 100 V, T_p = 420 K; (c, *3*; d, *3*, *3'*) U_p = 300 V, T_p = 300 K; and (c, *4*; d, *4*, *4'*) U_p = 100 V, T_p = 520 K. Inset shows the low-temperature peak in ε'(T) isolated from curve a, *2*. The right-hand axes are appropriate for curves *1'*, *2'*, *3'*, and *4'*, and the left-hand ones, to the remaining curves.

a G3-118 external sine-voltage generator, and an S1-64A oscillograph as a null indicator. The measurements were conducted in a computer-programmed linear heating mode at a rate of 0.16 K s^{-1}. We studied the original (unpolarized) and polarized samples. The polarization conditions were varied in the following ranges: polarizing voltage U_p = 10–10^3 V (electric field $E = 2 \times 10^2$–2×10^4 V cm^{-1}), polarization temperature T_p = 300–600 K, and the polarization duration of 30 min was fixed. These conditions provide the thermoelectret state in BSO : Cr crystals [12].

2. RESULTS AND DISCUSSION

The temperature dependences of the real part of the complex permittivity ε'(T) and tanδ(T) are essentially different from those observed for undoped BSO [4, 9, 13]. They exhibit clearly pronounced features characteristic of the Debye-type relaxation processes involving many relaxators throughout the temperature range studied (Figs. 1a, 1b). In the range T_1 = 400–600 K, one can see a broad, low-intensity peak of ε'(T) with steep low-temperature and smooth, structured high-temperature sides, and a group of peaks in tanδ(T). For $T > T_1$, one observes a region of an intense, close-to-exponential rise in ε'(T), with kinks in ε(T) superposed on it visible up to $T \sim 700$ K and maxima in tanδ(T) detected in the same range.

The locations of the maxima in ε'(T), which were isolated by subtracting the highest-temperature exponential falloff (with E_a = 0.9 eV) from the ε'(T) curve, lie close to those of tanδ(T). As the field frequency increases, the peaks of tanδ(T) and ε'(T) shift to higher temperatures, as expected, and ε' and tanδ drop in magnitude. The shift was used to calculate the relaxator activation barriers

$$E_a = \{kT_{\max 1}T_{\max 2}/(T_{\max 2} - T_{\max 1})\}\ln(\nu_1/\nu_2), \quad (1)$$

Parameters of relaxators in silico- and germanosillenite crystals

Parameters derived from the dependences $\varepsilon'(\nu, T)$ and $\tan\delta(\nu, T)$					Parameters derived from the dependences $\sigma_\sim(T)$ and $\sigma_\sim(\omega)$ and equation (3)		
No.	$T_{i\,\max}$, K	${}^1E_{ai}$, eV	${}^2E_{ai}$, eV	ν_0, s^{-1}	T, K	${}^\sigma E_a$, eV, crystal, reference	n, crystal, reference
1	395	0.69	0.67	10^{11}	~300		0.8, *BGO, [14]
2	480	0.72	0.72	2×10^{10}	~300		0.7, *BGO : Cr, [14]
3	550	0.77	0.78	10^{10}	~300		0.6, *BSO, [15]
4	595	0.8	0.81	3.2×10^9	~300		0.42, **BSO : Cr
5	635	0.81	0.84	10^9	600–800	0.83, BGO : Cr, [15]	
6	680	0.92	0.94	2.5×10^9	600–800	1.0, BGO, [15]	

Note: $i = 1, 2, \ldots, 6$ are numbers of peaks in the $\varepsilon'(\nu, T)$ and $\tan\delta\,(\nu, T)$ spectra; $T_{i\,\max}$ are the temperatures of the corresponding maxima at $\nu = 500$ Hz; ${}^1E_{ai}$ and ${}^2E_{ai}$ are the activation energies calculated from the shifts of the peaks in the $\varepsilon'(\nu, T)$ and $\tan\delta\,(\nu, T)$ spectra, respectively; and ${}^\sigma E_a$ is the activation energy of ac electric conduction for the $\sigma_\sim(\nu, T)$ dependences. * The exponents n for the $\sigma_\sim(\omega)$ dependences. ** The value of n derived in this work from relationship (3) at $T = 300$ K.

where k is the Boltzmann constant, $T_{\max 1}$ and $T_{\max 2}$ are the temperatures of the maxima, and ν_1 and ν_2 are the corresponding measuring frequencies (see table). From the temperature dependences of the relaxation time $\tau = \tau_0\exp(E_0/kT)$ for the peaks of the $\tan\delta(T)$ spectra, we derived the attempt frequencies of the normal relaxator vibrations $\nu_0 = 1/\tau_0 = 10^{11} - 2.5 \times 10^9\ s^{-1}$, which are substantially lower than the limiting lattice-vibration frequencies (see table).

Subtraction of the high-temperature exponential contribution from the $\varepsilon'(T)$ spectra permitted us also to isolate the first low-temperature peak (see inset in Fig. 1c). Its steep low-temperature falloff does not allow a straightforward analytical description, and the high-temperature falloff can be fitted by the expression $\varepsilon'(T) \sim \varepsilon_\infty + K/T$, where the Curie constant $K = 8 \times 10^3$ K, and $\varepsilon_\infty = 13$ is the high-frequency permittivity characterizing the elastic forms of polarization of the crystals under study.

Within the temperature range $T \geq 350$ K, where anomalies in $\varepsilon'(T)$ and $\tan\delta(T)$ occur, we have failed to obtain a Cole–Cole diagram in the form of simple monotonic dependences of the imaginary part of complex permittivity on the real part $\varepsilon''(\varepsilon')$, which apparently should be due to a considerable difference in the parameters of a large set of relaxators.

The relaxators in BSO : Cr crystals could be Cr-containing impurity–vacancy-type quasi-dipoles. They are believed [10] to be responsible for the internal-friction peaks in the temperature range $T = 400$–700 K. Quasi-dipoles similar to those considered in [10] form when the Cr^{3+} ions substitute for M cations at the centers of the oxygen tetrahedra, which requires (by the charge-neutrality condition) the presence of an oxygen vacancy with a captured electron V_O^- at one of the sites. The hopping of the V_O^- vacancy in the field of the multi-well potential produced by distorted oxygen tetrahedra is responsible for the participation of the Cr^{3+}–V_O^- quasi-dipoles in thermally oriented polarization. Other scenarios are also conceivable, because Cr exists in several charge states and can also be localized by substituting Bi in the distorted octahedra [16].

Taking into account that V_O^- hopping takes place in the strongly polarizable BSO crystal lattice, we believe that the efficient coupling of such quasi-dipoles mediated by the lattice considerably complicates the pattern of the $\varepsilon''(\varepsilon')$ diagrams. However, this aspect of the problem requires additional studies.

The shape of the $\varepsilon'(T)$ and $\tan\delta(T)$ spectra depends on the actual prepolarization conditions. A slight increase in the polarizing voltage and in the polarization temperature (up to $U_p \sim 300$ V, $T_p \sim 400$ K) shifts the first low-temperature peak (the peak isolated above, with E_{a1}) toward lower temperatures, with some of the other peaks becoming suppressed. As the values of U_p and T_p increase still more, the remaining low-temperature peaks become better resolved, after which the peaks in the $\varepsilon'(T)$ and $\tan\delta(T)$ spectra are suppressed throughout the temperature range studied, and ε' and $\tan\delta$ decrease in magnitude. The low-temperature shift of the first peak in $\varepsilon'(T)$ and $\tan\delta(T)$ can be associated with an increase in the internal field of the residual thermoelectret polarization [17]. The behavior of the other peaks remains unclear; we note only that their temperature location does not depend on the polarization conditions (Figs. 1c, 1d).

Close to room temperature ($T < 350$ K), the Cole–Cole diagrams were found to be monotonic. However, the $\varepsilon''(\varepsilon')$ dependences constructed on a complex plane (where ε'' is the imaginary part of the permittivity) do not resemble the classical Cole–Cole semicircle (Fig. 2). In their major part, they are close to linear or

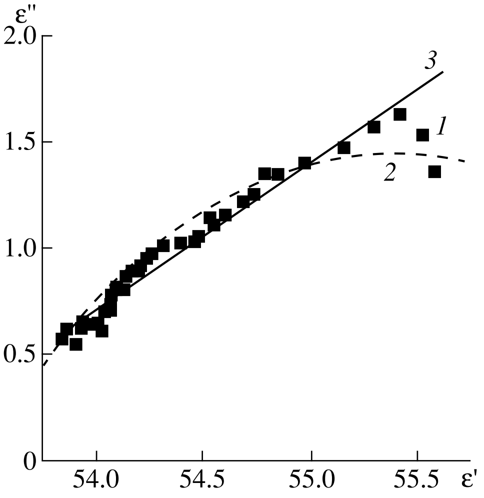

Fig. 2. The Cole–Cole diagram for BSO : Cr crystals: (*1*) the experimental data and the fitting with (*2*) lemniscate and (*3*) linear relation.

can be approximated with a lemniscate-like arc described by the expression

$$(\varepsilon^*)^{-1} = (1 + i\omega\tau)^{\gamma}, \quad (2)$$

where ω is the circular frequency, and the parameter $\gamma \sim 0.3$ (Fig. 2).

Lemniscates of type (2) are conventionally used to describe strongly distorted Debye dispersion spectra of the complex permittivity ε* [14]. The experimental data obeying equation (2) are scanty, and they relate primarily to polymers, with the γ quantity interpreted as a measure of interaction between dipole structural units [17].

The shift or distortion of the Debye semicircles are characterized in various models (Cole–Cole, Davidson–Cole, Fuoss–Kirkwood, Fröhlich, Gavriliak–Nagami) by a parameter similar to γ, which either relates to the distribution of the relaxation times τ or represents the measure of relaxator coupling. Note, however, that the above models are not based on a specific microscopic polarization mechanism, and, therefore, the physical nature of the τ distribution, as well as the mechanism of relaxator interaction, remain unclear.

We believe it appropriate now to describe the close-to-linear ε''(ε') relationship obtained here in terms of the Jonscher law, which is based on an energy approach and is applicable to all dielectrics [18]. The Jonscher model relates the polarization to the hopping of ions or electrons over long or short chains. The discrete displacement of charges is accompanied by the screening of the polarization thus created through lattice relaxation. One can write the following relation

$$\frac{\chi''(\omega)}{\chi'(\omega)} = \frac{W_1}{W_2} = \cot\left(\frac{n\pi}{2}\right) = \text{const}, \quad (3)$$

where $\chi'(\omega)$ and $\chi''(\omega)$ are the real and imaginary parts of the permittivity, W_1 is the energy lost per period, W_2 is the energy gained per period, and n is a constant determined by the slope of the ε''(ε') plot with respect to the ε'' axis (Fig. 2). By this model, n is the exponent characterizing the frequency dependence of the ac conductivity presented in the form

$$\sigma_{\sim}(\omega) \sim \omega^{n}, \quad (4)$$

where ω is the circular frequency, provided $0 < n < 1$. Such relations are associated with the hopping mechanism of conduction involving the hopping of electrons (holes) over localized energy states near the Fermi level. The value of n depends on the spatial and energy distribution of these states and the localization length of their wave functions and differs for different multiplicities, i.e. the number of links in a hopping chain [19, 20].

The literature data argue for the hopping mechanism of electric conductivity in BGO [14, 21], BSO [15], and Cr-doped BGO [14] crystals, and, therefore, it appeared of interest to compare some relevant quantitative characteristics (based on [22], we assume the ionic transport in the crystals under study to be insignificant).

We note, first of all, that the values of n, which is the exponent in the frequency dependence of electric conductivity (4) and enters into expression (3), are fairly close at temperatures $T \le T_1$. The trend of the value of n decreasing as one crosses over from BGO to BSO crystals, and from undoped BGO or BSO to Cr-doped crystals, is also retained (see table). A decrease in n is associated with an increase in the hopping multiplicity (at $n = 8$, hops between pairs of localized states occur [19]). This provides a support for the validity of the model chosen by us and an indication that the hops have a higher than pair multiplicity.

Interestingly, the imaginary part of electric conductivity of BGO : Cr crystals was observed to be larger near room temperature than the real part by 1.5–2 orders of magnitude [14]. This is believed [19, 20] to indicate a weak wave-function overlap and strong electron localization. This situation provides favorable conditions for the realization of the hopping mechanism of electric conduction and can account for the ε''(ε') diagrams of the type under study here [18].

A certain deviation of the ε''(ε') diagram obtained here from a linear relation (Fig. 2) suggests that additional polarization mechanisms, which also affect the formation of the thermoelectret state in BMO crystals, are operative here.

In the range $T > T_1$, where $\sigma_{\sim}$ of BGO : Cr crystals grows exponentially with temperature and depends only weakly on frequency, we observe a correlation between the thermal activation energy ${}^{\sigma}E_a$ of the ac electric conductivity $\sigma_{\sim}$ and the activation barriers E_{a5} and E_{a6} for the relaxators observed by us in the given range (see table). On the strength of these observations, as well as bearing in mind that Cr ions create in BSO, as in BGO, acceptor levels increasing the compensation of the dc electric conductivity (by about 20%), one can assume, following [14], that the high-temperature range is dominated by carrier hops over long chains connecting localized states near the valence band. This situation manifests itself in a strong increase in the permittivity with an increase in temperature.

REFERENCES

1. *Acoustic Crystals*, Ed. by M. P. Shaskol'skaya (Nauka, Moscow, 1982).
2. B. N. Litvin, Yu. V. Shaldin, and I. E. Pitovranova, Kristallografiya **13**, 1106 (1968) [Sov. Phys. Crystallogr. **13**, 971 (1968)].
3. G. M. Safronov, V. N. Batog, Yu. I. Krasilov, *et al.*, Izv. Akad. Nauk SSSR, Neorg. Mater. **6**, 284 (1970).
4. A. V. Firsov, A. A. Bush, A. A. Mar'in, *et al.*, Izv. Akad. Nauk SSSR, Neorg. Mater. **21**, 447 (1985).
5. V. M. Pashkov, Yu. M. Poplavko, and V. M. Skorikov, Fiz. Tverd. Tela (Leningrad) **26**, 844 (1984) [Sov. Phys. Solid State **26**, 510 (1984)].
6. J. Link, J. Fontanella, and C. G. Andeen, J. Appl. Phys. **51**, 4352 (1980).
7. P. K. Grewal and M. J. Lea, J. Phys. C: Solid State Phys. **16**, 247 (1983).
8. W. Rehwald, K. Frick, G. R. Lang, *et al.*, J. Appl. Phys. **47**, 1292 (1976).
9. Y. R. Reddy and L. Sirdeshmukh, Phys. Status Solidi A **103**, K157 (1987).
10. M. D. Volnyanskiĭ, A. Yu. Kudzin, and I. L. Chertkov, Fiz. Tverd. Tela (Leningrad) **34**, 225 (1992) [Sov. Phys. Solid State **34**, 119 (1992)].
11. T. V. Panchenko and G. V. Snezhnoĭ, Fiz. Tverd. Tela (Leningrad) **35**, 3248 (1993) [Phys. Solid State **35**, 1598 (1993)].
12. T. V. Panchenko and L. M. Karpova, Fiz. Tverd. Tela (S.-Peterburg) **40**, 472 (1998) [Phys. Solid State **40**, 432 (1998)].
13. T. V. Panchenko, Fiz. Tverd. Tela (S.-Peterburg) **39**, 1223 (1997) [Phys. Solid State **39**, 1085 (1997)].
14. V. I. Kalinin, Zh. S. Kuchuk, N. G. Gorashchenko, *et al.*, Izv. Akad. Nauk SSSR, Neorg. Mater. **24**, 637 (1988).
15. V. P. Avramenko, A. Yu. Kudzin, and G. Kh. Sokolyanskiĭ, Fiz. Tverd. Tela (Leningrad) **22**, 3149 (1980) [Sov. Phys. Solid State **22**, 1839 (1980)].
16. T. V. Panchenko and N. A. Truseeva, Ukr. Fiz. Zh. **29**, 1186 (1984).
17. Yu. M. Poplavko, *Physics of Dielectrics* (Vishcha Shkola, Kiev, 1980).
18. A. R. Jonscher, Scientific Papers of the Institute of Electrical Engineering Fundamentals, Seria Wspolpraca **16**, 5 (1977).
19. N. F. Mott and E. A. Davis, *Electronic Processes in Non-Crystalline Materials* (Oxford Univ. Press, Oxford, 1971; Mir, Moscow, 1974).
20. I. V. Klyatskina and I. K. Shlimak, Fiz. Tekh. Poluprovodn. (Leningrad) **12**, 134 (1978) [Sov. Phys. Semicond. **12**, 76 (1978)].
21. V. P. Avramenko, L. P. Klimenko, A. Yu. Kudzin, *et al.*, Fiz. Tverd. Tela (Leningrad) **19**, 1201 (1977) [Sov. Phys. Solid State **19**, 702 (1977)].
22. I. A. Kilner, I. Drennan, P. Dennis, *et al.*, Solid State Ionics **5**, 527 (1981).

Translated by G. Skrebtsov

Physics of the Solid State, Vol. 42, No. 4, 2000, pp. 694–696. Translated from Fizika Tverdogo Tela, Vol. 42, No. 4, 2000, pp. 676–678.
Original Russian Text Copyright © 2000 by Berzin, Morozov, Sigov.

DEFECTS, DISLOCATIONS, AND PHYSICS OF STRENGTH

Cluster Mobility in a System of Light Interstitial Impurities

A. A. Berzin, A. I. Morozov, and A. S. Sigov
Moscow State Institute of Radio Engineering, Electronics, and Automation (Technical University),
pr. Vernadskogo 78, Moscow, 117454 Russia
e-mail: morosov@eot-gw.eot.mirea.ac.ru

Received October 7, 1999

Abstract—The contribution of cluster mobility to the low-temperature diffusion coefficient in a system of light interstitial impurities has been studied by computer simulation. It is shown that the magnitude of this contribution is dominated by the parameters of the impurity interaction potential, and the nonmonotonic character of its temperature behavior is related to a variation of cluster shape or freezing-out of one of several mobility mechanisms. *© 2000 MAIK “Nauka/Interperiodica”.*

It was shown by us earlier [1, 2], that the alternating pattern of long-range interaction (elastic and through Friedel electron-density oscillations) generates a large number of bound states for any pair of point defects in a metal (as well as for a pair of neutral defects in an insulator), irrespective of the actual form of the short-range part of the pairwise interaction. Therefore, a decrease of temperature inevitably gives rise to clustering of mobile defects.

Clustering in the low-temperature domain should initiate separation into phases with a high and a low defect concentration. However, at low defect concentrations, large-scale phase separation is replaced with decreasing temperature by a transition of the system into one of the metastable states, which are characterized by a large number of small clusters. These states turn out to be long lived, because clustering dramatically reduces the impurity mobility. Metastable states differ from one another in the mutual location, number, and shape of the clusters.

This situation is realized in the hydrides of group-III metals, MH_x, with relative hydrogen concentrations $x \lesssim 0.01$–0.1 (see review [2] and references therein).

Clustering of interstitial impurities results in a sharp decrease of their diffusion coefficient, which precludes observation of the quantum diffusion of hydrogen isotopes at low temperatures [3]. For temperatures $T < T_{\mathrm{cl}}$ (T_{cl} is the clustering temperature), two major diffusion mechanisms are operative: (i) via single impurities, which separate from the clusters for a certain time (“evaporation”), to be subsequently trapped again by the latter (“condensation”) (the fraction of such impurities decreases exponentially with temperature), and (ii) through the mobility of the clusters themselves. The mobility may be determined by either impurity diffusion over the cluster periphery [4, 5], or the diffusion of excitations (vacancies [4, 5] and dislocations [6, 7]) through the cluster itself.

The relative contribution of the processes of the second type should, in principle, grow with decreasing temperature, because the activation energy of these processes is, as a rule, lower than that for the evaporation mechanisms.

This work deals with a study of the temperature dependence of the relative contribution of cluster mobility to the coefficient of low-temperature ($T < T_{\mathrm{cl}}$) diffusion of light interstitial impurities in the bulk of a crystal, i.e., with an investigation of the diffusion mechanism.

A number of publications on adatom diffusion over the crystal surface have appeared recently [4–9]. The interest in surface diffusion is associated with the possibility of a direct observation of the cluster behavior. No such problems have thus far been studied for bulk diffusion. Besides, the diffusion was studied at $T \ll T_{\mathrm{cl}}$ temperatures, whereas we have focused our attention on a transition region $T \lesssim T_{\mathrm{cl}}$.

The first part of the work deals with a description of the model, and the second one, with the results obtained.

1. DESCRIPTION OF THE MODEL

We assume that the impurities can occupy the sites of a simple cubic interstice lattice corresponding to tetrahedral pores in a fcc crystal. The position of an impurity is specified by three integer coordinates (expressed in lattice constants).

The short-range part of the model interaction potential coupling the impurities characterizes repulsion and precludes occupation by two impurities of the same lattice site. The long-range part of the pairwise interaction energy has the form [3]

$$W_{ij} = \frac{b[3/5 - (X/\rho)^4 - (Y/\rho)^4 - (Z/\rho)^4] + (1-b)\cos(\gamma\rho)}{\rho^3}, \qquad (1)$$

where the first term corresponds to elastic interaction in a cubic crystal with a weak anisotropy [10], and the second, to interaction through the Friedel electron-density oscillations. The constant $b < 1$ specifies the relative magnitude of these contributions. The vector $\boldsymbol{\rho} = (X, Y, Z)$ with integer coordinates connects two interacting impurities (the axes of the coordinate frame coincide with the crystallographic axes of the crystal). The constant $\gamma = 2k_F d$, where k_F is the Fermi wave vector of the conduction electrons, and d is the interstice lattice constant.

With the potential chosen in this way, the temperature is reduced to the characteristic interaction energy of impurities occupying neighboring lattice sites [3].

The simulation was performed for a cube with 30 × 30 × 30 interstices, which is continued periodically to eliminate boundary effects. The number of the impurities was set equal to 30 ($x = 1.1 \times 10^{-3}$ per interstice and 2.2×10^{-3} per host atom).

The dynamics of the impurity system was studied by the Metropolis Monte Carlo algorithm [11]. The probability w_{ij} for a randomly chosen impurity to jump from interstice i to an as randomly chosen neighboring interstice j was determined by the energy difference $\xi_{ij} = \xi_j - \xi_i$, where ξ_i is the energy of the impurity at interstice i, which is equal to the sum of the pairwise interaction energies

$$w_{ij} = \begin{cases} 1, & \xi_{ij} \le 0 \\ \exp(-\xi_{ij}/T), & \xi_{ij} > 0. \end{cases} \qquad (2)$$

It was shown [3] that the choice of w_{ij} in this manner reproduces adequately the behavior of quantum interstitial impurities in a metal matrix; however, the simulation gives not the diffusion coefficient D but the quantity D/D_0, where D_0 is the diffusion coefficient of a system of noninteracting impurities.

To find the quantity D/D_0, one made use of the Einstein relation $D = T\mu$, where μ is the impurity mobility. One generated a weak potential gradient along one of the crystallographic axes. The impurity distribution was found by simulation annealing from the high-temperature region [3]. After this, one determined the impurity flux generated by a constant force. The ratio of the flux to the force yielded the value of μ.

If both the initial and the final impurity positions were found to be separated by a distance shorter than the critical distance a from any other impurity, the jump process was classed among processes of the second type, and, in the opposite case, among those of the first type.

2. DISCUSSION OF RESULTS

The temperature dependences of D/D_0, as well as of the quantity $\tilde{Z}$, the relative cluster-mobility contribution to the diffusion coefficient, are presented graphically in Figs. 1 and 2.

The results of the simulation reveal a fast drop of D/D_0 for $T < T_{cl}$ for all the values of b and γ characterizing the impurity pairwise interaction potential stud-

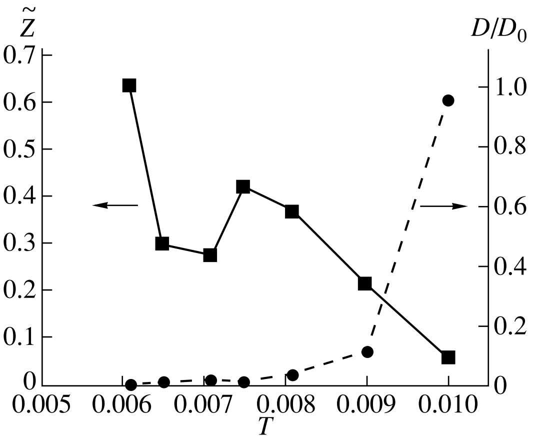

Fig. 1. Temperature dependences of the diffusion coefficient and of the contribution to the latter due to cluster "creep" plotted for $b = 0.5$ and $\gamma = 0.75$.

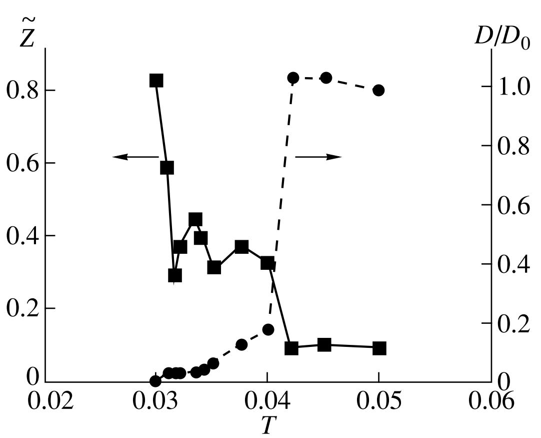

Fig. 2. Same as in Fig. 1 or $b = 0.5$ and $\gamma = 1.2$.

ied, whereas the behavior of $\tilde{Z}$ was found to depend substantially on the parameters b and γ.

For $b = 0.8$, i.e., for the case where elastic interaction dominates in the long-range pairwise potential, annealing generates a sudden formation at $T = T_{\text{cl}}$ in the (001) or equivalent plane of a plane cluster, in which impurities occupy neighboring lattice sites. For two values of γ studied, 0.75 and 1.2, particle transport occurred only through evaporation and condensation down to the temperature $T = 0.4\ T_{\text{cl}}$. At lower temperatures, the impurity mobility is so low that accumulation of reasonable statistics with the PCs employed for the study would require too long a time.

The negligible cluster mobility at $b = 0.8$ is associated with the anisotropy of the elastic interaction. An impurity migrating over the periphery of a cluster has to overcome a fairly high potential barrier. The probability of this process is lower than that of the “evaporation.” At the same time, the formation of a vacancy or dislocation in the closely packed cluster structure is also unlikely.

However, if $b = 0.5$, then for $\gamma = 0.75$ a plane cluster formed gradually in the (001) plane as the temperature dropped below $T_{\text{cl}} = 0.009$, with the impurities making up a square lattice with a spacing of 2 (in units of d). The $\tilde{Z}(T)$ and $D(T)/D_0(T)$ dependences are plotted in Fig. 1. The nonmonotonic behavior of the $\tilde{Z}(T)$ relation is accounted for by cluster rearrangement. While for $T < 0.0075$, it is planar, in the $0.0075 < T < T_{\text{cl}}$ interval, the cluster consists of two parallel plane fragments spaced by 3 (in units of d).

Now if $b = 0.5$ and $\gamma = 1.2$, then for $T < T_{\text{cl}}$ one also observes a plane cluster to form in the (001) plane, but the period of the corresponding square impurity lattice is unity. In contrast to the $\gamma = 0.75$ case, the formation (breakup) of such a cluster occurs not gradually but practically in a jump at $T_{\text{cl}} = 0.04$. This accounts for the jump in the $\tilde{Z}(T)$ plot (Fig. 2). For $T > T_{\text{cl}}$, we have $\tilde{Z}(T) \neq 0$, because randomly spaced impurities form a certain number of small clusters consisting of two to three impurities at high temperatures as well.

The peak in $\tilde{Z}(T)$ at $T = 0.0335$ is not connected with a noticeable cluster rearrangement. The nonmonotonic behavior of the $\tilde{Z}(T)$ relation may be caused by a freezing-out of one of the diffusion mechanisms in the clusters. For instance, the contribution of particle diffusion in a plane parallel to the cluster plane (in the case of adatoms on a crystal surface, this mechanism is called terrace diffusion [4, 5]) may become much less than that of in-plane diffusion along the cluster perimeter.

Thus, the shape and mobility of the clusters forming in the clustering of mobile impurities depend substantially on the parameters of the impurity pairwise interaction potential.

In a number of cases, cluster mobility plays an essential part already at $T = T_{\text{cl}}$, where a sizable fraction of impurities combine to form clusters. The relative contribution $\tilde{Z}(T)$ of cluster “creep” to the diffusion process becomes dominant at temperatures $T = (0.6–0.75)T_{\text{cl}}$.

The nonmonotonic character of the $\tilde{Z}(T)$ dependence can be due either to cluster rearrangement or to freezing-out of one of several impurity diffusion mechanisms responsible for the cluster mobility.

ACKNOWLEDGMENTS

Partial support of the Russian Foundation for Basic Research (project no. 97-02-17627) is gratefully acknowledged.

REFERENCES

1. A. I. Morozov and A. S. Sigov, Zh. Éksp. Teor. Fiz. **95**, 170 (1989) [Sov. Phys. JETP **68**, 97 (1989)].
2. A. I. Morozov and A. S. Sigov, Usp. Fiz. Nauk **164**, 243 (1994).
3. A. A. Berzin, A. I. Morozov, and A. S. Sigov, Fiz. Tverd. Tela (S.-Peterburg) **40**, 475 (1998) [Phys. Solid State **40**, 435 (1998)].
4. S. V. Khare and T. L. Einstien, Phys. Rev. B **54**, 11752 (1996).
5. J. Heinonen, I. Koponen, J. Merikoski, *et al.*, Phys. Rev. Lett. **82**, 2733 (1999).
6. J. C. Hamilton, M. S. Daw, and S. M. Foiles, Phys. Rev. Lett. **74**, 2760 (1995).
7. J. C. Hamilton, Phys. Rev. Lett. **77**, 885 (1996).
8. S. C. Wang, U. Kurpick, and G. Ehrlich, Phys. Rev. Lett. **81**, 4923 (1998).
9. S. Renisch, R. Schuster, J. Wintterlin, *et al.*, Phys. Rev. Lett. **82**, 3839 (1999).
10. R. A. Masumura and G. Sines, J. Appl. Phys. **41**, 3930 (1970).
11. *Monte Carlo Methods in Statistical Physics*, Ed. by K. Binder (Springer, Heidelberg, 1979; Mir, Moscow, 1982).

Translated by G. Skrebtsov

Physics of the Solid State, Vol. 42, No. 4, 2000, pp. 697–700. Translated from Fizika Tverdogo Tela, Vol. 42, No. 4, 2000, pp. 679–682.
Original Russian Text Copyright © 2000 by Ocelik, Fursova, Khonik, Csach.

DEFECTS, DISLOCATIONS, AND PHYSICS OF STRENGTH

Non-Newtonian Deformation of Co-Based Metallic Glass at Low Stresses

V. Ocelik[2], Yu. V. Fursova[1], V. A. Khonik[1, 3], and K. Csach[2]
[1]*Voronezh State Pedagogical University, ul. Lenina 86, Voronezh, 394611 Russia*
[2]*Institute of Experimental Physics, Slovak Academy of Sciences, 04353 Košice, Slovakia*
[3]*Kanazawa University, 920-8667 Kanazawa, Japan*
e-mail: khonik@vspu.ac.ru, khonik@t.kanazawa-u.ac.jp

Received, in final form, October 5, 1999

Abstract—The results of precision measurements of creep in Co-based metallic glass are presented. It is shown that, in spite of generally accepted concepts, plastic flow at low stresses under intense structural relaxation conditions is of a non-Newtonian type. Consequences of this fact are considered. *© 2000 MAIK “Nauka/Interperiodica”.*

Rheological properties of metallic glasses (MGs) are interesting from purely scientific, as well as applied, points of view. Attempts to find out whether the plastic flow is of a linear Newtonian or a nonlinear type were made soon after the discovery of metallic glasses [1, 2]. In the former case, the rate $\dot{\varepsilon}_s$ of plastic shear strain is directly proportional to the applied shear stress σ_s, while in the latter case the dependence of the strain rate on stress is nonlinear.

The σ_s vs. $\dot{\varepsilon}_s$ dependence can be described in terms of shear viscosity, which is defined as

$$\eta = \sigma_s/\dot{\varepsilon}_s = \sigma/3\dot{\varepsilon}, \qquad (1)$$

where σ and $\dot{\varepsilon}$ are the tensile stress and the rate of longitudinal strain, respectively. On the other hand, the same dependence can be characterized by the so-called strain-rate sensitivity defined as

$$m = \frac{\partial \ln \dot{\varepsilon}_s}{\partial \ln \sigma_s} = 1 - \frac{\sigma_s}{\eta}\frac{\partial \eta}{\partial \sigma_s}. \qquad (2)$$

If the viscosity defined as (1) is independent of stress, plastic flow is Newtonian and $m = 1$. Otherwise ($\eta = f(\sigma_s)$), the σ_s vs. $\dot{\varepsilon}_s$ dependence is nonlinear, and $m > 1$.

First experiments [1–4] made with MGs at temperatures $T > 300$ K and low shear stresses proved that plastic deformation is Newtonian, while measurements at relatively high stresses (exceeding 200–400 MPa depending on the temperature, thermal previous history, and chemical composition of an MG) indicated a nonlinear type of the flow with $1 < m < 12$ [5–9].

At the present time, it is generally accepted that such behavior is typical of MGs. However, our recent precision measurements of creep [10] proved that the plastic flow of nickel-based glass is non-Newtonian at low tensile stresses, and accordingly viscosity (1) is a function of stress. It would be interesting to find the extent to which the nonlinearity of plastic flow is typical of metallic glasses. In order to solve this problem, we studied a magnetically soft MG with a standard chemical composition.

1. EXPERIMENTAL TECHNIQUE

We investigated industrial MG $Co_{70}Fe_5Si_{15}B_{10}$ (at. %) obtained by spinning in the form of a strip, having a thickness of 48 ± 5 μm and width $d = 21$ mm. The noncrystallinity of the structure was controlled by x-ray analysis. According to the results of differential scanning calorimetry (on a Rigaku-Denki calorimeter DSC-8230), the temperature corresponding to the onset of crystallization was 762 K at a heating rate of 3.3 K/min. The creep was measured in the argon flow under a tensile stress on a thermomechanical analyzer Setaram TMA92 with an absolute resolution of approximately 10 nm. The samples had the shape of a double blade and were prepared by the mechanical grinding of a part of the strip in a special mount. The sample length was $l_0 = 15$ mm and the working width was 1.2 mm. The temperature of the experiment was chosen to be 675 K, which was dictated, on the one hand, by the tendency to carry out measurements at the maximum possible temperature for increasing the creep rate (and accordingly for reducing the errors in calculating the strain rate at low stresses) and, on the other hand, by the tendency to avoid crystallization as a result of prolonged isothermal holding. The sample was heated to the experimental temperature (which was subsequently maintained to within ±0.2 K) at a rate of 10 K/min without overheating, annealed at this temperature during the time $\tau = 288 \pm 3$ s, and loaded by a tensile stress (determined

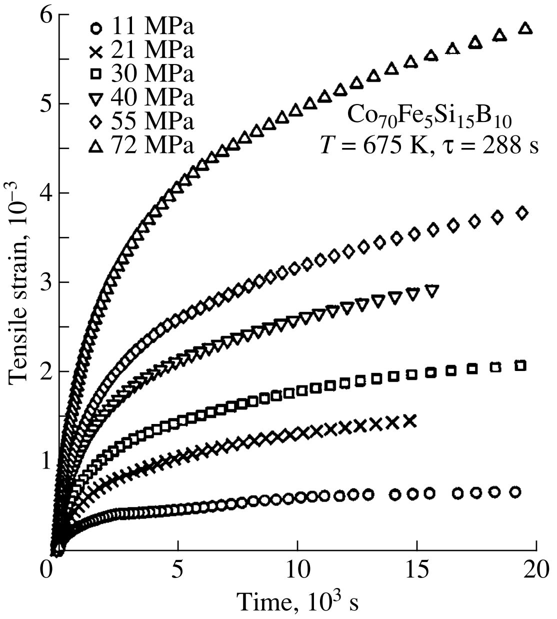

Fig. 1. Creep kinetics of the $Co_{70}Fe_5Si_{15}B_{10}$ metallic glass at $T = 675$ K under different stresses.

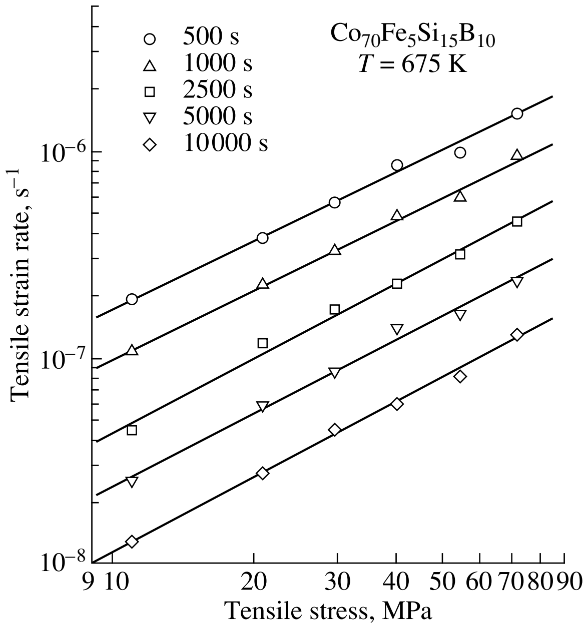

Fig. 2. Dependence of strain rate on tensile stress for indicated instants of time.

approximately to within 15%), after which the sample elongation Δl was measured automatically with the help of a computer, and the strain $\varepsilon = \Delta l/l_0$ was calculated. The interval between measurements was 0.8 s immediately after loading and then increased in proportion to the logarithm of time. X-ray tests of the samples under investigation did not reveal any traces of crystallization.

2. EXPERIMENTAL RESULTS

Preliminary experiments demonstrated the lack of admissible reproducibility of the results for samples prepared from different segments corresponding to an arbitrary coordinate X along the strip width. Creep measurements for samples prepared from seven segments with different coordinates $0 \le X \le d$ proved that the reason is the inhomogeneity in the strip's properties. As a result, the rate of viscosity growth at the experimental temperature, which characterizes the rate of structural relaxation and, accordingly, the structural state of the strip, can vary (other conditions being equal) by 40–50%, depending on X. Taking this into account, all subsequent experiments were carried out using the samples corresponding to a constant X coordinate along the strip width.

To the determination of the strain rate sensitivity from the data presented in Fig. 2

t, s	m	R	S
500	1.11	0.995	0.04
100	1.12	0.995	0.04
2500	1.19	0.995	0.04
5000	1.17	0.994	0.04
10 000	1.21	0.997	0.03

Figure 1 shows the creep curves obtained for various stresses 11 MPa $\le \sigma \le$ 72 MPa. As usual, the creep rate increases significantly with the applied load.

The standard way to find out whether a flow is Newtonian is to calculate the strain-rate sensitivity according to equation (2). For this purpose, the $\varepsilon(t)$ dependence was differentiated numerically through calculating the average slope between the ith point $(\varepsilon_i(t_i))$, the next point $(\varepsilon_{i+1}(t_{i+1}))$, and the previous point $(\varepsilon_{i-1}(t_{i-1}))$. Using the cross sections of the obtained strain rate vs. time graphs, we calculated the stress dependences of the strain rate for various instants t. Figure 2 shows such dependences for t = 500, 1000, 2500, 5000, and 10000 s in logarithmic coordinates. It can be seen that a close linear approximation is possible in all cases. This approximation was carried out by the least-squares method, and then we calculated the strain-rate sensitivity m, the pair correlation coefficient R characterizing the extent of deviation of the $\ln\sigma$ vs. $\ln\dot{\varepsilon}$ dependence from linearity, and the standard deviation S. The values of these are given in the table, which shows that the $\ln\dot{\varepsilon}$ vs. $\ln\sigma$ dependences are linear with the pair correlation coefficient $R \approx 0.995$ ($R = 1$ for a straight line) and the standard deviation $S \approx 0.04$. The mean value of $m = 1.16$, which indicates the non-Newtonian nature of the plastic flow. However, this conclusion requires additional substantiation in view of the smallness of the deviation.

On the other hand, it is clear that, in the presence of even an insignificant nonlinearity, it is more convenient to analyze the kinetics of viscosity defined by equation (1) than the $\ln\dot{\varepsilon}\,(\ln\sigma)$ dependences. Indeed, in this case, the viscosity is a function of stress, and the difference in the viscosities of samples loaded by different stresses will build up with time, which makes it possible to identify a non-Newtonian flow, even with an insignificant nonlinearity, more reliably.

In order to accomplish this approach, we calculated the kinetics of viscosity growth under various stresses. It was found that, in accordance with numerous available data (see, for example, [11, 12]), viscosity increases linearly with time except in initial measurements during a few hundred seconds, when the viscosity growth rate is higher.[1] The dependence of the viscosity growth rate $d\eta/dt$ on the stress is depicted in Fig. 3 (the initial nonlinear segment of the $\eta(t)$ curve was disregarded in calculations). The same figure shows the results of calculation of the pair correlation coefficient R. The main conclusion that can be drawn from Fig. 3 is obvious: the kinetics of viscosity growth is determined by stress. This means that plastic deformation is non-Newtonian in the entire range of stresses. The decrease in the standard deviation in determining $d\eta/dt$ and the increase in R with the stress reflect the decrease in the error of calculation of strain rate due to the general increase in the creep strain.

3. DISCUSSION OF RESULTS

The creep of MGs in the initial state at temperatures $T \geq 400$ K can be interpreted as a structural relaxation oriented by the applied stress [14, 16, 17]. We can assume that the observed nonlinearity is a typical feature of structural relaxation in MGs. Indeed, as mentioned above, the standard method of analysis of the stress dependence of plastic strain rate is based on plotting the $\ln\dot{\varepsilon}\,(\ln\sigma)$ curve. The example considered above shows that such an analysis may lead to a unconvincing result in the case of insignificant nonlinearity. The identification of nonlinearity requires an analysis of the data of the kinetics of viscosity obtained for different stresses.

It should also be noted that, apart from the small nonlinearity observed in [10], some indications of nonlinearity were also obtained by Deng *et al.* [18]. An analysis of creep in the $Pd_{40}Ni_{40}P_{20}$ metallic glass proved that the kinetics of viscosity at temperatures 453 K $\leq T \leq$ 568 K under very low (1.6–6.6 MPa) and moderate (60–100 MPa) stresses exhibits a clearly pronounced dependence on the load (see Fig. 7 in [18]). Deng *et al.* [18] calculated the strain rate sensitivity to be $1.1 \leq m \leq 1.5$, depending on the experimental temperature. This fact, however, was not discussed in [18] at all.

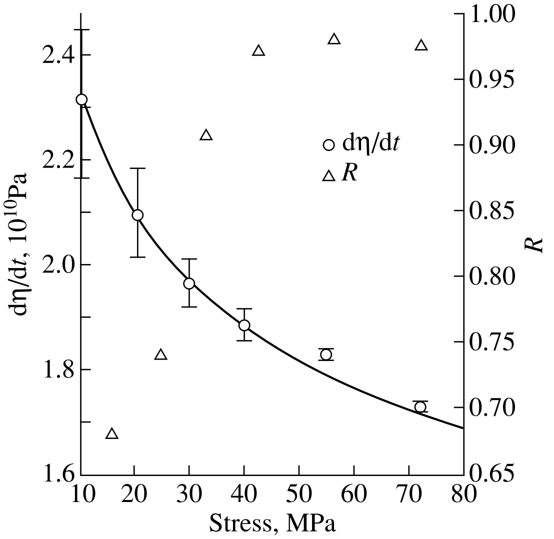

Fig. 3. Shear viscosity growth rate and pair correlation coefficients as functions of stress. The solid curve corresponds to the power law of creep (6) for $m = 1.16$.

According to the concepts developed in [14, 16, 17], the plastic shear strain rate for long periods of time ($t \gg \tau$, where τ is the time of preliminary annealing at the experimental temperature T) can be presented in the form

$$\dot{\varepsilon}_s = \sigma_s kTN_0\Omega C/t, \qquad (3)$$

where k is the Boltzmann constant, N_0 is the volume density of active relaxation centers per unit interval of activation energy, Ω is the volume involved in an elementary act of structural relaxation, and C is a parameter characterizing the orienting effect of external stress on elementary acts of structural relaxation. If none of the quantities N_0, Ω, and C is a function of stress, equation (3) describes a Newtonian flow with $m = 1$. An increase in at least one of these quantities with stress causes a nonlinear deformation with the strain-rate sensitivity

$$m = 1 + \partial\ln N_0\Omega C/\partial\ln\sigma_s > 1. \qquad (4)$$

This formula leads to the following expression for the product $N_0\Omega C$ in the case of a nonlinear deformation:

$$N_0\Omega C = A\sigma_s^{m-1}, \qquad (5)$$

where lnA is the integration constant. The value $m \approx 1.16$ we determined here indicates that the product $N_0\Omega C$ increases, in accordance with formula (5), upon an increase in stress from $\sigma_1 = 11$ MPa to $\sigma_2 = 72$ MPa by a factor of $(\sigma_2/\sigma_1)^{m-1} \approx 1.35$.

---

[1] Similar anomalies were also observed by us earlier for some other MGs [13–15].

Using formulas (3)–(5), we obtain expressions for the strain rate

$$\dot{\varepsilon}_s = \frac{kTA}{t}\sigma_s^m \tag{6}$$

and the viscosity growth rate at a constant temperature:

$$\dot{\eta} = \frac{1}{kTA}\sigma_s^{1-m}. \tag{7}$$

It follows from (7) that, in accord with the experiment, viscosity increases linearly with time, while its growth rate decreases with increasing stress. The functional dependence of the form σ^{1-m} for $m = 1.16$ is shown by the solid curve in Fig. 3, indicating that relation (7) correctly describes (to within the experimental error) the dependence of $\dot{\eta}$ on stress. It should also be noted that formula (6) is just the so-called power law often used for interpreting experiments on plastic flow of MGs (see, for example, [19]). In the case of a Newtonian flow, formulas (3) and (6) are equivalent and $A = N_0\Omega$.

Nonlinearity of a plastic flow must directly affect the low-frequency ($f < 0.1$–1 Hz) internal friction associated with structural relaxation of the MG. Using (3), we can prove that in this case, internal friction is of the viscoplastic type and can be described using the simple Maxwell two-element rheological model [20–22]

$$Q^{-1} = G/\eta\omega, \tag{8}$$

where G is the unrelaxed shear modulus, ω is the cyclic frequency, and the time-dependent viscosity is determined from the relation

$$\eta^{-1} = kTN_0\Omega C/t. \tag{9}$$

Equations (5), (8), and (9) show that, in the case of a non-Newtonian flow, internal friction must be independent of the amplitude of the applied stress (strain). Otherwise, the nonlinearity of plastic deformation, emerging when $N_0\Omega C = f(\sigma_s)$, causes an amplitude-dependent internal friction.

Thus, we can predict that the low-frequency internal friction associated with structural relaxation of an MG under nonlinear plastic-flow conditions is a function of the stress amplitude. It should be emphasized that this question has not been investigated experimentally as yet.

The main conclusions of the present communication can be formulated as follows.

(1) The plastic flow of the metallic glass $Co_{70}Fe_5Si_{15}B_{10}$ under low stresses is non-Newtonian with the strain-rate sensitivity $m \approx 1.16$. This fact can be interpreted as the result of the stress dependence of the structural relaxation parameters N_0, Ω, and/or C determining the kinetics of plastic flow in accordance with equation (3).

(2) Structural relaxation of non-Newtonian metallic glasses at low frequencies of loading must lead to an amplitude-dependent viscoplastic internal friction.

ACKNOWLEDGMENTS

The authors are grateful to the reviewer for valuable remarks.

This research was partly supported by the Ministry of General and Professional Education of the Russian Federation (fundamental natural science grant no. 97-0-7, 0-161).

REFERENCES

1. H. S. Chen and D. Turnbull, J. Chem. Phys. **48**, 2560 (1968).
2. T. Masumoto and R. Maddin, J. Mater. Sci. **19**, 1 (1975).
3. J. Logan and M. F. Ashby, Acta Metall. **22**, 1047 (1974).
4. A. I. Taub and F. Spaepen, Scr. Metall. **13**, 195 (1979).
5. R. Maddin and T. Masumoto, Mater. Sci. Eng. **9**, 153 (1972).
6. J. C. Gibeling and W. D. Nix, Scr. Metall. **12**, 919 (1978).
7. D. Lee, Metall. Trans. A **12**, 419 (1981).
8. T. D. Hadnagy, D. J. Krenitsky, D. G. Ast, *et al.*, Scr. Metall. **12** (1), 45 (1978).
9. J. P. Patterson and D. R. H. Jones, Acta Metall. **28**, 675 (1980).
10. K. Csach, Yu. V. Fursova, V. A. Khonik, *et al.*, Scr. Mater. **39**, 1377 (1998).
11. A. I. Taub and F. E. Luborsky, Acta Metall. **29**, 1939 (1981).
12. A. I. Taub and F. Spaepen, J. Mater. Sci. **16**, 3087 (1981).
13. A. T. Kosilov, V. A. Mikhaĭlov, V. A. Khonik, *et al.*, Fiz. Met. Metalloved. **82**, 172 (1996).
14. A. T. Kosilov, V. A. Mikhaĭlov, V. V. Sviridov, *et al.*, Fiz. Tverd. Tela (S.-Peterburg) **39**, 2008 (1997) [Phys. Solid State **39**, 1796 (1997)].
15. K. Csach, V. A. Khonik, A. T. Kosilov, *et al.*, in *Proceedings of the 9th International Conference on Rapid Quenching Metastable Materials, Bratislava, Slovakia*, Ed. by P. Duhaj, P. Mrafko, and P. Svec (Elsevier, Amsterdam, 1997), Suppl., p. 357.
16. A. T. Kosilov and V. A. Khonik, Izv. Akad. Nauk, Ser. Fiz. **57**, 192 (1993).
17. O. P. Bobrov, A. T. Kosilov, V. A. Mikhaĭlov, *et al.*, Izv. Akad. Nauk, Ser. Fiz. **60** (9), 124 (1996).
18. D. Deng, F. Zheng, Y. Xu, *et al.*, Acta Metall. **41**, 1089 (1993).
19. J. P. Patterson and D. R. H. Jones, Acta Metall. **28**, 1089 (1980).
20. V. I. Belyavskiĭ, O. P. Bobrov, A. T. Kosilov, *et al.*, Fiz. Tverd. Tela (S.-Peterburg) **38**, 30 (1996) [Phys. Solid State **38**, 16 (1996)].
21. V. A. Khonik, J. Phys. (Paris) IV **6** (C8), 591 (1996).
22. Yu. V. Fursova and V. A. Khonik, Izv. Akad. Nauk, Ser. Fiz. **62**, 1288 (1998).

Translated by N. Wadhwa

Physics of the Solid State, Vol. 42, No. 4, 2000, pp. 701–702. Translated from Fizika Tverdogo Tela, Vol. 42, No. 4, 2000, pp. 683–684.
Original Russian Text Copyright © 2000 by Gerasimov, Chiradze, Kutivadze, Bibilashvili, Bokhochadze.

DEFECTS, DISLOCATIONS, AND PHYSICS OF STRENGTH

On the Mechanism of Residual Photomechanical Effect

A. B. Gerasimov, G. D. Chiradze, N. G. Kutivadze,
A. P. Bibilashvili, and Z. G. Bokhochadze
Tbilisi State University, Tbilisi, 280028 Georgia
Kutaisi State University, Kutaisi, 384000 Georgia

Received September 13, 1999

Abstract—The results of investigation of the residual photomechanical effect (PME) in a monocrystalline *n*-Si sample at various temperatures by the method of microindentation following exposure to light are considered. It is shown that a decrease in the residual PME is an exponential function of time and temperature. *© 2000 MAIK “Nauka/Interperiodica”.*

In our previous publication [1], we reported that the depth of imprints on Si samples in experiments on photomechanical effect (PME) [2] (effect of light on microhardness (MH)) was a function of the time during which the sample was loaded after its exposure to light. In particular, the longer the action of the indentor was, the larger the imprint depth; after a certain time, the indentation was the same as during MH measurements in the dark. In order to explain this effect, we proposed a mechanism that can be briefly described as follows [1]. After the exposure of the crystal to light, nonequilibrium charge carriers in it experience rapid recombination, but some of these carriers in the surface layer remain at corresponding minima separated in space and formed due to nonuniform bending of energy bands in this layer of Si (see Fig. 1b in [1]). The recombination of such carriers can take place after the surmounting of the corresponding barrier, i.e., in an activation manner. For this reason, the surface layer of the crystal subjected to illumination preserves softening for a certain time (residual PME). It was proved earlier [1, 3, 4], that crystal softening is due to nonequilibrium electrons and holes referred to as anticoupling quasiparticles.

The above considerations concerning the physical origin of the residual PME lead to the conclusion that an increase in the sample temperature must lead to an exponential decrease in the magnitude of residual PME as well as its lifetime due to an increase in the rate of expulsion of electrons and holes from the corresponding minima, and, hence, an increase in the rate of their recombination. For this reason, it was interesting to investigate this effect at various temperatures.

In this communication, we consider the results of investigation of the residual PME at various temperatures by the method of microindentation of the sample after its illumination.

The experiments were made on the (100) face of a dislocation-free Si single crystal exhibiting *n*-type conductivity and having a resistivity of 200 Ωcm. The surfaces of the experimental samples were ground and polished mechanically and then subjected to chemical cleaning followed by etching in a H_2SO_4 + H_2O_2 mixture (in the 4 : 1 ratio) at a temperature of 40°C for 30 s. The method of MH measurements in the dark and under illumination is described in [1]. The load was chosen equal to 25 g, and the main diagonal of the Knoop pyramid used in the experiment always coincided with a ⟨100⟩ direction in the (100) plane under investigation for anisotropy being taken into account [5].

The experiments were made as follows. First, the surface of the sample under investigation was illuminated for 10 s (which ensured complete saturation of the value of residual microhardness associated with illumination). Then, imprints were impressed with an indentor in certain time intervals. The experiments were repeated at various temperatures of the sample.

Figure 1 shows that a decrease in the residual PME is an exponential function of time (Fig. 1a) and temperature (Fig. 1b). For convenience of graphic representation, the change in the residual PME is measured in rel-

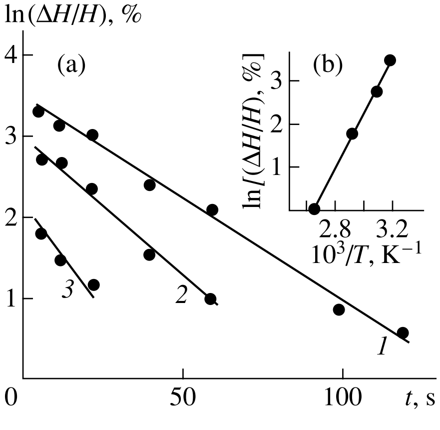

Fig. 1. Residual PME as a function of (a) time at 298 (curve *1*), 325 (curve *2*), and 348 K (curve *3*), and (b) temperature. Indentation started immediately after the switching off the illumination.

ative units $\Delta H/H$ (where $\Delta H = H - H_i$ is the value of MH measured in the dark at a given temperature and H_i is the residual MH under illumination, corresponding to a certain ith instant of time after illumination at the same temperature). It was found that the maximum time during which the residual PME could be determined in our experiments was also an exponential function of temperature.

In order to estimate the average height of the barrier that should be surmounted for the charge carrier recombination to occur in the surface layer, we can use the well-known expression [6] for lifetime $\tau = \tau_0 \exp(\Delta/kT)$, where Δ is the barrier height, τ_0 is the lifetime in the bulk, k is Boltzmann's constant, and T is the temperature. Proceeding from the established correlation between the magnitude of PME and the corresponding concentration of anticoupling quasiparticles [1], it is natural to assume that the longer τ, the larger the magnitude of residual PME, i.e., $\Delta H/H \sim \tau$. In this case, $\Delta H/H \sim \exp(\Delta/kT)$, and we can write a simple relation $\Delta H/H = \alpha \exp(\Delta/kT)$, where α is a coefficient, which can be regarded as constant in the time and temperature intervals under investigation. In order to determine Δ, it is convenient to write the latter equation in the form $\ln(\Delta H/H) = \ln\alpha + (\Delta/k)(1/T)$. The value of Δ estimated from a graph plotted according to this expression proved to be 0.3 eV.

It should be noted that the value of Δ we estimated here is of illustrative nature since it corresponds only to our samples with an appropriate treatment of their surfaces and is not a physical parameter of the material under investigation since the microhardness itself is determined by experimental conditions to a considerable extent.

REFERENCES

1. A. B. Gerasimov, G. D. Chiradze, N. G. Kutivadze, *et al.*, Fiz. Tverd. Tela (S.-Peterburg) **40**, 503 (1998) [Phys. Solid State **40**, 462 (1998)].
2. G. K. Kuczynski and R. H. Hochman, Phys. Rev. **108**, 946 (1957).
3. I. G. Gverdtsiteli, A. B. Gerasimov, Z. V. Jibuti, *et al.*, Poverkhnost' **11**, 132 (1985).
4. A. B. Gerasimov, in *Proceedings of the 4th International Conference Materials Science Forum* (New York, 1990), Vol. 65–66, p. 47.
5. P. D. Waren, S. G. Roberts, and P. B. Hirsch, Izv. Akad. Nauk SSSR, Ser. Fiz. **51**, 812 (1987).
6. V. I. Fistul', *Introduction to Semiconductor Physics* (Vysshaya Shkola, Moscow, 1984).
7. V. M. Glazov and V. N. Vigdorovich, *Microhardness of Metals and Semiconductors* (Metallurgiya, Moscow, 1969).

Translated by N. Wadhwa

Physics of the Solid State, Vol. 42, No. 4, 2000, pp. 703–705. Translated from Fizika Tverdogo Tela, Vol. 42, No. 4, 2000, pp. 685–687.
Original Russian Text Copyright © 2000 by Fedorov, Pluzhnikova, Tyalin.

DEFECTS, DISLOCATIONS, AND PHYSICS OF STRENGTH

Healing of Cracks Arrested at Asymmetric Cleavage in Alkali-Halide Crystals and Calcite

V. A. Fedorov, T. N. Pluzhnikova, and Yu. I. Tyalin
Tambov State University, Tambov, 392622 Russia
e-mail: feodorov@feodorov.tstu.ru

Received September 30, 1999

Abstract—Plastic-strain regions near the tips of cracks are investigated. Possible mechanisms of self-healing of cracks are considered. It is shown that heating and exposure to visible light affect the evolution of microplastic shear strains at the crack tip. It is found that the dislocation density at the tips of cracks depends exponentially on temperature and time of exposure to light. © *2000 MAIK "Nauka/Interperiodica".*

In an asymmetric cleaving of a crystal with cleavage, the probability that a narrower part of the sample splits off due to the transition of the crack from the (100) plane to the orthogonal plane (001) is quite high [1]. In this case, the crack remaining in the crystal after splitting off exhibits self-healing [2].

This communication is devoted to an analysis of the morphology of plastic-strain regions formed near the tip of an arrested crack and to the establishment of the mechanism of spontaneous healing of cracks and the effect of heating and visible-range radiation on this process.

The experiments were made on alkali-halide crystals (AHCs) of LiF, NaCl, KCl, and on $CaCO_3$. The impurity concentration in the crystals did not exceed $\sim 10^{-3}$. The samples having a size of $15 \times 30 \times 2$ mm were cleaved along the (100) plane at a certain distance S_1 from the symmetry axis of the crystal (see inset to Fig. 2). The asymmetry of the cleavage was characterized by the ratio of S_1 to the sample half-width $S_2/2$. The cleavage was made by a calibrated blow with an energy of ~17 mJ. Then, the crystal was additionally split into two parts along the (010) plane to obtain the reference and the experimental sample.

Some samples were heated in a furnace from 300 to 365 K. An other part of samples was subjected to radiation emitted by a 100-W tungsten incandescent lamp with emission spectrum peak corresponding to the wavelength $\lambda = 1$ μm ($E = 1.24$ eV), which simultaneously heated the samples to ~355 K. The exposure time varied from 2 to 1400 hours. The illuminance of the sample surface amounted to ~15 klx.

It was established experimentally that, after the arrest of the initial crack, the lateral cleavage in an AHC occurs predominantly along the (001) plane (~73%) and, with a lower probability (~22%), along the (101) plane. The lateral cleavage in calcite takes place only along the (001) plane. A rectangular cleft is generated, as a rule, at a distance of 2–5 mm from the tip of the initial crack. The cleavage at an angle of 45° evolves, however, directly from the tip of the arrested crack. The crack remaining in the crystal after cleavage and unloading of the sample is self-healed in most cases.

The length of the healed segment of a crack decreases with increasing asymmetry of the cleavage. Unhealed cracks were also observed. At the tips of such cracks, microplasticity is significant. Plastic opening $\delta = (nb\sqrt{2})/2$ exceeded 40 nm for these cracks (b is the Burgers vector for [100]{101} dislocations and n is the number of dislocations in the slip band). No microplasticity was detected at the tips of cracks in $CaCO_3$. In individual cases, no dislocation "rosettes" were observed at the tip of cracks in AHCs as well as in $CaCO_3$.

With increasing asymmetry of the cleavage, AHCs exhibit a tendency to lowering the symmetry of etch patterns relative to the plane of cracks. The number of rays decreases, and their length changes together with the relative size of the rays on different sides of the crack plane. It was also noted that the dislocation density near the tip of a crack changes from 10^{10} m^{-2} for the asymmetry ratio 0.2 to 3×10^{10} m^{-2} for the asymmetry ratio 0.8. The dislocation density at the rays of "rosettes" decreases exponentially with increasing distance from the tip of the crack. In the immediate vicinity of the crack tip, there is a bounded region free of dislocations.

Annealing or prolonged holding at room temperature does not affect the length of the healed segment, but significantly changes the dislocation pattern near the crack tip.

The same result is also obtained after simultaneous annealing and exposure to visible light (Fig. 1), but the dislocation structure changes more intensely in this case (Fig. 2).

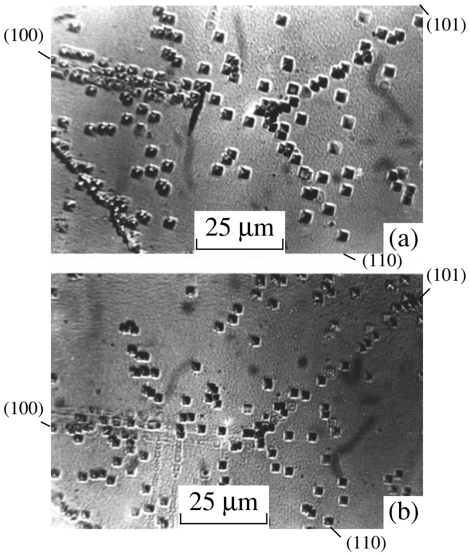

Fig. 1. Dislocation structure near the tips of cleavage cracks in LiF crystals: (a) a reference crystal at room temperature and (b) a crystal exposed to radiation in the optical range, E = 1.24 eV, T = 355 K, 15 klx, 20 hours.

Analyzing the deformation of fragments of the crystal being destroyed in the beam approximation, we can state that the narrower part of the crystal is subjected to stronger deformation and, hence, is preferential for cleavage. Cleavage cracks can originate at various defects of the type of cleavage steps or sub-boundaries. Intense stress relaxation at the tips of cracks can occur due to slip along the (101) planes. The cleavage at 45° becomes possible in this case due to embrittlement of the material in the slip band.

The nonuniform distribution of stresses in the vicinity of the crack tip affects the evolution of microplastic shear strains in this region. An increase in the cleavage asymmetry and, hence, in the nonuniformity of the stress field is accompanied by a change in the etch pattern at the crack tip from symmetric to asymmetric patterns containing predominantly one of slip systems.

The mechanism of crack healing can be visualized as follows.

As a result of lateral cleavage, the sample is unloaded and the initial crack becomes arrested. As long as the sample loading differs from zero, a noticeable emission of dislocations takes place at the crack tip [3]. Depending on the number of dislocations and the slip geometry, the plastic opening δ of the crack can assume different values. Some of the possible shapes of the tips of such cracks are shown in Fig. 3.

At a certain instant, emission of dislocations ceases, and a further decrease in loading initiates the first "rapid" stage of healing, i.e., plastic closing of the crack. It can develop both as a result of reversible discharge of emitted dislocations into the crack, and due to the motion of new dislocations of the opposite polarity along neighboring parallel slip planes or the planes perpendicular to them (which is observed much less frequently) if the motion of dislocations in the primary slip band is hampered. The former is due to the action of repulsive forces among dislocations lying in the same slip plane and image forces, while the latter is due to the action of elastic stresses in the sample (Fig. 3). If

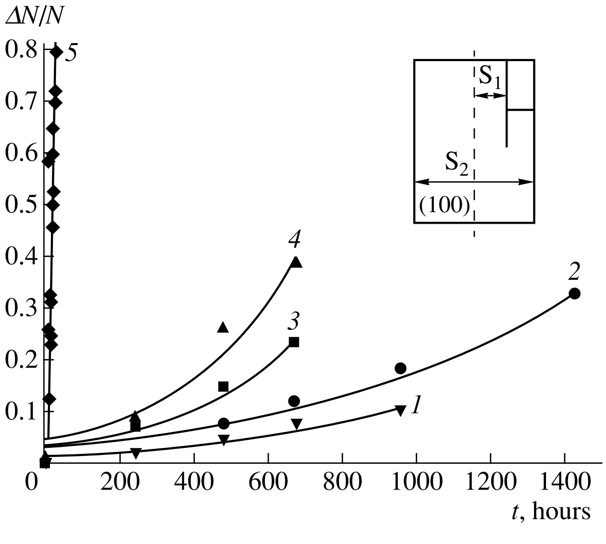

Fig. 2. Relative variation of the number of dislocations near the crack tip ($\Delta N/N$) as a function of time of action (t): T = 263 K (curve *1*), 288 K (curve *2*), 325 K (curve *3*), and 365 K (curve *4*); curve *5* corresponds to simultaneous illumination and heating. The inset schematically shows the cleavage of crystals.

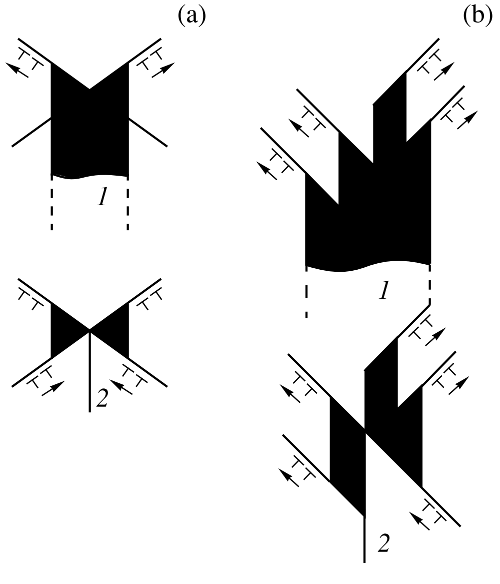

Fig. 3. Schematic diagrams illustrating the shape of tips of self-healing cracks: (a) without a relative displacement of crack surfaces and (b) with a relative shift; the tip of plastic opening of cracks (*1*) and the tip of a crack after the first stage of "rapid healing" (*2*).

the resultant (ultimate) opening δ is quite small ($\delta <$ 40 nm), the parts of the crystal moving towards each other by inertia come into contact. Since the process develops quite rapidly, most of the crack surface remains juvenile, which also facilitates the restoration of ionic bonds. The perfection of healing is obviously determined by the difference in the number of emitted and “new” dislocations (and their slip geometry). When these values are comparable, a microvoid in the shape of a narrow channel is preserved at the front of the arrested tip of the crack (position *2* in Fig. 3a). The size of this channel can be reduced at a later stage (second stage of healing) if a fraction of remaining dislocations is absorbed in it as a result of an external factor. In our experiments, such stimulating factors were sample heating and exposure to radiation in the optical wavelength range, which affect the mobility of dislocations and the resistance offered to their motion.

In the “rapid” healing stage, an important factor is obviously the matching of the reliefs of the surfaces coming into contact, which can be perfect.

In the case of considerable plasticity at the tip of the crack, its opening δ is quite large ($\delta >$ 40 nm), and only partial convergence of the opening banks is possible due to the processes described above. An external force action is required for the convergence of the surfaces that are not juvenile any longer. After they come in contact, rows of conventional and reanimating dislocations can be seen on the surface of observation [4–6].

The presence of regions free of dislocations in front of the crack tip is ensured by the relation between the friction forces confining dislocations to the slip band, repulsive forces, and image forces.

Sample annealing activates healing processes due to increasing mobility of dislocations associated with the temperature dependence of friction stress.

On the other hand, the exposure to radiation in the visible range leads to a change in the energy state of dislocations and stoppers and in the photomobility of dislocations [7, 8]. The latter is a function of radiation intensity and the spectral composition of incident light. The simultaneous action of radiation and heating enhances the healing effect.

ACKNOWLEDGMENTS

This research was supported financially by the Russian Foundation for Basic Research (project no. 98-01-00617) and by the Ministry of General and Professional Education (grant for fundamental research in natural science no. 97-0-4.3-185).

REFERENCES

1. J. J. Gilman, *Cleavage, Plasticity, and Viscosity of Crystals: Atomic Mechanism of Fracture* (Metallurgiya, Moscow, 1993).
2. V. A. Fedorov, I. V. Ushakov, and T. N. Pluzhnikova, Vestn. Tambov. Univ. **2**, 291 (1997).
3. N. V. Dorokhova, Ph.D. thesis (1994).
4. V. M. Finkel’ and B. B. Konkin, Fiz. Tverd. Tela (Leningrad) **25**, 1553 (1983) [Sov. Phys. Solid State **25**, 896 (1983)].
5. V. M. Finkel’, O. G. Sergeeva, and V. V. Shegaĭ, Kristallografiya **36**, 170 (1991).
6. V. M. Finkel’ and O. G. Sergeeva, Fiz. Tverd. Tela (Leningrad) **29**, 857 (1987) [Sov. Phys. Solid State **29**, 489 (1987)].
7. G. A. Ermakov and É. M. Nadgornyĭ, Dokl. Akad. Nauk SSSR **181**, 76 (1968).
8. S. I. Bredikhin, Yu. A. Osip’yan, and S. Z. Shmurak, Zh. Éksp. Teor. Fiz. **68**, 750 (1975) [Sov. Phys. JETP **41**, 373 (1975)].

Translated by N. Wadhwa

Physics of the Solid State, Vol. 42, No. 4, 2000, pp. 706–711. Translated from Fizika Tverdogo Tela, Vol. 42, No. 4, 2000, pp. 688–693.
Original Russian Text Copyright © 2000 by Malygin.

**DEFECTS, DISLOCATIONS,
AND PHYSICS OF STRENGTH**

Amplitude-Dependent Internal Friction and Similarity of Temperature Dependences of Microflow and Macroflow Stresses of a Crystal

G. A. Malygin

Ioffe Physicotechnical Institute, Russian Academy of Sciences,
ul. Politekhnicheskaya 26, St. Petersburg, 194021 Russia
e-mail: malygin.ga@pop.ioffe.rssi.ru

Received October 14, 1999

Abstract—A dislocation-kinetic mechanism is discussed of amplitude-dependent internal friction and of the similar temperature dependences of the microflow and yield stresses of a crystal. The similarity of these dependences is shown to be due to the similarity of strain- (dislocation-) strengthening curves of the crystal in the microplastic- and macroplastic-strain ranges, respectively. *© 2000 MAIK “Nauka/Interperiodica”.*

INTRODUCTION

In experiments on amplitude-dependent internal friction (ADIF), it was established that, for microplastic strains $\varepsilon \sim 10^{-9}$–10^{-5}, the temperature dependences of oscillatory stresses are identical to those of the yields at $\varepsilon \sim 10^{-4}$–10^{-3} for the same crystals [1–5]. The microflow and macroflow stresses differ greatly in magnitude (by one or two orders) in the same crystal, and the similarity of their temperature dependences is very difficult to interpret in terms of the models in which ADIF is associated with dislocation hysteresis.

The best known of them is the Granato–Lücke model, according to which dislocations break away from their pinning points and then are again pinned at the same points when the oscillatory stress becomes lower during a cycle [6]. However, it has been clearly demonstrated [4, 7, 8] that this model is only of limited usefulness. There is another (friction stress) model of ADIF [7, 8], which agrees better with the experimental data. In this model, dissipation of the energy of vibrations is associated with the movement of dislocations through large distances and their interaction with a great number of point obstacles.

However, the friction stress model also fails to explain the similarity of the temperature dependences of the microflow and macroflow stresses. Indeed, it is almost unbelievable that, in one crystal, there are two friction stresses (initial micro- and macroflow stresses) having identical temperature dependences. Besides, according to this model, internal friction should increase with the concentration of impurity atoms in the crystal, whereas, experimentally, ADIF decreases with increasing impurity concentration [9].

In this paper, we propose a possible mechanism for ADIF, using a fairly simple dislocation-kinetic model. In terms of this mechanism, we explain the temperature and impurity concentration dependences of ADIF and the similarity of the temperature dependences of the microflow and macroflow stresses of a crystal.

1. THE PHENOMENOLOGICAL MODEL OF ADIF

The hypothesis that ADIF is associated with microplastic deformation of the crystal had been put forward by Davidenkov [10] even before the concept of a dislocation came into wide use in treating the plastic properties of crystalline materials. In this approach, the applied stress σ is commonly assumed [1–5] to be a power low function of the microplastic dislocation strain ε_d,

$$\sigma = \chi_d \varepsilon_d^{1/m}, \tag{1}$$

where χ_d and m are strain-independent parameters. Substituting (1) into a general expression for the coefficient of hysteretic internal friction [8]

$$\delta_h = \frac{2E}{\sigma_0^2}\left[\sigma_0\varepsilon_d(2\sigma_0) - \int_0^{2\sigma_0} \varepsilon_d(\sigma)d\sigma\right], \tag{2a}$$

we find the amplitude dependence of ADIF

$$\delta_h(\varepsilon_0) = 2^{m+1}\frac{m-1}{m+1}\left(\frac{E}{\chi_d}\right)^m \varepsilon_0^{m-1}, \tag{2b}$$

where $\varepsilon_0 = \sigma_0/E$, and σ_0 is the amplitude of oscillatory stresses. The modulus defect ($\Delta E/E \ll 1$) is given by the expression

$$\frac{\Delta E}{E} = \frac{\varepsilon_d}{\varepsilon_0} = \left(\frac{E}{\chi_d}\right)^m \varepsilon_0^{m-1}. \tag{3}$$

Therefore, δ_h is proportional to $\Delta E/E$ [4],

$$r = \delta_h/(\Delta E/E) = 2^{m+1}\frac{m-1}{m+1}, \tag{4}$$

where the coefficient of proportionality r is dependent only on the exponent in (1). Relations (2b)–(4) form the basis of currently available phenomenological models of ADIF and the modulus defect, which are consistent with the experimental data [1–5].

Combining (2b), (3), and the relation $\varepsilon_d = r^{-1}\delta_h\varepsilon_0 = (\sigma_0/\chi_d)^m$, one obtains

$$\sigma_0 = \chi_d\varepsilon_d^{1/m}. \tag{5}$$

Hence, the phenomenological model predicts that the temperature dependences of the decrement in (2b) and the microflow stress (5) are dictated by the temperature dependences of the parameters χ_d and m. Experiment shows that, in most cases, the exponent m in expression (2b) for the internal friction coefficient is temperature independent in a wide temperature range [1–5]; hence, the temperature dependences of δ_h and σ_0 in the same crystal are controlled by that of the parameter χ_d. In a number of cases, as was shown in [1–4], the temperature dependence of σ_0 can be approximated by an exponential function

$$\sigma_0(T) = \chi_d(0)\exp(-BT)\varepsilon_d^{1/m}, \tag{6}$$

where $\chi_d(0)$ is the value of χ_d at zero temperature and B is a constant.

At the initial stage of macroplastic deformation of a crystal, the stress σ_p is also a power-low function of the strain ε_p (see below),

$$\sigma_p = \chi_p\varepsilon_p^{1/p}. \tag{7}$$

Therefore, the temperature independence of the ratio between the macroplastic and microplastic stresses

$$\Pi = \frac{\sigma_p}{\sigma_0} = \left(\frac{\chi_p}{\chi_d}\right)\frac{\varepsilon_p^{1/p}}{\varepsilon_d^{1/m}} \tag{8}$$

is due to the similarity of the temperature dependences of the coefficients χ_d and χ_p, entering the phenomenological relations (5) and (7), respectively.

2. A MICROSCOPICAL MECHANISM OF ADIF

A microscopic (dislocation) model of hysteretic internal friction and the yield should elucidate the origin of relations (1) and (7) with typical values of the exponents equal to $m = 2$–4 [4] and explain the temperature dependences of oscillatory stresses (6) and ADIF decreasing in doped samples.

We will assume that the generation of dislocations by their sources and multiplication of dislocations through the mechanism of double cross glide (DCG) of screw dislocations occur even in the range of microplastic deformations. In this case, the rate of increase of the density of mobile dislocations ρ is given by the kinetic equation [11]

$$\frac{d\rho}{dt} = \frac{n_s u}{l_F} + \frac{u}{\lambda_s}\rho, \tag{9a}$$

where t is the time, u is the velocity of dislocations, n_s is the density of dislocation sources per unit area of a glide plane, l_F is the critical length for the operation of a dislocation source of the Frank–Read type, and λ_s is the path that dislocations travel between successive acts of dislocation multiplication by the DCG mechanism.

With the left-hand side of (9a) written as $d\rho/dt = (d\rho/d\varepsilon)\dot{\varepsilon}$, where $\dot{\varepsilon} = b\rho u$ is the plastic strain rate and b is the Burgers vector, equation (9a) becomes

$$\rho\frac{d\rho}{d\varepsilon} = \frac{n_s}{bl_F} + \frac{\rho}{b\lambda_s}. \tag{9b}$$

At the very initial stage of crystal deformation, the increase of the density of dislocations is due to their generation from dislocation sources. Keeping only the first term in the right-hand side of (9b) and integrating the equation, we obtain the dislocation density as a function of the amount of plastic strain ε,

$$\rho = \left(\frac{2n_s}{bl_F}\right)^{1/2}\varepsilon^{1/2}. \tag{10}$$

But if the density of sources is low and multiplication of dislocations by the DCG mechanism is dominant in (9b), we have

$$\rho = \frac{\varepsilon}{b\lambda_s}. \tag{11}$$

Under single-glide conditions, the flow stress due to the Taylor interaction between dislocations opposite in sign on adjacent glide planes is equal to $\sigma = \alpha\mu b\rho^{1/2}$, where α is the dislocation interaction constant and μ is the shear modulus. Substituting (10) and (11), we obtain expressions (5) and (7), respectively, for the stress as a function of strain,

$$\sigma = \chi_F\varepsilon^{1/4}, \quad \chi_F = \alpha\mu b\left(\frac{n_s}{bl_F}\right)^{1/4}, \tag{12a}$$

$$\sigma = \chi_s\varepsilon^{1/2}, \quad \chi_s = \alpha\mu b\left(\frac{1}{b\lambda_s}\right)^{1/2}. \tag{12b}$$

The strain dependences of the dislocation density and stress, similar to (10)–(12), were observed [11, 12] at the initial stage of crystal deformation. The exponents intermediate between (12a) and (12b) ($\sigma \sim \varepsilon^{1/3}$) were observed in the single copper crystals for strain amounts $\varepsilon = 10^{-5}$–10^{-3} [13]. A dislocation model describing such a strain dependence of the stress was proposed in [14].

A power dependence similar to (5) and (7) was also observed in the case of cyclic plastic deformation in experiments on the mechanical fatigue of crystals for cyclic-strain amplitudes $\varepsilon = 10^{-5}$–10^{-2}; the exponent in the fatigue strengthening law $\sigma \sim \varepsilon^s$ was measured to be $s = 0.2$–0.3 [15, 16]. It is of interest that small values of s were observed when the oscillatory stress applied to a crystal had no constant component. When the latter was nonzero, the exponent increased and was as large as 0.5 [16]. In terms of the kinetic model proposed in this paper for the initial stage of plastic deformation of crystals, this means that, in the case where the constant component of the oscillatory stress is absent, the paths traveled by dislocations generated by dislocation sources are not large enough for the dislocation multiplication to occur through the DCG mechanism. In the presence of a constant stress component, the paths of dislocations become larger and, hence, more favorable to the operation of the DCG mechanism.

Thus, the power dependences of oscillatory-stress amplitudes on dislocation strain [relation (1)] observed in experiments on ADIF are not of the nature typical for this type of crystal loading. The same power dependences with exponents between 0.2 and 0.5 take place under fatigue conditions and in the usual case of deforming with a constant strain rate at the initial stage of plastic deformation. Therefore, in order to develop a microscopic model of ADIF, one should refine some of the assumptions forming the basis for the dislocation models proposed earlier for hysteretic internal friction.

The first assumption is that no new dislocations are generated in the process of ADIF, and, hence, dissipation of the energy of vibrations is associated with the movement of the dislocations already existing in the crystal at the instant the oscillatory stress is applied. This is suggested by the fact that, if the stress amplitude does not exceed a certain critical value, the amplitude dependence of the decrement shows no hysteresis and the amplitude-independent component of internal friction remains unchanged after cyclic loading of the crystal.

The second assumption is about the shape of dislocations that perform reciprocating motion under the action of oscillatory stresses. It is commonly assumed that they are straight lines and their number remains constant during a loading cycle. When the stress changes its sign, the dislocations reverse their direction of motion and displace in the opposite direction with respect to their initial equilibrium positions.

Both assumptions provide no explanation for the nonlinear, power-low dependence of the stress amplitude on the amount of plastic strain [relation (5)]. This dependence can be explained in terms of the kinetic model based on (9)–(12). According to this model, the application to a crystal of oscillatory stresses of even a very small amplitude causes the generation of dislocation loops from a number of efficient sources. The dislocation loops expand to a certain size and then, as the oscillatory stress falls to zero, they contract (under the action of the line tension) to a size depending on the magnitude of the friction stress. When the applied stress changes its sign, the dislocation loops collapse (to zero radius) and then they are again generated during the negative stress half-cycle. The cyclic dynamic process of the expansion and contraction of dislocation loops in the crystal and their interaction with each other leads to hysteresis in stress–strain curves, which manifests itself either in the form of a Davidenkov hysteresis loop [10] (in the presence of a restoring force due to the line tension of dislocations) or in another form (in the absence of a restoring force) [4] if the friction stress far exceeds the stress due to the dislocation line tension.

Since this dynamic process is not accompanied by irreversible accumulation of dislocations in the crystal, it does not give rise to hysteresis in the amplitude dependence of internal friction. However, when the amplitude of oscillatory stress becomes large enough for the dislocation multiplication to occur through the DCG mechanism during the expansion of dislocation loops [17], dislocations will be accumulated in the form of immobile dislocation dipoles, which will not take part in the dissipation of the energy of vibrations. The density of mobile dislocations also increases in this case, but the increase is not large enough to give rise to a noticeable hysteresis in the amplitude dependence of the decrement of vibrations, because the magnitude of the applied stress is small. The situation is reversed for large amplitudes of vibration, corresponding to the yield of the crystal, where large-scale multiplication of dislocations occur in the form of broadening slip bands [17, 18].

In the experiments on ADIF, dislocations travel large distances during a cycle of vibration. This was demonstrated in [19] in experiments on internal friction in polycrystalline copper, where it was established that the decrement becomes sensitive to the size of crystallites when the latter is less than 80 μm. The microflow stress increases with decreasing grain size, whereas internal friction, on the contrary, decreases. This agrees well with the kinetic model, according to which, if the paths of dislocations are restricted to the grain size d [i.e., $\lambda_s = d$ in (12b)], we have $\chi_s \sim d^{-1/2}$ and, hence, $\sigma_0 \sim d^{-1/2}$ [20] (Hall–Petch relationship) and $\delta_h = d^{m/2}$. Taking the paths of dislocations to be of the order of 80 μm and the Burgers vector to be 0.3 nm, we obtain that the density of dislocations corresponding to the microplastic strain $\varepsilon_d \approx 10^{-10}$–$10^{-8}$ in experiments on internal friction should be equal to $\rho = \varepsilon_d / b\lambda_s \approx 1 - 10^2$ cm^{-2}, which is far less than, for instance, the density of growth dislocations in copper, $\rho_0 = 10^4$–10^6 cm^{-2} [21]. This means that, under ADIF conditions, only a small proportion of all dislocations and, hence, a small fraction of the crystal volume are involved in the process of dissipation of the vibration energy. At the values of the microplastic strain indicated above and frequencies $\omega = (10$–$100)$ kHz, the average microplastic strain rate $\dot{\varepsilon}_d = \omega\varepsilon_d$ is of the same order 10^{-6}–10^{-3} s^{-1} as under conditions of macroplastic strain. These results should be taken into account in quantitative evaluations of the absolute magnitudes of ADIF and microplastic stresses.

3. THE SIMILARITY LAW OF THE TEMPERATURE DEPENDENCES OF STRESSES

As indicated above, the temperature dependences of the decrement δ_h and microplastic stresses σ_0 are dictated by the temperature dependence of the parameter χ_d or, according to the microscopic model of ADIF under consideration, by the temperature dependences of the parameters l_F and λ_s in expressions (12a) and (12b). Substituting (12a) and (12b) into (2b), we obtain, respectively,

$$\delta_h(\varepsilon_0) = \frac{12\beta}{5\alpha^4}\left(\frac{l_F}{b^3 n_s}\right)\varepsilon_0^3, \tag{13a}$$

$$\delta_h(\varepsilon_0) = \frac{2\beta}{3\alpha^2}\left(\frac{\lambda_s}{b}\right)\varepsilon_0, \tag{13b}$$

where β is the fraction of the crystal volume involved in the process of dissipation of the energy of vibration.

In experiments on alkali halide crystals, it was found [17] that the coefficient of dislocation multiplication by the DCG mechanism $(b\lambda_s)^{-1}$ increases linearly with the friction stress $\sigma_f = \sigma^* + \sigma_C$, where σ^* is the friction stress component due to thermally activated motion of dislocations (dependent on the temperature and strain rate) and σ_C is the friction stress component associated with the presence of athermic obstacles to the motion of dislocations. One can write an empirical relationship between λ_s and σ_f in the form

$$\lambda_s = g_s\frac{\mu}{\sigma_f}b, \tag{14}$$

where $g_s \approx (1–2) \times 10^2$. As for the temperature dependence of the critical length for the operation of a Frank–Read source l_F, it was found, by modeling the operation of a dislocation source in the field of thermally activated obstacles and athermal ones [22], that the time length for the operation of a source is temperature dependent. Therefore, the stress and the critical length for the operation of a source also depend on the temperature, and one can write

$$l_F = g_F\frac{\mu}{\sigma_f}b, \tag{15}$$

where $g_F \approx 3$–5.

Thus, according to our model, the dependences of ADIF and vibration amplitudes on the temperature, strain rate, and concentration of obstacles are determined by the dependence of the friction stress σ_f on the temperature, strain rate, and concentrations of thermic (c) and athermic (C) obstacles to the dislocation motion ($\sigma_f \sim c^n$ and $\sigma_f \sim C^n$ with $n = 0.5$–1 [23]). Therefore, if the mechanisms of microflow and macroflow of a crystal are identical (generation of dislocations from sources or multiplication of dislocations through the DCG mechanism), the coefficient Π, defined in (8), will be temperature independent,

$$\Pi = \left(\frac{\varepsilon_p}{\varepsilon_d}\right)^{1/m}, \tag{16}$$

and the similarity law of the microflow and macroflow stresses will take place. Otherwise we will have $p \neq m$ in (8) and, as is seen from (12), the similarity of the stresses will be absent. Experimentally, both the situations occur [1].

As for the temperature dependence of the friction stress and of the microflow and macroflow stresses in the form of (6), $\sigma \sim \exp(-BT)$, it is of importance to elucidate the origin of this non-Arrhenius dependence, because, in the cases where experimental data are closely approximated by a dependence of this type, the fairly radical inference is made that the dislocation movement in crystals is due to thermal vibrations of atoms, rather than to thermal fluctuations [24].

This form of the temperature dependence of the microflow and macroflow stresses is the consequence of the approximation of the stress dependence of the plastic strain rate by a power-low function

$$\dot{\varepsilon} = \dot{\varepsilon}_\nu\left(\frac{\sigma - \sigma_C}{\sigma_c}\right)^{m_c}, \tag{17a}$$

where $m_c = H_c/kT$, H_c is a constant with dimensions of energy, k is the Boltzmann constant, and σ_C is the critical stress above which the plastic deformation begins. Indeed, it follows from (17a), that

$$H(\sigma) = H_c\ln\frac{\sigma_c}{\sigma - \sigma_C} = kT\ln\frac{\dot{\varepsilon}_\nu}{\dot{\varepsilon}}, \tag{17b}$$

$$\sigma = \sigma_C + \sigma_c\exp(-BT), \quad B = (K/H_c)\ln(\dot{\varepsilon}_\nu/\dot{\varepsilon}). \tag{17c}$$

Although logarithmic dependences of the activation energy H on the stress occur in theory of thermally activated motion of dislocations, they refer to special cases and cannot be associated with empirical relations (17), universal in some sense.

As indicated in [25], this universality is due to the fact that, in the cases where dislocations have to overcome fairly high athermal barriers for their thermally activated movement to begin (as, for example, in the Orowan process of pushing dislocations through a system of particles or precipitates), the stress dependence of the activation energy has the form $H(\sigma) = H(\sigma - \sigma_C)$, where σ_C is the critical stress for overcoming the barri-

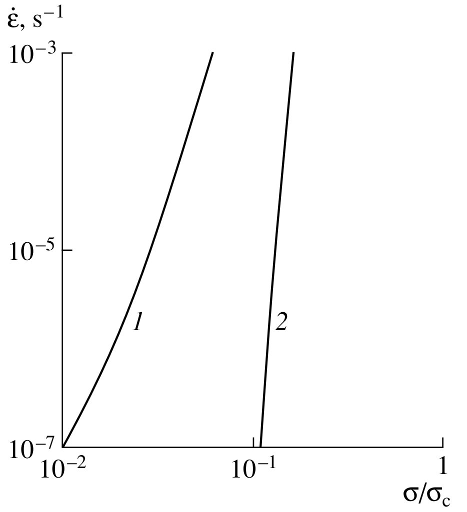

Fig. 1. Stress dependence of the plastic strain rate in the absence (curve *1*) and presence (curve *2*) of athermic obstacles to thermally activated motion of dislocations.

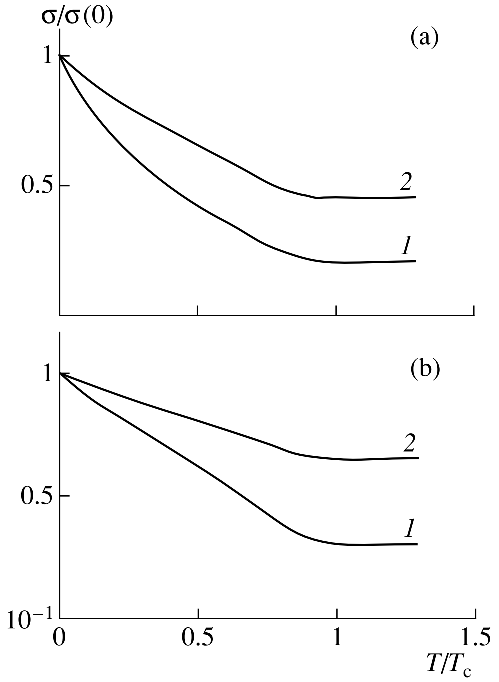

Fig. 2. (a) Temperature dependences of the microflow and macroflow stresses as given by (12a) (curve *1*) and (12b) (curve *2*) and (b) the same dependences at the semilogarithmic scale.

ers. This expression can be represented in a more general form [25]

$$H = H_c\left[1 - \left(\frac{\sigma - \sigma_C}{\sigma_c}\right)^p\right]^q, \qquad (18)$$

where $0 < p < 1$ and $1 < q < 2$. Substituting (18) into the Arrhenius equation for the plastic strain rate, we obtain

$$\dot{\varepsilon} = \dot{\varepsilon}_\nu \exp[-H(\sigma)/kT]. \qquad (19)$$

Figure 1 presents log–log plots of the $\dot{\varepsilon}(\sigma)$ dependence given by (19) for the athermal stress σ_C equal to zero (curve *1*) and for $\sigma_C = 0.1\sigma_c$ (curve *2*). The calculation is performed for the parameters $H_c/kT = 40$, $\dot{\varepsilon}_\nu = 10^7$ s^{-1}, $p = 1/2$, and $q = 3/2$. It is seen that, in the case of a nonzero critical stress, a $\log\dot{\varepsilon} - \log\sigma$ curve can be closely approximated by a straight line; hence, it is described by the power law of (17a), even though the dislocation movement is determined by the Arrhenius law (19).

It follows from (18) and (19), that the temperature dependence of the friction stress has the form

$$\begin{aligned} \sigma_f(T) &= \sigma_C + \sigma_c[1 - (T/T_c)^{1/q}]^{1/p}, \\ T_c &= H_c/k\ln(\dot{\varepsilon}_\nu/\dot{\varepsilon}). \end{aligned} \qquad (20)$$

Substituting this expression for σ_f into (14) and (15) and the results into (12a) and (12b), respectively, we obtain the temperature dependences of the microflow and macroflow stresses of the crystal. Figure 2a shows these dependences for the stresses normalized to their value $\sigma(0)$ at $T = 0$ and for the values of parameters $p = 1/2$, $q = 3/2$, and $\sigma_C/\sigma_c = 0.04$. Figure 2b shows $\log\sigma$–T plots of the same dependences. It is seen that the curves can be approximated by the exponential dependence (17c), which is often done for experimental data. Clearly, the possibility of such an approximation does not necessarily mean that the mechanism of dislocations overcoming barriers has nothing to do with thermal fluctuations [24].

Substituting (14) and (15) into (13b) and (13a), respectively, we arrive at the result that the coefficient of internal friction varies in inverse proportion to the friction stress,

$$\delta_h = A_s\left(\frac{\mu}{\sigma_f}\right)\varepsilon_0, \quad A_s = \frac{2\beta g_s}{3\alpha^2}, \qquad (21a)$$

$$\delta_h = A_F\left(\frac{\mu}{\sigma_f}\right)\varepsilon_0^3, \quad A_F = \frac{12\beta g_F}{5\alpha^4 b^2 n_s}. \qquad (21b)$$

Therefore, the temperature and concentration dependences of ADIF are dictated by the corresponding dependences of the friction stress (20). Hence, the internal friction coefficient decreases with increasing concentration of impurity atoms, in accordance with [9].

CONCLUSION

Thus, we have shown that, if the physical mechanisms of dislocation strengthening in the process of microflow and macroflow of a crystal are identical, the similarity of the temperature dependences of the corresponding stresses will be observed. In this case, the scaling factor (8) is determined by the amount of strain. For instance, at $\varepsilon_p/\varepsilon_d = 10^4$ and $p = m = 2–4$, we have $\Pi = 10–10^2$. The absence of the similarity does not imply that the physical mechanisms of micro- and macroflow of the crystal are radically different, but it merely means that, at a given crystal structure, different mechanisms of multiplication or interaction of dislocations operate in the processes of microflow and macroflow. The dislocation-kinetic model considered in this paper allows one to consistently explain this fact and the effect of factors determining the magnitude of ADIF.

REFERENCES

1. A. B. Lebedev and S. B. Kustov, Phys. Status Solidi A **116**, 645 (1989).
2. A. B. Lebedev, Fiz. Tverd. Tela (Leningrad) **34**, 1889 (1992) [Sov. Phys. Solid State **34**, 1008 (1992)].
3. A. B. Lebedev, J. Alloys Compd. **211/212**, 177 (1994).
4. A. B. Lebedev, J. Phys. IV (Paris) **6** (C8), 255 (1996).
5. Y. Nishino, Y. Okada, and A. Asano, Phys. Status Solidi A **129**, 409 (1992).
6. A. V. Granato and K. Lücke, J. Appl. Phys. **52**, 7136 (1981).
7. V. A. Chelnokov and N. L. Kuz'min, Fiz. Tverd. Tela (Leningrad) **22**, 3000 (1980) [Sov. Phys. Solid State **22**, 1751 (1980)].
8. A. Asano, Jpn. J. Phys. **29**, 952 (1970).
9. K. V. Sapozhnikov, S. N. Golyandin, S. B. Kustov, *et al.*, Philos. Mag. A **77**, 151 (1998).
10. N. N. Davidenkov, Zh. Tekh. Fiz. **8**, 483 (1938).
11. G. A. Malygin, Fiz. Tverd. Tela (Leningrad) **35**, 1328 (1993) [Phys. Solid State **35**, 855 (1993)].
12. J. Man, M. Holzmann, and B. Vlach, Phys. Status Solidi A **19**, 543 (1967).
13. A. S. Argon and W. T. Bridges, Philos. Mag. **18** (154), 817 (1968).
14. F. R. N. Nabarro, in *Strength of Metals and Alloys* (ICSMA7), Ed. by H. J. McQueen *et al.* (Pergamon, 1985), Vol. 3, p. 1667.
15. A. Giese, A. Styzcynski, and Y. Estrin, Mater. Sci. Eng. A **124**, L11 (1990).
16. P. Lucas, L. Kunz, B. Weiss, *et al.*, Mater. Sci. Eng. A **118**, L1 (1989).
17. B. I. Smirnov, *Dislocation Structure and Hardening of Crystals* (Nauka, Leningrad, 1981).
18. É. P. Belozerova and N. A. Tyapunina, Kristallografiya **11**, 651 (1966).
19. H. Goto, Y. Nishino, and S. Asano, J. Jpn. Inst. Met. **55**, 848 (1991).
20. V. A. Chelnokov and N. L. Kuz'min, Fiz. Tverd. Tela (Leningrad) **24**, 3166 (1982) [Sov. Phys. Solid State **24**, 1796 (1982)].
21. H. Mecking and G. Bulian, Acta Metal. **24**, 249 (1976).
22. T. N. Golosova, M. I. Slobodskoĭ, and L. E. Popov, Izv. Vyssh. Uchebn. Zaved., Fiz. **35**, 20 (1992).
23. P. Haazen, in *Dislocations in Solids*, Ed. by F. R. N. Nabarro (North Holland, 1979), Vol. 4, p. 157.
24. A. B. Lebedev, in *Strength of Materials* (ICSMA10), Ed. by H. Oikawa *et al.* (Jpn. Inst. Met., Sedai, 1994), p. 195.
25. U. F. Kocks, A. S. Argon, and M. F. Ashby, in *Thermodynamics and Kinetics of Slip* (Pergamon, New York, 1975), pp. 141–170.

Translated by Yu. Epifanov

Physics of the Solid State, Vol. 42, No. 4, 2000, pp. 712–718. Translated from Fizika Tverdogo Tela, Vol. 42, No. 4, 2000, pp. 694–700.

MAGNETISM AND FERROELECTRICITY

Features of the Phonon Localization near the Surface of a Low-Temperature Antiferromagnet

S. V. Tarasenko

Donetsk Physicotechnical Institute, National Academy of Sciences of Ukraine,
Donetsk, 340114 Ukraine

Received August 6, 1999

Abstract—Necessary conditions are determined under which elastic surface shear waves can exist in a crystal with magnetic long-range order, even if no account is taken of the magnetic dipole–dipole interaction, in both the case of the mechanically free surface of the crystal and the case of an acoustically continuous interface between the magnetic crystal and a nonmagnetic medium. © *2000 MAIK "Nauka/Interperiodica".*

INTRODUCTION

It is well known that, in terms of both the crystal-lattice dynamics and the elastic-continuum theory, the mechanically free surface of a half-space of an elastic medium can be considered as a local distortion of an infinite perfect medium [1]. In this case, a surface acoustic wave (SAW) propagating along the crystal boundary can be treated as a localized vibration mode of an infinite crystal with a planar defect [2]. The problem of existence and uniqueness of solutions to the equations of the elasticity theory in the form of SAWs has been analytically solved for a mechanically free surface [3–5], as well as for a loaded boundary of a nonmagnetic crystal [6]. In particular, it was shown that, in the case of the mechanically free crystal surface, a SAW can propagate in any direction except a few certain ones. For the latter directions, the boundary conditions are fulfilled for a pure shear bulk wave, and the problem of existence of SAWs should be solved separately in this geometry; the bulk elastic wave is unstable and transforms into a SAW even when the boundary conditions are varied only slightly. An example is the formation of a wave of the Bleustein–Gulyaev type when allowances are made for the piezoelectric [7, 8] or the piezomagnetic [9, 10] interaction in the crystal, or the formation of a Love wave in the case where the surface of a semi-infinite crystal (medium 1) is in hard acoustic contact with the surface of a layer (medium 2) and the elastic constants of the media satisfy the condition

$$s_1 > s_2, \tag{1}$$

where s_1 and s_2 are the velocities of an elastic shear wave in unbounded media 1 and 2, respectively. If the inequality opposite to (1) takes place, only the Bleustein–Gulyaev mechanism will govern the formation of an elastic shear wave, with its wave vector $\mathbf{k} \parallel x$ and particle displacements $\mathbf{u} \parallel z$, propagating near the mechanically free surface of a semi-infinite medium or near the acoustically continuous interface between media 1 and 2 (no matter how thick the layer of the nonpiezoelectric insulating medium is) when an external electric field $\mathbf{E} \parallel z$ is applied along the z axis parallel to the interface. (The coordinate system is set with the y axis along the normal $\mathbf{n} \parallel y$ to the surface of semi-infinite medium 1.)

This is also true in the case of the mechanically free boundary of a magnetic medium, or the acoustically continuous interface between a magnetic and a nonmagnetic insulating medium, if the temperature T is higher than the Curie temperature T_C, an external magnetic field $\mathbf{H}$ is applied along the z axis parallel to the interface, and, in addition, $\mathbf{k} \parallel x$, $\mathbf{u} \parallel z \parallel \mathbf{H}$, and $\mathbf{n} \parallel y$. At $T < T_C$, the magnetic long-range order significantly affects the spectrum of surface shear waves in the magnet as compared to the spectrum at $T > T_C$. This was first shown by Parekh in [11], where the formation of shear SAWs was studied in a half-space of a ferromagnetic medium with a mechanically free surface in the case of $\mathbf{k} \parallel x$, $\mathbf{u} \parallel z \parallel \mathbf{H} \parallel \mathbf{M}$, and $\mathbf{n} \parallel y$, $\mathbf{H}$, and $\mathbf{M}$ along the z axis (here, $M = M_0$ is the saturation magnetization). The Parekh SAW, as well as the Bleustein–Gulyaev wave at $T > T_C$, is a combination of two partial waves when the magnetic dipole–dipole interaction and the magnetoelastic coupling are taken into account. However, in a ferromagnet with $M_z \neq 0$ ($\mathbf{M} \perp \mathbf{k}_\perp$; $\mathbf{M} \perp \mathbf{n}$), the dispersion relation for the Parekh wave $\omega(\mathbf{k}_\perp)$ ($\mathbf{M} \perp \mathbf{k}_\perp$) has several branches and $\omega(k_\perp) \neq \omega(-k_\perp)$; that is, there is no reciprocity with respect to the inversion of the propagation direction.

To elucidate the mechanisms of the formation of the Parekh SAW, let us consider the basic relations [12] determining the spectrum and spatial structure of this wave

$$\alpha = \frac{\omega_{\mathrm{me}}(\omega - s\omega_+)(\omega + s\omega_-)}{(\omega_{DE} - s\omega)[\omega^2 - \omega_0(\omega_0 + \omega_M - \omega_{\mathrm{me}})]}, \qquad \omega_\pm = \frac{[\omega_0(\omega_0 + 2\omega_M)]^{1/2} \pm \omega_0}{2}, \tag{2}$$

$$\frac{\omega^2}{s_t^2 k_\perp^2} = (1 - \alpha^2)\frac{\omega_0(\omega_0 + \omega_M) - \omega^2}{\omega_0(\omega_0 + \omega_M - \omega_{\mathrm{me}}) - \omega^2}. \tag{3}$$

Here, $\omega_{DE} = (2\omega_0 + \omega_M)/2$, $s \equiv k_\perp/|\mathbf{k}_\perp|$, $\omega_0 = \omega_{\mathrm{a}} + \omega_H + \omega_{\mathrm{me}}$, ω_{a} is the “activation frequency” for the FMR spectrum due to uniaxial magnetic anisotropy, $\omega_H = gH$, ω_{me} is the magnetoelastic gap, $\omega_M = 4g\pi M_0$, g is the gyromagnetic ratio, M_0 is the saturation magnetization, and s_t is the phase velocity of an elastic shear (SH) wave in the unbounded medium at $T > T_C$.

The structure of the amplitude of the magnetostatic potential in nonmagnetic medium 1 ($y < 0$) and magnetic medium 2 ($y > 0$) is presented as

$$\begin{aligned}\phi_{1,2} &= [A_{1,2}\exp(i\omega t - \alpha_{1,2}k_\perp y) \\ &+ B_{1,2}\exp(i\omega t - \beta_{1,2}k_\perp y)]\exp(i\omega t - ik_\perp x),\end{aligned} \tag{4}$$

In (4), we have $\alpha_1 = -1$ and $\beta_1 = B_1 = 0$ for $y > 0$, and $\beta_2 = 1$ and $\alpha_2 = \alpha$ is determined from (2) for $y < 0$. Analysis of (2)–(4) shows that the elastic surface shear wave calculated by Parekh in [11] differs in properties from the Bleustein–Gulyaev wave at $T > T_C$. Indeed, in the paramagnetic phase ($T > T_C$), the formation of the Parekh wave at $H_z \neq 0$ is due to the hybridization of the magnetic dipolar and magnetoelastic interactions in the vicinity of the planar crystal surface, whereas at $T < T_C$, this wave is not delocalized ($\alpha \neq 0$) even when the magnetic dipolar interaction is absent, as is seen from (2)–(4), in which we should formally put 4π equal to zero in order to go to this limit. At the same time, going to the analogous limit in relations for the spectrum of the Bleustein–Gulyaev wave leads to the delocalization of this surface wave ($\alpha \longrightarrow 0$) at $T > T_C$ and in the same geometry ($\mathbf{H} \parallel z$, $\mathbf{k}_\perp \parallel x$, and $\mathbf{n} \parallel y$).

Let us elucidate why the spontaneous magnetization of a crystal $\mathbf{M} \parallel \mathbf{H} \parallel z$ leads to the formation of a SAW ($\mathbf{n} \perp \mathbf{u} \parallel \mathbf{H} \perp \mathbf{k}_\perp$) on the mechanically free surface of the magnet even if the magnetic dipole–dipole interaction is not taken into account. For the geometry indicated above, we can write the following system of dynamic equations [12] describing the propagation of an elastic shear wave $\mathbf{u} \parallel z$ of a frequency ω, coupled with a spin wave, in a ferromagnet in the magnetostatic approximation (B_{44} is the magnetostriction constant and c_{44} is the elastic constant):

$$\begin{aligned} i\omega m_x &= \omega_0 m_y + \frac{gB_{44}}{M_0}\frac{\partial u_z}{\partial y} + \frac{\omega_M}{4\pi}\frac{\partial \phi_2}{\partial y}, \\ i\omega m_y &= -\omega_0 m_x - \frac{gB_{44}}{M_0}\frac{\partial u_z}{\partial x} - \frac{\omega_M}{4\pi}\frac{\partial \phi_2}{\partial x}, \\ \frac{\omega^2}{s_t^2}u_z &= \Delta u_z + \frac{B_{44}}{c_{44}}\left(\frac{\partial m_x}{\partial x} + \frac{\partial m_y}{\partial y}\right), \\ \Delta\phi_2 &= 4\pi\left(\frac{\partial m_x}{\partial x} + \frac{\partial m_y}{\partial y}\right). \end{aligned} \tag{5}$$

The boundary conditions at $y = 0$ have the form (σ_{ik} is the elastic stress tensor)

$$\sigma_{xy} = 0, \quad \phi_1 = \phi_2, \quad \frac{\partial \phi_2}{\partial y} + 4\pi m_y = \frac{\partial \phi_1}{\partial y}. \tag{6}$$

Analysis of (5) and (6) in the formal limit of $4\pi \longrightarrow 0$ shows that a shear SAW is formed on the mechanically free surface of the ferromagnet even in the absence of the magnetic dipole–dipole interaction; this is because the magnetic medium possesses acoustic activity in the plane of propagation (xy) of the elastic SH wave (in the geometry under consideration). It is easy to verify that the spectrum of this surface wave has no symmetry with respect to the inversion of the propagation direction [$\omega(k_\perp) \neq \omega(-k_\perp)$] and consists of several branches separated by gaps.

Passing to another formal limit as $B_{44} \longrightarrow 0$ in (2)–(6), that is, neglecting the coupling between the spin and elastic subsystems, we obtain (for the same mutual orientation of the vectors $\mathbf{n}$, $\mathbf{M}$, and $\mathbf{k}_\perp$) the dispersion relation for the magnetic surface *TE*-type polariton (Damon–Eshbach wave) in the magnetostatic approximation.

Thus, the Parekh two-partial surface acoustic wave [11] is the result of hybridization between two types of partial surface excitations in the magnetic gyrotropic crystal, namely, the magnetic surface *TE*-type polariton and the shear surface *SH* wave (with no magnetic dipole–dipole interaction). In fact, the Parekh wave [11, 12] is a particular case of the surface phonon–magnon TE-type polariton that originates from an acoustic, rather than optical, phonon.

However, the efficiency of this mechanism of the transverse-phonon localization is rather low in ferromagnets because of the relative smallness of the magnetoelastic effect as compared to that of the magnetic dipole–dipole interaction. At the same time, it is well known [13] that, in antiferromagnets (AFMs), the exchange interaction enhances the magnetoelastic coupling and weakens the magnetic dipole–dipole interaction, so that the above-mentioned (nonmagnetodipolar) mechanism of the formation of a shear SAW may be important in these materials. The conditions under which the magnetic surface *TE* polaritons are formed and propagate in AFMs of the easy-axis type in the absence of the magnetoelastic coupling were investigated in detail in [14–16] with and without allowances made for electromagnetic retardation effects.

There are a lot of papers in which the conditions for the formation and propagation of shear SAWs in antiferromagnets were analyzed (see, e.g., [12]). However, in all of them, a number of restrictive assumptions were made: (1) Only the magnetodipolar mechanism for the formation of two-partial shear SAWs (Bleustein–Gulyaev mechanism) was treated in them. (2) The SAW spectrum was analyzed under the assumption that the wave frequency ω satisfies the condition

$$\omega \ll \omega_{\mathrm{AFM}}, \tag{7}$$

where ω_{AFM} is the AFMR frequency. Hence, the calculations are valid for high-temperature AFMs ($T_{\mathrm{N}} > T_{\mathrm{D}}$, where T_{N} and T_{D} are the Néel and Debye temperatures, respectively [17]) for any value of the wave number $k_{\perp}$, whereas in the case of low-temperature AFMs ($T_{\mathrm{D}} > T_{\mathrm{N}}$ [17]), the results of [11] are true, because of (7), only in the range of small wave numbers as compared to k_{mph} (k_{mph} is determined from the conditions for the magnetoacoustic resonance). (3) The effect of gyrotropy on the formation of a shear SAW has not been considered in all of those papers. (4) The case of a mechanically free surface of the magnet was only investigated. Finally, (5) calculations were made for the case of a half-space of a magnetic material rather than for an actual magnet of a finite size.

In this paper, we neglect the magnetic dipole–dipole interaction in AFMs, because it is small as compared to the magnetoelastic coupling, and investigate the localization of transverse phonons due to mechanisms other than the magnetodipolar one in the vicinity of either the mechanically free surface of a low-temperature AFM or the acoustically continuous interface between a low-temperature AFM and a nonmagnetic medium. We assume that the elastic parameters of the magnetic and nonmagnetic media are such that inequality (1) takes place at $T > T_N$, with medium 1 being nonmagnetic and medium 2, antiferromagnetic.

In Section 1 of this paper, we present the basic equations and formulate the corresponding boundary-value problem. In Section 2, in an exchangeless approximation (ignoring the nonhomogeneous exchange interaction), we analyze nonmagnetodipolar mechanisms of the formation of a shear SAW and its dispersion properties in the case of a semi-infinite low-temperature AFM in a collinear phase. The dependence on an external magnetic field, which is assumed to be applied along the easy axis parallel to the surface of the AFM is investigated. We consider both the case of the mechanically free AFM surface and the case where this surface is in continuous acoustic contact with a nonmagnetic film of a finite thickness. The effect of the finite sizes of a magnet and its nonmagnetic cover on the spectrum of shear SAWs under study is analyzed in Section 3. The dispersion features of these SAWs associated with the nonlocal nature of the Heisenberg mechanism of the spin–spin exchange and with dissipation processes are also discussed in that section. Finally, in the last section, we formulate the main conclusions reached in this paper.

1. THE BASIC EQUATIONS

We consider a two-sublattice AFM of the easy-axis type with sublattice magnetizations $\mathbf{M}_1$ and $\mathbf{M}_2$ ($|\mathbf{M}_1| = |\mathbf{M}_2| = M_0$) and with the easy axis being along the z axis. The magnetoelastic and elastic properties of both the magnetic and nonmagnetic media are assumed to be isotropic for simplicity. To describe the AFM, we use a phenomenological model that takes into account the coupling between the spin and elastic subsystems but ignores the nonlocal Heisenberg exchange. In terms of the ferromagnetism ($\mathbf{m}$) and antiferromagnetism ($\mathbf{l}$) vectors, the energy density W of the AFM can be written in the form [13, 17]

$$\begin{gathered} W = W_m + W_{\mathrm{me}} + W_e, \\ W_m = 2M_0^2\left(\frac{\delta}{2}\mathbf{m}^2 + \frac{\alpha}{2}(\nabla\mathbf{l})^2 - \frac{\beta}{2}l_z^2 - 2\mathbf{m}\cdot\mathbf{h}\right); \\ W_{\mathrm{me}} = \gamma l_i l_k u_{ik}; \quad W_e = \frac{\lambda}{2}u_{ii}^2 + \mu u_{ik}^2; \\ \mathbf{m} = \frac{\mathbf{M}_1 + \mathbf{M}_2}{2M_0}; \quad \mathbf{l} = \frac{\mathbf{M}_1 - \mathbf{M}_2}{2M_0}. \end{gathered} \tag{8}$$

where u_{ik} is the elastic strain tensor; $\mathbf{H}$ is an external magnetic field; δ, α, and γ are the homogeneous exchange, nonhomogeneous exchange (exchange stiffness), and magnetostriction constants, respectively; λ and μ are Lamé's constants; $\mathbf{h} = \mathbf{H}/2M_0$; and $\beta > 0$ is the uniaxial magnetic anisotropy constant. In what follows, we assume that

$$|\mathbf{m}| \ll |\mathbf{l}|. \tag{9}$$

It can be shown [17] that, under the assumption of (9), both the linear and nonlinear spin dynamics of the magnet are described, in the model under consideration, by a closed system of dynamic equations involving only the antiferromagnetism vector $\mathbf{l}$ and the lattice displacement vector $\mathbf{u}$. In the collinear phase of the easy-axis AFM with $\mathbf{l} \parallel \mathbf{H} \parallel z$, the spectrum of normal magnetoelastic vibrations with $\mathbf{k}$ lying in the xy plane and $\mathbf{u} \parallel z$ has the form ($k^2 = k_x^2 + k_y^2$)

$$\begin{gathered} \omega^2 = s_t^2 k^2 \mu; \\ \mu = ((\omega^2 - \omega_0^2 + \omega_H^2 - c^2k^2) \\ \times (\omega^2 - \omega_0^2 + \omega_H^2 - \omega_{me}^2 - c^2k^2) - 4\omega^2\omega_H^2)\Delta^{-1}, \\ \Delta = (\omega^2 - \omega_0^2 + \omega_H^2 - \omega_{me}^2 - c^2k^2) - 4\omega^2\omega_H^2, \end{gathered} \tag{10}$$

where ω_{me} is the magnetoelastic gap, ω_0 is the "activation frequency" of the spin-wave spectrum due to the uniaxial anisotropy, and $\omega_H = gH$ (g is the gyromagnetic ratio).

Since our interest here is with the magnetoelastic dynamics of a thin magnetic film, the system of dynamic equations should be supplemented by the corresponding boundary conditions. If a film is covered with a metal layer on both sides and magnetized in its plane, the spectrum of its surface exchangeless spin oscillations (magnetostatic surface spin waves) is well known to be dispersionless [18]. For this reason, we will consider a metal–magnet interface in what follows. If the metallic overlayer is very thin ($k_\perp D \ll 1$, where D is the overlayer thickness), its influence on the elastic properties of the magnet can be neglected [19] and the interface can be considered as a mechanically free surface of the magnet. In this case, we have (ξ is the coordinate along a normal to the interface)

$$\sigma_{ik} n_k = 0; \quad \xi = 0. \tag{11}$$

But if the surface of the magnet (medium 2) is in continuous acoustic contact with a nonmagnetic metal and the condition $k_\perp D \ll 1$ is not fulfilled, the boundary conditions at the interface can be written as

$$\sigma_{ik}^{(1)} = \sigma_{ik}^{(2)}; \quad u_i^{(1)} = u_i^{(2)}, \quad \xi = 0. \tag{12}$$

In both the case of the mechanically free surface of the crystal and the case of the interface between two half-spaces, the elastic wave will be localized in the vicinity of this planar defect if, in addition to (11) or (12), the following condition is met:

$$u_z(\xi \longrightarrow \pm\infty) \longrightarrow 0. \tag{13}$$

In what follows, we will separately consider the case of a half-space of a magnetic medium and the case of a thin magnetic film covered with a nonmagnetic layer on one or both sides. We shall also analyze the conditions under which a shear SAW is formed by a nonmagnetodipolar mechanism, even in the exchangeless limit ($c \longrightarrow 0$) in the vicinity of the mechanically free surface of a magnet or near the acoustically continuous interface between two (magnetic and nonmagnetic) media.

2. A HALF-SPACE OF A MAGNETIC MEDIUM (EXCHANGELESS APPROXIMATION)

From (13), one can obtain an expression for the component of the wave vector normal to the surface, $q_2 \equiv \alpha k_\perp$ ($k_2 \equiv k_\perp^2(1 - \alpha^2)$). At $\mathbf{n} \parallel y$ and $\mathbf{k}_\perp \parallel x$, we have

$$\alpha^2 = 1 - \frac{\omega^2}{s_t^2 k_\perp^2 \mu} > 0. \tag{14}$$

Therefore, the wave under study is a partial one in both the magnetic and nonmagnetic media; in nonmagnetic medium 1 ($y < 0$), we have $q_1 \equiv -k_\perp$, while in magnetic medium 2 ($y > 0$), q_2 is determined from (14). Thus, we have

$$u_{1,2} = A_{1,2}\exp(-q_{1,2}y)\exp(i\omega t - ik_\perp x). \tag{15}$$

In both the case of the mechanically free surface of a magnet [with boundary conditions (11) and (13)] and the case of the interface between two (magnetic and nonmagnetic) half-spaces with boundary conditions (12) and (13), the dispersion relation for the transverse elastic surface wave has the same form,

$$\omega^2 = s_t^2 \mu (k_\perp^2 - q_2^2). \tag{16}$$

However, using (13), for the mechanically free surface of the magnetic half-space, we obtain

$$\alpha = -\frac{s\mu_*}{\mu} > 0, \qquad \mu_* = \frac{2\omega\omega_{me}^2\omega_H}{\Delta}, \tag{17}$$

whereas in the case of the acoustically continuous interface between the magnetic and nonmagnetic half-spaces,

$$\alpha = -\frac{a + s\mu_*}{\mu} > 0 \tag{18}$$

with $a \equiv \mu_1/\mu_2$. The limit case of a mechanically free surface, given by (17), can be obtained from (18) by putting the shear modulus of the nonmagnetic medium μ equal to zero.

Using (16)–(18), the dispersion relation of the shear SAW under study can be written as $k_\perp = k_\perp(\omega)$ for $\mu_1 \neq 0$ and $H_z \neq 0$; namely,

$$k_\perp^2 = \frac{\omega^2}{s_t^2}\frac{\mu^2 - (a + s\mu_*)^2}{\mu}. \tag{19}$$

Analysis of (19) shows that, if no account is taken of the magnetic dipole–dipole interaction, the shear SAW on the mechanically free surface of a low-temperature AFM in a collinear phase is delocalized when $|\mathbf{H}| = 0$. As is seen from (15)–(19), in the case of the magnet being in continuous acoustic contact with a nonmagnetic dielectric medium, the shear SAW is formed, in the geometry under consideration, even in the absence of a magnetic field $\mathbf{H} \parallel \mathbf{l} \parallel z$. The important features of the spectrum of the SAW [relations (17)–(19)] under study forming on the magnetic–nonmagnetic medium interface are as follows: (i) The frequency spectrum consists of several bands separated by gaps when $H_z \neq 0$. (ii) The spectrum is asymmetric with respect to the inversion of the propagation direction, $\omega(k_\perp) \neq \omega(-k_\perp)$, if $H_z \neq 0$. (iii) A dispersion curve of the SAW, described by (19), has end points $k_\perp = k_*$ at which $\alpha(k_*) = 0$.

If the acoustic retardation is ignored, ($\alpha \longrightarrow 1$) and $H_z \neq 0$, the SAW under study is dispersionless; that is,

$\omega(k_\perp) = \text{const}$. The frequencies can be found in an explicit form to be

$$\Omega_\pm = \omega_0 \pm s\omega_H \quad (\mu_1 = 0), \tag{20}$$

$$\Omega_\pm = \left(\omega_0^2 + \omega_{\text{me}}^2 \frac{a}{1+a}\right)^{1/2} \pm s\omega_H \quad (\mu_1 \neq 0). \tag{21}$$

In the case of the nonmagnetic medium having a finite thickness $t < \infty$ and its outer surface being traction-free, expression (18) for α is replaced by another one, appropriate for the case of a finite t,

$$\alpha = -\frac{a\tanh k_\perp t + s\mu_*}{\mu} > 0. \tag{22}$$

The spectrum of the SAW localized on the interface between the low-temperature AFM and the nonmagnetic metal layer can be found, as before, from (14) combined with (22). However, now, the spectrum cannot be analytically represented in the form $k_\perp = k_\perp(\omega)$, as in (17)–(19), for arbitrary values of the wave number $k_\perp$.

In the short-wavelength limit, the dispersion relation for the SAW under study can be found in an explicit form from (16) and (22) in the elastostatic approximation ($\alpha \longrightarrow 1$). The result is

$$\Omega_\pm^2 = \omega_0^2 + \omega_{\text{me}}^2 \frac{a\tanh(k_\perp t)}{1 = a\tanh(k_\perp t)}. \tag{23}$$

Thus, even in the case of a magnetic half-space where both the magnetic dipole–dipole interaction and acoustic retardation are neglected, the presence of a nonmagnetic overlayer leads to dispersion of the spectrum of the shear SAW under study in the short-wavelength limit. The dispersion is determined by the magnetoelastic and elastic parameters of the acoustically rigidly bound magnetic and nonmagnetic media.

Now, let us consider the effect of the thickness of the magnet on the spectrum of the shear SAW. For this purpose, we investigate the propagation of the SAW in the same geometry ($\mathbf{H} \parallel \mathbf{u} \parallel z$, $\mathbf{n} \parallel y$, and $\mathbf{k}_\perp \parallel x$) in a film of a thickness d of an easy-axis AFM in a collinear phase ($\mathbf{l} \parallel \mathbf{H} \parallel z$) described by expressions (8). The film is assumed to be covered with a nonmagnetic overlayer on either one or both sides. As before, the elastic parameters of the magnetic and nonmagnetic media are assumed to be such that inequality (1) takes place with a large margin and, hence, shear elastic waves can be considered as propagating with an infinite velocity in the nonmagnetic medium.

3. A MAGNETIC FILM. NONHOMOGENEOUS-EXCHANGE EFFECTS

Let us consider a film of a low-temperature AFM under conditions $\mathbf{H} \parallel \mathbf{l} \parallel z$, $\mathbf{k}_\perp \parallel x$, and $\mathbf{n} \parallel y$. On both sides, the film is covered with nonmagnetic metal overlayers of thicknesses t and f, respectively, which are in acoustically continuous contact with the film. If both the outer surfaces of this three-layer structure are traction-free, one can write the following equation for α, using (11), (12), and (17):

$$\begin{aligned}\mu^2\alpha^2 + \mu\alpha(\tanh(k_\perp t) + \tanh(k_\perp f))\coth(\alpha k_\perp d)\\ - sa\mu_*(\tanh(k_\perp t) - \tanh(k_\perp f)) - \mu_*^2\\ + a^2\tanh(k_\perp t)\tanh(k_\perp f) = 0.\end{aligned} \tag{24}$$

Thus, in the case of an AFM film covered with nonmagnetic layers on both sides, the dispersion relation for the shear SAW is found solving the set of equations (14) and (24). From (24), it follows that (i) the spectrum of the shear SAW under study is asymmetric with respect to the inversion of the direction of propagation in the case where $H_z \neq 0$, $\mu_1 \neq 0$, and $t \neq f$, and (ii) the dispersion curve may have segments with $\partial\omega/\partial k_\perp = 0$ at $k_\perp \neq 0$. Expression (22), valid for the case of a magnetic half-space covered with a nonmagnetic overlayer, is obtained from (24) by going to the limit as $k_\perp d \longrightarrow \infty$ and $k_\perp f \longrightarrow 0$.

Analysis of (14) and (24) shows that, when the spectrum described by dispersion relation (24) becomes symmetric (namely, when $H_z = 0$ at $t \neq f$, or $H_z \neq 0$ at $t = f$), the spectrum of the shear SAW under study has the following explicit form in the elastostatic approximation ($\alpha \longrightarrow 1$):

$$\begin{aligned}\Omega_\pm^2 &= \omega_0^2 + \omega_{\text{me}}^2 \frac{A \pm \sqrt{B}}{A \pm \sqrt{B} + 1}, \quad H_z = 0, \quad t \neq f,\\ A &= \frac{a}{2}(\tanh k_\perp t + \tanh k_\perp f)\coth k_\perp d,\\ B &= \frac{a^2}{4}((\tanh k_\perp t + \tanh k_\perp f)^2\coth^2 k_\perp d\\ &\quad - 4\tanh k_\perp t\tanh k_\perp f);\end{aligned} \tag{25}$$

$$\begin{aligned}\Omega_\pm^2 &= \frac{P_1}{2} \pm \left(\frac{P_1^2}{4} - P_2\right)^{1/2}, \quad H_z = 0, \quad t = f,\\ P_1 &= (1 + R_1 + R_2)^{-1}(2(\omega_0^2 + \omega_H^2) - R_1\omega_{\text{me}}^2\\ &\quad + 2(R_1 + R_2)(\omega_0^2 + \omega_{\text{me}}^2 + \omega_H^2)),\\ P^2 &= (1 + R_1 + R_2)^{-1}((\omega_0^2 - \omega_H^2)^2 + R_1(\omega_0^2 - \omega_H^2)\\ &\quad \times(\omega_0^2 - \omega_{\text{me}}^2 + \omega_H^2) + R_2(\omega_0^2 + \omega_{\text{me}}^2 + \omega_H^2)^2),\\ R_1 &= 2a\tanh k_\perp t\coth k_\perp d,\\ R_2 &= a^2\tanh^2 k_\perp d.\end{aligned} \tag{26}$$

Thus, if the surface of the magnetic film is mechanically free or the film is covered with nonmagnetic overlayers on both sides, the spectrum of elastic shear surface waves consists of two branches.

In the case where $H_z \neq 0$ and $t \neq f$, the spectrum of the shear SAW can be found from (14) and (24) in the form $k_\perp = k_\perp(\omega)$ in the limit as $k_\perp t \longrightarrow \infty$ and $k_\perp f \longrightarrow 0$; namely,

$$k_\perp = \frac{1}{2d}\ln\frac{A+1}{A-1}, \quad A = \frac{as\mu_* + \mu_*^2}{\mu^2}. \tag{27}$$

The structure of the spectrum of the SAW under study is very sensitive to the elastic boundary conditions at the free surfaces of the nonmagnetic overlayers. For example, if the outer surface of the nonmagnetic layer of the thickness t (or f) of the three-layer structure is rigidly fixed ($\mathbf{u} = 0$) and $t \neq f$, $\mathbf{l} \parallel \mathbf{H} \parallel z$, $\mathbf{k}_\perp \parallel x$, $\mathbf{n} \parallel y$, then the expression for α that, in combination with (17), describes the spectrum of transverse phonons localized on the magnetic–nonmagnetic layer interface has the form of (24) with $\tanh(k_\perp t)$ and $\tanh(k_\perp f)$ being replaced by $\coth(k_\perp t)$ and $\coth(k_\perp f)$, respectively.

So far, we have ignored the acoustic retardation in the magnetic film and the nonmagnetic overlayers. If we take into account that $s_{1,t} < \infty$, the dispersion relation for the shear SAW in the thin magnetic film with nonmagnetic overlayers on both sides will still have the form of (24) with $\alpha_1^2 \equiv 1 - \omega^2/(s_1 k_\perp)^2$ and with $\tanh(k_\perp t)$ and $\tanh(k_\perp f)$ being replaced by $\alpha_1\tanh(\alpha_1 k_\perp t)$ and $\alpha_1\tanh(\alpha_1 k_\perp f)$, respectively, where $\alpha^2 \equiv 1 - \omega^2/\mu(s_t k_\perp)^2$. It follows from (24) and (29), that acoustic retardation [due to which $0 < (\alpha^2, \alpha_1^2) < 1$] leads to the occurrence of end points $\alpha(k_\perp) = 0$ at $k_\perp = k_*$ (for $s_1 < s_t$) in each of the two branches of the dispersion curve of the SAW under study. The position of the end points is independent of the relative thicknesses of the magnetic and nonmagnetic layers (t/d and f/d). Thus, if $s_1 < s_t$, the SAW under study exists only at $k_\perp > k_* \neq 0$.

Besides, it follows from (24) and (29), that the finiteness of the velocity of elastic waves leads to the change over of the asymptotic form of the spectrum in the vicinity of the point of condensation k_* (as compared to the case of $\alpha, \alpha_1 \longrightarrow 1$) from an exponential to a power form (as $k_\perp d \longrightarrow \infty$).

To this point, we have ignored the nonlocal character of the Heisenberg spin–spin exchange (nonhomogeneous exchange interaction) and considered (16) in the limit as $c \longrightarrow 0$. Analysis of (14) shows that, at $c \neq 0$, an elastic shear wave with $\mathbf{u} \parallel z$ in the magnetic medium is a combination of three partial waves, and the spatial dependence of the z component of the elastic displacement vector $\mathbf{u}$ in (magnetic) medium 2 has, rather than (15), the form

$$u_2 = \sum_{j=1}^{3} A_j \exp(-q_j y)\exp(i\omega t - ik_\perp x), \tag{28}$$

where $q_1^2 = k_\perp^2$, and $q_{2,3}^2$ are the roots of the equation

$$q^4 - Aq^2 + B = 0,$$
$$A = (2(\tilde{\omega}_0^2 - \omega_H^2 - \omega^2) + \omega_{\mathrm{me}}^2)c^{-2}, \tag{29}$$
$$B = (\tilde{\omega}_0^2 - \omega_H^2 - \omega^2)(\tilde{\omega}_0^2 - \omega_H^2 + \omega_{\mathrm{me}}^2)c^{-4}.$$

with $\tilde{\omega}_0^2 \equiv \omega_0^2 + c^2 k_\perp^2$.

Thus, the partial wave with $q_1^2 = k_\perp^2$ is the shear SAW under study. Over the ranges of frequencies ω and wave numbers $k_\perp$ in which we have $q_{2,3}^2 < 0$ ($j = 2, 3$), the nonhomogeneous exchange interaction causes the SAW under study to be an outgoing wave, for the attendant partial waves in (29) become bulk (sinusoidal) ones. The latter waves make an oscillatory contribution to the dispersion relation $F(\omega, k_\perp) = 0$ that describes the spectrum of the shear SAW under study including the effect of the nonhomogeneous exchange. Physically, these waves are bulk spin exchange waves. In the particular case of a magnetic film of a thickness d, the spins are absolutely free at both the surfaces of the film ($\partial l/\partial\xi = 0$ at $\xi = 0, d$); in the range of small wave vectors ($k_\perp d \ll \pi\nu/d$, $\nu = 1, 2, \ldots$), their dispersion law can be written in an explicit form

$$\Omega_{2\nu,3\nu}^2 = \frac{T_1}{2} \pm \left(\frac{T_1^2}{4} - T_2\right)^{1/2},$$
$$T_1 = 2(\omega_{0\nu}^2 + \omega_H^2) + \omega_{\mathrm{me}}^2, \tag{30}$$
$$T_2 = (\omega_{0\nu}^2 - \omega_H^2)(\omega_{0\nu}^2 + \omega_{\mathrm{me}}^2 + \omega_H^2),$$

where $\omega_{0\nu}^2 \equiv \omega_0^2 + c^2(k_\perp^2 + (\pi\nu/2d)^2$. At the same time, the dispersion relation for the SAW in the long-wavelength limit is still given by (24) if the outer surfaces of the nonmagnetic overlayers are mechanically free.

A comparison of (30) and (24) shows that these spectra have degeneracy points at $\Omega_\pm > \min(\Omega_{2\nu}, \Omega_{3\nu})$ and $k_\perp \neq 0$, in the vicinity of which repulsion between the dispersion curves occur and frequency gaps arise. The physical picture described above is qualitatively similar to that observed in the case of nonhomogeneous spin–spin resonance between a Damon–Eshbach magnetostatic surface wave and bulk spin waves (see, e.g., reviews [20, 21]). Calculations show that the analogy takes place even if dissipation is included. In particular, the line width of the SAW under study may oscillate as the wave number $k_\perp$ is varied.

CONCLUSION

Thus, the investigation performed in this paper shows that, at $T < T_N$, in contrast to the case of $T > T_N$, the formation of a shear one-partial SAW near the surface of a magnetic medium is governed by nondipolar mechanisms owing to the presence of the long-range order in the magnet. In particular, it is found that

(i) a one-partial SAW is formed on the mechanically free surface of a magnet, as well as on the acoustically continuous interface between a magnet and a nonmagnetic medium, if an external magnetic field is applied along the normal to the plane of propagation of the elastic shear wave with $\mathbf{u} \parallel \mathbf{H} \perp \mathbf{n}$ (acoustically active crystal), and (ii) a one-partial shear SAW with $\mathbf{u} \perp \mathbf{n}$ and $\mathbf{u} \perp \mathbf{k}_\perp$ is formed on the interface between a magnet and a nonmagnetic medium rigidly bonded to each other if $|\mathbf{H}| = 0$. In the latter case, the shear modulus of the nonmagnetic medium (μ_1) should be nonzero.

Thus, under the conditions indicated above, additional types of a one-partial shear SAW can be formed on the mechanically free surface of a magnetically ordered crystal even if the magnetic dipole–dipole interaction is ignored.

The effect of the nonlocality of the Heisenberg mechanism of the spin–spin exchange (nonhomogeneous exchange interaction) on the spectrum of the one-partial shear SAW investigated in this paper, as well as the influence of dissipation in the spin subsystem of the magnet, is qualitatively similar to that for the Damon–Eshbach magnetostatic surface spin wave.

It should be noted that there is a close analogy between the conditions for the formation of surface polaritons of the *TE* (or *TM*) type and those of the one-partial shear SAWs considered in this paper.

In order to show this, it is convenient to consider an infinite magnetic crystal in terms of the Green's functions. At $T_N > T_D$, the effect of the spin subsystem of the crystal on its elastic properties can be taken into account by introducing a set of effective elastic moduli, which will possess spatial and temporal dispersion and characterize a certain effective elastic medium. If one compares the equation of motion describing the propagation of the shear *SH* wave in this elastic medium with the equation determining the spectrum of the bulk *TE* (or *TM*) polariton propagating in the infinite crystal [22], it will be seen that, in certain geometries of the wave propagation, there is a one-to-one correspondence between the effective elastic moduli involved in the equation for the normal shear *SH* wave in the infinite crystal, on one hand, and the components of the permittivity (permeability) tensor, on the other. In this way, considering elastic shear waves propagating along the surface of a magnet, one can find analogs of the surface, as well as bulk, polaritons of the *TE* (*TM*) type.

In particular, if a crystal has no acoustic activity, i.e., $(\mathbf{H} \cdot \mathbf{l}) = 0$, the shear SAW arising on the acoustically continuous magnetic–nonmagnetic medium interface and characterized by dispersion relation (19) is an analog of the surface phonon polariton [22]. A new type of a two-partial shear SAW arising in the presence of the nonhomogeneous exchange interaction (investigated in [23]) is analogous to the surface excitonic polariton [22].

The effect of the magnetic dipole–dipole interaction (magnetic surface *TE* polaritons) on the spectrum of the one-partial shear SAWs investigated here and on the conditions for their formation on the surface between a low-temperature AFM and a nonmagnetic medium will be considered elsewhere.

ACKNOWLEDGMENTS

The author is grateful to E.P. Stefanovskiĭ, T.N. Tarasenko, and I.E. Dragunov for encouragement and helpful discussions.

REFERENCES

1. I. M. Lifshitz and L. N. Rozentsveig, Zh. Éksp. Teor. Fiz. **18**, 1012 (1948).
2. S. V. Biryukov, Yu. V. Gulyaev, V. V. Krylov, and V. A. Plesskiĭ, *Acoustic Surface Waves in Inhomogeneous Media* (Nauka, Moscow, 1991).
3. J. Lothe and D. M. Barnett, J. Appl. Phys. **47**, 428 (1976).
4. V. I. Al'shits and K. Lote, Kristallografiya **23**, 901 (1978).
5. J. Lothe and D. M. Barnett, Wave Motion **1**, 107 (1979).
6. V. I. Al'shits, V. N. Lyubimov, and A. L. Shuvalov, Zh. Éksp. Teor. Fiz. **106**, 828 (1994) [JETP **79**, 455 (1994)].
7. Yu. V. Gulyaev, Pis'ma Zh. Éksp. Teor. Fiz. **9**, 63 (1969) [JETP Lett. **9** (1969)].
8. J. L. Bleustein, Appl. Phys. Lett. **13**, 412 (1968).
9. Yu. V. Gulyaev, Yu. A. Kuzavko, I. N. Oleĭnik, *et al.*, Zh. Éksp. Teor. Fiz. **87**, 674 (1984) [Sov. Phys. JETP **60**, 386 (1984)].
10. M. I. Kaganov and Yu. A. Kosevich, Poverkhnost' **5**, 148 (1986).
11. J. P. Parekh, Electron. Lett. **5**, 322 (1969).
12. Yu. V. Gulyaev, I. E. Dikshteĭn, and V. G. Shavrov, Usp. Fiz. Nauk **167**, 735 (1997) [Phys. Usp. **167** (1997)].
13. E. A. Turov and V. G. Shavrov, Usp. Fiz. Nauk **140**, 429 (1983) [Sov. Phys. Usp. **26**, 593 (1983)].
14. R. E. Camley and D. L. Mills, Phys. Rev. B **26**, 1280 (1982).
15. B. Luthi, D. L. Mills, and R. E. Camley, Phys. Rev. B **28**, 1475 (1983).
16. R. L. Stamps and R. E. Camley, J. Appl. Phys. **56**, 3497 (1984).
17. V. I. Ozhogin and V. L. Preobrazhenskiĭ, Usp. Fiz. Nauk **155**, 593 (1988) [Sov. Phys. Usp. **31**, 713 (1988)].
18. A. G. Gurevich and G. A. Melkov, *Magnetic Oscillations and Waves* (Nauka, Moscow, 1994).
19. H. van de Vaart, J. Appl. Phys. **42**, 5305 (1971).
20. C. E. Patton, Phys. Rep. **103**, 251 (1984).
21. Yu. V. Gulyaev and P. E. Zil'berman, Izv. Vyssh. Uchebn. Zaved., Fiz. **31**, 6 (1988).
22. *Surface Polaritons. Electromagnetic Waves on Surfaces and Medium Interfaces*, Ed. by V. M. Agranovich and D. L. Mills (Nauka, Moscow, 1985).
23. S. V. Tarasenko, Fiz. Tverd. Tela (S.-Peterburg) **40**, 299 (1998) [Phys. Solid State **40**, 272 (1998)].

Translated by Yu. Epifanov

Physics of the Solid State, Vol. 42, No. 4, 2000, pp. 719–721. Translated from Fizika Tverdogo Tela, Vol. 42, No. 4, 2000, pp. 701–703.
Original Russian Text Copyright © 2000 by Samokhvalov, Arbuzova, Viglin, Naumov, Smolyak, Korolev, Lobachevskaya.

MAGNETISM AND FERROELECTRICITY

An Anomaly in the Magnetic Susceptibility of the $Mg_{1-x}Cu_xO$ Solid Solutions with $0.01 \le x \le 0.20$

**A. A. Samokhvalov*, T. I. Arbuzova*, N. A. Viglin*, S. V. Naumov*, I. B. Smolyak*,
A. V. Korolev*, and N. I. Lobachevskaya****

**Institute of Metal Physics, Ural Division, Russian Academy of Sciences, ul. S. Kovalevskoĭ 18, Yekaterinburg, 620219 Russia
e-mail: magsemi@ifm.e-burg.su*

***Institute of Solid State Chemistry, Ural Division, Russian Academy of Sciences,
ul. Pervomaĭskaya 91, Yekaterinburg, 620219 Russia*

Received July 21, 1999

Abstract—The problem of localized superconductivity has motivated the preparation of $Mg_{1-x}Cu_xO$ solid solutions with NaCl structure and $0.01 \le x \le 0.20$, as well as a study of the magnetization and magnetic susceptibility χ in the 2–400 K temperature range and in magnetic fields of up to 5 T. The temperature dependence of χ is described for all compositions by the Curie–Weiss law, $\chi = C/(T - \theta)$, where the constant C is close to the value calculated for each composition for $\mu_{eff} = 1.7–1.9\mu_B$, and θ is close to zero. For $T < 30$ K, $\chi(T)$ deviates for all compositions toward lower χ, which can be attributed to magnetic ordering of exchange-coupled clusters in the solid solution. At $T \sim 320–330$ K, an anomaly of a diamagnetic type, i.e., a decrease of χ by 6–30% of its paramagnetic value, has been observed for all compositions against the background of the generally paramagnetic $\chi(T)$. A discussion is presented of alternative reasons for this anomaly and of its possible connection with localized superconductivity. © *2000 MAIK “Nauka/Interperiodica”.*

Studies of localized (impurity) superconductivity are of a certain interest as a possible way to increase the T_c temperature of high-temperature superconductors [1]. This superconductivity with T_c as high as 200–300 K is quite frequently observed not only in the well-known cuprate superconductors [2], but in a number of other transition-metal compounds, in particular, in copper monoxide-based heterophase systems [3–5]. It was shown, for instance, that the Cu–$Mg_{1-x}Cu_xO$ heterostructure exhibits for $x = 0.15$ and 0.20 magnetic screening [5], which is possibly related to the interface-type superconductivity. The magnetic screening setting in under cooling near 320–330 K coincides with the onset of a magnetic anomaly (of the diamagnetic type) for the same compositions. The present study was performed over broader temperature and magnetic-field ranges with the purpose of obtaining more complete and detailed information on this anomaly and on the specific magnetic properties of the $Mg_{1-x}Cu_xO$ solid solutions with the NaCl structure favorable for high-temperature superconductivity.

1. SAMPLES AND MEASUREMENT TECHNIQUES

Polycrystalline samples of $Mg_{1-x}Cu_xO$ solid solutions were prepared by solid-phase reactions in the $0.01 \le x \le 0.20$ composition region (for more details, see [5]). The starting components and solid solutions were subjected to x-ray structural and phase analyses, and one also studied their EPR spectra to reveal the presence of possible magnetic impurities. The x-ray diffraction analyses showed the samples to be single phase, and the parameter of their NaCl-type crystal lattice to increase linearly with x from 4.212 ± 0.001 Å for $x = 0$ to 4.218 ± 0.001 Å for $x = 0.20$. EPR measurements made at 300 K, as well as low-temperature magnetic-susceptibility studies revealed in MgO, which was used to prepare the $Mg_{1-x}Cu_xO$ solid solutions, showed the presence of a small amount of the impurity ions Cu^{2+}, Mn^{2+}, and Cr^{3+} (≤0.1%). The measurements of magnetic susceptibility were carried out on two setups, namely, with a SQUID magnetometer in the 2–400 K range and in magnetic fields of up to 5 T, and on a Faraday magnetic balance within the 50–600 K region and at H of up to 1.5 T. Both setups have about the same sensitivity, 5×10^{-8} cm^3/g.

2. RESULTS

It was shown [5] that the temperature dependences of the magnetic susceptibility of the $Mg_{1-x}Cu_xO$ solid solutions, $\chi(T)$ and $\chi^{-1}(T)$, follow the paramagnetic behavior and obey the Curie–Weiss law $\chi = C/(T - \theta)$ with θ close to zero. However, a more careful consideration of these relationships leads to the conclusion that the paramagnetic $\chi(T)$ relations have anomalies of a “diamagnetic” character. To more clearly reveal these anomalies, it is more reasonable to consider the experimental data in the $\chi T = f(T)$ coordinates. If $\chi(T)$ follows a pure paramagnetic course with $\theta = 0$, the experimental points should fit in this case on a temperature-

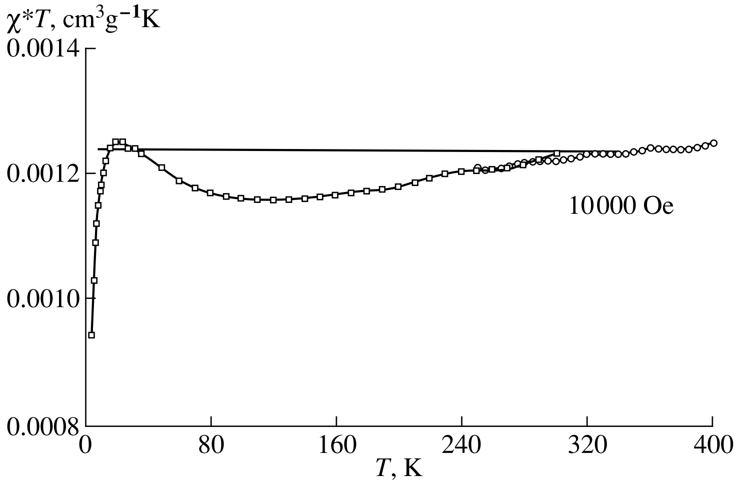

Temperature dependence of the Curie constant $C = \chi T$ for the $Mg_{0.85}Cu_{0.15}O$ solid solution in a magnetic field of 1 T.

independent line with the intercept on the vertical axis equal to the constant of the Curie law $\chi = C(T)$. The figure presents a $\chi T = f(T)$ plot typical of all the solid solutions with $x = 0.15$ studied. Above 320–330 K, the experimental points are seen to fit closely to a temperature-independent straight line with $C = 1.27 \times 10^{-3}$ cm^{3}K/g calculated for the $x = 0.15$ composition. Below 320–330 K, the experimental points lie below the calculated value of C. A similar result was obtained also for other compositions with x = 0.04, 0.05, 0.10, and 0.20. The relative magnitude of the $\Delta\chi/\chi$ anomaly is ~6% for $x = 0.15$ and lies within 20–30% for the compositions with x = 0.05 and 0.10.

The figure shows that, as the temperature decreases to 20 K, the experimental values of χ approach the C line, to subsequently fall rapidly off with temperature down to 2 K. A similar result for the low-temperature part of the $\chi T = f(T)$ plot was found with the other compositions studied, but the temperature T at which χT starts to decrease was approximately proportional to x, i.e., to the content of Cu^{2+} ions in the solution. For instance, we found $T' = 30$ K for $x = 0.20$ and $T' = 14$ K for $x = 0.10$.

It should be pointed out that the temperature dependences $\chi(T)$ were measured in magnetic fields $H = 0.5$ and 1 T, and for some samples, at 4.5 T. The results obtained in all these fields were practically identical. No noticeable dependence of the magnitude of the anomaly on H was observed. An attempt was also made to reveal hysteretic phenomena in the “diamagnetic” susceptibility, which are characteristic of type-II hard superconductors. With this purpose in mind, the sample was cooled in a zero field (the ZFC regime) and in a magnetic field $H = 80$ Oe (FC) below 320–330 K. The ZFC and FC temperature dependences of the magnetization coincided within experimental error, which can be assigned either to a low diamagnetic susceptibility of the localized superconductivity regions, or to a reversible nature of the $M(H)$ magnetization curves because of a weak magnetic-vortex pinning.

One also measured the field dependences of the magnetization of the solid solutions at fixed temperatures of 2, 100, and 300 K. The $M(H)$ plots obtained at T = 100 and 300 K were practically linear. The $M(H)$ relation obtained at 2 K for the $x = 0.2$ composition is satisfactorily reproduced by a Brillouin function, but with an effective magnetic moment substantially smaller than the theoretical value of $1.73\mu_B$ derived for the Cu^{2+} ion with spin 1/2. This decrease of M is apparently associated with the existence at low temperatures of some antiferromagnetically coupled complexes of Cu^{2+} ions.

3. DISCUSSION

The results presented here are evidence of the existence of an anomaly of a “diamagnetic” nature at $T \leq$ 320–330 K, superposed on a paramagnetic temperature dependence of the magnetic susceptibility of the $Mg_{1-x}Cu_xO$ solid solutions ($0.01 \leq x \leq 0.20$). The absence of a detectable difference between the ZFC and FC magnetizations $M(T)$ may be due to the localized superconductivity regions having a small volume and to the specific features of the process of their magnetization in this case. Therefore, one cannot rule out the possibility of formation of regions with localized superconductivity in $Mg_{1-x}Cu_xO$ solid solutions ($x \leq$ 0.20). It is the relatively small fraction of the regions (fragments) with localized superconductivity in the total volume of the paramagnetic phase that underlies certain difficulties met in studies of this phenomenon (see [1]). The main argument for the conjecture of the observed anomaly being of the superconducting nature is the coincidence in temperature of the beginning of this anomaly (under cooling) at 320–330 K with the onset of the magnetic screening observed earlier on the same solid-solution samples (see [5]). An analysis of this effect suggests that its nature is related to the interface-type localized superconductivity [3–5]. It should be also pointed out that the observed anomalies exhibit a metastable character, which is typical of localized (impurity) superconductivity with a high critical temperature [2].

The assumption of the observed $\chi(T)$ anomaly being due to magnetic impurities appears less likely. If one accepted this assumption, some ferro- or antiferromagnetic uncontrollable impurities would create an anomaly opposite in sign to the observed “diamagnetic” one, i.e., their presence would have increased rather than reduced χ against the background of the paramagnetic $\chi(T)$ under cooling. No such situation was seen to occur in our experiments. The anomaly was “diamagnetic” in all cases and for all samples of the solid solutions, including those prepared from different Mg^{2+} and Cu^{2+} oxides and salts. Thus, the assumption of the magnetic anomaly observed in the solid solutions studied being of a superconducting nature appears most probable.

ACKNOWLEDGMENTS

The authors are indebted to A. V. Mitin for interest in the work and valuable criticisms.

Support of the Federal Program “Surface Atomic Structures” (project no. 2.4.99) is gratefully acknowledged.

REFERENCES

1. A. V. Mitin, Perspekt. Tekhnol. **3** (17), 7 (1996).
2. C. Y. Huang and M. Rabinowiz, Mod. Phys. Lett. **4**, 567 (1990).
3. A. A. Samokhvalov, T. I. Arbuzova, V. V. Osipov, *et al.*, Fiz. Tverd. Tela (S.-Peterburg) **38**, 3277 (1996) [Phys. Solid State **38**, 1788 (1996)].
4. A. A. Samokhvalov, T. I. Arbuzova, N. A. Viglin, *et al.*, Fiz. Tverd. Tela (S.-Peterburg) **40**, 295 (1998) [Phys. Solid State **40**, 268 (1998)].
5. A. A. Samokhvalov, T. I. Arbuzova, N. A. Viglin, *et al.*, Fiz. Tverd. Tela (S.-Peterburg) **41**, 293 (1999) [Phys. Solid State **41**, 262 (1999)].

Translated by G. Skrebtsov

Physics of the Solid State, Vol. 42, No. 4, 2000, pp. 722–725. Translated from Fizika Tverdogo Tela, Vol. 42, No. 4, 2000, pp. 704–707.
Original Russian Text Copyright © 2000 by Krynetskiĭ, Popkov.

MAGNETISM AND FERROELECTRICITY

Low-Temperature Relaxation of Metastable States and Quantum Tunneling in Antiferromagnets with Ising Rare-Earth Ions: Dysprosium Orthoaluminate

I. B. Krynetskiĭ* and A. F. Popkov**
**Moscow State University, Vorob'evy gory, Moscow, 119899 Russia*
e-mail: krynets@plms.phys.msu.su
***Lukin Scientific Research Institute of Physical Problems, Zelenograd, Moscow, 103460 Russia*

Received April 12, 1999; in final form, September 6, 1999

Abstract—The paper reports the first observation of a magnetic relaxation of metastable states in an antiferromagnet (dysprosium orthoaluminate $DyAlO_3$) at low temperatures in zero magnetic field made by magnetostriction measurements. The metastable states were excited with the heat shock at the transition through the λ point of liquid helium in the course of thermal cycling. A possible mesoscopic mechanism of thermally activated and quantum magnetic relaxation is discussed. © *2000 MAIK "Nauka/Interperiodica".*

1. Magnetic relaxation phenomena exhibiting quantum saturation at helium temperatures were observed to occur in amorphous and single-crystal, film, and bulk magnets [1–3]. Metastable states form here usually in a remagnetizing magnetic field, the strength of which does not exceed the coercive force of the material, and one measures the sample magnetization. Magnetic relaxation occurs in this case primarily by thermally activated and quantum creep of domain walls [4–7]. The highest temperature of the transition from the thermally activated to quantum mode and the highest quantum-tunneling frequency for the same volume are observed in antiferromagnetic materials [8–12]. However, the use of a magnetic field to create metastable states in a pure antiferromagnet meets with difficulties, because Zeeman interaction is compensated and the sample magnetization is zero in the fields traditionally employed for observation ($H < 100$ Oe).

2. This paper reports the first observation in antiferromagnetic single crystals (dysprosium orthoaluminate) of magnetic relaxation of metastable states induced by a strong thermal excitation of magnetic crystals immersed in liquid helium at a temperature close to the superfluidity point, at which the heat conductivity of helium undergoes a jump. The dramatic decrease (down to 10^{-7}) of heat removal occurring in the crossover through the λ phase-transition point during the reverse temperature run in thermal cycling created a heat shock, which was due to the release of Joule heat in the strain gauge attached to the sample, and the single crystal was driven to an excited state [13, 14].

A new method is proposed for studying the relaxation of this state, which consists in measuring the magnetostriction in metamagnetic transitions. The sample used in the experiment was a single crystal of dysprosium orthoaluminate $DyAlO_3$ measuring $4 \times 4 \times 1$ mm, which was grown by spontaneous crystallization from a melt solution. The magnetostriction was measured with a tensometric dilatometer (with a relative strain sensitivity of 5×10^{-7}) in fields of up to 4.2 T generated by a superconducting coil within a temperature interval from 4.2 to 1.57 K. The magnetic field was applied along the *a* axis, and the strain was measured along the [110] direction. Below the Néel temperature ($T_N = 3.52$ K [15]), a metamagnetic transition with an $A_yG_x \longrightarrow A_xG_y$ magnetic-structure rearrangement (by the notation of Wollan–Koehler [16]) is observed in $DyAlO_3$ in this experiment geometry. We have found that the metamagnetic transition is accompanied by an anomaly in magnetostriction, and it is the latter that serves in this study as an indicator of the state of the rare-earth subsystem. The experiment was conducted as follows. In the first stage, we measured magnetostriction curves as the sample temperature was lowered from 4.2 down to 1.57 K (with the sample residing in an equilibrium state). For illustration, Figs. 1 and 2 present magnetostriction isotherms of $DyAlO_3$ obtained at $T_1 = 2.3$ K and $T_2 = 2.9$ K. The curves are seen to have a characteristic cupola-shaped anomaly caused by the metamagnetic transition. Curves *1* correspond, in these figures, to the equilibrium state. On attaining the lowest temperature $T = 1.5$ K reached in this experiment, the sample temperature starts to increase. As the liquid-helium bath temperature passes through the λ point, the sample is subjected to a short heat shock (because of the experimental conditions crossing over from isothermal to adiabatic), which excites the crystal. With the sample in this state, the second stage of the experiment begins. The sample temperature is fixed, for instance, at $T = 2.3$ K, and we start to study the tempo-

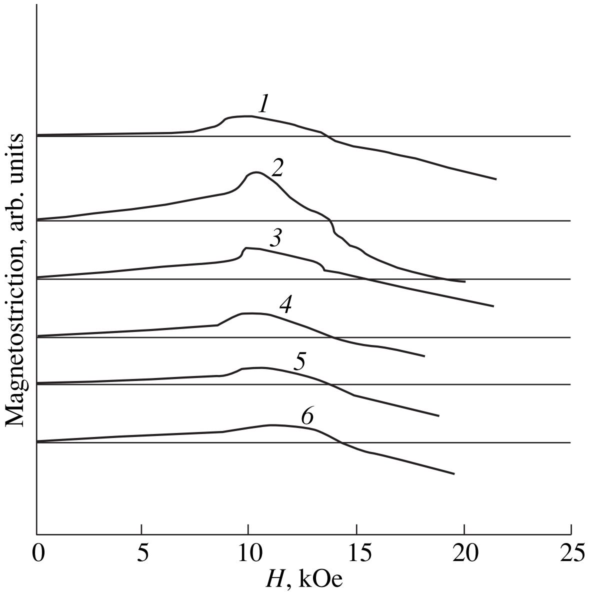

Fig. 1. Magnetostriction isotherms of a $DyAlO_3$ single crystal along the *a* axis at $T = 2.3$ K: (*1*) sample in an equilibrium state and (*2–6*) temporal dependence in the metastable state, *t* (s): (*2*) 0, (*3*) 280, (*4*) 1120, (*5*) 1680, and (*6*) 2240.

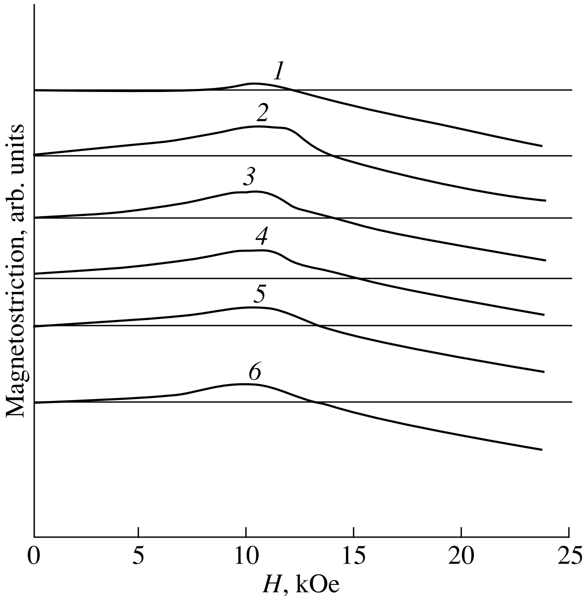

Fig. 2. Magnetostriction isotherms of a $DyAlO_3$ single crystal along the *a* axis at $T = 2.9$ K: (*1*) sample in an equilibrium state and (*2–6*) temporal dependence in the metastable state, *t* (s): (*2*) 0, (*3*) 840, (*4*) 1400, (*5*) 3080, and (*6*) 3920.

ral behavior of the magnetostriction anomaly at the metamagnetic transition by successively obtaining magnetostriction isotherms with a time step $\Delta t = 240$ s (curves *2–6* in Figs. 1 and 2). The subsequent treatment of the results of measurements consists in calculating, for each curve, the ratio of the anomaly amplitude A_n (in the metastable state) to the amplitude A_0 (in the equilibrium state), and in plotting the dependence of $\ln(A_n/A_0)$ on the time of measurement for the given temperature. Fig. 3 presents such plots obtained at $T_1 =$ 2.3 K and $T_2 = 2.9$ K. These plots were used to derive the relaxation constants Γ for the given temperatures ($\Gamma_1 = 1.24 \times 10^{-4}$ s^{-1} and $\Gamma_2 = 1.53 \times 10^{-4}$ s^{-1}). It should be stressed that the values of Γ we determined are in good agreement with those obtained [3] in a study of the low-temperature relaxation in an isomorphous single crystal of terbium orthoferrite $TbFeO_3$ by traditional magnetization measurements. Our experiment differs radically in that it studies the relaxation of metastable states of strongly anisotropic rare-earth ions, which possess large *J* (for the dysprosium ion Dy^{3+}, we have $M_J = \pm 15/2$) and are characterized by pseudo-Ising properties, whereas the authors of [3] dealt with an investigation of the relaxation of the magnetic subsystem formed by Fe^{3+} ions ($S = 5/2$), which represent a classical example of weakly anisotropic ions.

3. Let us now discuss possible mechanisms of thermally activated relaxation and quantum relaxation in the magnetic subsystem of the antiferromagnet under study. One of them could be associated with the formation of domains of a metastable antiferromagnetic phase, which relax through domain wall displacement. Consider this mechanism in more detail. The rare-earth (RE) orthoaluminate $DyAlO_3$ has a distorted perovskite structure described by the space group D_{2h}^{16}. It is characterized by the existence of two nonequivalent sites for rare-earth ions, to which two Ising axes correspond lying in the *ab* plane of the crystal at an angle to one another, and by four pairwise-coupled antiferromagnetic sublattices, whose magnetizations are directed along the Ising axes [17]. Denoting by m_i ($i = 1, 2, 3, 4$) the sublattice magnetizations, the energy of the antiferromagnet in a magnetic field can be presented in the form

$$\begin{aligned} E = E_0 + 1/4\Big[&-H_x\cos\alpha_0(m_1+m_2+m_3+m_4) \\ &-H_y\sin\alpha_0(m_1+m_2-m_3-m_4) \\ &-\frac{1}{2}\lambda_{11}(m_1^2+m_2^2+m_3^2+m_4^2)-\lambda_{12}(m_1m_2+m_3m_4) \\ &-\lambda_{13}(m_1m_3+m_2m_4)-\lambda_{14}(m_1m_4+m_2m_3)\Big], \end{aligned} \tag{1}$$

where H_x and H_y are the magnetic-field components along the *a* and *b* axes, respectively; λ_{ij} are the exchange constants; and α_0 is the angle between the Ising axes and the *a* axis. By minimizing the energy (1) in zero magnetic field, one obtains two twofold-degenerate antiferromagnetic phases [17]: the (A_yG_x) phase, in which $m_1 = m_3 = -m_2 = -m_4 = \pm m$, and the (A_xG_y)

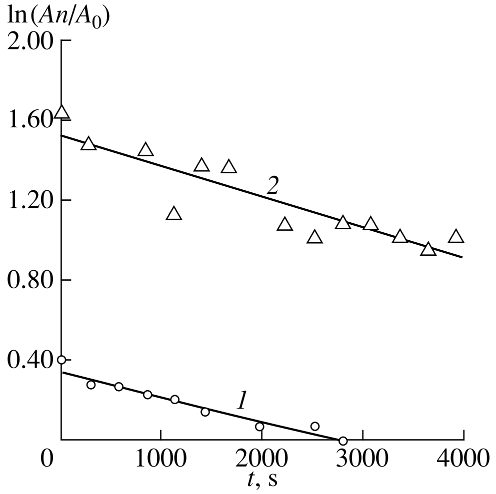

Fig. 3. Time dependence of the logarithmic ratio of the magnetostriction amplitude of the metamagnetic transition in a metastable state, A_n, to the amplitude in an equilibrium state, A_0, for $DyAlO_3$ measured at (*1*) $T_1 = 2.3$ K and (*2*) $T_2 = 2.9$ K.

phase with $m_1 = m_4 = -m_2 = -m_3 = \pm m$. The energies of these phases can be written, respectively, as

$$E(A_yG_x) = \frac{1}{2}[-\lambda_{11} + \lambda_{12} - \lambda_{13} + \lambda_{14}]m^2, \qquad (2)$$

$$E(A_xG_y) = \frac{1}{2}[-\lambda_{11} + \lambda_{12} + \lambda_{13} - \lambda_{14}]m^2. \qquad (3)$$

One of these phases is metastable and will transfer to a more stable one by the thermally activated or quantum relaxation mechanism owing to the difference between their specific energies $\Delta E = E(A_yG_x) - E(A_xG_y) = [-\lambda_{13} + \lambda_{14}]m^2$. The phase transformation can occur by a local displacement of the interface, which represents, in the case of a strong (Ising) anisotropy in question, two adjacent sublattice layers of rare-earth ions with a compensated antiferromagnetic exchange field generated by the neighboring layers. We will arbitrarily call the states of magnetic ions in these boundary layer the "±" states. Because of the Ising character of the RE ion anisotropy, a boundary ion crossing over from the "+" to "–" state has to overcome an energy barrier caused by the ferromagnetic interaction in the sublattice boundary layer, $\Delta E_\pm = \frac{1}{2}\lambda_{11}m\mu$, where μ is the ion magnetic moment. This barrier can be overcome by thermal activation at a finite temperature. Because the Ising properties of the Kramers RE ions in the orthoaluminate are not ideal, i.e., there exists a finite, though strong *g*-factor anisotropy destroying the axial local crystal-field symmetry, quantum tunneling is also not forbidden in the system under study (in a system of non-Kramers Ising ions, this mechanism was considered in [18]). Let us estimate the possible number of ions taking part in boundary phase-transformation events. From the relaxation constant $\Gamma(T) = \omega\exp(-\Delta U/k_BT)$ measured at two temperatures ($T_1 = 2.3$ K and $T_2 = 2.9$ K), we obtain $\Delta U = [k_BT_1T_2/(T_1 - T_2)]\ln(\Gamma_1/\Gamma_2) \sim 3.2 \times 10^{-16}$ erg. On the other hand, $\Delta E_\pm = \frac{1}{2}\lambda_{11}m\mu = \frac{1}{2}H_{11\mathrm{exch}}\mu$, where μ is the rare-earth ion magnetic moment, so that $\Delta E_\pm \sim 1.67 \times 10^{-17}$ erg, in full accord with the data [19] obtained for $DyAlO_3$. A comparison of the two energies shows that a boundary region displacement event involves $\sim 10^1$–10^2 ions. Therefore, the possible quantum tunneling described here is a mesoscopic process in this case. It should be noted that expansion of the metastable phase in the direction perpendicular to the sublattice antiferromagnetic planes is energetically preferable to that in the *ab* plane of the crystal, because in the latter case, the ion would also have to overcome the antiferromagnetic coupling energy required to form the boundary plane. Therefore, the creation of metastable phase formations extended along the *c* axis in each pair of the antiferromagnetically coupled sublattices appears more likely. The overlap of the metastable phases gives rise to the formation of a stable phase with an oppositely directed antiferromagnetism vector in both sublattices. The probability of formation of the above metastable states is high, because the estimated thermal energy built up in the crystal is more than sufficient to transfer all of the crystal to the metastable phase. Indeed, if one takes into account that the observed short jump of the sample temperature in the crossover through the λ point is $\Delta T = 5$ K [13, 14], the specific thermal energy will constitute $\Delta E_T = \rho c\Delta T \sim 3.9 \times 10^7$ erg/cm^3, and the energy of the metastable phase, $\Delta E = E(A_y, G_x) - E(A_x, G_y) = |-H_{13} + H_{14}|m \sim 3.0 \times 10^6$ erg/cm^3. Thus, the above estimates are not at odds with the possibility of existence of the magnetic relaxation mechanism described. The colossal magnitude of the observed thermal expansion, as well as the associated frequency shift of the optical absorption spectrum of $DyAlO_3$ [20] ($\Delta\varepsilon = 10^{-4}$) following the heat shock, may be due to metastable changes in the magnetic subsystem of the crystal, because no such colossal thermal expansion is observed to occur in the $YAlO_3$ yttrium orthoaluminate, the nonmagnetic analog of the sample studied. It should be pointed out that the relative magnitude of the frequency shift of the optical absorption spectrum correlates with the observed colossal thermal expansion $\Delta\varepsilon = 3 \times 10^{-5}$ [13].

One should also bear in mind that thermal excitation in a crystal gives rise to a strong elastic distortion of the lattice, which results in a change of the crystal field and, as a consequence, in a change of the rare-earth ion ground state (the energy spectrum, *g*-tensor components, the character of the wave functions). Magnetostriction measurements permit one to follow the relaxation of such distortions in time. To clarify the nature of the observed colossal metastable strain in the crystal, one has to carry out additional experiments, such as a study of the antiferromagnetic domain structure using magneto-optic methods.

4. This study has revealed an exponential relaxation of metastable magnetic states in rare-earth orthoaluminates with Ising ions. We propose a new method of its investigation, namely, by measuring the temperature and temporal dependences of the magnetoelastic anomalies in metamagnetic transitions.

ACKNOWLEDGMENTS

Support of the Russian Foundation for Basic Research (grant no. 98-02-16469) and of the RF Ministry of Education "Basic Natural Sciences" (grant no. 97-0-7.3-157) is gratefully acknowledged.

REFERENCES

1. B. Barbara, L. C. Sampaio, J. E. Wegrowe, *et al.*, J. Appl. Phys. **73**, 6703 (1993).
2. J. Tejada, X. X. Zhang, and L. I. Ballsells, J. Appl. Phys. **73**, 6709 (1993).
3. X. X. Zhang, J. Tejada, A. Roig, *et al.*, J. Magn. Magn. Mater. **137**, L235 (1994).
4. P. C. E. Stamp, Phys. Rev. Lett. **66**, 2802 (1991).
5. E. M. Chudnovsky, O. Iglesias, and P. C. E. Stamp, Phys. Rev. B **46**, 5392 (1992).
6. S. Takagi and G. Tatara, Phys. Rev. B **54**, 9920 (1996).
7. V. V. Dobrovitskiĭ and A. K. Zvezdin, Zh. Éksp. Teor. Fiz. **109**, 1420 (1996) [JETP **82**, 766 (1996)].
8. B. Barbara and E. M. Chudnovsky, Phys. Lett. A **145**, 205 (1990).
9. E. V. Krive and O. B. Zaslavskiĭ, J. Phys.: Condens. Matter **2**, 9457 (1990).
10. E. N. Bogachek and I. V. Krive, Phys. Rev. B **46**, 14559 (1992).
11. Ji-Min Duan and A. Garg, J. Phys.: Condens. Matter **7**, 2171 (1995).
12. V. Yu. Golyshev and A. F. Popkov, Europhys. Lett. **29**, 327 (1995).
13. N. P. Kolmakova, I. B. Krynetskiĭ, and E. V. Sinitsin, in *Proceedings of the First International Meeting on Magnetoelastic Effects and Applications* (Naples, 1993), p. 297.
14. I. B. Krynetskiĭ, N. P. Kolmakova, and E. V. Sinitsyn, Fiz. Tverd. Tela (S.-Peterburg) **38**, 391 (1996) [Phys. Solid State **38**, 216 (1996)].
15. L. M. Holmes, L. G. van Uitert, R. R. Hecker, *et al.*, Phys. Rev. B **5**, 138 (1972).
16. W. C. Koehler and E. O. Wollan, J. Phys. Chem. Solids **2**, 100 (1957).
17. A. K. Zvezdin, V. M. Matveev, A. A. Mukhin, and A. I. Popov, *Rare-Earth Ions in Magnetically Ordered Crystals* (Nauka, Moscow, 1985).
18. A. K. Zvezdin and A. F. Popkov, Pis'ma Zh. Éksp. Teor. Fiz. **57**, 548 (1993) [JETP Lett. **57**, 562 (1993)].
19. I. B. Krynetskiĭ, V. M. Matveev, and V. V. Matveev, Fiz. Tverd. Tela (S.-Peterburg) **37**, 1548 (1995) [Phys. Solid State **37**, 840 (1995)].
20. B. T. Borowiec, I. B. Krynetskiĭ, M. M. Lukina, *et al.*, in *Abstracts of the International Conference on Magnetism* (Warsaw, 1994), p. 373.

Translated by G. Skrebtsov

Physics of the Solid State, Vol. 42, No. 4, 2000, pp. 726–729. Translated from Fizika Tverdogo Tela, Vol. 42, No. 4, 2000, pp. 708–711.
Original Russian Text Copyright © 2000 by Dolotenko, Zvezdin, Musaev, Platonov, Plis, A. Popov, V. Popov, Tatsenko, Filippov.

MAGNETISM AND FERROELECTRICITY

Faraday Effect of Europium Organic Glass in Megagauss Magnetic Fields

M. I. Dolotenko*, A. K. Zvezdin**, G. G. Musaev**, V. V. Platonov***, V. I. Plis*, A. I. Popov*, V. N. Popov**, O. M. Tatsenko***, and A. V. Filippov*****

** Moscow State Institute of Electronic Engineering (Technical University),*
Zelenograd, Moscow oblast, 103948 Russia

*** Institute of General Physics, Russian Academy of Sciences,*
ul. Vavilova 38, Moscow, 117942 Russia

**** All-Russia Research Institute of Experimental Physics (VNIIEF), Russian Federal Nuclear Center,*
Sarov, Nizhegorodskaya oblast, 607200 Russia

Received July 16, 1999; in final form, September 13, 1999

Abstract—The Faraday rotation of europium organic glass (based on polymethyl methacrylate) in megagauss fields is investigated experimentally and theoretically. The experiment was performed using an MK-1 magnetic explosion generator and laser radiation at the wavelength $\lambda = 0.85$ μm at $T = 30$ K. It is found that the dependence of the rotation angle of the polarization plane on the magnetic field is nonlinear. The theoretical results are compared with the experimental data. The contribution of the orbital angular momentum of europium ions to the Faraday effect is revealed. The conclusion is drawn that the previously found anomalies of the Faraday effect for the laser radiation at the wavelength $\lambda = 0.63$ μm are brought about by the magnetooptical resonance, which is induced by the ultrastrong field. *© 2000 MAIK "Nauka/Interperiodica".*

Earlier [1], we predicted and theoretically investigated a new phenomenon—the substantial transformation of the spin and orbital structure of light rare-earth atoms under the action of ultrastrong (megagauss) magnetic fields. It is known that the ground state (ground multiplet) with a small magnitude of the total angular momentum is realized in light rare-earth ions due to the spin–orbit interaction (for example, in Eu^{3+}, $J = 0$; in Sm^{3+}, $J = 5/2$; etc.), whereas the multiplets with large magnitudes of the angular momentum are the excited ones. In the quasi-classical terminology, the spin and the orbital angular momentum can be considered to be antiparallel to each other in the ground state and parallel in the highest-lying multiplet of the fundamental term. It was demonstrated [1] that the strong magnetic field, when competing with the spin–orbit interaction, changes the mutual orientation of the spin and orbital angular momentum from the antiparallel orientation to the parallel one. This mutual reorientation occurs via series of quantum jumps, rather than continuously. Investigation of this phenomenon seems to be promising, because it provides information on complex many-electron objects such as rare-earth atoms, actinides, high-spin organic molecules, etc. Moreover, the observation and investigation of quantum jumps are also of interest for the physics of ultrastrong magnetic fields, specifically for the development of measuring techniques employed in these fields, since these jumps can be considered as the atomic standards of megagauss fields. The measurement of the Faraday rotation in ultrastrong magnetic fields in the optical and ultraviolet ranges is of considerable promise for the study of quantum reorientation of magnetic moments. This is explained by the fact that, according to [1–5], the Faraday effect brought about by ions with the nonzero orbital angular momentum responds to only the orbital angular momentum of the ion rather than the total magnetic moment (excluding the narrow spectral regions adjacent to the resonant frequencies of the forbidden *f*–*f* transitions).

Traditionally, investigations into the magnetic and magnetooptical properties of rare-earth materials are reduced to consideration of only the ground multiplet of rare-earth ions [5, 6]. In this case, the average orbital angular momentum is proportional to the total magnetic moment of the ion ($J \neq 0$). The inclusion of the multiplet mixing (J–J mixing) results in an additional contribution to the orbital angular momentum and, consequently, to the Faraday rotation, which, in relatively weak fields, linearly depends on the magnetic field [2–5]. In ultrastrong magnetic fields, when the splitting of the levels in the ion becomes comparable to the spin–orbit interaction, the dependence of the average orbital angular momentum on the magnetic field becomes substantially nonlinear [1]. Among the rare-earth ions, the Eu^{3+} ions ($L = 3$, $S = 3$) are of special interest. The ground state of these ions is the singlet with zero total angular momentum. For this reason, the paramagnetic contribution to the Faraday rotation due to the difference in populations of the levels of the ground multiplet split by the magnetic field is not observed.

In [7], the Faraday effect was measured in the organic glass containing the Eu^{3+} ions in magnetic fields up to 11 MOe with the use of laser radiation at the wavelength $\lambda = 0.63$ μm, which is rather close to the absorption line for this ion [8]. The latter circumstance considerably complicates the interpretation of the experimental results, because, in this case, it needs to take into account the resonance contribution to the Faraday effect.

In order to investigate the phenomenon of rotation of the angular momenta of the Eu^{3+} ion, it is necessary to examine the Faraday effect of europium-containing media with the use of the radiation at a frequency well apart from resonant frequencies, which was accomplished in the present work.

1. EXPERIMENT

The Faraday rotation of the organic glass (based on polymethyl methacrylate) containing 5 wt % Eu^{3+} ions was measured in magnetic fields up to 6 MOe at $T \sim 30$ K. The schematic diagram of the experiment is presented in Fig. 1a. A sample of the organic glass 18 mm thick was placed in a flow-type helium cryostat (Fig. 1b). The Faraday effect was measured using the laser radiation at the wavelength $\lambda = 0.85$ μm. The light passed through a polarizer, the sample, analyzers, and two photomultipliers. One of the photomultipliers recorded the Faraday rotation, and the second photomultiplier measured the dependence of absorption on the magnetic field. The absorption of the sample was constant over the entire range of magnetic fields. The ultrastrong magnetic fields were produced by an MK-1 magnetic explosion generator [9]. The error in the measurement of the field was no more 5%. The experimental dependence of the Faraday rotation of the sample is shown in Fig. 2a. It is worth noting that the obtained curve differs drastically from the corresponding dependence, which was observed under radiation at the wavelength $\lambda = 0.63$ μm [7]. Note also the fact that, despite the low content of europium ions in the sample, the dependence of the Faraday rotation on the magnetic field is essentially nonlinear.

2. THEORY

The magnitude of the Faraday effect in the system under investigation is the sum of contributions from the matrix (organic glass) and optical transitions in the Eu^{3+} ions. The contribution from the matrix is of diamagnetic character and linearly depends on the magnetic field up to fields of about 10^2 MOe [10].

The specific rotation of the polarization plane (the Faraday effect) can be represented by the following formula (see, for example, [5, 6]):

$$\alpha_F = \frac{\pi N e^2 L}{mcn}\sum_{a,b}\rho_a \frac{f^+_{ab} - f^-_{ab}}{\omega_{ab}}\varphi(\omega, \omega_{ab}),$$

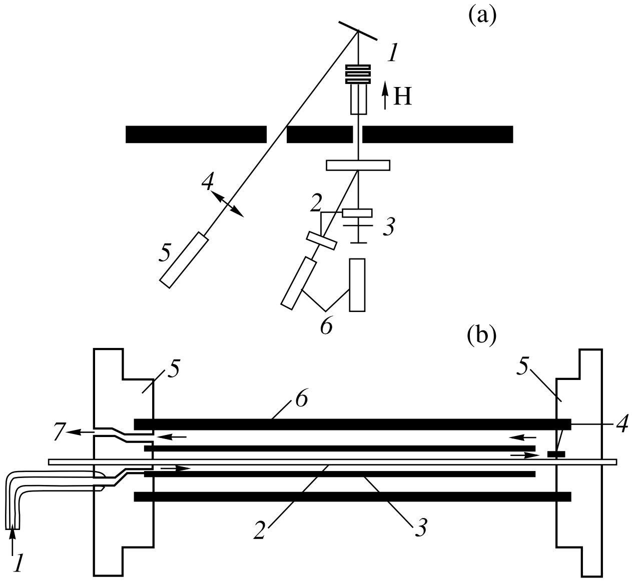

Fig. 1. (a) Schematic diagram for measuring the Faraday rotation in ultrastrong magnetic fields produced by magnetic explosion generator: (*1*) cryostat and sample, (*2*) interference filter ($\lambda = 0.85$ μm), (*3*) analyzer, (*4*) polarizer, (*5*) laser ($\lambda = 0.85$ μm), and (*6*) photoelectric multipliers. (b) Schematic diagram of the flow-type helium cryostat: (*1*) helium inlet, (*2*) optical sensor for measuring the Faraday rotation, (*3*) glass pipe, (*4*) temperature-sensitive element, (*5*) plastic flanges, (*6*) internal cascade of the MK generator, and (*7*) helium outlet.

where

$$f^+, f^- = (\hbar e^2)^{-1} m\omega_{ab}(d^x_{ab} \pm i d^y_{ab})^2$$

are the oscillator strengths, $|a\rangle$ and $|b\rangle$ are the ground and excited states, $\omega_{ab} = \frac{1}{\hbar}(E_b - E_a)$ is the population of the ground state, $L = [(n^2 + 2)/3]^2$, n is the refractive index of the medium, N is the number of ions,

$$\varphi(\omega, \omega_{ab}) = \frac{\omega_{ab}\omega(\omega^2_{ab} - \omega^2 - \Gamma^2_{ab})}{(\omega^2_{ab} - \omega^2 - \Gamma^2_{ab})^2 + 4\omega^2\Gamma^2_{ab}},$$

and Γ_{ab} is the half-width of the a–b transition.

Let us consider in greater detail the contribution from the Eu^{3+} ions to the Faraday effect. The ground state of Eu^{3+} is the singlet $^7F_0$ with $J = 0$, and the energies of excited multiplets are as follows: $E(^7F_1) = 310\ \text{cm}^{-1}$, $E(^7F_2) = 925\ \text{cm}^{-1}$, and $E(^7F_3) = 2 \times 10^3\ \text{cm}^{-1}$. In the general case, the contribution of magnetic ions to the Faraday effect is comprised of the frequent-independent gyromagnetic rotation of polarization plane, which is proportional to the magnetization of ions $\alpha^M_F = C_M M$, and the gyroelectric rotation, which depends on the frequency of the incident wave. The rotation angle of polarization plane in the visible and ultraviolet spectral ranges is predominantly determined

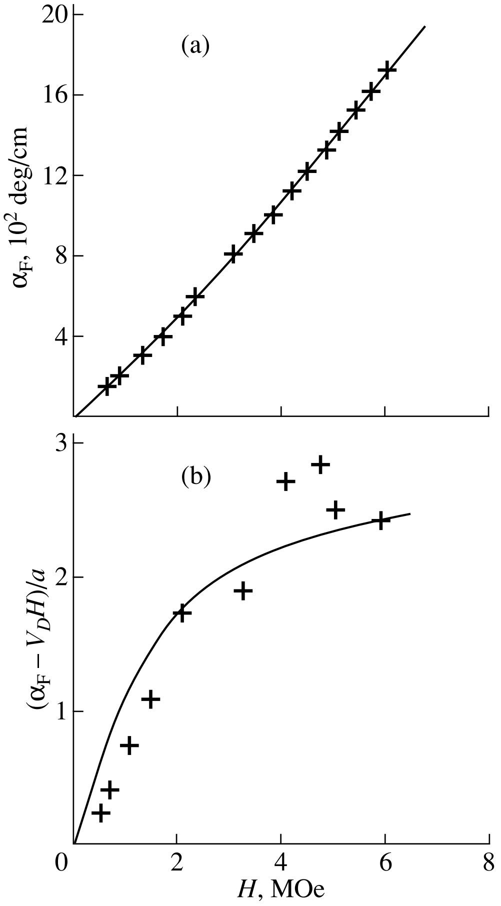

Fig. 2. (a) Dependence of the Faraday rotation angle of the organic glass containing europium ions (5 wt %) on the magnetic field at $T = 30$ K. Crosses correspond to the experimental data obtained under laser radiation at the wavelength $\lambda = 0.85$ μm, and the solid line is the linear approximation of the dependence of the Faraday rotation on the magnetic field. (b) Dependence of the mixing contribution (*J–J* mixing) to the Faraday effect of europium ions on the magnetic field. Crosses correspond to the processing of the experimental data, and the solid line is the calculated field dependence of the average orbital angular momentum for europium ions at $T = 30$ K.

by the gyroelectric contribution due to the electric susceptibility of the medium. For rare-earth ions, which occur in dielectric media, the gyroelectric Faraday effect is formed, for the most part, by the $4f^N - 4f^{N-1}5d$ electric dipole transitions, except the narrow spectral regions close to the resonant frequencies of the forbidden *f–f* transitions. It was demonstrated [2, 4] (see also [5]) that the contribution to the Faraday effect from the $4f^N - 4f^{N-1}5d$ transitions for the magnetic ions with the nonzero orbital angular momentum is equal to

$$\alpha_F = a\langle L_Z\rangle + V_DH. \qquad (1)$$

The first term is the combination of the paramagnetic contribution and mixing contribution, i.e., the contribution due to the multiplet interaction (*J–J* mixing), and the second term is the diamagnetic contribution. In this case, the Faraday effect in the organic glass containing the Eu^{3+} ions can be analyzed with expression (1), in which the second term is the combination of diamagnetic contributions of europium ions and the matrix. It is important that the deviation of the Faraday rotation from the linear dependence with an increase in the external magnetic field H is determined solely by the nonlinear behavior of the average orbital angular momentum of the Eu^{3+} ion as a function of H.

In this work, the average orbital angular momentum $\langle L_Z\rangle$ of the Eu^{3+} ion in ultrastrong magnetic fields at $T = 30$ K was calculated, and the experimental dependence $\alpha_F(H)$ obtained at $\lambda = 0.85$ μm was compared with the theoretical curve described by formula (1). It is seen from Fig. 2a that the theoretical results, which were obtained at $V_D = 3.14 \times 10^4$ deg/(cm Oe) and $a = 75.67$ deg/cm, are in good agreement with the experimental data. In order to determine the contribution from the orbital angular momentum of europium ions to the Faraday effect, we subtracted the diamagnetic term (V_D), which linearly depends on the magnetic field, from α_F and, thus, determined the dependence of the mixing contribution (*J–J* mixing) on the magnetic field. Then, this dependence was compared with the field dependence of the average orbital angular momentum of europium ions, which was also calculated in the present work (Fig. 2b). It is seen that the theoretical results, as a whole, are in reasonable agreement with the experimental data. Note that such a treatment of the results requires the high accuracy of the measurements of H and α_F at a low concentration of the Eu^{3+} ions. For $\delta = \Delta h/h = \Delta\alpha_F/\alpha_F = 2\%$, the $\langle L_Z\rangle$ values obtained from the treatment of the experimental results (Fig. 2b) and the calculated data coincide within the limits of error.

Now, we describe the Faraday effect in ultrastrong magnetic fields in the vicinity of the resonant frequencies of the forbidden *f–f* transitions. This situation is apparently realized under laser radiation at the wavelength $\lambda = 0.63$ μm. To accomplish this, it is necessary to add the contribution of the adjacent forbidden absorption line α_R to expression (1). Then,

$$\alpha_F = a\langle L_Z\rangle + V_DH + \alpha_R(H). \qquad (2)$$

The resonant frequency ω_0 of the actual forbidden optical transition depends on the magnetic field strength H and, in a certain field, can achieve the frequency of the laser radiation used. In other words, we believe that the optical resonance induced by the magnetic field takes place in this case. For the qualitative description of the contribution of the field-induced optical resonance to the Faraday rotation, let us use the linear approximation of the dependence of the resonant frequency on the magnetic field $\omega(h) = \omega_0 + \gamma H$, where γ is the rate of frequency change. In this case, it follows

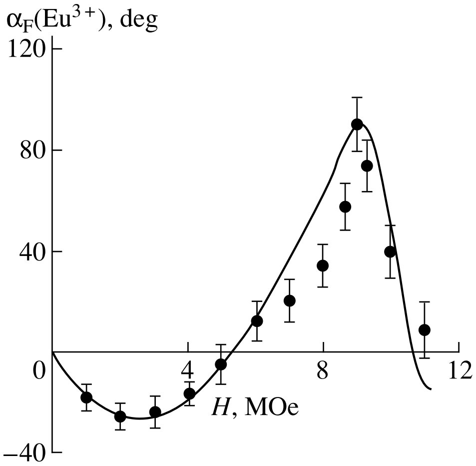

Fig. 3. Dependence of the Faraday rotation of europium ions on the magnetic field at room temperature. Points correspond to the experimental data obtained in [7] under laser radiation at the wavelength $\lambda = 0.63$ μm, and the solid line is the result of calculations by formulas (2)–(5) at H_1 = 8.8 MOe, H_2 = 10.2 MOe, $a = 55$, A = 74 deg/cm, and V_D = 13 deg/(cm MOe).

from formula (1) that

$$\alpha_R(H) = f(H) - f(-H), \tag{3}$$

where

$$f(H) = \frac{C(\omega_0^2(H) - \omega_1^2 - \Gamma^2)\omega_1^2}{(\omega_0^2(H) - \omega_1^2 + \Gamma^2)^2 + 4\omega_1^2\Gamma^2}. \tag{4}$$

Here, Γ is the width of the forbidden line (for rare-earth ions, the spectral lines are very narrow $\Gamma \sim 10^{13}$ s^{-1}), ω_1 is the frequency of the laser radiation (for the radiation at the wavelength $\lambda = 0.63$ μm, $\omega_1 = 3 \times 10^{15}$ s^{-1}), and C is the coefficient proportional to the oscillator strength for this transition. Parameters γ and $\Delta\omega = \omega_0 - \omega_1$ can be expressed through the magnitudes of the fields H_1 and H_2 [where H_1 is the field at which $f(H) = 0$ (according to [7], H_1 = 10 MOe), and H_2 is the field at which $f(H)$ reaches the maximum value (according to [8], H_2 = 9 MOe)], as follows:

$$\Delta\omega = \Gamma H_1/(H_1 - H_2),$$

$$\gamma = \Gamma/(H_1 - H_2).$$

Then, $f(H)$ [see (4)] takes the form

$$f(H) = A\frac{2(H_1 - H_2)(H_1 - H)}{(H_1 - H)^2 + (H_1 - H_2)^2}, \tag{5}$$

where $A = C\omega_0/4\Gamma$.

Expressions (2)–(5) permit us to describe the experimental field dependence of the contribution of the Eu^{3+} ions to the Faraday rotation. Figure 3 shows the comparison between the experimental data obtained in [7] and the results of calculations at H_1 = 8.8 MOe, H_2 = 10.2 MOe, $a = 55$, A = 74 deg/cm, and V_D = 13 deg/(cm MOe).

Thus, the anomalies of α_F, which were found in [7] with the use of the laser radiation at the wavelength $\lambda = 0.63$ μm, are most likely due to the magnetooptical resonance induced by the ultrastrong field.

Investigations into similar optical resonances that are induced by the magnetic field are of interest in determining reference points on the scale of magnetic fields. These points are necessary for grade-up of the technique for measuring the megagauss fields.

The significant result of this work is that the contribution from the average orbital angular momentum of Eu^{3+} ions to the Faraday effect is uniquely determined for the first time. This is an important step toward the experimental revelation of quantum magnetooptical jumps, which are caused by magnetic field-induced reorientation of the orbital angular momentum and the spin of the Eu^{3+} ion from the antiparallel to parallel mutual alignment.

ACKNOWLEDGMENTS

This work was supported by the Russian Foundation for Basic Research (project no. 97-02-17-972), the Foundation for Basic Natural Sciences of the Ministry of Education of the Russian Federation (project no. 97-0-7.036), the International Scientific and Technical Program (MNTP) (project no. 97-1071), and the Federal Program “Integration” (project no. K-0573).

REFERENCES

1. A. K. Zvezdin, A. S. Ovchinnikov, V. I. Plis, *et al.*, Zh. Éksp. Teor. Fiz. **109**, 1742 (1996).
2. U. V. Valiev, A. K. Zvezdin, G. S. Krinchik, *et al.*, Zh. Éksp. Teor. Fiz. **85**, 311 (1983) [Sov. Phys. JETP **58**, 181 (1983)].
3. U. V. Valiev and A. I. Popov, Fiz. Tverd. Tela (Leningrad) **27**, 2729 (1985) [Sov. Phys. Solid State **27**, 1636 (1985)].
4. A. K. Zvezdin, A. I. Popov, and Kh. N. Turkmenov, Zh. Éksp. Teor. Fiz. **28**, 1760 (1986).
5. A. K. Zvezdin and V. A. Kotov, *Modern Magnetooptics and Magnetooptical Materials* (IOP Publishing, UK, 1997).
6. A. K. Zvezdin and V. A. Kotov, *Magnetooptics of Thin Films* (Nauka, Moscow, 1988).
7. A. I. Pavlovskiĭ, V. V. Druzhinin, O. M. Tatsenko, *et al.*, Pis’ma Zh. Éksp. Teor. Fiz. **31**, 659 (1980) [JETP Lett. **31**, 622 (1980)].
8. P. Görlich, H. Karras, and G. Kötitzand, and R. Lehmann, *Spectroscopic Properties of Activated Laser Crystals* (Physica Status Solidi **5**, (1964); **6** (1964); **8** (1965); Nauka, Moscow, 1966), p. 207.
9. A. D. Sakharov, Usp. Fiz. Nauk **88**, 725 (1966) [Sov. Phys. Usp. **88**, 294 (1966)].
10. V. V. Druzhinin and O. M. Tatsenko, Opt. Spektrosk. **36**, 733 (1974).

Translated by N. Korovin

Physics of the Solid State, Vol. 42, No. 4, 2000, pp. 730–733. Translated from Fizika Tverdogo Tela, Vol. 42, No. 4, 2000, pp. 712–715.
Original Russian Text Copyright © 2000 by Loseva, Ovchinnikov, Chernov, Ivanova, Kiselev, Bovina.

Correlation between the Magnetic and Electrical Properties of the $(VS)_x(Fe_2O_3)_{2-x}$ Oxysulfide System

G. V. Loseva, S. G. Ovchinnikov, V. K. Chernov, N. B. Ivanova,
N. I. Kiselev, and A. V. Bovina

Kirenskiĭ Institute of Physics, Siberian Division, Russian Academy of Sciences,
Akademgorodok, Krasnoyarsk, 660036 Russia
e-mail: sgo@post.krascience.rssi.ru

Received July 9, 1999; in final form, October 5, 1999

Abstract—The correlation between the magnetic and electrical properties of the $(VS)_x(Fe_2O_3)_{2-x}$ $(0.9 < x < 1.25)$ oxysulfide solid solutions has been studied. The crossover of conductivity from the semimetallic to semiconducting type is accompanied by changes in the magnetic susceptibility, which are characteristic of the transition from delocalized to localized electrons. For $x = 1.25$, a region of the ferromagnetic ordering has been established in the temperature range 90–120 K. *© 2000 MAIK “Nauka/Interperiodica”.*

The observation of a colossal magnetoresistance in $La_{1-x}Ca_xMnO_3$ doped manganites has raised interest in other magnetically ordered materials, in which a change in the magnetic properties is accompanied by changes in the electrical ones, namely, by a reversal of the conductivity type and a sharp increase in the magnetoresistance.

The magnetically ordered mixed 3*d*-metal compounds, among which are the $Me^{I}Me^{II}A$ and $MeA^{I}A^{II}$ doped chalcogenides (Me is 3*d* metal, and A = S or Se), chalcogenide spinels, e.g., $M_{1-x}Cu_xCr_2Se_4$ (M = Zn, Ca, or Hg), and the $(MeO)_x(MeA)_{1-x}$-type compounds, exhibit a broad spectrum of exchange interactions and electrical properties [1]. By varying the composition of these compounds, as well as by properly changing external factors (temperature, electric and magnetic fields, irradiation, etc.), one can tailor new materials to the desired physicotechnical requirements, as well as make possible such phenomena as the photomagnetic effect, the metal–insulator transition, the onset of the ferromagnetic state in an antiferromagnetic phase, etc. In view of the specific features of their electronic and magnetic states, these mixed magnetically ordered 3*d*-metal compounds deserve comprehensive experimental and theoretical investigations.

This work reports the results of investigations into structural, thermal, electrical, and magnetic properties of the $(VS)_x(Fe_2O_3)_{2-x}$ oxysulfide system with a spinel structure of the Fe_3O_4 magnetite type.

1. SAMPLE PREPARATION

Polycrystalline samples of the $(VS)_x(Fe_2O_3)_{2-x}$ oxysulfide system with compositions in the range $0.9 < x < 1.25$ were prepared by sintering the appropriate amounts of vanadium monosulfide VS and oxide α-Fe_2O_3 in evacuated silica tubes at 1100 K for three days, with subsequent cooling at a rate of 40 K/h.

The vanadium monosulfide VS was prepared by annealing of pure, electrolytically produced vanadium metal and 99.999%-pure sulfur in evacuated silica tubes at 1200 K for three days. The monosulfide thus obtained had at 300 K the β-VS structure (MnP type, P_{mcn}, D_{2h}^{16}).

The finely dispersed powder of α-Fe_2O_3 hematite was prepared as the final product of the dehydration of synthesized iron α-hydroxide (α-FeOOH-goethite) by calcination at 558 K. The α-Fe_2O_3 thus obtained had an Al_2O_3-type structure (D_{3d}^{6}, $R3C$) with the unit cell parameters corresponding to the tabulated values for the α-Fe_2O_3 hematite at 300 K. The dehydration temperature of α-FeOOH was derived from the differential thermal analysis (DTA) data. Besides, the Mössbauer spectra of our α-Fe_2O_3 hematite yielded the estimate $H_{eff} = 515.5$ kOe, which likewise is in agreement with the tabulated value for α-Fe_2O_3 at 300 K.

2. EXPERIMENTAL TECHNIQUE

The X-ray diffraction patterns of the samples were recorded on a DRON-3 diffractometer with CuK_α radiation at 300 K. The X-ray diffraction pattern of the sample with $x = 1.25$ was also obtained at 120 K.

DTA curves were measured with a MOM derivatograph in the range 300–1400 K at a rate of 10 deg/min. The powder samples of the oxysulfides under study were placed in specially-shaped evacuated silica tubes. For each composition, the DTA curves were obtained in three to five heating–cooling runs.

1063-7834/00/4204-0730$20.00 © 2000 MAIK “Nauka/Interperiodica”

The electrical resistivity ρ was measured by the four-probe dc potentiometric method in the range 77–300 K. The parallelepiped-shaped pressed-powder samples 10 × 5 × 3 mm in size were annealed in evacuated silica tubes at 1300 K for 1 h.

The temperature behavior of the real part of the initial magnetic susceptibility χ' was studied on a setup comprising an inductance bridge and a phase-sensitive detector in the range 77–300 K. The measurements of χ' were carried out on oxysulfide powders placed in a special container 2 mm in diameter and 15 mm long. The powders used in the χ'(*T*) measurements were then pressed into the samples for the ρ(*T*) studies.

3. RESULTS

3.1. X-ray diffraction analysis. X-ray diffraction analysis of the $(VS)_x(Fe_2O_3)_{2-x}$ system with compositions $x = 0.9$, 1.1, and 1.25 showed that at 300 K the samples have a 90–95% spinel structure of the $FeO \cdot Fe_2O_3$ magnetite type (H_1; O_h^7–$Fd3m$) with a similar cubic-lattice parameter ($a \sim 8.39$ Å [2]). No additional clearly pronounced phases were revealed. The earlier measurement [3] made for $x = 1.0$ showed a sulfospinel phase with a Fe_3O_4-type structure that constituted up to 80%. It was found that the cooling of the sample with $x = 1.25$ from 300 to 120 K is accompanied by structural changes with a lowering of the symmetry. Note that the electronic transition in Fe_3O_4 (the Verwey transition at $T_V = 119$ K) with a decrease in the temperature $T < T_V$ is accompanied by a small orthorhombic lattice distortion of ~0.05% [2]. Above T_V, the Fe^{2+} and Fe^{3+} ions randomly occupy the octahedral sites, and below T_V, they are ordered.

3.2. Differential thermal analysis. The DTA curves revealed a reversible endothermic effect for all the compositions at $T \sim 880$ K, which, by analogy with the DTA curves obtained for the Fe_3O_4 magnetite and $FeS \cdot Fe_2O_3$ sulfomagnetite (the endothermic effects at 830 and 850 K correspond to the Curie temperatures T_c), can be identified with the Curie points of the vanadium oxysulfides. Besides, the T_c temperature for the $(VS)_{1.0}(Fe_2O_3)_{1.0}$ composition prepared by sintering equimolar amounts of the monosulfide and oxide, which was derived earlier from magnetic measurements and the corresponding DTA endothermic peak, is approximately 870 K [3].

The DTA curves of the compositions studied yielded a melting temperature of 1340 K for $x = 0.9$, which increases to 1370 K for $x = 1.25$.

3.3. Electrical properties. Figure 1 presents the logarithm of the resistivity as a function of temperature, log[ρ(*T*)], plotted for the compositions $x = 0.9$, 1.1, and 1.25 in the range 77–300 K. One can readily see that the log[ρ(*T*)] dependences for $x = 0.9$ and 1.1 at temperatures from 80 to 240 K have semiconducting character, and at $T > 240$ K, the oxysulfide with $x = 0.9$ undergoes a smooth crossover from the semiconducting to semimetallic type of conductivity. The composition with $x = 1.1$ in the range 240–280 K exhibits a decrease in the resistivity by about an order of magnitude with the activated character of conductivity retained up to 300 K. Earlier measurements for the composition with $x = 1.0$ revealed a decrease in ρ by a factor of seven or eight in the range 280–330 K, with activated conductivity persisting above 350 K [3].

It is also seen from Fig. 1 that the temperature behavior ρ(*T*) for samples with $x = 0.9$ and 1.1 has an activated character in the range 160–240 K, whereas for $x = 1.25$, the conductivity is semimetallic. According to [4], such a concentration behavior of the curves for the oxysulfide system under study is characteristic of disordered systems with a concentration-driven Anderson-type metal–insulator transition at a critical concentration x_c. Note that the concentration $x_c = 1.25$ is critical for the $(VS)_x(Fe_2O_3)_{2-x}$ system, because it is at this concentration that the conductivity crosses over from the semiconducting to semimetallic type.

As the monosulfide concentration *x* in the vanadium oxysulfide system increases, the drop in ρ within the range 77–300 K increases from 1.5 orders of magnitude for $x = 0.9$ to nine orders for $x = 1.25$.

The oxysulfide with $x = 1.25$ in the range 150–180 K undergoes a change in the conductivity type from the semiconductor to the semimetal with a change in the electrical resistivity from 10^8 to 10^{-1} Ω cm.

3.4. Magnetic properties. Figure 2 shows temperature dependences of the real component of the initial magnetic susceptibility for the $(VS)_x(Fe_2O_3)_{2-x}$ system with compositions $x = 0.9$ and 1.1. The composition with $x = 0.9$ was found to have an anomaly in the χ'(*T*)

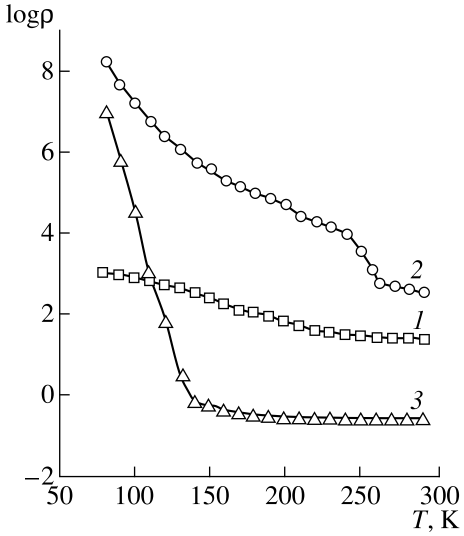

Fig. 1. Temperature dependences of the electrical resistivity of the $(VS)_x(Fe_2O_3)_{2-x}$ system: $x =$ (*1*) 0.9, (*2*) 1.1, and (*3*) 1.25.

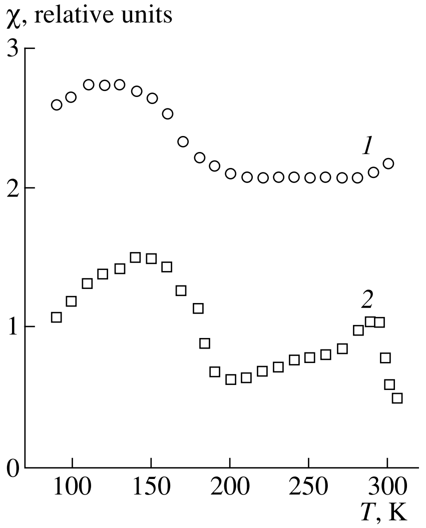

Fig. 2. Temperature dependences of the magnetic susceptibility of the $(VS)_x(Fe_2O_3)_{2-x}$ system. x: (*1*) 0.9 and (*2*) 1.1.

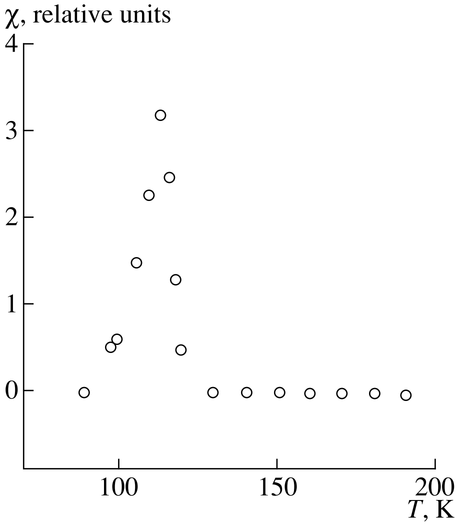

Fig. 3. Temperature dependence of the magnetic susceptibility of the $(VS)_{1.25}(Fe_2O_3)_{0.75}$ composition.

curve in the range 80–210, which peaks at 125 K. In the range 210–280 K, the $\chi'(T)$ curve is temperature independent, with subsequent increase in the susceptibility as one approaches 300 K. The composition with $x = 1.1$ exhibits two broad peaks in the $\chi'(T)$ curve at 145 and 298 K.

Figure 3 displays the $\chi'(T)$ curve for the composition with $x = 1.25$. As is seen from the temperature dependence of the magnetic susceptibility, this composition reveals the magnetization within a limited temperature range from 90 to 120 K with a peak at 115 K and two magnetic transformation points at 90 and 120 K.

The present experimental studies of the physical properties of the $(VS)_x(Fe_2O_3)_{2-x}$ oxysulfide system with compositions in the range $0.9 < x < 1.25$ allow the following conclusions on the correlation between the electrical and magnetic characteristics.

(1) As the sulfide concentration x in samples of the system increases, one has observed (i) a concentration-driven semiconductor–semimetal transition at $x_c = 1.25$; and (ii) an anomaly in the magnetic susceptibility in the range 80–210 K for compositions with $x = 0.9$ and 1.1, followed by an increase in the susceptibility, which is replaced by the onset of magnetization within the limited temperature range 90–120 K for $x = 1.25$.

(2) Measurements of the temperature behavior of the electrical resistivity and susceptibility showed that (i) for the composition with $x = 0.9$, a monotonic change in the conductivity type at $T > 240$ K is accompanied by a change in the $\chi'(T)$ curve from a temperature-dependent to temperature-independent character in the range $210 < T < 290$ K; and (ii) for the composition with $x = 1.1$, similar to $x = 1.0$ [3], the change in ρ by an order of magnitude at 240–300 K is accompanied by the appearance of a peak in the $\chi'(T)$ curve at 298 K.

(3) The results obtained for the composition with $x = 1.25$ appear interesting. The semiconductor–semimetal crossover in the conductivity type entailing a change in ρ by nine orders of magnitude in the range 160–180 K is accompanied by structural changes and a symmetry lowering. One has also observed the existence of magnetization at 90–120 K with a peak at 115 K in the $\chi'(T)$ curve and two magnetic-transition points.

4. DISCUSSION

The electronic structure of the $FeS \cdot Fe_2O_3$ oxysulfides has recently been discussed [3] in terms of the band structure of the Fe_3O_4 magnetite. Both compounds are characterized by ferrimagnetic ordering of the iron ions. Below the Verwey point, the formula of the iron oxysulfide can be presented in the form $Fe_A^{3+}S^{2-}Fe_B^{2+}Fe_B^{3+}O_3^{2-}$. The current carriers are the t_{2g} electrons in the B sublattice moving in a narrow d band characterized by strong electron correlations. Based on the data obtained for $FeS \cdot Fe_2O_3$, and assuming the spinel lattice is retained, one can propose the formula $V_A^{3+}S^{2-}Fe_B^{2+}Fe_B^{3+}O_3^{2-}$ for the $VS \cdot Fe_2O_3$ compound. The V^{3+} ion occupying a tetrahedral site has two d electrons in the e_g orbitals; the e_g band formed by these electrons is half-filled and also experiences the effects of strong electron correlations. The correlations make the vanadium e_g band split into a lower and upper Hubbard subbands with the Fermi level falling in the Mott–Hubbard gap for $x = 1$. In compositions with $x = 1$, the e_g band is filled less than one half for $x < 1$, and above one half for

$x > 1$. Electron transfer from the vanadium to iron bands, and electron collectivization to form narrow *d* bands, complicates the pattern of the electronic structure. Nonetheless, there is no question that the carriers in the compounds under study are strongly correlated electrons from the narrow *d* bands, for which transitions between localized and delocalized states induced by slight variations of external parameters (temperature, composition, etc.) are typical [4]. One can thus visualize various modes of behavior, which should affect both the electrical and magnetic properties.

Because V^{3+} has $S = 1$, the $(VS)_x(Fe_2O_3)_{2-x}$ system should be ferrimagnetic. A comparison of curves *1* and *2* in Figs. 1 and 2 shows that, in the region of semimetallic conductivity, the susceptibility follows the Pauli-type temperature dependence, which implies that the *d* electrons are delocalized. As the temperature decreases to the level where the conductivity is activated, the temperature dependence of the susceptibility takes on the form characteristic of localized electrons. Thus, the changes in the temperature behavior of the electrical and magnetic properties for compositions with $x = 0.9$ and 1.1 are correlated.

For the composition with $x = 1.25$, the situation is more complex. Here, the ferromagnetic region existing in a narrow temperature range appears below $T = 160$ K, where the conductivity crosses over from the semimetallic to semiconducting character. Magnetic phases of this type were predicted in [1] as the result of the temperature-induced exchange in the system of band carriers, whose concentration in the semiconducting phase increases with a rise in the temperature. Another possible reason may be that the ferron states becoming stabilized [5] inside the two-sublattice matrix, ferrimagnetic in our case. A similar temperature dependence of the magnetization with a narrow peak near 473–533 K is known to occur in the FeS_x iron sulfide system with $x = 1.11$ [6, 7].

ACKNOWLEDGMENTS

This work was supported by the Russian Foundation for Basic Research, project no. 99-02-17405.

REFERENCES

1. A. A. Berdyshev, *Exchange Interactions in Magnetically Ordered Solids and the Associated Effects*, Doctoral Dissertation in Mathematical Physics (Sverdlovsk, 1975).
2. L. R. Bickford, Rev. Mod. Phys. **25**, 75 (1953).
3. G. V. Loseva, G. M. Mukoed, S. G. Ovchinnikov, *et al.*, Fiz. Tverd. Tela (Leningrad) **34**, 1765 (1992) [Sov. Phys. Solid State **34**, 940 (1992)].
4. N. F. Mott, *The Metal–Insulator Transitions* (Taylor & Francis, London, 1974; Nauka, Moscow, 1979).
5. É. L. Nagaev, *Physics of Magnetic Semiconductors* (Nauka, Moscow, 1979).
6. T. Hihara, J. Sci. Hirosima Univ., Ser. A **24**, 31 (1960).
7. G. V. Loseva, S. G. Ovchinnikov, and G. A. Petrakovskiĭ, *The Metal–Dielectric Transition in 3d Metal Sulfides* (Nauka, Novosibirsk, 1983).

Translated by G. Skrebtsov

Physics of the Solid State, Vol. 42, No. 4, 2000, pp. 734–738. Translated from Fizika Tverdogo Tela, Vol. 42, No. 4, 2000, pp. 716–720.

MAGNETISM AND FERROELECTRICITY

Anisotropy of the Magnetoelectric Effect in β'-$Gd_2(MoO_4)_3$

B. K. Ponomarev*, E. Stiep, H. Wiegelmann**, A. G. M. Jansen**,**
P. Wyder, and B. S. Red'kin***

**Institute of Solid-State Physics, Russian Academy of Sciences, Chernogolovka, Moscow oblast, 142432 Russia*
e-mail: ponom@issp.ac.ru
***Grenoble High Magnetic Field Laboratory, Grenoble Cedex 9, F-38042 France*

Received August 9, 1999

Abstract—An experimental study is reported of the nonlinear magnetoelectric effect in the metastable orthorhombic ferroelectric ferroelastic paramagnetic β' phase of $Gd_2(MoO_4)_3$ in magnetic fields of up to 20 T and at temperatures of 4.2 and 0.4 K. It is shown that the present models of the paramagnetoelectric effect can be reconciled with experiments only for low magnetic fields. A new approach to the description of the magnetoelectric effect in rare-earth molybdates is proposed, which is based on a model of single-ion magnetostriction. *© 2000 MAIK "Nauka/Interperiodica".*

The metastable orthorhombic ferroelectric β' phase of $Gd_2(MoO_4)_3$ (gadolinium molybdate) exists at temperatures below 159°C [1]. Gadolinium molybdate crystallizes at 1165°C in a tetragonal β phase, which belongs to the space group $P\bar{4}2m$. Further cooling transforms it from the tetragonal β to a monoclinic α phase. The β–α phase-transition point for $Gd_2(MoO_4)_3$ is 857°C. However, this transformation proceeds very slowly, and the high-temperature phase can be preserved by fast cooling. If the thermodynamically metastable tetragonal β phase of $Gd_2(MoO_4)_3$ is cooled still more, it undergoes a second phase transformation at 159°C. This transformation produces the ferroelastic ferroelectric orthorhombic β' phase with a lower symmetry *Pba*2. While this phase is also thermodynamically metastable, it is very stable kinetically.

Rare-earth ions in rare-earth molybdates are trivalent and have large magnetic moments. The magnetic moment of a Gd^{3+} ion in gadolinium molybdate is $M_S = 7\mu_B$. A magnetic-field-induced change in the orientation of the magnetic moment of a rare-earth ion should give rise to a perturbation of the molybdate lattice, which cannot but affect the electric polarization of the ferroelectric lattice. This accounts for the interest in the possible existence of the magnetoelectric effect in rare-earth molybdates. The first member of the family of rare-earth molybdates where the magnetoelectric effect was observed is $Tb_2(MoO_4)_3$ [2]. It was explained as being due to the electric polarization of the ferroelectric subsystem in $Tb_2(MoO_4)_3$ being affected by the single-ion magnetostriction of the Tb^{3+} ions. This interpretation was confirmed by measurements of the magnetoelectric effect in $Tb_2(MoO_4)_3$ [3]. It was also shown experimentally that at $T = 77$ K, the magnetically induced electric polarization in $Gd_2(MoO_4)_3$ in a field $H = 11$ T is $P \leq 10^{-10}$ C/cm^2. This is several orders of magnitude lower than the value for $Tb_2(MoO_4)_3$. The magnetoelectric effect in $Gd_2(MoO_4)_3$ was measured at temperatures ranging from 300 to 5 K and in magnetic fields of up to 19 T oriented along the [100] and [010] axes [4]. The $P(H)$ isotherms had a hysteresis induced by the drift of the electric polarization. A paramagnetism–antiferromagnetism magnetic phase transition was reported [5] to occur at $T \approx 0.3$ K.

This work presents the results of measurements of the magnetoelectric effect in $Gd_2(MoO_4)_3$ made at temperatures of 4.2 and 0.4 K and magnetic fields of up to 20 T for various magnetic-field directions in the (001) plane. It is shown that the field dependences undergo a qualitative change in pattern as the temperature is lowered from 4.2 to 0.4 K. This is not accompanied by any change in the character of the angular dependences. Electric polarization vs. induced magnetization plots $P(m)$ have been constructed. It is shown that calculations based on the frequently employed approximation $P \sim m^2$ very strongly differ from the experiment. On the other hand, calculations making use of the theory of single-ion magnetostriction agree much better with the experiment.

1. SAMPLES AND EXPERIMENT

$Gd_2(MoO_4)_3$ single crystals were grown by the Czochralski technique [6]. The sample was a rectangular parallelepiped measuring $7 \times 7 \times 1$ mm. The large faces were parallel to the (001) plane. Prior to the measurements, the sample was made a single domain. The details of the corresponding technique can be found in [7–9]. The magnetoelectric effect measurements in a constant magnetic field are described in [10, 11]. Cooling the sample to 0.4 K was achieved by ^{3}He pumping.

The electric polarization was determined by the dc technique. The potential difference V between the electrodes deposited on the (001) sample faces was measured with a Keithley-617 electrometer. The electrometer input capacitance was $C_{em} = 435.5$ pF. The sample capacitance was $C_{sample} = 3.76$ pF. An additional capacitor $C_{add} = 291$ pF was connected parallel to the sample to achieve an electrometer-input time constant long enough to enable prolonged measurements in a dc magnetic field. The input circuit time constant was several hours long. Measurement of a magnetoelectric-effect isotherm $P(H)$ took 10 min. The measurement error was ~5%.

The magnetically induced electric polarization $P(H)$ was measured along the [001] axis. The magnetic field was applied in the (001) plane. The angle φ between the [010] axis and the magnetic field was varied from 0 to 90°. The measurements were carried out in magnetic fields of up to 20 T. When obtaining a $P(H)$ isotherm, the magnetic field was increased from zero to the maximum magnitude of 20 T for 5 min. The maximum field was maintained for approximately 30 s, after which it was brought down for 5 min. The magnetic field H and the potential difference V between the (001) sample faces were recorded automatically in 1-s increments.

The experimental plots exhibited a hysteresis. The electric polarization grew noticeably in magnitude at a constant magnetic field. This was considered an unambiguous indication of a drift of the sample electric polarization in time. The correction for the drift was determined in the following way. Measurements of the drift rate were repeated three times for each $P(H)$ isotherm: in a zero field directly before beginning an isotherm measurement, at the maximum field, and immediately after the field reached zero. The differences between the three values of the drift rate for the same isotherm were not large, about 10%, but for different isotherms they could differ by several times. The drift rate for each given isotherm was assumed to be time independent. It was determined by averaging these three values. After finding the drift rate for each isotherm, its dependence on time was calculated. It was subtracted from the experimental time dependence of the polarization. The time was eliminated between the $P(t)$ and $H(t)$ dependences, and in this way we obtained $P(H)$ isotherms corrected for the drift of the electric polarization. The correction varied from 5 to 25% for different isotherms. The isotherms $P(H)$ corrected for the drift showed practically no hysteresis at all. The direction of the drift did not change when the magnetic-field derivative with respect to time reversed its sign, but did change under the sign reversal of the magnetoelectric effect. The drift always occurred in the direction of increasing absolute value of the electric polarization.

2. RESULTS

Figure 1 presents $P(H)$ plots obtained on gadolinium molybdate at a temperature of 4.2 K and various values of φ. The $P(H)$ plots are nonlinear. In weak fields, below approximately 1 T, the field dependences of polarization are quadratic to within $\delta P/P < 8\%$. Above 5 T, a trend to saturation is seen, but the growth of polarization does not stop at the maximum field $H = 20$ T. Curve *1* in Fig. 1 is obtained at $\varphi = 6.2°$. At $H = 20$ T, the magnetically induced electric polarization is $P \approx 0.3 \times 10^{-9}$ C/cm^2 $= 0.0014P_s$. As φ increases, the polarization decreases, and at $\varphi \approx 45°$ the sign of the effect is reversed. Within the $45° < \varphi < 90°$ interval, the $P(H)$ dependences differ from those for $0° < \varphi < 45°$ only in the sign.

Figure 2 shows $P(H)$ plots obtained at 0.4 K for different φ. They qualitatively differ from those measured at 4.2 K. In weak fields $H < 1$T, a comparatively fast growth of the electric polarization is observed. For $H > 1$T, the growth rate slows down considerably, and subsequently remains practically constant up to $H = 20$T.

Curve *1* in Fig. 2 was obtained at $\varphi = 6.2°$. At $H \approx 1$ T, the electric polarization on this curve reaches $P \approx 0.2 \times 10^{-9}$ C/cm^2. At $H = 20$ T, the electric polarization reaches $P \approx 0.3 \times 10^{-9}$ C/cm^2.

Figure 3 displays $p_{red}(\varphi) = P(\varphi)/P_0$ reduced relations taken at $H = 20$ T at the temperatures of 4.2 K (circles)

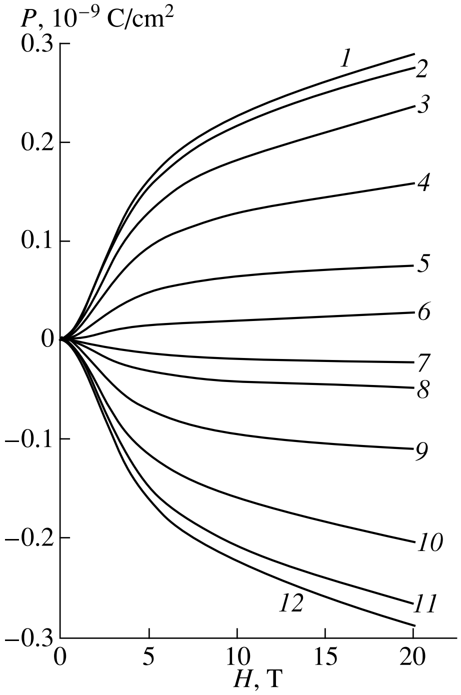

Fig. 1. Electric polarization in $Gd_2(MoO_4)_3$ along the [001] axis induced by a magnetic field applied in the (001) plane. The measurements were performed at $T = 4.2$ K at different angles φ between the field and the [010] axis. φ (deg): (*1*) 6.2°, (*2*) 10.6°, (*3*) 19.5°, (*4*) 28.4°, (*5*) 37.3°, (*6*) 43.9°, (*7*) 48.4°, (*8*) 50.6°, (*9*) 59.5°, (*10*) 68.4°, (*11*) 77.2°, and (*12*) 95°.

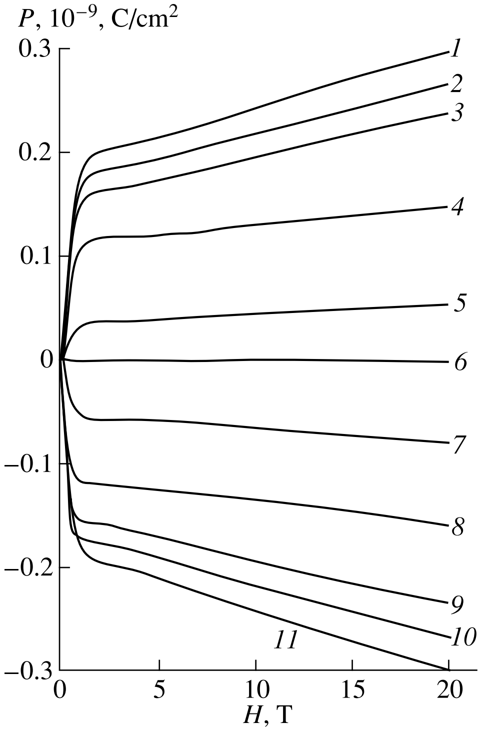

Fig. 2. Same as in Fig. 1, but for $T = 0.4$ K. φ (deg): (*1*) 6.2, (*2*) 15.1, (*3*) 19.5, (*4*) 28.4, (*5*) 41.7, (*6*) 46.2, (*7*) 55.0, (*8*) 63.9, (*9*) 72.8, (*10*) 77.3, and (*11*) 90.6.

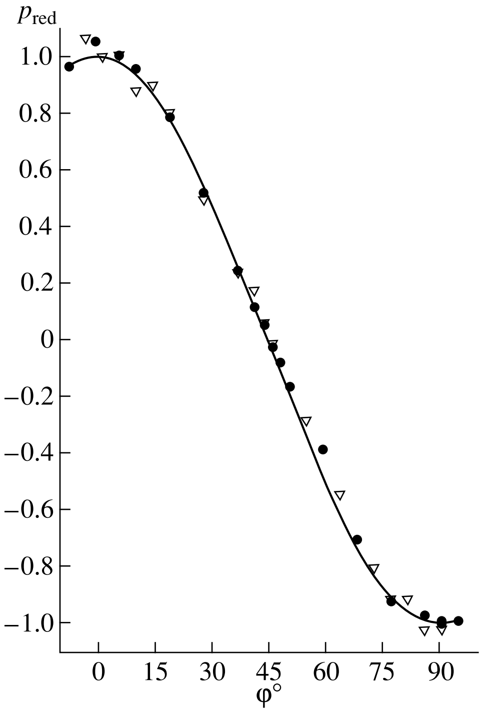

Fig. 3. Reduced electric polarization $p_{red}(\varphi) = P(\varphi)/P_0$ in $Gd_2(MoO_4)_3$ as a function of the angle φ between the [010] axis and the magnetic-field direction. Magnetic field $H = 20$T. The temperature: 4.2 K (circles) and 0.4 K (triangles).

and 0.4 K (triangles). The values of P_0 were obtained by least-squares fitting the angular dependences $P(\varphi)$ measured at $H = 20$ T by the function $P(\varphi, H) = P_0(H)\cos(2\varphi)$. They are $P_0(4.2\text{ K}) \approx P_0(0.4\text{ K}) \approx 0.29 \times 10^{-9}$ C/cm^2. The curve in Fig. 3 is a plot of the expression $p_{red}(\varphi) = \cos 2\varphi$. One readily sees that the experimental angular dependences of the electric polarization presented here for the above two temperatures do not practically differ from one another and are satisfactorily fitted by this expression.

Figure 4 plots the magnetically induced electric polarization as a function of reduced magnetization $P(m) = P(M/M_S)$. They were obtained by eliminating the magnetic field H between the experimental field dependences of the magnetization, $M(H)$, and electric polarization, $P(H)$. The magnetization data for $Gd_2(MoO_4)_3$ were taken from [10] for the temperature of 4.2 K, and from [12, 13] for 0.4 K. The character of the $P(m)$ relation undergoes qualitative changes as the temperature is lowered from 4.2 to 0.4 K. This appears only natural, because by [5], a magnetic phase transition from the paramagnetic to antiferromagnetic state takes place near 0.3 K. At $m = 1$, the $P(m)$ dependences exhibit a strong anomaly at both temperatures. The lines through the plots *1* and *3* measured at 0.4 K are drawn to aid the eye. The lines approximating relations *2* and *4* measured at 4.2 K were calculated using the expressions of the theory of single-ion magnetostriction [14].

3. DISCUSSION

The theory of the paramagnetoelectric effect treated in [15] proposes the following expression for the magnetically induced electric polarization

$$P(H) = -(1/2)\xi H^2 \sin 2\varphi. \quad (1)$$

Here, φ is the angle between the tetragonal axis c and the magnetic field. The experimental angular dependences of the magnetoelectric effect in $Gd_2(MoO_4)_3$, as seen from Fig. 3, are fitted satisfactorily by an equation of type (1). This does not apply, however, to the field dependences. When fitted to $Gd_2(MoO_4)_3$ at 4.2 K and for sufficiently weak fields, equation (1) describes the field dependences of the magnetoelectric effect with a constant $\xi \approx 5 \times 10^{-11}$ C cm^{-2} T^{-2}. The field interval within which equation (1) is valid is very narrow. At $H = 1$ T, the error is 8%, while at $H = 2$ T it is already as high as 40%.

The author of [16] proposes the following expression for the magnetically induced electric polarization

$$P(m) = \Gamma_1 m_x^2 + \Gamma_2 m_y^2. \quad (2)$$

Here, $m_{x,y} = M_{x,y}/M_S$, and Γ_1 and Γ_2 are constants of the theory. The experimental $P(m)$ relations obtained for $Gd_2(MoO_4)_3$ at 4.2 K are fitted satisfactorily by a quadratic equation of type (2) only in weak fields. For $m = 0.4$ ($H = 1$ T), the deviation of the experimental $P(m)$ relation from a quadratic law is $\delta P/P = 0.07$, and for $m = 0.7$ it is 0.2. The deviation of the calculations from the experiment has a systematic character. The scatter of the experimental values is an order of magnitude less than this systematic discrepancy. Thus, the quadratic dependence of the electric polarization on magnetization frequently used in the literature has a very narrow region of applicability in this case. At $T = 0.4$ K, relations (1) and (2) deviate from the experimental $P(m)$ dependences still stronger than at $T = 4.2$ K.

It was shown experimentally [3] that the magnetic field-induced variation of the electric polarization measured in terbium molybdate at $T = 77$–290 K, i.e., for small m, depends linearly on the single-ion magnetostriction of Tb^{3+} ions. Assuming the electric polarization in gadolinium molybdate also to depend linearly on magnetostriction, and the latter to be described by the theory of single-ion magnetostriction [14], one readily obtains an expression describing the dependence of the electric polarization on reduced magnetization

$$P(m) = P_0 \hat{I}_{l+1/2}[L^{-1}(m)]. \qquad (3)$$

Here, P_0 is a coefficient, $\hat{I}_{l+1/2}(x)$ is the lth order reduced hyperbolic Bessel function:

$$\hat{I}_{l+1/2}(x) = \frac{I_{l+1/2}(x)}{I_{1/2}(x)}; \qquad (4)$$

$$I_{l+1/2}(x) = \int_{-1}^{1} P_l(y)\exp(xy)dy; \qquad (5)$$

$P_l(y)$ is the Legendre polynomial, and $L^{-1}(m)$ is the inverse Langevin function of reduced magnetization. The order $l = 2$ of the reduced hyperbolic Bessel function is determined by the twofold symmetry of the $P(\varphi)$ plot in Fig. 3. For $l = 2$, the reduced hyperbolic Bessel function has the form

$$\hat{I}_{5/2}(x) = 1 + \frac{3}{x^2} - \frac{3}{x}\coth x. \qquad (6)$$

The results of the calculations made using (3)–(6) are shown in Fig. 4 by solid lines *2* and *4*. The values of the coefficient P_0 for the [100] and [010] directions are, respectively, 0.18×10^{-9} and 0.17×10^{-9} C/cm^2. They were chosen so as to match the calculated to experimental values at $m = 0.8$. These coefficients provide the best fit of the calculation to the experimental data within the $0 < m < 0.8$ interval. In this interval, the error does not exceed 2%. This error has a random character. For $m > 0.8$, the calculation is seen to deviate systematically from the experiment. Thus, the theory of single-ion magnetostriction agrees with the experiment much better than the quadratic relations (1) and (2) do. The agreement of the calculation with the experiment observed for $m < 0.8$ indicates that the proposed approach offers a correct interpretation of the main features of the magnetoelectric effect in paramagnetic gadolinium molybdate at the temperature of 4.2 K.

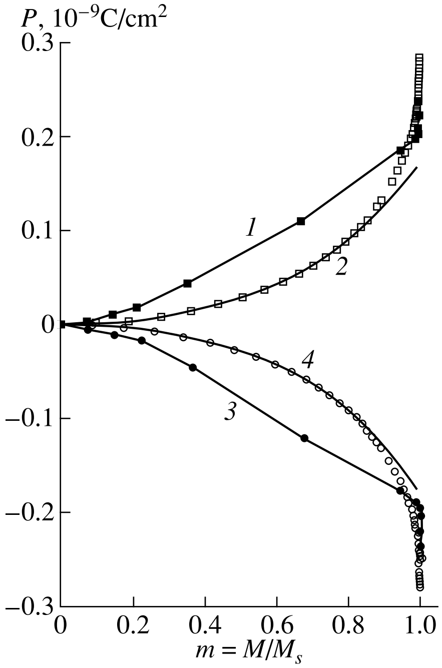

Fig. 4. Electric polarization in $Gd_2(MoO_4)_3$ along the [001] axis as a function of reduced magnetization $m = M/M_S$ measured at different temperatures and magnetic-field directions. The field along the [010] axis: (*1*) $T = 0.4$ K and (*2*) 4.2 K. The field along the [100] axis: (*3*) $T = 0.4$ K and (*4*) 4.2 K.

The experimental $P(m)$ dependences obtained at $T = 0.4$ K fit neither of these theories. These relations qualitatively differ in character from relations (1), (2), and (3). This is apparently associated with the closeness of the magnetic phase transition at $T = 0.3$ K. The theory of single-ion magnetostriction [14] considers a one-sublattice magnet, which can be in the paramagnetic or the ferromagnetic state, depending on the temperature. In the paramagnetic temperature region, the relations derived in this theory turn out to be applicable to a description of the magnetoelectric effect in gadolinium molybdate within a substantial part of the interval of reduced magnetizations m. However, as the temperature is reduced to below 0.3 K, gadolinium molybdate undergoes antiferromagnetic rather than ferromagnetic ordering [5], which was not treated by the single-ion magnetostriction theory [14]. Therefore, the relations derived in terms of the single-ion magnetostriction theory in its present form cannot reproduce the behavior of the magnetoelectric effect in gadolinium molybdate for $T < 0.3$ K, as well as at temperatures close to 0.3 K.

An important result obtained in this study is establishing the existence of anomalies in the experimental $P(m)$ relations near $m = 1$. These anomalies are observed at both temperatures studied. The existence of these anomalies is the only feature common for the $P(m)$ relations measured at 0.4 and 4.2 K. None of the (1)–(3) expressions reproduces these anomalies. The physical meaning of the anomalies consists in that at certain magnetic fields, the magnetization m saturates and practically does not grow with increasing field, whereas the electric polarization P continues to increase in this field interval. At $T = 4.2$ K and in a field $H = 7.5$ T, the experimental $m(H)$ dependence reaches $m = 0.98$. As the field continues to increase from 7.5 to 20 T, the relative growth of the magnetization is $\Delta m/m \approx 0.02$ [10]. The relative increase of the electric polarization in this field interval is, as evident from Fig. 1, $\Delta P/P \approx 0.4$. This accounts for the steep increase of the P/m derivative in the vicinity of $m = 1$.

One of possible reasons for the existence of this anomaly could be that it contributes to the magnetostriction of gadolinium molybdate from the mixing of the wave functions among different multiplets of the excited term of the Gd^{3+} ion. A calculation was made of the influence of the excited term of the Gd^{3+} ion on the field behavior of the Faraday effect in paramagnetic gallium-gadolinium garnet [17]. It was shown that due to the excited term, the Faraday rotation contains a contribution depending on the magnetic field only and is independent of magnetization. This contribution can result in a strong dependence of the Faraday effect on the magnetic field within the field interval where the magnetization is practically field independent due to paramagnetic saturation. This calculation permitted one to offer a qualitative interpretation of the experimental field dependence of the Faraday effect obtained in [17]. One cannot rule out the possibility that the mixing of wave functions belonging to different multiplets of the Gd^{3+} excited term provides a similar contribution to the magnetostriction of gadolinium molybdate. If this is indeed so, then the strong magnetic field dependence of the electric polarization of gadolinium molybdate in the region of magnetic saturation finds an explanation.

ACKNOWLEDGMENTS

The authors are indebted to R.Z. Levitin for fruitful discussions.

Support of the Russian Foundation for Basic Research (project no. 98-02-16635), project “School” (grant 96806), and INTAS (grant 94-935) is gratefully acknowledged.

REFERENCES

1. L. H. Brixner and J. R. Barkley, *Handbook on the Physics and Chemistry of Rare Earths* (North-Holland, Amsterdam, 1979), pp. 610–655.
2. S. A. Ivanov, V. N. Kurlov, B. K. Ponomarev, *et al.*, Pis’ma Zh. Éksp. Teor. Fiz. **52**, 1003 (1990) [JETP Lett. **52**, 394 (1990)].
3. B. K. Ponomarev, S. A. Ivanov, B. S. Red’kin, *et al.*, Physica B **177**, 327 (1992).
4. B. K. Ponomarev, B. S. Red’kin, H. Wiegelmann, *et al.*, Ferroelectrics Lett. **18**, 394 (1994).
5. R. A. Fisher, E. W. Hornung, G. E. Brodale, *et al.*, J. Chem. Phys. **56**, 193 (1972).
6. B. S. Red’kin, V. N. Kurlov, I. S. Pet’kov, *et al.*, J. Crystal Growth **104**, 77 (1990).
7. B. K. Ponomarev, S. A. Ivanov, B. S. Red’kin, *et al.*, Pis’ma Zh. Éksp. Teor. Fiz. **55**, 353 (1992) [JETP Lett. **55**, 356 (1992)].
8. B. K. Ponomarev, V. D. Negrii, B. S. Red’kin, *et al.*, J. Phys. D **27**, 1995 (1994).
9. B. K. Ponomarev, S. A. Ivanov, Yu. F. Popov, *et al.*, Ferroelectrics **161**, 43 (1994).
10. H. Wiegelmann, B. K. Ponomarev, J. van Tol, *et al.*, Ferroelectrics **183**, 195 (1996).
11. B. K. Ponomarev, Yu. F. Popov, I. M. Shmyt’ko, *et al.*, Ferroelectrics **169**, 97 (1995).
12. E. W. Hornung, G. E. Brodale, R. A. Fisher, *et al.*, J. Chem. Phys. **56**, 5007 (1972).
13. G. E. Brodale, R. A. Fisher, E. W. Hornung, *et al.*, J. Chem. Phys. **56**, 6118 (1972).
14. H. B. Callen and E. Callen, J. Phys. Chem. Solids **27**, 1271 (1966).
15. S. L. Hou and N. Bloembergen, Phys. Rev. **138**, A1218 (1965).
16. I. E. Chupis, Fiz. Nizk. Temp. **21**, 941 (1995).
17. A. K. Zvezdin, S. V. Koptsik, G. S. Krinchik, *et al.*, Pis’ma Zh. Éksp. Teor. Fiz. **37**, 331 (1983) [JETP Lett. **37**, 393 (1983)].

Translated by G. Skrebtsov

Physics of the Solid State, Vol. 42, No. 4, 2000, pp. 739–742. Translated from Fizika Tverdogo Tela, Vol. 42, No. 4, 2000, pp. 721–724.

Effect of Sample Thickness on Electron Emission from the TGS Ferroelectric Crystal

A. S. Sidorkin*, N. Yu. Ponomareva*, S. D. Milovidova*, and A. S. Sigov**

**Voronezh State University, Universitetskaya pl. 1, Voronezh, 394693 Russia*

***Moscow State Institute of Radioengineering, Electronics, and Automation (Technical University), pr. Vernadskogo 78, Moscow, 117454 Russia*

e-mail: sidorkin@dom.vsu.ru

Received August 12, 1999

Abstract—An experimental study of electron emission from nominally pure triglycine sulfate crystal samples of various thicknesses is reported. It is shown that the threshold field of emission, similar to the coercive field, increases with decreasing sample thickness d in inverse proportion to d. *© 2000 MAIK "Nauka/Interperiodica".*

The present stage of development of emission electronics stimulates the search for new emission materials, with ferroelectrics showing good promise. Indeed, it turns out that emission is an integral part of relaxation processes, which accompany practically any change in macroscopic polarization of ferroelectric materials [1–4].

The most radical and, hence, capable of the maximum emission effect method of changing the macroscopic polarization of a ferroelectric is its reversal [2]. A wealth of experimental material accumulated to date shows the emission and polarization reversal processes in ferroelectrics to be related. It was shown, in particular, that, first, emission is observed, as a rule, only in the ferroelectric phase, where spontaneous polarization exists. Second, it appears only when the polarization in a sample is reversed. If an ac electric field is applied to a ferroelectric sample, the emission signal is observed only in the half-period of the external field when a negative uncompensated electric charge forms near the emission-active sample surface [5].

An analysis of the totality of the above observations suggests [1, 6] that this emission is most likely due to the total uncompensated charge appearing near the surface of the material when the sample polarization is reversed.

The connection of the reversal with electron emission from a ferroelectric should manifest itself in a correlation between the main parameters characterizing these processes. Studies of the relation of reversal parameters with the emission characteristics [7–9] revealed the existence of a similar dependence on temperature, defect concentration in a sample, the type of the ferroelectric (weak or ordinary) for the coercive field E_c, and the emission threshold field E_{th}. In particular, an investigation of the threshold fields in chromium-doped triglycine sulfate showed that an increase of the impurity concentration, together with a growth of E_c, results in a corresponding increase of the threshold field within the 25–49°C temperature interval [7, 8].

A comparative analysis of experimental data on E_{th} on the weak ferroelectric lithium heptagermnanate and the ordinary ferroelectric triglycine sulfate also provides support for the idea of a correlation between the threshold and coercive fields [9]. Indeed, in weak ferroelectrics, the E_c field is very high, 5–25 kV/cm, even near the Curie point, which exceeds by one to two orders of magnitude that observed in classical ferroelectrics. A similar relation was observed experimentally also for the threshold fields E_{th} measured in weak and ordinary ferroelectrics in the same conditions.

In view of the fact that the coercive field depends substantially on the thickness of the materials studied, it appears natural to assume that the emission threshold field should likewise depend on the sample thickness. It is at the checking of this assumption that the present work was aimed.

1. EXPERIMENTAL TECHNIQUES AND RESULTS

Similar to our preceding works, the emission current density j_{em} was measured here by the standard technique [10] in a vacuum of 6.5×10^{-3} Pa. All measurements were carried out on 0.4–2 mm-thick polar-cut samples of a nominally pure triglycine sulfate (TGS) single crystal with an area of 20–30 mm^2. The electrodes on the samples were of goldleaf. The electron emission was measured in the gap region near the electrode closest to a secondary-emission multiplier. The gap width was about 1 mm. The 50-Hz sinusoidal electric field applied was 5–5000 V/cm in amplitude. The studies were carried out in the temperature interval from 25 to 55°C.

1063-7834/00/4204-0739$20.00 © 2000 MAIK "Nauka/Interperiodica"

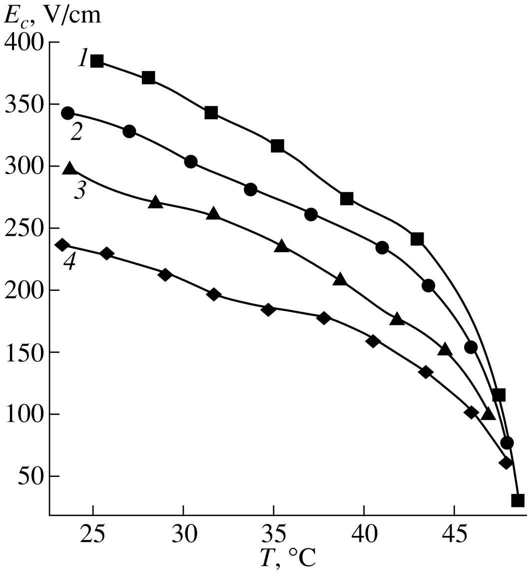

Fig. 1. Coercive field E_c as a function of temperature for samples of pure TGS single-crystal of various thicknesses, d (mm): (*1*) 0.45, (*2*) 1.03, (*3*) 1.3, and (*4*) 1.98.

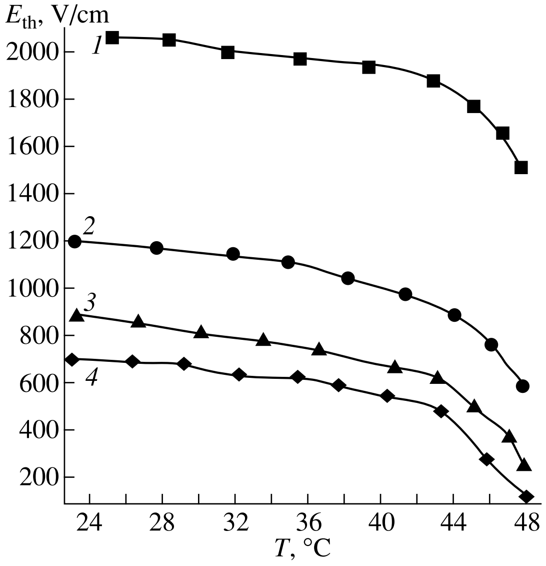

Fig. 2. Threshold field E_{th} as a function of temperature for samples of pure TGS single-crystal of various thicknesses, d (mm): (*1*) 0.45, (*2*) 1.03, (*3*) 1.3, and (*4*) 1.98.

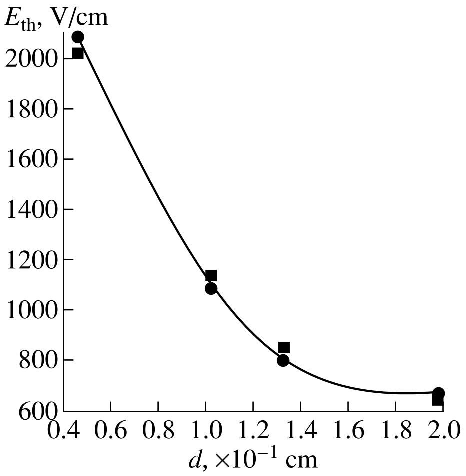

Fig. 3. Threshold field E_{th} as a function of thickness of pure TGS single-crystal samples obtained at T = 25°C.

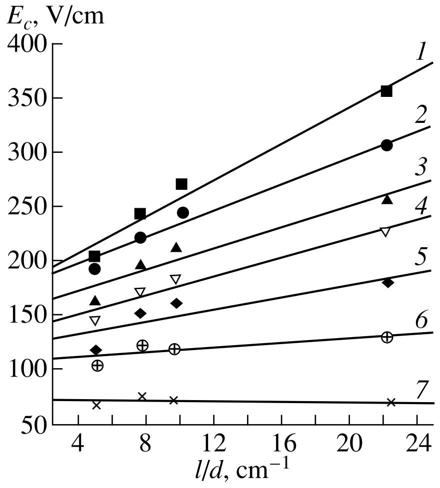

Fig. 4. Coercive field E_c as a function of inverse sample thickness for pure TGS single-crystal obtained at various temperatures T (°C): (*1*) 24, (*2*) 27, (*3*) 30, (*4*) 35, (*5*) 40, (*6*) 45, and (*7*) 48.

The results of the measurements can be summed up as follows.

As in the previous experiments, all the samples produced electron emission only when in the ferroelectric phase. The upper limit of the temperature interval within which electron emission was observed is approximately equal to the temperature of transition to the nonpolar state, T_c.

Throughout the temperature range studied, the coercive field of a sample decreases as one approaches the phase-transition temperature and vanishes altogether at T_c. As is evident from a comparison of the temperature dependences of the coercive field calculated from the dielectric hysteresis loops for various sample thicknesses (Fig. 1), a decrease in sample thickness brings about a corresponding growth of the coercive field within the temperature region studied.

Similar experimental relations were obtained also for the electron-emission threshold field E_{th}. As the coercive field, the emission threshold field is a decreasing function of temperature (Fig. 2). One observes also a nonlinear increase (Fig. 3) of the emission threshold field E_{th} with decreasing sample thickness throughout the temperature range where the ferroelectric phase exists. As follows from an analysis of these relations, the emission threshold field, similar to the coercive field, increases with decreasing sample thickness d in inverse proportion to it (Figs. 4 and 5). The threshold field is observed also to slightly exceed the coercive field E_c. The numerical value of this difference does not remain constant for the material under study; it depends on the dimensions of a sample and, in particular, on its thickness. This effect manifests itself particularly strongly for thin (below 1 mm) samples.

2. DISCUSSION OF THE RESULTS

Practically all of the results obtained are in accord with the above scheme, which relates the onset of emission at polarization reversal in ferroelectrics to the release of charges from surface electronic states induced by the field of uncompensated charge. The surface of a ferroelectric carries a bound surface charge caused by the discontinuity in the spontaneous polarization vector P_s. In the equilibrium state, the bound-charge field is balanced at a given temperature by the free charge flowing to the surface due to the intrinsic conductivity of ferroelectric materials (which is always nonzero in real crystals) or of the medium surrounding them. Violation of this charge balance, which can occur, for instance, under polarization reversal, creates an electric field of the net charge in the surface layer, which sets in during the short time required for the vector P_s to reverse its direction. When oriented in the favorable direction, this field is capable of accelerating electrons and initiating emission.

As already mentioned, polarization reversal is one of the most efficient methods of creating unbalanced charge on the surface of a ferroelectric. To reverse the polarization of a sample, one has to apply an external field in excess of the coercive one. A change in the coercive field E_c, forming for one reason or other, will also cause an increase of the emission threshold field.

It is known that the coercive field, rather than being a universal parameter of a material, depends on a number of factors, including the sample thickness. Most of the theoretical models [11] and experiments [12] point out an inverse proportionality of the coercive field to sample thickness, $E_c(d, T) = E_c^0(T) + \dfrac{A_c(T)}{d}$. As seen from Fig. 4, this relation also fits the data on the triglycine sulfate crystal obtained in the present work. For room temperature, we obtained $E_c^0 = 200$ V/cm and $A_c = 8$ V. As the temperature is increased, the values of E_c^0 and A_c characterizing the ordinate at the origin and the slope of the corresponding straight lines decrease.

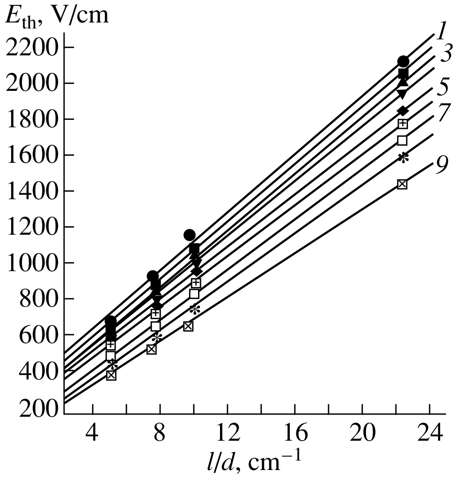

Fig. 5. Threshold field E_{th} as a function of inverse thickness of pure TGS single-crystal samples obtained at various temperatures T (°C): (*1*) 24, (*2*) 27, (*3*) 30, (*4*) 35, (*5*) 38, (*6*) 40, (*7*) 44, (*8*) 47, and (*9*) 48.

As follows from Fig. 5, the emission threshold field can be approximated by a similar function, $E_{\mathrm{th}}(d, T) = E_{\mathrm{th}}^0(T) + \dfrac{A_{\mathrm{th}}(T)}{d}$. Here, E_{th}^0 is the hypothetical threshold field for infinitely thick samples, which is 270–300 V/cm at room temperature. This value decreases as one approaches the phase-transition point, which should apparently be assigned to a similar dependence of the corresponding term in the coercive field. The $A_{\mathrm{th}}(T)$ parameter is 70 V at room temperature, and it likewise decreases as one approaches the Curie point. Thus, the behavior of the emission threshold field for triglycine sulfate samples of various thicknesses is similar to that of the coercive field, which implies that the above quantities are related.

There is nothing strange in that the quantities E_c and E_{th} behave somewhat differently, because the development of the emission process is governed not just by the polarization reversal itself, but rather by the reversal-induced field of the unbalanced charge, which should be high enough to stimulate emission.

ACKNOWLEDGMENTS

Partial support of the “Universities of Russia: Fundamental Research” program (grant no. 2801) is gratefully acknowledged.

REFERENCES

1. A. M. Kostsov, A. S. Sidorkin, V. S. Zal’tsberg, *et al.*, Fiz. Tverd. Tela (Leningrad) **24**, 3436 (1982) [Sov. Phys. Solid State **24**, 1952 (1982)].
2. G. I. Rozenman, V. A. Okhapkin, Yu. L. Chepelev, *et al.*, Pis’ma Zh. Éksp. Teor. Fiz. **39**, 397 (1984) [JETP Lett. **39**, 477 (1984)].

3. K. Biedrzycki, Phys. Status Solidi A **109**, K79 (1988).
4. H. Gundel, J. Handerek, and H. Riege, J. Appl. Phys. **69** (2), 975 (1991).
5. K. Biedrzycki and R. Bihan, Ferroelectrics **126**, 253 (1992).
6. A. S. Sidorkin and B. M. Darinskiĭ, Ferroelectrics **111**, 325 (1997).
7. A. S. Sidorkin, S. D. Milovidova, N. Yu. Ponomareva, *et al.*, Ferroelectrics **219**, 23 (1998).
8. A. S. Sidorkin, N. Yu. Ponomareva, and S. D. Milovidova, Fiz. Tverd. Tela (S.-Peterburg) **41**, 1675 (1999) [Phys. Solid State **41**, 1534 (1999)].
9. A. S. Sidorkin, P. V. Loginov, A. M. Savvinov, *et al.*, Fiz. Tverd. Tela (S.-Peterburg) **38**, 624 (1996) [Phys. Solid State **38**, 344 (1996)].
10. A. S. Sidorkin, B. M. Darinskiĭ, A. P. Lazarev, *et al.*, Ferroelectrics **143**, 209 (1993).
11. A. K. Tagantsev, Ferroelectrics **184**, 79 (1996).
12. G. A. Smolenskiĭ, V. A. Bokov, V. A. Isupov, N. N. Kraĭnik, A. I. Sokolov, and N. K. Yushin, *The Physics of Ferroelectric Phenomena* (Nauka, Leningrad, 1985).

Translated by G. Skrebtsov

Physics of the Solid State, Vol. 42, No. 4, 2000, pp. 743–744. Translated from Fizika Tverdogo Tela, Vol. 42, No. 4, 2000, pp. 725–726.
Original Russian Text Copyright © 2000 by A. A. Sidorkin, Milovidova, Rogazinskaya, A. S. Sidorkin.

MAGNETISM AND FERROELECTRICITY

Kinetics of Electron Emission from the TGS Ferroelectric Crystal

A. A. Sidorkin, S. D. Milovidova, O. V. Rogazinskaya, and A. S. Sidorkin
Voronezh State University, Universitetskaya pl. 1, Voronezh, 394693 Russia
e-mail: sidorkin@dom.vsu.ru

Received August 13, 1999

Abstract—A study is reported on the behavior in time of the electron emission current density from a triglycine sulfate ferroelectric crystal measured at fixed temperatures. This relation is shown to have an exponential nature. The characteristic emission relaxation time depends on temperature and decreases as one approaches the phase-transition point. The magnitude of the relaxation time and its temperature dependence can be accounted for both within a mechanism in which the emission decay is associated with the emptying of surface electron states, and in terms of the Maxwellian relaxation process. *© 2000 MAIK "Nauka/Interperiodica".*

Electron emission from ferroelectric crystals is a problem of considerable significance both from the standpoint of basic research and in terms of the application potential involved. The kinetics of the emission occupy an important place among various aspects of this process. The characteristic emission-current decay times suggest that ferroelectrics are promising materials for fabricating cold emitters. On the other hand, studying the kinetics of emission processes in ferroelectrics in more detail could provide a better understanding of the basic emission mechanisms in these crystals.

Our earlier studies [1, 2] of the emission kinetics in ferroelectric materials, in particular, in crystalline triglycine sulfate, determined the relaxation time of the emission current after the stabilization of the polarized state, which was created by preliminary polarization of the sample in an electric field [2] or by properly varying its temperature [1]. In both cases, all measurements were carried out at one fixed temperature. This work was aimed at an investigation of the dependence of the relaxation processes in thermally stimulated emission on the material temperature.

The electron emission current density j_{em} was measured by the standard technique [3] in a vacuum of 6.5×10^{-3} Pa. The samples used for the study were *Y*-cuts of a triglycine sulfate crystal, 20 mm^2 in area and 1 mm thick. The sample temperature was measured with a copper–constantan thermocouple and checked by simultaneously measuring the capacitance of another TGS sample. The error in temperature measurements was 5%. The temperature of the samples used in various experiments varied from +20 to +48°C.

The measurements yielded the following results. As seen from the experimental plot displayed in Fig. 1, thermionic emission from a TGS ferroelectric crystal is observed only at the instant of a change of the macroscopic polarization. After the temperature has stabilized at a distance from the Curie point, one observes a characteristic exponential decay of the emission current density. The characteristic relaxation time of this current (within the temperature region studied it is a few minutes long) decreases as one approaches the phase-transition point, from ≈10 min at 37°C to ≈4 min at 48°C. As seen from Fig. 2, in some cases (see, e.g., curve *2*) the same process may evolve over more than one relaxation time. Note that, as this should be in the approximation of small enough perturbations, the relaxation time of thermally stimulated emission coincides here in order of magnitude with that of the emis-

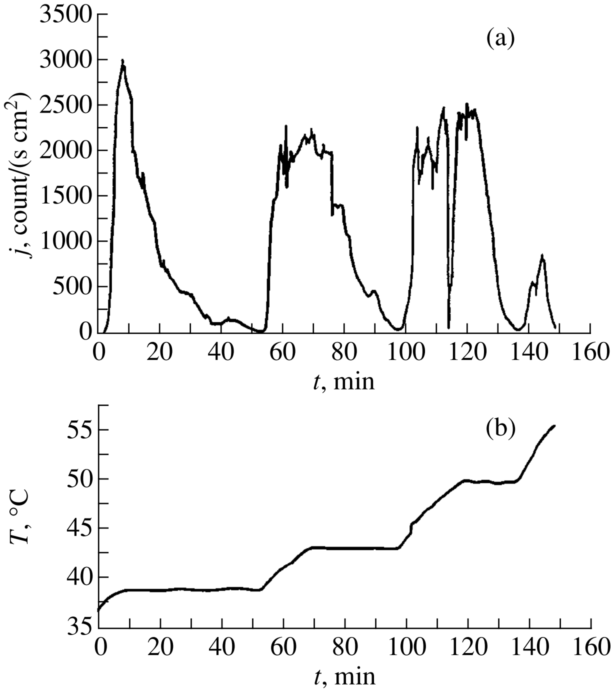

Fig. 1. (a) Emission current density vs. time plot for the given (b) temperature variation with time, measured on samples of pure TGS single crystal.

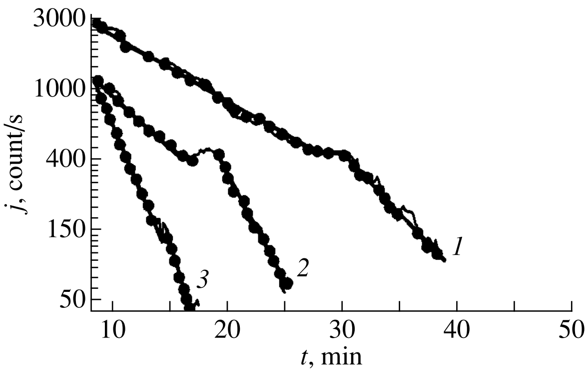

Fig. 2. Log emission current density vs. time plot obtained on a sample of pure TGS single crystal at different temperatures *T* (°C): (*1*) 37, (*2*) 43, and (*3*) 48.

sion current in TGS crystals in the case of electric field-induced emission [2].

The observed thermionic activity of the ferroelectrics under study can be explained as due to field emission of electrons from surface electron states induced by the charge screening of the spontaneous polarization. At equilibrium, the spontaneous polarization charge field is usually balanced, for instance, by the charge settling down from the atmosphere, so that the surface of the ferroelectric does not exhibit electrical activity. A lack of balance between these fields resulting from a decrease of spontaneous polarization as one approaches the Curie point will bring about development of a nonzero net field, whose direction will be determined now by the field of the balancing charge. It is this field that is responsible for the ejection of electrons trapped in the surface electron states [4].

Estimate the characteristic time taken by the electron traps to empty by the field-emission mechanism. The emission current density [3]

$$j_{\mathrm{em}}(T) = en(T)W(T), \qquad (1)$$

where $n(T)$ is the surface density of the filled surface states at the given temperature, and

$$W(T) = \frac{2\sqrt{2mA}\zeta}{mS}\exp\left(-\frac{4\sqrt{2m}A^{3/2}}{\hbar eE}\right) \qquad (2)$$

is the probability for a surface trap of depth A to become ionized in a field E. Here, ζ is the width of the potential well corresponding to the electron trap, and S is the ferroelectric surface area involved in the emission.

The field E of the spontaneous-polarization screening charge can be written as

$$E = \frac{2\pi}{\varepsilon_s}\left(P_S - \sqrt{\frac{\alpha_0(T-T_c)}{\beta}}\right), \qquad (3)$$

where ε_s is the permittivity of the nonferroelectric surface layer, P_S is the saturation polarization, and α and β are the coefficients of expansion of the thermodynamic potential for the crystal under study.

Substituting this field into (2), we obtain the characteristic electron trap emptying time

$$\tau = W^{-1}$$

$$= \frac{mS}{2\sqrt{2mA}\zeta}\exp\left(-\frac{4\sqrt{2m}A^{3/2}\varepsilon_s}{\hbar e 2\pi(P_S - \sqrt{\alpha_0(T-T_c)/\beta})}\right). \qquad (4)$$

As seen from (4), the time τ should decrease for $T \longrightarrow T_c$, exactly that which is observed in the experiment. Numerical estimation of the time τ made for the ordinary parameters $\varepsilon_s \approx 5$, $P_S \approx 10^4$, $S \approx 1$, $\zeta \approx 10^{-8}$ typical of $T \approx 45$°C for the TGS crystal with $\alpha_0 \approx 4 \times 10^{-3}$ and $\beta \approx 8 \times 10^{-10}$ for $A \approx 10^{-12}$ yields $\tau \approx 10^3$, which likewise, is in a good agreement with the value measured in the experiment.

The emission associated with the Maxwellian relaxation of a screening charge can, in principle, compete in kinetics with that involving the emptying of surface electron states. Near the phase-transition temperature, the electric conductivity of crystalline triglycine sulfate is $10^{-12}\ \Omega^{-1}\ \mathrm{cm}^{-1}$, and the permittivity of the ferroelectric material $\varepsilon \approx 10^3$, which yields for the Maxwellian relaxation time $\tau_M = \varepsilon/4\pi\sigma \approx 10^3$ s. In principle, this time is also close to the experimentally observed emission relaxation time, but it follows a radically different temperature behavior than the relaxation time found from the experiment. Indeed, the electric conductivity does not exhibit a critical behavior near the phase-transition point, and therefore the evolution of the Maxwellian relaxation time τ_M will be dominated here by the behavior of the permittivity, which exhibits an anomalous growth in the vicinity of T_c.

ACKNOWLEDGMENTS

Partial support of the “Universities of Russia: Fundamental Research” program (grant no. 2801) is gratefully acknowledged.

REFERENCES

1. A. S. Sidorkin, A. M. Kostsov, and V. S. Zal’tsberg, Fiz. Tverd. Tela (Leningrad) **27**, 2200 (1985) [Sov. Phys. Solid State **27**, 1320 (1985)].
2. A. S. Sidorkin, P. V. Loginov, A. M. Savvinov, *et al.*, Fiz. Tverd. Tela (S.-Peterburg) **38** (2), 624 (1996) [Phys. Solid State **38**, 344 (1996)].
3. A. M. Kostsov, A. S. Sidorkin, V. S. Zal’tsberg, *et al.*, Fiz. Tverd. Tela (Leningrad) **24**, 3436 (1982) [Sov. Phys. Solid State **24**, 1952 (1982)].
4. A. S. Sidorkin and B. M. Darinskiĭ, Ferroelectrics **111**, 325 (1997).

Translated by G. Skrebtsov

Physics of the Solid State, Vol. 42, No. 4, 2000, pp. 745–750. Translated from Fizika Tverdogo Tela, Vol. 42, No. 4, 2000, pp. 727–732.
Original Russian Text Copyright © 2000 by Sidorkin, Sigov, Khoviv, S. Yatsenko, O. Yatsenko.

MAGNETISM AND FERROELECTRICITY

Preparation and Properties of Lead Titanate Thin Ferroelectric Films

A. S. Sidorkin, A. S. Sigov, A. M. Khoviv, S. O. Yatsenko, and O. B. Yatsenko
Voronezh State University, Universitetskaya pl. 1, Voronezh, 394693 Russia
e-mail: sidorkin@dom.vsu.ru

Received August 23, 1999

Abstract—A new technique is proposed for preparing lead titanate ferroelectric films. The technique involves a solid-phase reaction in an oxygen environment between titanium and lead layers deposited on a substrate. The thicknesses of the component films being deposited are chosen based on the stoichiometric ratio in the compound to be synthesized. The composition and structure of the film obtained are checked by x-ray phase analysis. The films exhibit a dielectric hysteresis loop and a temperature dependence of the permittivity characteristic of ferroelectrics. A study has been made of the temperature and thickness dependences of the film coercive field. They also are shown to follow a pattern typical of ferroelectrics. *© 2000 MAIK "Nauka/Interperiodica".*

Of the various methods of preparation of ferroelectric materials, thin-film technologies unquestionably hold the lead. This is due both to the present trends in applications of ferroelectrics, for example, in microelectronics, and to the interest in the basic aspects of the behavior of a substance in two- and quasi-two-dimensional structures (in our case, in the so-called two-dimensional ferroelectricity).

Considered from the standpoint of their chemical composition, ferroelectric films currently enjoying the widest popularity are still those with a perovskite unit cell, with lead titanate $PbTiO_3$ films on various substrates also being of considerable interest.

Preparation of new materials by thin-film technologies has both advantages and drawbacks. In theory, thin-film techniques have a fundamental merit in that they allow increasing the reactivity of components through the use of the excess surface energy of the system and, thus, lowering the temperature of the reaction and its duration. In thin-film systems, the requirements imposed on the composition and structure of final products by the phase equilibrium conditions specified in the corresponding phase diagrams are less stringent. On the one hand, this considerably broadens the experimental potentialities in a specific problem of synthesis, and, on the other, offers a way to a better understanding of the nature (mechanism and kinetics) of the processes involved in the formation and operation of the structures to be prepared, to specify and study the most interesting and important metastable states of the system, the conditions and limits of their existence, and the means of their control.

One should, however, point out that the use of thin-film technologies for the preparation and investigation of materials of a complex chemical composition, to which ferroelectrics belong, meets with difficulties of a purely technological nature.

Lead titanate can be prepared in the form of bulk single crystals and thin films by a number of techniques [1–5]. All the known methods of fabricating this material involve chemical reactions between the lead and titanium oxides, PbO and TiO_2, synthesized preliminarily, for instance, by the sol–gel technology and taken in the corresponding stoichiometric ratio. The reaction can be run both in the original melt and in a solid-phase process. The optimum conditions of the synthesis [the charge (melt) composition and thermal-processing temperature] are determined from the PbO–TiO_2 phase diagram. These data suggest that the optimum lead oxide-enriched charge compositions, which permit one to grow crystals of two compounds, are $PbTiO_3$ (PbO–TiO_2) and Pb_2TiO_4 (2PbO–TiO_2).

In our opinion, the main difficulties met in the preparation of both films and bulk crystals consist in that one employs the already available oxides of lead and titanium as starting components for the synthesis of lead titanate in any form. These oxides, particularly TiO_2, are very stable compounds. Their metal–oxygen bonds are nearly saturated, and therefore the formation of new bonds required to produce $PbTiO_3$ is a hard process. This is why, in order, for example, to grow lead titanate crystals from melt, one has to enrich the latter with lead oxides (low-melting components) and operate at a temperature of 1000°C and higher.

1. PREPARATION OF LEAD TITANATE THIN FILMS: STUDY OF THEIR STRUCTURE AND PHASE COMPOSITION

This paper proposes a number of novel steps in the preparation of heterostructures, including $PbTiO_3$ thin films exhibiting ferroelectric properties. The first of them involves the use as starting components thin (~1000 Å) lead and titanium layers produced in a certain way in the form of heterostructures on various substrates. This approach permits one to fully meet the requirements of present-day microelectronics and lifts the constraints imposed on the possibilities of synthesis in solid-phase reactions specified above. At the same time, it offers a possibility of producing and studying individual parts of thin-film structures by comparing their size with that of the solid-body regions where their properties (metallic, semiconducting, dielectric, or ferroelectric) appear and develop. The most essential of them are the transition layers forming at the interfaces between various starting thin-film elements in the course of their interaction during the synthesis.

1. 1. Preparation of Lead Titanate Films on Single-Crystal Silicon Substrates

To solve the problems posed in this work, we carried out several series of experiments using different substrates and different synthesis regimes. In the first series, the material used for the substrates was KÉF- or KOB-grade silicon single crystal cut from a [100] plate measuring 20 × 20 × 1 mm, which was treated preliminarily by standard techniques [6]. Next, layers of metallic lead, and subsequently, of titanium were deposited by magnetron sputtering on the substrates prepared in this way. The magnetron sputtering of the metals was chosen because of its being one of the most promising methods for producing thin-film structures employed widely in microelectronics today. This method permits one to vary within broad limits the composition and structure of deposited systems and the conditions of their interaction with one another and the substrate. The lead-to-titanium thickness ratio, Pb : Ti = 2 : 1, was chosen in accordance with the stoichiometry of $PbTiO_3$. The total thickness of the films thus obtained (without the substrate) varied from 200 to 450 nm.

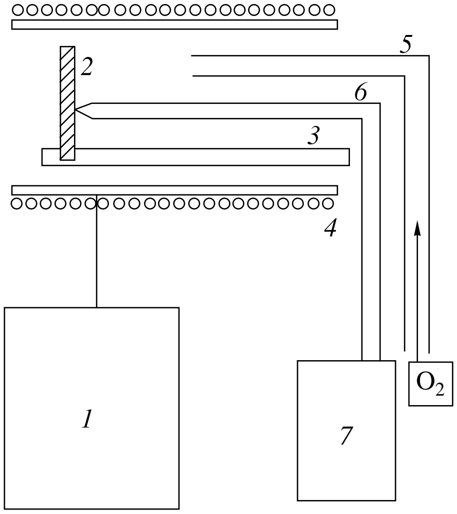

Fig. 1. Block diagram of the experimental setup for the preparation of lead titanate films. (*1*) VRT-2 temperature control unit, (*2*) sample, (*3*) quartz holder, (*4*) resistance furnace, (*5*) quartz tube for oxygen admission, (*6*) Chromel–Alumel thermocouple, and (*7*) PP-63 potentiometer.

To obtain a film of the $PbTiO_3$ complex oxide, the Si/Pb/Ti structure was thermally annealed in a resistance furnace having an oxygen flow with an average rate of 40 l/h. The reactor temperature was controlled by a VRT-2 unit to within 1–2°C. The temperature was measured by a Chromel–Alumel thermocouple contacting the back side of the sample. The temperature and duration of the process varied within the 327–627°C and 30–180 min intervals, respectively. Figure 1 shows the block diagram of the setup.

The temperature was increased in steps, namely, the sample was placed into the furnace at an initial temperature of 300–350°C and maintained in it for 30–60 min, after which the temperature was raised to 500–700°C. In some experiments, the heating was performed in three stages with intermediate temperature stabilization.

The phase composition of the samples thus obtained was checked by x-ray diffraction on a DRON-3M instrument. The x-ray phase analysis revealed phase transformations occurring in the structures in the course of the thermal treatment. The diffraction patterns of the starting samples (before the thermal treatment) contained lines of polycrystalline metallic lead (Fig. 2a) and revealed the presence of amorphous titanium. No silicon (substrate) lines were detected. Annealing at $T = 320°C$ for 60 min (Fig. 2b) results in the disappearance of the amorphous titanium, oxidation of a part of the lead to PbO_2, and the onset of formation of one of the titanium-enriched titanate phases ($PbO–3TiO_3$). An increase in the annealing time to 90 min gives rise to the formation of other titanate phases, evidenced by the appearance of $PbTiO_3$ and $PbTi_3O_7$ lines with a part of the lead remaining unreacted, and to complete disappearance of the amorphous titanium. A stepped increase of the annealing temperature from 335°C for 60 min, to 410°C for 30 min, and finally to 600°C for 5 min brings to the end the formation of the $PbTiO_3$ and $PbTi_3O_7$ titanate phases (Fig. 2c).

These results suggest the following. Interaction in the Pb–Ti thin-film structure on a silicon substrate in an oxygen environment is essentially different from what could be expected based on the phase equilibrium diagram for the $PbO–TiO_2$ system.

The presence of a thin amorphous layer of titanium improves substantially the reactivity of the system. The transformations involved occur at appreciably lower temperatures than those in the oxide system (320°C). Titanium interacts actively with lead and its oxide to form stable TiO_2 (which hinders this interaction when one uses preliminarily synthesized PbO and TiO_2 oxides as starting compounds). Also, the enrichment of the titanate phases in lead oxide to $PbTiO_3$ here is higher than that found for the bulk samples. Finally, no reflections due to titanium silicide phases are observed. Thus, the thin-film structure proposed here permits one to control the interaction of titanium with Pb, Si, and O toward the formation of the titanates, including the $PbTiO_3$ of interest to us here.

1.2. Preparation of Lead Titanate Films on Polycrystalline Titanium Substrates

The lead titanate films prepared on Si substrates did not exhibit clearly pronounced ferroelectric properties. One of the reasons for this is the difficulties associated with attaching electrical contacts to high-resistivity silicon samples.

To overcome these difficulties, to simplify the heterosystem to be fabricated, and to broaden its functional potential, we have developed the techniques of preparing $PbTiO_3$ samples on substrates of metallic titanium. Plates of VT-10-grade titanium measuring $20 \times 20 \times 2$ mm were polished mechanically and rinsed in distilled water and isopropyl alcohol, after which layers of lead 100 to ~1000 nm in thickness were deposited on them by magnetron sputtering. These structures were annealed isothermally in a quartz reactor in an oxygen environment. Thin (100-nm-thick) lead films on Ti were annealed in regimes similar to those used for films deposited on silicon, and thick (up to 1000 nm) films, at 700–750°C for 5–15 min. A phase analysis of films on titanium made after the thermal treatment revealed primarily the $PbTiO_3$ phase, with inclusions of $PbTi_3O_7$ (Fig. 3).

Note that the use of metallic titanium as a substrate solved also the problem of the second electrode in the formation and study of ferroelectric structures; indeed, the ferroelectric forms on the metal, which serves as one of the starting components of the heterostructure being fabricated.

The results obtained in the study of the Ti–Pb–Si structures permitted one to determine the optimum conditions for synthesis of $PbTiO_3$ ferroelectric films on a titanium substrate, to simplify substantially the synthesis procedure, and to broaden, at the same time, its functional potentialities. We have succeeded in purposefully changing the interaction of Pb, Ti, and O in our technique toward preferential formation of the $PbTiO_3$ film. The lead layer formed on the titanium plays a specific role here. It permitted the stabilization of the titanium surface by protecting it against uncontrollable transformation to the TiO_2 oxide, which hinders the formation of $PbTiO_3$. At the same time, the interaction of lead with titanium controls the formation of PbO in the way that favors the optimum lead distribution between the titanium and oxygen for the formation of $PbTiO_3$. Lead and titanium in a thin-film structure interact both with one another and, simultaneously, with the oxygen, so that we have here the oxidation not of the pure Pb (to PbO) and Ti (to TiO_2), but rather of an intermediate Pb–Ti composition, which starts to form at the Pb–Ti interface.

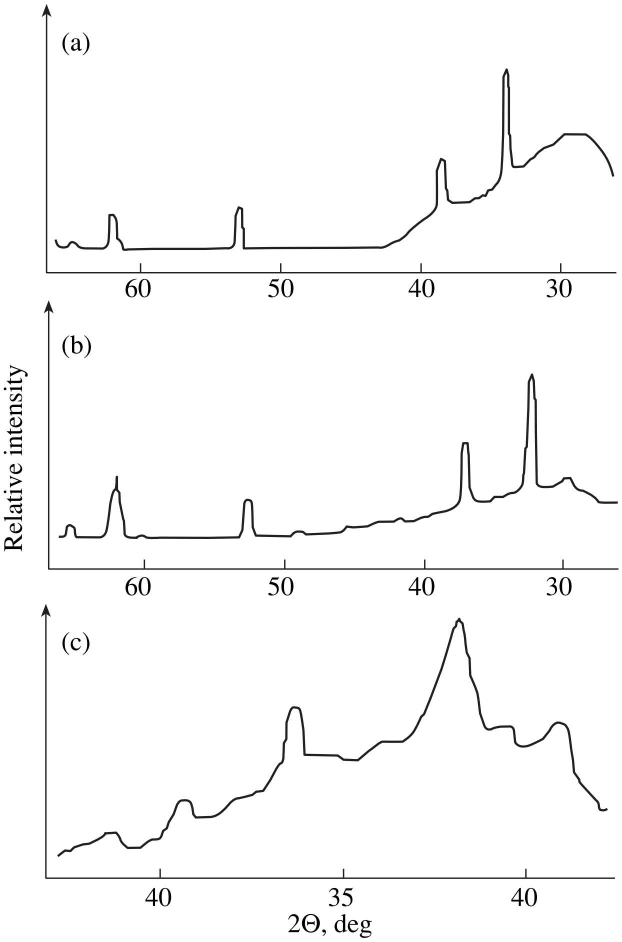

Fig. 2. X-ray diffraction patterns of the Si/Pb/Ti heterostructure. (a) before the annealing, (b) thermal annealing (T = 320°C, 60 min), and (c) stepped annealing (T_1 = 335°C, 60 min; T_2 = 410°C, 30 min; T_3 = 600°C, 5 min).

2. DIELECTRIC PROPERTIES OF THE SYNTHESIZED FILMS

To prove that the films thus synthesized are indeed ferroelectric, we subjected them, besides x-ray diffraction analysis, to measurements of the principal dielectric properties as well. Silver was deposited for this purpose on the surface of the prepared films as the upper electrode. The deposition was performed through a mask with holes 1 mm in diameter. In the case of a silicon substrate, the lower contact was provided by depositing on the latter an indium–gallium eutectic,

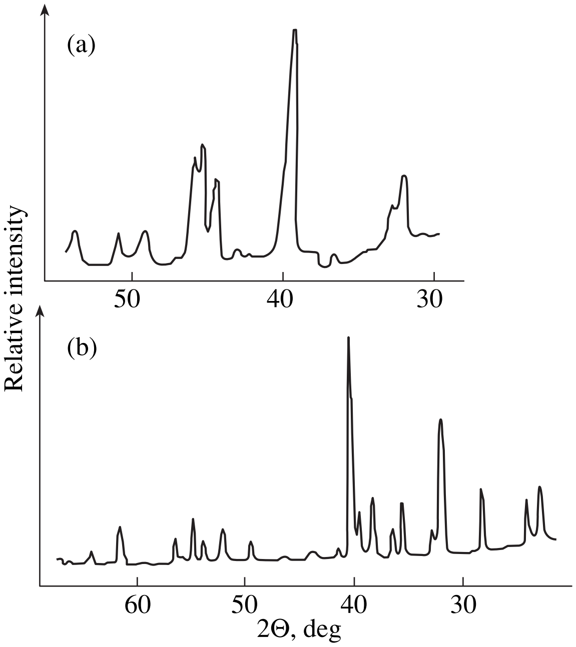

Fig. 3. Diffraction patterns of the Pb/Ti structure. The Pb layer thickness: (a) 100 nm and (b) 1000 nm. Annealing regime: (a) T_1 = 350°C, 30 min and (b) T = 650°C, 15 min.

and when titanium was used as a substrate, it served as the lower electrode.

2.1. Hysteresis Loops

The dielectric hysteresis loops were observed for an improved Sawyer–Tower circuit with a holder adapted for operation with thin films. The sample was placed on a metallic platform serving as one of the contacts. The second contact was provided with the help of a needle pressed to the deposited silver. An S1-48B oscillograph and a G3-56/1 audio-signal generator were employed. The measurement frequency was 50 Hz, and the voltage across the sample monitored by a V7-26 millivoltmeter was 0.5 V.

Measurements showed that, similar to [7, 8], the loops observed in films on silicon substrates had a poorly pronounced, distorted form (Fig. 4a). The loops were unsaturated and broad, which can probably be assigned to diffusion occurring at the film–substrate interface.

The dielectric hysteresis loops observed on comparatively thin films prepared on titanium substrates and slowly annealed, likewise, did not exhibit saturation and were broad (Fig. 4b). Thin film are known to have anomalously high coercive fields. Therefore, the above loop pattern can be accounted for by an excessively high coercive field, which exceeds the electrical strength of a film and, hence, would hinder its complete polarization reversal. The thickness ranges and the temperature and deposition time regimes used to prepare these films were similar to those employed for the films on silicon.

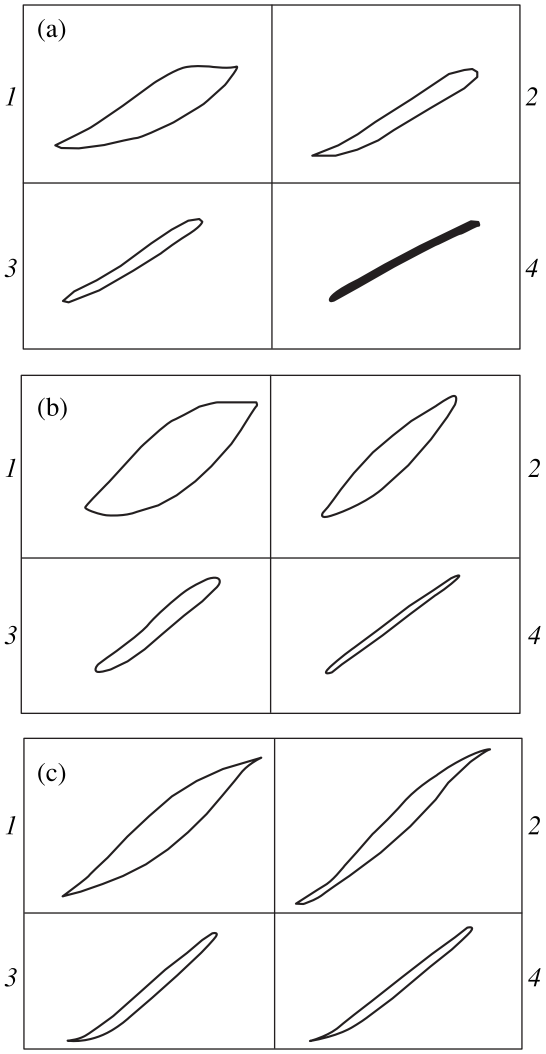

Fig. 4. Temperature variation of the hysteresis loops of films prepared on various substrates: (a) on silicon (d = 150 nm), (b) on titanium (d = 150 nm), and (c) on titanium (d = 1000 nm). T (°C): (*1*) 25, (*2*) 250, (*3*) 370, (*4*) 480.

A qualitatively different hysteresis loop is observed in the oscillographic trace of comparatively thick (1 μm) films prepared by rapid annealing at a high temperature (600–700°C) [9]. The hysteresis loop displayed in Fig. 4c has the form typical of ferroelectric films and, in particular, of lead titanate films prepared by other techniques. The spontaneous polarization and the coercive field derived from the loop were 15 μC/cm^2 and 18 kV/cm, respectively, which likewise correlates with the results obtained by other authors.

Figure 4 demonstrates the temperature-induced variation of the dielectric hysteresis loops of lead titanate films prepared on silicon and titanium substrates

(0.2–1 μm). One readily sees that as one approaches the temperature of transition to the nonpolar phase, both the spontaneous polarization and the coercive field of the material decrease. Besides, at temperatures above the Curie point T_C, the hysteretic dependence of polarization on the switching field, $P(E)$, degenerates into a linear relation. All this argues for the ferroelectric nature of the synthesized films.

2.2. Temperature Dependence of the Permittivity

The temperature behavior of the permittivity was measured on a computerized all-purpose setup. The sample was placed on a cylindrical resistance furnace, which served at the same time as the lower contact. The second contact was pressed from the above. The furnace temperature was varied by means of a transformer and monitored with a chromel–alumel thermocouple placed in the immediate vicinity of the sample, with its cold end immersed into a Dewar flask filled with thawing ice. The thermocouple emf was measured with a V7-23 digital voltmeter. In the course of an experiment, one measured the capacitance of the parallel-plate capacitor thus formed, as well as the film conductivity and the loss tangent. The measurements were performed with the use of a digital RLC meter, with the readings of all instruments entered automatically into the computer memory. The sample heating rate was 10–15 K/min. After the transition through the Curie point, the sample was cooled at the same rate, and a reverse run of the $\varepsilon(T)$ relation and of the loss tangent $\tan\delta(T)$ were measured. The measurement frequency was 1 kHz.

Figure 5a presents the $\varepsilon(T)$ dependence for lead titanate films on a 1 μm-thick titanium substrate. We readily see that the films exhibit a characteristic growth of ε as one approaches the phase-transition temperature (495°C). Measurements at higher temperatures are made difficult by film degradation. The film conductivity measurements are plotted in Fig. 5b.

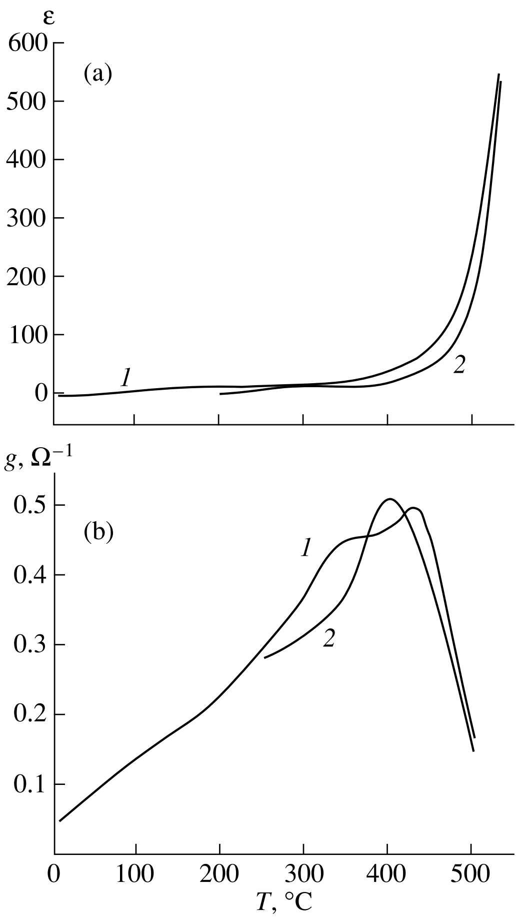

Fig. 5. Temperature dependence of (a) permittivity and (b) conductivity of a lead titanate film. (*1*) heating run, (*2*) cooling run.

2.3. Dependence of the Coercive Field of the Films on Their Thickness

The coercive field of thin ferroelectric materials is known to increase rapidly with decreasing film thickness [10, 11]. A comparison of the dielectric hysteresis loops obtained for films of different thickness permits one to follow the thickness dependence of E_c for the films that we prepared. The results of study of this dependence plotted in Fig. 6 also exhibit a clearly pronounced inverse proportionality $E_c(d^{-1})$ characteristic of ferroelectrics.

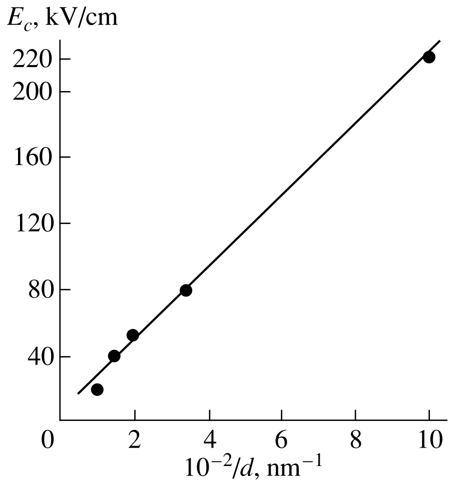

Fig. 6. Coercive force as a function of inverse film thickness.

Thus, the above results show that lead titanate films possessing ferroelectric properties can be obtained by reacting lead with titanium in the solid phase in an oxygen environment. By precluding the formation of highly stable oxides, this technique permits one to considerably lower the temperature of the synthesis and, hence, to partially remove the problems arising due to the substrate material diffusing into the film.

REFERENCES

1. N. J. Phillips, J. Non-Cryst. Solids **147**, 285 (1992).
2. R. P. Tandon, V. Raman, K. A. Arora, *et al.*, Ferroelectrics **152**, 151 (1994).
3. G. R. Bai, H. L. M. Chang, and H. K. Kim, Appl. Phys. Lett. **61**, 408 (1992).
4. B. D. Qu, W. Zhong, and K. M. Wang, J. Appl. Phys. **74**, 2896 (1993).
5. K. Sangsub, K. Youngmin, and B. Sunggi, Ferroelectrics **152**, 1 (1994).
6. A. M. Khoviv, I. Ya. Mittova, and S. I. Dubov, Zh. Tekh. Fiz. **57**, 151 (1996) [Tech. Phys. **41**, 716 (1996)].
7. V. P. Afanas’ev, E. Yu. Kaptelov, G. P. Kramar, *et al.*, Fiz. Tverd. Tela (S.-Peterburg) **36**, 1657 (1994) [Phys. Solid State **36**, 906 (1994)].
8. Q. X. Jia, L. H. Chang, and W. A. Anderson, Electron. Mater. **23**, 551 (1994).
9. A. M. Khoviv, A. S. Sidorkin, S. O. Yatsenko, *et al.*, Neorg. Mater. **34**, 462 (1998).
10. G. A. Smolenskiĭ, V. A. Bokov, V. A. Isupov, *et al.*, *Fundamentals of Ferroelectric Phenomena* (Nauka, Leningrad, 1985).
11. A. K. Tagantsev, Ferroelectrics **184**, 79 (1996).

Translated by G. Skrebtsov

Physics of the Solid State, Vol. 42, No. 4, 2000, pp. 751–759. Translated from Fizika Tverdogo Tela, Vol. 42, No. 4, 2000, pp. 733–740.
Original Russian Text Copyright © 2000 by Slezov.

LATTICE DYNAMICS AND PHASE TRANSITIONS

Method of Virtual Media in the Theory of First-Order Phase Transitions

V. V. Slezov

Kharkov Institute of Physics and Technology, National Scientific Center,
ul. Akademicheskaya 1, Kharkov, 310108 Ukraine
e-mail: slt@mail.vl.net.ua

Received in final form, October 20, 1999

Abstract—The method of deriving a set of equations describing the first-order phase transitions under different conditions has been proposed. A set of equations is obtained for a medium in which a decrease in the pressure leads to the formation of bubbles filled with a dissolved gas. *© 2000 MAIK "Nauka/Interperiodica".*

One of the most important problems in the physics of first-order phase transitions is to devise a method for deriving a fundamental system of equations representing these processes in various media under different conditions.

Discrete kinetic equations for describing the precipitation of particles involving atoms of the same sort in the course of phase transition have long been deduced [1–4]. Similar equations in a continual form were derived by Zel'dovich [5].

The equations for first-order phase transitions contain coefficients that depend on the quantities governing these processes. The determination of these coefficients is the basic problem in the formulation of closed equations describing phase transitions. Despite numerous investigations in this field, up to now, there has been no regular method for determining these coefficients (specifically for complex systems) without invoking additional assumptions regarding the possible application of the detailed balancing principle and a certain equilibrium size distribution of particles. These assumptions are questionable in the case when a system is nonequilibrium. In the simplest cases, these assumptions can be considered as limitations imposed on the relationships applicable to an equilibrium system.

In these cases, which, as a rule, have already been treated, the obtained coefficients take the correct form.

The present work is devoted to the formulation of a method for determining the coefficients of kinetic equations describing the first-order phase transitions in the sufficiently general form without invoking the above assumptions. As an example, we considered the formation of bubbles of a gas dissolved in a medium with a decrease in the external pressure.

1. THE BASIC SYSTEM OF EQUATIONS

The evolution of gas bubbles in viscous liquids and melts at the given instant t is determined by the distribution function $f(V, N, t)$ over the bubble volume V and the number of gas atoms N per unit volume of a gas bubble. When deriving the basic system of equations, it is convenient to introduce the dimensionless quantity $N_1 = V/V_0$, where V_0 is the change in the bubble volume for time δt. Then, $f(V, N, t)dV = \bar{f}(N_1, N, t)dN_1$, and $f(V, N, t) = V_0^{-1}\bar{f}(N_1, N, t)$.

Let δt be sufficiently small so that the change in volume by V_0 leads to the change in the number of gas atoms by unity. Then, we can write

$$\frac{\partial \bar{f}}{\partial \tau} = -(I_N - I_{N-1}) - (I_{N_1} - I_{N_1-1}) = -\frac{\partial I}{\partial N} - \frac{\partial I}{\partial N_1},$$

$$I_N = \nu_{N,N+1}\bar{f}(N_1, N, t) - \nu_{N+1,N}\bar{f}(N_1, N+1, t), \quad (1)$$

$$I_{N_1} = \nu_{N_1,N_1+1}\bar{f}(N_1, N, t) - \nu_{N_1+1,N_1}\bar{f}(N_1+1, N, t).$$

Here, I_N is the flux in space N; I_{N_1} is the flux in space N_1, and $\nu_{N,N+1}$ is the frequency of transition from state N to state $N + 1$. The meaning of the remaining frequencies of transitions is obvious. Since equation (1) is linear in $\bar{f}$, and $\bar{f}$ and f differ only by a constant multiplier, hereafter, the bar over f will be omitted.

The flux I_N can be represented as

$$I_N = \nu_{N,N+1}\left[f(N_1, N, t) - \frac{\nu_{N+1,N}}{\nu_{N,N+1}}f(N_1+1, N, t)\right]. \quad (2)$$

The flux I_{N_1} has a similar form.

2. CALCULATION OF RATIO BETWEEN FREQUENCIES OF TRANSITIONS—THE METHOD OF VIRTUAL MEDIA

In order to calculate the ratio between the frequency of liberation of a structural element $\nu_{N+1,N}$ and the frequency of absorption $\nu_{N,N+1}$, we employ the method of equilibrium virtual media [6, 7]. This becomes possible in the systems for which the notion of a "physical point" is applicable; i.e., in the case when a system can be described in terms of local thermodynamic quantities. Then, the frequency of liberation or absorption of particles upon growth of a new phase (or upon transfer from one physical point to another physical point) is, in the general case, the product of the kinetic factor responsible for the transfer rate and the probability of a favorable configuration, which is determined by the local thermodynamic potential.

This approach implies a rather small variation in the local thermodynamic potential in the range of a physical point, which is also determined by the characteristic length of interaction between particles in a system. Parameters of the system can depend on external conditions in an arbitrary way, provided that they only slightly vary over the length of a physical point.

In condensed media, there is a short-range interaction, and the characteristic length of the interaction between atoms is of the order of interatomic distance. Under these conditions, a physical point should contain a sufficiently large number of atoms. Its size should be less than the least characteristic size determined by the external conditions of the existence of the system under consideration.

To calculate the ratios $\nu_{N+1,N}/\nu_{N,N+1}$ and $\nu_{N_1+1,N_1}/\nu_{N_1,N_1+1}$, we introduce accessory virtual media. These media are chosen so that, for a given gas bubble, they provide the fulfillment of equilibrium conditions (detailed balancing principle) with respect to any process responsible for its evolution. In our case, these are the change in bubble size and the change in amount of a gas in the bubble.

In the calculation of the $\nu_{N+1,N}/\nu_{N,N+1}$ ratio, the virtual medium is in equilibrium with a gas bubble with respect to the exchange of atoms, i.e., in the chemical equilibrium. When choosing such a medium, it is essential that the kinetic coefficient for the frequency of transfer of a gas atom into a bubble would coincide with the actual coefficient and the local chemical potential would be equal to the chemical potential of gas atoms in the bubble.

For a bubble with $\mu^L \geq \mu^V$ (where μ^L is the chemical potential of a gas atom in a liquid, and μ^V is the chemical potential of a gas atom in a bubble with volume V), this medium is an actual medium in which a fraction of atoms is frozen (i.e., atoms are assumed to be fixed). Their interaction with mobile atoms in a medium remains unchanged. This implies that the environment of mobile atoms in the course of displacements and their interaction with the surrounding gas atoms are identical to those in an actual medium. Correspondingly, the kinetic coefficient for the transfer of a mobile gas atom into a bubble is the same as in an actual medium. Naturally, the entropy of mobile atoms is less than the entropy of all atoms in the medium. The number of frozen gas atoms in the medium is determined by the equality between the chemical potentials for mobile atoms and the chemical potentials for gas atoms in a bubble with allowance made for their interaction with frozen gas atoms. (This condition permits one to determine the number of frozen atoms as may be required.) The condition for applicability of the above approach assumes that the transfer of a gas atom from a medium into a bubble, or from a bubble into a medium, occurs for the time during which the environment of these atoms does not undergo substantial changes.

Therefore, for a gas bubble with the specified size and the given number of atoms, one can find a virtual medium being in a detailed equilibrium with this bubble, and, hence,

$$\nu_{N+1,N} = \tilde{\nu}_{N,N+1}, \tag{3}$$

where $\tilde{\nu}_{N,N+1}$ is the equilibrium frequency of the transfer of gas atoms from a virtual medium into a bubble. Since the bubble size remains constant during the process, the corresponding variable can be omitted. As a result, we can write

$$\frac{\nu_{N+1,N}}{\nu_{N,N+1}} = \frac{\tilde{\nu}_{N,N+1}}{\nu_{N,N+1}} = \frac{\tilde{W}}{W} = \exp(\Delta S - \Delta\tilde{S}) = \exp\Delta S_n. \tag{4}$$

This relationship takes into account the fact that, according to the conditions of construction of the virtual medium, its kinetic coefficient for the transfer of a gas atom into a bubble is equal to the kinetic coefficient for the transfer of the gas atom in an actual medium. These coefficients are cancelled to give the ratio between the probability of the favorable configuration for the transfer of a gas atom from the virtual medium into a bubble $\tilde{W}$ and the probability of the favorable configuration for its transfer from an actual medium into the bubble W. Let us now consider the Gibbs microcanonical distribution for a closed system—an actual medium, a virtual medium, and a gas bubble. Then, after the appropriate integration in a usual way, we obtain the following expressions for the probability of the transfer of one atom from a virtual medium into a bubble $\tilde{W}$ and the probability of its transfer from an actual medium into the bubble W:

$$\tilde{W}(E, N, \tilde{E}, \tilde{N}-1, E_p, N_p+1) = \text{const}\exp[S(E, N) + S(\tilde{E}, \tilde{N}-1) + S(E_p, N_p+1)] = Be^{-\Delta S},$$

$$B = \text{const}\exp[S(E, N) + S(\tilde{E}, \tilde{N}) + S(E_p, N_p + 1)],$$

$$\Delta\tilde{S} = S(\tilde{E}, \tilde{N}) - S(\tilde{E}, \tilde{N} - 1),$$

$$W(E, N-1, \tilde{E}, \tilde{N}, E_p, N_p + 1) = Be^{-\Delta S},$$

$$\Delta S = S(E, N) - S(E, N-1).$$

Here, N, $\tilde{N}$, N_p, E, $\tilde{E}$, and E_p are the mean numbers of particles in subsystems and their mean energies. From the ratio $W/\tilde{W}$, we obtain formula (4). In this formula, $\Delta S_n = \Delta S - \Delta\tilde{S}$ is the change in the total entropy of the closed system, which consists of the actual subsystem (ΔS) and the virtual subsystem ($\Delta\tilde{S}$). In the general case, each of these subsystems is in equilibrium by itself, but not with each other. The deficit of the total entropy ΔS_n upon transfer of a gas atom from a bubble (i.e., from an actual medium into a virtual medium) can be determined by the general relationships.

In the case when the conditions for the transfer are such that the entropy deficit increases by $\Delta S_n < 0$ as compared to the equilibrium entropy under the given conditions, we have

$$\Delta S_n = -\frac{\Delta S_n}{\Delta E}R_{\min} = -\frac{1}{T}R_{\min}, \tag{5}$$

where $R_{\min} > 0$ is the minimum work that should be done to increase the energy of the system by $\Delta E > 0$ and, thus, to increase the deficit of the total entropy with respect to the initial total entropy of a metastable system by $\Delta S_n < 0$ at its constant value. For our case of the transfer from the virtual medium (in which the chemical potential of a gas atom is μ^V) to an actual medium (the chemical potential of a gas atom is μ^L), at $\mu^L \geq \mu^V$, we have $R_{\min} = \mu^L - \mu^V > 0$.

If the conditions of the transfer are such that the entropy deficit decreases by $\Delta S_n > 0$ as compared to the equilibrium entropy under the given conditions, we obtain

$$\Delta S_n = \frac{\Delta S_n}{|\Delta E|}|R_{\max}| = \frac{1}{T}|R_{\max}| = \frac{1}{T}|R_{\min}|, \tag{6}$$

where $|R_{\max}| > 0$ is the maximum work that can be done by the metastable system to decrease its energy by $\Delta E < 0$ and, thus, to decrease the deficit of the total entropy of a system by $\Delta S_n > 0$ at its constant value. In our case, at $\mu^L \leq \mu^V$, $|R_{\max}| = |\mu^L - \mu^V| = -(\mu^L - \mu^V) = |R_{\min}|$. Thus, as follows from equations (5) and (6), at any ratio between the chemical potentials μ^L and μ^V, the quantity ΔS_n can be written as

$$\Delta S_n = -\frac{1}{T}R_{\min} = -\frac{1}{T}(\mu^L - \mu^V), \tag{7}$$

where $R_{\min}$ is the minimum work defined above [see formula (5)]. Note that, as is well known, $|R_{\max}| = |R_{\min}|$.

As can be seen from formula (4), the ratio between frequencies is a function rapidly varying with its parameters. This means that its argument ΔS_n should be represented as a difference, so that the expansions rapidly converge. Hence, we rewrite relationship (7) in the form

$$\begin{aligned}\Delta S_n &= -\frac{1}{T}(\mu^L - \mu^V)\\ &= \frac{F(N+1, V) - F(N, V)}{T} = \frac{1}{T}\frac{\delta F}{\delta N},\end{aligned} \tag{8}$$

where $F(N, V)$ is, as will be shown below, the difference between the free energy of the medium containing a bubble (with the volume V and the number of gas atoms N) and the free energy of the medium involving dissolved gas without bubble.

Then, the ratio between the transfer frequencies is given by

$$\begin{aligned}\frac{\nu_{N+1, N}}{\nu_{N, N+1}} &= \frac{\tilde{\nu}_{N, N+1}}{\nu_{N, N+1}} = \exp\left[-\frac{1}{T}(\mu^L - \mu^V)\right]\\ &= \exp\frac{F(N+1, V) - F(N, V)}{T}.\end{aligned} \tag{9}$$

In calculations of the frequencies ν_{N_1, N_1+1} and ν_{N_1+1, N_1} for the process attended by changes in the size of a gas bubble, the virtual medium is the medium being in a mechanical equilibrium with a given bubble. The local thermodynamic potential of this medium is determined by the pressure at the bubble surface $p^L + 2\sigma/R$, where p^L is the pressure in a viscous liquid, R is the bubble radius, and σ is the surface tension coefficient at the liquid–vacuum interface (we assume that the gas in a bubble does not affect the surface tension). By using the above relationships, we substitute $R_{\min}$ for this process into formula (7).

An increase in the volume of virtual medium by the elementary volume V_0 implies a decrease in the bubble volume, because the bubble is in a detailed equilibrium with the virtual medium, and the number of elementary volumes N_1 in the bubble decreases by unity. Therefore, for $p^V > p^L + 2\sigma/R$ (where p^L is the gas pressure in a viscous liquid), we can write

$$\begin{aligned}\Delta S_n &= \Delta S - \Delta\tilde{S} = -\frac{1}{T}R_{\min}\\ &= -\frac{1}{T}\left(p^V - p^L - \frac{2\sigma}{R}\right)|V_0|.\end{aligned} \tag{10}$$

In this expression, we took into account that a decrease in N_1 by unity signifies a decrease in the bubble volume $V \longrightarrow V - V_0$ and an increase in the volume of an actual medium by V_0. As shown above, formula (10) can be used at any ratio between p^V and p^L

$$\begin{aligned}\Delta S_n &= -\frac{1}{T}\left(p^V - p^L - \frac{2\sigma}{R}\right)V_0 \\ &= \frac{F(N, V+V_0) - F(N, V)}{T} = \frac{1}{T}\frac{\delta F}{\delta V}V_0\end{aligned} \qquad (11)$$

(the modulus sign is omitted). Relationship (11) permits us to obtain the ratio between the transfer frequencies

$$\begin{aligned}\frac{\nu_{N_1+1,\,N_1}}{\nu_{N_1,\,N_1+1}} &= \frac{\tilde{\nu}_{N_1,\,N_1+1}}{\tilde{\nu}_{N_1,\,N_1+1}} = \exp\left[-\frac{1}{T}\left(p^V - p^L - \frac{2\sigma}{R}\right)V_0\right] \\ &= \exp\frac{F(N, V) - F(N, V-V_0)}{T} = \exp\frac{1}{T}\frac{\delta F}{\delta V}V_0.\end{aligned} \qquad (12)$$

Let us reconstruct $F(N, V)$ from its derivatives (8) and (12)

$$\begin{aligned}F(V, N) &= \int_0^V \frac{\delta F}{\delta V}\bigg|_{N=0} dV + \int_0^N \frac{\delta F}{\delta N}\bigg|_V dN \\ &= V(p^L - p^V) + N(\mu^V - \mu^L) + 4\pi R^2\sigma.\end{aligned} \qquad (13)$$

Indeed,

$$\int_0^V \frac{\delta F}{\delta V}\bigg|_{N=0} dV = \int_0^V \left(p^L + \frac{2\sigma}{R}\right)dV = p^L V + 4\pi R^2\sigma,$$

$$p^V\big|_{N=0} = 0,$$

$$\begin{aligned}\int_0^N \frac{\delta F}{\delta N}\bigg|_V dN' &= \int_0^N (\mu^V - \mu^L)dN' \\ &= N(\mu^V - \mu^L) - \int_0^N N'\frac{\partial\mu^V}{\partial p^V}\frac{\partial p^V}{\partial N'}dN' \\ &= N(\mu^V - \mu^L) - Vp^V, \quad F(0, 0) = 0.\end{aligned} \qquad (14)$$

Here, μ^V is the chemical potential of gas atoms in a bubble with constant volume V upon integration with respect to N, and $\partial\mu^V/\partial p^V = V'$, where V' is the volume of a gas bubble (with the volume V and the number of gas atoms N') per atom. Since the volume upon integration with respect to N' is constant, $N'V' = V = \text{const}$, and this quantity can be factored outside the integral sign. Therefore, $F(V, N)$ is an analog of the change in the free energy upon formation of a bubble (with the volume V and the number of gas atoms N) in the medium.

If the pressure in the medium $p^L > p$ (where p is the saturation gas pressure), under all conditions, we obtain $F(V, N) > 0$. When $p^L < p$, at certain parameters, we have $F(V, N) < 0$. This implies that the system is metastable and, thus, will break down.

3. CHANGE-OVER TO DIFFERENTIAL EQUATION

For macroscopic volumes of gas bubbles at N_1 and $N \gg 1$, relationships (8) and (12) enable us to change-over from difference equation (1) to the differential equation. As a result, we obtain

$$\begin{aligned}I_N &= \nu_{N,\,N+1}\exp(-F(N, V)/T) \\ &\quad\times[\exp(F(N, V)/T)f(N, V, t) \\ &\quad - \exp(F(N+1, V)/T)f(N+1, V, t)] \\ &= -\nu_{N,\,N+1}\left[\frac{1}{T}\frac{\delta F}{\delta N}f(N, V, t) + \frac{\partial f(N, V, t)}{\partial N}\right].\end{aligned} \qquad (15)$$

In the right-hand side of this equation, the first term is the “hydrodynamic flux,” and the second term is the diffusion flux in the space of numbers of gas atoms in a bubble

$$D(N) = \nu_{N,\,N+1}, \quad \frac{dN}{dt} = -D(N)\frac{1}{T}\frac{\delta F}{\delta N}. \qquad (16)$$

For I_{N_1} (as for I_N), the expression is similar to formula (15), that is,

$$I_{N_1} = -\nu_{N_1,\,N_1+1}\left[\frac{1}{T}\frac{\delta F}{\delta V}V_0 f + \frac{\partial f}{\partial V}V_0\right].$$

In going to the continuous variable $V = N_1V_0$ with allowance made for the relationship

$$\frac{\partial f}{\partial N_1} = \frac{f}{\partial V}V_0,$$

we obtain

$$\begin{aligned}I_V &= I_{N_1}V_0 = -\nu_{N,\,N+1}V_0^2\left[\frac{1}{T}\frac{\delta F}{\delta V}f + \frac{\partial f}{\partial V}\right], \\ \frac{\partial I_V}{\partial V} &= \frac{\partial I_{N_1}}{\partial N_1}.\end{aligned} \qquad (17)$$

In formula (17), the first term is the hydrodynamic flux, and the second term is the diffusion flux in the space of the bubble volumes. Therefore,

$$D(V) = \nu_{N_1,\,N_1+1}V_0^2, \quad \frac{dV}{dt} = -D(V)\frac{1}{T}\frac{\delta F}{\delta V}. \qquad (18)$$

From relationships (17) and (18), it follows that the diffusion coefficients $D(N)$ and $D(V)$ can be determined if the rate of hydrodynamic flux is known. This rate can be found by solving the corresponding problem or from analysis of the processes proceeding at the boundary of a new phase.

Then, equation (1) can be rewritten in the form

$$\frac{\partial f}{\partial t} = -\frac{\partial I_N}{\partial N} - \frac{\partial I_V}{\partial V}, \qquad (19)$$

where

$$I_N = \frac{dN}{dt}f - D(N)\frac{\partial f}{\partial N}, \quad I_V = \frac{dV}{dt}f - D(V)\frac{\partial f}{\partial V}.$$

For equation (19), it is necessary to determine the initial and boundary conditions. Note that equation (19) is rigorously applicable when N and V are the macroscopic quantities; however, in the case when N is of the order of unity and V is of the order of atomic volume, this equation leads to a qualitatively correct description of the process of the gas bubble formation.

4. CALCULATION OF THE RATES OF CHANGE IN BUBBLE VOLUME AND ITS FILLING WITH GAS

Now, in order to calculate dN/dt, we should take into consideration the fact that, at the initial and transient stages, gas bubbles do not involve “diffusion clouds” of gas atoms, even though they can appear at the transient stage under certain conditions.

Consequently, the boundary kinetics of filling a bubble by gas atoms takes place at these stages. To put it differently, under these conditions, there is an exchange of gas atoms between the medium and the bubble. Then, by assuming that the gas in the bubble is ideal, we obtain

$$\frac{dN}{dt} = -D(N)\frac{1}{T}\frac{\delta F}{\delta N} = \alpha\frac{D}{2l}4\pi R^2 n\frac{1}{T}(\mu^L - \mu^V), \quad (20)$$

$$D(N) = \alpha\frac{D}{2l}4\pi R^2 n^L = \nu_{N,\,N+1},$$

$$-\frac{1}{T}\frac{\delta F}{\delta N} = \frac{1}{T}(\mu^L - \mu^V), \quad \frac{1}{T}(\mu^L - \mu^V) = \ln\frac{p}{p^V}. \quad (21)$$

Here, p is the saturation gas pressure responsible for the gas density in a liquid $n^L(p)$, $D(N)$ is determined by the conditions at the medium–bubble interface, D is the diffusion coefficient of gas atoms in the medium, α ($0 \le \alpha \le 1$) is the coefficient accounting for an additional barrier that can exist for the last jump of a gas atom into the bubble, and l is the length of an elementary displacement (of the order of interatomic distance in the liquid) of gas atoms in the medium. Note also that $D/2l^2$ is the frequency of jumps of gas atoms in a certain direction, $4\pi R^2 l$ is the volume from which gas atoms migrate into the bubble, and $4\pi R^2 l n^L$ is the number of gas atoms in this volume (where n^L is the density of gas atoms in the solution). By multiplying these quantities, we obtain $D(N)$.

The rate of change in the volume or in the size of a bubble in an incompressible viscous liquid (or a melt) can be calculated using the Navier–Stokes equation for incompressible viscous liquids and the continuity equation. As is known,

$$\frac{\partial v_i}{\partial t} + (\mathbf{v}\cdot\boldsymbol{\nabla})v_i = -\frac{1}{\rho}(\nabla_i p - \eta\Delta v_i) = \frac{1}{\rho}\frac{\partial\sigma_{ik}}{\partial x_k}, \quad (22)$$

$$\operatorname{div}\mathbf{v} = 0, \quad v|_{r=R} = \frac{dR}{dt}. \quad (23)$$

Here, R is the bubble size; v_i is the ith component of the velocity field in an incompressible liquid, for which $\Delta\rho/\rho = kp^L \ll 1$ [where $k = (1/V)(dV/dp)$ is the compressibility coefficient of a liquid, and V is the volume of a liquid]; ρ is the liquid density; η is the dynamic viscosity of a liquid; p is the pressure in a liquid; and σ_{ik} is the stress tensor

$$\sigma_{ik} = -p\delta_{ik} + \eta\left(\frac{\partial v_i}{\partial x_k} + \frac{\partial v_k}{\partial x_i}\right), \quad (24)$$

where δ_{ik} is the Kronecker symbol. For a spherical bubble, v_i (σ_{ik}) has only one nonzero component V_r (σ_{rr}) in the spherical coordinate system

$$\Delta v_i \longrightarrow \frac{1}{r^2}\frac{\partial}{\partial r}r^2\frac{\partial V_r}{\partial r} - \frac{2V_r}{r}.$$

For a liquid with sufficiently large viscosity, any term in the left-hand side of equation (21) is considerably less than any term in the right-hand side.

This implies that, for such a liquid, it is possible to use the quasi-equilibrium condition at the boundary, that is,

$$\frac{\partial\sigma_{rr}}{\partial r} \cong 0.$$

The conditions of mechanical equilibrium are met at the bubble surface

$$-\left(p^V - \frac{2\sigma}{R}\right) = \sigma_{rr}|_{r=R} = -p|_{r=R} + 2\eta\frac{\partial V_r}{\partial r}. \quad (25)$$

From equation (22), we obtain the velocity field in a liquid

$$V_r = \frac{F(t)}{r^2} = \frac{dR}{dt}\left(\frac{R}{r}\right)^2. \quad (26)$$

Substituting equation (26) into formula (25) gives the growth rate of a pore dR/dt, that is,

$$\frac{dR}{dt} = \frac{R}{4\eta}\left(p^V - p^L - \frac{2\sigma}{R}\right). \quad (27)$$

According to relationship (27), the rate of change in the volume V can be written as

$$\begin{aligned}\frac{dV}{dt} &= \frac{3V}{4\eta}\left(p^V - p^L - \frac{2\sigma}{R}\right)\\ &= \frac{3VT}{4\eta}\frac{1}{T}\left(p^V - p^L - \frac{2\sigma}{R}\right) = -\frac{3VT}{4\eta}\frac{1}{T}\frac{\delta F}{\delta V},\end{aligned} \quad (28)$$

Then, using expression (18), we have

$$D(V) = \frac{3VT}{4\eta}. \tag{29}$$

For a sufficiently viscous liquid, the difference between the pressure $p(R, t)$ at the bubble boundary and the pressure p^L is small, and, hence, $p(R, t)$ is replaced by p^L in formulas (27) and (28). By integrating expression (21) from R to infinity and substituting V_r from formula (26) into the integrated expression, we obtain the equation for determination of $p(R, t)$

$$\begin{aligned} &\frac{1}{\rho}[p(r,t) - p^L]\big|_{r=R} \\ &= \int_R^{\infty}\left\{\frac{R^2}{r^2}\frac{d}{dt}\left(\frac{dR}{dt}\right) - \frac{1}{2}\frac{R^4}{r^4}\left(\frac{dR}{dr}\right)^2\right\}dr \\ &= R\frac{d}{dt}\left(\frac{dR}{dt}\right) - \frac{1}{2}\left(\frac{dR}{dt}\right)^2 \simeq \frac{1}{2}\left(\frac{dR}{dt}\right)^2. \end{aligned} \tag{30}$$

From relationship (30), it follows that

$$\begin{aligned} \frac{(p(R,t) - p^L)}{p^L} &= \frac{1}{2}\left(\frac{dR}{dt}\right)^2\frac{\rho}{p^L} \\ &= \frac{\rho R^2}{16\eta^2 p^L}\left(p^V - p^L - \frac{2\sigma}{R}\right)^2 \ll 1. \end{aligned} \tag{31}$$

Inequality (31) determines the possibility of replacing $p(R, t)$ by p^L.

It is evident from expression (31) that the inequality is fulfilled even at large R and the sufficiently high viscosity η. This also immediately follows from the fact that the inequality has the second order in the low rate $(dR/dt)^2$.

By determining dN/dt from equation (20), dV/dt from formula (28), $D(N)$ from relationship (26), and $D(V)$ from expression (30), kinetic equation (19) can be represented as

$$\begin{aligned} \frac{\partial f}{\partial t} &= \frac{\partial}{\partial N}D(N)\left[\frac{1}{T}\frac{\delta \Delta F}{\delta N}f + \frac{\partial f}{\partial N}\right] \\ &\quad + \frac{\partial}{\partial V}D(V)\left[\frac{1}{T}\frac{\delta F}{\delta V}f + \frac{\partial f}{\partial V}\right], \end{aligned} \tag{32}$$

where f is normalized to the unit volume, and $fdVdN$ is the number of bubbles per unit volume. The boundary and initial conditions will be specified below. Equation (32) should be complemented by the law of conservation of gas atoms in bubbles and in the medium

$$\begin{aligned} &n^L(p|_{t=0})\left(1 - \int_0^{\infty}\int_0^{\infty} Vf(V,N,t)dNdV\right) \\ &= n^L(p(t))\left(1 - \int_0^{\infty}\int_0^{\infty} Vf(V,N,t)dNdV\right) \\ &\quad + \int_0^{\infty}\int_0^{\infty} Nf(V,N,t)dNdV, \end{aligned} \tag{33}$$

where $n(p)$ is the gas density corresponding to the saturation pressure p in a liquid, and $p(t)$ is the saturation pressure corresponding to the density of gas atoms at a given instant. In other words, it is the pressure of atoms of the gas being in equilibrium with the gas dissolved in a liquid.

The multiplier $1 - \int_0^{\infty}\int_0^{\infty} Vf dNdV$ accounts for the fraction of the free unit volume of the medium after the formation of gas bubbles (the reciprocal of this quantity determines the “expansion” of the unit volume, i.e., the volume occupied by the unit volume of a liquid with bubbles). This means that the volume of a liquid with bubbles is given by

$$V = V_0\left(1 - \int_0^{\infty}\int_0^{\infty} Vf(N,V)dVdN\right)^{-1}. \tag{34}$$

Equations (32) and (33) comprise the complete set of equations determining $f(V, N, t)$ and $n^L(t)$.

5. CHARACTERISTIC TIMES OF ADJUSTING THE NUMBER OF GAS ATOMS IN BUBBLE TO PORE SIZE OR ADJUSTING THE BUBBLE SIZE TO AMOUNT OF GAS IN BUBBLE

The finding of the general solution of equations (32) and (33) is a very complex problem. It is easier to take the general solution of these equations in the case when kinetic equation (32) can be reduced, with good accuracy, to the one-dimensional equation. To accomplish this, the parameters of a system should provide a rapid attainment of an equilibrium with respect to the exchange of gas atoms between bubbles and the medium, that is, $\mu^L = \mu^V$, and the subsequent slow change in the pore sizes. In the process, the chemical equilibrium is adjusted to the current bubble size. In this case, equation (20) rapidly relaxes to zero at a constant bubble size. For an ideal gas in a bubble, equation (20) takes the form

$$\frac{dN}{dt} = \frac{D}{2l}4\pi R^2\delta\frac{p}{T}\ln\frac{p}{p^V}. \tag{35}$$

Assume that the gas dissolved in a liquid obeys the Henry law $n^L = \delta p/T$, where δ is the solubility of the gas in a liquid, p is the pressure corresponding to the gas density in liquid $n(t) = n^L(t)$, and p^V is the pressure in the bubble of volume V.

At the nucleation stage, the gas density in liquid remains virtually constant $n^L(t) = n^L(0) = \delta p_0/T$ and $p = p_0$, where p_0 is the saturation gas pressure at the initial instant of time. Then, at $dN/dt|_{t \gg \tau_g} \longrightarrow 0$, we have

$$p^V = \frac{NT}{V} = p_0, \quad V = \frac{4\pi}{3}R^3 = N\frac{T}{p_0}, \qquad N = V\frac{p_0}{T}. \tag{36}$$

Consequently, in this case, V and N are related by relationship (36).

The relaxation time required for adjusting the gas amount to the bubble size can be obtained by the linearization of expression (35) with respect to N in the vicinity of a given bubble size with the use of relationships (36)

$$\frac{d\Delta N}{dt} = -\frac{D}{2l}4\pi R^2\delta\frac{\delta\Delta N}{4\pi R^3/3}. \tag{37}$$

Hence, it follows that the characteristic time of chemical relaxation τ_g ($\mu^L = \mu^V$) is determined as

$$\tau_g = \frac{2lR}{3\delta D}. \tag{38}$$

If the gas in a bubble cannot be treated as ideal, it is necessary to perform the substitution $T/V \longrightarrow \partial p^V/\partial N$ with the use of the equation of state $p^V = p^V(N/V, T)$. In the case when the bubble sizes vary so fast (at a sufficiently low viscosity of the liquid) that the mechanical equilibrium between the bubble and the medium has managed to be maintained, we obtain from relationship (27) that

$$\left.\frac{dR}{dt}\right|_{t \gg \tau_R} \longrightarrow 0, \quad p^V - p^L - \frac{2\sigma}{R} \longrightarrow 0. \tag{39}$$

Substitution of $p^V = NT(4\pi R^3/3)^{-1}$ gives the relationship between R and N

$$R^2(N) = \frac{3T}{8\pi}\frac{N}{\sigma},$$

$$p^L \ll \frac{2\sigma}{R} \text{ or } p^L \ll \sqrt{\frac{32\pi}{3}}\frac{\sigma^{3/2}}{(NT)^{1/2}} = p^L, \tag{40}$$

$$R^3(N) = \frac{NT}{4\pi p^L/3}, \quad p^L > \frac{2\sigma}{R} \text{ or } p^L \gg \tilde{p}^L.$$

By linearizing relationship (27) in the vicinity of $R(N)$ and using expression (39), we obtain

$$\frac{d\Delta R}{dt} = -\frac{1}{4\eta}\left(3p^L + \frac{8\sigma}{R(N)}\right)\Delta R. \tag{41}$$

Therefore, the relaxation time required for adjusting the bubble size to the amount of gas in the bubble N is written as

$$\tau_R = \frac{4\eta}{3p^L + 8\sigma/R(N)}. \tag{42}$$

At small p^L, we have $3p^L \ll 8\sigma/R(N)$, and relationship (42) can be simplified to yield

$$\tau_R = \frac{4\eta}{8\sigma}R(N), \quad R(N) \le R_c \simeq \frac{2\sigma}{p_0}, \quad \tau_r = \frac{\eta}{p_0}, \tag{43}$$

where $R(N)$ is specified by equation (40).

Note that expression (43) is more probable for the initial and transient stages. After the transfer of a considerable part of excess gas into bubbles, and, correspondingly, a sufficient increase in the mean size of bubbles to $\bar{R} \gg 2\sigma/p^L$, formula (42) can be rearranged to give

$$\tau_R = \frac{4\eta}{3p^L} = \frac{4t_0}{3}\frac{p_0}{p_L}, \quad t_0 = \frac{\eta}{p_0}. \tag{44}$$

Relationship (44) is more probable at the later stage when bubbles have not already nucleated, their mean size increases, and the number decreases.

6. REDUCED EQUATIONS FOR TIME EVOLUTION OF GAS BUBBLES IN VISCOUS LIQUID

For liquids and melts with rather high viscosities and solubilities, the following inequalities most likely should be met:

$$\tau_g = \frac{2lR}{3\delta D} \ll \tau_R = \frac{4\eta}{8\sigma}R \tag{45}$$

or

$$\frac{4l\sigma}{3\delta D\eta} \ll 1. \tag{46}$$

Thus, the simplified reduced equations can be derived from expression (32) for liquids with sufficiently high viscosities when condition (46) is fulfilled. In this case, the chemical equilibrium ($\mu^L = \mu^V$) is rapidly attained at a constant bubble size. The pressure in a bubble becomes equal to the equilibrium pressure corresponding to the pressure $p(n^L)$ of the gas dissolved in the liquid, that is, $p^V = p(n^L(t))$, and does not depend on the bubble volume. This adjustment leads to a considerable decrease in the number of independent variables. Indeed, at $t \gg \tau_g$, under the assumption that the gas in bubbles is ideal ($p^V = NT/V$) and with the use of relationship $p^V = p$, we can obtain the expressions

$$f(V, N, t) = \varphi(V, t)\delta(N - N(R)), \tag{47}$$

$$N(R) = \frac{4\pi}{3}R^3\frac{p}{T}, \tag{48}$$

$$\frac{dR}{dt} = \frac{R}{4\eta}\left(p - p^L - \frac{2\sigma}{R}\right), \quad p = p(n^L) \tag{49}$$

[where $\delta(x)$ is the delta function], which corresponds to the adjustment of the number of gas atoms in a bubble to its size. Substitution of formula (47) into equation (32) and the integration with respect to the adjusting variable [1] lead to the equation for $\varphi(V, t)$

$$\frac{\partial\varphi}{\partial t} = -\frac{\partial I_V}{\partial V}$$
$$= \frac{\partial}{\partial V}D(V)\left[\frac{1}{T}\left(p - p^L - \frac{2\sigma}{R}\right)\varphi + \frac{\partial\varphi}{\partial V}\right], \tag{50}$$

$$D(V) = \frac{3}{4}\frac{VT}{\eta}, \quad N(V) = \frac{4\pi}{3}R^3\frac{P}{T} = \frac{PV}{T},$$
$$\mu^L - \mu^V = 0. \tag{51}$$

As follows from relationships (51), the distribution of bubbles over volumes or sizes also determines the gas amount in bubbles due to the adjustment of the gas content to the bubble size. It is quite reasonable that, in the case when the gas density in a bubble is sufficiently high, it is necessary to employ the equation for a real gas

$$F(V, t) = \int f(V, N, t)dN = \varphi(V, t),$$
$$\tilde{F}(N, t) = \int f(V, N, t)dV = \left(\frac{dN}{dV}\right)^{-1}\varphi(V(N), t). \tag{52}$$

Here, F and $\tilde{F}$ are the distributions of bubbles over sizes and amounts of gas, respectively.

In order to write the closed set of equations, the law of conservation of the number of gas atoms should be taken into consideration

$$n_0\left(1 - \int_0^\infty \varphi V dV\right)$$
$$= n^L(t)\left(1 - \int_0^\infty V\varphi dV\right) + \int_0^\infty N(V)\varphi(V, t)dV, \tag{53}$$

where $n_0 = n^L(t = 0)$ is the initial gas density in a liquid, and $n^L(t)$ is the gas density at a given instant. The third term is the amount of gas in bubbles per unit volume.

The multiplier $1 - \int_0^\infty V\varphi dV$ accounts for the fraction of the unit volume occupied by the liquid. Thus, the expansion of a liquid or a melt is governed by the relationship

$$\frac{V}{V_0} = \left(1 - \int_0^\infty V\varphi(V, t)dV\right)^{-1}, \tag{54}$$

where V is the volume of the liquid, and V_0 is the initial volume of the liquid. For low-viscosity liquids, when $\tau_g \gg \tau_R$, the mechanical equilibrium between the gas and the bubble is rapidly established; i.e., the bubble size is adjusted to the amount of gas in the bubble. Consequently, from the fulfillment of the inequality

$$\tau_g \gg \tau_R, \text{ or } \frac{4l\sigma}{3\delta D\eta} \gg 1,$$
$$\text{or } \frac{1}{2}\frac{l\bar{R}}{\delta D}\frac{p^L}{p_0} \gg t_0 \text{ if } p^L > \frac{2\sigma}{R}, \tag{55}$$

it follows that $f(V, N, t) \longrightarrow \psi(N, t)\delta(V - V(N))$. Correspondingly, as a result of adjustment, when the bubble volume "follows" the amount of gas in the bubble, we have

$$\frac{\partial\psi}{\partial t} = \frac{\partial}{\partial N}D(N)\left[\psi\ln\frac{p(n^L)}{p^L + 2\sigma/R} + \frac{\partial\psi}{\partial N}\right],$$
$$D(N) = \alpha\frac{D}{2l}4\pi R^2 n^L; \quad p^V = p^L + \frac{2\sigma}{R}. \tag{56}$$

At the nucleation stage, $p(n^L) \simeq p(n^L(0)) = p_0$ is the initial pressure. The $R(N)$ quantity is defined by equations (40). It is more probable that $p^L \ll 2\sigma/R$; however, at sufficiently high pressures when p^L is maintained in the liquid by external conditions, it is quite possible that $p^L \gg 2\sigma/R$. The law of conservation of the number of gas atoms in this case takes the form

$$n_0\left(1 - \int_0^\infty V(N)\psi(N, t)dN\right)$$
$$= n^L(t)\left(1 - \int_0^\infty V(N)\psi(N, t)dN\right) + \int_0^\infty N\psi(N, t)dN. \tag{57}$$

Under these conditions, $\left(1 - \int_0^\infty V(N)\psi(N, t)dN\right)^{-1}$ is the expansion coefficient of the liquid, $\int_0^\infty N\psi dN$ is the total number of gas atoms in all bubbles per unit volume, and $n_0 = n^L(0)$.

7. LIMITING VALUES OF DISTRIBUTION FUNCTION AT SMALL VALUES OF VARIABLES

For equations (50) and (56), it is necessary to specify the boundary and initial conditions. To accomplish this, let us divide volume V into elementary volumes $V_0 = T/P$ equal to the volume per gas atom in a bubble [see equation (50)].

According to equation (50), when the bubble absorbs a gas atom, the bubble volume changes by V_0. This elementary volume will be treated as the minimum volume of the bubble. Then, the probability that n gas atoms occupy the volume V_0 is determined by the Poisson distribution

$$W(n) = \frac{n^{-n}e^{-\bar{n}}}{n!}, \tag{58}$$

where $\bar{n} = n^L V_0 = \delta$, $\delta = n^L/n = n^L T/p$ is the gas solubility; n is the gas density at pressure p; and n^L is the equilibrium density of dissolved gas, provided that the Henry law is fulfilled. The probability that a bubble with one gas atom occurs in the volume V_0 is given by

$$W(1) = \delta e^{-\delta}. \tag{59}$$

The total number of these bubbles per unit volume depends on the gas density in the liquid. Each of the gas atoms in the liquid can form an elementary bubble of volume V_0

$$\tilde{\varphi}(V/V_0, t)\big|_{V/V_0 \to 1} = n^L \delta e^{-\delta}. \tag{60}$$

By going from the variable V_0/V to the variable V, we finally obtain

$$\varphi(V, t)dV = \tilde{\varphi}(V/V_0, t)\frac{dV}{V_0},$$

$$\varphi_0 = \varphi(V, t)\big|_{V \to V_0} = \frac{\tilde{\varphi}}{V_0} = n^L \frac{p}{T}\delta e^{-\delta} \tag{61}$$

$$= (n^L)^2 e^{-\delta} = \delta^2 \frac{p^2}{T^2} e^{-\delta}.$$

Limiting relationship (61) is the sought boundary condition for the $\varphi(V, t)$ function.

If the fluctuations in the bubble formation are ignored, the initial condition is defined as

$$\varphi(V, t)\big|_{t = 0} = 0. \tag{62}$$

Therefore, the set of equations for φ (50) and $n^L(t)$ (53) becomes closed with boundary condition (61) and initial condition (62). In the case when $\tau_g \gg \tau_R$, each atom is the nucleus of the gas bubble. The extension of the macroscopic approach to the bubbles of atomic sizes leads to

$$\psi(N, t)\big|_{N \to 1} \longrightarrow n^L. \tag{63}$$

By neglecting the fluctuations, the initial condition is represented by

$$\psi(N, t)\big|_{n \geq 1,\, t = 0} = 0. \tag{64}$$

Thus, equations (56) and (57) with boundary conditions (63) and initial conditions (64) form the complete closed set.

The general relationships obtained can be applied to determine the coefficients in kinetic equations in other different cases of first-order phase transitions. The above-derived kinetic equations, as applied to the evolution of the first-order phase transitions in viscous liquids and melts, will be considered in a separate work.

REFERENCES

1. M. Folmer, *Kinetic der Phasenbildung* (Th. Steinkopf, Dresden, 1939).
2. L. Farkas, Z. Phys. Chem. **125**, 236 (1927).
3. Z. Doring, Z. Phys. Chem. **36**, 371 (1937); Z. Phys. Chem. **38**, 292 (1938).
4. W. Bekker and Z. Doring, Ann. Phys. (Paris) **24**, 719 (1935).
5. Ya. B. Zel'dovich, Zh. Éksp. Teor. Fiz. **12**, 525 (1942).
6. V. V. Slezov and J. Schmelzer, Fiz. Tverd. Tela (S.-Peterburg) **36**, 353 (1994) [Phys. Solid State **36**, 193 (1994)].
7. V. V. Slezov and J. Schmelzer, J. Phys. Chem. Solids **55**, 243 (1994).
8. V. V. Slezov, Phys. Rep. **288**, 389 (1997).

Translated by O. Borovik-Romanova

Physics of the Solid State, Vol. 42, No. 4, 2000, pp. 760–766. Translated from Fizika Tverdogo Tela, Vol. 42, No. 4, 2000, pp. 741–746.
Original Russian Text Copyright © 2000 by Andrievskiĭ, Kalinnikov, Shtanskiĭ.

LOW-DIMENSIONAL SYSTEMS AND SURFACE PHYSICS

High-Resolution Transmission and Scanning Electron Microscopy of Boride–Nitride Nanostructured Films

R. A. Andrievskiĭ[1], G. V. Kalinnikov[1], and D. V. Shtanskiĭ[2, 3]
[1]*Institute of New Chemical Problems, Russian Academy of Sciences,*
p/o Chernogolovka, Noginskiĭ raĭon, Moscow oblast, 142432 Russia
[2]*Bardin Central Research Institute for the Iron and Steel Industry, Vtoraya Baumanskaya ul. 9/23, Moscow, 107005 Russia*
[3]*Department of Materials Science and Engineering, Ehime University, 3 Bunkyo-cho, Matsuyama 790-77, Japan*

Received May 12, 1999; in final form, August 6, 1999

Abstract—The results of electron-microscopic studies of grain boundaries and the structure of fractures of titanium boride- and nitride-based films obtained by nonreactive magnetron sputtering are considered. The chemical and phase composition of the films is analyzed with the help of Auger electron spectroscopy and microscopic electron diffraction analysis. The structure of boundaries and the presence of amorphous inclusions, dislocations, and other structural distortions are discussed and the nature of the deformation under indentation is considered. *© 2000 MAIK "Nauka/Interperiodica".*

In the continuation of our previous research [1], it was interesting to obtain more detailed information on the structure of grain boundaries in boride–nitride films and to study the nature of their fractures. The structure of boride and nitride films has been investigated by many authors (see, for example, [2–11] and the review [12]). Some of them [4–6, 12] noted the possibility of amorphous phases forming as a result of nonequilibrium conditions of deposition. However, the data are not systematic, and the information on the type of boundaries, the presence of dislocations, and peculiarities of deformation in films based on interstitial phases is extremely scarce. This stimulated the present research using high-resolution transmission and scanning electron microscopy.

1. SAMPLES AND EXPERIMENTAL TECHNIQUE

The method of obtaining films using TiB_2–TiN targets of various compositions was described in [1]. Some of the characteristics of the investigated films deposited on silicon substrates are given in the table. The structure was studied with the help of a JEM-3010 microscope with an accelerating voltage of 300 kV. The experimental foils were prepared from films deposited on razor blades and thinned by subsequent electrolytic and ionic polishing. The crystallite size was estimated on the basis of dark- and light-field images. The phase composition was determined from x-ray diffraction and microscopic electron diffraction data. The chemical and structural composition of the films was estimated from the Auger electron spectroscopic data (obtained on a Varian Scanning Auger electron spectrometer).

The microhardness of the films on silicon substrates was measured by the Vickers hardness test on a PMT-3 instrument using loads of 0.2–0.3 N; on the basis of 5–7 measurements, the value of H_0 corresponding to the hardness of films proper was estimated by the method [13] that makes it possible to eliminate the

Characteristics of investigated films

Film type	Sputtering regime (target)	Thickness, μm	Structural type	Lattice parameters, nm		Crystallite size, nm	Hardness H_V, GPa, under load P, N		H_0, GPa	Composition
				a	*c*		0.2	0.3		
I	DC(TiB_2)	1	AlB_2	Unknown		2–5	34	24	70–80	Unknown
II	HF(TiB_2)	1.7	AlB_2	0.3048	0.318	3–5	31	21.5	40–49	$Ti(B_{0.92}O_{0.05}C_{0.03})_{1.61}$
III	HF(50TiB_2–50TiN)	0.4	NaCl	~0.428		0.5–3	26	21	47–54	$Ti(B_{0.34}N_{0.49}O_{0.12}C_{0.05})_{1.49}$
IV	HF(25TiB_2–75TiN)	1.3	NaCl	~0.4307		5–15	23	19	42–43	Unknown

Note: DC indicates sputtering under direct current conditions and HF is the high-frequency mode.

effect of the substrate and film thickness on the results of measurements.

Fractographic measurements were made on a scanning microscope Hitachi S-4000 using a technique [3, 8] allowing one to observe the behavior of the material at the center of deformation. In other words, we studied the surface of cracks passing through pricks appearing as a result of microindentation (under loads of 1–5 N).

Preliminary results concerning the structure and fractography of films I and IV (see table) were reported in [8, 14].

2. DISCUSSION OF RESULTS

2.1. Structure and Composition

Figure 1 shows some dark-field images of films that visually indicate the presence of a nanocrystalline structure with a crystallite size generally smaller than 5–15 nm (films I, II, and IV). Especially small grains are observed for films III, deposited by sputtering from targets of an equimolar composition and having the smallest thickness.

Figure 2 illustrates several microscopic electron diffraction patterns of the synthesized films. The electron diffraction pattern obtained from one of the largest crystallites of film IV (Fig. 2c) confirms the presence of a structure of the NaCl type. The values of lattice parameters presented in the table were calculated predominantly from microscopic diffraction data, and, hence, their accuracy is not high. In our earlier publication [1], we discussed the difference between the lattice parameters and the tabulated data, which is due to the composition and the presence of a large number of impurities, as well as to deformation-induced displacements of diffraction maxima. According to Deng *et al.* [5], considerable compressive residual stresses can be expected in nitride–boride films.

A general analysis of x-ray and microscopic electron diffraction patterns also leads to the conclusion that, in view of the absence of a visible halo, amorphous phases are either absent or scarce.

According to the results of the Auger analysis, the distribution of elements over the film thickness was quite uniform except in a thin surface layer ($\delta \sim 30$ nm). It should be noted that these data correlate well with our previous results [1] and confirm the formation of a prestoichiometric phase on the basis of titanium diboride and a superstoichiometric phase on the basis of titanium nitride. As before [1], while writing the structural composition, we presumed that the film structure contains only one phase (judging from x-ray and electron diffraction patterns), and all interstitial atoms are in the nonmetallic sublattice.

We did not observe any difference in the phase composition and structure between the films deposited on silicon and steel substrates.

2.2. High Resolution

Figure 3 shows some photographs obtained in the direct resolution mode. It can be seen that, in contrast to noncrystalline materials prepared by consolidating ultrafine powders and normally characterized by a certain number of residual pores [15], film-type nanostructured objects are virtually free of pores. It can also be observed that the overwhelming number of grains have a stripe structure typical of the crystalline state, although individual regions could be characterized as amorphous. One such region denoted by A is shown in Fig. 3c. The number of regions with a blurred image, a violation of the stripe structure, and an indication of "amorphism" becomes so significant in the structure of film III (Fig. 3e) that it creates the impression that crystalline grains of size 0.5–2 nm are located in an amorphous matrix. It should be noted that the number of NaCl unit cells ($a \sim 0.43$ nm) in a crystallite having a size ~1 nm is just eight, and according to simple estimates, the fraction of boundary regions for crystallites

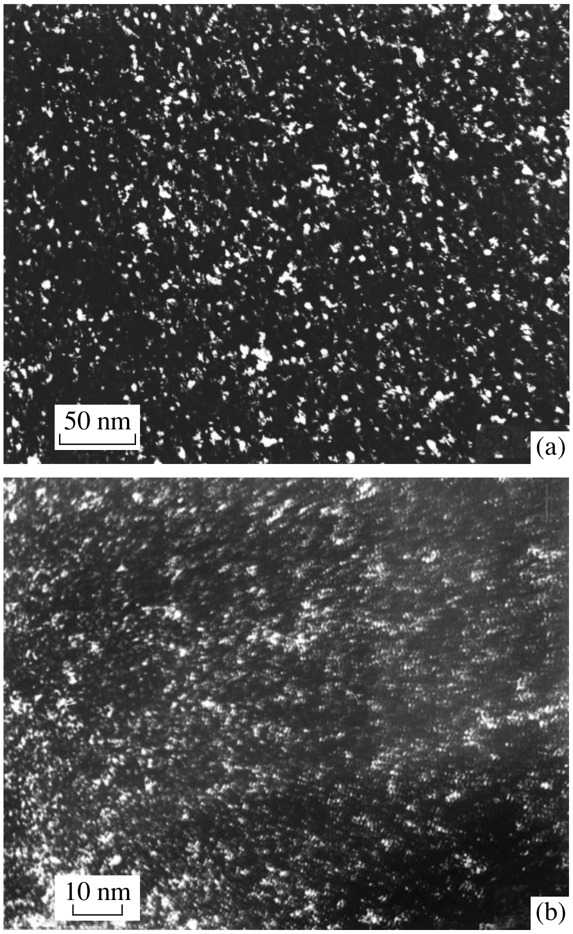

Fig. 1. Dark-field electron micrographs: (a) film I and (b) III.

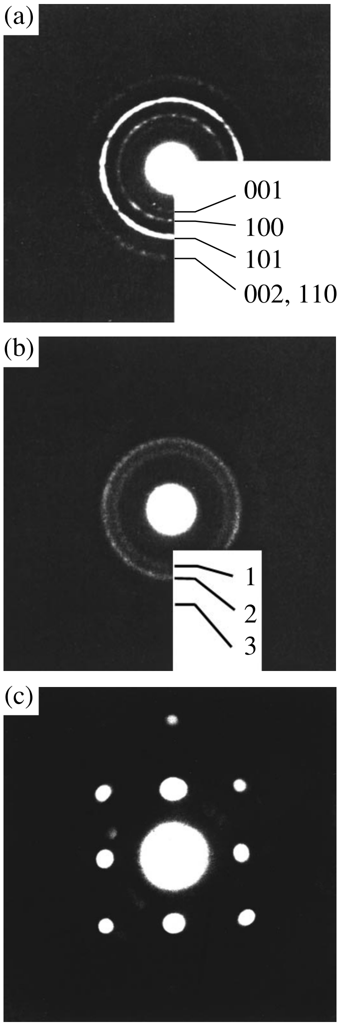

Fig. 2. Microscopic electron diffraction patterns: (a) film II, (b) III, and (c) IV (single crystal, axis [001]).

of this size can be 50%, and even higher for a boundary width ~0.3 nm. In the case of film III, whose image differs in general from those of other films, we are actually dealing with a sort of crystallite-like clusters displaying considerable structural distortions, which was also detected from displacements of diffraction lines.

In all probability, the “amorphous” nature of some other regions is associated with the effect produced on the image by numerous boundaries between crystallites, which are not parallel to the electron beam, and by above-mentioned possible internal stresses in the films. Besides, the blurring of images is also quite likely for crystallites having a size < 5 nm, whose number over the thickness of a foil under investigation (normally close to 5 nm) can be two or more, so that the interpretation of the presence or absence of amorphous inclusions becomes quite problematic. This looks significant for films I–III (especially for film III) with fine crystallites dominating in the structure (see table). Thus, the absence of amorphous inclusions in films IV, as well as in films I and II to a considerable extent, appears quite probable, while the situation with the object having finest grains (film III) is unclear on account of the large fraction of boundary regions, although the absence of a visual halo on x-ray and electron diffraction patterns was noted for all types of the films under investigation (see above).

In Figs. 3a and 3c, the boundaries between grains, at which the crystalline structure of both grains is seen more or less clearly, can be observed in many regions; atomic stripes terminate at the boundaries whose structure is of the crystalline form (arrows in Fig. 3c). The width of large-angle boundaries constitutes ~0.5 nm or even less. In some cases, the presence of coherent boundaries was detected.

Figure 3d shows, under a large magnification, the lower right corner of the image of film IV depicted in Fig. 3c, where there is a large grain approximately 20 nm in diameter. The clearly manifested inhomogeneous contrast (the focusing varied over distances shorter than 5 nm) can be attributed to internal stresses and the difference in composition, but the latter is unlikely.

Finally, an important point in observing direct-resolution structures is the detection of dislocations and other structure distortions. Bending of stripes in stripe patterns is noticeable in many cases (see, for example, Fig. 3a). We can also distinguish several edge dislocations, which are also seen clearly in the limits of the large nanocrystal in film IV (see Fig. 3d). In the structure of hexagonal films (Figs. 3a and 3b), dislocations are observed less frequently and are mainly located near boundaries.

It is well known [16, 17] that the presence and motion of dislocations in small crystalline objects is limited not only by frictional forces of the lattice (Peierls–Nabarro stress σ_{PN}), but also to a considerable extent by the so-called image forces emerging at interfaces and determining the stability of dislocations. The estimates obtained by Gryaznov *et al.* [17] for a number of metallic nanocrystals (Cu, Al, Ni, and Fe) indicate that the characteristic linear size for these materials, below which the existence of edge dislocations is highly improbable, is 2–24 nm. Unfortunately, the information on σ_{PN} for the refractory compounds under investigation is extremely scarce. If we use the estimate of the critical shear stress for TiN (σ_{cr} = 3.7 GPa) [18] and assume, as is usually done for refractory compounds [19], that $\sigma_{PN} \sim \sigma_{cr}$), then from the expression $\Lambda = 0.04Gb/\sigma_{PN}$ [17], where G is the shear modulus (248 GPa [1, 19]) and b is the Burgers vector (0.298 nm), we obtain the characteristic linear size, $\Lambda \sim$ 0.8 nm, below which the probability of existence of edge dislocations in nanocrystals is very low. This value is in satisfactory agreement with our experimental results. The approximate nature of the estimates for

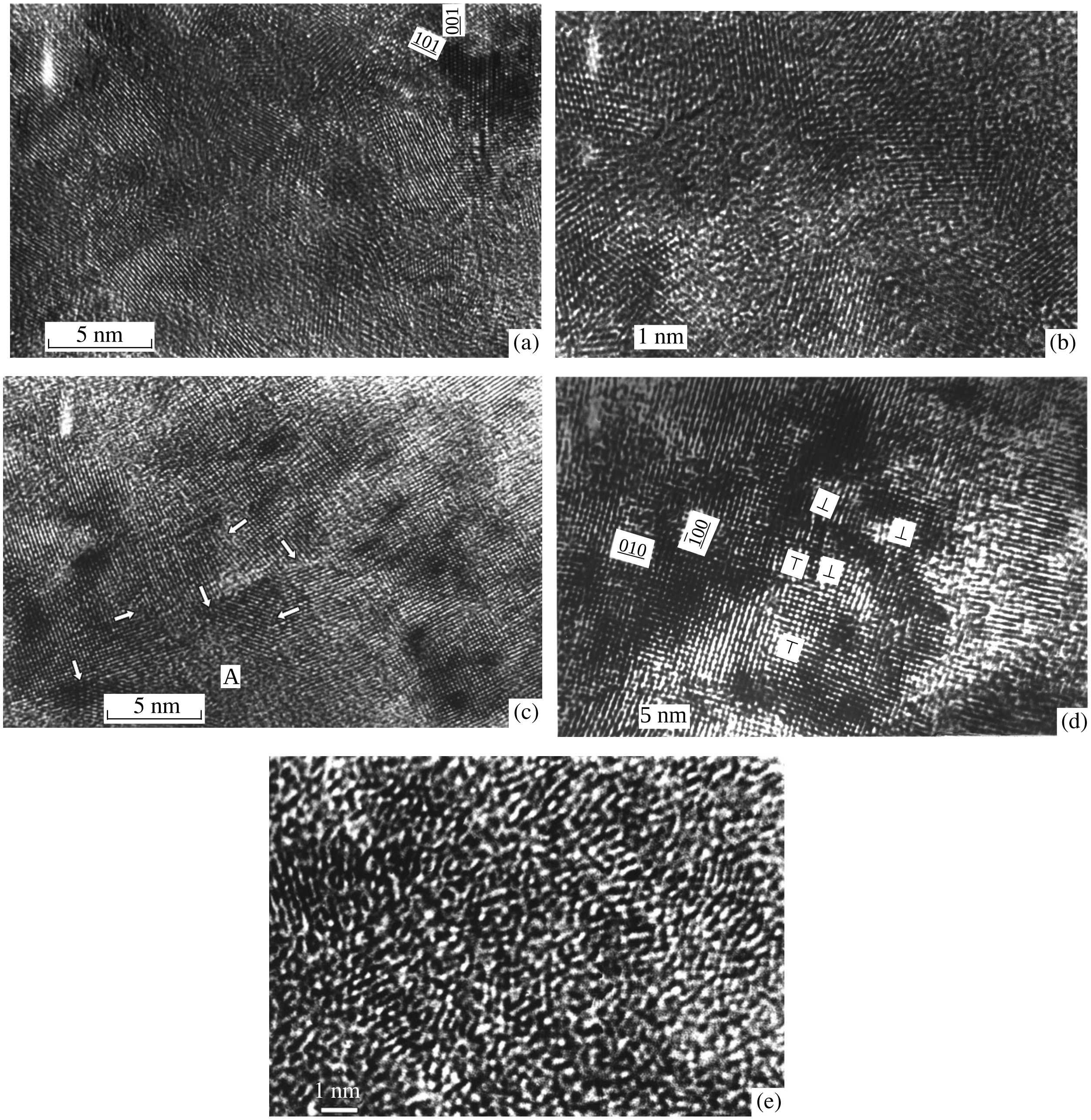

Fig. 3. Photographs of a film structure made in direct resolution mode: (a) film I, (b) II, (c) IV, (d) IV (one crystallite), and (e) III.

Λ does not allow us, however, to find the difference between phases based on TiN and TiB_2 nanocrystals.

2.3. Fractography

Figure 4 shows characteristic fractures of films with a cubic (a–c) and a hexagonal (d, e) structure. Judging from the plane of imprint and fracture, the deformation in the former case is more or less homogeneous, while in the latter case the step formation and localization of shear strains in the direction of force exerted by an indentor are quite obvious, and the deformation appears to be nonhomogeneous. When large loads (>1 N) are applied during indentation, annular and radial cracks are formed at the imprint surfaces in the case of cubic films (see Fig. 4b), as is usually observed in the case of hardness measurements in brittle solids, but no shear steps were observed in the load range under investigation (up to 5 N). An analysis of fractures of hexagonal films shows that the height and width of steps vary from ~100 nm to several hundred nanometers.

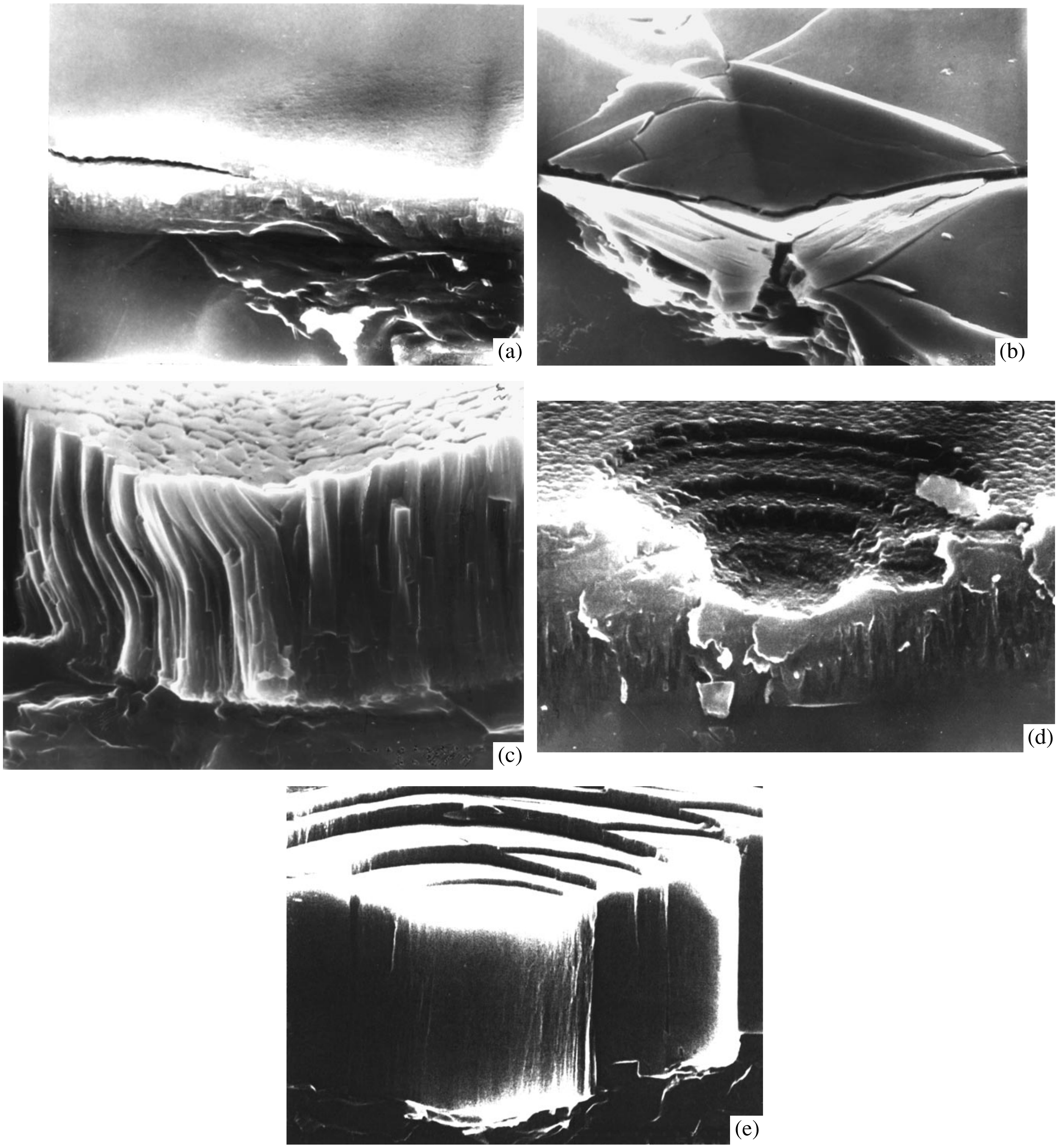

Fig. 4. Fractographs of fractures in (a–c) TiN-based films with a cubic structure and (d, e) TiB_2-based films with a hexagonal structure. (Courtesy of K.Y. Ma and A. Bloyce [27].)

Localized nonhomogeneous deformation is known to occur in many types of solids: metallic glasses, metals and alloys (including single crystals), ionic crystals, polymers, etc. The nature of this phenomenon is being discussed widely, although no satisfactory explanation of this effect have been obtained as yet (see, for example, [20–23]). On the other hand, in recent publications concerning the deformation of nanostructured materials (prepared from ultrafine powders of Fe, Fe–Cu, and $ZrO_2 + 3\%Y_2O_3$), the step formation and localization of shear strains were also reported [24–26]. In this connection, the nonhomogeneous deformation we detected for the first time [8] in nanostructured TiB_2-based films with a hexagonal structure is not surprising. However, it is not clear why TiN-base nanostructured films with a cubic structure are deformed homogeneously, which can also be confirmed by an analysis of the fractures of this type of films in [3, 8, 27]. It was proposed [14, 28] that this is due to different numbers of independent slip systems in TiB_2 (two systems of the type $\{10\bar{1}0\}\langle 11\bar{2}0\rangle$) and in TiN (five systems of the type $\{111\}\langle 110\rangle$). However, recently information on the behavior of dislocations in monocrystalline films and polycrystalline compacts of TiN [18, 29] convincingly proves the preferred slip along the $\{110\}$-type planes in the same direction $\langle 110\rangle$ (the number of independent slip systems is also two in this case).

Peculiarities of the deformation of cubic and hexagonal boride–nitride films can also be attributed hypothetically to the difference in the behavior of boundaries between columns in these films. In the former case, a clearly manifested columnar structure is observed as a rule (see Fig. 4c), and a uniform slip along columns under the action of the indentor is obvious. In the latter case, the columnar structure is less pronounced (see Fig. 4d), and deformation is localized through step formation, although the mechanism of this phenomenon (as for other objects listed above [20–26]) remains unclear and requires further investigations.

It is important to note that the objects under investigation are brittle by nature and are characterized by intercrystallite fracture [28]. Nevertheless, the presence of intracrystallite dislocations noted above (see Fig. 3d) facilitates the manifestation of plastic deformation, a unique example of which is depicted in Fig. 4c. The residual deformation of a part of “columns” in brittle TiN after indentation can be seen clearly; hence dislocations in compounds of this type may be not only of the sessile type, although the destruction pattern is often of the brittle (cleavage) type.

Note that the microhardness of film I (see table, reduced values of H_0), displaying typically nonhomogeneous deformation, is considerably higher than that of film IV being deformed homogeneously. The difference in the hardness of hexagonal films (I and II) obtained under different conditions of magnetron synthesis, which was also observed by other authors (see [15]), remains unclear.

Thus, the high-resolution transmission and scanning electron microscopy revealed that amorphous inclusions and interlayers at the boundaries between crystallites are absent for most nanostructured nitride–boride films under investigation and the boundaries have a predominantly crystalline structure. For film III, with a crystallite size 0.5–3 nm, the situation remains unclear and requires further investigation. The presence of intracrystallite edge dislocations is confirmed by estimates obtained in [16, 17]. The deformation under indentation of films can be of a homogeneous or a nonhomogeneous, localized type, which is hypothetically attributed to the difference in the behavior of the columnar structure of the films. The proposed possibility of plastic deformation of “columns” of TiN correlates with the presence of intracrystallite dislocations revealed experimentally.

ACKNOWLEDGMENTS

The authors are grateful to A.S. Aronin, A.M. Glezer, N.I. Noskova, and R.Z. Valiev for fruitful discussions of the results and to K. Ma (Taiwan) and D. Hull (Great Britain) for their assistance in fractographic and Auger experiments. We are also grateful to the Departments of Materials Science at the Universities of Ehime (Japan), and Birmingham and Loughborough (Great Britain) for letting us use their equipment.

This research was carried out under the support of INTAS program (project no. 96-2232) and “Integration” program (project no. 855).

REFERENCES

1. R. A. Andrievskiĭ, G. V. Kalinnikov, N. P. Kobelev, *et al.*, Fiz. Tverd. Tela (S.-Peterburg) **39**, 1859 (1997) [Phys. Solid State **39**, 1661 (1997)].
2. J.-E. Sundgren and L. Hultman, in *Materials and Processes for Surface and Interface Engineering*, Ed. by Y. Pauleau (Kluwer, Dordrecht, 1995), p. 453.
3. M. Shiwa, E. Wepelmann, D. Munz, *et al.*, J. Mater. Sci. **31**, 5985 (1996).
4. J. P. Riviere, Ph. Guesdon, J. Delafond, *et al.*, Thin Solid Films **204**, 151 (1991).
5. H. Deng, J. Chen, R. B. Inturi, *et al.*, Surf. Coat. Technology **76–77**, 609 (1995).
6. X. Wang, P. J. Martin, and T. J. Kinder, Surf. Coat. Technology **78**, 37 (1996).
7. R. Wiedemann, H. Oettel, and M. Jerenz, Surf. Coat. Technology **97**, 313 (1997).
8. K. Ma, A. Bloyce, R. A. Andrievskiĭ, *et al.*, Surf. Coat. Technology **94–95**, 322 (1997).
9. R. A. Andrievskiĭ, J. Solid State Chem. **133**, 249 (1997).
10. E. Kelesoglu and C. Mitterer, Surf. Coat. Technology **98**, 1483 (1998).
11. R. A. Andrievskiĭ, in *Surface-Controlled Nanoscale Materials for High-Added-Value Application*, Ed. by K. E. Gonsalves, M.-I. Baraton, R. Singh, *et al.* (Mater. Res. Soc., Warrendale, 1998), **501**, p. 149.
12. R. A. Andrievskiĭ, Usp. Khim. **66**, 57 (1997).
13. B. Jonsson and S. Hogmark, Thin Solid Films **114**, 257 (1984).
14. R. A. Andrievskiĭ, Materialovedenie No. 8 (1999) (in press).
15. R. A. Andrievskiĭ, Usp. Khim. **63**, 431 (1994).
16. V. G. Gryaznov, A. M. Kaprelov, and A. E. Romanov, Pis’ma Zh. Tekh. Fiz. **15** (2), 55 (1989) [Sov. Tech. Phys. Lett. **15**, 39 (1989)].
17. V. G. Gryaznov, I. A. Polonsky, A. E. Romanov, *et al.*, Phys. Rev. B **44**, 42 (1991).
18. M. Odén, H. Ljungcrantz, and L. Hultman, J. Mater. Res. **12**, 2134 (1997).

19. R. A. Andrievskiĭ and I. I. Spivak, *Strength of Refractory Compounds and Materials on Their Basis* (Metallurgiya, Chelyabinsk, 1989).
20. A. M. Glezer and B. V. Molotilov, *Structure and Mechanical Properties of Amorphous Alloys* (Metallurgiya, Moscow, 1992).
21. V. I. Al’shits and G. V. Berezhkova, in *Physical Crystallography* (Nauka, Moscow, 1992) [Phys. Solid State **39** (1995)].
22. N. P. Skvortsova, Fiz. Tverd. Tela (S.-Peterburg) **37**, 3347 (1995).
23. G. Spathis, J. Mater. Sci. **32**, 1943 (1997).
24. D. S. Yan, Y. S. Zheng, and L. Gao, J. Mater. Sci. **33**, 2719 (1998).
25. J. E. Garsley, A. Fisher, W. W. Milligan, *et al.*, Metall. Mater. Trans. A **29**, 2261 (1998).
26. T. R. Malow and C. C. Koch, Metall. Mater. Trans. A **29**, 2285 (1998).
27. K. J. Ma and A. Bloyce, Surf. Eng. **11**, 71 (1995).
28. R. A. Andrievskiĭ, in *Nanostructured Materials: Science and Technology*, Ed. by G.-M. Chow and N. I. Noskova (Kluwer, Dordrecht, 1998), p. 263.
29. R. Yamamoto, S. Murakami, and K. Maruyama, J. Mater. Sci. **33**, 2047 (1998).

Translated by N. Wadhwa

Physics of the Solid State, Vol. 42, No. 4, 2000, pp. 767–771. Translated from Fizika Tverdogo Tela, Vol. 42, No. 4, 2000, pp. 747–751.
Original Russian Text Copyright © 2000 by Sedrakyan, Badalyan, Khachatryan.

LOW-DIMENSIONAL SYSTEMS AND SURFACE PHYSICS

Electron Scattering at One-Dimensional Chain with Composition Disorder

D. M. Sedrakyan*, D. A. Badalyan*, and A. Zh. Khachatryan**
**Yerevan State University, ul. A. Manukyana 1, Yerevan, 375049 Armenia*
e-mail: dsedrak@www.physdep.r.am
***Armenian State Engineering University, Yerevan, 375046 Armenia*
e-mail: akhachat@www.physdep.r.am

Received August 9, 1999

Abstract—A new method is proposed for determining average kinetic parameters of one-dimensional disordered systems. Electron scattering at a one-dimensional chain with structural and composition disorders is considered. The solution of a finite-difference equation derived for the average resistance shows that the dependence of the average resistance on the number of scatterers (sample length) for all states of the one-electron spectrum is a sum of three exponential functions irrespective of the type of random field in the system. It is proved that, in the case of a mixed disorder, all one-electron states are localized in a chain of δ potentials. *© 2000 MAIK “Nauka/Interperiodica”.*

The study of the behavior of a quantum particle (or a system of particles) in a static external field with statistically defined parameters is an important problem in the theory of disordered systems. Such a field is referred to as a statistical field. A random field appears, for example, in strongly doped semiconductors due to a disordered distribution of impurities in the lattice (the so-called composition disorder) or in amorphous, glass-like, and liquid semiconductors or metals due to structural peculiarities of the materials (structural disorder).

An analysis of the type of electrical conductivity of two- and three-dimensional disordered systems encounters enormous mathematical difficulties. For this reason, one-dimensional models, which are of physical and applied interest in themselves, acquire special importance, for they permit exact solutions and, at the same time, possess considerable generality from the physical point of view. The methods of solutions of one-dimensional problems developed at present (e.g., the methods of transfer matrices, determinant method, and the method of invariant immersion) have made it possible to solve the problem for special types of random potentials, for weak and strong scattering fields, or for definite values of the electron energy [1–16].

In this paper, we propose a new effective method for exact calculation of the average resistance for a one-dimensional system formed by a finite number of randomly arranged scatterers of an arbitrary type, in which the parameters characterizing the scattering field are independent random variables.

Let us consider the space of possible realizations of a random field whose general form is of the type

$$V(x) = \sum_{n=1}^{N} V_n(x - x_n), \tag{1}$$

where $V_n(x - x_n)$ are individual potentials, which do not overlap and are localized at the points x_n. The individual potentials $V_n(x)$ are random independent functions with a uniform distribution density P in a certain space E of possible realizations. For example, the mean field of an individual potential can be written as

$$\langle V_n(x)\rangle = \int_E P[V_n(x)]V_n(x)DV_n(x). \tag{2}$$

If $V_n(x)$ is a parametrized potential, the continual integral (2) reduces to an ordinary integral in which integration is carried out over the random parameters of the function $V_n(x)$. In expression (1), the points x_n form a certain chain in which the distances $x_n - x_{n-1}$ ($n = 2, 3, \ldots, N$) are determined randomly and independently of one another and have the same mean value a:

$$\begin{gathered}\langle x_n - x_{n-1}\rangle = a,\\ \int f(\Delta x_{n-1})\Delta x_{n-1} d\Delta x_{n-1} = 0,\end{gathered} \tag{3}$$

where $\Delta x_{n-1} = x_n - x_{n-1} - a$, and $f(\Delta x_{n-1})$ is an (even) distribution function for the random quantity Δx_{n-1}, normalized to unity.

The model of a disordered system with the random static field (1)–(3) describes a large class of systems with so-called mixed disorder, in which structural disorder is combined with composition disorder. For example, the random parameters Δx_{n-1} characterize the structural disorder of the system, while the functions $V_n(x)$ determine the composition disorder. Special cases of this model, which are important from the physical point of view, are systems with structural order and composition disorder, with structural disorder and composition order, as well as various perfect lattices defined as systems possessing structural and composition orders simultaneously.

According to the ergodic hypothesis, a mean physical quantity pertaining to the system as a whole is calculated as the average over the random field existing in the bulk of the system. The procedure of averaging of a physical quantity Ω_N over the ensemble of possible realizations of the random field (1)–(3) can be written in the form

$$\begin{aligned}\langle\Omega_N\rangle = \int\ldots\int\Omega_N f(\Delta x_1)\ldots f(\Delta x_{N-1})P[V_1(x)] \\ \ldots P[V_N(x)]d\Delta x_1\ldots d\Delta x_N DV_1(x)\ldots DV_1(x).\end{aligned} \tag{4}$$

Integration in (4) is carried out over the entire range of the quantities Δx_{n-1} and over the entire space of possible realizations of the functions $V_n(x)$.

In Section 1, we will obtain the recurrence equation defining the average resistance $\langle\rho_N\rangle$ of the system. The dependence of $\langle\rho_N\rangle$ on the parameters of the problem will be determined in Section 2. In Section 3, we will analyze a chain of δ potentials with a mixed disorder and consider a class of exotic disordered systems comprising so-called nonreflecting wells.

1. EQUATION FOR AVERAGE RESISTANCE OF A SYSTEM WITH MIXED DISORDER

Let us consider the problem of calculating the average resistance $\langle\rho_N\rangle$ of a system with mixed disorder (1)–(3). We will use the Landauer formula defining the resistance of a finite system as the ratio of the reflection and transmission coefficients for an electron passing through the potential field of the system [17]:

$$\rho_N = |R_N|^2/|T_N|^2, \tag{5}$$

where R_N and T_N are the amplitudes of reflection and transmission of the electron, respectively.

It was proved by us earlier [18], that the problem of determining R_N and T_N for field (1) in the general form can be reduced to the solution of the following system of finite-difference equations:

$$D_N = r_N/t_N\bar{D}_{N-1}e^{i2kx_N} + 1/t_N D_{N-1}, \tag{6a}$$

$$\bar{D}_N = r_N^*/t_N^* D_{N-1}e^{-i2kx_N} + 1/t_N^*\bar{D}_{N-1}, \tag{6b}$$

where $D_N = 1/T_N$; $\bar{D}_N = R_N^*/T_N^*$; and r_N and t_N correspond to the amplitudes of reflection and transmission, respectively, through an individual potential field $V_N(x)$. It should be noted that D_{N-1} and $\bar{D}_{N-1}$ correspond to the first $N-1$ potentials of field (1).

Using the law of conservation of the number of particles ($|T_N|^2 + |R_N|^2 = 1$), we can write the resistance of the system in the form

$$\rho_N = |D_N|^2 - 1 = |\bar{D}_N|^2. \tag{7}$$

In order to calculate the average resistance $\langle\rho_N\rangle$, we introduce the auxiliary function

$$S_N = D_N\bar{D}_N^*e^{-2ikx_N}. \tag{8}$$

Then, we can obtain from (6)–(8) the following system of difference equations for ρ_N and S_N:

$$\begin{aligned}\rho_N = (2\alpha_N - 1)\rho_{N-1} + \beta_N^*\eta_{N-1}^*S_{N-1} \\ + \beta_N\eta_{N-1}S_{N-1}^* + \alpha_N - 1,\end{aligned} \tag{9a}$$

$$\begin{aligned}S_N = 2\gamma_N\rho_{N-1} + \chi_N\eta_{N-1}^*S_{N-1} \\ + \delta_N\eta_{N-1}S_{N-1}^* + \gamma_N,\end{aligned} \tag{9b}$$

where

$$\begin{aligned}\alpha_N = 1/|t_N|^2, \quad \beta = r_N/|t_N|^2, \quad \gamma_N = r_N/t_N^2, \\ \delta_N = r_N^2/t_N^2, \quad \chi_N = 1/t_N^2, \quad \eta_{N-1} = e^{i2k(a+\Delta x_{N-1})}.\end{aligned} \tag{10}$$

It can be seen from (9), that the coefficients of equations (9a) and (9b) contain scattering parameters only for the Nth individual potential of field (1) and the distance Δx_{n-1}. Since the quantities ρ_{N-1} and S_{N-1} depend by definition only on the first $N-1$ potentials of the system and on the distances Δx_{n-1} ($n = 2, 3,\ldots, N-1$), all the coefficients and the variables corresponding to them are averaged independently in averaging the system of equations (9) in accordance with (4). For example, we have

$$\langle(2\alpha_N - 1)\rho_{N-1}\rangle = \langle(2\alpha_N - 1)\rangle\langle\rho_{N-1}\rangle.$$

and so on.

Thus, the system of equations (9) averaged over the random field can be written in the form

$$\begin{aligned}\langle\rho_N\rangle = (2\alpha - 1)\langle\rho_{N-1}\rangle \\ + \beta^*\eta^*\langle S_{N-1}\rangle + \beta\eta\langle S_{N-1}^*\rangle + \alpha - 1,\end{aligned} \tag{11a}$$

$$\langle S_N\rangle = 2\gamma\langle\rho_{N-1}\rangle + \chi\eta^*\langle S_{N-1}\rangle + \delta\eta\langle S_{N-1}^*\rangle + \gamma, \tag{11b}$$

where

$$\begin{aligned}\alpha = \langle\alpha_N\rangle, \quad \beta = \langle\beta_N\rangle, \quad \gamma = \langle\gamma_N\rangle, \quad \delta = \langle\delta_N\rangle, \\ \chi = \langle\chi_N\rangle, \quad \eta = \langle\eta_{N-1}\rangle.\end{aligned} \tag{12}$$

The system of equations (11) allows us to obtain a finite-difference equation for the average resistance

$\langle\rho_N\rangle$ of the chain with mixed disorder (1)–(3). It has the form (see Appendix)

$$\langle\rho_N\rangle = A\langle\rho_{N-1}\rangle + B\langle\rho_{N-2}\rangle + C\langle\rho_{N-3}\rangle + D, \quad (13)$$

where

$$\begin{gathered} A = 2\alpha - 1 + \theta, \quad B = 2d - \nu - (2\alpha - 1)\theta, \\ C = (2\alpha - 1)\nu - 2u, \\ D = (\alpha - 1)(1 - \theta + \nu) + d - u \end{gathered} \quad (14)$$

and

$$\begin{gathered} d = 2\mathrm{Re}(\beta\eta\gamma^*), \quad u = 2\mathrm{Re}(\Gamma\eta\gamma^*), \\ \theta = 2\mathrm{Re}(\eta^*\chi), \quad \nu = |\eta|^2(|\chi|^2 - |\delta|^2). \end{gathered} \quad (15)$$

It can be seen from (13), that the average resistance $\langle\rho_N\rangle$, as a function of the number of scattering centers in the system, satisfies a nonhomogeneous linear difference equation. Equation (13) is the main result of this section. Let us go over to its solution.

2. SOLUTION OF THE EQUATION FOR THE AVERAGE RESISTANCE $\langle\rho_N\rangle$

We seek the solution of equation (13) in the form

$$\langle\rho_N\rangle = \sum_{j=1}^{p} L_j z_j^N + L_0, \quad (16)$$

where L_j and L_0 are arbitrary constants.

Substituting (16) into (13), we obtain a characteristic equation defining the quantities z_j ($j = 1, 2, 3$), and an equation for L_0:

$$z_j^3 - Az_j^2 - Bz_j - C = 0, \quad (17)$$

$$L_0 = L_0(A + B + C) + D. \quad (18)$$

It can be seen from (17), that $p = 3$. Substituting the values of A, B, C, and D from (14) and (15) into (18), we find that $L_0 = -1/2$. Consequently, solution (16) can be written in the form

$$\langle\rho_N\rangle = \sum_{j=1}^{3} L_j z_j^N - 1/2. \quad (19)$$

The coefficients L_j in solution (19) can be expressed in terms of $\langle\rho_2\rangle$, $\langle\rho_1\rangle$, $\langle\rho_0\rangle$, and the roots z_j of equation (17) by solving the system of equations

$$\begin{cases} L_1 + L_2 + L_3 = \langle\rho_0\rangle + \dfrac{1}{2} \\ L_1 z_1 + L_2 z_2 + L_3 z_3 = \langle\rho_1\rangle + \dfrac{1}{2} \\ L_1 z_1^2 + L_2 z_2^2 + L_3 z_3^2 = \langle\rho_2\rangle + \dfrac{1}{2}. \end{cases} \quad (20)$$

The quantities $\langle\rho_2\rangle$, $\langle\rho_1\rangle$, and $\langle\rho_0\rangle$ can be determined directly from (4) and (6):

$$\begin{gathered} \langle\rho_0\rangle = 0, \quad \langle\rho_1\rangle = \alpha - 1, \\ \langle\rho_2\rangle = 2\alpha(\alpha - 1) + d. \end{gathered} \quad (21)$$

Then the solution of system (20) gives

$$L_1 = \frac{2d - (2\alpha - 1)(z_2 + z_3 - 2\alpha - 1) + z_2 z_3}{(z_2 - z_1)(z_3 - z_1)}; \quad (22)$$

the quantities L_2 and L_3 can be obtained from (22) by cyclic permutation of the quantities z_1, z_2, and z_3.

Thus, it has been proved rigorously that the dependence of the average resistance of a one-dimensional system on its length for all the states of the one-electron spectrum is a sum of three exponential functions irrespective of the type of the random field.

3. A MODEL OF δ SCATTERERS WITH MIXED DISORDER

By way of example of the application of formulas derived above, let us consider a chain consisting of δ potentials

$$V(x) = \sum_{n=1}^{N} V_n \delta(x - x_n), \quad (23)$$

where V_n are random variables independent of one another and of the coordinates x_n.

In the case of a solitary δ potential, we have

$$\frac{1}{t_n} = 1 + \frac{iV_n}{2k}, \quad \frac{r_n}{t_n} = -\frac{iV_n}{2k} e^{2ikx_n}. \quad (24)$$

Using (10) and (24), we obtain from (12) the following expressions for the average values α, β, γ, δ, χ, and η:

$$\begin{gathered} \alpha = 1 + p, \quad \beta = -(p + iq), \quad \gamma = p - iq, \\ \delta = -p, \quad \chi = 1 - p + 2iq, \\ \eta = n^2 \exp(i2ka), \end{gathered} \quad (25)$$

where

$$p = \langle V_n^2\rangle/4k^2, \quad q = \langle V_n\rangle/2k$$

are parameters of composition disorder and

$$n^2 = \langle \exp(i2k\Delta x_{N-1})\rangle$$

is a parameter of structural disorder.

Substituting (25) into (14) and (15), we obtain the following expressions for the coefficients of the characteristic equation (17):

$$A = n^2(l+m) + (1-n^2)(1+2p),$$
$$B = -n^2(l-m) + n^2(1-n^2)(1-2p+4q^2), \quad (26)$$
$$C = n^4,$$

where

$$m = 2(p-q^2)(1-\cos 2ka), \quad l = 4\cos^2\varphi - 1,$$
$$\cos\varphi = \cos ka + q\sin ka.$$

A knowledge of the coefficients A, B, and C allows us to determine the roots z_j of equation (17). Substituting z_j into (22), we can find the coefficients L_j. Using the expressions for L_j and formula (19), we obtain the dependence of the average resistance $\langle\rho_N\rangle$ on the sample length, on the disorder parameters p, q, and n^2 of the system, and on the energy k of an incident electron.

Let us go over to an analysis of the solution (19) for $\langle\rho_N\rangle$ in the case of $N \longrightarrow \infty$. We will prove that, in this limit, all the one-electron states are localized irrespective of the nature of scattering at a solitary δ potential, i.e., that the localization radius

$$\zeta = \lim_{N\to\infty}\frac{Na}{\ln\langle\rho_N\rangle} \quad (27)$$

is finite and independent of N. For this purpose, we analyze the roots of the characteristic equation (17) [with coefficients (26)]. According to Vieta's theorem, we have

$$z_1 z_2 z_3 = C = n^4 \geq 0. \quad (28)$$

It follows from this relation, that if all the three roots of equation (17) are real-valued, either all of them are positive, or one root is positive and the other two are negative. If, however, equation (17) has only one real root, it is positive.

Let us prove that, among the roots of equation (17), there is always at least one real root greater than unity.

We consider the function

$$G(z) = z^3 - Az^2 - Bz - C, \quad (29)$$

whose zeros determine the roots of equation (17). Using (26), we can easily verify that, for all values of the coefficients A, B, and C, the function $G(z)$ is negative at points $z = \pm 1$, $G(z) \longrightarrow \infty$ for $z \longrightarrow \infty$, and $G(z) \longrightarrow -\infty$ for $z \longrightarrow -\infty$. From the properties listed above and from the fact that the function $G(z)$ has two extrema, we can conclude that the maximum root of the equation $G(z) = 0$ is always greater than unity. It follows, hence, that the average Landauer resistance (19) has the following asymptotic form for $N \longrightarrow \infty$:

$$\langle\rho_N\rangle = L_1 z_1^N - 1/2. \quad (30)$$

Here, z_1 stands for the root of the characteristic equation (17); $z_1 \geq 1$ and $1 \geq |z_2|, |z_3|$, where z_2 and z_3 are the remaining two roots.

Substituting (30) into (27), we obtain

$$\zeta = \frac{a}{\ln z_1}. \quad (31)$$

It follows from this expression, that the radius of localization depends in a complex way on the energy spectrum of one-electron states and disorder parameters of the system.

It is interesting to consider the case of a weak composition ($m \ll 1$) and structural ($1 - n^2 = s \ll 1$) disorders for the model under investigation for the energy of an incident electron corresponding to the allowed band ($\cos\varphi \leq 1$). In this case, the root of equation (17) determining the localization radius (31) can be sought in the form

$$z_1 = 1 + \Delta z \quad (32)$$

and $\Delta z \ll 1$. Substituting (32) into (17) and retaining only the terms linear in Δz, s, and m, we obtain

$$\Delta z = \frac{2m + 4q^2 s}{4\sin^2\varphi}. \quad (33)$$

The application of relations (31)–(33) leads to the formula

$$\zeta = \frac{4a\sin^2\varphi}{2m + 4q^2 s}. \quad (34)$$

In the particular case of only composition disorder in the system, in the absence of structural disorder ($m \neq 0$, $s = 0$), formula (34) is transformed into the corresponding formula derived in [19]. Relation (34) shows that, in the case of complete order ($s = 0$, $m = 0$), the localization radius tends to infinity.

The method we developed in this paper makes it possible to determine the average resistance of a one-dimensional disordered system with arbitrary composition and structural disorders. In particular, the formulas derived here can be readily applied to structures with random rectangular barriers (or wells). The approach developed can also be used for calculating other average kinetic parameters of one-dimensional disordered systems and for studying the problem of self-averaging of ρ_N.

In conclusion, let us consider a class of disordered systems comprising so-called random nonreflecting wells, for which [20]

$$r(k) = 0 \text{ and } |t(k)| = 1 \quad (35)$$

for all k and for all realizations of the well field.

In this case, relations (35) and (10) lead to the following expressions for the parameters of equation (13):

$$\alpha = 1, \quad \beta = 0, \quad \gamma = 0, \quad \delta = 0,$$
$$\chi = \langle\chi_N\rangle, \quad \eta = \langle\eta_{N-1}\rangle. \quad (36)$$

Then it follows from (13), that

$$\langle\rho_N\rangle = 0 \quad (37)$$

for any k and N. This result indicates complete delocalization of one-electron states in the one-dimensional disordered system, which is the distinctive feature of the model (35) under investigation. A similar result was obtained by Shalaev [21] by the inverse scattering method.

APPENDIX

We will write (11a) for $\langle\rho_{N-1}\rangle$ and $\langle\rho_{N-2}\rangle$ and (11b) for $\langle S_{N-1}\rangle$, $\langle S_{N-2}\rangle$, and $\langle S_{N-3}\rangle$ and their complex conjugates. This leads to the following system of difference equations:

$$\begin{aligned}\langle\rho_{N-1}\rangle &= (2\alpha-1)\langle\rho_{N-2}\rangle \\ &+\beta^*\eta^*\langle S_{N-2}\rangle+\beta\eta(S^*_{N-2})+\alpha-1, \\ \langle\rho_{N-2}\rangle &= (2\alpha-1)\langle\rho_{N-3}\rangle \\ &+\beta^*\eta^*\langle S_{N-3}\rangle+\beta\eta(S^*_{N-3})+\alpha-1, \\ \langle S_{N-1}\rangle &= 2\gamma\langle\rho_{N-2}\rangle \\ &+\chi\eta^*\langle S_{N-2}\rangle+\delta\eta\langle S^*_{N-2}\rangle+\gamma, \\ \langle S^*_{N-1}\rangle &= 2\gamma\langle\rho_{N-2}\rangle \\ &+\chi\eta^*\langle S^*_{N-2}\rangle+\delta\eta\langle S_{N-2}\rangle+\gamma, \\ \langle S_{N-2}\rangle &= 2\gamma\langle\rho_{N-3}\rangle \\ &+\chi\eta^*\langle S_{N-3}\rangle+\delta\eta\langle S^*_{N-3}\rangle+\gamma, \\ \langle S^*_{N-2}\rangle &= 2\gamma\langle\rho_{N-3}\rangle \\ &+\chi\eta^*\langle S^*_{N-3}\rangle+\delta\eta\langle S_{N-3}\rangle+\gamma.\end{aligned} \tag{A.1}$$

The system of equations (A.1) can be regarded as a linear nonhomogeneous system of algebraic equations for the unknown quantities $\langle S_{N-1}\rangle$, $\langle S_{N-2}\rangle$, and $\langle S_{N-3}\rangle$ and their complex conjugates. Determining $\langle S_{N-1}\rangle$ and $\langle S^*_{N-1}\rangle$ from (A.1) and substituting them into (11a), we obtain an equation for $\langle\rho_N\rangle$. Indeed, from (A.1) we obtain

$$\langle S_{N-1}\rangle = F/F_1, \tag{A.2}$$

where

$$\begin{aligned}F &= A_{N-1}F_1-A_{N-2}F_2 \\ &+A^*_{N-2}F_3-B_{N-1}F_4+B_{N-2}F_5, \\ F_1 &= |\eta|^2(\beta^*\Gamma-\beta\Gamma^*),\quad F_2=|\eta|^2|\Gamma|^2, \\ F_3 &= -|\eta|^2\eta/\eta^*\Gamma, \\ F_4 &= |\eta|^2(\delta\Gamma^*-\chi\Gamma),\quad F_5=-|\eta|^2\eta(|\chi|^2-|\delta|^2), \\ \Gamma &= \eta^*(\chi\beta-\delta\beta^*),\quad A_{N-1}=\gamma(2\langle\rho_{N-2}\rangle+1), \\ B_{N-1} &= \langle\rho_{N-1}\rangle-(2\alpha-1)\langle\rho_{N-2}\rangle-\alpha+1.\end{aligned} \tag{A.3}$$

Substituting (A.2) and (A.3) into (11a), we arrive at equation (13).

REFERENCES

1. I. M. Lifshits, S. A. Gredeskul, and L. A. Pastur, *Introduction to the Theory of Disordered Systems* (Wiley, New York, 1988).
2. P. W. Anderson. D. J. Thouless, E. Abrahams, *et al.*, Phys. Rev. B **22**, 3519 (1980).
3. T. Hirota and K. Ishii, Prog. Theor. Phys. **45**, 1713 (1971).
4. D. J. Thouless, J. Phys. C **5**, 77 (1972).
5. V. N. Prigodin, Zh. Éksp. Teor. Fiz. **79**, 2338 (1980) [Sov. Phys. JETP **52**, 1185 (1980)].
6. V. N. Mel'nikov, Fiz. Tverd. Tela (Leningrad) **22**, 2404 (1980) [Sov. Phys. Solid State **22**, 1398 (1980)].
7. A. Abrikosov, Solid State Commun. **37**, 997 (1981).
8. M. Ya. Azbel, Phys. Rev. B **28**, 4106 (1983).
9. V. N. Perel' and D. G. Polyakov, Zh. Éksp. Teor. Fiz. **86**, 352 (1984) [Sov. Phys. JETP **59**, 204 (1984)].
10. I. V. Klyatskin, *Immersion Method in the Theory of Wave Propagation* (Nauka, Moscow, 1986).
11. A. N. Dmitriev, Zh. Éksp. Teor. Fiz. **95**, 234 (1989) [Sov. Phys. JETP **68**, 132 (1989)].
12. A. G. Aronov, V. M. Gasparian, and Ute Yummich, J. Phys.: Condens. Matter **3**, 3023 (1991).
13. P. Erdos and R. C. Herndon, Adv. Phys. **31**, 65 (1982); Solid State Commun. **98**, 495 (1996).
14. O. N. Dorokhov, Zh. Éksp. Teor. Fiz. **101**, 2001 (1992) [Sov. Phys. JETP **74**, 1071 (1992)].
15. A. Abrahams and R. Berkovits, Phys. Rev. Lett. **70**, 1509 (1993).
16. D. M. Sedrakyan, D. A. Badalyan, V. M. Gasparyan, *et al.*, Zh. Éksp. Teor. Fiz. **109**, 243 (1996) [JETP **82**, 129 (1996)]; Zh. Éksp. Teor. Fiz. **111**, 575 (1997) [JETP **84**, 317 (1997)].
17. R. Landauer, Philos. Mag. **21**, 863 (1970).
18. D. M. Sedrakyan and A. Zh. Khachatryan, Izv. Nats. Akad. Nauk Arm. **34**, 138 (1999).
19. D. M. Sedrakyan, D. M. Badalyan, and A. Zh. Khachatryan, Izv. Nats. Akad. Nauk Arm. **33**, 166 (1998).
20. F. Calogero and A. Degasperis, *Spectral Transform and Solitons* (North Holland, Amsterdam, 1982).
21. B. N. Shalaev, Fiz. Tverd. Tela (Leningrad) **32**, 3586 (1990) [Sov. Phys. Solid State **32**, 2079 (1990).

Translated by N. Wadhwa

Physics of the Solid State, Vol. 42, No. 4, 2000, pp. 772–779. Translated from Fizika Tverdogo Tela, Vol. 42, No. 4, 2000, pp. 752–758.

LOW-DIMENSIONAL SYSTEMS AND SURFACE PHYSICS

Electron Tunneling through Thin Barrier with Smooth Potential at GaAs/AlAs(001) Heterointerfaces

S. N. Grinyaev and G. F. Karavaev

Kuznetsov Siberian Physicotechnical Institute, pl. Revolyutsii 1, Tomsk, 634050 Russia

e-mail: kanc@spti.tsu.ru

Received May 13, 1999; in final form, September 6, 1999

Abstract—The influence of actual microscopic potential on the characteristics of resonant electron tunneling from the Γ valley in GaAs through the AlAs barrier with thickness of one lattice constant has been investigated by the methods of pseudopotential and scattering matrix factorized by the irreducible representations of the symmetry group of the heterostructure. The transition regions between the potentials of components and the barrier region are treated as the components of the $Ga_2Al_2As_4$ superlattice spacing to provide the continuity of the crystal potential at the boundaries of the matching of wave functions. It is demonstrated that, compared to the results obtained in the abrupt-interface model, the inclusion of the actual potential in the calculation leads to changes in the number and location of the Fano resonances, an enhancement in the localization of electron density within the barrier, and a drastic increase in the tunneling time. *© 2000 MAIK "Nauka/Interperiodica".*

At present, the metalloorganic hydride and molecular-beam epitaxy techniques have been used to produce heterostructures with thin atomic layers in which the transition regions of the potentials of adjacent layers are comparable in size to the layers themselves. The physical properties of these heterostructures essentially depend on the nature of the interface region. In this respect, their electronic states should be described by the methods accounting for the actual microscopic potential. However, this circumstance is ignored in many cases. In the effective-mass method that is widely accepted in the present time, the potential at interfaces is usually taken to be discontinuous. This is justified for structures with sufficiently thick layers and also for the energy range, in which the mixing of states from different valleys is insignificant.

In other cases, this method can lead to quantitative discrepancies with the experimental characteristics. For example, the method gives the underestimated quantum levels in a narrow quantum well of GaAs inside $Ga_{1-x}Al_xAs$ [1] and underestimated times of tunneling through the GaAs/AlAs superlattices with thin barriers and wells [2]. The discrepancies can be avoided by smoothing the discontinuous potential with certain model functions whose form is sufficiently arbitrary [1, 3]. At the same time, consideration of the interface potential within the envelope wave function method results in a multiband system of equations with nonlocal interaction [4], which renders its application more complex and difficult-to-use. In more exact tight-binding and pseudopotential calculations [5–14], the absence of translational symmetry along the heterostructure axis necessitates the use of the so-called flat-band approximation, in which the bending of energy bands near heterointerfaces is neglected, and the potential in each layer is taken to be equal to the potential of the corresponding ideal bulk material. In general, the results of these calculations depend on the choice of boundaries, along which the wave functions of components are matched, and, for structures with thin layers, this problem becomes especially acute.

On the other hand, the self-consistent calculations of electronic states in superlattices demonstrate [15, 16] that, in the vicinity of heterointerfaces, there are regions with thickness of several monolayers, in which the crystal potentials of adjacent materials are continuously transformed into each other. Generally speaking, corrections applied to the discontinuous potential are not smooth functions, have a lower symmetry than the potentials of components, and, moreover, are nonlocal, which leads to certain problems of their inclusion in the description of resonant electron tunneling.

To our knowledge, only a few attempts have been made to introduce these corrections in a simplified way. For example, Cuypers and van Haeringen [10] applied the corrections to the discontinuous potential by steps from each side of the interface. Within this approximation, these corrections lead to a considerable change in the probability amplitudes of the resonant tunneling of electrons from GaAs through sufficiently thick AlAs barriers (~$10a_0$, where a_0 is the lattice constant), specifically in the range of mixing of states from the Γ and X valleys, but almost do not affect the energy location of resonances. It is obvious that a decrease in the barrier width brings about an increase in the contribution of the interface potential, which should be described more precisely. In the framework of the flat-band approximation, this can be achieved by division of the structure into such layers that they contain transition regions as components, for example, being the fragments of superlattices whose potentials at the boundaries of the matching of wave functions are continuously transformed into each other.

In the present work, this approach was applied to the electron tunneling from GaAs through the thin AlAs barrier with thickness of one lattice constant, for which the influence of the interface potential is particularly important. The resonances and antiresonances in the coefficient of transmission through a single barrier are associated with the Γ–*X* intervalley mixing effects. The pseudopotential and scattering-matrix calculations demonstrated that inclusion of the actual microscopic potential near the heterointerfaces is especially important for the quantitative description of these resonances, because this leads not only to a change in their number and energy, but also to a substantial increase in the collision times and the electron charge density within the barrier.

1. COMPUTATIONAL TECHNIQUE

As in the earlier works [12–14], the transmission coefficient of electrons was investigated within the discontinuous-potential model, but the barrier built up from the AlAs layer and adjacent transition layers was treated as a superlattice spacing. This made it possible to obtain a small jump of the crystal potential and wave functions at the matching boundaries. The determination of electronic states with complex values of the wave vector in multiatomic superlattices involves considerable computational problems, which can be partly resolved by invoking the symmetrized wave function basis set. Hence, in this work, we applied the scattering-matrix technique to multilayer systems with allowance made for their symmetry. In structures with the matched lattice constants of components, the *G* point symmetry group is the intersection of point groups of layers and consists of the symmetry elements in the interface plane. In this case, an additional symmetry arising at a certain structural configuration is ignored.

Let us consider a structure involving *N* interfaces with the z_n coordinates along the growth axis *z*. These interfaces separate *N* + 1 media. At the specified energies and the wave vector component $\mathbf{k}_\parallel$ parallel to the interface, the general solution of the Schrödinger equation for the *n*th medium $\Psi^{\alpha n}_{\mathbf{k}_\parallel}(\mathbf{r})$, which is transformed along the *s*th row of the *f*th irreducible representation of the *G* group [$\alpha \equiv (s, f)$], can be written as a superposition of the specific solutions $\Psi^{\alpha n}_{\mathbf{k}_\parallel}(\mathbf{r})$ corresponding to the incident ($\xi = \nu$) and reflected ($\xi = \mu$) waves [13]

$$\Psi^{\alpha n}_{\mathbf{k}_\parallel}(\mathbf{r}) = \sum_\nu A^{\alpha n}_\nu \Psi^{\alpha n}_{\mathbf{k}_\parallel \nu}(\mathbf{r}) + \sum_\mu B^{\alpha n}_\mu \Psi^{\alpha n}_{\mathbf{k}_\parallel \mu}(\mathbf{r}),$$
$$\Psi^{\alpha n}_{\mathbf{k}_\parallel \xi}(\mathbf{r}) = U^{\alpha n}_{\mathbf{k}_\parallel k^n_{z\xi}}(\mathbf{r}) \exp(i(\mathbf{k}_\parallel \cdot \boldsymbol{\rho} + k^n_{z\xi})), \qquad (1)$$
$$\mathbf{k} = \mathbf{k}_\parallel + \mathbf{e}_z k^n_{z\xi}.$$

Here, $\mathbf{e}_z$ is the unit vector along the *z*-axis, ρ is the projection of the radius vector **r** onto the interface plane, and $U^{\alpha n}_{\mathbf{k}_\parallel k^n_{z\xi}}(\mathbf{r})$ are the periodic wave functions expanded in the orthonormal basis set of symmetrized combinations of plane waves $\chi^\alpha_p(\mathbf{r})$

$$U^{\alpha n}_{\mathbf{k}_\parallel k^n_{z\xi}}(\mathbf{r}) = (1/\sqrt{V}) \sum_p Q^{\alpha n}_{p\xi} \chi^\alpha_p(\mathbf{r}),$$
$$\chi^\alpha_p(\mathbf{r}) = \sum_m R^\alpha_{pm} \exp(i\mathbf{b}^p_m \mathbf{r}), \qquad (2)$$

where $\mathbf{b}^p_m$ are the three-dimensional reciprocal-lattice vectors, *p* is the number of the symmetrized combination of plane wave, and *V* is the volume of the block of crystal periodicity. The projection of $\chi^\alpha_p(\mathbf{r})$ onto the heterointerface plane gives the orthonormal basis set of symmetrized combinations of surface plane waves

$$\varphi^\alpha_q(\boldsymbol{\rho}) = (1/\sqrt{S_0}) \sum_l T^\alpha_{ql} \exp(i\mathbf{a}^q_l \cdot \boldsymbol{\rho}),$$

where $\mathbf{a}^q_l$ are the two-dimensional reciprocal-lattice vectors, *q* is the number of the symmetrized combination of surface plane waves, and S_0 is the area of the surface unit cell. The matching conditions at boundaries of the $\Psi^{\alpha n}_{\mathbf{k}_\parallel}(\mathbf{r})$ wave functions and their first derivatives are written as

$$\sum_\nu A^{\alpha n}_\nu D^{\alpha n}_{q\nu} \exp(ik^n_{z\nu} z_n) + \sum_\mu B^{\alpha n}_\mu D^{\alpha n}_{q\mu} \exp(ik^n_{z\mu} z_n)$$
$$= \sum_\nu A^{\alpha(n+1)}_\nu D^{\alpha(n+1)}_{q\nu} \exp(ik^{(n+1)}_{z\nu} z_n)$$
$$+ \sum_\mu B^{\alpha(n+1)}_\mu D^{\alpha(n+1)}_{q\mu} \exp(ik^{(n+1)}_{z\mu} z_n),$$
$$\sum_\nu A^{\alpha n}_\nu P^{\alpha n}_{q\nu} \exp(ik^n_{z\nu} z_n) + \sum_\mu B^{\alpha n}_\mu P^{\alpha n}_{q\mu} \exp(ik^n_{z\mu} z_n)$$
$$= \sum_\nu A^{\alpha(n+1)}_\nu P^{\alpha(n+1)}_{q\nu} \exp(ik^{(n+1)}_{z\nu} z_n)$$
$$+ \sum_\mu B^{\alpha(n+1)}_\mu P^{\alpha(n+1)}_{q\mu} \exp(ik^{(n+1)}_{z\mu} z_n),$$
$$D^{\alpha n}_{q\xi} = \sqrt{S_0} \sum_p Q^{\alpha n}_{p\xi} C^{\alpha n}_{qp}, \qquad (3)$$

$$C_{qp}^{\alpha n} = \langle \varphi_q^\alpha | \chi_p^\alpha \rangle$$

$$= \sum_{m,l} (T_{ql}^\alpha)^* R_{pm}^\alpha \delta((\mathbf{b}_m^p)_\parallel - \mathbf{a}_l^q)\exp(ib_{mz}^p z_n),$$

$$P_{q\xi}^{\alpha n} = \sqrt{S_0}\left[\sum_p Q_{p\xi}^{\alpha n}\partial C_{qp}^{\alpha n}/\partial z + ik_{z\xi}^n D_{q\xi}^{\alpha n}\right],$$

$$\partial C_{qp}^{\alpha n}/\partial z$$

$$= i\sum_{m,l} (T_{ql}^\alpha)^* R_{pm}^\alpha \delta((\mathbf{b}_m^p)_\parallel - \mathbf{a}_l^q) b_{mz}^p \exp(ib_{mz}^p z_n),$$

$$b_{mz}^p = \mathbf{b}_m^p \cdot \mathbf{e}_z.$$

The order of the $D_{q\xi}^{\alpha n}$ and $P_{q\xi}^{\alpha n}$ matrices is determined by the number of incident (reflected) waves, which is equal to the number of symmetrized combinations of surface plane waves. The matching conditions can be reduced to the recurrence relations for the factorized scattering-matrix elements $S_{ij}^\alpha(n)$ [where $i, j = 1, 2$ are the subscripts numbering the incident (1) and reflected (2) waves] at one interface ($n = 1$), two interfaces ($n = 2$), and so on [13]

$$S_{11}^\alpha(n) = [(L_1^n)^{-1} J_{11}^\alpha(n) L_1^{(n+1)}$$

$$- S_{12}^\alpha(n-1)(L_2^n)^{-1} J_{21}^\alpha(n) L_1^{(n+1)}]^{-1} S_{11}^\alpha(n-1),$$

$$S_{12}^\alpha(n) = S_{11}^\alpha(n)(S_{11}^\alpha(n-1))^{-1}$$

$$\times [S_{12}^\alpha(n-1)(L_2^n)^{-1} J_{22}^\alpha(n) L_2^{(n+1)}$$

$$- (L_1^n)^{-1} J_{12}^\alpha(n) L_2^{(n+1)}], \tag{4}$$

$$S_{21}^\alpha(n) = S_{21}^\alpha(n-1)$$

$$+ S_{22}^\alpha(n-1)(L_2^n)^{-1} J_{21}^\alpha(n) L_1^{(n+1)} S_{11}^\alpha(n),$$

$$S_{22}^\alpha(n) = S_{22}^\alpha(n-1)(L_2^n)^{-1}[J_{22}^\alpha(n) L_2^{(n+1)}$$

$$+ J_{21}^\alpha(n) L_1^{(n+1)} S_{12}^\alpha(n)],$$

where $J_{ij}^\alpha(n)$ are the elements of the matching matrix

$$J_{ij}^n(n) = [(P_{3-i}^{\alpha n})^{-1} P_i^{\alpha n} - (D_{3-i}^{\alpha n})^{-1} D_i^{\alpha n}]^{-1}$$

$$\times [(P_{3-i}^{\alpha n})^{-1} P_j^{\alpha(n+1)} - (D_{3-i}^{\alpha n})^{-1} D_j^{\alpha(n+1)}],$$

$$L_{\xi\xi'}^n = \delta_{\xi\xi'}\exp(ik_{z\xi}^n z_n).$$

The sought matrix $S^\alpha(N)$ of scattering through N interfaces is determined by solving these equations at the initial condition $S^\alpha(0) = I$, where I is the unit matrix. The transmission and reflection coefficients of electrons are expressed in terms of the matrix elements $S_q^\alpha(N)$ (normalized to fluxes) for open channels. By using the intermediate matching matrices $J^\alpha(n)$ taken from (4), it is possible to determine the $A_\nu^{\alpha n}$ and $B_\mu^{\alpha n}$ coefficients and the wave function of a heterostructure. The general solutions in layers are conveniently sought with the use of the same large unit cell of a superlattice by the complex band structure method with local pseudopotentials.

In the present work, we studied the transmission of electrons at the normal incidence ($\mathbf{k}_\parallel = 0$) on the barrier with the (001) heterointerfaces. In this case, the wave function of the heterostructure has a maximum symmetry and can be transformed according to the identical representation Λ_1 of the C_{2v} group of the wave vector lying on the Λ line of the Brillouin zone of a tetragonal lattice [17]. The $Al_2Ga_2As_4$ superlattice spacing was chosen as the barrier region. This allowed us to take into account the principal part of the exact microscopic potential of transition layers in relatively simple calculations. In these calculations, we applied the pseudopotentials [18] determined from the experimental data and *ab initio* calculations of the band spectrum. With the kinetic-energy cutoff parameters taken from [18], in the basis set consisting of 243 three-dimensional plane waves constructed around the Γ reference point of the superlattice, we formed 98 symmetrized combinations of plane waves, eight symmetrized combinations of surface plane waves, and also eight incident and eight reflected waves transformed by the identical representation of the C_{2v} group. The inclusion of this number of waves provides a high accuracy in the description of electronic states in the neighborhood of the conduction-band bottom (~1 eV), and the error in the band energies does not exceed 0.02 eV.

2. RESULTS AND DISCUSSION

The features of resonant electron tunneling in heterostructures are governed by the complex band structure of their components. Note that the dominant role is played by the states with the least damping decrements. In the neighborhood of the conduction-band bottom, these are the states originating from the Γ_1, X_1, and X_3 valleys of the low-lying conduction bands of the GaAs and AlAs compounds. Figure 1 depicts the fragments of complex band structures along the Λ line of the tetragonal Brillouin zone ($\mathbf{k}_\parallel = 0$) for these states in $Al_2Ga_2As_4$, AlAs, and GaAs. The energies are measured from the bottom of the conduction band of GaAs. The imaginary and real parts of k_z are located to the left and to the right of the Γ point, respectively. The Λ direction of the superlattice is matched by the Δ line of the Brillouin zone in sphalerite, and the Γ, X, and Δ(0, 0, 1/2) sphalerite points are equivalent to the Γ point of the superlattice. The states of the superlattice with the Λ_1 symmetry are connected with the Γ_1, Γ_3, Z_1,

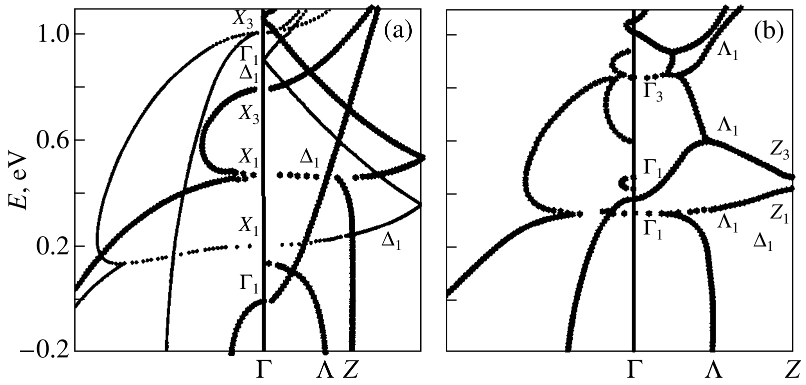

Fig. 1. Complex band structures along the Λ line of the tetragonal Brillouin zone ($\mathbf{k}_{||} = 0$) for (a) GaAs (heavy lines), AlAs (fine lines), and (b) the $Al_2Ga_2As_4$ superlattice.

and Z_3 states at the symmetric points by the consistency relations. The tetragonal component of the crystal potential in the superlattice leads to the removal of degeneracy and brings about the mixing of sphalerite states from the Γ and X valleys of the virtual crystal and the Δ line. The extrema of the split states are connected by loops in the complex region of the wave vector. The splitting gives rise to new valleys Z_1 and Z_3 near the lateral point Z with extrema at energies of 0.428 and 0.47 eV in the band spectrum of the superlattice. Even larger splitting is observed in the region of the intersection of sphalerite states from the Γ and X valleys. The gap in the range ~0.6–0.8 eV corresponds to the latter splitting. Analysis of the overlap integrals of wave functions for the superlattice and binary compounds shows that the X_1 sphalerite states of GaAs and AlAs are dominant in the low-lying state of the conduction band of the superlattice with the symmetry $\Gamma_1^{(1)}$ ($E = 0.3406$ eV), whereas the next energy state of the superlattice $\Gamma_1^{(2)}$ ($E = 0.3864$ eV) involves the Γ_1 states of GaAs and AlAs and, moreover, is substantially contributed by the states of AlAs from the Δ line. The mean value of masses $m(X_1) = 2.2$ (in terms of free electron mass) in the X_1 valley of AlAs and $m(\Delta) \approx 6$ in the Δ minimum of GaAs corresponds to the effective mass of the low-lying valley $m(\Gamma_1^{(1)}) = 4.4$. Along the tetragonal axis, the wave functions of the superlattice are smoothly transformed from the GaAs-like states to the AlAs-like states. The energies of extrema of the conduction band in the binary compounds are as follows: $E_{X_1} = 0.4818$ eV, E_{Δ_1}(GaAs) = 0.4673 eV, E_{X_3}(GaAs) = 0.7955 eV, E_{Γ_1}(AlAs) = 1.0040 eV, E_{X_1}(AlAs) = 0.2083 eV, and E_{X_3}(AlAs) = 1.0099 eV. These energies furnish a means of reconstructing the profile of bands along the axis of the $GaAs/Al_2Ga_2As_4/GaAs$ heterostructure. However, owing to the mixing of sphalerite states not only at heterointerfaces, as in the sharp-potential model, but also inside the superlattice, the connection of lines becomes ambiguous. For an electron incident from GaAs, the superlattice can be considered a superposition of the barriers (wells) with different heights (depths) and different effective masses from the $\Gamma_1^{(1)}$, $\Gamma_1^{(2)}$, Z_1, and Z_3 valleys, with which the electron interacts simultaneously, but with different probabilities proportional to the weights of states from the Γ_1 and Z_1 valleys in the wave function of the superlattice. In general, from the aforesaid it follows that, for thin layers, the band discontinuities determined up to now should be refined and newly interpreted.

In order to analyze the actual microscopic potential of the heterostructure, we calculated the crystal potential (averaged over the interface plane, $\mathbf{a}_l^q = 0$) of the superlattice along the z-axis and the difference ΔV between this potential and the potential in the model with abrupt interfaces (Fig. 2), which correspond to the locations of the As_{av} atoms surrounded by two Ga atoms and two Al atoms. Here, we took into account the fact that the arsenic pseudopotentials [18] depend on the type of the nearest atoms. An increase in the superlattice spacing does not essentially affect the ΔV potential in the vicinity of the barrier, and its form is similar to the corresponding profiles of nonlocal pseudopotential components [15, 16]. The main difference between the actual and discontinuous potentials is observed within the first four atomic layers near the interfaces covering the barrier region, where ΔV is a sharply varying function. It is evident that ΔV is poorly approximated by a stepwise potential. A similar behavior is also characteristic of the other Fourier components of the crystal potential ($\mathbf{a}_l^q \neq 0$). Hence, the matching of wave functions for the superlattice and GaAs was carried out at the boundaries separated from each other by the superlattice spacing ($2a_0$) and coinciding with the location of the As_1 atoms (surrounded by the Ga atoms), at which the difference in the crystal potentials of GaAs and the superlattice is minimum. The calcula-

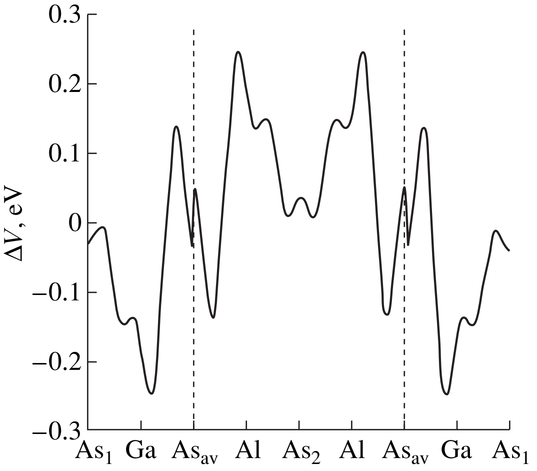

Fig. 2. Averaged (over the interface plane) difference between the crystal potential of the $Al_2Ga_2As_4$ superlattice and the potential in the abrupt-interface model. Vertical dashed lines indicate the locations of abrupt heterointerfaces.

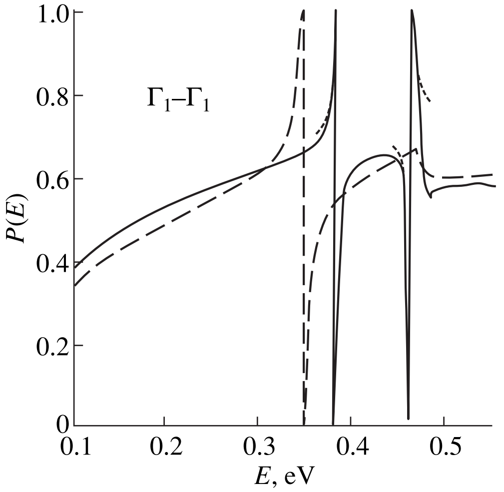

Fig. 3. Calculated coefficient of transmission of electrons from the Γ_1 valley to the Γ_1 valley of GaAs through the AlAs (a_0) barrier. Solid and dashed lines demonstrate the results of calculations within the diffuse-interface and abrupt-interface models, respectively. The dotted line shows the results of calculations according to formula (5).

tions were also performed for the matching boundaries coinciding with the locations of the Ga atoms adjacent to the As_1 atoms. The results obtained in both cases are close to each other, which indicates the convergence achieved in the description of the interface potential with the use of the $Al_2Ga_2As_4$ superlattice. The amplitude of the ΔV potential is comparable in magnitude to the band discontinuities. The same order of magnitude should have corrections to the electronic states calculated within the discontinuous-potential model. The largest changes can be expected for the quasi-stationary X states of AlAs, which are localized in the perturbing potential region.

Figure 3 displays the calculated coefficient for transmission of electrons from the Γ valley of GaAs (the Γ_1–Γ_1 channel) across the AlAs (a_0) barrier. Considerable differences between the results of calculations within the diffuse-interface and abrupt-interface models are observed over the entire energy range. In terms of the effective-mass approximation parameters, these differences are connected with the change in the band profiles, masses, and intervalley coupling constants at the interfaces. In the low-energy range ($E <$ 0.3 eV), the barrier calculated with due regard for the actual interface potential is 20% more transparent, predominantly due to the smaller damping decrement for the Γ_1 wave in the superlattice as compared to that in AlAs. More appreciable differences are found in the region of overlapping the profiles of different valleys in which the Fano resonances arise. These resonances correspond to the quasi-stationary states in the X_1 well of AlAs ($E_1 = 0.28$ eV, $E_2 = 0.45$ eV) and the $\Gamma_1^{(1)}$ well of the superlattice ($E_1 = 0.39$ eV, $E_2 = 0.45$ eV). The energy levels calculated within the one valley approximation for isolated wells are given in parentheses. With allowance made for the multiband structure, the locations of these levels change somewhat, and these changes are more pronounced for the narrower X_1 well of AlAs (the levels are shifted upward). As a result, the second level in this well becomes higher than the Δ_1 minimum of GaAs ($E_2 = 0.48$ eV). Analysis of the wave function for the heterostructure shows that the state of the low-lying Fano resonance within the barrier region is composed of three states originating from the $\Gamma_1^{(1)}$ (scattering state), $\Gamma_1^{(2)}$ [state with small Im(k_z)], and $\Gamma_1^{(1)}$ [state with large Im(k_z)] valleys of the superlattice. Upon normalization of the periodic parts of the wave functions to unity, the ratio between the amplitudes $A_\nu^{\alpha n}$ (or $B_\mu^{\alpha n}$) of these states is equal to 7 : 3 : 3. Consequently, the low-lying resonance is a hybridized state, which can be approximately treated as a quasi-stationary state in the $\Gamma_1^{(1)}$ well. The differences in the results of two calculations are due to the features in the behavior of the ΔV correction to the discontinuous potential, which, on the average, reduces the barrier height in the region between the As_{av} and As_1 atoms and raises the bottom of the well in the region between the As_{av} atoms. As a consequence, the well for the X-like states in the superlattice becomes wider, but shallower, and the effective mass of these states increases by a factor of two. This leads to an increase in the energy of the low-lying state in the X_1 well of AlAs and a lowering of the high-lying level below the extremum of a double humped structure for GaAs. Unlike the first Fano reso-

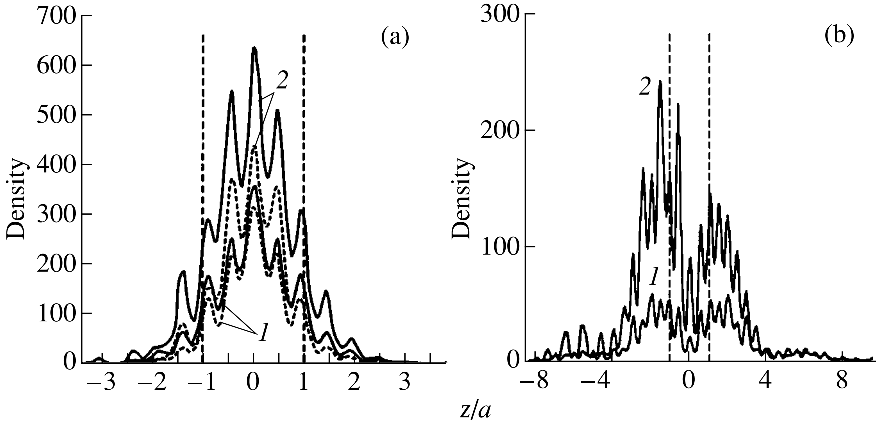

Fig. 4. Probability densities (averaged over the heterointerface plane) of states in the vicinity of the (a) first and (b) second Fano resonances: (*1*) the states correspond to the peaks of resonances and (*2*) the states correspond to the dips of resonances. Solid and dotted lines demonstrate the results of calculations within the diffuse-interface and abrupt-interface models, respectively. Vertical dashed lines indicate the boundaries of the superlattice period.

nance, the minimum of $P(E)$ for the second resonance does not become identically equal to zero. Tekman and Bagwell [19] pointed to the possibility of incomplete destructive and incomplete constructive interference between waves owing to the influence of other bands. In our case, near the second Fano resonance, there are three interacting states originating from the $\Gamma_1^{(2)}$ (scattering state), Z_3 [state with the small imaginary part $\mathrm{Im}(k_z)$], and $\Gamma_1^{(1)}$ [state with the large imaginary part $\mathrm{Im}(k_z)$] valleys of the superlattice. In the wave function of the heterostructure, the amplitudes of the second state are the largest, and, hence, the electron predominantly tunnels across the barrier via the gap state arising from the splitting of the band spectrum of the superlattice at the Brillouin zone edge. Within the abrupt-interface model, the electron at the same energies predominantly tunnels via the Γ_1 state of AlAs.

An increase in the X potential well size and the effective mass due to allowance made for the actual microscopic potential brings about an increase in the charge density of electronic states corresponding to the peak ($A_{\max}$) and the dip ($E_{\min}$) of the low-lying Fano resonance in the AlAs region (Fig. 4). In the calculations of the density, the wave function of the heterostructure was normalized according to the condition that the amplitude of incident wave is equal to unity. The charge density of states in the vicinity of the peak of low-lying resonance is maximum within the barrier region. In the GaAs direction, the charge density of states exponentially [with the decrement corresponding to $\mathrm{Im}(k_z)$ of the X_1 valley in GaAs] transforms to an oscillating superposition of incident and reflected waves (on the left) or to an oscillating passed wave (on the right). For the states with the energies $E_{\min}$, the function is bounded in one direction, which is accompanied by an increase in the density in the AlAs region. The charge density of states corresponding to the second Fano resonance is less localized and, for the most part, is located outside the AlAs layer.

The pole–zero nature of the Fano resonances clearly manifests itself in the dependence of the real part of the scattering-matrix element S_{11} (for the open Γ_1–Γ_1 channel) on the imaginary part (Fig. 5). In this diagram, S_{11} is the vector whose energy evolution is bounded by a unit circle. In the vicinity of resonances, this vector most drastically changes, which is convenient for the simulation of the scattering matrix. Diagrams of a similar type (the Argand diagrams [20]) are often used in interpretation of the structures in optical characteristics (in the form of dependences of the real and imaginary parts of permittivity ε_1 (ε_2), optical constants $n(k)$, etc. [21]) in terms of the parameters of separate or coupled oscillators. It can be seen from Fig. 5 that, for the most part, the trajectories of S_{11} near both Fano resonances

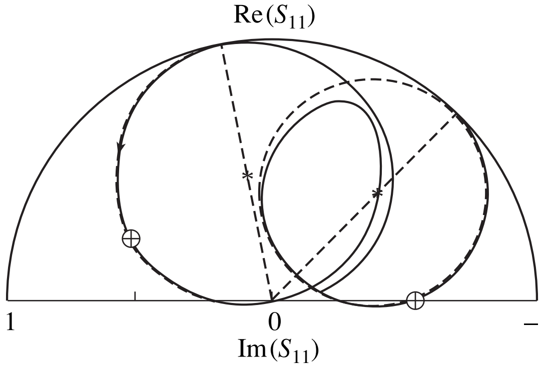

Fig. 5. Dependence of the real part of the scattering-matrix element $(S_{11})_{\Gamma_1\Gamma_1}$ on the imaginary part. The arrow indicates the direction of an increase in the energy. Small circles correspond to the location of real parts of the energies E_r at the poles. Dashed lines are constructed by formula (5). Crosses represent the centers of circles.

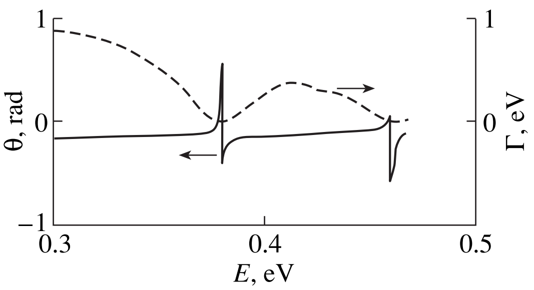

Fig. 6. Energy dependences of the phase shift $\Theta(E)$ and the broadening parameter $\Gamma(E)$ for the scattering-matrix element $(S_{11})_{\Gamma_1\Gamma_1}$.

are circles. The circle radius is equal to 0.5 for the low-lying resonance and is somewhat less than 0.5 for the second resonance, because the $P(E)$ value corresponding to the dip is nonzero. The parameters of these circles are related to the poles and zeros of the scattering matrix in the complex energy region. Since the resonances are sufficiently far apart in energy, their "coupling" can be ignored, and, in the neighborhood of each resonance, the canonical expansion of the scattering matrix can be approximately represented in the form [22]

$$S_{11}(E) \approx S_{\text{pot}} + A/(E-E_p) = B\frac{(E-E_n)}{(E-E_p)}, \qquad (5)$$

where S_{pot} is the term describing the potential scattering, which slightly depends on the energy; $E_p = E_r - i\Gamma$ $(\Gamma > 0)$ is the energy of the pole; $E_n = E_0 - i\gamma$ is the energy of zero of the scattering-matrix element in the complex energy plane; and B is the complex number. Formula of type (5) was used by Ivchenko *et al.* [23] in analysis of the electron transmission through several AlAs monolayers within the perturbation theory approximation. For the specific case $\gamma = 0$, this formula was employed by Porod *et al.* [24] for interpreting the non-Lorentzian features in the probabilities of electron tunneling through quantum waveguides with coupled cavities. This formula also leads to the scattering cross-section obtained by Fano [25] for resonance states in atoms and molecules. In the general case, the parameters of formula (5) can be determined from the results of exact calculations of the minimum $[P(E_{\min})]$ and maximum $[P(E_{\max}) = 1]$ transmission coefficients in the range of the Fano resonance and the extrema of the phase delay time [26] $\tau(E) = \hbar\frac{\partial\Theta(E)}{\partial E}$ (where $\Theta(E)$ is the phase shift of the matrix element S_{11}) at the energies E_r and E_0. The energy dependences of the phase shift $\Theta(E)$ and the broadening parameter $\Gamma(E) = \hbar/\tau(E)$ are displayed in Fig. 6. For the low-lying Fano resonance, $E_{\min} = E_0 = 0.3799$ (0.348) eV, $E_{\max} = 0.3781$ (0.343) eV, $\gamma = 0$, and the pole parameters are as follows: $E_r = 0.3793$ (0.3459) eV, $\Gamma = 0.00085$ (0.00246) eV, and $\tau(E_r) = 0.387$ (0.134) ps. The parameters calculated within the discontinuous-potential model are given in parentheses. Therefore, the consideration of the actual microscopic potential leads to an increase in the time of collision between an electron and the barrier in the range of the first Fano resonance almost by a factor of three. This change is directly determined by an increase in the localization of the wave function within the barrier region and a decrease in the Γ_1–$\Gamma_1^{(1)}$ intervalley coupling constant $\left|(J_{11})_{\Gamma_1\Gamma_1^{(1)}}\right| = 0.03$ at the $GaAs/Al_2Ga_2As_4$ interface as compared to the Γ_1–X_1 intervalley coupling constant $\left|(J_{11})_{\Gamma_1X_1}\right| = 0.05$ at the abrupt interface GaAs/AlAs. The ratio between the squares of magnitudes of these constants yields an estimate of the ratio between collision times. A decrease in the Fano resonance width (and the corresponding increase in the collision time) with a decrease in the intervalley coupling constant was observed earlier in [19]. The influence of interface potential on the tunneling time also provides an explanation for the results obtained in [2], in which the experimental times of tunneling through the GaAs/AlAs superlattices with thin barriers and wells proved to be longer than those calculated by the effective mass method with a stepwise potential. In [2], this discrepancy was explained by an additional scattering from phonons and the Coulomb interaction between electrons and holes. However, the discrepancies in [2] increase with a decrease in the layer thickness, which most likely indicates the influence of the interface. The second Fano resonance is characterized by the following parameters: $E_r = 0.4605$ eV, $\Gamma = 0.00126$ eV, $\tau(E_r) = 0.261$ ps, $E_0 = 0.45975$ eV, $E_{\max} = 0.4626$ eV, and $\gamma = -0.00022$ eV. Since γ is small, $E_{\min} \approx E_0$, and the trajectory of S_{11} in the diagram, as can be easily seen from formula (5), is close to a circle. The shorter times of a collision between the wave packet and the barrier correspond to the more weakly localized states of the second Fano resonance in the AlAs region.

In conclusion, we note that the results of multiband calculations are well reproduced when the matching matrices $J^{\alpha}(n)$ account for only the states from the $\Gamma_1^{(1)}$, $\Gamma_1^{(2)}$, Z_1, and Z_3 low-lying valleys of the superlattice. Another model that efficiently accounts for the actual profile of a microscopic potential through the band parameters of these valleys in the GaAs/AlAs(001) superstructures will be elaborated in a separate work.

ACKNOWLEDGMENTS

This work was supported by the "Surface Atomic Structures" Program of the Ministry of Science and Technology of the Russian Federation, project no. 5.12.99.

REFERENCES

1. D. F. Nelson, R. C. Miller, C. W. Tu, *et al.*, Phys. Rev. B **36**, 8063 (1987).
2. K. Fujiwara, K. Kawashima, and T. Imanashi, Phys. Rev. B **54**, 17724 (1996).
3. B. A. Foreman, Phys. Rev. Lett. **80**, 3823 (1998).
4. G. F. Karavaev and I. N. Krivorotov, Fiz. Tekh. Poluprovodn. (S.-Peterburg) **30**, 177 (1996) [Semicond. **30**, 102 (1996)].
5. D. Y. Ko and J. C. Inkson, Phys. Rev. B **38**, 9945 (1988).
6. D. Y. Ko and J. C. Inkson, Semicond. Sci. Technol. **3**, 791 (1988).
7. T. Ando, S. Wakahara, and H. Akera, Phys. Rev. B **40**, 11609 (1989).
8. T. Ando and H. Akera, Phys. Rev. B **40**, 11619 (1989).
9. J. P. Cuypers and W. van Haeringen, Physica B (Amsterdam) **168**, 58 (1991).
10. J. P. Cuypers and W. van Haeringen, J. Phys.: Condens. Matter **4**, 2587 (1992); J. P. Cuypers, *Scattering of Electrons at Heterostructure Interfaces*, Ph.D. Thesis (The Eindhoven University of Technology, Eindhoven, 1992).
11. T. Osotchan, V. W. L. Chin, and T. L. O. Tansley, Phys. Rev. B **54**, 2059 (1996).
12. G. F. Karavaev, S. N. Grinyaev, and V. N. Chernyshov, Izv. Vyssh. Ucheb. Zaved., Fiz. **35** (9), 64 (1992).
13. S. N. Grinyaev and V. N. Chernyshov, Fiz. Tekh. Poluprovodn. (Leningrad) **26**, 2057 (1992) [Sov. Phys. Semicond. **26**, 1157 (1992)].
14. S. N. Grinyaev, G. F. Karavaev, and V. N. Chernyshov, Fiz. Tekh. Poluprovodn. (S.-Peterburg) **28**, 1393 (1994) [Semicond. **28**, 784 (1994)].
15. C. G. van de Walle and R. M. Martin, Phys. Rev. B **35**, 8154 (1987).
16. D. M. Bylander and L. Kleinmann, Phys. Rev. B **36**, 3229 (1987).
17. O. V. Kovalev, *Irreducible and Induced Representations and Corepresentations of Fedorov Groups* (Nauka, Moscow, 1986).
18. K. A. Mader and A. Zunger, Phys. Rev. B **50**, 17393 (1994).
19. E. Tekman and P. F. Bagwell, Phys. Rev. B **48**, 2553 (1993).
20. T. S. Moss, *Optical Properties of Semiconductors* (Butterworths, London, 1959; Inostrannaya Literatura, Moscow, 1961).
21. V. V. Sobolev and V. V. Nemoshkalenko, *Methods of Computational Physics in Solid State Physics* (Naukova Dumka, Kiev, 1988).
22. H. M. Nussenzveig, *Causality and Dispersion Relations* (Academic Press, New York, 1972; Mir, Moscow, 1976).
23. E. L. Ivchenko, A. A. Kiselev, Y. Fu, *et al.*, Phys. Rev. B **50**, 7747 (1994).
24. W. Porod, Z.-an Shao, and C. S. Lent, Phys. Rev. B **48**, 8495 (1993).
25. U. Fano, Phys. Rev. **124**, 1866 (1961).
26. Ta-You Wu and Takashi Ohmura, *Quantum Theory of Scattering* (Prentice Hall, New York, 1962; Nauka, Moscow, 1969).

Translated by O. Borovik-Romanova

Physics of the Solid State, Vol. 42, No. 4, 2000, pp. 780–784. Translated from Fizika Tverdogo Tela, Vol. 42, No. 4, 2000, pp. 759–763.

LOW-DIMENSIONAL SYSTEMS AND SURFACE PHYSICS

Electron-Stimulated Desorption of Lithium Atoms from Oxidized Molybdenum Surface

V. N. Ageev and Yu. A. Kuznetsov

Ioffe Physicotechnical Institute, Russian Academy of Sciences, Politekhnicheskaya ul. 26, St. Petersburg, 194021 Russia

Received August 10, 1999

Abstract—The yield and energy distributions of lithium atoms upon electron-stimulated desorption from lithium layers adsorbed on the molybdenum surface coated with an oxygen monolayer have been measured as functions of the impact electron energy and lithium coverage. The measurements are performed using the time-of-flight technique and a surface ionization detector. The threshold of the electron-stimulated desorption of lithium atoms is equal to 25 eV, which is close to the ionization energy of the O 2*s* level. Above a threshold of 25 eV, the yield of lithium atoms linearly increases with an increase in the lithium coverage. In the coverage range from 0 to 0.45, an additional threshold is observed at an energy of 55 eV. This threshold can be associated with the ionization energy of the Li 1*s* level. At the electron energies above a threshold of 55 eV, as the coverage increases, the yield of lithium atoms passes through a maximum at a coverage of about 0.1. Additional thresholds for the electron-stimulated desorption of the lithium atoms are observed at electron energies of 40 and 70 eV for the coverages larger than 0.6 and 0.75, respectively. These thresholds correlate with the ionization energies of the Mo 4*s* and Mo 4*p* levels. Relatively broad peaks in the range of these thresholds indicate the resonance excitation of the bond and can be explained by the excitation of electrons toward the band of free states above the Fermi level. The mean kinetic energy of the lithium atoms is equal to several tenths of an electronvolt. At electron energies less than 55 eV, the energy distributions of lithium atoms involve one peak with a maximum at about 0.18 eV. For the lithium coverages less than 0.45 and electron energies higher than 55 eV, the second peak with a maximum at 0.25 eV appears in the energy distributions of the lithium atoms. The results obtained can be interpreted in the framework of the Auger-stimulated desorption model, in which the adsorbed lithium ions are neutralized after filling holes inside inner shells of the substrate and lithium atoms. *© 2000 MAIK “Nauka/Interperiodica”.*

The electron-stimulated desorption is widely used in analysis and modification of adsorbed layers and film coatings. However, the current state of the art in the understanding of physical processes underlying this phenomenon is still not sufficient for its all-round application. This is primarily due to the fact that only charged particles have hitherto been recorded in the majority of works, and the data on the electron-stimulated desorption of neutral particles were obtained by the indirect method [1].

Earlier [2, 3], we employed a surface ionization detector for the recording of desorbed neutral particles. This enabled us to measure the cross-sections and energy distributions of alkali metal atoms upon electron-stimulated desorption from layers adsorbed on oxidized tungsten and to put forward the model of this process on the basis of the Auger-stimulated desorption with allowance made for the relaxation of the local surface field. The yields of K, Na, and Cs atoms and their energy distributions upon electron-stimulated desorption from the layers adsorbed on the molybdenum surface coated with an oxygen monolayer were measured in our earlier work [4]. It was demonstrated that the electron-stimulated desorption can be initiated not only by the ionization of the O 2*s* level, but the Mo 4*p* and Mo 4*s* levels as well. Note that, in the latter case, the ionization is a resonance process and is accompanied by the extension of the energy distribution of alkali metal atoms toward the range of very low energies [4].

In the present work, we measured the yield and energy distributions of lithium atoms upon electron-stimulated desorption from the lithium layer adsorbed on the molybdenum surface coated with an oxygen monolayer. This work is a part of the program concerned with the elucidation of the mechanism for electron-stimulated desorption of alkali metal atoms from the surface of transition metal oxides.

1. EXPERIMENTAL TECHNIQUE

The yield and energy distributions of alkali metal atoms upon electron-stimulated desorption were measured using the time-of-flight technique with a surface ionization detector. The procedure of measurements and an instrument were described in detail earlier in [5]. Here, we only briefly recall their main features. The measurements were carried out in a heated stainless steel chamber at a residual gas pressure below 5×10^{-10} Torr. The desorbed lithium atoms were ionized in a surface ionization detector consisting of a textured iridium ribbon, which was heated up to $T = 1800$ K. The amplitude modulation of an electron beam, followed by the synchronous detection of a signal at the output of the detector, made it possible to improve the signal-to-noise ratio. The energy distributions of the desorbed lithium atoms were measured by the time-of-flight technique upon irradiation of a target with electron pulses of duration 1 μs at a frequency of 1 kHz.

A textured molybdenum ribbon $70 \times 2 \times 0.01$ mm^3 in size was used as a target. In order to provide the preferable orientation of the (001) surface, the ribbon was heated by an alternating current under a high vacuum at $T = 2000$ K for 5 h. The ribbon was cleaned from carbon by the annealing in an oxygen atmosphere at a pressure of 1×10^{-6} Torr at $T = 1800$ K for 3 h. After the evacuation of oxygen from the chamber, the ribbon was heated up to $T = 2200$ K for 3 min in order to desorb oxygen. The purity of the ribbon was checked by the Auger electron spectroscopy, work function measurements, and temperature-controlled desorption technique. A monolayer oxygen coating was produced by the treatment of the ribbon in oxygen at a pressure of 1×10^{-6} Torr at the temperature $T = 1400$ K for 10 s.

Lithium was applied on the oxidized surface of a molybdenum ribbon at $T = 300$ K from an evaporator, in which lithium oxide was reduced by aluminum upon passage of electric current. The concentration of deposited lithium was determined from the deposition time at a constant flux. The intensity of lithium flux was measured from the total current of surface ionization on the ribbon heated to $T > 1750$ K. The adsorbed-lithium concentration corresponding to a monolayer coating on the oxidized Mo(100) face was taken to be equal to 1×10^{15} at/cm^2, because the yield of lithium atoms at this concentration reached a maximum.

The composition of residual gases and the purity of lithium atom fluxes was checked with a quadrupole mass spectrometer. The density of electron current was no more than 10^{-6} A/cm^2 at an electron energy of 100 eV, and, hence, the electron bombardment did not lead to considerable heating of the ribbon.

2. RESULTS

The yield of lithium atoms upon electron-stimulated desorption from the lithium layer adsorbed on the molybdenum surface coated with an oxygen monolayer depends on the energy of bombarding electrons and the lithium coverage of the surface. Note that, unlike the electron-stimulated desorption of lithium atoms from oxidized tungsten, the yield of lithium atoms desorbed from oxidized molybdenum is not a linear function of the lithium coverage [4]. Figure 1 displays the yields of lithium atoms q from the molybdenum surface coated with an oxygen monolayer as a function of the bombarding electron energy for different lithium coverages at $T = 300$ K. It can be seen that the threshold of the electron-stimulated desorption is equal to 25 eV and does not depend on the lithium coverage. Taking into account the contact potential difference between an electron emitter and the target, this value of threshold energy can be treated to be close to the ionization energy of the O 2s level. At the lithium coverages $\Theta < 0.45$, the dependences of the yield of lithium atoms on the electron energy exhibit a stepwise increase in the yield at the electron energy $E_e \approx 55$ eV, which corresponds to the ionization energy of the Li 1s level. It is interesting that the yield of lithium atoms due to this threshold reaches a maximum at the lithium coverage $\Theta \approx 0.1$, decreases with a further increase in the coverage, and becomes negligibly small at $\Theta > 0.45$. An increase in the lithium coverage above 0.6 leads to the appearance of a broad peak in the $q(E_e)$ curves at $E_e \approx 40$ eV, which correlates with the ionization energy of the Mo 4p level. At the lithium coverage $\Theta > 0.75$, the curves show the second broad peak at the electron energy $E_e \approx 70$ eV, which is close to the ionization energy of the Mo 4s level [6]. The location of these features in the electron energy scale is independent of the lithium coverage. As the electron energy increases, the yield of lithium atoms gradually increases and does not reach saturation up to $E_e \approx 160$ eV. The shape of the features at $E_e \approx 40$ and 70 eV suggests that the resonance excitation of bonds is responsible for the electron-stimulated desorption of lithium atoms in the range of these energies.

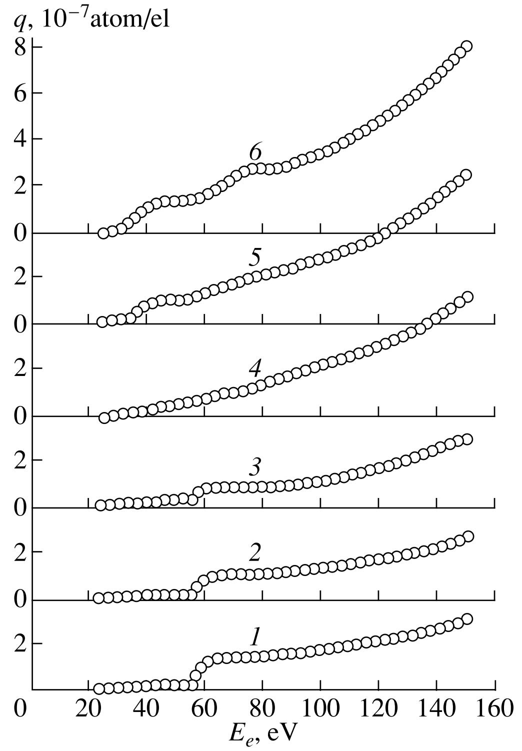

Fig. 1. Dependences of the yield of lithium atoms q on the bombarding electron energy E_e upon electron-stimulated desorption from the molybdenum surface coated with an oxygen monolayer at $T = 300$ K for different lithium coverages Θ: (*1*) 0.10, (*2*) 0.15, (*3*) 0.25, (*4*) 0.45, (*5*) 0.60, and (*6*) 0.75.

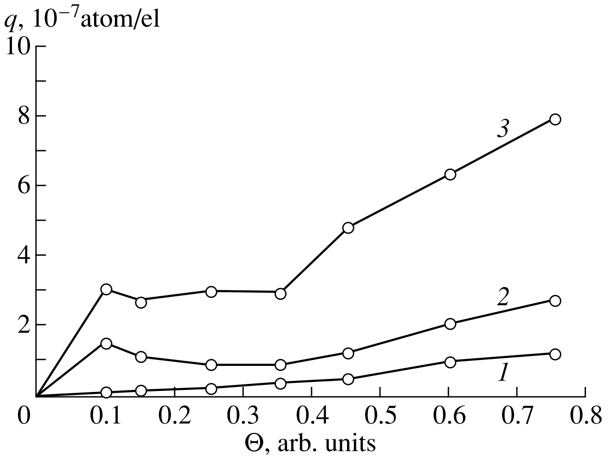

Fig. 2. Dependences of the yield of lithium atoms *q* on the lithium coverage Θ of the molybdenum surface coated with an oxygen monolayer at $T = 300$ K for different energies of bombarding electrons E_e (eV): (*1*) 50, (*2*) 80, and (*3*) 150.

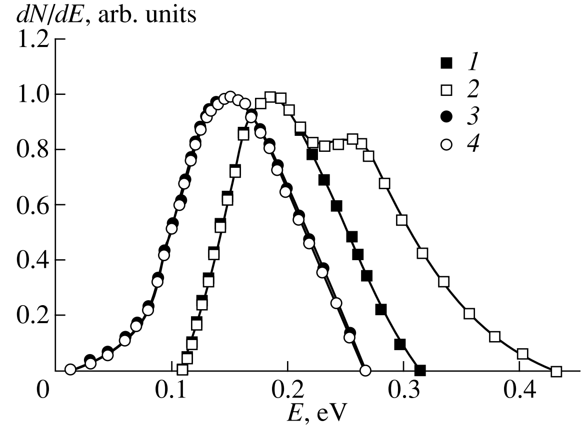

Fig. 3. Normalized energy distributions of lithium atoms upon electron-stimulated desorption from the molybdenum surface coated with an oxygen monolayer for the lithium coverages Θ = (*1*, *2*) 0.10 and (*3*, *4*) 0.75 and the electron energies E_e = (*1*, *3*) 50 and (*2*, *4*) 80 eV.

Figure 2 depicts the dependences of the yield of lithium atoms *q* on the lithium coverage Θ of the molybdenum surface coated with an oxygen monolayer for different energies of bombarding electrons E_e. As can be seen, at $E_e < 50$ eV, the yield *q* of lithium atoms almost linearly increases with an increase in the lithium coverage Θ. At $E_e > 50$ eV, the yield of lithium atoms in the coverage range $0 < \Theta < 0.45$ is not a linear function of the coverage and passes through a maximum at $\Theta \sim 0.1$. At $\Theta > 0.45$, the yield *q* again linearly increases with an increase in Θ.

The normalized energy distributions of lithium atoms upon electron-stimulated desorption from the molybdenum surface coated with an oxygen monolayer are demonstrated in Fig. 3 for two electron energies $E_e = 50$ and 80 eV and two lithium coverages $\Theta = 0.10$ and 0.75. At $E_e < 50$ eV, the energy distribution resembles a Gaussian curve slightly broadened to the high-energy range. As the lithium coverage increases, the energy distributions are shifted toward the low-energy range. At $E_e = 80$ eV, the energy distributions show a high-energy peak with a maximum at $E = 0.275$ eV. At $\Theta > 0.45$, this peak disappears, and the energy distributions are broadened toward the low-energy range.

3. DISCUSSION

Alkali metals adsorbed on the surface of transition metal oxides reduce the work function of the surface. A decrease in the work function depends on the coverage and the ionization potential of an alkali metal. At small coverages, alkali metals are likely adsorbed in the ionic form. As the coverage increases, the ionic form gradually converts into the neutral form, because the rate of decrease in the work function smoothly decreases to zero at a monolayer coating. This can be explained by the mutual depolarization of dipoles induced by adjacent adsorbed particles. An increase in the coverage brings about a continuous decrease in the heat of adsorption of alkali metals due to the repulsion of adjacent dipoles, and the bonding between adsorbed particles and the surface becomes weaker. Correspondingly, the distance between adsorbed particles and the surface increases [7].

The main regularities in the electron-stimulated desorption of lithium atoms can be interpreted in the framework of the Auger-stimulated desorption model, which was advanced earlier for the electron-stimulated desorption of alkali metal atoms and ions from the layers adsorbed on the surface of oxidized tungsten [2, 3] and then was applied to the description of the electron-stimulated desorption of the Na, K, and Cs atoms from their layers adsorbed on the surface of oxidized molybdenum [8, 9].

Let us assume that a primary electron produces a hole at the O 2*s* level whose ionization energy is close to the threshold of the onset in the electron-stimulated desorption of lithium atoms (~25 eV). This hole can be filled with an electron of the higher-lying O 2*p* level to initiate the Auger process. An emitted Auger electron can be captured by an adjacent adsorbed Li^+ ion. In the case when the O^+ ion formed in the Auger process regains its original negative charge by capturing electrons from a substrate more rapidly than the lithium atom ionizes, the O^- ion begins to repel the lithium atom due to the overlap of their valence shells, and the lithium atom leaves the surface. The larger the overlap of the shells, the higher the kinetic energy of the desorbed lithium atom. An increase in the lithium coverage leads to an enhancement in the repulsion between lithium atoms and, correspondingly, to an increase in the equilibrium distance between Li adatoms and O^- ions. Therefore, the mean kinetic energy of desorbed lithium atoms decreases with an increase in the coverage. The difference between the atomic and ionic radii decreases in going from Cs to Li, and, hence, the mean kinetic energies of desorbed atoms also decrease [4].

In the case when a primary electron removes an electron from the 1*s* level of the Li^+ adatom (the ionization energy is ~55 eV), the formed Li^{++} ion begins to move toward the substrate due to an increase in the image potential and a decrease in the repulsion between outer orbitals [10]. The interatomic Auger process occurs at a certain distance from an O^- ion. As a result of this process, the Li^{++} ion again transforms into the Li^+ ion, which, in turn, can capture an Auger electron to be converted into the Li atom. An increase in the lithium coverage brings about an increase in the equilibrium distance between lithium adatoms and the substrate. Therefore, the lithium atoms acquire a higher kinetic energy prior to the turning point, and, correspondingly, the desorbed lithium atoms acquire a higher kinetic energy as compared to the lithium atoms leaving the surface from the equilibrium distance after the ionization of the O 2*s* level (a high-energy peak shown in Fig. 3). With an increase in the kinetic energy, the lithium atoms moving toward the surface come closer to positive O^+ ions, and their ionization potential decreases under the action of image forces, which increases the probability of their reionization [11]. As a consequence, the yield of lithium atoms due to the ionization of the Li 1*s* level decreases with an increase in the lithium coverage.

Among alkali metal atoms, the lithium atoms possess the highest ionization potential and, hence, the least probability of the reionization during the motion toward the surface. Hence, it is not surprising that the electron-stimulated desorption of only the lithium atoms is observed after the ionization of their core levels. The electron-stimulated desorption of lithium atoms from oxidized tungsten after the ionization of the Li 1*s* level likely is not seen, because of a sharp increase in the yield of lithium atoms with an increase in the energy of primary electrons in this case.

Additional features in the $q(E_e)$curves at electron energies of 40 and 70 eV can be caused by the resonance ionization of the Mo 4*p* and Mo 4*s* levels [6]. The presence of these features implies that there exist the Auger processes involving the Mo 4*p* and Mo 4*s* levels, which lead to the neutralization of the adsorbed Li^+ ions. These ions cannot be neutralized by the Auger electrons liberated directly from the valence band after filling holes at the Mo 4*p* and Mo 4*s* levels, because the energies of these Auger electrons are too high. This is corroborated by the absence of the yield of alkali metal atoms upon electron-stimulated desorption from alkali metal layers adsorbed on the tungsten surface coated with silicon film [12], for which the least energy of Auger electrons is equal to about 90 eV. It seems likely that the adsorbed Li^+ ions can be more efficiently neutralized by way of capturing electrons liberated in the cascade Auger processes involving the Mo 4*p*, Mo 4*s*, O 2*s*, and O 2*p* levels. A peak-like character of the features can be explained by assuming that, upon ionization of the Mo 4*p* and Mo 4*s* levels, electrons transfer from these levels to the band of free states above the Fermi level. These electrons decrease the relaxation time of oxygen ions and, thus, increase the yield of lithium atoms. The density of states in the band of free states increases with an increase in the lithium coverage of the surface. It should be noted that, for an isolated lithium layer, the density of states in the band of free states is considerably more uniform than that in the corresponding Cs, K, and Na layers [13]. As a result, the features at 40 and 70 eV for the lithium atoms appear at larger coverages and are less pronounced as compared to the electron-stimulated desorption of the Cs, K, and Na atoms [8, 9].

An increase in the energy of a core hole can lead to an increase in its relaxation time [14] and, correspondingly, to an increase in the probability of the reionization of lithium atoms and a decrease in their yield upon electron-stimulated desorption. For this reason, the feature at $E_e \approx 40$ eV is observed at smaller lithium coverages than the feature at $E_e \approx 70$ eV. The features at $E_e \approx$ 40 and 70 eV are not observed in the $q(E_e)$ dependences for the electron-stimulated desorption from lithium layers adsorbed on molybdenum oxide. This is likely explained by the fact that the relaxation of the charge on positive oxygen ions is too slow in this case.

The low-energy "tails" in the energy distributions of lithium atoms can be associated either with the reverse motion of the lithium atoms in the field of positive oxygen ions, or with an incomplete relaxation of the charge on oxygen ions, and, possibly, with the polarization of outer orbitals of negative oxygen ions in the filed of positive molybdenum ions. The lithium atom formed in the neighborhood of a positive oxygen ion moves toward this ion. The smaller the spacing between the atom and the ion, the higher the kinetic energy acquired by atom after the relaxation of the charge on oxygen. Therefore, the less the atomic mass, the shorter the low-energy tail in the energy distributions of the atoms. This is in agreement with an increase in the tail lengths in going from Li to Cs [8, 9]. Since the equilibrium distance between alkali metal ions and the surface increases with an increase in the coverage, the length of tails in the energy distributions also increases with an increase in Θ.

On the other hand, the extension of the energy distributions of lithium atoms toward the low-energy range can be caused by the partial relaxation of the charge on positive oxygen ions, which, nonetheless, brings about the repulsion of lithium atoms. In this case, the lithium atoms experience a weaker repulsion as compared to the complete relaxation of the charge on oxygen and acquire a lower energy. It is quite probable that electrons captured in the band of free states are responsible for the partial relaxation of the charge on oxygen. Then, the tail length should increase with an increase in the coverage.

Finally, the polarization of the outer orbitals of negative oxygen ions in the field of positive molybdenum ions should lead to a decrease in the density of charge between oxygen ion and alkali metal atom. This should result in a weaker repulsion between the oxygen ion and the alkali metal atom and, correspondingly, in the appearance of the low-energy tails in the energy distributions of the alkali metal atoms. It is clear that, in this case, the length of the low-energy tails also should increase with an increase in the alkali metal coverage of the surface. Moreover, it is important that the appearance of the low-energy tails should correlate with the appearance of additional thresholds in the $q(E_e)$ curves, which is observed in the experiment.

ACKNOWLEDGMENTS

This work was supported by the “Surface Atomic Structures” Program of the Ministry of Science and Technology of the Russian Federation (project no. 4.5.99) and, in part, by the Russian Foundation for Basic Research (project no. 99-02-17972).

REFERENCES

1. V. N. Ageev, Prog. Surf. Sci. **47**, 55 (1994).
2. V. N. Ageev, Yu. A. Kuznetsov, B. V. Yakshinskiĭ, *et al.*, Nucl. Instrum. Methods Phys. Res., Sect. B **101**, 69 (1995).
3. V. N. Ageev, Yu. A. Kuznetsov, and N. D. Potekhina, Surf. Sci. **367**, 113 (1996).
4. V. N. Ageev and Yu. A. Kuznetsov, Phys. Low-Dim. Struct., No. 1/2, 113 (1999).
5. V. N. Ageev, O. P. Burmistrova, and Yu. A. Kuznetsov, Fiz. Tverd. Tela (Leningrad) **29**, 1740 (1987) [Sov. Phys. Solid State **29**, 1000 (1987)].
6. D. Briggs and M. P. Seah, *Practical Surface Analysis by Auger and X-ray Photoelectron Spectroscopy* (Wiley, Chichester, 1983).
7. C. T. Campbell, Surf. Sci. Rep. **27**, 1 (1997).
8. V. N. Ageev, Yu. A. Kuznetsov, and T. E. Madey, Surf. Sci. **390**, 146 (1997).
9. V. N. Ageev, Yu. A. Kuznetsov, and T. E. Madey, Phys. Rev. B **58**, 2248 (1998).
10. P. R. Antoniewicz, Phys. Rev. B **21**, 3811 (1980).
11. V. N. Ageev and S. Yu. Davydov, Surf. Sci. **425**, 152 (1999).
12. V. N. Ageev, O. P. Burmistrova, A. M. Magomedov, *et al.*, Fiz. Tverd. Tela (Leningrad) **32**, 801 (1990) [Sov. Phys. Solid State **32**, 472 (1990)].
13. E. Wimmer, J. Phys. F: Met. Phys. **13**, 2313 (1983).
14. P. J. Feibelman, Surf. Sci. **102**, L51 (1981).

Translated by O. Borovik-Romanova

Physics of the Solid State, Vol. 42, No. 4, 2000, p. 785.
Original Russian Text Copyright © 2000.

ERRATA

Erratum: “On the Role of Spectral Diffusion in Single-Molecule Spectroscopy” [*Phys. Solid State* 42 (3), 477 (2000)]

V. V. Palm, K. K. Rebane, and A. Zabrodskiĭ
Institute of Physics, Academy of Sciences of Éstonia, Riia 142, Tartu, EE2400 Éstonia
e-mail: rebanek@fi.tartu.ee

The editorial board of the journal *Fizika tverdogo tela* apologizes for indicating A. Zabrodskiĭ as an author of the article “On the Role of Spectral Diffusion in Single-Molecule Spectroscopy” published in *Phys. Solid State* **42** (3), 477 (2000).

The authors of this article are V. V. Palm and K. K. Rebane.